A physicist explores the brain's tangled networks *p. 118*

Treating depression with ketamine *pp. 129 & 147*

How predator loss affects an ecosystem *p. 173*

Science

$15
12 APRIL 2019
sciencemag.org

AAAS

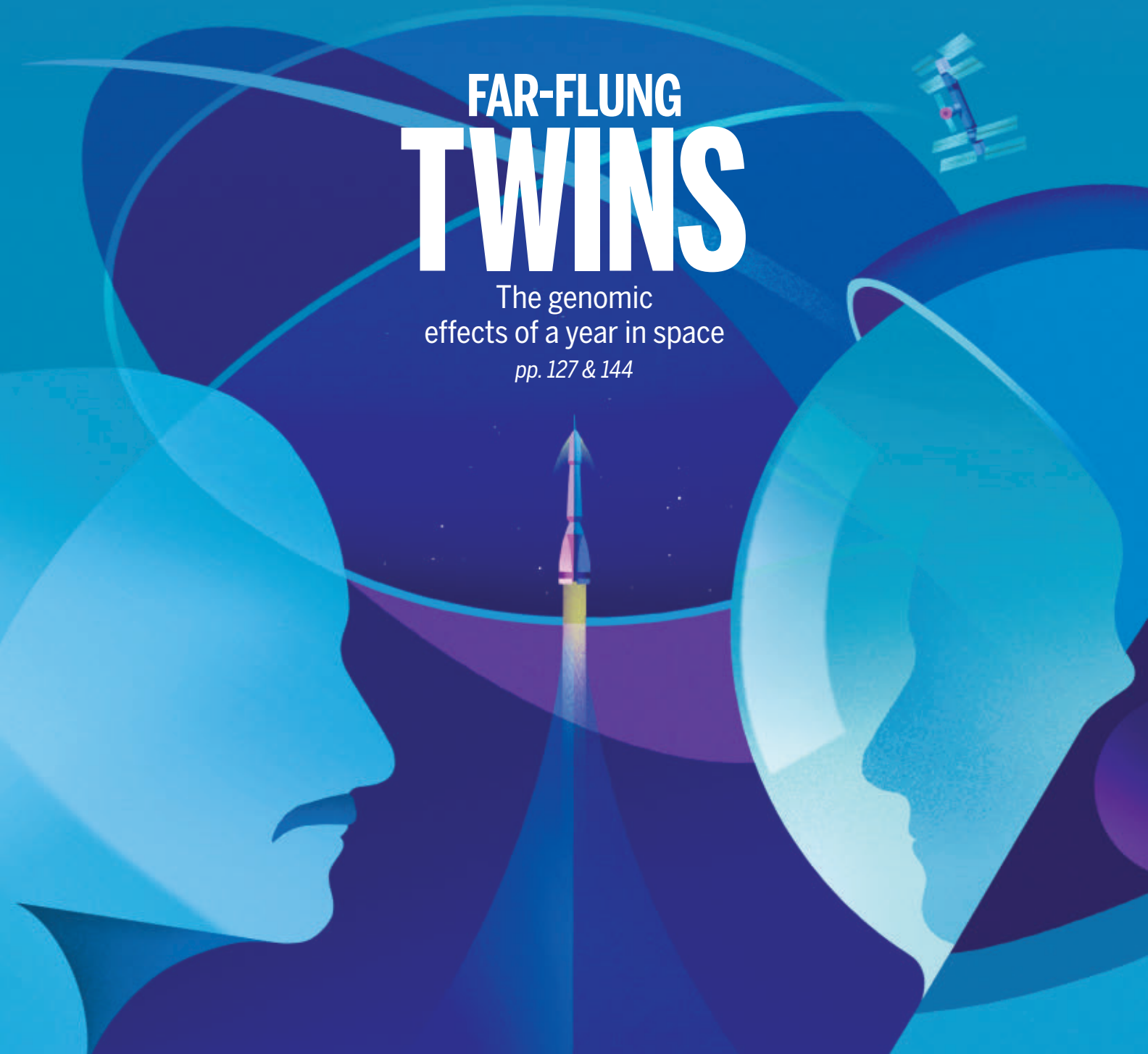

FAR-FLUNG TWINS

The genomic effects of a year in space

pp. 127 & 144

eppendorf

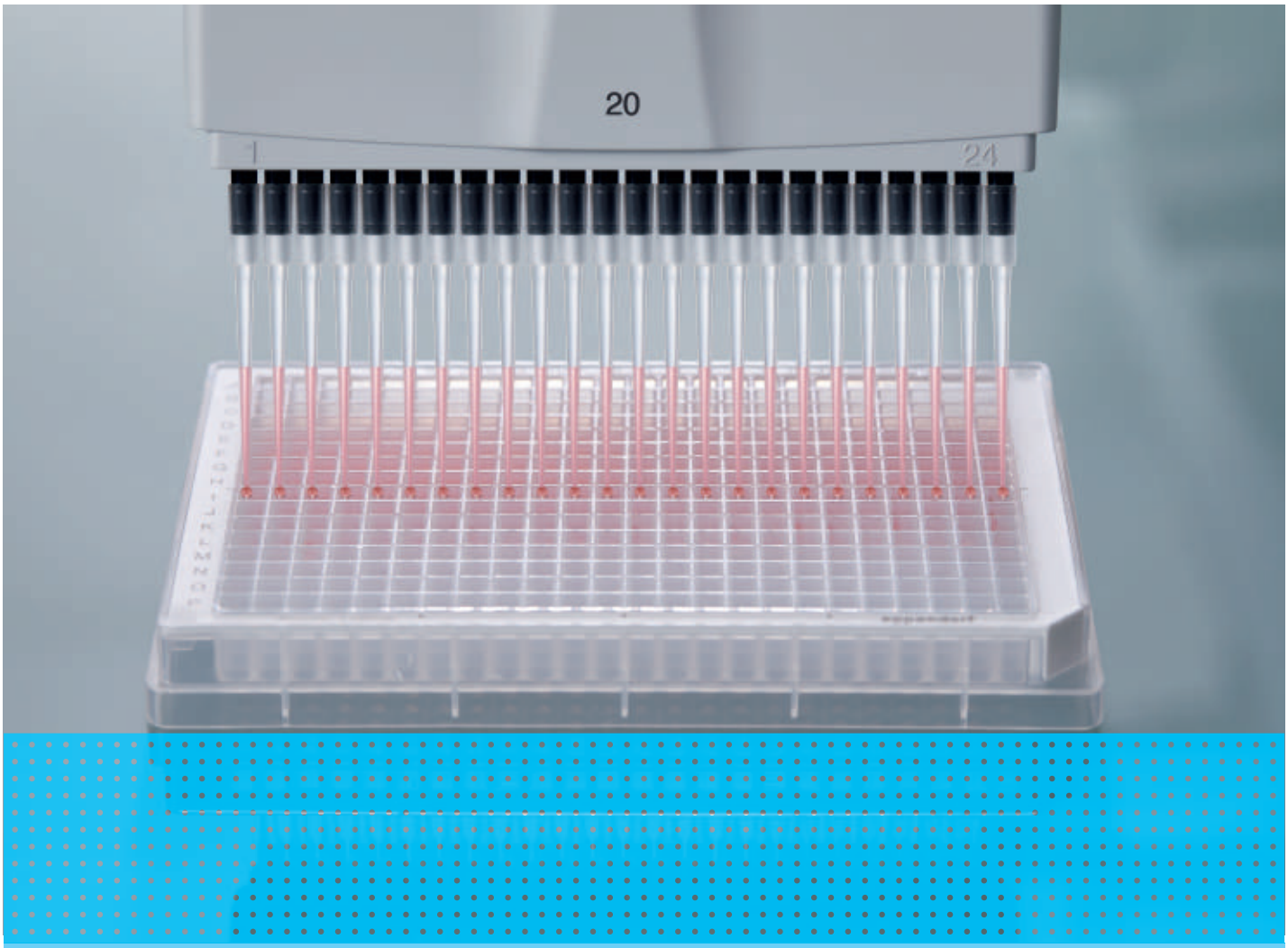

384. Ready. Set. Pipette!

Manual pipetting of 384-well-plates made easy

Do you work with 384-well-plates and strive for more efficient manual pipetting methods? Your worries are over. The new Eppendorf Research® plus and Eppendorf Xplorer® plus 16- and 24-channel pipettes and pipette tips epT.I.P.S.® 384/ep Dualfilter T.I.P.S.® 384 make working with 384-well-plates convenient, ergonomic and safe. Feel the magic of filling a 384-well-plate within a minute.

> No more mistakes or tedious work due to inconvenient alternate well pipetting with 8- and 12-channel pipettes.
> Set up or validate an automated process manually, and have a back-up system in case automation fails.
> Increase your throughput and change from 96- to 384-well-plates. There´s no reason to hesitate anymore!

www.eppendorf.com/ready-set-pipette

Eppendorf®, the Eppendorf Brand Design, Eppendorf Research®, Eppendorf Xplorer®, ep Dualfilter T.I.P.S.®,and epT.I.P.S.® are registered trademarks of Eppendorf AG, Germany.
U.S. Design Patents are listed on www.eppendorf.com/ip. All rights reserved, including graphics and images. Copyright © 2019 by Eppendorf AG.

CONTENTS

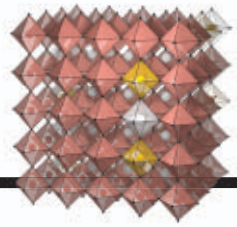

116
Perovskite gives a boost to a tandem solar cell

12 APRIL 2019 • VOLUME 364 • ISSUE 6436

108
A surprise find in a Philippine cave

116 SOLAR CELL BUILT FOR TWO LOOKS SWEET
Simple tandem design uses perovskite layer to feed photons to silicon cell
By R. F. Service

FEATURES

118 THE TRESPASSER
Physicist Danielle Bassett searches for simple rules that govern the brain's tangled networks *By K. Servick*

INSIGHTS

PERSPECTIVES

122 POLLINATORS, HERBIVORES, AND THE EVOLUTION OF FLORAL TRAITS
Floral characters reflect plant adaptation to both bumble bees and leaf-eating insects *By J. Ågren*
▸ REPORT P. 193

123 LOST IN THE FIRE
Thyroid hormones tip the balance between regeneration and temperature regulation *By S. Marchianò and C. E. Murry*
▸ REPORT P. 184

125 AN EXOTIC QUANTUM FLUID IN GRAPHENE
Under the right conditions, electrons can move as fluids in graphene
By A. Lucas
▸ REPORTS PP. 158 & 162

126 PLATE TECTONICS, CARBON, AND CLIMATE
Enhanced weathering of uplifted rocks in the tropics may have driven past glaciations *By J. Hartmann*
▸ REPORT P. 181

127 HAZARDS OF HUMAN SPACEFLIGHT
A 1-year mission in space has many biological consequences
By M. Löbrich and P. A. Jeggo
▸ RESEARCH ARTICLE P. 144

129 DO ANTIDEPRESSANTS RESTORE LOST SYNAPSES?
Ketamine triggers changes in behavior, neuron microcircuitry, and dendritic spines *By A. Beyeler*
▸ RESEARCH ARTICLE P. 147

NEWS

IN BRIEF

106 News at a glance

IN DEPTH

108 NEW SPECIES OF ANCIENT HUMAN UNEARTHED
Homo luzonensis, from the Philippines, may have been a small-bodied tree climber *By L. Wade*
▸ PODCAST

109 CLOSURE OF U.S. *TOXOPLASMA* LAB DRAWS IRE
Scientists say political pressure threatens research on cause of blindness and birth defects *By M. Wadman*

110 BELIEFS IN ALIENS, ATLANTIS ARE ON THE RISE
Researchers take to Twitter, blogs to counter pseudoarchaeology's outlandish ideas *By L. Wade*

111 BRAZILIAN SCIENTISTS LAMENT 'FREEZE' ON RESEARCH BUDGET
Block on 42% of the science ministry's funds, coming on top of other cuts, puts flagship synchrotron at risk
By H. Escobar

112 ATMOSPHERIC SCIENTISTS JOIN PHEROMONE QUEST
Can measuring volatile compounds in real time save a field that is "in a bit of a crisis"? *By K. Kupferschmidt*

114 POLITICS COULD UPEND GLOBAL TRADE IN RARE EARTH ELEMENTS
Malaysian government asks "flagship" company to remove radioactive waste from the country or shut down
By Y.-H. Law
▸ PODCAST

115 REPORT URGES MASSIVE DIGITIZATION OF BIOSPECIMENS
"Extended specimens" would link images and data *By E. Pennisi*

IMAGES: (TOP TO BOTTOM) V. ALTOUNIAN/*SCIENCE*; © CALLAO CAVE ARCHAEOLOGY PROJECT

130 IMMUNOTHERAPY FOR NEURODEGENERATION?
The role of innate and adaptive immunity in neurodegeneration remains controversial
By Y. Liu and A. Aguzzi

POLICY FORUM

132 SENSITIVE INTERVENTION POINTS IN THE POST-CARBON TRANSITION
We must exploit socioeconomic tipping points and amplifiers
By J. D. Farmer et al.

BOOKS *ET AL.*

135 DIVING DEEP INTO THE SOUTHERN OCEAN
A major player in weather, climate, and biodiversity, the waters around Antarctica take center stage in a new history *By L. Fabiani*

136 HELPING EINSTEIN
Efforts to identify Mileva Marić's contributions highlight the trouble with telling the tales of early women in science *By M. Frappier*

LETTERS

138 ROHINGYA REFUGEES AND THE ENVIRONMENT
By S. A. Mukul et al.

139 ADDRESS THE ROOTS OF ENVIRONMENTAL CRIME
By B. Neimark

139 CONCERNS OF YOUNG PROTESTERS ARE JUSTIFIED
By G. Hagedorn et al.

RESEARCH

IN BRIEF

141 From *Science* and other journals

RESEARCH ARTICLES

144 HUMAN PHYSIOLOGY
The NASA Twins Study: A multidimensional analysis of a year-long human spaceflight
F. E. Garrett-Bakelman et al.
RESEARCH ARTICLE SUMMARY; FOR FULL TEXT: dx.doi.org/10.1126/science.aau8650
▸ PERSPECTIVE P. 127

145 PLANT SCIENCE
Glycosidase and glycan polymorphism control hydrolytic release of immunogenic flagellin peptides
P. Buscaill et al.
RESEARCH ARTICLE SUMMARY; FOR FULL TEXT: dx.doi.org/10.1126/science.aav0748

146 NEUROSCIENCE
Ultrapotent chemogenetics for research and potential clinical applications
C. J. Magnus et al.
RESEARCH ARTICLE SUMMARY; FOR FULL TEXT: dx.doi.org/10.1126/science.aav5282

147 NEUROSCIENCE
Sustained rescue of prefrontal circuit dysfunction by antidepressant-induced spine formation *R. N. Moda-Sava* et al.
RESEARCH ARTICLE SUMMARY; FOR FULL TEXT: dx.doi.org/10.1126/science.aat8078
▸ PERSPECTIVE P. 129

148 STRUCTURAL BIOLOGY
Structure and dynamics of the active human parathyroid hormone receptor-1
L.-H. Zhao et al.

REPORTS

154 PHYSICS
Electron-phonon instability in graphene revealed by global and local noise probes
T. I. Andersen et al.

GRAPHENE
158 Quantum-critical conductivity of the Dirac fluid in graphene
P. Gallagher et al.

162 Measuring Hall viscosity of graphene's electron fluid *A. I. Berdyugin* et al.
▸ PERSPECTIVE P. 125

166 THIN FILMS
Spin coating epitaxial films *M. V. Kelso* et al.

170 PHYSICS
Anti–parity-time symmetry in diffusive systems *Y. Li* et al.

173 TROPHIC CASCADES
Cascading impacts of large-carnivore extirpation in an African ecosystem
J. L. Atkins et al.

178 PLANT SCIENCE
Bacterial medium-chain 3-hydroxy fatty acid metabolites trigger immunity in *Arabidopsis* plants *A. Kutschera* et al.

181 GLACIAL CYCLES
Arc-continent collisions in the tropics set Earth's climate state
F. A. Macdonald et al.
▸ PERSPECTIVE P. 126

184 HEART REGENERATION
Evidence for hormonal control of heart regenerative capacity during endothermy acquisition *K. Hirose* et al.
▸ PERSPECTIVE P. 123

188 SIGNAL TRANSDUCTION
Deubiquitinase USP10 regulates Notch signaling in the endothelium
R. Lim et al.

193 EVOLUTIONARY BIOLOGY
Rapid plant evolution driven by the interaction of pollination and herbivory
S. E. Ramos and F. P. Schiestl
▸ PERSPECTIVE P. 122; PODCAST

DEPARTMENTS

105 EDITORIAL
Reverse global vaccine dissent
By Heidi J. Larson and William S. Schulz

202 WORKING LIFE
The way I am *By Artaza Gilani*

ON THE COVER

A study of identical twins identifies molecular, physiological, and cognitive changes specific to one twin who spent a year living aboard the International Space Station. The cover depicts the twins and their respective Earth-bound and space residencies, with a rocket and the International Space Station in the background. See pages 127 and 144. *Illustration: Ray Oranges @ Machas*

New Products 197
Science Careers 198

SCIENCE (ISSN 0036-8075) is published weekly on Friday, except last week in December, by the American Association for the Advancement of Science, 1200 New York Avenue, NW, Washington, DC 20005. Periodicals mail postage (publication No. 484460) paid at Washington, DC, and additional mailing offices. Copyright © 2019 by the American Association for the Advancement of Science. The title SCIENCE is a registered trademark of the AAAS. Domestic individual membership, including subscription (12 months): $165 ($74 allocated to subscription). Domestic institutional subscription (51 issues): $1971; Foreign postage extra: Mexico, Caribbean (surface mail) $55; other countries (air assist delivery): $98. First class, airmail, student, and emeritus rates on request. Canadian rates with GST available upon request, GST #125488122. Publications Mail Agreement Number 1069624. **Printed in the U.S.A.**
Change of address: Allow 4 weeks, giving old and new addresses and 8-digit account number. **Postmaster:** Send change of address to AAAS, P.O. Box 96178, Washington, DC 20090–6178. **Single-copy sales:** $15 each plus shipping and handling; bulk rate on request. **Authorization to reproduce** material for internal or personal use under circumstances not falling within the fair use provisions of the Copyright Act can be obtained through the Copyright Clearance Center (CCC), www.copyright.com. The identification code for *Science* is 0036-8075. *Science* is indexed in the *Reader's Guide to Periodical Literature* and in several specialized indexes.

PHOTO: ARCO IMAGES GMBH/ALAMY STOCK PHOTO

EDITORIAL

Reverse global vaccine dissent

This year, the World Health Organization named vaccine hesitancy as one of the top 10 global health threats, alongside threats as grave as climate change, antimicrobial resistance, Ebola virus, and the next influenza pandemic. What happened? How did vaccine reluctance and refusal become such a major risk?

The concerns driving antivaccine sentiment today are diverse. For example, from 2003 to 2004, a vaccine boycott in Nigeria's Kano State sparked the retransmission of polio across multiple countries as far as Indonesia. Rumors of vaccine contamination with antifertility agents contributed to distrust and reinforced the boycott, costing the Global Polio Eradication Initiative over U.S. $500 million to regain the progress that was lost. In Japan, vaccination against human papilloma virus plummeted to almost zero after young women complained of movement disorders and chronic pain, causing the government to suspend proactive recommendation of the vaccine nearly 6 years ago. Similar episodes occurred in Denmark, Ireland, and Colombia as YouTube videos of the girls' symptoms spread anxiety, despite evidence of the vaccine's safety.

The global surge in measles outbreaks has been exacerbated by vaccine refusers. In 2015, the measles strain that sparked the Disneyland outbreak came from visitors from the Philippines, infecting people who had refused vaccination. And in Indonesia, Muslim leaders issued a fatwa against a measles vaccine containing "haram" porcine compounds, while naturopathic "cupping" methods were promoted on Facebook as an alternative to vaccination. In 2018, a mix of political, religious, and alternative health antivaccine messages circulated on WhatsApp and Facebook in Southern India, disrupting a local measles-rubella vaccination campaign.

The phenomenon of vaccine dissent is not new. The pages of 18th-century London antivaccination pamphlets bristle with many of today's memes, but these ideas now spread over unprecedented distances with remarkable speed, clustering in online neighborhoods of shared beliefs. This clustering can tear the protective fabric—the "herd (community) immunity"—that the majority of vaccine acceptors have woven. As the portion of the community that is vaccinated decreases, there is less protection for others who may be too young, unable, or choose not to be vaccinated. For some diseases, it only takes a small minority to disrupt the protective cover.

It is just over 20 years since British physician Andrew Wakefield sowed seeds of doubt about the safety of the MMR (measles, mumps, rubella) vaccine, suggesting a link between the vaccine and autism. Suspicions around the vaccine traveled globally, instilling anxiety among the most and least educated alike. The discredited Wakefield alone, though, cannot be blamed for today's waves of vaccine discontent. He seeded a message on the eve of a technological revolution that disrupted business, politics, societies, and global health. The same year that Wakefield published his research, Google opened its doors. The launches of Facebook, YouTube, Twitter, and Instagram soon followed. These social media platforms have magnified individual sentiments that might have stayed local. Emotions are particularly contagious on social media, where personal narrative, images, and videos are shared easily.

"How did vaccine reluctance and refusal become such a major risk?"

Today's tech companies are now being called to account for their role in spreading vaccine dissent. Last month, the American Medical Association urged the chief executives of key technology companies to "ensure that users have access to scientifically valid information on vaccinations." But this is not merely an issue of correcting misinformation. There are social networks in which vaccine views and information are circulating in online communities, where vaccine choices become part of one's overall identity.

To mitigate the globalization of vaccine dissent, while respecting legitimate sharing of concerns and genuine questions, a mix of relevant expertise is needed. Technology experts, social scientists, vaccine and public health experts, and ethicists must convene and take a hard look at the different roles each group has in addressing this challenge. It needs everyone's attention.

–Heidi J. Larson and William S. Schulz

Heidi J. Larson *is a professor of Anthropology, Risk, and Decision Science in the Department of Epidemiology and Population Health and director of The Vaccine Confidence Project, London School of Hygiene and Tropical Medicine, London, UK. heidi.larson@lshtm.ac.uk*

William S. Schulz *is a Ph.D. student in the Department of Politics, Princeton University, and an affiliated researcher at the Vaccine Confidence Project, London School of Hygiene and Tropical Medicine, London, UK. wschulz@princeton.edu*

ILLUSTRATION: DOUG CHAYKA

10.1126/science.aax6172

NEWS

IN BRIEF

Edited by **Jeffrey Brainard**

Oil from the *Deepwater Horizon* spill reached this marsh in Venice, Louisiana.

ENVIRONMENT

Oil dispersants did little harm to ocean, academy says

The use of chemicals to disperse oil spills, such as the massive 2010 *Deepwater Horizon* disaster in the Gulf of Mexico, largely doesn't create a mixture more toxic than the oil itself, a blue-ribbon scientific panel reported last week. Dispersants, which can break slicks and clumps of oil into smaller droplets that sink, have long been dogged by questions about safety and effectiveness. Of particular concern was whether oil became more poisonous to marine life when mixed with dispersant. Although that can happen at high concentrations, levels in the ocean during a spill are usually much lower, says the report from the U.S. National Academy of Sciences in Washington, D.C. As for effects on people, recent studies of Coast Guard workers and *Deepwater Horizon* spill responders found evidence that those exposed to a dispersant suffered higher incidences of respiratory problems such as coughing and wheezing, as well as skin irritation. But the academy report warns the studies could not clearly separate the dispersants' effects from those of the toxic fumes produced by the oil itself. The panel said questions remain about the dispersants' effectiveness. To get answers, researchers should be ready to deploy monitoring instruments in the event of another major oil spill, the report said.

Japan blasts hole in asteroid

PLANETARY SCIENCE | Japan's Hayabusa2 mission continued its novel exploration of the asteroid Ryugu last week by blowing a crater in it so the spacecraft can collect samples. Scientists are eager to study rock from beneath the surface because it has not undergone eons of space weathering, and may hold clues about materials present in the early solar system. In the precisely timed operation, the Hayabusa2 mothership first released a tiny spacecraft called the Small Carry-on Impactor, then darted to the other side of the asteroid for safety. Forty minutes later, the impactor exploded, sending a 2-kilogram copper projectile into Ryugu. Hayabusa2 has already collected surface rock fragments and is scheduled to return the samples to Earth in 2020 for analyses.

NIH restricts foreign visitors

NATIONAL SECURITY | The U.S. National Institutes of Health (NIH) has begun to restrict visitors from certain countries at its campus in Bethesda, Maryland, for security reasons, sparking concerns from NIH staff scientists. In March, NIH admitted an Iranian graduate student and green card holder who had applied for a postdoctoral position, only to eject him during his presentation. Campus police had decided, without notice, to begin to enforce a 2011 Department of Health and Human Services (HHS) policy requiring a clearance process for visitors from "state sponsors of terrorism," currently Iran, North Korea, Sudan, and Syria, according to *The Washington Post*; clearance takes at least 10 days. NIH Director Francis Collins wrote to staff on 5 April that he was "deeply troubled" by the student's removal and has apologized to him and another visitor who missed half of a 2-day meeting because of the clearance rules. Collins said NIH is reviewing its implementation of the HHS policy so that "all our guests … are treated with the utmost respect and consideration." NIH's actions come amid growing concern from President Donald Trump's administration about the risk that other countries are stealing secrets from U.S. researchers.

PHOTO: CARRIE VONDERHAAR/OCEAN FUTURES SOCIETY/GETTY IMAGES

Google shutters AI ethics panel

COMPUTER SCIENCE | Only 10 days after Google created an external advisory council on the ethics of artificial intelligence (AI) research, the company pulled the plug last week amid controversy. Employees of Google, based in Mountain View, California, had circulated a petition to remove Kay Cole James, president of the conservative Heritage Foundation in Washington, D.C., from the eight-member panel, citing her past remarks critical of the rights movement for lesbian, gay, bisexual, transgender, and questioning people. Google employees and others also separately called for the removal of Dyan Gibbens, head of Trumbull Unmanned, a drone technology company in Houston, Texas. Last year, Google ended work with the U.S. military to develop AI for analyzing drone footage because of employees' concerns that the project would support drone attacks. The council was to have considered military uses and other ethical issues, such as facial recognition and bias in algorithms. Google said it "will find different ways of getting outside opinions on these topics."

Genetics pioneer Brenner dies

PEOPLE | Sydney Brenner, the Nobel laureate who made seminal discoveries in genetics and developmental biology, died last week in Singapore at age 92. He discovered fundamental steps in how cells use DNA to make the proteins that enable life. Working at the Laboratory of Molecular Biology in Cambridge, U.K., he found that sequences of three DNA bases code for the amino acids that form proteins, and he discovered that RNA molecules carry that information to ribosomes, the cellular machines that synthesize proteins. In another major breakthrough, Brenner identified and developed the transparent worm *Caenorhabditis elegans* as an ideal animal model; the worm is used today in labs worldwide. That work led to the Nobel Prize in Physiology or Medicine, which he won in 2002 with two colleagues, John Sulston and Robert Horvitz.

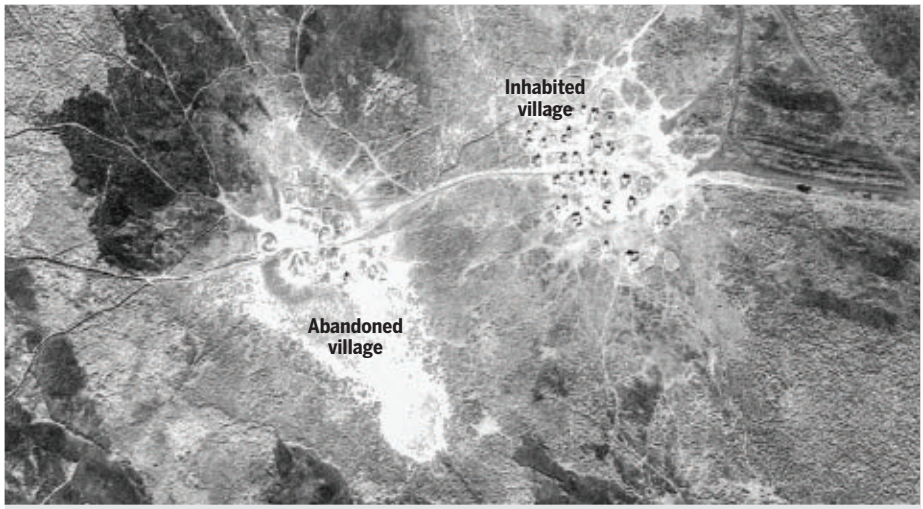

PHOTO: E. HAMMER *ET AL.*, *ADVANCES IN ARCHAEOLOGICAL PRACTICE* 10.1017 (2019)

RESEARCH TOOLS

Once-secret spy photos reveal lost sites

High-resolution photos taken by U.S. spy planes during the Cold War could help archaeologists investigate historical sites lost or damaged because of war and development, a study reports. Its authors examined photos shot by U-2 planes at 21,000 meters using sophisticated cameras; declassified in 1997, the images provide higher resolution than old satellite photos. The U-2 images lack details about their precise locations, but the study, in *Advances in Archaeological Practice,* shows how to reconstruct that information based on the spy planes' flight paths. The paper also describes how to request the photos, which are not digitized, from the Federal Records Center in Lenexa, Kansas, and the National Archives in College Park, Maryland. Historical sites described in the study include a village of traditional reed huts in Iraq's once-marshy wetlands (above), which former Iraqi President Saddam Hussein systematically drained in the early 1990s to quell rebels. When the photo was taken in 1960, a neighboring village had already been abandoned.

THREE QS

Cracking free will's mysteries

A new research program on free will has brought together eight neuroscientists and nine philosophers from 17 universities. The collaboration intends to tackle two questions: What is required to have free will? And does the human brain have mechanisms to support that? The effort is backed by a 4-year grant of more than $7 million from the John Templeton Foundation in West Conshohocken, Pennsylvania, and the Fetzer Institute in Kalamazoo, Michigan. A recent conference helped inaugurate the project, and its leader, Uri Maoz, a psychologist and computational neuroscientist at Chapman University in Irvine, California, described the work to *Science*. This interview has been edited for clarity; a longer version is available at https://scim.ag/QAfreewill.

Q: Why do we need to study free will?
A: I think studying it is important because it teaches us about processes in the brain and how things like volition come about. That has implications for the legal system, for example, which distinguishes between voluntary and involuntary actions. It may also have implications for motor disorders like Parkinson's disease, where people have a hard time with self-initiated movements.

Q: Have the two fields collaborated before?
A: Previously, different groups of philosophers and neuroscientists worked separately, and once a year met and told each other what they were doing. Now, we can start working together rather than each group in their own silos.

Q: What would a collaboration look like?
A: Every project has at least two neuroscientists and at least one philosopher involved. What we would hope to get from [philosophers] is to first help in deciding what are the right questions to ask. As a scientist, I don't know what it entails to have free will. That is a philosophical question that our philosopher colleagues should discuss. Then, how do we design the experiment that would answer exactly that question? It may be that we don't have the technology to measure it, but that is at least an empirical question that we could get at. Once the experiment is done, [the philosophers] would help interpret what the results mean and produce joint publications.

IN DEPTH

About 67,000 years ago, Callao Cave on Luzon in the Philippines was home to an unusual human.

HUMAN EVOLUTION

New species of ancient human unearthed

Homo luzonensis, from the Philippines, may have been a small-bodied tree climber

By **Lizzie Wade**

A strange new species may have joined the human family. Human fossils found in a cave on Luzon, the largest island in the Philippines, include tiny molars suggesting their owners were small; curved finger and toe bones hint that they climbed trees. *Homo luzonensis*, as the species has been christened, lived some 50,000 to 80,000 years ago, when the world hosted multiple archaic humans, including Neanderthals and Denisovans, and when *H. sapiens* may have been making its first forays into Southeast Asia.

"This is a truly sensational finding," says Adam Brumm, an archaeologist at Griffith University in Nathan, Australia. The paper, published this week in *Nature*, "sent shivers down my spine."

The discovery echoes that of another unusual ancient hominin—the diminutive *H. floresiensis*, or "hobbit," found on the island of Flores in Indonesia. "One is interesting. Two is a pattern," says Jeremy DeSilva, an expert on *Homo* foot bones at Dartmouth College. He and others suspect the islands of Southeast Asia may have been a cradle of diversity for ancient humans, and that *H. luzonensis*, like *H. floresiensis*, may have evolved small body size in isolation on an island.

In 2007, a team led by Armand Mijares, a paleoanthropologist at the University of the Philippines in Quezon City, found a metatarsal—one of the bones that runs along the top of the foot—in Callao Cave on Luzon. The shape of the bone clearly marked its owner as a member of our genus, the team reported in 2010. The ratio of uranium to its decay products in the bone revealed its probable age range, between 50,000 and 80,000 years old, with a likely minimum age of about 67,000 years. Intrigued, Mijares's team went back in 2011 and 2015—and excavated what he calls a fossil "bonanza."

Teeth show a new find is *Homo*.

In the same layer as the metatarsal, the team discovered five teeth from the right upper jaw of the same individual, two isolated teeth, two finger bones, two toe bones, and a broken femur. The bones represent at least three individuals, the team says, all presumably from the same species.

The teeth show a unique mosaic of traits found separately in other *Homo* species. The premolars are about the size of ours, but instead of a single root they have two or three—a primitive feature. The molars are much more modern, with single roots, but "incredibly small" at only 10 millimeters across and 8 millimeters long, says Florent Détroit, a paleoanthropologist at the Museum of Man in Paris who worked with Mijares. That's even smaller than those of *H. floresiensis*. Tooth size tends to correlate with body size, so it's possible that *H. luzonensis* itself was tiny, Détroit says. But only a complete arm or leg bone will say for sure.

The long, curved fingers and toes resemble those of australopithecines like Lucy, an early human ancestor thought to have both walked upright and swung through the trees. "This is a very strong indication of climbing," says paleoanthropologist Tracy Kivell, who studies hand bones at the University of Kent in Canterbury, U.K.

Not everyone is ready to embrace these teeth and skeletal fragments as a separate species, rather than a locally adapted population of, say, *H. erectus*, an older hominin that lived in Asia for millennia.

"I see what they're saying, but at the same time, I want more," says Susan Antón, a paleoanthropologist at New York University in New York City. A skull bone could clinch the case for a new species, as could ancient DNA. But DNA breaks down fast in hot, humid conditions like those at the cave, and the fossils have not yielded genetic material.

Regardless of whether *H. luzonensis* was its own species, it may have evolved in isolation for hundreds of thousands of years. Butchered rhino bones on Luzon date to 700,000 years ago, though researchers don't yet know which human species was responsible.

Mijares is already back in the field. Many more pieces of the human story could be hidden on Southeast Asia's islands. When it comes to human evolution, Antón says, "We know a lot less than we thought we did." ■

PHOTOS: © CALLAO CAVE ARCHAEOLOGY PROJECT

INFECTIOUS DISEASE

Closure of U.S. Toxoplasma *lab draws ire*

Scientists say political pressure threatens research on cause of blindness and birth defects

By **Meredith Wadman**

For the past 37 years, a small research lab in Beltsville, Maryland, has been the world's leading hub for scientists working on *Toxoplasma gondii*, a parasite that infects more than 1 billion people globally, causing death, blindness, and birth defects. Operated by the U.S. Department of Agriculture (USDA), the facility is a source of expertise and rare, sought-after materials for researchers working to stop the parasite, which can be transmitted by food and has no human vaccine and no cure.

But last week, the lab fell victim to pressure from animal welfare activists and members of Congress concerned about its use of cats, the only animal in which *T. gondii* completes the sexual stages of its life cycle. USDA abruptly announced it was shutting down the lab's work, saying the program, which cost $625,000 annually to operate, had "reached its maturity" and "achieved" its agricultural research goals.

The 2 April decision, which lab chief Jitender Dubey learned about from media reports, has left researchers scrambling for alternatives. "I'm really angry about this," says Laura Knoll, a parasitologist at the University of Wisconsin in Madison who relies on samples from the laboratory. During a December 2018 external review of the lab she took part in, she says, "The validity and necessity of the research never seemed to be in question." (USDA declined to answer a list of questions from *Science* and denied a request to interview Dubey.)

The laboratory is "an incredible resource," says Robert Yolken, a pediatric infectious disease specialist at Johns Hopkins University School of Medicine in Baltimore, Maryland. "It's a loss for *Toxoplasma* research in the U.S. and around the world."

But parasitologist Jim Keen, a former USDA scientist now at the University of Nebraska in Lincoln, sees things differently. Last month, he and the White Coat Waste Project, a Washington, D.C.–based advocacy group, released a report that argues the laboratory's work is "unnecessary and unjustifiable." The 14-page document, titled *USDA Kitten Cannibalism*, details how researchers fed infected meat, including cat meat, to kittens, in order to harvest parasite oocysts—infective, hardy forms of the organism—from their feces. Researchers then euthanized the animals, killing dozens each year, because they might spread the parasite if adopted as pets. Keen reviewed 121 *Toxoplasma* studies published between 1985 and 2018 that involved killing cats or dogs and had Dubey as a co-author. He concluded that much of the lab's recent work is "irrelevant to American public health and the USDA's mission."

Outside scientists disagree. The lab has made several key contributions in the past decade, says David Sibley, a *Toxoplasma* researcher at Washington University in St. Louis, Missouri. One was developing a blood test that can inform parasite control strategies. The test indicates whether a person has become infected by eating undercooked meat or by ingesting parasite oocysts shed by cats.

A closed laboratory relied on cats to sustain its research program.

PHOTO: WHITE COAT WASTE PROJECT VIA FREEDOM OF INFORMATION ACT

The report marked the latest salvo in White Coat Waste's efforts to end cat use at USDA's Animal Parasitic Diseases Laboratory in Beltsville, which housed the *Toxoplasma* facility. The group has placed billboards attacking USDA on buses and this year persuaded 61 members of Congress to sponsor the Kittens In Traumatic Testing Ends Now (KITTEN) Act. One KITTEN Act co-sponsor, Representative Brian Mast (R–FL), called closing the program "a decisive victory against government animal abuse and wasteful spending."

But many researchers say the lab's demise will undermine efforts to fight the devastating parasite, which is the world's leading infectious cause of blindness and causes roughly 190,000 babies to be born with defects each year. In the United States, which has about 1 million new infections annually, it is the second-leading food-borne killer, causing about 750 deaths.

"There is no laboratory in the world" that produces *T. gondii* oocysts with the same efficiency, says one U.S. researcher, who asked for anonymity to avoid being targeted by animal activists. "Centralizing production actually minimized waste and the number of cats required." (Several scientists predict the closure will drive cat use to less-expert U.S. labs, or offshore.)

The loss of the lab will slow efforts to develop a vaccine to protect cats from infections, scientists say. That's a top public health priority, and one that Dubey was pursuing, because it would stop the animals from shedding the oocysts that infect both livestock and people.

The closure will affect collaborations by U.S. and European researchers to develop better methods of detecting parasite oocysts in drinking water and soil. Other imperiled studies focus on keeping *T. gondii* out of the food supply. One—requested by USDA inspectors—is examining whether U.S. rules for curing hams are stringent enough. Another is testing methods for cleaning oocysts from fresh fruits and leafy greens. Other studies are probing why the parasite makes only some infected people very sick.

Scientists are also worried about the fate of the Beltsville lab's unparalleled collection of more than 1000 *T. gondii* strains and its trove of tissue samples and reagents. "They can't just throw them away," says geneticist Chunlei Su of the University of Tennessee in Knoxville, who used the lab's DNA samples to study the parasite's global genetic diversity.

Knoll, for her part, says losing access to oocysts from the lab will disrupt her studies—which aim to find alternatives to cats in *Toxoplasma* research. ■

ARCHAEOLOGY

Beliefs in aliens, Atlantis are on the rise

Researchers take to Twitter, blogs to counter pseudoarchaeology's outlandish ideas

By **Lizzie Wade**, *in Albuquerque, New Mexico*

In February, the popular podcast *The Joe Rogan Experience* referred to an idea made famous by some books and TV shows: that an image of the Mayan King K'inich Janaab' Pakal, carved onto the lid of his sarcophagus when he died in 683 C.E., shows him taking off in a spaceship. Host Rogan was skeptical of the notion, which has been used to argue that extraterrestrial visitors seeded sophisticated ancient societies like the Maya. He asked what mainstream archaeologists made of it.

For David Anderson, that request was a call to action. Anderson, an archaeologist at Radford University in Virginia, jumped on Twitter: "Dear @joerogan, speaking as a 'mainstream' archaeologist … it depicts [Pakal] falling into the underworld at the moment of his death." The rocket-propelling "fire" below Pakal is a personification of the underworld, and the "spaceship" is a world tree, a common feature in Mayan art. Rogan retweeted Anderson's thread, bringing him more than 1000 likes and many grateful comments—plus some angry ones.

Pakal's supposed seat in a spaceship is just one example of what Anderson and others call "pseudoarchaeology," which ignores the cultural context of ancient artifacts and uses them to support predetermined ideas, rather than test hypotheses, about the past. Common beliefs include that aliens helped build the Egyptian and Mayan pyramids, that refugees escaping Atlantis brought technology to cultures around the world, and that European immigrants were the original inhabitants of North America.

These outlandish beliefs have been circulating for decades, but archaeologists like Anderson are now mobilizing to counter them. They are taking to Twitter, blogs, podcasts, YouTube, and newspapers to debunk false claims and explain real archaeological methods, and they plan to compare notes this week during a symposium at the Society for American Archaeology (SAA) meeting here. "My profession … needs to do a better job of speaking out," Anderson says.

He and others are alarmed by the rising popularity of pseudoarchaeological ideas. According to the annual *Survey of American Fears* by Chapman University in Orange, California, which catalogs paranormal beliefs, in 2018, 41% of Americans believed that aliens visited Earth in the ancient past, and 57% believed that Atlantis or other advanced ancient civilizations existed. Those numbers are up from 2016, when the survey found that 27% of Americans believed in ancient aliens and 40% believed in Atlantis.

"I look at these numbers and say … something has gone massively wrong," Anderson says. He can't say exactly what is driving the rise in such ideas, but cable TV shows like *Ancient Aliens* (which has run for 13 seasons) propagate them, as does the internet.

These beliefs may seem harmless or even amusing, says Jason Colavito, an author in Albany who covers pseudoarchaeology in books and on his blog. But they have "a dark side," he says. Almost all such claims assume that ancient non-European societies weren't capable of inventing sophisticated architecture, calendars, math, and sciences like astronomy on their own. "It's racist at its core," says Kenneth Feder, an archaeologist at Central Connecticut State University in New Britain, who is slated to present at the SAA session and began to write about the dangers of these ideas long before most other scholars paid attention to them.

Mayan King K'inich Janaab' Pakal is not taking off in a spaceship in this image from his seventh century sarcophagus, but falling into the underworld.

PHOTO: CHRONICLE/ALAMY STOCK PHOTO

Adding to archaeologists' sense of responsibility is that "many of these ideas started within mainstream archaeology," says Jeb Card, an archaeologist at Miami University in Oxford, Ohio. "We have to own these stories."

For example, white settlers and early archaeologists in 19th century North America excavated elaborate pre-Columbian burial mounds—but ascribed them to a lost "moundbuilder race" that was killed by the ancestors of Native Americans. Former President Andrew Jackson used those ideas to justify displacing Native Americans from their lands.

Today, white nationalists make similar claims. To argue for Europeans' deep roots in the Americas, they have latched onto Vinland, a short-lived medieval Viking settlement in eastern Canada, and the "Solutrean hypothesis," which argues that the Americas were first peopled by arrivals from Western Europe. Neither claim started as pseudoarchaeology—Vinland was real, and the Solutrean hypothesis was proposed by mainstream archaeologists, then tested and ruled out—but they have been twisted for ideological ends. A

white supremacist accused of murdering two people on a train in Portland, Oregon, in 2017 included the words "Hail Vinland!!!" in a Facebook post less than a month before the attack.

"It's really a life-or-death issue," says Stephennie Mulder, an archaeologist and art historian at the University of Texas in Austin, who organized a 30 March symposium there called "Aliens, Atlantis, and Aryanism: 'Fake News' in Archaeology and Heritage," at which Anderson was the keynote speaker.

Yet archaeologists have historically been hesitant to tackle pseudoarchaeology. As the field matured in the 20th century, archaeologists moved into the academy and abdicated the public sphere, says Sara Head, an independent cultural resources archaeologist in Philadelphia, Pennsylvania, and the author of the Archaeological Fantasies blog, who is co-organizing the SAA session. "We've created a vacuum" that pseudoarchaeology has filled.

Today, "Most archaeological research is unavailable to the public," she says, obscured by jargon and locked behind paywalls. "But you want something from pseudoarchaeology? I can find you 15 references," all easily accessible online and on TV.

Re-engaging with the public is an uphill battle, Head says. Debunking specific claims, as Anderson did with Pakal's "spaceship," is merely a first step. To make a lasting impact, she and others say, archaeologists must proactively share their work and, in particular, explain their methods step by step. That's important to counter the common pseudoarchaeological claim that researchers are hiding evidence for aliens or Atlantis.

This isn't easy work, especially online. All the women interviewed for this article have been harassed online after tackling pseudoarchaeological interpretations. Mulder recently fielded replies that included a knife emoji after she tweeted about research showing that people of diverse ancestries, rather than only Western Europeans, lived in Roman Britain. Colavito reports receiving death threats after a host of *Ancient Aliens* urged his fans to send Colavito hate mail.

Ironically, the popularity of pseudoarchaeology also reveals intense public interest in the past. Anderson understands: His own interest in archaeology was spurred at age 18 when he read a book about a now-vanished advanced civilization that supposedly helped develop the cultures of ancient Egypt and the Maya. He was inspired to take archaeology courses in college—and found that the reality was even more exciting than the myths. "Archaeology was even better than [the book] had presented it." ■

RESEARCH FUNDING

Brazilian scientists lament 'freeze' on research budget

Block on 42% of the science ministry's funds, coming on top of other cuts, puts flagship synchrotron at risk

By **Herton Escobar**, *in São Paulo, Brazil*

The latest federal budget news coming out of Brasília has Brazilian scientists fearing the worst. On 29 March, faced with a stagnant economy and falling tax revenues, the government announced it was "freezing" nearly 30 billion reais ($7.5 billion) of the country's public funds for the year, including a 2.2 billion real slice of the science ministry's budget. If the freeze isn't lifted, funds for scholarships and research will be cut by 42%—a blow that would come on top of a series of other cuts in recent years (see graphic, below.)

"We were running on a flat tire; now they took out the wheel," says Ildeu de Castro Moreira, a physicist at the Federal University of Rio de Janeiro in Rio de Janeiro and president of the Brazilian Society for the Advancement of Science (SBPC) here. If made permanent, the freeze could have "tragic" consequences, Moreira predicts. Many laboratories and research institutions might be pushed into stagnation, including federally funded facilities that provide crucial services such as weather monitoring and public health surveillance.

A freeze means the money remains in the government's budget, but is locked down as "contingency funds" that can be spent only if the economy improves or new sources of revenue are found. For now, Brazil's Ministry of Science, Technology, Innovation and Communications (MCTIC) is authorized to spend only 2.9 billion reais in support of R&D this year—less than what NASA typically spends on a single Mars mission. "We knew there might be another contingency measure on the way, but we never expected it to be so extreme," Moreira says. "When you have so little to begin with, every loss is a major loss." Even Brazil's flagship science project, the synchrotron light source Sirius, is at risk; 80% of the funds it depends on to complete construction and start to commission the facility by the end of this year have been frozen.

In a press statement, MCTIC says it is "committed to recuperate investment in research," and is still analyzing how the freeze will be implemented throughout its many agencies and programs, including the National Council for Scientific and Technological Development (CNPq) in Brasília, Brazil's agency for basic research funding. Even before the freeze was announced, CNPq's management had warned it didn't have enough money to make it through the year.

During previous freezes, scientists have pressured the government into releasing some of the frozen funds. It's unclear whether that will happen again; President Jair Bolsonaro has done little so far to make good on his promise to make science and technology a priority and raise Brazil's spending on R&D from 1% to 3% of gross domestic product.

The funding collapse threatens to "dismantle" an R&D system that took decades to build and is pushing a new generation away from science, says former CNPq President Hernan Chaimovich, a biochemist of the University of São Paulo here. "I really hope we can reverse this situation," adds Luiz Davidovich, president of the Brazilian Academy of Sciences in Rio de Janeiro. "We can't take another hit like this. It's just too little to survive on." ■

Herton Escobar is a science journalist in São Paulo, Brazil.

Science in decline

Even without the freeze, the Brazilian science ministry's budget for R&D—adjusted for inflation—has declined sharply the past few years.

Budget in Brazilian reais

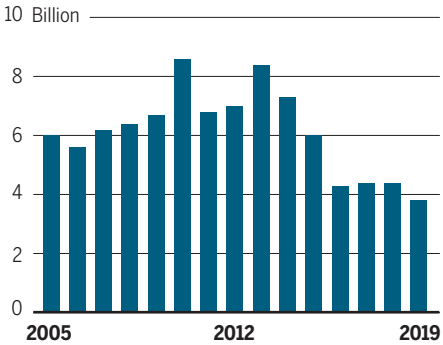

CREDITS: (GRAPHIC) A. CUADRA/*SCIENCE*; (DATA) BRAZILIAN ASSOCIATION FOR THE ADVANCEMENT OF SCIENCE

HUMAN BEHAVIOR

Atmospheric scientists join pheromone quest

Can measuring volatile compounds in real time save a field that is "in a bit of a crisis"?

By **Kai Kupferschmidt**, *in Chicheley, U.K.*

Jonathan Williams mostly studies the molecules that oceans and rainforests give off into the atmosphere. He's an unlikely recruit to a new cause: rescuing the decadeslong search for a human pheromone—a chemical signal in human body odor—from the doldrums.

Williams, who is at the Max Planck Institute for Chemistry in Mainz, Germany, joined two other atmospheric chemists here last week at a small Royal Society meeting on chemical communication in humans to describe how their workhorse technique for studying trace chemicals in the atmosphere, proton transfer reaction mass spectrometry (PTR-MS), could aid the pheromone hunt. "It really feels like we are on the brink of something great," says one of the meeting's organizers, psychologist Craig Roberts of the University of Stirling in the United Kingdom.

Something great is what the field needs. Since 1959, when German biochemist Adolf Butenandt isolated the first pheromone—a compound named bombykol that female silkmoths use to attract partners—generations of researchers have looked for similarly powerful chemicals in humans. But they haven't identified a single one. The few high-profile claims, for example that women living together synchronize their menstrual cycle through chemical signals, have not stood the test of time. "The field is in a bit of a crisis," says Andreas Natsch, a researcher at the fragrance company Givaudan in Vernier, Switzerland.

Part of the reason is that it's a small field with relatively little funding. "Smell is the Cinderella of human senses," says zoologist Tristram Wyatt of the University of Oxford in the United Kingdom, who has written a textbook on pheromones. Past studies often used small numbers of volunteers and questionable statistical methods. And then there is the sheer complexity of the subject. The human body emits hundreds of volatile compounds. Most pheromone studies give no more than a snapshot of them, for instance by asking participants to wear a T-shirt for a night or putting pads under their armpits and then analyzing captured compounds with a mass spectrometer.

By contrast, PTR-MS—which works by transferring a proton to volatile compounds in the air and then analyzing their mass from how they move in an electric field—is more like producing a video; it allows researchers to measure compounds in real time and to identify those that change in abundance after a certain type of stimulation. "You can eliminate a lot of hay from the haystack we have been searching through," Roberts says.

Decades of research have failed to yield any human pheromones.

Williams glimpsed the technique's potential years ago, when he analyzed the air around soccer fans during a game at a stadium in Mainz. "We could follow people's behavior by following the chemicals they emitted," he says. For instance, acetonitrile, a component of smoke, peaked at half time, when many people lit up a cigarette.

Williams wondered what the chemical signature of the euphoria after a goal would look like. That match, however, offered no joy, as it ended with a 0-0 score. To avoid another disappointing outcome, Williams turned to a local cinema instead. He found not only that crowds watching funny and suspenseful movies generate different chemical signatures, but also that the emissions change with plot twists. "In *The Hunger Games*, you could tell exactly when the heroine starts the big showdown fight," Williams says. In a paper in *Scientific Reports*, he reported that carbon dioxide levels increased, probably as the audience breathed faster; so did isoprene, which could be given off by twitching muscles.

Another atmospheric scientist, Ben Langford at the Centre for Ecology & Hydrology in Edinburgh, was so intrigued by the work that he decided to team up with Roberts, who was excited to learn about PTR-MS. Langford says: "It was almost like I was handing him a key to a door he had always wanted to open." In studies that they are preparing for publication, the duo has been showing movie clips to volunteers while analyzing the air under their armpits. They have identified some compounds that change in abundance during frightening scenes and plan to investigate further; whether the molecules constitute an actual chemical signal, however, is still unclear.

That study joins other work focusing on fear or aggression—a change after many years when pheromone research has searched for signals linked to sexual attraction and mate choice, which some now think may be harder to find. ("It used to be all about love and now in the age of [U.S. President Donald] Trump fear and aggression are the important topics," Natsch says.) In one ongoing study presented at the meeting, scientists collect sweat from Israeli soldiers before their first parachute jump and compare it with sweat collected in a different setting. Such extreme, life-or-death situations might present the best shot at identifying a chemical signal, Roberts says.

That signal may well turn out to be not a specific "fearomone" but a complicated series of changes in the abundance of several compounds, just the kind of thing Williams and his colleagues are accustomed to tracing in the atmosphere. That his new field is less mature than atmospheric chemistry only makes it more attractive, Williams says: "There is such an opportunity for discovery here." ■

PHOTO: © LOUIE PSIHOYOS

eppendorf & Science

PRIZE FOR NEURO BIOLOGY

Application Deadline
June 15, 2019

Now It's Your Turn!

Eppendorf & Science Prize for Neurobiology
The annual Eppendorf & Science Prize for Neurobiology is an annual international prize which honors young scientists for their outstanding contributions to neurobiological research based on methods of molecular and cell biology. The winner and finalists are selected by a committee of independent scientists, chaired by *Science's* Senior Editor, Dr. Peter Stern. If you are 35 years of age or younger and doing great research, now is the time to apply for this prize.

As the Grand Prize Winner, you could be next to receive
> Prize money of US$25,000
> Publication of your work in *Science*
> Full support to attend the Prize Ceremony held in conjunction with the Annual Meeting of the Society for Neuroscience in the USA
> 10-year AAAS membership and online subscription to *Science*
> Complimentary products worth US$1,000 from Eppendorf
> An invitation to visit Eppendorf in Hamburg, Germany

It's easy to apply! Write a 1,000-word essay and tell the world about your work. Learn more at:

www.eppendorf.com/prize

eppendorf Science AAAS

AAAS® and Science® are registered trademarks of the American Society for the Advancement of Science, USA. Eppendorf® and the Eppendorf logo are registered trademarks of Eppendorf AG, Germany. All rights reserved, including graphics and images. Copyright © 2019 by Eppendorf AG. Kurstin Roe Photography.

Hills of radioactive residue, covered in black sheeting, are stored at Lynas's facility in Malaysia.

ENVIRONMENT

Politics could upend global trade in rare earth elements

Malaysian government asks "flagship" company to remove radioactive waste from the country or shut down

By **Yao-Hua Law**, *in Kuantan, Malaysia*

Companies and governments worldwide are anxiously watching the fate of a sprawling industrial facility 30 kilometers north of this city on the east coast of peninsular Malaysia.

The 100-hectare Lynas Advanced Materials Plant (LAMP) produces 10% of the world's output of rare earth oxides (REOs), minerals needed in technologies including mobile phones, hard drives, surgical lasers, and cruise missiles. Lynas, an Australian company, imports concentrated ores from mines in Australia and refines them in Malaysia, where costs are lower; it sells REOs—which include cerium compounds, used in catalytic converters, and neodymium, critical to permanent magnets—to Japan, the United States, and other countries. The plant produced almost 18,000 tons of REOs in 2018.

Now, LAMP faces closure, barely 7 years after it opened. Environmental groups have long opposed the on-site storage of slightly radioactive waste from the extraction process, and they found a sympathetic ear in a new government elected in May 2018. In December 2018, the government demanded that LAMP ship its radioactive waste back to Australia if it wants to renew its operating license, which expires on 2 September. The company says exporting the residue by the deadline is "unachievable."

The standoff has caused Lynas's stock to lose almost half its value and has worried many countries hungry for REOs. A shutdown would be "a significant event with a ripple effect," says Ryan Castilloux, a metals and minerals analyst at Adamas Intelligence in Amsterdam. For one thing, it would strengthen China's position as the dominant supplier of REOs, which many countries deem a strategic risk. Japan's electric vehicle industry, for instance, would lose its main supplier of REOs for permanent magnets.

Rare earth elements include those with atomic numbers 57 to 71, the "lanthanide series" of the periodic table, as well as scandium and yttrium. Their exceptional magnetic and conductive traits make them critical to clean energy technology, such as hybrid fuel cells, solar panels, and wind turbine magnets. Industries worth trillions of dollars depend on REOs worth only billions, Castilloux says.

Rare earth deposits are found in more than 800 locations worldwide. Refining them takes lots of corrosive chemicals and generates huge amounts of residue. China was long the sole supplier; when it reduced exports in 2010, citing environmental concerns, prices jumped as much as 26-fold and major consumers scrambled for alternate sources. The United States and Myanmar mine REOs as well, but these are also processed in China, which now produces about 89% of the global REO output (see graphic, below). Lynas has become a "flagship" of REO production outside China, Castilloux says.

But the company is running aground in Malaysia. At LAMP, ores are roasted with acids to dissolve the REOs and then diluted with water. This creates a solution of concentrated REOs and a pastelike residue—more than 1.5 million tons so far, of which 30% is slightly radioactive because it retains thorium and uranium from the ores. Some REO facilities elsewhere have built permanent, secure facilities to store such waste, says Julie Klinger, a geographer and expert in REO mining at Boston University; others are secretive about what they do with it. "Residues are definitely the main issue," says Tracy Moore, CEO of Canada Rare Earth Corporation in Vancouver.

In a plan approved by the previous government, Lynas aimed to recycle its residues; the company has sponsored Malaysian researchers to turn them into soil enhancers. These efforts have not yielded commercial products, however. And in December 2018, a new executive committee, appointed by the government to evaluate LAMP, cautioned against using the radioactive waste in agriculture as it might accumulate in the environment. Retired radiochemist Amran Majid of the National University of Malaysia in Bangi and others have suggested a different strategy—extract the thorium, which accounts for almost all of the radioactivity, for use as fuel for nuclear reactors.

So far, LAMP has been storing residues on-site instead, in rapidly growing hills. The specter of piled up radioactive waste has sparked public fears, which experts say are exaggerated. Workers at the site are exposed to about 1.03 millisieverts (mSv) per year, Lynas reports, far below the 20-mSv threshold advised by the International Atomic Energy

Made in China

Rare earth oxides (REOs) are mined worldwide but are mostly processed in China. Lynas is the only notable REO supplier outside of China.

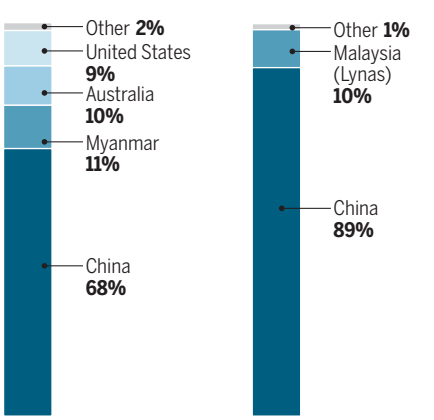

CREDITS: (PHOTO) SAVE MALAYSIA STOP LYNAS; (GRAPHIC) N. DESAI/*SCIENCE*; (DATA) ADAMAS INTELLIGENCE

Agency (IAEA) for workers exposed to radiation. The health effects of such low doses are "negligible," says Kwan Hoong Ng, a medical physicist at the University of Malaya in Kuala Lumpur. People outside the facility are at an even lower risk, Amran adds.

Still, in 2011 and 2014 IAEA found that Lynas lacked adequate plans for a permanent facility if recycling fails. The executive committee has suggested Lynas build one immediately, citing the potential for natural disasters to disperse the residues. (Monsoon storms and floods are common in the area.) Radioactivity isn't the only risk, says Bun Teet Tan, chair of Save Malaysia Stop Lynas, a nongovernmental organization here. A 2013 review by the Öko-Institute in Darmstadt, Germany, commissioned by Tan's group, found that heavy metals such as nickel, chromium, lead, and mercury could contaminate groundwater.

Neither the ministry in charge nor Lynas responded to interview requests from *Science*. In a financial report issued in late February, Lynas directors said the company has lived up to the terms of its operating license and will build permanent storage if necessary; exporting the residue should be a last resort, they said.

Saleem Ali, an expert in energy and the environment at University of Delaware in Newark, says the anti-Lynas fervor in Malaysia is "a classic case of the not-in-my-backyard syndrome." He says recycling is a commendable option but worries activists are now "stigmatizing the waste." Because REOs are crucial for green technology, "The industry needs to make the case more effectively that [it] benefits not just the local, but also the global community," Saleem says. Klinger says the conflict offers an "exciting opportunity" to develop new solutions for clean REO production that could serve as a model for others.

How the impasse will end is unclear. On 5 April, Prime Minister Mahathir Muhamad announced that Lynas can continue to operate if it imports only nonradioactive materials. In a statement, Lynas said it "sees value" in that idea. But shifting the processes that produce radioactive waste to Australia would be expensive, Castilloux says. "A slowdown in production or outright shutdown is certain." And Mahathir didn't say whether waste already stored at LAMP can stay.

Meanwhile, REO producers from developed countries are establishing new footholds worldwide. A Lynas shutdown would offer "greater market opportunities" for other players, but could also "discourage financing" as investors might fear similar problems, Moore says. ■

Yao-Hua Law is a science journalist in Kuala Lumpur.

MUSEUMS

Report urges massive digitization of biospecimens

"Extended specimens" would link images and data

By **Elizabeth Pennisi**

The United States should create an all-encompassing database of the billion stuffed, dried, and otherwise preserved plants, animals, and fossils in museums and other collections, a U.S. National Science Foundation (NSF)–sponsored white paper released last week urges. The report also calls for new approaches to cataloging digitized specimens and linking them to other data. If the plan is carried out, "There will be [a] huge potential impact for the research community to do new types of research," says NSF biology Program Director Reed Beaman in Alexandria, Virginia.

But the effort could take decades and cost up to half a billion dollars, and some fear the white paper will not win over policymakers. "I just wish that the report focused more on the potential benefits for noncollections communities," says James Hanken, director of the Harvard Museum of Comparative Zoology in Cambridge, Massachusetts.

A standard lightbox setup is used to digitize museum specimens such as fish.

For the past 8 years, NSF has sponsored the $100 million, 10-year Advancing Digitization of Biodiversity Collections program, which has paid for nearly 62 million specimens to be digitally photographed from multiple angles for specific research studies. New technology has greatly sped up the process (*Science*, 13 May 2016, p. 762). Already, natural history and evolutionary studies are benefiting from easy access to information previous locked in museums.

Other, smaller digitization efforts have also paid off. Since the 1993 outbreak of the deadly mouse-transmitted hantavirus in the U.S. southwest, the Museum of Southwestern Biology at the University of New Mexico in Albuquerque has been warehousing mammals used in public health studies and natural history research. It has digitized those specimens and linked them to relevant pathogen and genome data, enabling disease experts, microbiologists, and others to tap into the database, says Joseph Cook, the museum's curator of mammals.

The Advancing Digitization program ends in 2021, so NSF set up a a multigroup network to survey managers and users of biological collections and plan the next steps. It is now proposing an expanded effort that would also target smaller collections and develop a standardized, upgradable system for linking disparate databases to create an "extended specimen." Users will see not only a specimen, but also associated data such as DNA sequences, isotopic clues to its diet and climate, and environmental information from its collection site. "We want to pull together everything that's known about a specimen," says the network's Barbara Thiers, a botanist at the New York Botanical Garden in New York City.

Cook calls the new plan "a great opportunity to build important infrastructure for the big questions that society is going to ask," such as assessing environmental change and shifts in animal and disease ranges.

Thiers estimates it will take up to $500 million to realize this vision and "get all the bells and whistles we would like." For that reason, some collection experts are calling for stronger advocacy. "Somebody needs to hit the pavement and convince other agencies to support this [effort]," Hanken says. Otherwise, it risks being dismissed as "another in a long line of calls to the community to imagine a new future for biological collections," adds Scott Edwards, an evolutionary biologist at Harvard University.

Thiers sees it differently, calling the plan "a novel approach" that will combine "diverse data types in ways that have not been considered." NSF's Beaman is noncommittal about its prospects. "It's premature for me to say we would develop new programs" to support it, he says. But he acknowledges the value of expanding access to museum collections, noting the huge cost and effort of building them. "It's not stamp collecting," he says. "The potential for use and societal impact is huge." ■

PHOTO: KRISTEN GRACE/FLORIDA MUSEUM

MATERIALS SCIENCE

Solar cell built for two looks sweet

Simple tandem design uses perovskite layer to feed photons to silicon cell

By **Robert F. Service**, *in Orlando, Florida*

The promising solar cell materials called perovskites need a partner. Researchers marry a layer of perovskite, which absorbs high-energy blue photons in sunlight, with standard silicon, which gobbles up lower-energy light. In theory, such tandem cells should deliver a double dose of power, with electricity coming from both layers. But building two complete solar cells, one atop the other, adds cost and other challenges. Last week, a team reported advancing a potentially simpler, cheaper way to make a tandem.

The team's perovskite converts light instead of generating current, transforming blue photons to near-infrared (near-IR) photons, which the silicon cell below then turns into electricity. The researchers say the design could boost the efficiency of silicon solar cells by nearly 20%. If it does, it could be key to realizing the promise of perovskites, a class of compounds that share a crystal structure and are made from common elements such as lead, bromine, and chlorine.

"This is one of the most exciting results I've seen in a long time," says Michael McGehee, a perovskite expert at Stanford University in Palo Alto, California. "The boost in efficiency they are claiming is very significant." Silicon solar cell–makers, a $30 billion a year industry in 2016, grasp at every tenth of a percentage point gain in efficiency.

Silicon dominates the solar industry not because it's the best solar converter, but because it's serviceable and relatively cheap. Still, manufacturers must use expensive clean rooms to purify and prepare it. Perovskites, in contrast, are easy to coax into a thin, powerfully light-absorbing layer. Most perovskites are best at absorbing blue light, so they must be paired with other materials to snag the full solar spectrum.

The solar industry is racing to commercialize perovskites by placing them atop conventional silicon modules, which discard much of the energy in bluer light photons, releasing it as heat rather than electric current (*Science*, 9 December 2016, p. 1214). But in addition to the expense of adding device layers, manufacturers must also grapple with practical challenges such as designing tandems so the amount of current coming out of each cell is the same. If they don't, the overall current is limited by the weaker of the two cells.

Two years ago, researchers led by electrical engineer Hongwei Song at Jilin University in Changchun, China, reported a way around these challenges. By sprinkling a small amount of the rare earth metal ytterbium into a standard cesium- and lead-based perovskite, they found they could build a perovskite tandem with a different, simpler architecture. Like conventional perovskites, the ytterbium-doped version absorbs blue photons, energizing electrons in the material. But these electrons aren't turned into current. Instead, they immediately pass their energy to the ytterbium atoms, which re-emit virtually all of it as near-IR light. Most of these photons zip into the silicon cell below, which absorbs nearly all their energy and efficiently converts it to electricity, losing very little as heat. "For solar energy conversion, this combination of materials is almost exactly what you want," says Daniel Gamelin, a chemist at the University of Washington in Seattle.

The perovskites Song's team created were nanoparticles, however, which are hard to lay down uniformly on a silicon cell. The challenge is acute with the best-performing commercial cells, in which silicon is topped with a protective layer of glass that is intentionally roughened. The miniature glass mountains help light enter the cell instead of reflecting off its top surface, but the perovskite nanoparticles don't always form an even layer on the rough surface.

At last week's American Chemical Society meeting here, Gamelin reported that he and his colleagues have solved this problem. They used a common solar cell–growing technique known as vacuum deposition to create thin, smooth layers of ytterbium-doped perovskite on roughly 14-centimeter silicon solar cells. The technique coats the miniature glass mountain range with an even perovskite film.

In the resulting tandem, nearly all the blue light absorbed by the perovskite is converted to near-IR photons, Gamelin reported. As a result, he predicts, topping a high-end silicon cell with the ytterbium perovskite should enable it to convert 32.2% of the energy it absorbs as sunlight into electricity, up from 27%—a 19.2% boost. Gamelin's team is doing experiments now to confirm those predictions. "I am a little skeptical of the numbers," McGehee says. But even a fraction of that increase "would be a big deal," he says.

Michael Graetzel, a photovoltaic expert at the Swiss Federal Institute of Technology in Lausanne, agrees. But he says practical concerns such as emitted near-IR photons escaping may limit gains to less than 10%.

Last month, Gamelin and his colleagues launched a startup, BlueDot, to commercialize the technology. They have plenty of competition. Perovskite startups such as Oxford PV in the United Kingdom and Saule Technologies in Warsaw are already field testing their perovskite-silicon tandems or preparing to do so. But BlueDot hopes to leapfrog the other companies, because its simpler tandem design should enable standard silicon solar cell manufacturers to integrate perovskites into their manufacturing lines more easily—and get perovskites onto the roofs of the world. ■

A perfect match

A new tandem solar cell design uses a perovskite layer (pink), which absorbs energy from blue and purple photons and re-emits it as near-infrared (near-IR) photons. Along with other colors of light, these photons are absorbed by a silicon (gray) solar cell and converted to electricity.

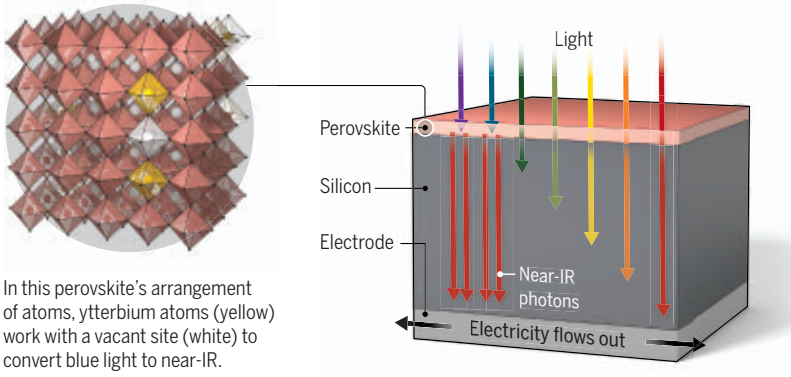

In this perovskite's arrangement of atoms, ytterbium atoms (yellow) work with a vacant site (white) to convert blue light to near-IR.

GRAPHIC: V. ALTOUNIAN/*SCIENCE*

Science
JOURNALS AAAS

Editor-in-Chief

Science family of journals

The American Association for the Advancement of Science (AAAS) is the world's largest general scientific society and publisher of the journal *Science* and the *Science* family of journals (*Science Translational Medicine*; *Science Signaling*; a digital, open-access journal, *Science Advances*; *Science Immunology*; and *Science Robotics*). *Science* has the largest paid circulation of any peer-reviewed general science journal in the world.

The *Science* family of journals performs a critical and distinctive role within scientific scholarly communications upon which thousands of global researchers depend to publish, promote, protect, and ensure access (in perpetuity) to their research results. Rigorous standards of review at the journals include not only review of technical merit, but also confirmation of adherence to editorial policies. AAAS is a leading organizational voice in ongoing global discussions on the changing nature of scientific publishing, including open-access publishing.

AAAS has initiated a search for a new **Editor-in-Chief** (EIC) for its international journal *Science* and the *Science* family of journals. The journals are essential to fulfilling the AAAS mission to "advance science, engineering, and innovation throughout the world for the benefit of all people." By publishing the very best in scientific research, commentary, and news, the *Science* family of journals furthers the AAAS goal to "enhance communication among scientists, engineers, and the public."

The AAAS Board of Directors seeks a bold, visionary, and wise EIC who, ideally, brings a record of significant achievement in scientific research, editorial experience, and creativity, as well as an awareness of leading trends and ideas in science and scientific publishing.

The EIC must demonstrate the ability to be a thought leader in science and scientific publishing globally, as well as the capacity to work collaboratively with multiple stakeholders. The EIC will lead a highly skilled team to ensure the *Science* journals maintain their standards of scientific and editorial rigor and advance their mission of fostering communication among scientists and between scientists and the public.

The EIC is the principal architect of the content of the *Science* family of journals. S/he ensures the journals continue to be recognized for their high quality and their scientific and technical significance. S/he ensures that the journals solicit and attract authors and research that are among the very best. Through editorials, appearances, and other interactions with scientists and others, s/he serves as a public voice for the *Science* family of journals and shows that *Science* and AAAS set high standards for the practice of science and its communication now and in the future.

The EIC must be well-known and well-regarded in scientific fields and must have impeccable credentials, exceptionally good judgment, a strong ethical compass, and a deep, proven commitment to ensuring that science is communicated broadly, accurately, and well.

AAAS and the editorial and publishing activities are headquartered in Washington, D.C., and the work of the EIC is centered there. The EIC will report to both the Board of Directors and the AAAS CEO.

To learn more about this position please visit: **https://koyapartners.com/search/editor-in-chief/**.

To express your interest in this role please submit your materials to Koya Leadership Partners at email **EIC-Science@koyapartners.com**. All inquiries and discussions will be considered strictly confidential.

AAAS is an equal opportunity employer and strongly encourages applications from people of color, persons with disabilities, women, and LGBT applicants. For more information on the *Science* family of journals, please visit www.sciencemag.org.

THE TRESPASSER

Physicist Danielle Bassett searches for simple rules that govern the brain's tangled networks

By **Kelly Servick**

At age 16, Danielle Bassett spent most of her day at the piano, trying to train her fingers and ignoring a throbbing pain in her forearms. She hoped to pursue a career in music and had been assigning herself relentless practice sessions. But the more she rehearsed Johannes Brahms's feverish *Rhapsody in B Minor* on her family's Steinway, the clearer it became that something was wrong. Finally, a surgeon confirmed it: Stress fractures would force her to give up the instrument for a year.

"What was left in my life was rather bleak," Bassett says. Her home-schooled upbringing in rural central Pennsylvania had instilled a love of math, science, and the arts. But by 17, discouraged by her parents from attending college and disheartened at her loss of skill while away from the keys, she expected that responsibilities as a housewife and mother would soon eclipse any hopes of a career. "I wasn't happy with that plan," she says.

Instead, Bassett catapulted herself into a life of research in a largely uncharted scientific field now known as network neuroscience. A Ph.D. physicist and a MacArthur fellow by age 32, she has pioneered the use of concepts from physics and math to describe the dynamic connections in the human brain. "She's now the doyenne of network science," says theoretical neuroscientist Karl Friston of University College London. "She came from a formal physics background but was … confronted with some of the deepest questions in neuroscience."

Now 37, Bassett runs a lab at the University of Pennsylvania (UPenn) that tackles a whiplash-inducing variety of questions. A sampling from one morning's worth of meetings: Do our brains navigate words in written text the way they navigate physical space? Does the structure of college students' brains interact with the structure of their social networks to influence their ability to abstain from alcohol? Does the network of connections in the mouse brain predict how a disease-causing protein will spread?

Other projects focus on a theme that has captivated her since her childhood passion for books and the piano: learning and mastery. Bassett wants to find ways to optimize learning by using networks to represent both the brain and the material it learns.

"If you came to most thinking scientists, who try to be conservative and skeptical and cautious, and you spelled out to them what Dani's research program was going to be, they'd question anybody's sanity who was going to bite off that big of a chunk of science," says Steven Schiff, a neurosurgeon at Pennsylvania State University in State College and an admirer of Bassett's work.

But Bassett routinely disregards disciplinary boundaries and follows her curiosity with abandon. "What I think is beautiful about network science," she says, "is that you can use it to derive very simple intuitions about really complex systems that … just look like a big hairball."

That bid to simplify one of nature's gnarliest hairballs—our 86-billion-neuron organ of thought—into a set of mathematical equations has been hard for some neuroscientists to get behind. Network science is "a new way of looking at the brain," says Martha Shenton, a neuroscientist at Harvard Medical School in Boston. "This is an advance in science—I do believe that—but it remains to be seen how much information it's going to give us." And whether Bassett's toolbox of equations can make reliable predictions that inform treatments, such as targeted stimulation for brain disorders, is still unknown.

But neuroscience is hungry for theory, says cognitive neuroscientist Michael Gazzaniga of the University of California (UC), Santa Barbara. "There's an uneasiness that I think is widespread that we're not quite capturing the framework … to understand how neurons generate behavior, mind, and all this," he says.

Bassett is part of a generation of physicists and mathematicians who are betting on new

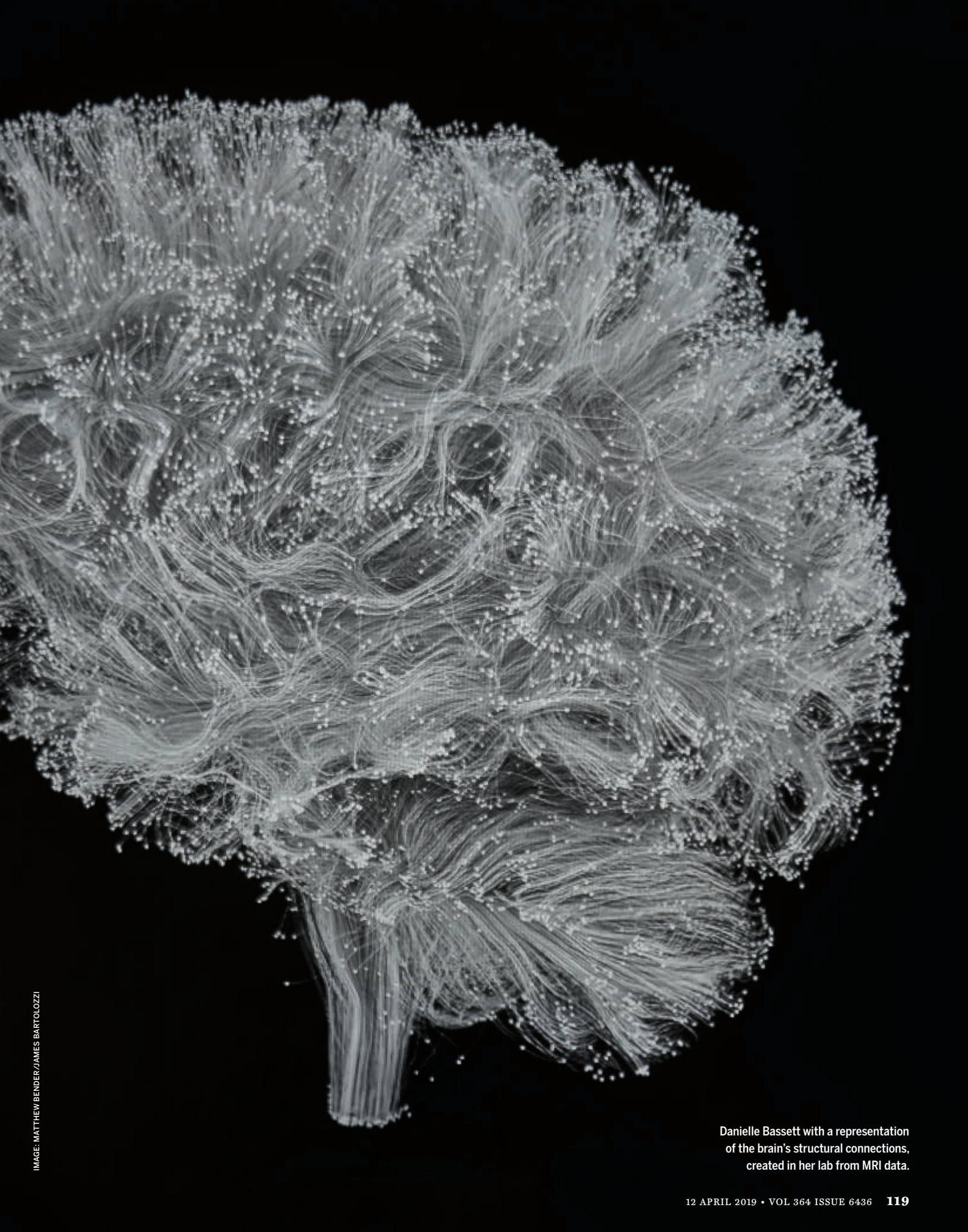

IMAGE: MATTHEW BENDER/JAMES BARTOLOZZI

Danielle Bassett with a representation of the brain's structural connections, created in her lab from MRI data.

theories to capture the brain's higher-order organization. "They [have] the math to back them up … and that just brings tremendous power to the biological scene," Gazzaniga says. "The great advances in science come from trespassing," he adds, paraphrasing pioneering psychologist Wolfgang Köhler. "And Dani is a trespasser."

ON A RECENT Tuesday afternoon, Bassett—a slight figure with short hair that persistently sneaks in front of her right eye—stands before her class with a large, gilded-edged volume of Claudius Ptolemy. The course teaches undergraduate and graduate students to represent the brain as a network—a set of "nodes" joined by pairwise connections, or "edges." Depending on the study, researchers might define nodes as individual neurons or larger brain regions. And they might draw edges between nodes that are physically connected by neural fibers or that tend to be active at the same time. The approach formalizes a basic premise of neuroscience: that our thoughts, sensations, and experiences emerge as the brain's connected components interact.

"She's now the doyenne of network science."
Karl Friston, University College London

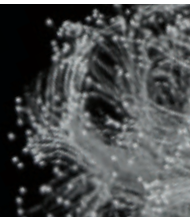

But first, Ptolemy. Bassett, in a characteristically composed and formal tone, reads aloud from the second century Greek astronomer's famous treatise, *The Almagest*: "It is proper to try and fit as far as possible the simpler hypothesis to the movements of the heavens; and if this does not succeed, then any hypothesis possible." He was addressing apparent contradictions in his geocentric explanation of planetary motion. His theory, we now know, was destined to fall apart. But his message was a good one, Bassett tells the class: Strive for the simplest hypothesis.

Bassett's penchant for quoting the ancients reflects her unusual education. Her mother, Zurn Perry, who home-schooled her 11 children, says her goal was "to teach them how to teach themselves anything they wanted to learn." Bassett was a natural autodidact. "When she decided that something interested her, she kind of couldn't stop until she knew everything there was about it," Perry says.

Bassett's twin brother, Perry Zurn, a philosopher at American University in Washington, D.C., describes their home schooling as research. They would choose a topic and build a constellation of projects around it, with little regard for where those projects fell among traditional school subjects.

Perry's insistence that her children prioritize primary texts stuck with Bassett. Reading antiquated, alien-sounding prose jolts the mind into "a much bigger space," she says. The twins now describe their education as "really wonderful" and "really fantastic." But their parents' conservative Christianity shaped what they could aspire to. "Because we both grew up being understood as female … we were actively discouraged from going to college," says Zurn, who is transgender.

After Bassett's hiatus from the piano, her father allowed her to attend nursing school. "He had finally given me a little bit of room, and I figured I should take it," she says. (Her father, John Perry, contends that he never discouraged his children from college or careers, though he says he "felt that being a good wife and mother was a high calling.")

An isolated childhood made the move to traditional school jarring for Bassett. "It took a long time to feel like I could laugh at the right times when somebody told a joke," she says. And nursing school was a bad fit. Confrontations with sickness and dying left her drained.

After a year and a half, she definitively broke with her family's expectations. She dropped out of nursing school and applied to Penn State to study physics. "I just wanted to do something that is clean and formal," she says, "and also, just with books."

AN HOUR INTO BASSETT'S Tuesday class, the students whip out their laptops and become subjects in one of her latest studies about learning. Their screens display a cloud of about 50 concepts she has selected from the course, such as prediction, network, behavior, and neurological disease. They draw lines to connect related words and phrases, stretching the lines to put distance between dissimilar concepts. Bassett will compare the structure of the maps at different points in the course, gauge the influence of class readings and lectures, and look for correlations between network structure and test scores.

The work seems miles away from Bassett's physics degree. But underlying that study—and nearly every other project in her lab—is a branch of math called graph theory. The approach, with roots in the 18th century, describes the structure of networks of discrete, interacting parts, be they friends linked on social media or grains in a sand pile.

Researchers first calculate the relationships between all nodes in a network: in the simplest case, either a zero (not connected) or a one (connected). Then, they ask questions about the features of the network: Is it a sparse web or a dense jungle of connections? Do certain nodes have an unusually large number of connections? Do nodes tend to organize themselves into tight-knit modules that mostly talk among themselves?

In the 1990s, a few researchers started to create such graphs to describe the layout of animal nervous systems. A graph for the nematode *Caenorhabditis elegans* could include all the connections among the 302 neurons that determine how the tiny worm wiggles through life. The brains of mammals were far too large and complex to map neuron by neuron, so researchers analyzed the connections between dozens of broad areas in the monkey and cat cortex according to the flow of tracer molecules along neurons.

"We worked in complete obscurity," neuroscientist Olaf Sporns says of the field that would become network neuroscience. Sporns, now at Indiana University in Bloomington, was among the first to use graph theory to analyze connections in the human brain. Few data sets were available, he says. But he and his collaborators hoped the approach could help explain how the brain's structure gives rise to thought and awareness.

By the mid-2000s, applications of graph theory were getting more ambitious. Neuropsychiatrist Edward Bullmore's group at the University of Cambridge in the United Kingdom used it to analyze human brain activity recorded with functional magnetic resonance imaging (fMRI), a technique that can indicate which regions are active in unison.

"It was a very exciting period, when [we] began to … explore these previously unmeasured properties of human brain networks," Bullmore says. "It was around that time when Dani started in the lab." Bullmore was one of Bassett's four advisers in a Ph.D. program sponsored by Cambridge and the U.S. National Institutes of Health. She took off running with graph theory, Bullmore recalls, stretching its uses to new types of brain data.

In one study, Bassett analyzed MRI data from people with and without schizophrenia. The condition seems to arise from broadly disorganized brain activity, not a defect in any one region. Bassett and colleagues showed that graph theory offered a new way to describe that disorganization. Brains with schizophrenia showed more random patterns of connectivity than healthy ones, and their hubs—the most highly connected regions—were less likely to be in the frontal cortex, the area that exerts executive control over the brain. That finding aligned with some of the symptoms of schizophrenia: deficits in executive functions such as planning, decision-making, and regulating behavior. But it didn't explain them.

IMAGE: MATTHEW BENDER/JAMES BARTOLOZZI

And some neuroscientists were unimpressed by early results from network science. Graphs of brain networks were "obviously a radical simplification of the nervous system," Bullmore says. "The main criticism has always been, 'Isn't this too simple to be meaningful, given the complexity of the system we're trying to understand?'"

Bassett saw a different limitation to graph theory. "It's great for characterizing the structure of something," she says, "but not necessarily what the thing does." A graph is static, but an active brain flows between connectivity patterns. So, as Bassett moved to her postdoc at UC Santa Barbara, she added another type of analysis to her study of networks: dynamical systems theory, a way of modeling how network structure changes. "Dani has excelled at bringing time into the game," Sporns says.

In a key experiment, Bassett studied people as they learned to tap their fingers quickly in a specific order by reading sequences of notes on a staff. The sequences weren't exactly Brahms rhapsodies; each was just 12 notes long. But participants took time to master them. During three training sessions, they lay in an fMRI scanner and practiced their finger work.

Bassett's group captured changes over time in the sets of brain areas that preferentially conversed with each other while participants learned. The researchers created a mathematical measure of overall "flexibility"—how likely regions were to change their "module allegiance" and sync up with a different set of partners. A brain's flexibility during a practice session, the researchers found, predicted how much faster the person would be able to play the note sequences in the next session.

The research, published in 2011, hinted that measurable, predictable features of the brain's configuration can prime it for learning. That "started to get a lot of people's attention," Bassett says, including representatives of the MacArthur Fellows Program, who pointed to the work in selecting Bassett for the 2014 award. Bassett, who was just getting her lab at UPenn off the ground, found herself in the academic spotlight. Her parents, who had separated when she was 18, cheered her on.

BASSETT IS NOW A HUB in a lively network—a role that doesn't always suit her. On an endless circuit of invited talks, she seeks solitude in her hotel room. She shies away from group interactions, preferring one-on-one communication with trainees and collaborators.

But some of those pairwise connections have had far-reaching effects. In 2013, on a bench overlooking the Pacific Ocean in Santa Barbara, she and mechanical engineer Fabio Pasqualetti, then a fellow postdoc, realized they shared an ambition. They wondered whether network science could go beyond describing the brain to offering ways to change it. Pasqualetti studies control theory, a branch of engineering that uses sensors and feedback to guide the behavior of a system, whether that's an electrical grid or a fighter jet. Was it possible, he and Bassett wondered, to apply principles of control theory to brain networks?

In their initial study, published in 2015, Bassett and Pasqualetti modeled brain structure with data from an MRI-based technique that traces the diffusion of water through the brain to identify regions connected by bundles of neuronal fibers. By feeding that information into an equation from control theory, they identified areas of the brain that, when active, might help it shift into various other states. "It was a big jump, honestly, to make the assumption that this thing could work," says Pasqualetti, now at UC Riverside.

Danielle Bassett at 12, wearing garb dictated by her family's religion.

PHOTO: DANIELLE BASSETT

"It's a very important contribution," computational neuroscientist Marco Zorzi of the University of Padua in Italy says of the paper. Scientists are already experimenting with zapping the brain to improve various conditions, including severe depression and disability after stroke. But the approach, which often relies on magnetic stimulation of the scalp, involves trial and error. Control theory could help researchers decide where in the brain to stimulate, and at which intensities, to reliably steer it into a healthier state.

Still, Zorzi says, "It's not ready yet." To develop stimulation protocols based on control theory, "we just need much more theoretical work," he says. That work should include studying how many points of stimulation are necessary to induce a desired brain state, he adds.

Bassett and her team are now refining their control theory approach and using it to predict the spreading patterns of activity in epileptic seizures. The results, they hope, will show how doctors could place seizure-stifling electrical implants more precisely or slice out less brain tissue during surgery.

Before any clinical trials, Bassett and colleagues will also have to defend the work against a familiar charge: that it oversimplifies the brain. Signals don't pass predictably along every connection between neurons. Some get amplified; others run into gating mechanisms that inhibit them, and equations from control theory don't fully capture those details. "That makes the control problem enormously difficult," says Schiff, a former epilepsy surgeon who studies control theory. "That's an enormous frontier that we're just starting to crack into."

In response, Bassett channels Ptolemy. "Physicists … start with relatively simple models, and then they expand those models as it becomes necessary," she says. "If there's more than a few parameters, it's very difficult to understand why something happens."

ON THE DRIVE HOME from class, Bassett's 4-year-old son, Simeon, recounts his day care exploits from the back seat of the car and dictates the playlist.

When Bassett entered college, she swore she would never be a wife or mother. On campus, she found that the homemaker role her family had insisted on was, at times, discouraged. But she met Lee Bassett, a fellow physics student whom she married in 2006. Both now teach at UPenn, and the first of their two children was born in 2011.

That evening, after bedtime reading (*The Berenstain Bears* for Simeon and the children's fantasy novel *Mossflower* for Silas), Bassett pops open a can of cherry-flavored sour beer and brings out one of her own favorites: British philosopher Joseph Glanvill's 17th century volume *The Vanity of Dogmatizing*. In it, Glanvill marvels at humanity's ignorance of the natural world and condemns blind faith in both science and religion. Bassett has peppered its margins with notes.

Down the hall in the living room sits a Steinway grand piano, testimony to her continuing love of music. It's the only purchase Bassett has made so far with her $625,000 MacArthur award; for now, her lab is not hurting for funding. But the unspent money means freedom. If an idea sparks her imagination and funders won't get behind her, she plans to chase it anyway. ■

INSIGHTS

PERSPECTIVES

PLANT EVOLUTION

Pollinators, herbivores, and the evolution of floral traits

Floral characters reflect plant adaptation to both bumble bees and leaf-eating insects

By **Jon Ågren**

Floral traits, including flower shape, color, nectar, and scent, affect pollination success and mating systems by influencing attractiveness to pollinators and efficiency of cross- and self-pollination. Traditionally, the evolution and maintenance of differences in these traits have been related to selective pressures imposed by pollinators, and pollen and mate limitation. Recent years have seen increasing evidence that antagonists such as grazers and seed predators also mediate selection on floral traits (*1*–*4*). On page 193 of this issue, Ramos and Schiestl (*5*) show that both pollinators and herbivores influence the evolution of floral display and of self-pollination efficiency and that their effects are not necessarily additive. The study provides a proof-of-concept that should inspire investigation of the interactive effects of mutualists and antagonists on the evolution of plant reproductive traits in additional systems.

There are several reasons why the evolution of floral display and efficiency of autonomous self-pollination might be affected by plant interactions with both pollinators and herbivores. For example, a prominent floral display may increase at-

Department of Ecology and Genetics, Evolutionary Biology Centre (EBC), Uppsala University, Uppsala, Sweden. Email: jon.agren@ebc.uu.se

PHOTO: ARCO IMAGES GMBH/ALAMY STOCK PHOTO

Selection mediated by both pollinators and herbivores affects the evolution of floral traits.

tractiveness to pollinators, but at the same time increase the risk of damage from herbivores. Optimal floral display will then be affected by the relative strength of these effects and their consequences for plant fitness (*6*). Moreover, because damage from herbivores can reduce attractiveness to pollinators, interactions with herbivores may influence the degree of pollen limitation and selection on traits affecting the ability to produce offspring through autonomous self-pollination (*2*). In addition, evolutionary response will depend not only on the strength and direction of selection, but also on the presence of genetic variation and genetically based correlations among traits.

Experimental evolution is a powerful approach to examine how environmental conditions affect evolutionary trajectories. Ramos and Schiestl combined pollination and herbivory treatments to determine their independent and interactive effects on the evolution of floral traits. A rapid-cycling population of the annual plant *Brassica rapa* evolved under one of four treatment combinations: hand-pollination with or without herbivory, and bee pollination with or without herbivory. In two treatment combinations, pollination by hand ensured that flowers received a surplus of pollen, whereas in the other two, bumble bees determined the pollination success of individual plants. As predicted, selection by bumble bees resulted in the evolution of plant phenotypes that were more attractive to bumble bees. This effect was reduced when plants evolved in the presence of both bumble bees and leaf herbivores (caterpillars of the butterfly *Pieris brassicae*). The observations are consistent with the idea that plant traits that influence attractiveness to pollinators may be subject to conflicting selection from herbivores. In addition, plants pollinated by bumble bees, which were presumably more strongly pollen-limited than were plants pollinated by hand, tended to evolve greater ability to produce offspring through autonomous self-pollination.

More unexpectedly, the presence of herbivores was associated with an increased efficiency of autonomous self-pollination also among plants pollinated by hand. This cannot be explained by an effect of herbivores on pollen limitation. Instead, Ramos and Schiestl suggest that this is the result of genetic correlations between traits affecting resistance to herbivory and floral traits affecting efficiency of autonomous self-pollination. This hypothesis could be tested by artificial selection (selective breeding) on these traits.

The experimental treatments were applied for six generations, which was sufficient for selection lines to diverge in several traits. One reason is that the population of *B. rapa* used in the study is genetically highly variable. The population was established through crosses between early-flowering genotypes and many generations of selection for early flowering, rapid seed maturation, absence of seed dormancy, small plant size, and high female fertility (*7*). Despite its history of long-term artificial selection, the population has maintained considerable genetic variation and has been used to examine the genetic basis of a wide range of traits and constraints to adaptive evolution [for example, (*8*, *9*)].

Future studies should examine how frequently and how rapidly evolutionary trajectories of natural plant populations are affected by changes in pollination regime and herbivore abundance. This should depend on the strength of selection by pollinators and herbivores and the importance of indirect and nonadditive effects (*10*, *11*). It will also depend on available genetic variation in traits subject to selection. Do natural populations harbor genetic variation that allows them to adapt rapidly to changes in pollination regime and abundance of herbivores? The extent to which adaptive evolution is constrained by genetic correlations among traits affecting these interactions is also unclear. Such investigations should improve predictions of the evolutionary response of plant populations to global environmental change, which involves strong effects on biotic interactions in a wide range of systems. ■

REFERENCES AND NOTES

1. S. Y. Strauss, J. B. Whittall, in *Ecology and Evolution of Flowers*, L. D. Harder, S. C. H. Barrett, Eds. (Oxford Univ. Press, 2006), pp. 120–138.
2. M. T. J. Johnson, S. S. Campbell, S. C. H. Barrett, *Annu. Rev. Ecol. Evol. Syst.* **46**, 191 (2015).
3. N. Sletvold, K. K. Moritz, J. Ågren, *Ecology* **96**, 214 (2015).
4. J. S. Santangelo, K. A. Thompson, M. T. J. Johnson, *J. Evol. Biol.* **32**, 4 (2019).
5. S. E. Ramos, F. P. Schiestl, *Science* **364**, 193 (2019).
6. J. Ågren, F. Hellström, P. Toräng, J. Ehrlén, *Proc. Natl. Acad. Sci. U.S.A.* **110**, 18202 (2013).
7. P. H. Williams, C. B. Hill, *Science* **232**, 1385 (1986).
8. P. Zu, W. U. Blanckenhorn, F. P. Schiestl, *New Phytol.* **209**, 1208 (2016).
9. S. J. Franks *et al.*, *Int. J. Plant Sci.* **179**, 175 (2018).
10. P. R. Guimarães Jr., M. M. Pires, P. Jordano, J. Bascompte, J. N. Thompson, *Nature* **550**, 511 (2017).
11. M. Thomann, J. Ehrlén, J. Ågren, *Ecology* **99**, 2167 (2018).

ACKNOWLEDGMENTS

This work was financially supported by the Swedish Research Council and Formas.

10.1126/science.aax1656

EVOLUTION

Lost in the fire

Thyroid hormones tip the balance between regeneration and temperature regulation

By **Silvia Marchianò**[1,2,3] *and* **Charles E. Murry**[1,2,3,4,5]

Like all mammals studied, humans are born with considerable regenerative capacity, but for unknown reasons, this is lost in early childhood (*1*). For example, in adulthood, human hearts and brains have minimal ability to regenerate after injury, and age-associated diseases of cell deficiency are major causes of human death. By contrast, amphibians, fish, and invertebrates can regenerate throughout their lives (*2*). This comparative biology has captivated researchers, who hope that understanding natural regeneration might lead to clinical treatments, such as for heart disease (*2*). On page 184 of this issue, Hirose *et al.* (*3*) identify thyroid hormone as a culprit in preventing mammalian heart regeneration. By comparing multiple mammalian species, they propose that regeneration was lost as a trade-off for the ability to regulate body temperature (endothermy).

Natural heart regeneration involves the division of preexisting cardiac muscle cells (cardiomyocytes), rather than the generation of new muscle from stem cells (*4*, *5*). As the mammalian heart matures postnatally (first week in mice and first decade in humans), cardiomyocytes undergo a final round of DNA synthesis with no cell division (*6*). Most adult cardiomyocytes, therefore, have multiple copies of the genome (polyploid), with only a minority remaining diploid (containing a single copy of the genome) (*7*). By contrast, cardiomyocytes of regenerative animals are almost entirely diploid (*8*). Diploid cardiomyocytes divide more frequently, whereas polyploidy inhibits regeneration (*8*, *9*). Thus, logical questions are what causes

[1]*Department of Pathology, University of Washington, 850 Republican Street, Seattle, WA 98109, USA.* [2]*Center for Cardiovascular Biology, University of Washington, 850 Republican Street, Brotman Building, Seattle, WA 98109, USA.* [3]*Institute for Stem Cell and Regenerative Medicine, University of Washington, 850 Republican Street, Seattle, WA 98109, USA.* [4]*Department of Medicine and Cardiology, 1959 NE Pacific Street, University of Washington, Seattle, WA 98195, USA.* [5]*Department of Bioengineering, University of Washington, 3720 15th Avenue NE, Seattle, WA 98105, USA. Email: murry@uw.edu*

polyploidy and can it be manipulated to allow regeneration?

Hirose *et al.* tackled these questions by evaluating the percentage of diploid cardiomyocytes across 41 species. Adult fish, amphibians, and reptiles are mostly (77 to 98%) diploid. Notably, there is a wide range in mammals: Bowhead whales possess 34 to 59% diploid cardiomyocytes, whereas humans have only 4% diploid cardiomyocytes. When correlating the frequency of diploid cardiomyocytes with multiple biometric parameters, they found that ploidy is independent of body weight, heart rate, and blood pressure but strongly correlates with body temperature.

Endothermy, the ability to regulate body temperature within a narrow range, is restricted to birds and mammals (and some species of fish). Amphibians, reptiles, and most fish are ectothermic, meaning that their body temperature is dependent on the environment. As a result, the metabolic rates of ectothermic animals are an order of magnitude less than in endotherms (*10*). In mammals, within minutes of birth, the cold temperature of the environment activates thermogenesis, increasing heat production and metabolic rate to maintain a constant body temperature (*11*). Hirose *et al.* found that as temperature and metabolic rate increase, there is a linear decrease in the numbers of diploid cardiomyocytes. This suggests that there is a mechanistic link between metabolic rate and cardiac regeneration.

Thyroid hormones are important regulators of metabolism and development, and they are thought to drive acquisition of endothermy during development (*12*). Indeed, ectothermic animals exhibit lower concentrations of thyroid hormone compared with endothermic animals. Moreover, soon after birth, the amount of circulating thyroid hormone in neonatal mice increases up to 50-fold (*13*). Hirose *et al.* demonstrated that impairing thyroid hormone signaling by either pharmacological inhibition or gene-editing approaches caused an increase in diploid cardiomyocytes from 9 to 30% in mice at postnatal day 14. Moreover, blocking thyroid signaling increased cardiomyocyte proliferative rates, such that the hearts of these mice were 37% larger than controls and contained around twice as many cardiomyocytes.

The increased regenerative capacity of the gene-edited mice was demonstrated by inducing a myocardial injury in the adult mice. At 28 days postinjury, these mice exhibited a 10-fold increase in proliferating mononucleated and diploid cardiomyocytes, associated with a 62% reduction of scar area and 11% improvement in cardiac function. Hirose *et al.* also demonstrated that thyroid signaling could inhibit natural heart regeneration in zebrafish. Administering thyroid hormone to zebrafish with injured hearts increased cardiomyocyte polyploidy by fivefold, accompanied by a 45% reduction in proliferation, impaired regeneration, and healing by scar formation.

The study of Hirose *et al.* establishes the role of thyroid hormone as an important regulator of cardiomyocyte ploidy and regenerative capacity across the animal kingdom (see the figure). These results agree with previous studies in human pluripotent stem cell–derived cardiomyocytes, in which treatment with thyroid hormone reduced cardiomyocytes' cell-cycle activity (*14*). However, manipulating the amount of thyroid hormone as a clinical approach to improve cardiac regeneration is challenging. Indeed, low concentrations of circulating thyroid hormones (hypothyroidism), due to thyroid gland dysfunction, alter cardiac gene expression and increase vascular resistance, both resulting in reduced cardiac performance. Moreover, failing hearts may be functionally hypothyroid, owing to impaired local signaling. Thus, thyroid hormone supplementation has been proposed as a treatment for heart failure patients (*15*). This emphasizes the need for a more detailed understanding of how thyroid signaling regulates regenerative capacity. It will be interesting to evaluate the regenerative capacity of mature cardiomyocytes in which thyroid hormone signaling is impaired in adulthood.

Regenerative capacity in the animal kingdom

Endotherms gained thyroid signals over the course of evolution and became thermogenic, perhaps in a trade-off with regeneration capacity.

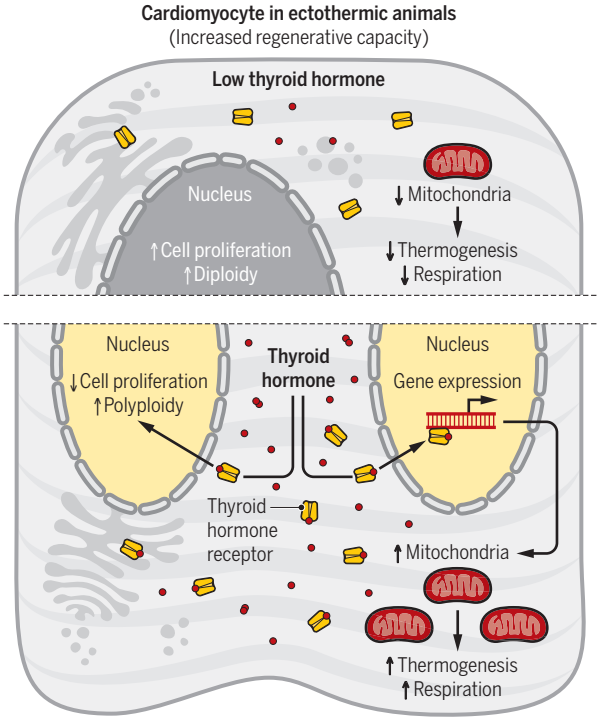

Frogs, whose metamorphosis requires a transient increase in thyroid hormones, are still capable of heart and skin regeneration, but not of limb or spinal cord. Humans, by contrast, can regenerate part of the liver and the skin but not other organs (including the heart). Hirose *et al.* demonstrate that, although thyroid hormone inhibits regeneration in zebrafish hearts, it does not limit their fin regeneration, demonstrating tissue specificity. Further experiments to understand differences among different organs and different species may give new insight into regenerative capacity.

Why is regeneration lost in adult mammalian hearts? Hirose *et al.* suggest that the loss of regenerative capacity represents a trade-off for acquisition of endothermy. But it is not clear why endothermy should be incompatible with regeneration. Endothermy allows for faster and more constant biochemical flux rates, and this has allowed humanity to spread over a wide geographical distribution. Does the capacity to regenerate somehow reduce cardiac fitness? Identifying pathways, other than thyroid hormones, that are "extinguished" by evolution could lead to the discovery of new targets to promote tissue regeneration. ■

REFERENCES AND NOTES

1. M. H. Yun, *Int. J. Mol. Sci.* **16**, 25392 (2015).
2. A. E. Bely, K. G. Nyberg, *Trends Ecol. Evol.* **25**, 161 (2010).
3. K. Hirose *et al.*, *Science* **364**, 184 (2019).
4. K. R. Chien *et al.*, *Nat. Biotechnol.* **37**, 232 (2019).
5. S. E. Senyo *et al.*, *Nature* **493**, 433 (2013).
6. P. Ahuja, P. Sdek, W. R. MacLellan, *Physiol. Rev.* **87**, 521 (2007).
7. G. Olivetti *et al.*, *J. Mol. Cell. Cardiol.* **28**, 1463 (1996).
8. J. M. González-Rosa *et al.*, *Dev. Cell* **44**, 433 (2018).
9. M. Patterson *et al.*, *Nat. Genet.* **49**, 1346 (2017).
10. B. B. Lowell, B. M. Spiegelman, *Nature* **404**, 652 (2000).
11. H. Asakura *et al.*, *J. Nippon Med. Sch.* **6**, 360 (2005).
12. E. P. M. Broeders *et al.*, *PLOS ONE* **11**, e0145049 (2016).
13. R. Janssen *et al.*, *Eur. Thyroid J.* **6**, 130 (2017).
14. X. Yang *et al.*, *J. Mol. Cell. Cardiol.* **72**, 296 (2014).
15. C. Vale *et al.*, *Cardiovasc. Drugs Ther.* 10.1007/s10557-019-06870-4 (2019).

ACKNOWLEDGMENTS

C.E.M. is supported by NIH grants R01HL084642, R01HL128362, R01 HL128368, R01 HL141570, and U01HL100405 and a grant from the Fondation Leducq Transatlantic Networks of Excellence. C.E.M. is a scientific founder and equity holder in Cytocardia.

10.1126/science.aax1006

GRAPHIC: A. KITTERMAN/*SCIENCE*

GRAPHENE

An exotic quantum fluid in graphene

Under the right conditions, electrons can move as fluids in graphene

By **Andrew Lucas**

Liquids such as water lack rigid shape, can move around obstacles, and exert forces during their collective flow. However, these conventional liquids are only one of a vast array of fluids. One such fluid, postulated many decades ago (*1*) but only observed relatively recently (*2*–*5*), arises when electrons in a conducting material begin to interact strongly with one another. This quantum fluid of electrons flows on scales a hundred times shorter than the width of a human hair, yet can flow just like water. On pages 162 and 158 of this issue, Berdyugin *et al.* (*6*) and Gallagher *et al.* (*7*), respectively, present experimental evidence for a two-dimensional fluid of electrons in graphene, a membrane of carbon atoms just one atom thick. The experiments uncover quantum kinds of fluid flows that cannot be observed in water. The results may lead to new kinds of quantum materials and electronics.

Graphene can be charged with a few extra electrons by applying a local voltage, analogous to charging one side of a capacitor. The added electrons can easily move from one atom to the next. At low temperatures, these electrons effectively move past each other because of quantum effects, but at higher temperatures, the electrons begin to scatter off each other. Two electrons bounce off each other in a very different way than two water molecules. Yet because energy, momentum, and electric charge (analogous to molecule number) are conserved in every collision, the resulting fluid of electrons should flow in much the same way as water does.

However, there is one crucial complication. Unlike water molecules, the electrons have to flow in between an array of ions. If the electrons scatter off an ionic impurity or a vibration of the ionic lattice, they lose momentum and no longer flow like a conventional liquid (see the figure). In ordinary metals, the electron-lattice scattering is so strong that the analogy with water fails completely. It is only because of advances in materials science that scientists can make quantum materials where mobile electrons scatter off each other sufficiently fast to form a fluid. Graphene is one such material.

Department of Physics, Stanford University, Stanford, CA 94305, USA. Email: ajlucas@stanford.edu

Berdyugin *et al.* studied the electron fluid in graphene in the presence of a magnetic field that they applied perpendicular to the graphene atomic layer. Because the magnetic field prefers to swirl all mobile charged electrons in the same way (for example, clockwise), parity symmetry is broken. Two-dimensional parity-violating fluids, whether they are made up of thin films of large chiral molecules or of small quantum electrons in a magnetic field, have a Hall viscosity (*8*).

To understand the effects of Hall viscosity, consider a viscous fluid flowing over a rigid surface. Ordinary shear viscosity tries to pull the surface along with the fluid flow, whereas Hall viscosity tries to pull the surface into or out of the flow. By probing how the electron fluid flows from one point to another in a varying temperature and magnetic field, Berdyugin *et al.* found evidence that the magnetic field induces a Hall viscosity in the graphene electron fluid, in agreement with theoretical predictions (*9*). Their study is a clear demonstration of this unusual phenomenon in fluid dynamics.

Quantum flows made from hops

Reports by Berdyugin *et al.* and Gallagher *et al.* show how charge carriers in graphene act as liquids.

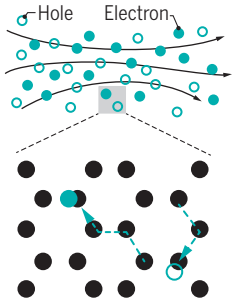

◀ **Seemingly continuous** On macroscopic length scales, the electron-hole plasma in graphene would appear to flow as a continuous, collective fluid of positively charged "holes" and negatively charged electrons.

▲ **Hopping along** At the scale of the graphene lattice, depicted as solid black carbon atoms, the electrons and holes hop in a discrete fashion and obey the laws of quantum mechanics.

Because of the peculiar quantum physics of graphene, an electron fluid exists even if all excess electrons are removed. At finite temperatures, the collective electronic system contains some extra energy that can excite some electrons out of their valence states to become mobile, conducting electrons. However, this excitation creates some atoms that are missing an electron, and these missing electrons appear to move as positively charged objects, or holes.

In graphene, the electrons and holes form a plasma that obeys equations similar to those for relativistic plasmas of hot quarks and gluons. Gallagher *et al.* have investigated this electron-hole plasma by studying its interplay with light. They confirmed existing theoretical predictions (*10*) and found an enhancement of electronic scattering relative to electron-lattice scattering, as was necessary for the fluid to emerge at all. They also confirmed that electronic scattering rates follow quantum critical behavior, just as do many "strange metals" that are non-Fermi liquids (*11*), with scattering rates set by the temperature and by fundamental constants of nature.

In the future, electronic fluids may be engineered to create thermoelectric materials, which efficiently convert electrical currents to heat currents (and vice versa) (*10*), to create excellent mesoscopic conductors (*5*), or to generate and detect terahertz radiation (*12*), a long-standing challenge in applied physics with many industrial applications. Unlike graphene, the more complicated structures and symmetries of crystals may give rise to new kinds of fluids, with new kinds of viscosity and unexpected patterns of fluid flow. Further, the rapid scattering rate of the electron-hole plasma in graphene suggests a connection with the physics of other strongly interacting quantum materials (*11*). Whether building industrial electronics on the micrometer scale or answering fundamental questions in condensed-matter physics, researchers at the interplay of fluid dynamics, quantum condensed-matter physics, and materials science will likely have their hands full for many years to come as they address these questions. ■

REFERENCES AND NOTES

1. R. N. Gurzhi, *Sov. Phys. JETP* **17**, 521 (1963).
2. M. J. M. De Jong, L. W. Molenkamp, *Phys. Rev. B* **51**, 11389 (1995).
3. D. A. Bandurin *et al.*, *Science* **351**, 1055 (2016).
4. J. Crossno *et al.*, *Science* **351**, 1058 (2016).
5. R. Krishna Kumar *et al.*, *Nat. Phys.* **13**, 1182 (2017).
6. A. I. Berdyugin *et al.*, *Science* **364**, 162 (2019).
7. P. Gallagher *et al.*, *Science* **364**, 158 (2019).
8. J. Avron, *J. Stat. Phys.* **92**, 543 (1998).
9. F. M. D. Pellegrino *et al.*, *Phys. Rev. B* **96**, 195401 (2016).
10. S. A. Hartnoll *et al.*, *Phys. Rev. B* **76**, 144502 (2007).
11. J. A. N. Bruin, H. Sakai, R. S. Perry, A. P. Mackenzie, *Science* **339**, 804 (2013).
12. M. Dyakonov, M. Shur, *Phys. Rev. Lett.* **71**, 2465 (1993).

ACKNOWLEDGMENTS

I am supported by the Gordon and Betty Moore Foundation through grant GBMF4302.

10.1126/science.aaw9869

GRAPHIC: V. ALTOUNIAN/SCIENCE

GEOSCIENCE

Plate tectonics, carbon, and climate

Enhanced weathering of uplifted rocks in the tropics may have driven past glaciations

By **Jens Hartmann**

Over the past 541 million years (the Phanerozoic eon), Earth's climate has been relatively stable compared to preceding eons. However, there have been periods of longer glaciations, which have been attributed to changes in the balance between CO_2 sources and sinks. The major CO_2 sources are thought to be mantle degassing at hotspot volcanoes, mid-ocean ridges, and rifts; subduction zone volcanoes; metamorphosis of carbonate rocks into silicate rocks; and oxidative weathering (see the figure) (*1*). The main CO_2 sink is chemical weathering and the subsequent transfer of carbon to the ocean, where carbonate sediments lock up CO_2 for long periods of time. During arc-continent collisions, rocks from volcanic arcs are accreted to continents. On page 181 of this issue, Macdonald *et al.* (*2*) propose that weathering can rise after the accreted rocks are exposed at Earth's surface. This mechanism may explain the glaciations seen during the Phanerozoic.

More specifically, the authors study ophiolite complexes, which are sections of oceanic crust and the upper mantle that have been uplifted and are exposed above sea level. They hypothesize that if these ophiolite complexes are exhumed (exposed at Earth's surface) in the intertropical zone, where precipitation rates are high, they weather faster, resulting in enhanced CO_2 consumption and shifting the balance between sources and sinks of CO_2 toward the sink side. If the resulting greenhouse gas reduction is substantial, it might cool the climate and cause glaciations.

Through detailed mapping of exhumed ophiolites at sutures (areas where tectonic plates merge) and reconstruction of their past location, Macdonald *et al.* show that the presence of exhumed ophiolite areas in the intertropical zone correlates with the four Phanerozoic glaciation periods in the Late Ordovician (455 to 440 million years ago), the Late Devonian (~360 million years ago), the Carboniferous-Permian (335 to 280 million years ago), and the Cenozoic time (the past ~35 million years). The results may be used in model and isotope studies to test the above hypothesis.

The authors' interpretations are based on a strong observed correlation between plate tectonic processes, paleogeography, and periods of colder and warmer climate. However, numerous processes modify global climate, and various problems must be solved before this hypothesis can be tested with Earth system models that predict weathering fluxes and CO_2 sources.

It is challenging to reconstruct the balance between CO_2 sources and sinks even for the modern era. Recent global inventories of CO_2 degassing from the mantle, subduction zones, and metamorphic sources show a high variability based on upscaling assumptions (*3*). Today, most degassed CO_2 seems to be recycled CO_2 from mantle sources, but the ratio may have been different in the past (*1*). Comparison of different studies shows that solid Earth degassing budgets still have large uncertainties (*3*, *4*).

Analysis of current weathering fluxes in areas where weathering is particularly high suggest that a small area of Earth's surface is responsible for most CO_2 consumption through weathering (*5*). Performing similar analyses for past time periods will only be possible if the size and past geographic location of areas with mafic silicate rock, which have high CO_2-sequestration potential (*5*), can be reconstructed in more detail. This will be challenging, particularly because the time since exhumation and the freshness of the surface as a result of erosive processes affect the weathering intensity and CO_2-consumption rate (*6*).

In addition, weathering releases geogenic (rock-derived) nutrients that may affect the terrestrial and marine biogeochemical carbon pump. Lenton *et al.* recently modeled this effect for phosphorus (*7*). Such an indirect effect of enhanced weathering on the biological carbon sink might add to the temporarily enhanced CO_2 sequestration.

Scientists have typically interpreted relatively high values of marine isotope proxies of weathering ($^{87}Sr/^{86}Sr$, $^{187}Os/^{188}Os$, and δ^7Li), particularly during the Cenozoic (the past 66 million years), as indicating enhanced weath-

Department of Geosciences, Center for Earth System Research and Sustainability (CEN), University of Hamburg, Hamburg, Germany. Email: geo@hattes.de

Geological sources and sinks of CO_2

Solar radiation, as well as the differences between sinks and sources of CO_2, contributes to the state of the climate. If a sink term, such as weathering of ophiolite complexes, increases, the system shifts to lower atmospheric CO_2 concentrations. This may lead to a period of cooling with glaciations.

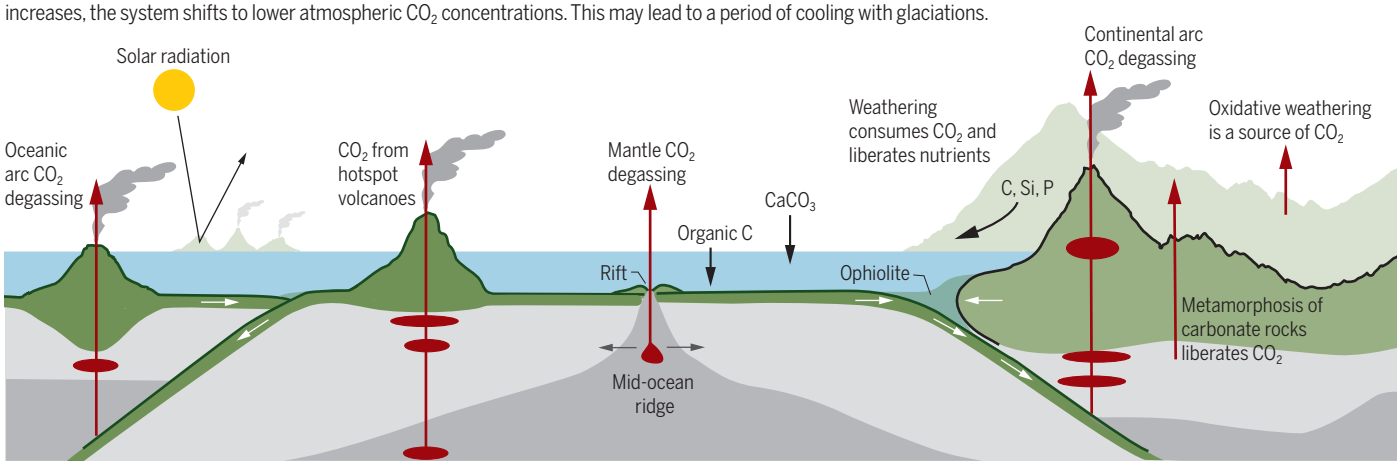

GRAPHIC: N. CARY/SCIENCE

ering of felsic continental crust (which is relatively rich in quartz and feldspar) rather than an increased mafic rock contribution (*8*). Reconciling the interpretations of these isotope records with Macdonald *et al.*'s record of tropical ophiolite exposure will help to elucidate the connection between climate, erosion, and weathering.

Future studies should test whether the findings are typical only for the Phanerozoic or also for the preceding eons. For example, if the convecting mantle is the main reservoir for CO_2 that newly enters Earth's surface-lithosphere-system, because most subducted carbon is not recycled back (*9*) and is incorporated into the lithosphere in the long term (*9*, *10*), then the mantle degassing rate might also decrease in the long term as the reservoir becomes depleted. This effect may be balanced by the long-term increase in solar radiation.

Advances in reconstructing paleogeographic settings, particularly subduction zones (*11*), may help to determine whether Macdonald *et al.*'s hypothesis is also relevant for previous glaciation periods, like those during the Neoproterozoic (1000 to 541 million years ago). In this case, further processes may also be considered, such as extensive ridge volcanism (*12*) or decreasing solid Earth degassing before the Neoproterozoic glaciations (715 to 595 million years ago) (*13*).

Researchers should also aim to reconstruct metamorphic and recycled CO_2 and its dynamics (*1*), because this source of CO_2 is a counterpart to the enhanced weathering of mafic rocks. Reconstructions of paleogeographic features such as those conducted by Macdonald *et al.* and others allow direct comparisons between observations related to CO_2 sinks and sources with long-term climate variability, and future improvements will trigger new modeling efforts to understand these observations. ■

REFERENCES AND NOTES

1. C.-T. A. Lee, J. S. Lackey, *Elements* **11**, 125 (2015).
2. F. A. Mcdonald *et al.*, *Science* **364**, 181 (2019).
3. M. R. Burton, G. M. Sawyer, D. Granieri, *Rev. Mineral. Geochem.* **75**, 323 (2013).
4. N.-A. Mörner, G. Etiope, *Global Planet. Change* **33**, 185 (2002).
5. J. Hartmann, N. Jansen, H. H. Dürr, S. Kempe, P. Kohler, *Global Planet. Change* **69**, 185 (2009).
6. A. J. West, *Geology* **40**, 811 (2012).
7. T. M. Lenton, S. J. Daines, B. J. W. Mills, *Earth Sci. Rev.* **178**, 1 (2018).
8. G. Li, H. Elderfield, *Geochim. Cosmochim. Acta* **103**, 11 (2013).
9. P. B. Kelemen, C. E. Manning, *Proc. Natl. Acad. Sci. U.S.A.* **112**, E3997 (2015).
10. J. M. Hayes, J. R. Waldbauer, *Philos. Trans. R. Soc. B Biol. Sci.* **361**, 931 (2006).
11. A. S. Merdith *et al.*, *Gondwana Res.* **50**, 84 (2017).
12. T. M. Gernon, T. K. Hincks, T. Tyrrell, E. J. Rohling, M. R. Palmer, *Nat. Geosci.* **9**, 242 (2016).
13. J. Hartmann, G. Li, A. J. West, *Geochem. Perspect. Lett.* **4**, 41 (2017).

ACKNOWLEDGMENTS

I thank J. C. Rugenstein for comments.

10.1126/science.aax1657

PHOTO: NASA/ROSCOSMOS/FLICKR/CC BY-NC-ND

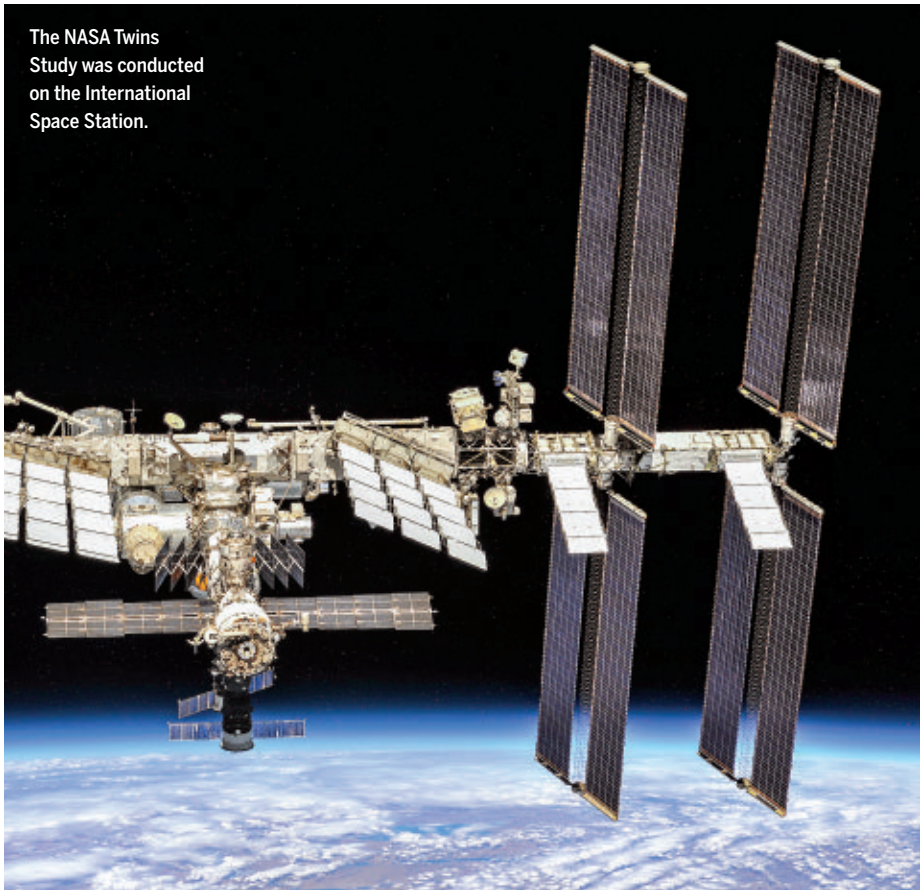

The NASA Twins Study was conducted on the International Space Station.

PHYSIOLOGY

Hazards of human spaceflight

A 1-year mission in space has many biological consequences

By **Markus Löbrich**[1] *and* **Penny A. Jeggo**[2]

In Einstein's famous twin paradox, the effect of special relativity causes aging to slow in one twin during travel in a high-speed rocket through space while the body of the Earth-bound twin undergoes the same wear and tear that all humans experience on Earth (*1*). However, real space travels present far more realistic challenges that can potentially compromise the health of the more adventurous twin. On page 144 of this issue, Garrett-Bakelman *et al.* (*2*) investigate the manifold biological consequences of a journey in space endured by an astronaut during a 1-year mission onboard the International Space Station (ISS) compared with his identical twin on Earth. The challenges encountered in space include noise, isolation, hypoxia, and disrupted circadian rhythm (body clock). Furthermore, exposure to ionizing radiation (IR) and weightlessness, also called microgravity, could cause important health risks.

IR is an omnipresent threat to human life because it can damage the integrity of important biomolecules, first and foremost the genetic information stored within our DNA. IR derives from radioactive material inside Earth, solar flares, and cosmic rays from outside the Solar System. Cosmic ionizing radiation comprises high-energy charged particles that are deflected and stopped by Earth's magnetic field and its atmosphere, effectively protecting us from excessive IR exposure. However, the IR load increases when we leave the shielded Earth, more so the further away we travel. Furthermore, surface gravity has shaped life on Earth, and most, if not all, physi-

[1]*Radiation Biology and DNA Repair, Darmstadt University of Technology, 64287 Darmstadt, Germany.* [2]*Genome Damage and Stability Centre, School of Life Sciences, University of Sussex, Brighton BN1 9RQ, UK. Email: lobrich@bio.tu-darmstadt.de; p.a.jeggo@sussex.ac.uk*

ological processes have adapted to it. It is, therefore, easy to envisage that weightlessness can have consequences for space travelers.

The largely unknown risks imposed by microgravity and IR exposure during spaceflight are currently limiting endeavors to visit Mars, warranting intensive research dedicated to their effects on astronauts. The ISS represents an ideal test bed to study long-term effects of weightlessness and increased IR exposure. Although the ISS orbits Earth relatively closely (~400 km from Earth's surface), its high speed and the concomitant centrifugal force counteract Earth's gravity, creating a weightless environment. The study by Garrett-Bakelman *et al.* followed an astronaut before, during, and after a 1-year stay at the ISS, the time approximately required for a return journey to Mars. The beauty of this study is the availability of an identical twin, serving as the perfect genetic control on Earth. Although the findings reflect the biological response of human beings with a particular genetic composition—that of the identical twins—and might differ for other astronauts, the availability of a genetic control minimizes false-positive results. Another strength of the study is the comprehensive biological analysis coupled with physiological and cognitive tests over the expected time frame needed to reach Mars, providing an unprecedented source of information. Biological samples were extensively monitored by state-of-the art techniques, including "-omics" approaches that identify global changes in gene or protein expression and connect them to the activation of particular stress response pathways.

The findings reveal many molecular, physiological, and behavioral changes induced by the space environment (see the figure), which Garrett-Bakelman *et al.* classified into low-risk, mid-level risk, and high-risk groups. The low-risk category included changes in the gastrointestinal microbiome and in body mass, whereas the mid-level risk category included alterations in collagen regulation and intravascular fluid management. Genomic instability, assessed by chromosomal aberrations, was placed into the potentially higher-risk group because it confers a risk of developing cancer. The structural abnormalities observed in the chromosomes of the traveling twin are typical of IR exposure (*3*). In particular, inversions of chromosomal fragments likely result from the space-specific charged particles and arose at a frequency consistent with the encountered radiation dose of 146 millisieverts (mSv) (a measure for the biological effectiveness of radiation), which is equivalent to 50 years of natural background radiation on Earth (*4*). Chromosome translocations, although observed previously in astronauts (*5*), arose with unexpectedly high frequency before declining postflight. Furthermore, telomeres—repetitive sequences that protect chromosome ends—predominantly became lengthened during the flight, but a few were shortened. Although largely returning to normal length postflight, critically short or lost telomeres persisted, a known consequence of exposure to charged particles (*6*). The expression of DNA repair genes remained up-regulated in the traveling twin postflight, reflecting the presence of persistent chromosomal damage.

Other severe biological effects could relate to microgravity, causing a headward fluid shift and pronounced changes in the vascular physiology, with distended arteries and veins in the upper body (*7*). The traveling twin showed increased carotid artery distension and thickening of the two innermost layers of the carotid wall, potentially representing early changes associated with cardiovascular and cerebrovascular diseases. He also exhibited abnormalities in the retinal vasculature, with choroid thickening and increased choroidal folding, features potentially compromising vision (*8*). Evaluations of the cognitive capacity of the traveling twin did not show major deficits during space travel but revealed significant diminutions postflight. Although impacts of microgravity on brain physiology have been reported, space-relevant IR exposure can affect cognition and neuronal circuit excitability in mice (*9*, *10*).

The observed effects reported by Garrett-Bakelman *et al.* are arguably broader and more pronounced than might have been expected, particularly for the more IR-specific responses such as genomic instability, persistently up-regulated expression of DNA damage response genes, and cognitive function decline. But the more microgravity-specific alterations in the neuro-ocular system and severe vascular physiology changes could also potentially couple with the known impact of IR on cataract formation and cardiovascular diseases. Both pathologies are known to arise at significant rates in people who have been exposed to IR doses above ~500 mSv (*11*). Such exposure levels, although not encountered during the 1-year ISS flight, will be received during travel to Mars, where the dose rate exceeds that on the ISS by about fivefold, and total dose estimates range up to 1000 mSv (*12*). Consequently, during Mars travel, the spectrum of biological effects will shift, placing more weight on IR-induced effects and those reacting synergistically with the microgravity responses. To understand the details of such shifts and their long-term consequences will be important for future studies and the development of countermeasures. Undoubtedly, the study by Garrett-Bakelman *et al.* represents more than one small step for mankind in this endeavor. ■

A year in orbit

A 1-year mission aboard the International Space Station (ISS) caused multiple alterations that arose from microgravity, ionizing radiation, and other stressors. These changes likely impose health risks.

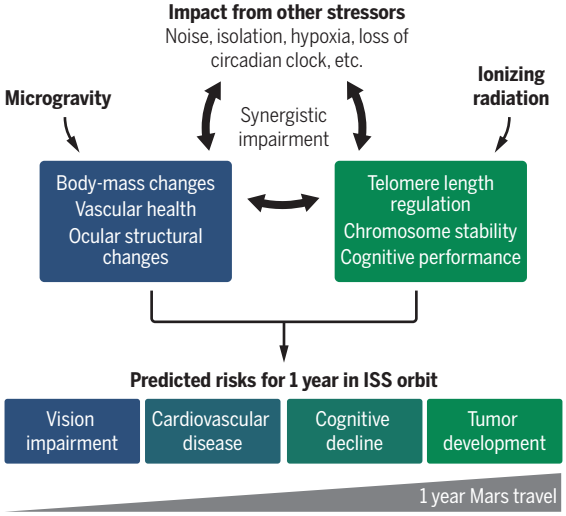

The impact of ionizing radiation will be five times greater for Mars travel.

GRAPHIC: V. ALTOUNIAN/*SCIENCE*

REFERENCES AND NOTES

1. T. A. Debs, M. L. G. Redhead, *Am. J. Phys.* **64**, 384 (1996).
2. F. E. Garrett-Bakelman *et al.*, *Science* **364**, eaau8650 (2019).
3. S. Behjati *et al.*, ICGC Prostate Group, *Nat. Commun.* **7**, 12605 (2016).
4. F. A. Ray *et al.*, *Radiat. Environ. Biophys.* **53**, 255 (2014).
5. K. George, J. Rhone, A. Beitman, F. A. Cucinotta, *Mutat. Res.* **756**, 165 (2013).
6. M. Durante, K. George, F. A. Cucinotta, *Radiat. Res.* **165**, 51 (2006).
7. P. Arbeille, R. Provost, K. Zuj, N. Vincent, *Eur. J. Appl. Physiol.* **115**, 2099 (2015).
8. R. Jandial, R. Hoshide, J. D. Waters, C. L. Limoli, *Surg. Neurol. Int.* **9**, 9 (2018).
9. D. R. Roberts *et al.*, *N. Engl. J. Med.* **377**, 1746 (2017).
10. V. K. Parihar *et al.*, *Exp. Neurol.* **305**, 44 (2018).
11. R. L. Hughson, A. Helm, M. Durante, *Nat. Rev. Cardiol.* **15**, 167 (2018).
12. F. A. Cucinotta, M. Durante, *Lancet Oncol.* **7**, 431 (2006).

ACKNOWLEDGMENTS

We thank M. Durante, C. Limoli, A. Elbakry, and J. Mirsch for comments.

10.1126/science.aaw7086

NEUROSCIENCE

Do antidepressants restore lost synapses?

Ketamine triggers changes in behavior, neuron microcircuitry, and dendritic spines

By **Anna Beyeler**

Depression is a mental illness characterized by episodes of a sad, despondent mood and/or a loss of interest or pleasure (*1*). This pathology affects nearly 20% of the population in the United States (*2*), and treatments are limited. Indeed, in the 5 years following remission, 80% of patients will endure relapse and more than 30% of patients suffer from treatment-resistant depression. Recently, the U.S. Food and Drug Administration (FDA) approved the clinical use of esketamine nasal spray for depression that is resistant to other treatments (*3*). Esketamine is an enantiomer of ketamine, a drug with antidepressant properties, although its mechanism of action remains unclear. Brain imaging studies suggest that neuronal circuitry in the medial prefrontal cortex (mPFC) is involved in the physiopathology of this disorder (*4*). On page 147 of this issue, Moda-Sava *et al.* (*5*) report that ketamine induces plasticity of dendritic spines on mPFC neurons and restores microcircuit activity and behavior in animal models of depression. This may expand therapeutic strategies for treating major depression.

Ketamine is a potent antagonist of the *N*-methyl-D-aspartate (NMDA) receptor, which is activated by the excitatory neurotransmitter glutamate. After ketamine was found to induce a trance-like state while providing pain relief and sedation, it was approved as an anesthetic by the FDA in 1970. In 2000, intravenous infusion of low doses of ketamine was discovered to have antidepressant properties (*6*). Despite such seminal studies and three clinical trials showing the benefit of esketamine nasal spray (*7*), the antidepressant mechanism has remained elusive.

Stress is a leading cause of depression and induces neural plasticity in the brain, altering multiple interdependent properties of neural circuits, including the coordination of electric activity between neurons (functional connectivity) and the number and strength of connections between neurons (synapses) (*8*). Moda-Sava *et al.* evaluated the functional connectivity within the mPFC microcircuit using single-cell two-photon calcium imaging in awake mice, based on the expression of a genetically encoded calcium sensor. To quantify the density and placement of synapses on the dendrites (spines), the authors used two-photon imaging in a mouse strain genetically engineered to express a fluorescent protein in a subset of excitatory neurons. Moda-Sava *et al.* further used a photoactivable probe to test the causal role of newly formed dendritic spines by selectively depleting them (*9*).

The study of Moda-Sava *et al.* makes a substantial breakthrough on the grounds of its longitudinal analysis of neuronal physiology, over weeks of stress (which induces symptoms of depression in mice), and after ketamine treatment. Repeated recordings of neuronal activity in the mPFC allowed the authors to identify a sequence of neural changes after ketamine treatment (by intraperitoneal injection) in experimentally stressed animals. Restoration of mPFC microcircuit functional connectivity was observed 3 to 6 hours after treatment, followed by dendritic spine restoration and formation 12 to 24 hours after ketamine administration (see the figure). The restoration of functional connectivity was concomitant with the behavioral restoration. By contrast, spine restoration and new spine formation appeared later, suggesting that they are not necessary for the short-term antidepressant effect of ketamine. However, the selective depletion of these restored and newly formed spines prevents some long-term antidepressant effects of ketamine. Thus, dendritic spine restoration and formation may be essential to sustain remission of depression-related behaviors after ketamine treatment.

Selective removal of ketamine-induced spine formation appeared to affect one type of depression-related behavior. Indeed, this ablation prevented ketamine restoration of defensive behavior during a challenge but did not alter sucrose preference restoration, a landmark of hedonic behaviors. This suggests that the mPFC plasticities control specific depression-like behaviors.

Another strength of this study is the duplication of findings in two animal models of depression-like states. These include a pharmacological approach by chronically treating mice with their principal stress hormone (corticosterone) for 3 weeks or by restraining mice daily for 3 weeks. In both model systems, similar influences of ketamine were observed on dendritic spine plasticity, and microcircuit activity in the mPFC.

Moda-Sava *et al.* provide data on the sequence of plastic changes induced by ketamine, which brings new questions. Examples include the origin of the synaptic inputs of the dendritic spines depleted during stress, as well as the origin of the synaptic inputs of the spines restored in response to ketamine. Moda-Sava *et al.* found that spine plasticity was not randomly distributed but was highly expressed in a subset of dendritic branches, suggesting that the inputs undergoing plastic changes originate from specific upstream regions in the brain. Similarly, the downstream targets of the mPFC neurons that undergo spine plasticity are unknown. Neurons from the mPFC project to different brain structures such as the dorsal raphe nucleus, the

Stress and ketamine alter dendritic spines

Dendritic spines are the site of synaptic connection with other neurons. In a stress-induced model of depression-like behaviors, spines of pyramidal neurons are depleted. Treatment with the antidepressant drug ketamine restores part of the lost spines and promotes the formation of new spines.

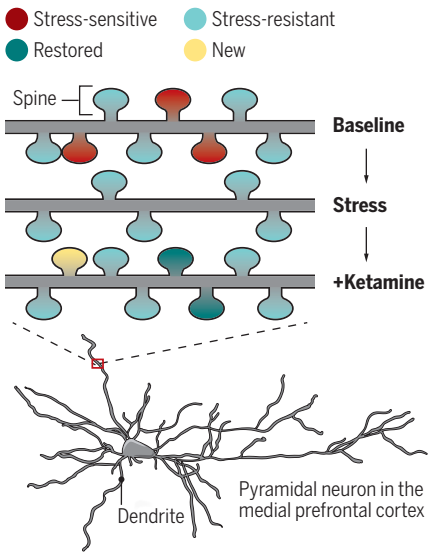

GRAPHIC: N. DESAI/SCIENCE

Neurocentre Magendie, INSERM 1215, Université de Bordeaux, 146 Rue Léo Saignat, 33000 Bordeaux, France. Email: anna.beyeler@inserm.fr

periaqueductal gray, or the nucleus accumbens, which differentially encode emotional valence or depression-like behaviors (*10–12*). Moreover, stress specifically alters dendritic spines of mPFC neurons projecting to the amygdala (*13*), which has roles in emotional responses including fear and anxiety. A recent study showed that the lateral habenula, activated by unpleasant stimuli, is necessary for the antidepressant effect of ketamine (*14*). Further analysis of spine formation and neural activity in response to ketamine within specific neuron populations of the mPFC targeting identified downstream targets might pinpoint circuit mechanisms of the drug's action.

Moda-Sava *et al.* have advanced our understanding of how ketamine can restore brain function. One concern about the use of esketamine is that although its effect on depression is apparent within hours, the drugs can have serious side effects including sedation, detachment from reality, and even addiction to the compound. Thus, the findings of Moda-Sava *et al.* are crucial not only for understanding the action of esketamine but also for the development of more innovative strategies to treat patients affected by treatment-resistant major depression (*15*). ■

"...dendritic spine restoration and formation may be essential to sustain remission of depression-related behaviors after ketamine treatment."

REFERENCES AND NOTES

1. American Psychiatric Association, *Diagnostic and Statistical Manual of Mental Disorders DSM-5* (2013).
2. R. C. Kessler, E. J. Bromet, *Annu. Rev. Public Health* **34**, 119 (2013).
3. FDA.gov, Press Announcements (2019); www.fda.gov/NewsEvents/Newsroom/PressAnnouncements/ucm632761.htm (2018).
4. H. He *et al.*, *Brain Struct. Funct.* **222**, 4051 (2017).
5. R. N. Moda-Sava *et al.*, *Science* **364**, 147 (2019).
6. R. M. Berman *et al.*, *Biol. Psychiatry* **47**, 351 (2000).
7. E. J. Daly *et al.*, *JAMA Psychiatry* **75**, 139 (2018).
8. W. Liu *et al.*, *Neural Plast.* **2017**, 6871089 (2017).
9. A. Hayashi-Takagi *et al.*, *Nature* **525**, 333 (2015).
10. J. M. Otis *et al.*, *Nature* **543**, 103 (2017).
11. C. M. Vander Weele *et al.*, *Nature* **563**, 397 (2018).
12. M. R. Warden *et al.*, *Nature* **492**, 428 (2012).
13. R. M. Shansky, C. Hamo, P. R. Hof, B. S. McEwen, J. H. Morrison, *Cereb. Cortex* **19**, 2479 (2009).
14. Y. Yang *et al.*, *Nature* **554**, 317 (2018).
15. K. D. Young *et al.*, *Psychiatry Clin. Neurosci.* **72**, 466 (2018).

ACKNOWLEDGMENTS

I thank A. Braine for help with this Perspective, and the Région Nouvelle-Aquitaine, the French NIH (INSERM), and the Brain and Behavior Research Foundation for financial support.

10.1126/science.aax0719

IMMUNOTHERAPY

Immunotherapy for neurodegeneration?

The role of innate and adaptive immunity in neurodegeneration remains controversial

By **Yingjun Liu** *and* **Adriano Aguzzi**

Alzheimer's disease (AD), Parkinson's disease (PD), and prion diseases such as Creutzfeldt-Jakob disease attack different parts of the central nervous system (CNS) and elicit distinct symptoms, yet they share many biochemical and neuropathological features. These include the formation of protein aggregates in the affected brain regions and progressive activation of non-neuronal cells in the brain that play crucial roles in immune responses. The activation of immune cells in the CNS ("neuroinflammation") is prominent in these diseases. However, it remains unclear whether boosting or suppressing the immune system, in the brain or in the periphery, may attenuate neurodegeneration. In the case of extraneural prion infections, genetic or pharmacological ablation of components of the immune system, such as B cells and complement, can prevent disease (*1*). However, immunotherapies, which have been successful in treating certain types of cancer, have yet to reverse neurodegeneration in any patients. Therefore, the therapeutic promise of this approach remains debatable.

Immunotherapy such as immune checkpoint blockade, which enhances the systemic adaptive immune response, may have potential in combating neurodegeneration, especially in AD (*2*, *3*). But recent studies have failed to observe any beneficial effects of immune checkpoint blockade in mouse models of AD (*4*) and of prion diseases (*5*, *6*), raising questions about the effectiveness of this approach. By contrast, findings from studies of human genetics and experimental models suggest that innate immunity in the brain has pivotal roles in the pathogenesis of neurodegenerative diseases. Therefore, targeting the immune reactions inside the brain may have enormous potential for treating these devastating disorders, yet a clear therapeutic path has not been discerned and well-defined, validated targets are still in demand.

Institute of Neuropathology, University of Zurich, CH-8091 Zurich, Switzerland. Email: yingjun.liu@usz.ch; adriano.aguzzi@usz.ch

The inhibition of immune checkpoint receptors, an approach to fighting cancers through boosting the adaptive immune system, has revolutionized cancer medicine (and was awarded a Nobel Prize in 2018). Immune checkpoint inhibition is mainly achieved by systemically blocking the activity of negative regulators of T cell activation, such as programmed cell death 1 (PD1), cytotoxic T lymphocyte–associated antigen 4 (CTLA4), and lymphocyte activation gene 3 (LAG3). The expression of these molecules, among others, establishes a state of immune suppression called tolerance toward cells of the body, which underlies the failure of the immune system to clear tumor cells (which are derived from cells of the body). Might systemic immune suppression contribute to the inefficient clearance of pathological protein aggregates in neurodegenerative diseases? Indeed, treatment with PD1-specific antibodies enhanced the infiltration of peripheral myeloid cells into the CNS and reduced the amount of β-amyloid (Aβ) plaques in the hippocampus and cortex (two brain regions most affected in AD) in two transgenic mouse models of AD (*2*). Moreover, LAG3 was found to facilitate the cell-to-cell spread of α-synuclein in a mouse model of PD (*7*).

Although PD1-specific antibodies are not harmless and can trigger autoimmunity, repurposing them for treating AD—an untreatable condition—could be justified. However, another study has found no effect of anti-PD1 antibody therapy on myeloid cell infiltration into the brain and Aβ load in these CNS regions in three other AD mouse models (*4*).

The brain Aβ load does not always correlate with cognitive performance, and the major determinant of cognitive decline is loss of synapses. Therefore, functional recovery tests deserve a high priority when evaluating therapeutic interventions for neurodegenerative diseases. The clearance of Aβ plaques was accompanied by recovery of cognitive performance in some of the anti-PD1 antibody–treated mouse models of AD, although effects on synapse dynamics were not studied (*2*). In other AD mouse models, however, the effects of anti-PD1 treatment on cognitive function were not investigated (*4*). Hence, the molecular underpinnings of functional recovery in

the successfully treated AD mouse models are still somewhat nebulous (see the figure).

Moreover, immune checkpoint blockade may affect cognition independently of plaque clearance. A plethora of immune modulators, including cytokines, complement components, and histocompatibility proteins, play vital roles in synapse formation, refinement, and excitability, as well as in structural and functional synaptic plasticity during development and in the adult brain (*8*). Treatment with anti-PD1 antibodies may induce the expression of these immune modulators and their entry into the CNS.

Mouse models of AD poorly represent the human condition. Could immune checkpoint blockade still hold therapeutic value for neurodegenerative diseases? Although there are limited data on how immunotherapy affects the human brain, anecdotal clinical reports yield little reason for optimism. In contrast to mouse models of AD, cognitive deterioration is frequent among patients undergoing cancer treatments, including immunotherapy. Even in preclinical animal tumor models, blocking the immune checkpoint receptor CTLA-4 (combined with radiotherapy) reduced tumor growth but resulted in cognitive impairment (*9*). In principle, because immune checkpoint blockade enhances the overall ability of the adaptive immune system to target multiple disease-associated factors, one could explore its usefulness in neurodegenerative diseases other than AD.

In prion diseases, however, targeting the immune checkpoint molecules PD1 and LAG3 did not alter prion deposition and the course of disease (*5*, *6*). Moreover, loss of PD1 did not induce myeloid mobilization to prion-infected brains (*6*). These results again suggest that PD1 inhibition may not suffice to promote the entry of peripheral myeloid cells into the CNS. Therefore, current evidence does not encourage the direct testing of immune checkpoint blockade in patients affected by neurodegenerative diseases. However, the increasing adoption of immune checkpoint inhibition against a growing variety of common cancers will enable statistically powered investigations of the effects of immunotherapy on human brain functions. Similarly, patients are increasingly subjected to anticancer immunotherapy, and some of them are likely to develop neurodegenerative diseases as they age. Analyzing the progression of disease in these patients, including neuropathological assessments of autopsied brains, may provide much-needed answers to these critical questions.

Targeting the innate arm of immunity inside the brain may hold more promise than targeting its adaptive arm through systemic immune checkpoint blockade. Genome-wide association studies of neurodegeneration have revealed correlations of neuroinflammatory genes in these diseases (*10*). Many biological processes can lead to the activation of astrocytes and microglia (non-neuronal cells in the brain), which in turn can be beneficial or deleterious. Hence, identifying specific pathways for intervention is crucial for the success of therapies targeting non-neuronal cell reactions in neurodegenerative diseases.

Progress in this area may be facilitated by the discovery of inflammasome activation in AD, PD, and other similar diseases such as amyotrophic lateral sclerosis (*11*–*13*). Inflammasomes are large complexes that play key roles in innate immune responses and in the maturation and secretion of proinflammatory cytokines such as interleukin-1β (IL-1β). An inflammasome consists of a sensor molecule, such as NLRP3 (NOD, LRR- and pyrin domain-containing 3), the adaptor protein ASC (apoptosis-associated speck-like protein containing CARD), and caspase-1, which together form a functional complex upon infection, tissue damage, or protein misfolding, such as Aβ pathologic aggregation.

In the brains of patients affected by AD and PD, the inflammasome is activated within reactive microglia (*11*, *12*). The cascade of inflammasome activation in these cells leads to the generation of ASC "specks," large assemblies of ASC protein that can self-propagate (much like prions), driving the neurotoxic inflammatory response and accelerating AD pathology by acting as seeds for further Aβ aggregation (*11*, *14*). In mouse models of AD, genetic inhibition of inflammasome activity reduces not only the Aβ load, but also proinflammatory cytokine production and cognitive impairment (*11*). Similarly, oral treatment with a small-molecule inhibitor of NLRP3 inflammasome prevented α-synuclein pathology and neurodegeneration in PD mouse models, resulting in improved motor function (*12*).

Furthermore, several nonsteroidal anti-inflammatory drugs (NSAIDs) of the fenamate class are effective inhibitors of NLRP3 inflammasome activation (*15*). Treatment with fenamates restored cognitive function in a mouse model of AD (*15*). These studies have laid a solid foundation for the clinical translation of inflammasome inhibitors and the repurposing of fenamates to treat AD and potentially other forms of neurodegeneration.

Although at first they may seem contradictory, these findings point to neuroinflammation as a driver of AD and possibly of other neurodegenerative conditions. These developments herald a paradigm shift away from the "amyloid cascade" hypothesis, which posits that in neurodegenerative diseases, pathologies stem from protein aggregation. Although nearly all therapeutic attempts are still aimed at quenching protein aggregation, it is increasingly evident that aggregation is only a part of the story. How the pathological accumulation of aggregated proteins affects innate (and perhaps adaptive) immunity, and vice versa, are likely to be addressed by future studies. Identifying the receptor, adaptor, and effector molecules involved in this cross-talk may represent the best path forward to identify therapies that are more effective than those hitherto tested. ■

Brain inflammation

Immune cells in the brain (microglia) promote inflammation and loss of neural connectivity, whereas other microglia and anti-inflammatory drugs (NSAIDs) counter this degeneration. It is not clear whether immunotherapy can stimulate the infiltration of immune cells and factors into the brain to modulate inflammation, such as in Alzheimer's disease.

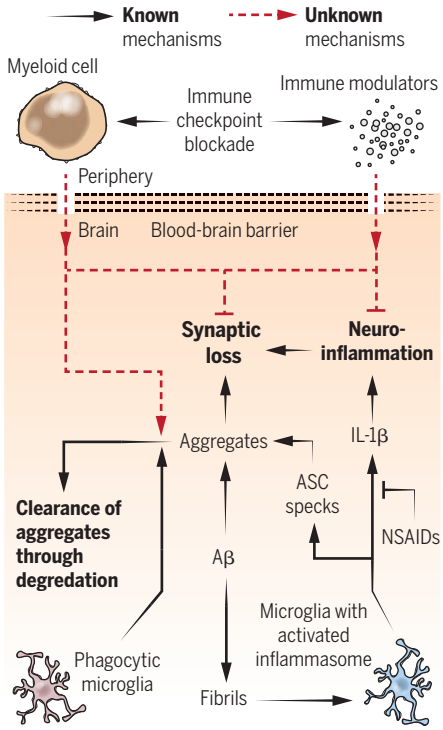

GRAPHIC: C. BICKEL/SCIENCE

REFERENCES AND NOTES

1. M. A. Klein *et al.*, *Nature* **390**, 687 (1997).
2. K. Baruch *et al.*, *Nat. Med.* **22**, 135 (2016).
3. M. Schwartz, *Science* **357**, 254 (2017).
4. M. Latta-Mahieu *et al.*, *Glia* **66**, 492 (2018).
5. Y. Liu *et al.*, *Sci. Rep.* **8**, 14600 (2018).
6. J. Obst *et al.*, *Brain Behav. Immun.* **73**, 708 (2018).
7. X. Mao *et al.*, *Science* **353**, aah3374 (2016).
8. L. M. Boulanger, *Neuron* **64**, 93 (2009).
9. G. J. McGinnis *et al.*, *Oncotarget* **8**, 9155 (2017).
10. R. Sims *et al.*, *Nat. Genet.* **49**, 1373 (2017).
11. M. T. Heneka *et al.*, *Nature* **493**, 674 (2013).
12. R. Gordon *et al.*, *Sci. Transl. Med.* **10**, eaah4066 (2018).
13. S. Johann *et al.*, *Glia* **63**, 2260 (2015).
14. C. Venegas *et al.*, *Nature* **552**, 355 (2017).
15. M. J. Daniels *et al.*, *Nat. Commun.* **7**, 12504 (2016).

ACKNOWLEDGMENTS

A. A. is supported by the European Research Council, the Swiss National Research Foundation, and the Nomis Foundation.

10.1126/science.aaw0685

Swedish student Greta Thunberg speaks at a climate demonstration at the Brandenburg Gate, Berlin, Germany, 29 March 2019.

PHOTO: MICHAEL KAPPELER/DPA/PICTURE-ALLIANCE/NEWSCOM

POLICY FORUM

CLIMATE CHANGE

Sensitive intervention points in the post-carbon transition

We must exploit socioeconomic tipping points and amplifiers

By **J. D. Farmer[1,2,3], C. Hepburn[1,4], M. C. Ives[1,4], T. Hale[5], T. Wetzer[1,6,7], P. Mealy[1,4,8], R. Rafaty[1], S. Srivastav[1,4], R. Way[1,4]**

Conventional approaches to mitigating climate change are not working. Despite the actions pledged under the 2015 Paris Agreement, actual progress is falling well short (*1*). Given limited time and resources, traditional efforts such as the climate stabilization wedge approach (*2*) are unlikely to be effective on their own. Physical science has shown how complex adaptive systems can cross critical thresholds ("tipping points") (*3*), such that a relatively small change can trigger a larger change that becomes irreversible (*4*), where nonlinear feedback effects act as amplifiers (*5*). We propose to examine how to exploit similar sensitive intervention points (SIPs) and amplification mechanisms in socioeconomic, technological, and political systems to advance climate change mitigation. We focus on research and policies in which an intervention kicks or shifts the system so that the initial change is amplified by feedback effects that deliver outsized impact.

[1]Institute for New Economic Thinking, Oxford Martin School, University of Oxford, Oxford, UK. [2]Mathematical Institute, University of Oxford, Oxford, UK. [3]Santa Fe Institute, Santa Fe, NM, USA. [4]Smith School of Enterprise and the Environment, University of Oxford, Oxford, UK. [5]Blavatnik School of Government, University of Oxford, Oxford, UK. [6]Faculty of Law, University of Oxford, Oxford, UK. [7]Oxford-Man Institute of Quantitative Finance, University of Oxford, Oxford, UK. [8]Bennett Institute for Public Policy, University of Cambridge, Cambridge, UK. Email: doyne.farmer@inet.ox.ac.uk; matthew.ives@smithschool.ox.ac.uk

SENSITIVE INTERVENTION POINTS

There are two types of SIPs. The first involves a kick to the current state of the system, moving it onto a new trajectory without any change in the underlying system dynamics. If the new trajectory diverges rapidly from the old trajectory, then a small kick at the right point can trigger a large change. A small kick can be effective when the system is chaotic or when it is near a critical point. Subsidizing renewable energy sources to lower their costs provides an example of a kick.

The second type of SIP involves a shift in the underlying system dynamics, where the rules of the system itself change and trajectories alter substantially. A shift can be effective even without a kick. In the socioeconomic-political sphere, a shift may entail a change in key concepts and institutions. For example, the shift from the rigid Kyoto regime to the more flexible (if still imperfect) Paris structure has altered the rules of the game, enabling new forms of cooperation (*6*). Although the distinction between kicks and shifts is clear in theory, in practice SIPs typically involve a mixture of the two and can be difficult to distinguish.

By emphasizing the potential for purposeful intervention to drive nonlinear amplification in complex systems, our approach augments previous studies of social transitions (*7*, *8*). However, we concentrate specifically on amplification effects (nonlinearities, positive feedbacks, or increasing returns) that can magnify the impact of an intervention. Knowing when this is possible requires an understanding of the underlying dynamics. Opportunities for SIPs may change over time as the system evolves, so paying attention to emerging windows of opportunity is essential (*8*).

SIPs can occur when nonlinearities cause trajectories to diverge rapidly. However, rates of divergence may vary markedly, and some intervention points may be much more effective than others. Interventions can be particularly powerful if they drive the system into a new basin of attraction, making them difficult to reverse. SIPs also commonly arise in the presence of a critical threshold or tipping point, where a system sits at a boundary between qualitatively different types of behavior. In this circumstance, a small intervention can tip a system from one behavior to another.

Applying this conceptual framework, we examine four SIPs with the potential to contribute to rapid decarbonization.

FINANCIAL DISCLOSURE

Relatively modest changes to financial accounting rules or disclosure guidelines regarding climate change risks could have outsized effects. Many companies are currently failing to disclose and account for the risks to their balance sheets from the transition necessary to limit warming to 1.5° or 2°C, as well as failing to account for the physical risks that climate change will bring. A recent

study of eight major oil and gas companies by a UK-based institutional investor suggests that, as a result of optimistic assumptions about long-term oil prices, there may be a systemic overstatement of capital and performance. Will oil prices really rise at 2% per annum from a baseline of $70 to $80 a barrel in 2020–2021? These assumptions are likely inconsistent with the Paris Agreement, which would reduce demand for oil and, other things being equal, imply prices that are closer to a range of $20 to $40 a barrel. Changing price assumptions makes a difference: In 2017, the oil and gas company Total S.A. reported that a reduction in assumed prices from $80 to $72 a barrel would lead to asset impairments of more than $4 billion, cutting profits in half (*9*). What would the impact be at $20 to $40 a barrel?

There is a committed minority of investors who are aware of climate risks and are pushing for more openness. A change in accounting standards or disclosure guidelines could cause a substantial repricing of fossil assets (e.g., fossil fuel reserves and securities valuations), reducing the ability of the oil and gas sector to develop new fields, hence reducing committed emissions. Preventing such investments lowers the economic, social, and political costs of transforming the energy industry, as it levels the playing field for renewables, reduces the likely quantum of stranded assets, and increases the credibility of climate targets. Regulators in many countries, including Australia, the Netherlands, and the United Kingdom, are demonstrating increasing awareness of the potential impact of accounting guidance.

CHOOSING TECHNOLOGY INVESTMENTS

A kick to clean energy technologies could trigger feedbacks that make the energy transition cheaper and faster. If costs fall predictably with deployment, as they have in the past, investment in specific clean technologies would push them past the tipping point where they become economically competitive with nonrenewable incumbents, even without a carbon price. Although the transition to renewables has so far only made a small reduction in emissions, it has the potential to accelerate decarbonization, providing another good example of a SIP.

Which technologies should we invest in? In standard portfolio theory, investments do not affect outcomes, and diversification is strongly favored. In contrast, technology investments strongly influence outcomes, making the portfolio allocation problem highly nonlinear and causing outcomes to be sensitive to investments (*10*). Too much diversification means that nothing makes much progress; rapid progress requires concentrating resources.

History suggests that in the long run, some technologies are much more responsive to investment than others. For energy technologies, the real costs of oil, coal, and natural gas have not changed much in more than a century. Nuclear power costs at least as much as it did 60 years ago. In contrast, renewable energy sources such as solar photovoltaics (PV) and wind have experienced rapid, persistent cost declines. The real cost of solar PV modules has dropped by more than a factor of 6000 since their inception in 1956 (*11*). Since 1990, costs have dropped at 10% per year, on average, while deployment has increased an average of 26% per year. Despite far greater investment and subsidies, fossil fuel costs have stayed within an order of magnitude for a century. Unless technological change is somehow "purely exogenous," this suggests that the cost of solar PV is, in the long run, more responsive to investment than fossil fuels or nuclear power.

"If a latent majority supports ambitious climate action ... then a small kick to raise the issue's political salience may have an outsized effect."

When there is a cheap incumbent and an initially expensive challenger (as is the case with fossil fuels and solar PV), a marginal investor solely focused on cost will always choose the incumbent. This creates a danger that the incumbent becomes stuck. A far-sighted public investor, in contrast, can invest in the most responsive technologies to make them cheaper. The optimal strategy is to invest heavily in the challenger early on (*10*).

Solar PV and wind have now been supported (or "kicked") to the extent that they are at, or near, the tipping point where they are competitive with the cheapest alternatives. If their deployment continues to increase at its present rate, by 2030 the prevailing cost of electricity will very likely become cheaper than it has been during the last century (*11*). This could pay handsome returns and substantially lower the cost of the green energy transition. To realize these gains, we must make intelligent choices about developing the energy storage technologies that are essential to deal with the intermittency of renewables.

A SIP strategy would seek to better understand the causal mechanisms of technological improvement, and then favor technologies where evidence supports the likelihood of rapid, investment-driven cost declines to outcompete incumbents. By raising the very real possibility that intelligent investments in the green energy transition could be financially profitable as well as environmentally beneficial, this SIP could accelerate progress by neutralizing resistance to change based on perceived economic costs.

POLITICAL MOBILIZATION

A regime shift toward green technologies will also require public support and adoption (*6*). However, despite widespread belief across countries that climate change exists and needs to be addressed, citizens have rarely prioritized the issue. This means that pro-climate policies have struggled to garner sufficient political salience to overcome powerful incumbent interest groups. Nonetheless, the existence of a "silent" pro-climate majority creates the possibility of a SIP, provided that political entrepreneurs can activate it.

Social scientists have long studied the power of small groups of influencers in, for example, political revolutions. A few "radicals" can spark a revolution simply by demonstrating to the majority that their beliefs are more commonly held than they had thought (*12*). The power of influencers has also been demonstrated in laboratory settings, where a committed minority with unwavering opinions can have an outsized effect on others whose opinions are less firm. Theoretical models show that the committed minority fails to grow if it is less than a critical threshold of the total population, but above the threshold it grows rapidly and becomes prevalent (*13*).

Such findings could have important implications for climate policy: If a latent majority supports ambitious climate action, and if the size of the committed minority is close to a critical threshold, then a small kick to raise the issue's political salience may have an outsized effect. Indeed, we observe an increasing number of political entrepreneurs attempting exactly this strategy. Student activists like Greta Thunberg who are driving a wave of school strikes around the world (see photo) are finding new discourses to change the political salience of the issue. Striking exhibits increasing returns: The costs of striking fall, and the benefits rise, as more students coordinate on the same behavior, as does the potential for political change. Similarly, proponents of the Green New Deal in the United States are attempting to harness the quiet pro-climate majority to generate a broader coalition formed around a wider social agenda. Will these movements have any impact? There are several key questions. Does the net benefit of political action rise as others take action? Is the current distri-

bution of political beliefs close to a critical point? Does the intervention kick the system into a different basin of attraction?

UK CLIMATE CHANGE ACT

The United Kingdom's political climate of 2007–2008 provided a window of opportunity that led to the Climate Change Act of 2008 (*14*), a good example of a SIP (in this case a shift). Drafted by a small number of policy entrepreneurs from NGOs, academia, and Parliament in the wake of the government-sponsored Stern Review on the economics of climate change, the Act passed with a near-unanimous vote during a rare multiparty consensus prior to the 2009 UN climate meeting in Copenhagen. The Act established the world's first national legislation mandating greenhouse gas reductions by 2050 of 80% relative to 1990 levels, unconditional on other countries' actions.

Although the Act itself did not immediately kick the system into a new state, it shifted the institutional conditions under which future governments decide on climate policy. It created new institutional bodies, including the expert-led Committee on Climate Change, tasked with formulating carbon budgets every 5 years and reporting regularly to Parliament and the cabinet. Government policies that fall short are publicly exposed, giving rise to legal challenges. By creating a long-term goal, an independent review body, and a regular ratcheting cycle, the Act makes it more difficult for future governments to backslide and creates additional pressure for ambitious steps in the future (*14*), creating self-fulfilling beliefs in the post-carbon transition. Over the decade since 2008, CO_2 emissions in the UK have fallen dramatically.

The UK Climate Change Act inspired the Paris Agreement's inclusion of a long-term target and ratchet mechanism, and its institutional features have been adopted by other jurisdictions, further amplifying its impact. Countries such as New Zealand, Chile, and Sweden are looking at similar approaches (*14*).

RESEARCH AND DEPLOYMENT

These examples illustrate how many areas of policy and practice could be transformed by taking the SIP perspective. But substantial work lies ahead. A first step is to proactively and systematically identify potential SIPs, informed by complex systems theory. Are there regions of the socioeconomic system with critical thresholds, windows of opportunity, or tipping points? If not, what shift might create such dynamics? How close is the system to a sensitive region? Is there an intervention to kick the system in the right direction? What are the possible mechanisms of amplification following a kick or a shift? These might include network externalities, self-fulfilling beliefs, norm cascades, learning curves, bandwagon effects, and other phenomena with positive feedback effects.

In some cases, this simply means thinking about familiar issues in a different way. There are connections here with the literature on sociotechnical transitions, particularly in the strategic management of niche technologies (*6*). In other cases, a climate strategy informed by SIPs would place an even stronger emphasis on exploiting positive feedbacks, nonlinearities, and the potential for chaotic behavior in complex systems. Each of the four examples discussed above came into being without an explicit complex systems perspective, but a holistic view could help to systemically identify such interventions and to target them most effectively.

"More realistic models may increase trust and interest in their results. ... This might itself constitute an intervention in a sensitive area of the sociopolitical system."

The second step involves empirically characterizing the system dynamics so that the intervention can be best designed. An excellent example is a study that tested and implemented approaches to prevent bullying in schools by identifying and recruiting key "social referent" students to alter social norms (*15*). Such a methodology might be applied to identifying tipping points in attitudes and actions toward climate change mitigation. Modeling the key actors in the system is necessary to specify the intervention: Who should do what, when?

Current integrated assessment models, used to evaluate the economics of climate mitigation, provide an example of why the SIPs approach is necessary. Most such general equilibrium models omit key nonlinear feedback effects that are essential for understanding SIPs and their impact. New analytical frameworks that incorporate methods from dynamical systems, network analysis, and agent-based modeling at a granular level can help to capture essential nonlinear feedback mechanisms. Such models could provide richer and more accurate insights into the costs and benefits of interventions with amplified effects. More realistic models may increase trust and interest in their results, and lead to better-informed policy. This might itself constitute an intervention in a sensitive area of the sociopolitical system.

Creating a world of zero greenhouse gas emissions is a revolutionary enterprise that will require vast changes to our physical infrastructure, economy, and society, and their interactions with each other. There is strong coupling among these different domains, which makes models built within silos unable to provide the guidance needed. This is already apparent from the four examples given above: Support for new green technologies depends on political mobilization and can be amplified by improved financial disclosures. All of these benefit from a regulatory framework that encourages decarbonization beyond political cycles.

We also need a multidisciplinary framework integrating perspectives from the social, physical, and natural sciences as well as the humanities. National and regional funding calls must seek to promote true interdisciplinary teams that span socioeconomic, political, environmental, and sociotechnical approaches, and are capable of generating conceptual or empirical breakthroughs that might not be reached in isolation. Fine-grained complex systems models of the economy and technological change should be coupled with models of opinion dynamics and of financial and legal systems. The change that we are about to make and the consequences of failure are so great that we cannot afford to fly blindly into the future. ■

REFERENCES AND NOTES

1. A. Pfeiffer, C. Hepburn, A. Vogt-Schilb, B. Caldecott, *Environ. Res. Lett.* **13**, 054019 (2018).
2. S. Pacala, R. Socolow, *Science* **305**, 968 (2004).
3. T. M. Lenton *et al.*, *Proc. Natl. Acad. Sci. U.S.A.* **105**, 1786 (2008).
4. D. H. Meadows, *Leverage Points: Places to Intervene in a System* (Sustainability Institute, Hartland, VT, 1999).
5. M. S. Torn, J. Harte, *Geophys. Res. Lett.* **33**, L10703 (2006).
6. T. Hale, *Catalytic Cooperation* (Blavatnik School of Government, Univ. of Oxford, 2018); www.bsg.ox.ac.uk/sites/default/files/2018-09/BSG-WP-2018-026.pdf.
7. B. K. Sovacool, D. J. Hess, *Soc. Stud. Sci.* **47**, 703 (2017).
8. F. W. Geels, B. K. Sovacool, T. Schwanen, S. Sorrell, *Science* **357**, 1242 (2017).
9. N. Landell-Mills, *Are Oil and Gas Companies Overstating Their Position?* (Sarasin & Partners, 2018); www.sarasinandpartners.com/docs/default-source/esg/are-oil-and-gas-companies-overstating-their-position.
10. R. Way, F. Lafond, F. Lillo, V. Panchenko, J. D. Farmer, *J. Econ. Dyn. Control* **101**, 211 (2019).
11. F. Lafond *et al.*, *Technol. Forecast. Soc. Change* **128**, 104 (2018).
12. T. Kuran, *Public Choice* **61**, 41 (1989).
13. D. Centola, J. Becker, D. Brackbill, A. Baronchelli, *Science* **360**, 1116 (2018).
14. M. Nachmany, S. Fankhauser, J. Setzer, A. Averchenkova, *Global Trends in Climate Change Legislation and Litigation: 2017 Update* (Grantham Research Institute on Climate Change and the Environment, London, 2017); http://eprints.lse.ac.uk/80447/.
15. E. L. Paluck, H. Shepherd, P. M. Aronow, *Proc. Natl. Acad. Sci. U.S.A.* **113**, 566 (2016).

10.1126/science.aaw7287

BOOKS *et al.*

Emperor penguins swim toward the surface of the Ross Sea, a pristine bay within the Southern Ocean.

PHOTO: PAUL NICKLEN/GETTY IMAGES

OCEANOGRAPHY

Diving deep into the Southern Ocean

A major player in weather, climate, and biodiversity, the waters around Antarctica take center stage in a new history

By **Louise Fabiani**

Of the vast, largely unknown marine environment, the most mysterious section arguably lies at the bottom of the world. In *Wild Sea*, historian Joy McCann has written a brief but delightfully comprehensive history of the Southern Ocean, "the most remote and inaccessible part of the planetary ocean, the only part that flows completely around Earth unimpeded by any landmass."

The ocean currents and winds originating there provide an engine for the world's climate, giving rise to El Niño years and their hemisphere-wide cascade of consequential weather patterns. The huge amount of Southern Ocean biomass alone, everything from tiny diatoms to the blue whale, also figures significantly in carbon sequestration—starting with phytoplankton, which are responsible for about half the planet's total photosynthesis—and thus in climate change's many complex feedback loops.

Wild Sea
A History of the Southern Ocean
Joy McCann
University of Chicago Press, 2019. 288 pp.

Seafarers from many nations who first caught and traded animals in the Southern Ocean quickly recognized those waters as a kind of marine El Dorado. In a way, they weren't far off in their assessment. Many species prefer colder water for their life cycles and find their food supply in the currents caused by upwelling (the mixing of colder water with the warmer layer on top of it) around 40 degrees latitude.

"By the early nineteenth century the oceans were perceived not only as a means to extend territorial ambitions but also as the source of inexhaustible riches unencumbered by any one nation's legal or administrative instruments," writes McCann. Factory ships returned home with holds laden with barrels of oils and other precious commodities.

Despite dire warnings and anecdotal evidence from experienced whalers and sealers, the impression of unending abundance persisted for centuries. When Rachel Carson's *The Sea Around Us* went into the second edition in 1960, some of the scientific community still saw the world's oceans "as an infinite resource akin to the emerging frontier of outer space." Others, however, advocated restraint, moratoriums on catch limits, and pollution guidelines.

Studies and international agreements were slow in coming. In 1959, 800 delegates from 38 countries met in New York to discuss the history and biodiversity of the world's oceans. It was a step in the right direction.

From seabirds to whales, many species had become commercially extinct by the mid-20th century. In 1965, the last South Georgia whaling station closed. And in 1986, the International Whaling Commission officially ended worldwide commercial whaling, though countries such as Iceland, Norway, and, infamously, Japan continue to kill hundreds of smaller cetaceans annually, circumventing the rulings.

Unfortunately, today's trawlers have not learned much from the heedless rapacity of the recent and distant past. The newest "limitless resource" is krill, the very basis of the immense southern food chain. Tiny crustaceans don't possess the charisma of blue whales, and that may explain relatively lackluster scientific and activist reactions to the declining numbers of krill. Yet their serious depletion would have far greater global reach than the loss of most marine mammals. As the supplement industry switches from fish to krill as a source of omega-3 fatty acids, regulation once again will be required to prevent ecological disaster in an area many beneficiaries consider out of sight, out of mind.

Though *Wild Sea* does feature plenty of grim statistics about disappeared or disappearing species in the Southern Ocean, the author's primary concern is neither conservation nor the sins of the Anthropocene. McCann successfully conveys the timeless mystery of the Southern Ocean and how it has figured in human history, adding a poet's touch to many passages.

In the preface to each chapter, for example, she relates impressions from her own voyage to the Southern Ocean. In chapter 2, she begins by describing the seabirds on Prion Island, South Georgia: "As I pause on the brow of a hill, I see two light-mantled sooty albatrosses wheel and soar in perfect unison. Then an apparition of an adult wandering albatross comes into view. ... Wings locked, it circles above the golden tussac grasses and skims the currents of silver air."

These personal impressions beautifully complement the history, biogeography, and oceanography, giving the reader a vivid sense of the remote, alien, but always changing marine environment upon which so much of the rest of the world depends. ■

The author is a freelance science writer and culture critic based in Montreal. Email: m.l.fabiani47@gmail.com

10.1126/science.aaw7754

SCIENCE LIVES

Helping Einstein

Efforts to identify Mileva Marić's contributions highlight the trouble with telling the tales of early women in science

Einstein's Wife
The Real Story of Mileva Einstein-Marić
Allen Esterson and David C. Cassidy
MIT Press, 2019. 336 pp.

By **Mélanie Frappier**

Mileva Marić entered the Zurich Polytechnic in 1896, becoming one of the first women who fought their way into a university physics program. As a student, she wrote with excitement about the kinetic theory of gases, read books on the ether, and completed a diploma dissertation on heat conduction in metals. She also fell in love with a younger classmate, Albert Einstein, who described in his letters the future he hoped they would share as a scientific couple.

Marić's academic ambitions sadly never materialized. She struggled with her dissertation and final exams. The Committee of Examiners decided against awarding her a degree, closing the door on her university career.

Still, after a traumatic and unplanned pregnancy, Marić did marry Einstein. In the end, the union was not a happy one. After an acrimonious divorce, Marić would be left to raise the couple's two sons alone in Switzerland, while a remarried Einstein rose to fame in Europe and America. But in their years together, did Marić and Einstein collaborate on scientific projects as they had promised each other? Might Einstein's prolific scientific output during his years with Marić be explained by her significant, but unacknowledged, scientific contributions to his work?

No direct evidence remains of such a collaboration. Only a few academic records, legal documents, letters, and uncertain recollections by acquaintances remain to bear witness to Marić's life. Yet, a growing number of popular historians argue that these documents prove that Marić did work closely with Einstein on many projects, including relativity theory, only to see her work subsumed under her husband's name.

Although a collaboration between Einstein and Marić would be a compelling story, it is, in the end, only a story, argue retired physics lecturer Allen Esterson and emeritus historian David Cassidy in their latest book, *Einstein's Wife*: *The Real Story of Mileva Einstein-Marić*. Central to Esterson and Cassidy's argument is the belief that historians, like scientists, must guard against speculation and anchor their claims in facts, especially when evidence is lacking.

The biographical outline of Marić's life with which Cassidy opens the book offers a prime example of such a fact-based approach. Cassidy carefully chooses his sources, presents rigorous arguments to support his conclusions, and refuses to ascribe thoughts or feelings to his actors, unless they have indisputably expressed them in their lifetimes.

Such an empirical approach is intrinsically limited. It demands that, when faced with missing evidence, we remain silent. But as the adage goes, "absence of evidence is not evidence of absence." Cassidy is right to say that we cannot conclude from Einstein's occasional references to "our work" or "our theory" when writing to Marić that the two were engaged in a real scientific collaboration, especially when in her own correspondence Marić ascribes the work to Einstein. But, as Cassidy readily admits, we cannot disprove such collaboration either.

Mileva, shown with Albert and their son Hans-Albert, was Einstein's classmate before she was his wife.

What are we then to make of popular accounts, such as the recent first season of the television series *Genius*, that have presented Marić as a close collaborator of Einstein? In the second part of *Einstein's Wife*, Esterson offers a convincing but exceedingly detailed reading of these accounts as nothing more than misleading fictions rooted in circumstantial arguments, hearsay, and overinterpreted evidence.

The problem is that, when it comes to reintegrating women into our historical narratives, underinterpreting evidence might be as problematic as overinterpreting it. If Senta Troemel-Ploetz has defended so forcefully—albeit unconvincingly—the idea that Marić made significant contributions to Einstein's work (*1*), it is because she is deeply aware that in cases like Marić's, where evidence is lacking, a historical account merely paralleling the available facts may be as misleading as a purely speculative one.

Historians try to guard themselves against such mistakes by embedding their biographical accounts of marginalized persons into their larger historical contexts. *Einstein's Wife* is no exception and includes an informative essay, penned by Ruth Lewin Sime, describing the barriers the 19th-century professionalization of science created for women.

Unfortunately, this otherwise excellent essay is much too short to fully balance the occasional failure of Esterson and Cassidy's arguments to be sensitive to the realities women continue to face in academia. In their evaluation of Marić's abilities, for example, they continuously rely on a comparison between Marić's and Einstein's grades. But given that even today, professors mark female students more harshly than their male counterparts, it is unclear why the two authors would give so much place to such data in their account (*2*).

Recovering in all their nuances the lives of women who, like Marić, were unable to pursue their scientific interests is essential for understanding the challenges female scientists still face today as they juggle academic ambitions, family duties, and social expectations. Evidence-based biographies such as *Einstein's Wife* are essential for this task, but given our fragmented historical records, they will not be sufficient. There may be a place here for fiction after all. ■

The reviewer is at the History of Science and Technology Program, University of King's College, Halifax, Nova Scotia B3H 2A1, Canada. Email: melanie.frappier@ukings.ca

REFERENCES AND NOTES

1. S. Troemel-Ploetz, *Women's Studies Int. Forum* **13**, 415 (1990).
2. C.A. Moss-Racusin *et al.*, *Proc. Natl. Acad. Sci. U.S.A.* **109**, 16474 (2012).

10.1126/science.aaw5438

PHOTO: ETH-BIBLIOTHEK ZÜRICH, BILDARCHIV/HS_1457-72

AAAS AWARDS & PRIZES

AAAS Mani L. Bhaumik Award for Public Engagement with Science

CALL FOR NOMINATIONS

The AAAS Mani L. Bhaumik Award for Public Engagement with Science recognizes scientists and engineers who demonstrate excellence in science communication that informs and engages the public.

The award recipient will receive a $5,000 cash prize and recognition at the 2020 AAAS Annual Meeting.

Applications for the 2020 AAAS Mani L. Bhaumik Award for Public Engagement with Science will be accepted through August 1, 2019.

For more information about this award, visit aaas.org/PESaward

AAAS is grateful to quantum physicist Mani L. Bhaumik for his generous contribution to endow this award, which has been honoring outstanding science communicators since 1987.

Bhaumik's gift will allow AAAS to continue, in perpetuity, to recognize and support individuals whose creative methods are engaging the public in significant ways.

HONORING EXCELLENCE IN SCIENCE

AMERICAN ASSOCIATION FOR THE ADVANCEMENT OF SCIENCE

AAAS

Nearly 1 million Rohingya refugees are living in camps in Bangladesh.

PHOTO: OMAR MUNNA

Edited by **Jennifer Sills**

Rohingya refugees and the environment

Violence in the Rakhine State of Myanmar has led to a humanitarian crisis as Rohingya people flee across the border to Bangladesh (*1*). With the rapid influx of nearly 700,000 arrivals between August 2017 and the beginning of 2018, the Bangladeshi city of Cox's Bazar is now under severe strain from a Rohingya population of almost 1 million, one of the largest concentrations of refugees in the world (*2*). The crisis seized global attention, and the international response was rapidly escalated to a Level 3 emergency (*3*).

In addition to the humanitarian challenges, the mass influx of Rohingya refugees has resulted in environmental degradation both within the refugee camps and in the surrounding areas (*2*). The expansion of existing campsites has led to more than 2000 ha of forest loss in the Cox's Bazar region (*4*). Expansion of the old Kutupalong camp blocked the only corridor used by the globally endangered Asian elephant as a migration route and trapped about 45 elephants in the western side of the camp (*5*). The latest Rohingya settlement has also amplified human-elephant conflict in the area, with 13 human casualties so far (*6*). The remaining elephant habitat is under severe pressure from uncontrolled fuelwood collection in the forest (*7*). The pressure on forests has caused tensions with local host communities, which rely on these forests for fuelwood, medicine, and food (*8*). The surrounding critical biodiversity areas, such as the Teknaf Wildlife Sanctuary, Himchari National Park, and Inani National Park, are also at risk (*2*). Soil erosion and landslides are already common in the area, affecting water resources, irrigation, and groundwater reserves (*9*). Local biodiversity, including marine resources, acoustic environment, and air quality, is being degraded at an unprecedented rate (*2*).

Repatriation is under negotiation, but it is likely that the Rohingya refugees will remain in Bangladesh for some time (*10*). The situation demands development of a long-term strategy at the landscape level not only to address humanitarian needs but also to mitigate both short- and long-term environmental effects. A forest and landscape restoration approach (*11*) will provide ample opportunities to integrate environmental and humanitarian interventions, both inside and outside the refugee camps. For instance, establishing fuelwood plantations to meet the local demand will reduce pressure on nearby forests. In addition, refugees and local host communities can use native species seedlings to plant trees, facilitating reforestation of degraded lands.

Sharif A. Mukul[1,2], Saleemul Huq[3,4], John Herbohn[2,5], Ainun Nishat[6], A Atiq Rahman[7], Raquibul Amin[8], Farid Uddin Ahmed[9]
[1]Department of Environmental Management, School of Environmental Science and Management, Independent University Bangladesh, Dhaka 1229, Bangladesh. [2]Tropical Forests and People Research Centre, University of the Sunshine Coast, Maroochydore DC, QLD 4558, Australia. [3]International Centre for Climate Change and Development, Dhaka 1229, Bangladesh. [4]International Institute for Environment and Development, London WC1X 8NH, UK. [5]Sustainable Minerals Institute, The University of Queensland, Brisbane, QLD 4072, Australia. [6]Centre for Climate Change and Environmental Research, BRAC University, Dhaka 1212, Bangladesh. [7]Bangladesh Centre for Advanced Studies, Dhaka 1212, Bangladesh. [8]IUCN Bangladesh, Dhaka 1212, Bangladesh. [9]Arannyak Foundation, Dhaka 1206, Bangladesh.
*Corresponding author. Email: smukul@iub.edu.bd

REFERENCES AND NOTES

1. S. Shevach *et al.*, *Humanit. Exch.* **73**, 16 (2018).
2. UN Development Programme, UN Women Bangladesh, Bangladesh Ministry of Environment and Forests, "Report on environmental impact of Rohingya influx" (Dhaka, 2018).
3. M. Bowden, *Humanit. Exch.* **73**, 5 (2018).
4. M. M. Hassan *et al.*, *Remote Sens.* **10**, 689 (2018).
5. M. A. Motaleb *et al.*, "Atlas: Elephant routes and corridors in Bangladesh" (IUCN, Dhaka, 2016).
6. K. McVeigh, D. Peri, "Fatal elephant attacks on Rohingya refugees push Bangladesh to act," *The Guardian* (2018); www.theguardian.com/global-development/2018/may/09/fatal-elephant-attacks-on-rohingya-refugees-push-bangladesh-to-act.
7. IUCN Bangladesh, The Office of the United Nations High Commissioner for Refugees (UNHCR), "Survey report on elephant movement, human-elephant conflict situation, and possible intervention sites in and around Kutupalong Camp, Cox's Bazar" (Dhaka, 2018).
8. M. A. S. A. Khan *et al.*, *Int. J. Biodivers. Sci. Manag.* **5**, 76 (2009).
9. S. Huq, "A note on the environmental aspects of Rohingya camps," *The Daily Star* (2018); www.thedailystar.net/opinion/politics-climate-change/note-the-environmental-aspects-rohingya-camps-1610368.
10. International Organization for Migration (IOM), "Rohingya refugee crisis response" (2018); www.iom.int/sitreps/bangladesh-iom-bangladesh-rohingya-refugee-crisis-response-external-update-december-2018.
11. P. Besseau *et al.*, "Restoring forests and landscapes: The key to a sustainable future" (Global Partnership on Forest and Landscape Restoration, Vienna, 2018).

10.1126/science.aaw9474

Address the roots of environmental crime

In their Letter "Madagascar: Crime threatens biodiversity" (22 February, p. 825), J. P. G. Jones *et al.* call on the new president of Madagascar, Andry Rajoelina, to get tough on environmental crime and corruption to protect what is left of the island's precious resources. However, in countries where enforcement-heavy conservation strategies take precedence, the rural poor and frontline environmental activists, rather than those truly at fault, often pay the price (*1*).

As Jones *et al.* point out, illegal activities are "often linked to local violence and insecurity," but such activities are also deeply connected to the political and economic marginalization of local communities and global demand for valuable resources (*2*). For instance, Madagascar's exports of rosewood (*Dalbergia* spp.), a high-value hardwood, increased in protected areas from 2002 to 2009 and continued unabated during Rajoelina's political coup d'état and the subsequent 5-year economic crisis (*3*, *4*). Neither local gangs nor rural communities engineered this international trade; rather, it was organized by large timber syndicates and those in positions of power with connections in global networks (*5*).

To date, top-down enforcement on environmental crime in Madagascar has mainly resulted in minor thieves held in jail indefinitely awaiting trial. Amnesty International reported that, as of October 2017, more than half the total prison population were petty offenders made up of rural poor who "lacked formal education and were underinformed of their rights" (*6*). Long-term incarceration will drive many rural inhabitants deeper into poverty, potentially reversing conservation objectives, and does little to target more powerful, centrally involved actors. Compounding the injustice, environmental activists and journalists speaking out on the government's role have also been arrested (*7*).

I agree with Jones *et al.* that enforcement is vital, but it must be implemented in a way that avoids overcriminalization of the rural poor. Fairer and more inclusive conservation policies would focus attention on important global drivers of environmental crime, including the role of complicit governments. Independent truth and justice commissions (*8*) adapted to specialize on international environmental crime could be used alongside in-depth investigations by United Nations special rapporteurs on human rights and the environment (*9*). Such programs are not meant to replace a country's judicial or enforcement systems, but rather to support existing institutions and work with transnational crime prevention programs. Interventions that directly address structural poverty at the local level could also combat counterproductive enforcement (*10*). Governments should fully adopt transparent benefit-sharing mechanisms, compensation for burdens of environmental harm, procedures to ensure diverse voices in natural resource allocation, and recognition of historical injustices (*11*).

Strengthened conservation enforcement involves not only national governments but also journalists and frontline activists, who often help hold those in power to account—including for their involvement in environmental crimes. These actors need to be able to live and work without the fear of arrest or worse. In 2017 alone, there were 207 activists and frontline environmental defenders killed worldwide (*12*). Now more than ever, we must ensure basic standards of human rights, freedom to protest, and protection of the press.

Benjamin Neimark
Lancaster Environment Centre, Lancaster, Lancashire LA1 4YQ, UK. Email: b.neimark@lancaster.ac.uk

REFERENCES AND NOTES

1. R. Duffy *et al.*, *Biol. Conserv.* **232**, 66 (2019).
2. J. Barlow *et al.*, *Nature* **559**, 517 (2018).
3. J. Tollefson, *Nature* **565**, 407 (2019).
4. H. Randriamalala, Z. Liu, *Madagascar Conserv. Dev.* **5**, 11 (2010).
5. A. Zhu, *Geoforum* **86**, 1 (2018).
6. Amnesty International, Madagascar, "Punished for being poor: Pretrial detention in Madagascar" (2018); https://www.amnesty.org/en/latest/campaigns/2018/10/madagascar-prison/.
7. J. Watts, "Madagascar's vanilla wars: Prized spice drives death and deforestation" (2018); www.theguardian.com/environment/2018/mar/31/madagascars-vanilla-wars-prized-spice-drives-death-and-deforestation.
8. International Center for Transitional Justice (2019); www.ictj.org/our-work/regions-and-countries/kenya.
9. United Nations Human Rights, "Special Rapporteur on human rights and the environment" (2019); www.ohchr.org/en/Issues/environment/SRenvironment/Pages/SRenvironmentIndex.aspx.
10. J. Phelps *et al.*, *Conserv. Lett.* **7**, 495 (2014).
11. R. Cooney *et al.*, *Conserv. Lett.* **10**, 367 (2017).
12. Global Witness, "At what cost?" (2018); www.globalwitness.org/en-gb/campaigns/environmental-activists/at-what-cost/.

10.1126/science.aax2701

Concerns of young protesters are justified

The world's youth have begun to persistently demonstrate for the protection of the climate and other foundations of human well-being. (*1*, *2*). As scientists and scholars who have recently initiated similar letters of support in our countries, we call for our colleagues across all disciplines and from the entire world to support these young climate protesters (*3*). We declare: Their concerns are justified and supported by the best available science. The current measures for protecting the climate and biosphere are deeply inadequate.

Nearly every country has signed and ratified the Paris Agreement of 2015, committing under international law to hold global warming well below 2°C above preindustrial levels and to pursue efforts to limit the temperature increase to 1.5°C (*4*). The scientific community has clearly concluded that a global warming of 2°C instead of 1.5°C would substantially increase climate-related impacts and the risk of some becoming irreversible (*5*). Moreover, given the uneven distribution of most impacts, 2°C of warming would further exacerbate existing global inequalities (*5*).

It is critical to immediately begin a rapid reduction in CO_2 and other greenhouse gas emissions. The degree of climate crisis that humanity will experience in the future will be determined by our cumulative emissions; rapid reduction now will limit the damage. For example, the Intergovernmental Panel on Climate Change (IPCC) has recently assessed that halving CO_2 emissions by 2030 (relative to 2010 levels) and globally achieving net-zero CO_2 emissions by 2050 (as well as strong reductions in other greenhouse gases) would allow a 50% chance of staying below 1.5°C of warming (*5*). Considering that industrialized countries produced more of and benefited more from previous emissions, they have an ethical responsibility to achieve this transition more quickly than the world as a whole (*4*, *6*).

Many social, technological, and nature-based solutions already exist. The young protesters rightfully demand that these solutions be used to achieve a sustainable society (*7*). Without bold and focused action, their future is in critical danger. There is no time to wait until they are in power.

Politicians have the huge responsibility of creating the necessary framework conditions in a timely manner. Policies are needed to make climate-friendly and sustainable action simple and cost-effective and make climate-damaging action unattractive and expensive. Examples include effective CO_2 prices and regulations; cessation of subsidies for climate-damaging actions and products; efficiency standards; social innovations; and massive, directed investment in solutions such as renewable energy, cross-sector electrification, public transport infrastructure, and demand reduction. A socially fair distribution of the costs and benefits of climate action will require deliberate attention, but it is both possible and essential (*8*).

The enormous grassroots mobilization (*2*) of the youth climate movement—including Fridays for Future, School (or Youth) Strike 4 Climate, Youth for (or 4) Climate, and Youth

Climate Strike (7)—shows that young people understand the situation. We approve and support their demand for rapid and forceful action. We see it as our social, ethical, and scholarly responsibility to state in no uncertain terms: Only if humanity acts quickly and resolutely can we limit global warming, halt the ongoing mass extinction of animal and plant species, and preserve the natural basis for the food supply and well-being of present and future generations. This is what the young people want to achieve. They deserve our respect and full support.

Gregor Hagedorn[1], Peter Kalmus[2]*, Michael Mann[3], Sara Vicca[4], Joke Van den Berge[4], Jean-Pascal van Ypersele[5], Dominique Bourg[6], Jan Rotmans[7], Roope Kaaronen[8], Stefan Rahmstorf[9], Helga Kromp-Kolb[10], Gottfried Kirchengast[11], Reto Knutti[12], Sonia I. Seneviratne[12], Philippe Thalmann[13], Raven Cretney[14], Alison Green[15], Kevin Anderson[16,17], Martin Hedberg[18], Douglas Nilsson[19], Amita Kuttner[20], Katharine Hayhoe[21]

[1]Berlin, Germany. [2]Joint Institute for Regional Earth System Science & Engineering, University of California, Los Angeles, Los Angeles, CA 90095, USA. [3]Earth System Science Center, Penn State University, University Park, PA 16802, USA. [4]Universiteit Antwerpen, Wilrijk, Antwerp, Belgium. [5]Université catholique de Louvain, 1348 Louvain-la-Neuve, Belgium. [6]Université de Lausanne, Lausanne, Switzerland. [7]Erasmus University, Rotterdam, 3000 DR Rotterdam, Netherlands. [8]Helsinki Institute of Sustainability Science, Faculty of Social Sciences, University of Helsinki, 00014 Helsinki, Finland. [9]Potsdam Institute for Climate Impact Research, 14473 Potsdam, Germany. [10]Center for Global Change and Sustainability, University of Natural Resources and Life Sciences, 1180 Vienna, Austria. [11]Wegener Center for Climate and Global Change, University of Graz, 8010 Graz, Austria. [12]Institute for Atmospheric and Climate Science, ETH Zürich, 8092 Zürich, Switzerland. [13]École Polytechnique Fédérale de Lausanne, 1015 Lausanne, Switzerland. [14]Department of Political Science and Public Policy, University of Waikato, Hamilton, Waikato, New Zealand. [15]Scientists Warning UK, Cambridge, UK. [16]The University of Manchester, UK. [17]Uppsala University, Uppsala, Sweden. [18]Polyfuture Institute SWC, Stockholm, Sweden. [19]Department of Environmental Science and Analytical Chemistry, Stockholm University, 106 91 Stockholm, Sweden. [20]University of California, Santa Cruz, Santa Cruz, CA 95064, USA. [21]Climate Center, Texas Tech University, Lubbock, TX 79409, USA.
*Corresponding author. Email: kalmus@ucla.edu

REFERENCES AND NOTES

1. M. Warren, *Nature* **567**, 291 (2019).
2. "Pictures from youth climate strikes around the world," *The New York Times* (2019); www.nytimes.com/2019/03/15/climate/climate-school-strikes.html.
3. Please show support by signing the open letter at www.scientistsforfuture.org/international/.
4. United Nations Framework Convention on Climate Change, "Decision 1/CP.21: Adoption of the Paris Agreement," (Paris, France, 2015); https://unfccc.int/files/essential_background/convention/application/pdf/english_paris_agreement.pdf.
5. IPCC, "Summary for policymakers: Global warming of 1.5 °C—An IPCC Special Report on the impacts of global warming of 1.5 °C above pre-industrial levels and related global greenhouse gas emission pathways, in the context of strengthening the global response to the threat of climate change, sustainable development, and efforts to eradicate poverty," V. Masson-Delmotte *et al*., Eds. (IPCC, World Meteorological Organization, United Nations Environment Programme, Geneva, Switzerland, 2018); www.ipcc.ch/report/sr15.
6. C. Kolstad *et al*., in *Climate Change 2014: Mitigation of Climate Change: Contribution of Working Group III to the Fifth Assessment Report of the Intergovernmental Panel on Climate Change*, O. Edenhofer *et al*., Eds. (Cambridge Univ. Press, Cambridge, UK, 2014).
7. Fridays for Future (www.fridaysforfuture.org).
8. IPCC, *Climate Change 2014: Synthesis Report: Contribution of Working Groups I, II and III to the Fifth Assessment Report of the Intergovernmental Panel on Climate Change*, Core Writing Team, R. K. Pachauri, L. A. Meyer, Eds. (IPCC, Geneva, Switzerland, 2014).

SUPPLEMENTARY MATERIALS

www.sciencemag.org/content/364/6436/139.2/suppl/DC1
List of signatories

10.1126/science.aax3807

Bial AWARD

IN BIOMEDICINE 2019

BIAL Award in Biomedicine 2019 - €300.000

Seeks to recognise a work published in the biomedical field (free theme) from 1 January 2010 onward, the results of which are considered to be of high quality and scientifically relevant.
Only works nominated by the Voting members of the Jury, the members of the Scientific Board of the BIAL Foundation, previous BIAL award winners and Scientific Societies may be considered candidates.
The Jury may also invite other scientific institutions to submit proposals.

Proposals must be sent by 30 June 2019 to fundacao@bial.com

Regulations and proposal form available at www.fundacaobial.com

Jury

President
Fernando Lopes da Silva

Members
European Research Council
Paola Bovolenta
Eva Kondorosi

Council of Rectors of the Portuguese Universities
Maria do Carmo Fonseca
Arsélio Pato de Carvalho

European Medical Association
Vincenzo Costigliola
Manuel Pais-Clemente

Scientific Board of the BIAL Foundation
Niels Birbaumer
Menno Witter

Previous winners of the BIAL Award
Vladimir Hachinski
Peter St. George-Hyslop

Scientific Journals
Howard Bauchner - JAMA
Richard Horton - The Lancet

FUNDAÇÃO Bial
Institution of public utility

Com o alto Patrocínio de Sua Excelência O Presidente da República

CRUP Conselho dos Reitores das Universidades Portuguesas

EMA

RESEARCH

A pack of African wild dogs (*Lycaon pictus*) takes advantage of a rural road in the Gorongosa National Park in Mozambique.

IN *SCIENCE* JOURNALS

Edited by **Michael Funk**

TROPHIC CASCADES

Ecosystems feel war's effects

War ravages human lives and landscapes, but nonhuman victims are no less affected. The Mozambican Civil War resulted in the rapid decline of predators in Gorongosa National Park and led to a trophic cascade that shifted prey behaviors and plant communities. Atkins *et al*. monitored this shift and found that the absence of wild dogs and leopards resulted in a change in habitat use and plant consumption by bushbuck, which are forest-dwelling antelopes. Experiments further showed that changes in prey behavior were reversible when signs of predator activity were introduced, supporting the impact of the predator loss. These results confirm patterns seen elsewhere and go further in providing mechanistic detail about the importance of the "landscape of fear" perceived by prey animals. —SNV

Science, this issue p. 173

STRUCTURAL BIOLOGY

Bone-cell regulation, fleshed out

One of many medically relevant G protein–coupled receptors, parathyroid hormone receptor-1 (PTH1R) functions in the control of calcium homeostasis and bone physiology. Zhao *et al*. used cryo–election microscopy to observe the structure of PTH1R in a complex with a modified form of parathyroid hormone and stimulatory G protein. The structural model helps explain how parathyroid hormone interacts with its receptor and the molecular basis for receptor activation. —LBR

Science, this issue p. 148

GRAPHENE

Electron hydrodynamics in graphene

Electrons can move through graphene in a manner reminiscent of fluids, if the conditions are right. Two groups studied the nature of this hydrodynamic flow in different regimes (see the Perspective by Lucas). Gallagher *et al*. measured optical conductivity using a waveguide-based setup, revealing signatures of quantum criticality near the charge neutrality point. Berdyugin *et al*. focused on electron transport in the presence of a magnetic field and measured a counterintuitive contribution to the Hall response that stems from hydrodynamic flow. —JS

Science, this issue p. 158, p. 162; see also p. 125

THIN FILMS

Epitaxial films through spin coating

A simple way to coat a surface with a uniform film is by spin coating. The substrate is spun at high speed, and a droplet of solution containing the coating is added at the center, spreads out, and evaporates. This method is used to make polycrystalline inorganic coatings and amorphous films, such as polymers used in lithography. Kelso *et al*. performed spin coating with single-crystal substrates, carefully controlling the thickness of the spreading solution on the basis of its viscosity and the rotation rate. In this way, they achieved epitaxial growth—in which the crystallites are oriented by the substrate—for perovskites, zinc oxide, and sodium chloride. —PDS

Science, this issue p. 166

GLACIAL CYCLES

Controlling cooling

On million-year time scales, Earth's climate state is

PHOTO: BRETT KUXHAUSEN, GORONGOSA MEDIA

determined by sources and sinks of carbon to the ocean-atmosphere system. But which specific mechanisms are important in controlling the timing of glacial intervals? Macdonald *et al*. identify arc-continent collisions in the tropics as a primary control (see the Perspective by Hartmann). They compiled a database of Phanerozoic arc-continent collisions and the latitudinal distribution of ice sheets, showing that ice coverage was greatest when those collisions were most widespread, maximizing global weatherability. —HJS

Science, this issue p. 181; see also p. 126

HEART REGENERATION

The price of staying warm

Among vertebrates, zebrafish and salamanders can regenerate their hearts, whereas adult mice and humans cannot. Hirose *et al*. analyzed diploid cardiomyocyte frequency as a proxy for cardiac regenerative potential across 41 vertebrate species (see the Perspective by Marchianò and Murry). They observed an inverse correlation of these cells with thyroid hormone concentrations during the ectotherm-to-endotherm transition. Mice with defects in thyroid hormone signaling retained significant heart regenerative capacity, whereas zebrafish exposed to excessive thyroid hormones exhibit impaired cardiac repair. Loss of heart regenerative ability in mammals may represent a trade-off for increases in metabolism necessary for the development of endothermy. —BAP

Science, this issue p. 184; see also p. 123

EVOLUTIONARY BIOLOGY

Adaptation by way of compromise

Many plants rely on animal pollinators to spread pollen and increase the genetic diversity of their offspring. However, there are trade-offs, because attracting pollinators may also attract herbivores and deterring predation may diminish floral displays. Ramos and Schiestl studied the interplay between mating system, flowers, and chemical defenses over several generations in *Brassica rapa* plants (see the Perspective by Ågren). Evolution driven by pollination and herbivory can be observed after only eight generations, suggesting that trade-offs have large evolutionary consequences. —LMZ

Science, this issue p. 193; see also p. 122

BACTERIAL INFECTIONS

Friend turned foe

Enterococci are commensal bacteria found in the gut of most humans, but strains adapted to survival in the bloodstream can be deadly. Because these bacteria spread patient-to-patient in hospitals, their adaptation can be tracked. Van Tyne *et al*. analyzed the genomes of enterococcal strains from an outbreak of bloodstream infection in a hospital in the mid-1980s. Genetic changes gradually accumulated in the enterococci to allow evasion of the host innate immune system and harden them against antibiotic therapy. —OMS

Sci. Transl. Med. **11**, eaat8418 (2019).

ENGINEERING

Pulling water from air

The scarcity of fresh water is a global problem in need of energy-efficient solutions. Sadeghpour *et al*. developed a dehumidifier that takes advantage of capillary instabilities produced by water's high surface tension to create water beads flowing down an array of cotton threads. The high surface area of the beads and the intrinsic low resistance to air flow yields devices that are very efficient in condensing water vapor carried in humid air. —LAA and KJP

Sci. Adv. 10.1126/sciadv.aav7662 (2019).

IN OTHER JOURNALS

Edited by **Caroline Ash** *and* **Jesse Smith**

ASTROBIOLOGY

Habitability impacts of molecular clouds

The Sun is currently located in a low-density region of interstellar space, but conditions would be very different if it were inside a giant molecular cloud (GMC). These vast assemblages of relatively dense gas and dust are concentrated within the Milky Way's spiral arms. Passing through a GMC would block visible light from other stars, owing to dust absorption, and reduce the habitability of Earth by scattering comets onto impact orbits. Kokaia and Davies calculated the expected encounter rate between the Sun and GMCs: 1.6 ± 1.3 per billion years, lasting a few million years each time. Fortunately for life on Earth, these disruptive encounters are rare. —KTS

Mon. Not. R. Astron. Soc., in press, arXiv:1903.08026 (2019).

NEUROSCIENCE

Remyelinating axons

The search for therapeutic targets to support remyelination in demyelinating diseases such as multiple sclerosis is challenging. Existing oligodendrocytes in the brain do not remyelinate demyelinated axons. Selective estrogen receptor modulators have been suggested to make oligodendrocyte precursor cells (OPCs) differentiate into functional, myelinating cells. In the search for myelinization-promoting agents, Rankin *et al*. selected bazedoxifene from a high-throughput screen and tested it in vitro and in vivo. This drug increased the differentiation of OPCs into functional oligodendrocytes (both in murine and human cells) and did so when axons were demyelinated after an induced lesion. A genetic knockout experiment revealed that the mechanism of action is independent of its presumed target, the estrogen receptor. Bazedoxifene is already approved by the Food and Drug Administration (as it is regularly prescribed for vasomotor menopausal symptoms in women) and is known for having relatively few side effects, which makes it a promising therapeutic drug for multiple sclerosis. —EACP

J. Neurosci. **39**, 2184 (2019).

PHOTO: NASA/JPL

ECOLOGY

Drought in tropical forests

In the context of a changing global climate, ecologists are examining the effects of drought on ecosystems. Drought has increased in several of the world's forested zones, including tropical West Africa, where Aguirre-Gutiérrez *et al*. have studied the multidecadal consequences of climate drying on forest composition and plant traits. In the Ghanaian study sites, drought has become more prevalent since the 1970s, and the authors were able to compare the responses of wetter and drier forests along a precipitation gradient. The drier forests were more able to adapt to further drought than were wetter forests and shifted toward a greater proportion of deciduous trees—a change that may enhance the resilience of the drier forest to further climatic change. —AMS

Ecol. Lett. **22**, 855 (2019).

Signs of climate change causing drought in a rain forest

SOIL MICROBES

Stinky molecules undermine competitors

Soil bacteria produce several earthy and unpleasant-smelling compounds, but for what reason? The filamentous bacterium *Streptomyces venezuelae* is known to both produce and respond to fishy trimethylamine as a volatile signaling molecule. Jones *et al*. found that airborne trimethylamine from *S. venezuelae* reduced growth and survival of other microbes growing nearby. This effect was reversed by iron supplementation, suggesting a role for trimethylamine in making iron less available to competing bacteria, likely by increasing the local pH. *S. venezuelae* may compensate for the unhospitable environment it has created by secreting iron-chelating compounds to recover recalcitrant iron. —MAF

mBio **10**, e00171-19 (2019).

PARKINSON'S DISEASE

Passing the sniff test

Parkinson's disease (PD) is a chronic progressive neurological disorder that largely affects movement. There is currently no diagnostic test. Trivedi *et al*. collected sebum samples from PD patients and unaffected volunteers to identify volatile metabolites that may serve as PD biomarkers. The research team included a woman with a sensitive sense of smell who reported to be able to detect PD by odor. In blinded studies, she identified the "musky" samples that belonged to the PD patients with high accuracy, which guided mass spectrometry to identify the volatile compounds that constituted a signature PD scent. These studies may pave the way for development of the first PD-specific diagnostic test. —PNK

ACS Cent. Sci. 10.1021/acscentsci.8b00879 (2019).

ELECTROCHEMISTRY

Tin and silver make a rough combination

There's a wide-ranging effort to find an efficient means of using electricity to transform carbon dioxide into value-added compounds. One persistent challenge in this context is identification of inexpensive catalysts that avoid competing production of hydrogen at the cathode. Choi *et al*. found that pretreating silver with an oxygen plasma initially favored carbon dioxide reduction, but hydrogen concentration rose over time. Depositing a tin oxide layer kept the hydrogen production at bay for at least 20 hours. X-ray spectroscopy suggested that the selectivity ensues from enduring surface roughness. —JSY

J. Am. Chem. Soc. **141**, 5261 (2019).

RESEARCH ETHICS

Research on wildlife

The use of animals in research has gained increasing attention and regulation, with the use of animals in laboratories now monitored by institutions and journals. Although there is still room for improvement for laboratory animals, monitoring of the welfare of animals studied in the wild has received much less attention. Field *et al*. investigated the legal and institutional oversight of animals studied in the field and found that legal guidelines are often unclear or absent and that institutional oversight, even when present, can be side-stepped. Furthermore, they found that journal requirements for publication collectively lack safeguards for the protection of wildlife during research, with only a third including any policy statement at all. —SNV

PLOS Biol. 10.1371/journal.pbio.3000193 (2019).

Wild-type and mutant *Streptomyces venezuelae* cultures growing on an agar medium

CREDIT: S. JONES *ET AL.*, *MBIO* **10**, E00171-19 (2019)

ALSO IN *SCIENCE* JOURNALS

Edited by **Michael Funk**

HUMAN PHYSIOLOGY

What to expect after a year in space

Space is the final frontier for understanding how extreme environments affect human physiology. Following twin astronauts, one of which spent a year-long mission on the International Space Station, Garrett-Bakelman *et al*. examined molecular and physiological traits that may be affected by time in space (see the Perspective by Löbrich and Jeggo). Sequencing the components of whole blood revealed that the length of telomeres, which is important to maintain in dividing cells and may be related to human aging, changed substantially during space flight and again upon return to Earth. Coupled with changes in DNA methylation in immune cells and cardiovascular and cognitive effects, this study provides a basis to assess the hazards of long-term space habitation. —LMZ

Science, this issue p. 144; see also p. 127

PLANT SCIENCE

Glycosylation goes back and forth

Plants produce receptors that recognize fragments of microbial flagellin, thus monitoring for infection by bacteria. Buscaill *et al*. studied how a flagellin fragment is made accessible for recognition by host glycosidases, which degrade the glycosylations shielding the peptide that triggers the immune response. The pathogen, in turn, evades detection by altering flagellin glycosylation and inhibiting the host glycosidase. This aspect of plant defense against infection plays out in the apoplast, the extracellular space within plant tissues. —PJH

Science, this issue p. 145

NEUROSCIENCE

Improved agonists for chemogenetics

Targeting ligand-responsive receptors to specific groups of cells, a strategy known as chemogenetics, is a powerful tool in many neurological applications. There is increasing interest in extending these tools for human treatment. Magnus *et al*. designed chemogenetic ion channels that improve currently available systems and are activated by the clinically used antismoking drug varenicline. They engineered a ligand-binding domain less responsive to endogenous signals and identified agonists that function at nanomolar concentrations. The combination of drug and introduced channels transiently silenced neurons, with slow but effective washout, and induced behavioral changes in animal models after brain administration. —PRS

Science, this issue p. 146

NEUROSCIENCE

Why is ketamine an antidepressant?

A better understanding of the mechanisms underlying the action of antidepressants is urgently needed. Moda-Sava *et al*. explored a possible mode of action for the drug ketamine, which has recently been shown to help patients recover from depression (see the Perspective by Beyeler). Ketamine rescued behavior in mice that was associated with depression-like phenotypes by selectively reversing stress-induced spine loss and restoring coordinated multicellular ensemble activity in prefrontal microcircuits. The initial induction of ketamine's antidepressant effect on mouse behavior occurred independently of effects on spine formation. Instead, synaptogenesis in the prefrontal region played a critical role in nourishing these effects over time. Interventions aimed at enhancing the survival of restored synapses may thus be useful for sustaining the behavioral effects of fast-acting antidepressants. —PRS

Science, this issue p. 147; see also p. 129

PHYSICS

Graphene: Driven to emission

Studying the electronic properties of graphene under extreme nonequilibrium conditions has provided a productive testbed to probe and monitor exotic transport phenomena. Andersen *et al*. report measurements of electron transport in ultraclean graphene devices where the electron drift velocity is extremely high. They found that direct current at high drift velocities generates a large increase in the noise at terahertz frequencies and that the noise grows exponentially in the direction of the current. The authors attribute the emission mechanism to amplification of acoustic phonons through the Cerenkov effect. —ISO

Science, this issue p. 154

PHYSICS

Making heat stand still

Dissipative oscillating systems (waves) can be described mathematically in terms of non-Hermitian physics. When parity-time symmetric systems have dissipative components, the interplay between gain and loss can lead to unusual and exotic behavior. Li *et al*. show theoretically and demonstrate experimentally that such behavior need not be limited to wave systems. Looking at the diffusion of heat, they devised an experimental setup comprising two thermally coupled disks rotating in opposite directions. The thermal energy transported by each disk is strongly coupled to the disk rotating in the opposite direction, providing a return path for the heat wave. For a particular rotation rate, there is an exceptional point where thermal coupling and counterrotating motion balance, resulting in the thermal energy profile being stationary over time. —ISO

Science, this issue p. 170

PLANT SCIENCE

A fatty acid triggers immune responses

Plants and animals respond to the microbial communities around them, whether in antagonistic or mutualistic ways. Some of these interactions are mediated by lipopolysaccharide—a large, complex, and irregular molecule on the surface of most Gram-negative bacteria. Studying the small mustard plant *Arabidopsis*, Kutschera *et al*. identified a 3-hydroxydecanoyl chain as the structural element sensed by the plant's lectin receptor kinase. Indeed, synthetic 3-hydroxydecanoic acid alone was sufficient to produce a response. A small microbial metabolite may thus suffice to trigger immune responses. —PJH

Science, this issue p. 178

SIGNAL TRANSDUCTION

Deubiquitinase fine-tunes Notch signaling

The branching of blood vessels is controlled in part by signaling through Notch receptor proteins. When NOTCH1 binds its ligand DLL4, the intracellular domain (NICD1) is cleaved from the receptor and works with other proteins to regulate gene transcription. In a screen for proteins that interacted with NICD1 in human cells in culture, Lim *et al*. identified the deubiquitinase USP10. NICD1 is rapidly ubiquitinated and degraded in cells, but interaction of NICD1 with USP10 counteracts ubiquitination of

NICD1 and stimulates Notch signaling. Genetic experiments in mice support a role for USP10 in fine-tuning Notch signaling during vascular morphogenesis. —LBR

Science, this issue p. 188

IMMUNOTHERAPY

Refocusing to target neurodegeneration

Given the success of immune checkpoint blockade in treating certain types of cancer and preclinical data connecting immune responses and neurodegeneration, might neurodegenerative disease be a viable future target of immunotherapy? In a Perspective, Liu and Aguzzi express words of caution about this approach, asserting that we do not yet know whether immune checkpoint blockade improves cognitive impairment that results from neurodegeneration. Instead, they suggest targeting inflammatory immune responses in the brain as a more promising approach consistent with preclinical data. —GKA

Science, this issue p. 130

AUTOIMMUNITY

Superagonist diabetogenic peptides

Type 1 diabetes is an autoimmune disease triggered in part by activation of $CD4^+$ T cells specific for insulin-derived autoantigens. Wang *et al*. prepared ternary complexes of a diabetogenic T cell receptor with insulin B-peptides and major histocompatibility complex class II proteins known to be associated with genetic susceptibility to diabetes. Fusion peptides with a covalent linkage of the carboxyl terminus of an insulin B-chain peptide to specific fragments of insulin C-peptide were highly potent ligands, enabling avid binding of both mouse and human T cell receptors. Transpeptidation reactions in lysosomes may therefore be a potential source of superagonist chimeric insulin peptides and play an important driver role in autoimmune diabetes. —IRW

Sci. Immunol. **4**, eaav7517 (2019).

CALCIUM SENSING

STIMulating basophils

The endoplasmic reticulum–resident calcium sensors STIM1 and STIM2 promote store-operated calcium entry, which is required for immune cell function. Using conditional knockout mice, Yoshikawa *et al*. found that the development of antigen-dependent allergic inflammation required STIM1 expression in basophils, but the response to a combination of the cytokines interleukin-3 and -33 required basophil expression of STIM2 (see the Focus by Alansary and Niemeyer). These results suggest that the STIM proteins in basophils have distinct roles in mediating responses to antigens or cytokines. —ERW

Sci. Signal. **12**, eaav2060, eaax0210 (2019).

RESEARCH ARTICLE SUMMARY

HUMAN PHYSIOLOGY

The NASA Twins Study: A multidimensional analysis of a year-long human spaceflight

Francine E. Garrett-Bakelman *et al.*

INTRODUCTION: To date, 559 humans have been flown into space, but long-duration (>300 days) missions are rare (n = 8 total). Long-duration missions that will take humans to Mars and beyond are planned by public and private entities for the 2020s and 2030s; therefore, comprehensive studies are needed now to assess the impact of long-duration spaceflight on the human body, brain, and overall physiology. The space environment is made harsh and challenging by multiple factors, including confinement, isolation, and exposure to environmental stressors such as microgravity, radiation, and noise. The selection of one of a pair of monozygotic (identical) twin astronauts for NASA's first 1-year mission enabled us to compare the impact of the spaceflight environment on one twin to the simultaneous impact of the Earth environment on a genetically matched subject.

RATIONALE: The known impacts of the spaceflight environment on human health and performance, physiology, and cellular and molecular processes are numerous and include bone density loss, effects on cognitive performance, microbial shifts, and alterations in gene regulation. However, previous studies collected very limited data, did not integrate simultaneous effects on multiple systems and data types in the same subject, or were restricted to 6-month missions. Measurement of the same variables in an astronaut on a year-long mission and in his Earth-bound twin indicated the biological measures that might be used to determine the effects of spaceflight. Presented here is an integrated longitudinal, multidimensional description of the effects of a 340-day mission onboard the International Space Station.

RESULTS: Physiological, telomeric, transcriptomic, epigenetic, proteomic, metabolomic, immune, microbiomic, cardiovascular, vision-related, and cognitive data were collected over 25 months. Some biological functions were not significantly affected by spaceflight, including the immune response (T cell receptor repertoire) to the first test of a vaccination in flight. However, significant changes in multiple data types were observed in association with the spaceflight period; the majority of these eventually returned to a preflight state within the time period of the study. These included changes in telomere length, gene regulation measured in both epigenetic and transcriptional data, gut microbiome composition, body weight, carotid artery dimensions, subfoveal choroidal thickness and peripapillary total retinal thickness, and serum metabolites. In addition, some factors were significantly affected by the stress of returning to Earth, including inflammation cytokines and immune response gene networks, as well as cognitive performance. For a few measures, persistent changes were observed even after 6 months on Earth, including some genes' expression levels, increased DNA damage from chromosomal inversions, increased numbers of short telomeres, and attenuated cognitive function.

CONCLUSION: Given that the majority of the biological and human health variables remained stable, or returned to baseline, after a 340-day space mission, these data suggest that human health can be mostly sustained over this duration of spaceflight. The persistence of the molecular changes (e.g., gene expression) and the extrapolation of the identified risk factors for longer missions (>1 year) remain estimates and should be demonstrated with these measures in future astronauts. Finally, changes described in this study highlight pathways and mechanisms that may be vulnerable to spaceflight and may require safeguards for longer space missions; thus, they serve as a guide for targeted countermeasures or monitoring during future missions. ■

ON OUR WEBSITE

Read the full article at http://dx.doi.org/10.1126/science.aau8650

The list of author affiliations is available in the full article online.
Email: nasa.twins.study@gmail.com
Cite this article as F. E. Garrett-Bakelman *et al.*, *Science* **364**, eaau8650 (2019). DOI: 10.1126/science.aau8650

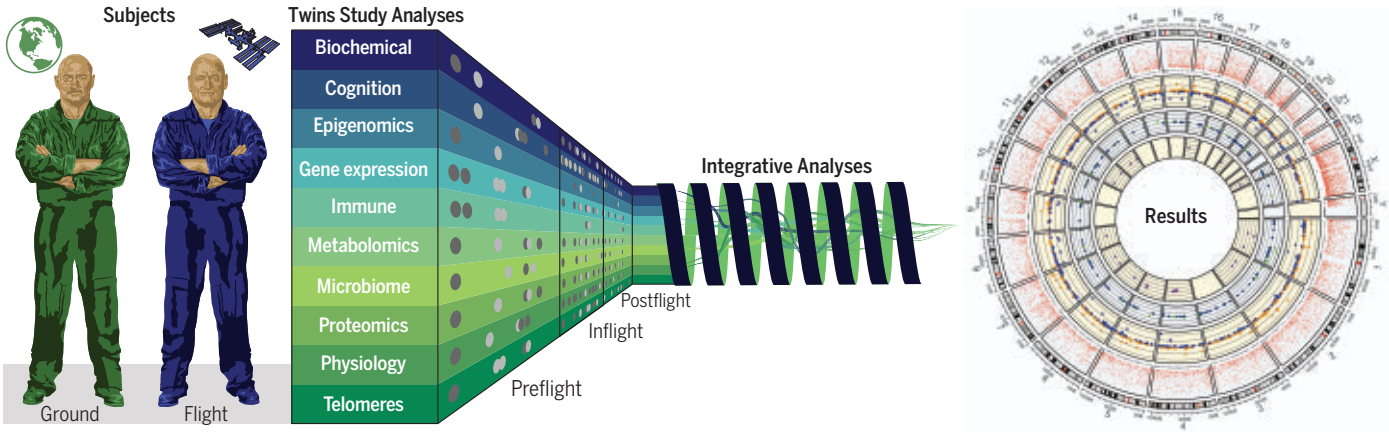

Multidimensional, longitudinal assays of the NASA Twins Study. (Left and middle) Genetically identical twin subjects (ground and flight) were characterized across 10 generalized biomedical modalities before (preflight), during (inflight), and after flight (postflight) for a total of 25 months (circles indicate time points at which data were collected). (Right) Data were integrated to guide biomedical metrics across various "-omes" for future missions (concentric circles indicate, from inner to outer, cytokines, proteome, transcriptome, and methylome).

RESEARCH ARTICLE

HUMAN PHYSIOLOGY

The NASA Twins Study: A multidimensional analysis of a year-long human spaceflight

Francine E. Garrett-Bakelman[1,2]*, Manjula Darshi[3]*, Stefan J. Green[4]*, Ruben C. Gur[5]*, Ling Lin[6]*, Brandon R. Macias[7]*, Miles J. McKenna[8]*, Cem Meydan[1,9]*, Tejaswini Mishra[6]*, Jad Nasrini[5]*, Brian D. Piening[6]*†, Lindsay F. Rizzardi[10]*‡, Kumar Sharma[3]*, Jamila H. Siamwala[11]*§, Lynn Taylor[8]*, Martha Hotz Vitaterna[12]*, Maryam Afkarian[13], Ebrahim Afshinnekoo[1,9], Sara Ahadi[6], Aditya Ambati[6], Maneesh Arya[7], Daniela Bezdan[1,9], Colin M. Callahan[10], Songjie Chen[6], Augustine M. K. Choi[1], George E. Chlipala[4], Kévin Contrepois[6], Marisa Covington[14], Brian E. Crucian[14], Immaculata De Vivo[15], David F. Dinges[5], Douglas J. Ebert[7], Jason I. Feinberg[10], Jorge A. Gandara[1], Kerry A. George[7], John Goutsias[10], George S. Grills[1]¶, Alan R. Hargens[11], Martina Heer[16]#, Ryan P. Hillary[6], Andrew N. Hoofnagle[17], Vivian Y. H. Hook[11], Garrett Jenkinson[10]**, Peng Jiang[12], Ali Keshavarzian[18], Steven S. Laurie[7], Brittany Lee-McMullen[6], Sarah B. Lumpkins[19], Matthew MacKay[1], Mark G. Maienschein-Cline[4], Ari M. Melnick[1], Tyler M. Moore[5], Kiichi Nakahira[1]††, Hemal H. Patel[11], Robert Pietrzyk[7], Varsha Rao[6], Rintaro Saito[11]‡‡, Denis N. Salins[6], Jan M. Schilling[11], Dorothy D. Sears[11], Caroline K. Sheridan[1], Michael B. Stenger[14], Rakel Tryggvadottir[10], Alexander E. Urban[6], Tomas Vaisar[17], Benjamin Van Espen[11], Jing Zhang[6], Michael G. Ziegler[11], Sara R. Zwart[20], John B. Charles[14]§§, Craig E. Kundrot[21]§§, Graham B. I. Scott[22]§§, Susan M. Bailey[8]§§, Mathias Basner[5]§§, Andrew P. Feinberg[10]§§, Stuart M. C. Lee[7]§§, Christopher E. Mason[1,9,23,24]§§, Emmanuel Mignot[6]§§, Brinda K. Rana[11]§§, Scott M. Smith[14]§§, Michael P. Snyder[6]§§, Fred W. Turek[12]§§

To understand the health impact of long-duration spaceflight, one identical twin astronaut was monitored before, during, and after a 1-year mission onboard the International Space Station; his twin served as a genetically matched ground control. Longitudinal assessments identified spaceflight-specific changes, including decreased body mass, telomere elongation, genome instability, carotid artery distension and increased intima-media thickness, altered ocular structure, transcriptional and metabolic changes, DNA methylation changes in immune and oxidative stress–related pathways, gastrointestinal microbiota alterations, and some cognitive decline postflight. Although average telomere length, global gene expression, and microbiome changes returned to near preflight levels within 6 months after return to Earth, increased numbers of short telomeres were observed and expression of some genes was still disrupted. These multiomic, molecular, physiological, and behavioral datasets provide a valuable roadmap of the putative health risks for future human spaceflight.

Hundreds of humans have flown in space since 1961, providing insight into the effects of environmental factors—including weightlessness, unloading, and radiation exposure—on the physiological responses of the human body and their functional consequences. Human physiological adaptation to short-duration (<1 month) and longer-duration (>4 months) spaceflight have been described, particularly for the cardiovascular, musculoskeletal, and sensorimotor systems (*1*). Some changes, such as headward fluid shift, are rapid and reach a new steady state relatively quickly (within days). By contrast, the nature of change in cardiovascular and muscular traits during longer missions is more pronounced, and their rate of return to baseline after spaceflight is prolonged (*2*). The headward fluid shift occurs immediately upon entry into weightlessness (*3*), resulting in a decrease in plasma and blood volume during the first few days of a mission (*4*) that plateaus in the first 2 weeks of flight. However, the decrease in plasma volume and red blood cells is not significantly different for short- or long-duration missions (*5*). Conversely, cardiovascular adaptations (e.g., left ventricular mass increase) and resulting downstream outcomes (e.g., orthostatic tolerance and maximal oxygen consumption losses) become more pronounced with longer-duration missions (*5*–*8*). Similarly, loss of muscle mass and strength are greater after longer-duration spaceflight (*9*–*11*). The adverse effects of these adaptations are especially clear upon return to Earth. Regular vigorous exercise, combined with adequate nutrition during spaceflight, mitigate some of the spaceflight-induced muscle (*9*, *12*) and bone loss (*13*) that occur during both short- and long-duration missions. However, recent evidence suggests that long-duration missions on the International Space Station (ISS) have resulted in some astronauts developing ocular changes, including optic disc edema and choroidal folds (*14*, *15*), termed spaceflight-associated neuro-ocular syndrome (SANS) (*16*). The incidence and severity of ocular symptoms varies, and the exact mechanism for the development of SANS is not well understood, which has limited NASA's ability to develop an effective countermeasure.

Although our understanding of the physiological and functional consequences of 4- to 6-month missions has increased greatly over the 18 years of continuous human presence on the ISS, there is almost no experience with spaceflight length greater than 6 months. Future missions, however, could be as long as 3 years, including transit to and from Mars and possible exploration of the planet, yet only four individuals have participated in spaceflight missions lasting 1 year or more. Moreover, investigations have not consistently implemented an integrated, cross-discipline study design or utilized multiomic approaches to biospecimen analyses. Thus, we have limited knowledge of the full range of the interactions of molecular, physiological, and cognitive dynamics that occur during long-duration spaceflight. Given the increasing number of vehicles providing access to spaceflight (*17*) and proposed missions to Mars, studies are needed to better understand the impact of prolonged spaceflight on human biology and health. Genetic, immune system, and metabolic functions are of particular concern given exposure to space radiations, restricted diet, reduced physical work requirements, disrupted circadian rhythms, and weightlessness. Importantly, longitudinal measures of biomarkers (such as genomic, epigenomic, biochemical, and physiological alterations) can provide critical metrics for astronaut health that could aid in assessment of increased risks and guide potential personalized interventions.

The NASA Twins Study investigators leveraged the opportunity to study identical twin astronauts, one in space and one on Earth. Data were generated from specimens collected and test protocols administered over 25 months, spanning time points before (preflight), during (inflight), and after (postflight) spaceflight with an integrated sampling scheme (Fig. 1A), including a wide variety of biological samples as well as cognitive and physiological measures (Fig. 1A and table S1). Our study also provides an example of inflight data and sample collection strategies used to generate a comprehensive, longitudinal, molecular, physiological, and cognitive profile, providing a scientific framework and baseline data for future studies. It is important to note that with a single test subject in the spaceflight environment for this

particular set of measures, it is impossible to attribute causality to spaceflight versus a coincidental event. Therefore, our study should be considered as hypothesis-generating and framework-defining and must be complemented in the future by studies of additional astronauts.

Results

A pair of male monozygotic twins were studied, one of whom spent 340 days aboard the ISS (flight subject; TW), while his identical twin remained on Earth (ground subject; HR). The subjects were 50 years of age at the time of study initiation and had accumulated different amounts of prior spaceflight exposure (Table 1). TW had, over the course of 12 years, a total of 180 days in space before the 1-year mission; there was a 4-year gap from the end of the previous long-duration mission until the start of this study. By contrast, HR had a total of 54 days in space and, at the time of this study, had not flown in space for almost 4 years.

Collected samples (n = 317) from both subjects throughout the duration of the study included stool, urine, and whole blood, which was also separated into peripheral blood mononuclear cells (PBMCs), sorted immune cells, and plasma. These samples were assayed for epigenomic, metabolomic, transcriptomic, proteomic, molecular, and microbiome changes (Fig. 1A and table S1). Additionally, subjects participated in physiological and cognitive tests in the laboratory during preflight and postflight ground-based testing and onboard the ISS (inflight).

Extensive multisystem changes occur in spaceflight

Data were generated from fresh (FR) and ambient return (AR) whole blood or PBMCs that were either directly processed and fractionated into subpopulations (T cells: CD4 and CD8; B cells: CD19; and lymphocyte depleted: LD) (fig. S1) or processed directly from frozen PBMCs. For fractionated subpopulations, the inflight collections were confounded by ambient return (AR specimens were collected on the ISS and returned to Earth via Soyuz capsule at room temperature). To simulate this effect, independent samples were generated to mimic FR and AR sample collection conditions and used for correction. Unsupervised analysis of gene expression profiles segregated TW's inflight from preflight and postflight samples, as well as from HR specimens, for all cell populations examined (fig. S2, A to E). Similar expression changes were observed for all cell types assessed (Fig. 1B). Differentially expressed genes (DEGs, DESeq2 multivariate negative binomial model, $q < 0.01$) were identified across all samples and cell types (n = 9317) with HR as the control and a particular focus on the differences that persisted postflight. In the LD cell population, of the 481 DEGs found inflight, compared with preflight, there were 112 (23.2%) that remained differentially expressed postflight (Fig. 1B and table S2). Across all sorted cell types, only 811 of the inflight DEGs remained disrupted postflight. Concomitant with an overall shift in mitochondrial RNA (mtRNA) levels (see below), far more DEGs (n = 8564, DESeq2 multivariate negative binomial model, $q < 0.01$) were observed in the 6- to 12-month inflight period compared with HR than in the 0- to 6-month inflight period (n = 1447) in PBMCs. This large (6×) shift in overall gene regulation upon exposure in TW to a year-long spaceflight suggests that overall gene regulation may be more affected by longer-duration spaceflight.

To assess physiological and immune signaling changes, the metabolome, proteome, and cytokine complement were measured using mass spectrometry and antibody-based methods. Targeted and untargeted metabolomics and proteomics were performed on plasma and urine samples, whereas cytokine profiling was performed only on plasma samples (fig. S3 and table S1). Untargeted analysis was focused on a high-confidence set of 719 metabolites (out of 4162 metabolic features) identified in plasma using a broad-spectrum liquid chromatography–mass spectrometry (LC-MS) metabolomics platform (*18*). Linear models demonstrate significant differences [false discovery rate (FDR) < 0.05] in the abundance of 245 metabolites among pre-, in-, and postflight samples between TW and HR, including those specific to the earlier or later halves of the flight period as well as those associated with time spent on the ISS (Fig. 1C and table S3). Additionally, 39 metabolites were significantly different (FDR < 0.05) between TW and HR at baseline (table S3). Metabolites indicative of genotoxic stress, inflammation, and altered amino acid metabolism were increased in TW inflight (table S3). Targeted metabolomic analysis using gas chromatography–tandem mass spectrometry (GC-MS/MS) was performed in plasma and urine to quantify metabolites involved in the tricarboxylic acid (TCA) cycle, glycolysis, and amino acid, fatty acid, ketone body, and pyrimidine metabolism. Of the 81 targeted metabolites, 60 and 66 metabolites were detected in plasma and urine, respectively (table S3). No significant changes were observed in plasma metabolites, but 32 urinary metabolites were significantly altered inflight for TW [FDR: $P < 0.05$, analysis of variance (ANOVA)]. To assess the epigenetic contribution to the changes observed, whole-genome bisulfite sequencing (WGBS) was performed on a subset of CD4 and CD8 samples from each subject. Global DNA methylation changes in TW were within the range of variation seen in HR throughout the study. However, ontology analysis of genes ranked on the basis of epigenetic discordance, as quantified by average promoter Jensen-Shannon distance (JSD) between samples, revealed distinct pathways enriched in TW when comparing preflight with inflight samples (Fig. 1D and tables S4 and S5). For example, in CD8 cells, enrichment in regulation of neutrophil activation or granulation was observed in TW [$q < 0.01$, hypergeometric test (HGT)], but not in HR (Fig. 1D). Similarly, in CD4 cells, enrichment in platelet aggregation (q = 0.0002, HGT) was observed only in TW.

To identify complex changes spanning diverse analyte classes that occur over time, the different data types were combined and scaled, and c-means clustering analysis was performed. Although this analysis (Fig. 1E) revealed that physiological levels for a large number of analytes were unaffected by spaceflight (Fig. 1E; clusters 1 and 2), several notable patterns were identified. These included a cluster of features, including cognitive performance, that for TW increased inflight and declined sharply upon return before reaching baseline (Fig. 1E, cluster 3; and Fig. 1F); this cluster was enriched for analytes involved in central carbon metabolism [$q < 0.0002$; integrated molecular pathway level analysis (IMPaLA) combined pathway analysis, Fisher's method]. Integrating gene expression changes with the other analytes revealed additional complex biochemical trajectories; for example, gene expression changes associated with neutrophil regulation were enriched ($q < 1 \times 10^{-12}$; IMPaLA combined pathway analysis, Fisher's method) in cluster 25 (fig. S5), illustrating an increase very early inflight followed by a steady decline, until increasing again postflight.

[1]Weill Cornell Medicine, New York, NY, USA. [2]University of Virginia School of Medicine, Charlottesville, VA, USA. [3]Center for Renal Precision Medicine, University of Texas Health, San Antonio, TX, USA. [4]University of Illinois at Chicago, Chicago, IL, USA. [5]University of Pennsylvania Perelman School of Medicine, Philadelphia, PA, USA. [6]Stanford University School of Medicine, Palo Alto, CA, USA. [7]KBRwyle, Houston, TX, USA. [8]Colorado State University, Fort Collins, CO, USA. [9]The Bin Talal Bin Abdulaziz Alsaud Institute for Computational Biomedicine, New York, NY, USA. [10]Johns Hopkins University, Baltimore, MD, USA. [11]University of California, San Diego, La Jolla, CA, USA. [12]Northwestern University, Evanston, IL, USA. [13]University of California, Davis, Davis, CA, USA. [14]National Aeronautics and Space Administration (NASA), Houston, TX, USA. [15]Harvard T.H. Chan School of Public Health, Boston, MA, USA. [16]University of Bonn, Bonn, Germany. [17]University of Washington, Seattle, WA, USA. [18]Rush University Medical Center, Chicago, IL, USA. [19]MEI Technologies, Houston, TX, USA. [20]University of Texas Medical Branch, Galveston, TX, USA. [21]Space Life and Physical Sciences Division, NASA Headquarters, Washington, DC, USA. [22]National Space Biomedical Research Institute, Baylor College of Medicine, Houston, TX, USA. [23]The Feil Family Brain and Mind Research Institute, New York, NY, USA. [24]The WorldQuant Initiative for Quantitative Prediction, New York, NY, USA.
*These authors contributed equally to this work. †Present address: Providence Portland Medical Center, Portland, OR, USA. ‡Present address: HudsonAlpha Institute for Biotechnology, Huntsville, AL, USA. §Present address: Brown University, Providence, RI, USA. ¶Present address: Augusta University, Augusta, GA, USA. #Present address: IUBH International University of Applied Sciences, Bad Reichenhall, Germany. **Present address: Mayo Clinic, Rochester, MN, USA. ††Present address: Nara Medical University, Nara, Japan. ‡‡Present address: Institute for Advanced Biosciences, Keio University, Tokyo, Japan.
§§Corresponding author. Email: jbcharle@gmail.com (J.B.C); craig.e.kundrot@nasa.gov (C.E.K.); graham_b_scott@yahoo.com (G.B.I.S.); susan.bailey@colostate.edu (S.M.B.); basner@pennmedicine.upenn.edu (M.B.); afeinberg@jhu.edu (A.P.F.); stuart.lee-1@nasa.gov (S.M.C.L.); chm2042@med.cornell.edu (C.E.M.); mignot@stanford.edu (E.M.); bkrana@ucsd.edu (B.K.R.); scott.m.smith@nasa.gov (S.M.S.); mpsnyder@stanford.edu (M.P.S.); fturek@northwestern.edu (F.W.T.)

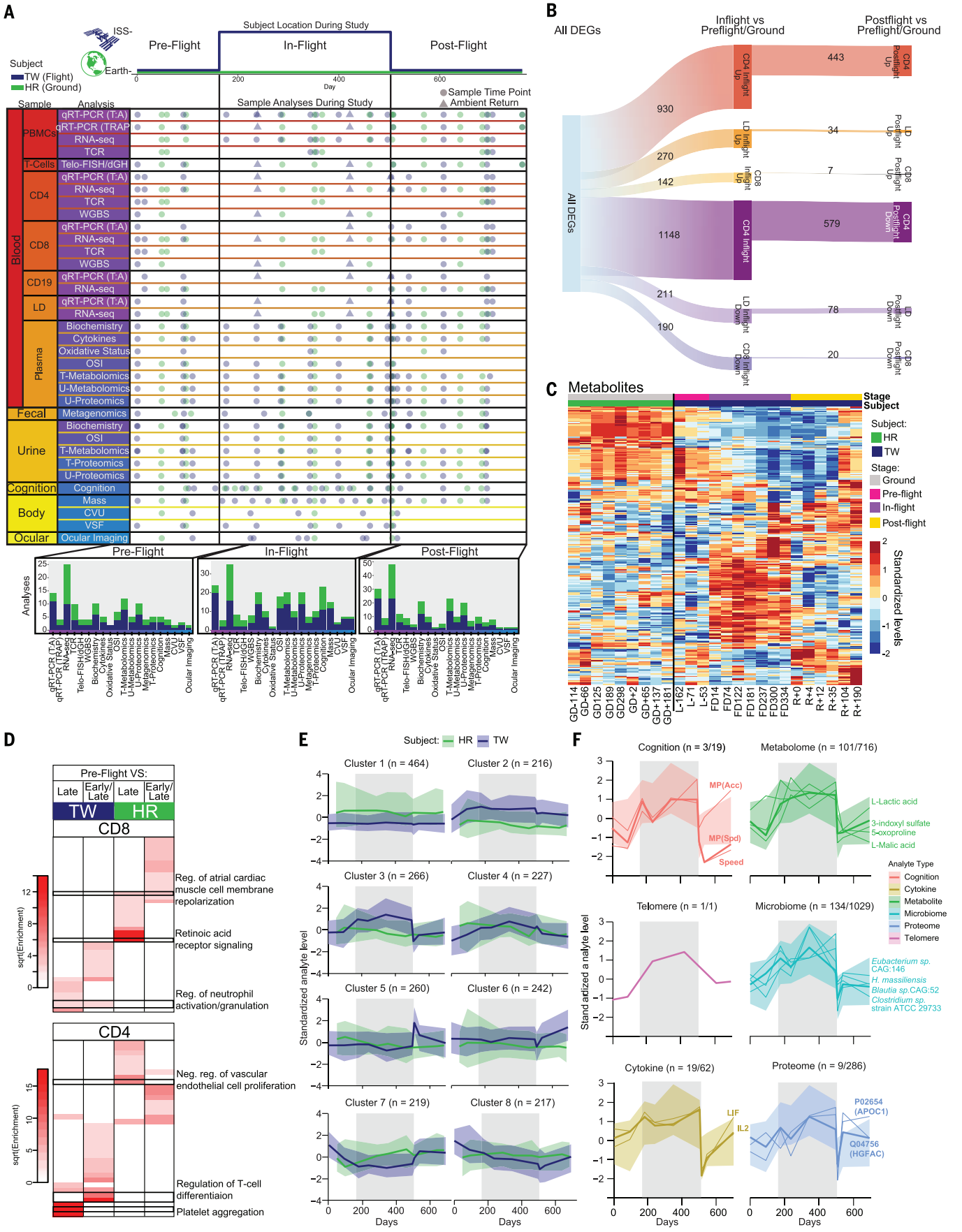
A
Subject Location During Study
Pre-Flight
In-Flight
Post-Flight
ISS-
Earth-
Subject
TW (Flight)
HR (Ground)
Sample Time Point
Ambient Return
Sample Analyses During Study
Sample
Analysis
Blood
PBMCs
T-Cells
CD4
CD8
CD19
LD
Plasma
Fecal
Urine
Cognition
Body
Ocular
Analyses
B
All DEGs
Inflight vs Preflight/Ground
Postflight vs Preflight/Ground
930
270
142
1148
211
190
443
34
7
579
78
20
C
Metabolites
Stage
Subject
Subject:
HR
TW
Stage:
Ground
Pre-flight
In-flight
Post-flight
Standardized levels
D
Pre-Flight VS:
Late
Early/Late
TW
HR
CD8
CD4
sqrt(Enrichment)
Reg. of atrial cardiac muscle cell membrane repolarization
Retinoic acid receptor signaling
Reg. of neutrophil activation/granulation
Neg. reg. of vascular endothelial cell proliferation
Regulation of T-cell differentiaion
Platelet aggregation
E
Subject: HR TW
Cluster 1 (n = 464)
Cluster 2 (n = 216)
Cluster 3 (n = 266)
Cluster 4 (n = 227)
Cluster 5 (n = 260)
Cluster 6 (n = 242)
Cluster 7 (n = 219)
Cluster 8 (n = 217)
Standardized analyte level
Days
F
Cognition (n = 3/19)
Metabolome (n = 101/716)
MP(Acc)
MP(Spd)
Speed
L-Lactic acid
3-indoxyl sulfate
5-oxoproline
L-Malic acid
Analyte Type
Cognition
Cytokine
Metabolite
Microbiome
Proteome
Telomere
Telomere (n = 1/1)
Microbiome (n = 134/1029)
Eubacterium sp. CAG:146
H. massiliensis
Blautia sp.CAG:52
Clostridium sp. strain ATCC 29733
Cytokine (n = 19/62)
Proteome (n = 9/286)
LIF
IL2
P02654 (APOC1)
Q04756 (HGFAC)

Fig. 1. Study design and human spaceflight metrics. The flight subject (TW, blue) and his identical twin (HR, green) were each studied over 25 months using a comprehensive set of health and biological metrics. (**A**) Earth-based and spaceflight collections include blood, sorted cells (CD4, CD8, CD19, and LD), stool, buccal, saliva, urine, and AR blood. TCR, T cell receptor sequencing; T- and U-Metabolomics, targeted and untargeted metabolomics; OSI, oxidative stress and inflammation; T- and U-Proteomics, targeted and untargeted proteomics; CVU, cardiac and vascular ultrasound; VSF, vascular structure and function. (**B**) Gene expression changes in TW inflight and postflight compared with the preflight period. All time points of HR were used to account for normal levels of variance and noise in gene expression. Genes that were significantly altered inflight after controlling for subject baselines and AR effect are reported. Gene expression changes were reported for any gene with $q < 0.05$ in a multivariate model that utilized expression values for polyadenylated [poly $(A)^+$] and ribosomal RNA depleted transcripts. (**C**) Metabolites present at significantly different levels in HR and TW or between pre-, in-, and postflight periods. Heatmap represents median-normalized $\log_2$ intensity for each analyte, scaled across all samples. Red color indicates relative enrichment, whereas blue indicates relative depletion. (**D**) GO analysis of genes ranked on the basis of epigenetic discordance at their promoters. Comparisons of preflight samples to inflight (early and late, and combined early and late) and postflight samples are shown for both CD4 and CD8 cells. Heatmaps represent transformed enrichment values [square root (sqrt) of enrichment] for GO categories with a raw enrichment value >5. Reg., regulation; neg. reg., negative regulation. (**E**) *C*-means clustering of multiomics data reveals longitudinal patterns associated with spaceflight. Analyte abundance (scaled) plotted over time for the identified clusters from the integrated metabolome, proteome, cytokine, cognition, and microbiome datasets is shown. Median abundance (bold) per cluster and 5th and 95th percentiles of abundance (shaded) are indicated. The gray shaded region indicates the inflight period. *n*, number of analytes in cluster. (**F**) Individual plots of the different analyte types that compose the spaceflight-dependent cluster, cluster 3, from (E). Telomere levels are plotted adjacent to the cluster members for reference. Median abundance (bold) per cluster and 5th and 95th percentiles of abundance (shaded) are indicated. Thin lines show annotated examples of analytes from cluster 3. For Cognition, accuracy [MP(Acc)] and speed [MP(Spd)] on the motor praxis task as well as standardized speed across cognitive domains (speed) are shown. *n*, number of analytes in cluster; CAG, coabundance gene groups.

Telomeres lengthened during spaceflight

Telomeres are repetitive features of chromosomal termini essential for maintaining genomic integrity; they protect physical DNA ends from degradation and prevent them from triggering inappropriate DNA damage responses (DDRs). Telomere length shortens with cell division and thus with age, as well as with a variety of lifestyle factors, such as stress, and environmental exposures, including air pollution and radiation. Here, average telomere length was evaluated pre-, in-, and postflight (DNA; PBMCs) using quantitative real-time polymerase chain reaction (qRT-PCR) (*19*, *20*). Consistent with a strong genetic component (*21*), HR and TW had similar telomere lengths at baseline (preflight $P = 0.942$; one-way ANOVA), and telomere lengths for HR remained relatively stable for the duration of the study (Fig. 2A). Most notable was a significant increase in telomere length during flight for TW (14.5%), as compared with his preflight and postflight measures as well as with those of HR ($P = 0.048$, 0.0003, and 0.0073, respectively; one-way ANOVA). TW's increased telomere length was observed at all inflight time points assessed [flight day (FD) 14 to FD334; fig. S6A], as well as in sorted CD4, CD8, and LD cells, but not in CD19 cells (Fig. 2B and fig. S6B). These results are consistent with recently reported cell type–specific responses to factors that contribute to telomere length regulation (*22*). Notably, telomere length shortened rapidly upon TW's return to Earth, within ~48 hours [FD340 ambient return to R+0 (R+ days post return); fig. S6B] and stabilized to near preflight averages within months.

Additionally, metaphase chromosomes were prepared from pre-, in-, and postflight samples (stimulated T cells; ambient whole blood), and thousands of individual telomeres were evaluated with telomere fluorescence in situ hybridization (Telo-FISH) (*23*, *24*), an independent measure that showed the same trends observed with qRT-PCR (fig. S6C). Importantly, Telo-FISH cell-by-cell analyses also enabled generation of telomere length distributions that confirmed HR's relatively stable telomere lengths throughout the study (Fig. 2C and fig. S6D). Consistent with TW's increased average telomere length during spaceflight, temporal shifts toward increased numbers of longer telomeres and concurrent decreases in the numbers of shorter telomeres were also observed (fig. S6D); for example, there was a significant shift in TW's inflight (FD259) telomere length distribution as compared to his preflight (L–162; L– days before launch) distribution ($P < 2.2 \times 10^{-16}$; Mann-Whitney U test) (Fig. 2D). After returning to Earth (R+190), TW's telomere length distribution shifted back toward increased numbers of shorter telomeres, more closely resembling his preflight distribution. However, an increased number of signal-free chromosome ends, indicative of complete loss and/or critically short telomeres (i.e., below our level of resolution), was also apparent (Fig. 2D). Spaceflight-specific shifts in telomere length dynamics were also supported by gene expression results, in that when inflight, TW's down-regulated DEGs were significantly enriched in packaging-of–telomere ends and telomere-maintenance pathways, in both CD4 and CD8 cells [gene set enrichment analysis (GSEA), all $q \leq 0.001$] (table S2). Similarly, changes in DNA methylation of the gene promoter for *TERT*, which encodes the regulatory subunit of telomerase, were observed when comparing preflight with the late inflight time point in both CD4 and CD8 T cells (JSD rank 248 and 32, respectively); by contrast, for HR, *TERT* was not highly ranked (428 or greater) (table S5).

Telomerase is the reverse transcriptase capable of de novo addition of species-specific telomeric repeats onto the ends of newly replicated chromosomes (*25*). Telomerase activity was evaluated pre-, in-, and postflight (PBMCs, ambient) with the qRT-PCR telomeric repeat amplification protocol (TRAP) (*24*, *26*). In general, TW had lower levels of telomerase activity than HR throughout the study, whereas levels for the two individuals were similar preflight and postflight (fig. S6E). Unfortunately, telomerase activity was lost in all inflight samples collected onboard the ISS. Given the sensitivity of enzymatic activity to sample handling conditions, we speculated that unavoidable transit time and/or temperatures associated with ambient return (via Soyuz) destroyed telomerase activity. To test this hypothesis, we compared ground control samples that had been in transit ≤24 hours with those that had been in transit ≥48 hours, mimicking the transit time from the ISS to Johnson Space Center. Loss of telomerase activity was observed in all blood samples experiencing transit times ≥48 hours ($P = 0.002$; Student's *t* test); however, telomere length and DNA integrity were unaffected (fig. S6, F to H).

DNA damage responses during spaceflight

Chromosome aberrations were analyzed in the same samples as above to evaluate potential telomere-related instability (e.g., fusions) as well as to assess DDRs to ionizing radiation (IR) exposure during spaceflight (*27*), specifically galactic cosmic ray (GCR)–induced cytogenetic damage, as has been done previously in blood lymphocytes of astronauts (*28*). Here, high-resolution directional genomic hybridization (dGH) paints (*29*) for chromosomes 1, 2, and 3 were used to enable simultaneous detection of interchromosomal translocations and intrachromosomal inversions (Fig. 2E). Baseline frequencies of these structural variants were similar for the two subjects, with inversions being more frequent than translocations (Fig. 2F). TW's inversion frequencies increased at a greater rate than translocations, consistent with inflight IR exposure, particularly to high linear energy transfer (LET) space radiation (*30*, *31*). Indeed, a physical dosimeter dose of 76.18 milligrays and an effective dose of 146.34 millisieverts were recorded by NASA. Also consistent with IR exposure, genes whose expression was

altered inflight were significantly enriched in pathways related to DNA damage responses in LD, CD4, CD8, and PBMCs [generalized linear model (GLM), all $q \leq 0.002$; table S2]. Furthermore, TW's inversion frequencies continued to rise postflight, indicative of instability and possibly reflective of IR-induced DNA damage to stem cell compartments. Although TW's translocation frequencies were variable, translocations were also increased inflight and postflight compared with preflight, additional evidence of inflight radiation exposure and the persistence of GCR-induced cytogenetic damage (*32*).

DNA methylation patterning during spaceflight

We also examined DNA methylation in FR and AR specimens (Fig. 1A and table S1). Genome-wide DNA methylation levels were measured in CD4 and CD8 lymphocytes isolated from both subjects at four time points throughout the study: one preflight, two inflight (early and late), and one postflight. Principal components analysis (PCA) revealed a distinction in global DNA methylation between the two cell types and between subjects for the CD4 samples (Fig. 3A). Moreover, TW's inflight samples were distinct from preflight and postflight samples for both cell types. Subtle differences in both genome-wide mean methylation levels (MML) and normalized methylation entropy (NME; a measure of methylation stochasticity) were detected inflight for TW, which returned to baseline postflight (Fig. 3B). Although for HR, the direction of these changes was consistent in CD4 and CD8 cells, it was reversed for TW, with a decrease in MML at FD259 for CD4 cells and an increase in CD8 cells. Although MML and NME are not necessarily predictive of one another (*33*), an inverse relationship between genome-wide medians of MML and

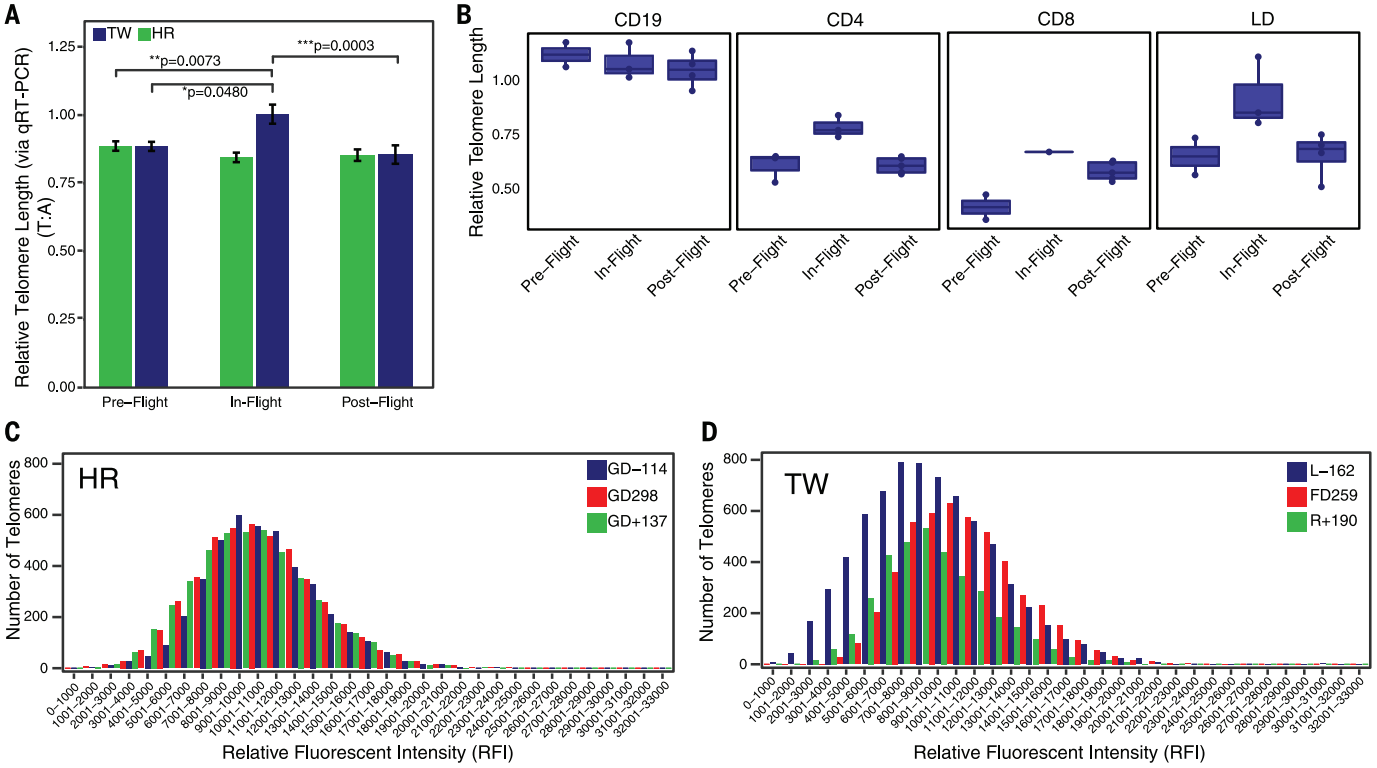

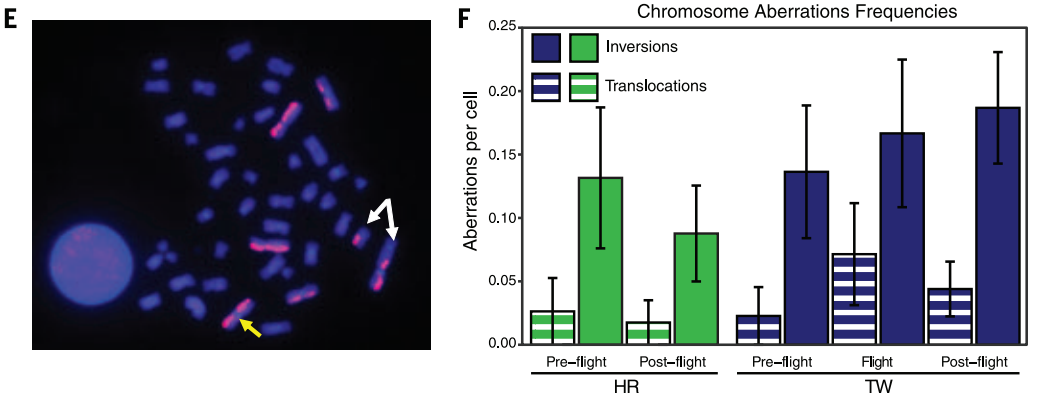

Fig. 2. Telomere length dynamics and DNA damage responses. (**A**) Relative average telomere length in PBMCs (DNA) pre-, in-, and postflight assessed by qRT-PCR for HR (green) and TW (blue). Significance was tested by one-way ANOVA, and error bars represent SEM. (**B**) Relative average telomere length for TW in sorted PBMC subpopulations, CD19 B cells, CD4 and CD8 T cells, and LD fractions, pre-, in-, and postflight. Boxplot whiskers show min and max. (**C** and **D**) Telo-FISH–generated histograms of individual telomere length distributions [shorter to longer, lower to higher relative fluorescent intensity (RFI)] for HR (C) and TW (D) preflight (blue), inflight (red), and postflight (green). (**E**) Cytogenetic analysis of DNA damage utilizing dGH paints (pink) for chromosomes 1, 2, and 3 facilitated simultaneous detection of translocations and inversions. Representative image of dGH on a metaphase chromosome spread illustrating an intrachromosomal inversion (yellow arrow) and an interchromosomal reciprocal translocation (white arrows). (**F**) Quantification of translocation (striped bars) and inversion (solid bars) frequencies for HR and TW pre-, in-, and postflight. Results were not statistically significant (one-way ANOVA). Error bars represent SEM.

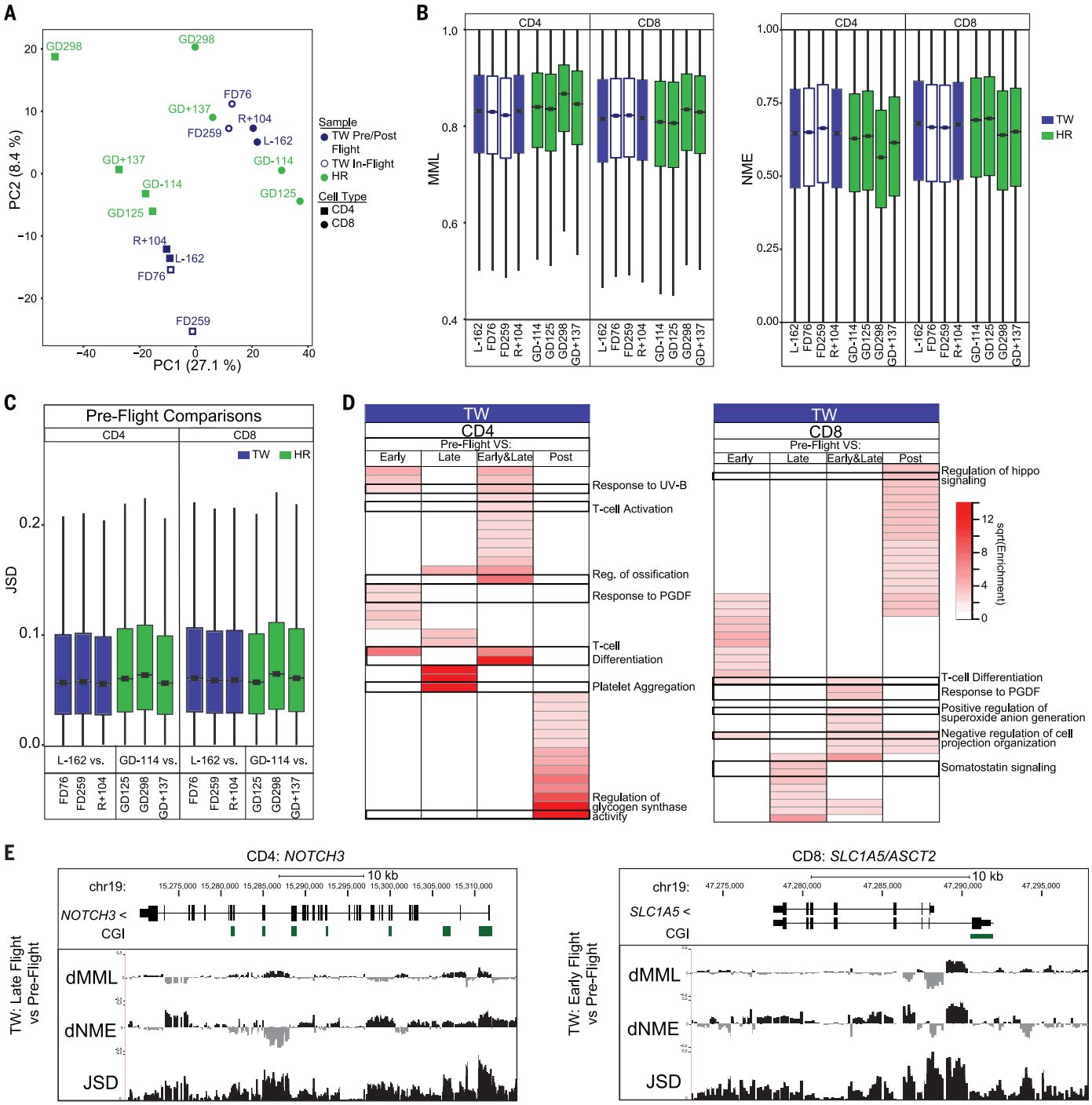

Fig. 3. Global changes in DNA methylation during spaceflight. (**A**) PCA of distances derived from average CpG methylation levels in 1-kb intervals along the chromosomes in each sample (CD4 and CD8 lymphocytes collected from each subject). (**B**) Genome-wide distributions of MML and NME values in CD4 and CD8 lymphocytes collected from each subject at indicated time points. (**C**) Genome-wide distributions of JSDs within each subject in comparisons of preflight to the indicated inflight and postflight time points in CD4 and CD8 cells. (**D**) Heatmaps representing transformed enrichment values (square root of enrichment) for GO categories with a raw enrichment value >5 in TW for comparisons of preflight (L−162) samples to inflight (early, FD76; late, FD259) and postflight (R+104) samples in CD4 and CD8 cells. (**E**) University of California, Santa Cruz, Genome Browser images of *NOTCH3* and *SLC1A5* with peaks of JSD at their promoters in TW when comparing inflight (FD259, for *NOTCH3*, and FD76, for *SLC1A5*) to preflight (L−162) samples from CD4 (for *NOTCH3*) and CD8 (for *SLC1A5*) cells. Differential MML (dMML) and differential NME (dNME) values are also plotted, with negative values indicating reduced MML or NME at the inflight time points compared with preflight time points. For all boxplots, center lines indicate median, boxes indicate interquartile range (IQR), and whiskers indicate 1.5 × IQR. CGI, CpG island; chr. 19, chromosome 19.

NME is evident across all samples. Importantly, the magnitude of changes in both MML and NME was greater for HR and did not fully return to baseline. These data indicate that genome-wide DNA methylation changes detected in CD4 and CD8 cells from TW were within the range of variation seen in HR.

These results identify only limited epigenetic discordance in global methylation and entropy levels. Therefore, we quantified both global and local epigenetic discordances between samples by calculating JSDs among all relevant pairwise comparisons within a cell type. Peaks of JSD indicate observable changes in the probability distributions of methylation levels within genomic regions, even if changes in mean methylation levels are small. Genome-wide JSD analysis revealed only subtle changes when comparing preflight with inflight or postflight samples within a subject (Fig. 3C). By contrast, we observed greater JSD changes in comparisons between subjects, particularly in CD4 cells (fig. S7A), consistent with our observation of higher MML and NME changes in that cell type (Fig. 3B). Similar to the results associated with methylation level and entropy, the magnitude of JSD changes was slightly greater for HR than for TW, again indicating that global methylation changes in TW were within the range observed for HR.

Although the observed genome-wide changes were minimal, we hypothesized that local changes at promoters of genes involved in environmental adaptation could be particularly affected in TW during flight. We therefore ranked genes according to their epigenetic discordance, as quantified by the JSD, and used these ranked lists for gene ontology (GO) enrichment analysis (table S4). When comparing inflight with preflight samples from TW, we observed enrichments for genes involved in the response to platelet-derived growth factor (PDGF) and T cell differentiation and activation pathways in both CD4 and CD8 cells (Fig. 3D). Genes involved in platelet aggregation (q = 0.028, HGT), regulation of ossification (q = 0.009, HGT), and cellular response to ultraviolet-B (UV-B) (q = 0.039, HGT) were also enriched in these comparisons, specifically in CD4 cells. By contrast, analysis of CD8 cells revealed enrichment in genes involved in the somatostatin signaling pathway (q = 0.016, HGT) and positive regulation of superoxide anion generation (q = 0.016, HGT). Importantly, for all time point comparisons, the most enriched GO terms for TW preflight versus inflight were not enriched in HR (Fig. 1D).

Immune response and inflammation during spaceflight

Differential gene expression analysis indicated that many immune-related pathways were significantly changed inflight across all cell types (GLM, $q < 0.001$), including the adaptive immune system, innate immune response, and natural killer cell–mediated immunity (table S2). Additionally, DNA methylation analysis revealed epigenetic discordance (indicated by JSD peaks) for TW in the promoters of *NOTCH3*, a well-known regulator of T cell differentiation (*34*), and *SLC1A5/ASCT2*, which promotes T cell activation (*35*), between preflight (L–162) and inflight samples (FD259 for *NOTCH3* and FD76 for *SLC1A5*) in CD4 and CD8 cells, respectively (Fig. 3E). This epigenetic discordance was associated with a peak of increased promoter methylation (from 10.7 to 20.2%) and entropy (from 41.4 to 71.3%) during flight and was observed in TW, but not in HR nor between HR and TW in preflight samples (fig. S7, B and C), and for *SLC1A5*, was associated with differential expression (down-regulation) (table S2).

To further evaluate T cell and immune functionality in spaceflight, we assessed cytokine data for inflammation signatures. Although none of the cytokines assayed were significantly different at

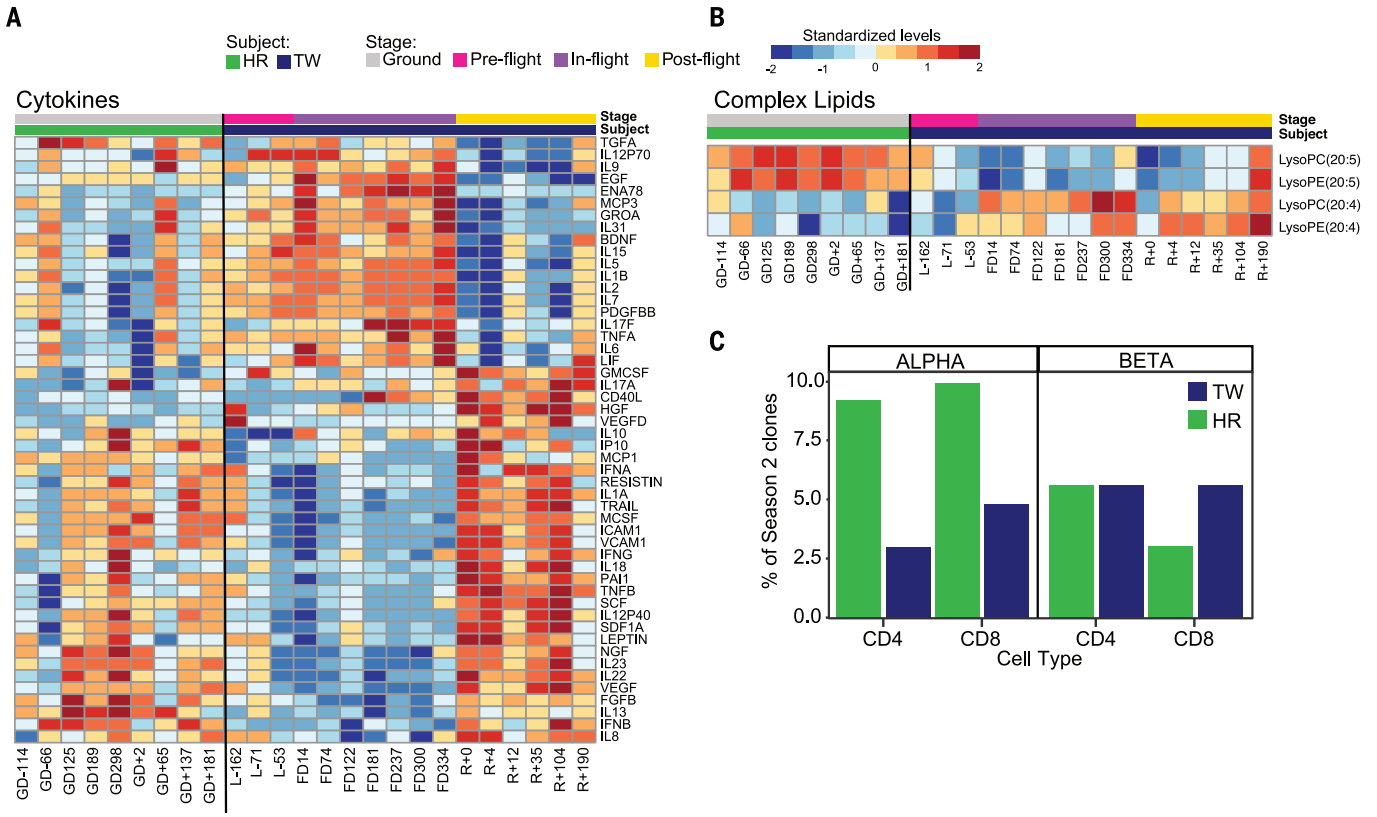

Fig. 4. Lipids and vaccine response. (**A**) Cytokines present at significantly different levels in HR and TW or between pre-, in-, and postflight periods. Heatmap represents median-normalized $\log_2$ intensity for each analyte, scaled across all samples. Red color indicates relative enrichment, whereas blue indicates relative depletion. (**B**) Relative levels (median-normalized, scaled $\log_2$ intensity) of complex lipids containing ω-3 and ω-6 fatty acids in HR and TW, from untargeted plasma metabolomics. Red color indicates relative enrichment, whereas blue indicates relative depletion. LysoPC, lysophosphatidylcholine; LysoPE, lysophosphatidylethanolamine. (**C**) Immunological and postvaccination response to spaceflight. For each subject, the proportion of season 2 clones present in the database of influenza vaccination-responsive CDR3 clones derived from year 1 and 3 vaccinations is shown for each cell type and respective TCR chain (FDR < 0.05).

baseline between TW and HR, 50 of the 62 cytokines assayed were differentially abundant between pre-, in-, and postflight in TW. We observed three notable signatures of inflammation. The first signature was composed of cytokines whose levels rose in TW's plasma in the days after return and continued to be increased 6 months after return. These return-associated cytokines included CSF2 (GM-CSF), HGF, IL10, IL17A, IL18, LEP (leptin), CD40LG (CD40L), LTA (TNFB), VEGFD, NGF, FGF2 (FGFB), IFNA2 (IFNA), IFNB1 (IFNB), IFNG, SERPINE1 (PAI1), RETN, ICAM1, VCAM1, TNFSF10 (TRAIL), and VEGFA (VEGF), among others (Fig. 4A and table S6). The second signature was composed of cytokines that were at relatively high levels in TW preflight, continued to be high inflight, and decreased after return. These cytokines included BDNF, EGF, CXCL5 (ENA78), CXCL1 (GROα), IL2, IL6, LIF, PGDF-BB, TGFA, and TNF (TNFA), with several of them involved in mediating inflammation, cell growth, and cell proliferation, as well as tumor proliferation and vascularization (Fig. 1E and table S6). Of note, IL2 stimulation in CD8 cells activates Hippo signaling (*36*), and we observed enrichment in this pathway (q = 0.033, HGT) when comparing average promoter JSD (a measure of methylation discordance) from TW's preflight with postflight samples in both CD4 and CD8 cells (table S4). The third signature of inflammation was seen immediately after landing (R+0 and R+4), with up to eightfold changes for CCL2 (MCP-1), C-reactive protein (CRP), and IL1RN (IL1RA; fig. S8, A to C; ANOVA, q < 0.001; table S8). Notably, CCL2 levels were increased at R+0, whereas CRP levels rose at R+0 and continued to rise at R+4 days. IL1RA levels only peaked at our R+4 data collection point. All three measures returned to baseline levels by the R+36 collection. During both inflight and postflight periods in TW, we detected increased levels of lysophospholipids containing proinflammatory omega-6 20:4 fatty acid (arachidonic acid) (*37*), together with a decrease in lysophospholipids containing anti-inflammatory omega-3 20:5 fatty acid (eicosapentaenoic acid) (*38*), suggestive of an increased inflammatory status (Fig. 4B and table S3).

Finally, we performed a vaccination response experiment to compare the effect of an influenza immunization in the spaceflight environment with that on Earth on the T cell receptor (TCR) repertoires in both subjects with the 2015–2016 trivalent unadjuvanted flu vaccination. Samples were obtained from TW and HR before and ~10 days after a trivalent flu immunization at three time points over the duration of the study. TW was sampled both on Earth (years 1 and 3) and on the ISS (year 2). For samples collected on Earth, repertoires for CD4 and CD8 T cells were separated, whereas frozen PBMCs from the ISS were expected to be a mixture of CD4 and CD8 repertoires. Vaccination-responsive clones were identified by matching complementarity-determining regions (CDR3s) pre- and postvaccination for each subject and cell type, with z scores as measures of change in a one-tailed approach. There were no significant differences (FDR > 0.05) in the percentage of unique CD4 or CD8 T cell receptor sequences (vaccination-responsive clones) that were noted as recruited by vaccination at 6 months inflight from the total PBMC fraction when compared with preflight and postflight responses in TW (Fig. 4C and fig. S9).

Taxonomic and functional microbial shifts during spaceflight

Changes over time in the gastrointestinal (GI) microbiota were examined with shotgun metagenome sequencing of genomic DNA extracted from serial fecal swabs of both subjects over the course of the study (tables S1 and S10). At the taxonomic level of genus, 1364 to 1641 taxa were detected in microbiome samples of both subjects. Although the richness of the fecal microbiome of HR was consistently higher than that of TW (P < 0.05, paired Wilcoxon signed-rank test, genus level) for the duration of the study, there were no significant differences between subjects in the Shannon index (SI; an index of diversity) (P = 0.82, paired Wilcoxon signed-rank test, genus level). Within TW, there was no decrease in richness or SI in inflight samples relative to preflight and postflight samples [median genera detected 1405.5 versus 1405; median SI ($\log_2$), 2.66 versus 2.42; Fig. 5A].

Fecal microbial communities from both subjects were dominated by bacteria from the phyla Firmicutes and Bacteroidetes, together representing >96% of all annotated sequences recovered. Actinobacterial and Proteobacterial sequences represented 1.97 and 1.27% of annotated sequences, respectively. The ratio of sequences derived from Firmicutes to those derived from Bacteroidetes (F/B ratio) ranged from 0.72 to 5.55. The F/B ratio in TW was higher in inflight samples relative to combined pre- and postflight samples (median F/B ratio 3.21 versus 1.45) but returned to preflight levels postflight (a maximum F/B ratio of 4.60 was observed in TW inflight; Fig. 5A). Yet, all TW F/B ratios were in the range of 0.01 to 5.96 observed in a healthy human cohort (*39*). Although HR had an increased F/B ratio at the second preflight sampling [ground day (GD)-56; GD- days before TW launch; F/B ratio of 5.55], this increased ratio was not sustained over time and was low throughout the remainder of the analysis period (range of F/B ratios was 0.72 to 1.76; Fig. 5A). Fecal microbiomes at all sampling time points from both subjects had high relative abundance of bacteria from the genus *Bacteroides* (ranging from 15.4 to 61.0% of reads annotated to the taxonomic level of genus).

When examining diversity among samples (beta diversity), fecal microbial communities of the subjects were significantly different [analysis of similarity (ANOSIM) sample statistic R = 0.587, P = 0.001] and remained distinct over time (Fig. 5B and fig. S10A). The microbial community structure observed in the four inflight TW samples was significantly different from the pre- and postflight samples combined (ANOSIM, R = 0.438, P = 0.016; Fig. 5B). No such effect was observed in HR samples (ANOSIM, R = −0.05, P = 0.579). Similar flight-associated trends were identified in targeted analyses of fungal and viral community structures (fig. S10B) and in analyses of functional gene content across all taxa (Fig. 5C). At the highest resolution of functional gene annotation (SEED function), the subjects had significantly different functional gene content (ANOSIM, R = 0.456, P = 0.003). For TW, the functional gene content observed in the four inflight samples was significantly different from the preflight and postflight samples (ANOSIM, R = 0.55, P = 0.016; Fig. 5C). No such change over time was observed for HR (ANOSIM, R = −0.094, P = 0.762).

To evaluate the extent of microbial community shifts in flight, we identified specific taxonomic groups and gene function features that were significantly altered during the inflight period in both subjects. Specifically, 0.5 to 4.5% of the detected microbial taxa—including 36 species, 13 genera, 8 families, 4 orders, 3 classes, and 3 phyla—were differentially abundant (FDR < 0.05), when inflight samples were compared with the combined pre- and postflight periods (Fig. 5D). However, we found a smaller number of altered microbial groups at each taxonomic level in HR for the same comparison (Fig. 5D). Similar observations were made when analyzing functional gene content. The spaceflight environment significantly (FDR < 0.05, EdgeR) altered the abundance of a moderate fraction (2 to 23%) of gene functional categories at each level in TW inflight compared with the combined preflight and postflight periods. The number of altered gene functional categories was smaller for HR during the inflight-equivalent period (Fig. 5E). Overall, TW's inflight samples had high similarity in taxonomic composition and functional gene content, as assessed with Bray-Curtis similarity (Fig. 5F). The level of similarity within TW's inflight samples was slightly higher than the inflight-equivalent samples from HR for both taxonomic and functional gene annotations (P = 0.03 and 0.31, paired Wilcoxon signed-rank test, respectively). Although TW had more similar preflight and postflight microbial communities than HR, these differences were not significant (P = 0.16 and 0.13, paired Wilcoxon signed-rank test, for taxonomy and functional gene annotations, respectively; Fig. 5F).

Finally, we examined metabolomic data for corroboration with the microbiome signatures. We observed several small-molecule markers of microbial metabolism in the untargeted LC-MS metabolomics data, including phenyls, secondary bile acid metabolites, and indole containing compounds, some of which are produced solely by microbial metabolism. Some metabolites, such as 3-indole propionic acid, have anti-inflammatory effects and were observed at lower levels in TW throughout the duration of the study (Fig. 5G and table S3).

Mitochondria-related adaptations during spaceflight

Our integrated analyses identified a number of mitochondria-related changes at the genomic and functional levels related to the 1-year mission.

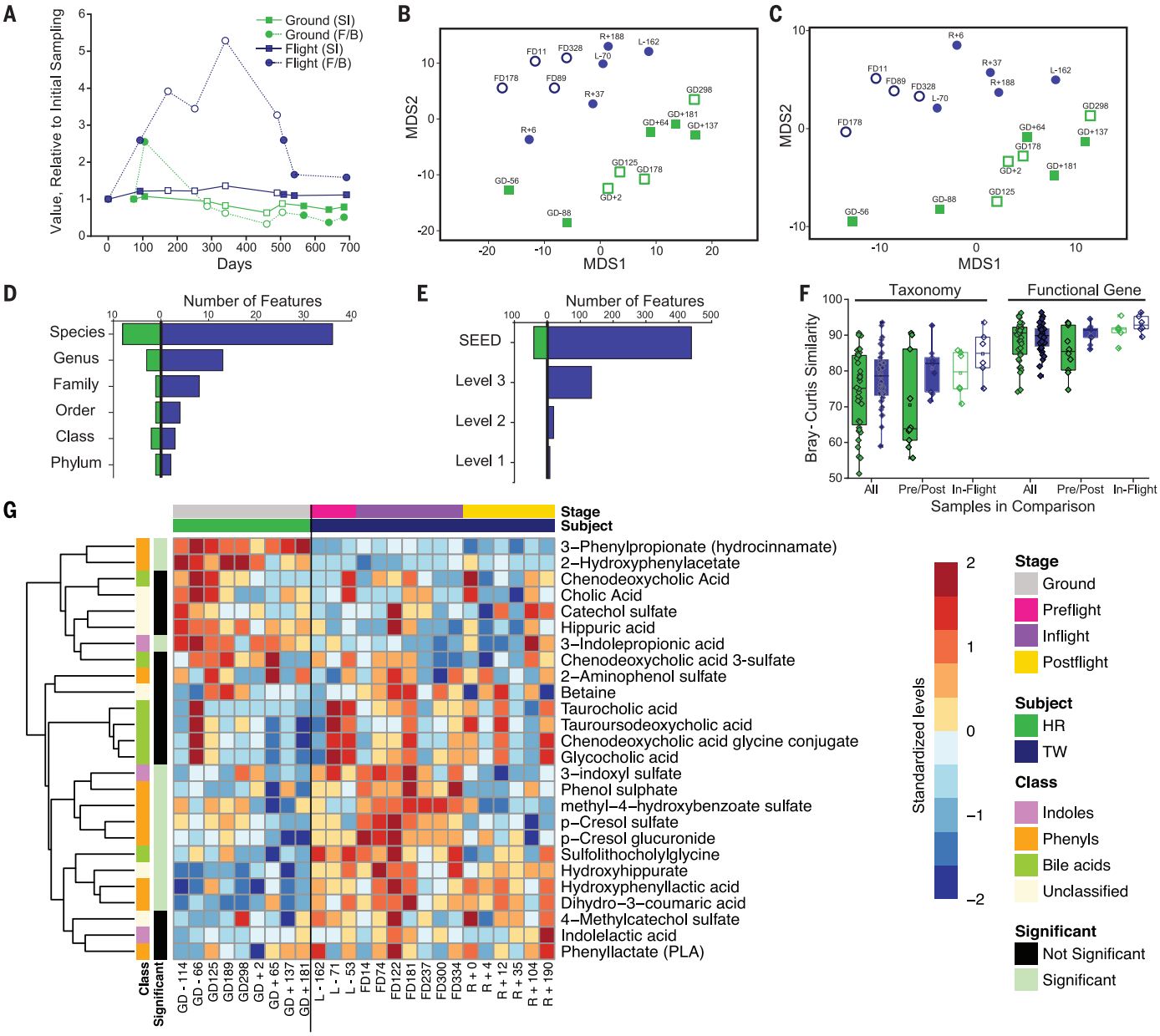

Fig. 5. Effect of spaceflight on the fecal microbial community structure of the flight subject relative to the twin ground subject. Samples are color coded by subject (TW, blue; HR, green), with open symbols representing flight samples from TW or flight-equivalent samples from HR. (**A**) Taxonomic alpha diversity parameters for HR and TW over nine sampling events, normalized to the value of the first sampling event for each subject. Shown are the normalized genus-level $\log_2$ SI values for both subjects and the F/B ratio. SI values at the first sampling event were 4.26 and 3.13 for HR and TW, respectively. F/B ratio values at the first sampling event were 2.18 and 0.87 for HR and TW, respectively. (**B** and **C**) Analysis of microbial community taxonomic structure at the genus level (B) and functional gene content (C) using mMDS of annotated shotgun metagenome sequence data. Data were $\log(x + 1)$ transformed, and a resemblance matrix, from Bray-Curtis dissimilarity, was generated. MDS axes 1 and 2 are plotted; two-dimensional stress values are 0.19 and 0.13 for taxonomic and functional gene analyses, respectively. Sample names represent dates relative to launch. (**D**) Number of microbial features at each taxonomic level that were differentially abundant between the inflight samples and the combined pre- and postflight samples of TW or between the equivalent sets of samples from HR. (**E**) Number of gene functional features at each level (ranged from SEED, that is, the most specific gene functions, to level 1, that is, the most general categories) that were differentially abundant between the inflight samples and the combined pre- and postflight samples of TW or between the equivalent sets of samples from HR. (**F**) Overall similarity of metagenomic sequence data from sample groups was assessed with Bray-Curtis similarity measurements for untransformed data and presented as boxplots. For each subject, all nine samples are compared and plotted (HR and TW; 36 comparisons), followed by pre- and postflight samples only (HR ground and TW ground; 10 comparisons) and flight samples only (HR flight and TW flight; six comparisons). (**G**) Metabolic products associated with microbial metabolism in humans. The heatmap shows relative levels of microbial metabolites detected in the metabolomics data (median-normalized, scaled, $\log_2$ intensity). Red color indicates relative enrichment, whereas blue indicates relative depletion. Row annotations mark different classes of microbial metabolites, including indoles (violet), phenyls (orange), and bile acids (green). Metabolites that were not significantly altered between HR and TW or between pre-, in-, and postflight periods are marked in black.

Genic annotation of RNA sequencing (RNA-seq) data (40, 41) revealed higher levels of mtRNA inflight as compared with preflight and postflight (Fig. 6A and fig. S11A). The time spent on the ISS was correlated [coefficient of determination (R^2) = 0.84] with increased mtRNA inflight ($P = 3.6 \times 10^{-6}$, ANOVA). Mitochondrial genome coverage was consistent across all samples (fig. S11B) and validated by qPCR in DNA from blood plasma and qRT-PCR in RNA from PBMCs, supporting this finding further (fig. S11, C to E). We also conducted an extracellular flux assay that monitors real-time changes in the mitochondrial oxygen consumption rate (OCR, a measure of mitochondrial oxidative phosphorylation) by treating muscle cells (L6 cell line) with plasma from the astronauts. The results can be characterized as twofold, whereby the plasma can (i) increase basal respiration (Fig. 6B) and (ii) decrease the spare reserve adenosine triphosphate (ATP) capacity (Fig. 6C). These trends show an increase in ATP-linked respiration, decrease in nonmitochondrial respiration, and no change in maximum respiration (Fig. 6, D and E), which may also reflect the changes in mtRNA levels observed during flight.

Additionally, a significantly increased level of lactic acid ($P = 0.018$; ANOVA) was detected in TW's urine inflight, which returned to baseline postflight. The highest lactic acid levels were observed in TW during the first 15 days and final 14 days of spaceflight (Fig. 6F). GC-MS/MS urine metabolomics data showed an increase in the lactic acid/pyruvic acid ratio (Fig. 6G), indicating a shift from aerobic to anaerobic metabolism. A similar trend in lactic acid levels, as observed in the urine, was also observed in plasma, although only the lactic acid/pyruvic acid ratio was significantly altered in plasma at an FDR of 0.05 (fig. S12, A

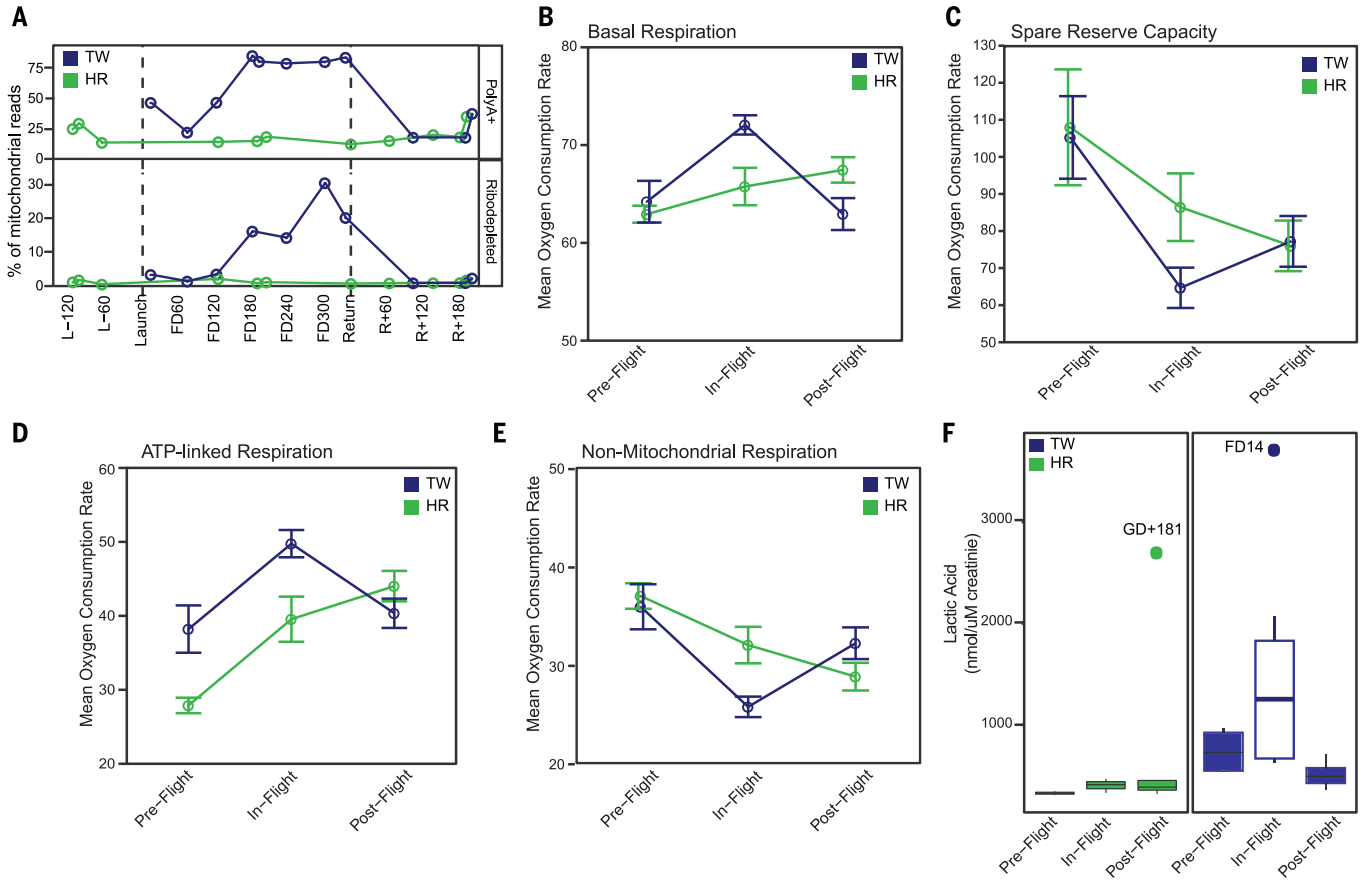

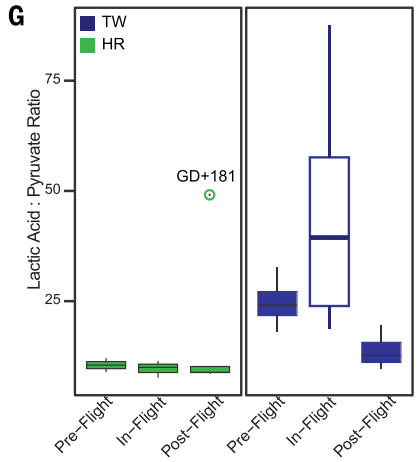

Fig. 6. Mitochondrial functions and Seahorse assays. (**A**) mtRNA content observed in RNA-seq data for the unsorted frozen PBMC (expressed relative to total number of aligned reads). Sequencing results after library preparation with both poly $(A)^+$ selection and ribosomal depletion. (**B** to **E**) Mean OCR during pre-, in-, and postflight for basal mitochondrial respiration (B), spare reserve capacity (C), ATP-linked respiration (D), and nonmitochondrial respiration (E). L6 muscle cells were treated with plasma from TW and HR collected pre-, in-, and postflight with six to eight assay replicates per time point. OCR was measured before and after the addition of inhibitors (oligomycin, a complex V inhibitor; FCCP, a protonophore; and antimycin A and rotenone, complex III and I inhibitors, respectively) to derive parameters of mitochondrial respiration. Mean OCR was calculated for each parameter after normalizing for baseline OCR of the L6 cells before the addition of plasma or inhibitors. Error bars represent 95% confidence intervals of the mean OCR of all replicates at each time point for each flight event. (**F**) Boxplots comparing the concentration of lactic acid in urine normalized to urine creatinines (determined by GC-MS targeted metabolomics) pre-, in-, and postflight in TW and HR. (**G**) Boxplots representing the ratio of urine lactic acid to pyruvate pre-, in-, and postflight in TW and HR revealing an inflight shift to anaerobic metabolism in the flight twin.

to C). Lactic acid production promotes higher extracellular acidification rates (42) that, in turn, are associated with increased expression of glycolysis-related genes. We also observed a trend for increased levels of plasma TCA cycle intermediates in the inflight period, such as citric acid and malic acid (FDR < 0.10), compared with preflight and postflight levels (fig. S12, D and E).

Given the previously noted changes in mitochondrial respiration, we examined TW's data for other related signatures. TW exhibited altered gene expression patterns in pathways related to oxygen and reactive species metabolic processes, mitochondrial transport, hypoxia, and apoptotic mitochondrial changes (GSEA, q < 0.0001) (table S2). Although differential expression of these genetic pathways is observed in response to hypoxic stimuli in a rodent model (43), the partial pressure of oxygen levels on ISS were near sea-level values (fig. S13).

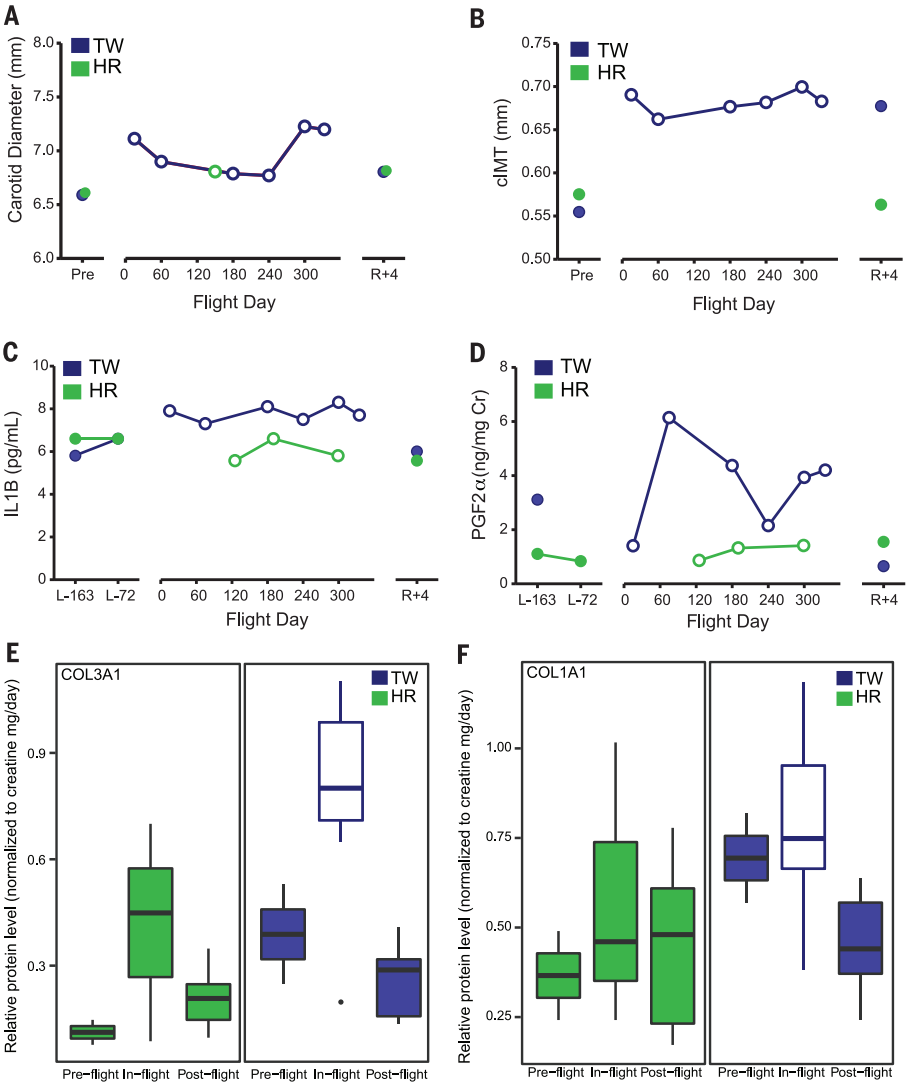

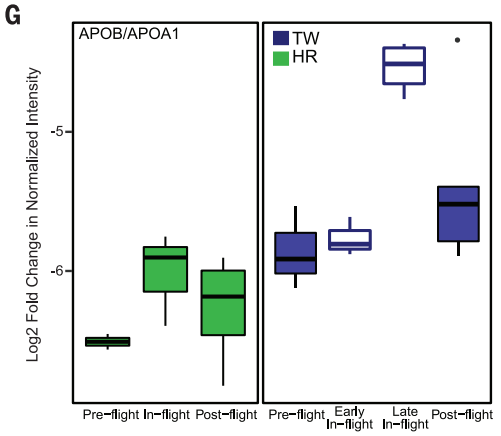

Fig. 7. Vascular adaptations. (**A** and **B**) Carotid artery diameter during diastole (A) and carotid intima-media thickness (cIMT) (B) measured while supine on the ground and during spaceflight in TW and HR. "Pre" indicates the mean of the two preflight measurements. (**C** and **D**) IL1B (C) and PGF2α (D) as examples of biomarkers of inflammation and oxidative stress that were measured in these two subjects. (**E** and **F**) Boxplots of relative COL3A1 (E) and COL1A1 (F) levels pre-, in-, and postflight for both subjects. (**G**) Ratio of relative plasma levels of proteins APOB and APOA1 (APOB/APOA1) in both subjects pre-, in-, and postflight, measured using untargeted proteomics (LC-MS).

Cardiovascular changes during spaceflight

Spaceflight-specific changes in cardiovascular structure and function were observed similar to those previously reported (44, 45) in astronauts during long-duration spaceflight, including a cardiac output increase of 10% (average of spaceflight measurements) (Fig. 7A) and a moderate decrease in systolic and mean arterial pressure (table S7) relative to the upright posture on Earth. Moreover, carotid artery distension developed early in flight during both systole and diastole and persisted throughout the mission (Fig. 7A). Concomitantly, carotid intima-media thickness increased in TW from preflight to inflight and remained thicker 4 days after landing (Fig. 7B). In addition, indices of inflammation, including cytokines [e.g., IL1A, IL1B, IL2, and prostaglandin F2α (PGF2α)] and chemokines, were increased during spaceflight in TW, whereas they remained unchanged in HR across all time points measured (Fig. 7, C and D; fig. S8; and table S6). Biomarkers of oxidative stress were not consistently increased [e.g., oxidized low-density lipoprotein (LDL), myeloperoxidase, and 8-hydroxy-2′-deoxyguanosine (8-OHdG)] in TW during spaceflight (table S8). However, targeted proteomics identified increased levels of two proteins that may be associated with observed changes in vascular wall dimensions. Collagen alpha-1(III) chain (COL3A1) and collagen alpha-1(I) chain (COL1A1) proteins in TW's inflight urine were increased compared with preflight levels, and these values returned to baseline levels postflight (Fig. 7, E and F). We also observed increased COL1A1, from measurements of two separate COL1A1 peptides, by untargeted proteomic analyses (Fig. 7F). This finding is consistent with enrichment of expression levels of genes in the collagen-related pathways [including but not limited to GO term "collagen trimer" and Reactome pathway "collagen formation" in PBMCs (DESeq2, q < 0.001)] (table S2). We also observed an increase in the ratio of plasma levels of apolipoprotein B (APOB; a major constituent of LDL particles) to apolipoprotein A1 [APOA1; a major constituent of high-density lipoprotein (HDL) particles] during the last 6 months inflight (late inflight; after FD180) in TW, compared with preflight and early inflight (ANOVA, P = 0.003, Fig. 7G). These levels decreased postflight and, then, were not significantly different from preflight levels. No significant increase was seen in HR, indicating an association of the APOB/APOA1 ratio with the long duration of the mission.

Body mass, nutrition, and hydration during spaceflight

Baseline and inflight values for HR and TW can be found in table S8. Similar to observations in other astronauts (46), TW lost 7% of his body

mass during flight, whereas HR gained ~4% of his body mass over the course of the study (Fig. 8A). TW had decreased urine volume (table S8) and increased urinary aquaporin-2 (AQP2) inflight compared with preflight, which both returned to baseline postflight (Fig. 8B). Serum sodium concentrations (Fig. 8B) and osmolality (Fig. 8C) followed urine AQP2 levels (Fig. 8D) for the duration of the study. TW's energy intake was about 66% of predicted requirements, and beyond the nominal vitamin D supplements provided to all astronauts, he did not report taking vitamin or mineral supplements during the mission. In TW, proteomic analysis revealed a decrease in urine angiotensinogen inflight relative to pre- and postflight that is correlated with the decline of body mass inflight (Fig. 8E).

Bone turnover markers for both breakdown (N-telopeptide; Fig. 8F) and formation (bone-specific alkaline phosphatase; Fig. 8G) increased 50 to 60% in TW during the first 6 months, as previously reported during 4- to 6-month spaceflights (*13*, *47*, *48*). However, these markers decreased in the last 6 months of the mission until immediately before landing. Similar trends were observed for other resorption (e.g., serum CTX-β) and formation markers (e.g., P1NP and osteocalcin; table S8), supporting these data. Bone formation and volume of resistive exercise before the blood draw followed similar trends (Fig. 8H), that is, when exercise volume was lower in the second half of the mission (due to injury), bone formation was correspondingly lower, as expected.

Neuro-ocular changes during spaceflight

Spaceflight resulted in a cephalad fluid shift and ocular changes in TW that were not present in HR. Internal jugular vein cross-sectional area, forehead tissue thickness, cardiac filling, stroke volume, and cardiac output increased, despite an average decrease in mean arterial pressure when compared with values associated with the seated position on Earth (Fig. 9, A and B). Increases in subfoveal choroidal thickness (primary vascular supply of the outer retina) and peripapillary total retinal thickness were observed, indicating retinal edema formation (Fig. 9, C and D). Moreover, although TW exhibited choroidal folds during preflight testing before this mission, the severity of the choroidal folds increased during spaceflight, as quantified by number and depth. These ocular structure parameters were unchanged in HR for the duration of the study, and choroidal folds were not present at the initiation of these data collection sessions (Fig. 9, A to D).

Of relevance to these ocular changes, untargeted proteomics revealed a decrease in urine leucine-rich alpha-2-glycoprotein (LRG1) levels in TW inflight relative to those pre- and postflight (Fig. 9E). LRG1 has been reported to play a role in retinal vascular pathology (*49*). The predisposition to develop these ocular changes during spaceflight has also been associated with B-vitamin status and the presence of specific single-nucleotide polymorphisms (SNPs) (*50*). Risk alleles in five SNPs predict incidence of ophthalmic issues (*49*), and six of the nine risk alleles are present in the twins (*50*). Furthermore, serum folate, a B vitamin that is often low in astronauts who experienced ophthalmic changes during flight (*51*), was also low in both TW and HR (Fig. 9F).

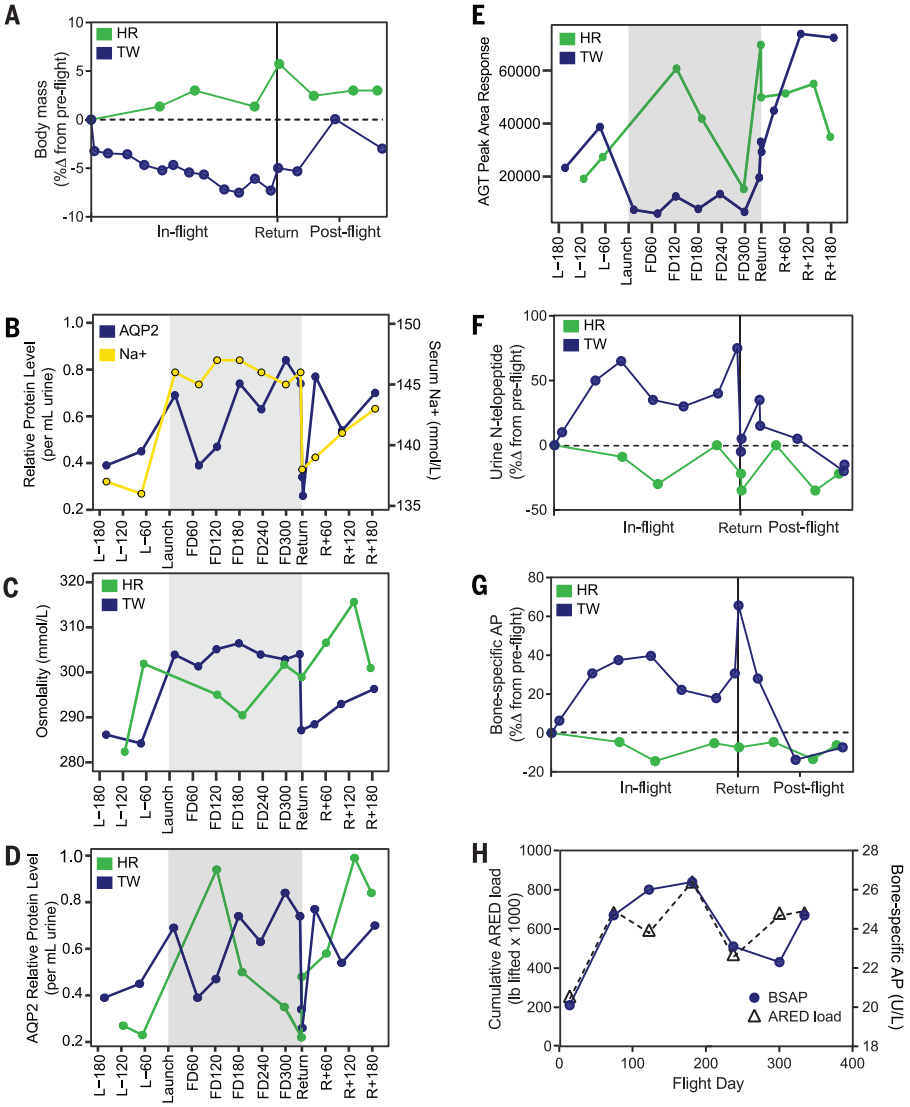

Fig. 8. Body weight, bone formation, fluid regulation, and biochemical activity during spaceflight. Biochemical and biophysical measures during the mission. Data are mean ± SD. (**A**) Body mass expressed as percent change (Δ) from preflight. (**B**) Relative urine AQP2 concentration in TW (blue circles) plotted along with serum sodium concentrations (yellow circles). (**C**) Calculated plasma osmolality for both subjects. (**D**) Relative urine AQP2 concentrations for both subjects. (**E**) Untargeted (LC-MS) urine proteomics reveals that relative angiotensinogen (AGT) levels inflight correspond with inflight weight loss. In (B) to (E), the shaded area represents inflight time points. (**F** and **G**) Bone breakdown (N-telopeptide) (F) and bone formation [bone-specific alkaline phosphatase (AP)] (G) markers. Data in (F) and (G) are expressed as percent change from preflight. (**H**) Exercise load using the advanced resistive exercise device (ARED) and bone-specific AP marker. 1 lb = 0.45 kg; U/L, units per liter.

Cognitive performance

Continuous high levels of astronaut cognitive performance are critical for mission success. Study subjects performed a computerized cognitive test battery (Cognition) (*52*) throughout all phases of the mission (Fig. 10A). TW's accuracy and speed scores were measured for the different phases of the mission [preflight, inflight months 1 to 6 (early flight), inflight months 7 to 12 (late flight), and postflight] (Fig. 10B). TW took more risk than HR on the balloon analog risk test (BART) during all phases of the mission, more so inflight compared with preflight and postflight. Compared with HR, TW did not exhibit significant deficits in either speed (−0.7 SD, $P = 0.3518$; Student's t test) or accuracy (−0.2 SD, $P = 0.6678$; Student's t test) across cognitive domains preflight. TW's cognitive speed increased across all cognitive domains early inflight relative to preflight. During

the same period, spatial orientation and motor praxis accuracy increased (>1 SD), whereas accuracy of visual object learning and abstract matching decreased (>1 SD) relative to HR. There was no significant decrease in performance from early to late inflight, with the following exceptions: (i) decline (>1 SD) in emotion recognition task (ERT) and digit symbol substitution task (DSST) speed and (ii) decline (>2 SD) in abstract matching (AM) accuracy (P = 0.0280; Student's t test; TW versus HR late flight, Fig. 10C). Performance trends across the study on key accuracy and speed metrics for all 10 tests in the Cognition battery are shown in fig. S14.

Most notably, cognitive speed decreased for all tests except for the DSST, and accuracy decreased for all domains except for spatial orientation postflight. TW's cognitive efficiency (a combination of speed and accuracy across cognitive domains) was similar pre- and inflight relative to HR but was significantly lower postflight (P = 0.0016, Student's t test). This postflight decline in cognitive performance persisted up to 6 months postflight in both speed and accuracy domains (Fig. 10C).

Discussion

The NASA Twins Study represents an integrated, multiomics, molecular, physiological, and cognitive portrait of an astronaut and reveals the biomedical responses of a human body during a year-long spaceflight. Our results demonstrate both transient and persistent changes associated

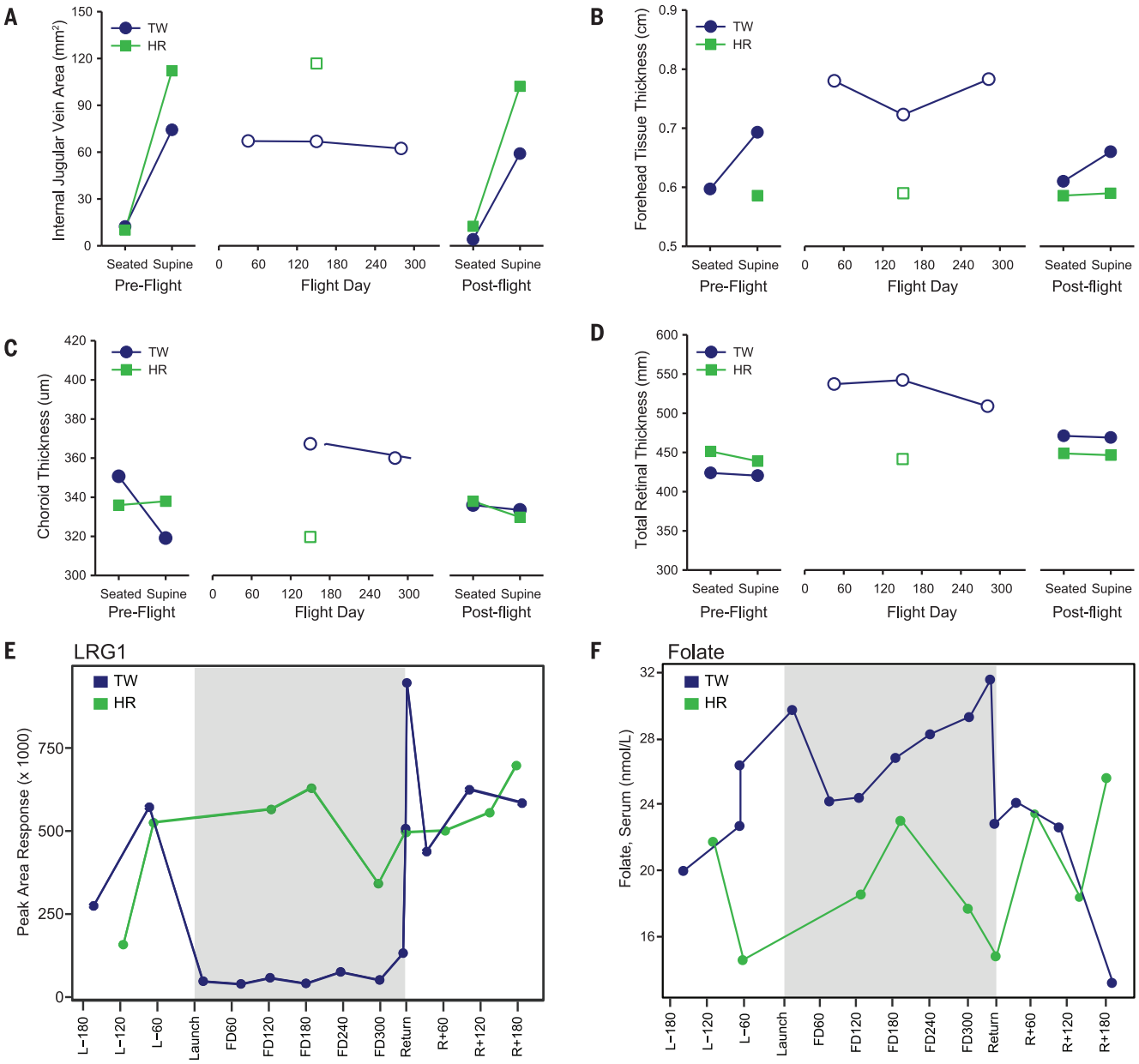

Fig. 9. Fluid shifts and ocular changes. (**A** and **B**) Internal jugular vein cross-sectional area (A) and forehead skin thickness (B) measured by ultrasound as indicators of acute fluid shifting during the transition from seated to supine during ground-based testing and the chronic fluid shift in weightlessness in TW. (**C** and **D**) Concurrently, ocular measures of choroid thickness (C) and total retinal thickness (D) measured by optical coherence tomography under the same conditions. (**E**) Untargeted proteomics reveals decreased urine excretion of LRG1 in TW during flight relative to ground time points. (**F**) Serum folate is lower in astronauts who experienced ophthalmic issues and was similarly relatively low in both twins. TW's serum folate increased during flight, mirroring the increase in telomere length.

with long-duration spaceflight across multiple cell types, tissues, genotypes, and phenotypes. These specific data, as well as the broader biomedical measures and sample collection methods, can now serve as a foundation for scientific and medical assessments of future astronauts, especially for those on prolonged, exploration-class missions.

NASA has announced plans for a Mars mission and a cis-lunar station, which will provide new opportunities for contextualizing human physiological and molecular dynamics during extended spaceflight. Data from this study indicate that at least 10 key physiological processes were influenced by long-duration spaceflight, which serve as targets for development of countermeasure interventions during future exploration-class human space travel. These include (i) body mass and nutrition, (ii) telomere length regulation, (iii) maintenance of genome stability, (iv) vascular health, (v) ocular structural adaptations, (vi) transcriptional and metabolic changes, (vii) epigenetic shifts, (viii) lipid level alterations, (ix) microbiome responses, and (x) cognitive function. These can further be classified as associations that are of potentially (i) low risk, (ii) medium or unknown risk, and (iii) high risk. These risk classifications are made on the basis of the degree of potential functional importance during spaceflight and their persistence for at least 6 months after returning to Earth.

Highly dynamic associations with potentially low risk

Many rapid physiological and molecular changes associated with spaceflight returned to near preflight levels, including average telomere length,

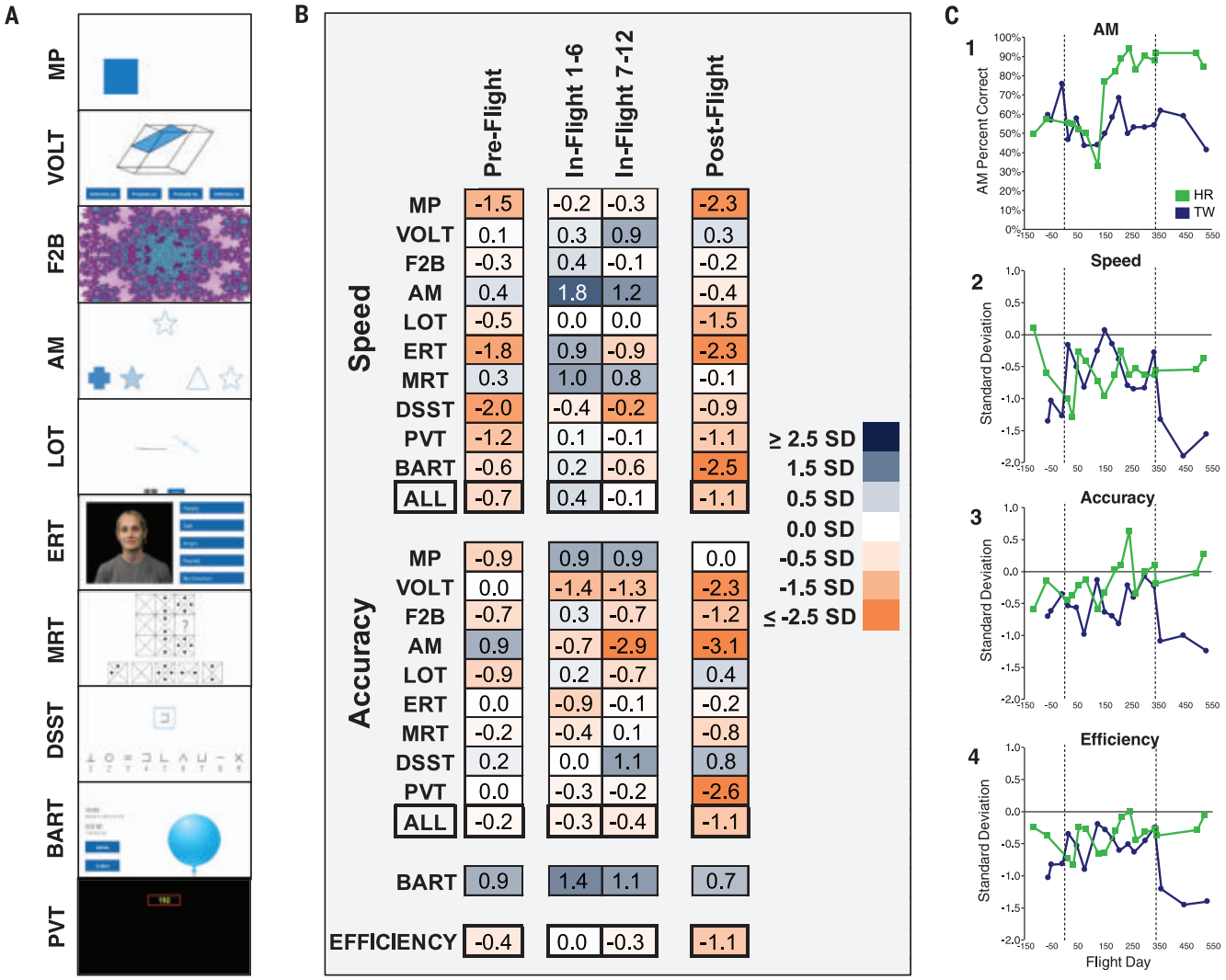

Fig. 10. Cognitive performance results. (**A**) Representative images of the Cognition battery (10 tasks). MP, motor praxis; VOLT, visual object learning test; F2B, fractal 2-back; AM, abstract matching; LOT, line orientation test; ERT, emotion recognition task; MRT, matrix reasoning test; DSST, digit symbol substitution task; BART, balloon analog risk test; PVT, psychomotor vigilance test. (**B**) Heatmap of cognitive performance scores of TW relative to HR during preflight (N = 3 tests), the first 6 months inflight (inflight 1 to 6, N = 6 tests), the second 6 months inflight (inflight 7 to 12, N = 5 tests), and postflight (N = 3 tests). Test scores were corrected for practice and stimulus set-difficulty effects. All data were then standardized relative to preflight ground data of 15 astronauts (including TW and HR). Test scores in the heatmap reflect TW scores minus HR scores expressed in SD units. The BART reflects risk-taking behavior and was thus not included in the accuracy score across cognitive domains (accuracy, ALL). Efficiency was calculated as the average of the speed score across cognitive domains (speed, ALL) and the accuracy score across cognitive domains (accuracy, ALL). (**C**) Standardized cognition performance scores for individual test bouts for the AM test (1) and speed (2), accuracy (3), and efficiency (4) across cognitive domains. The vertical lines indicate launch and landing dates for TW. The AM plot shows that HR (green) had a major insight mid-mission relative to the rules that govern the AM that TW (blue) did not have (50% is performance at chance level on the AM). The speed, accuracy, and efficiency plots demonstrate that the nature of the postflight decline in TW's performance was protracted.

body mass, microbiome composition, T cell function, and most cellular and tissue regulation (transcriptional and metabolic). Owing to their pronounced responses during spaceflight, these serve as important potential biomarkers for adaptation of the human body in space but likely represent minimal to low risks for long-duration missions.

Measures of gene function

The majority (91.3%) of the genes that changed expression in CD4, CD8, and LD cells during spaceflight returned to normal ranges within 6 months postflight (Fig. 1B and table S2). In addition, although some epigenetic loci were changed, the genome-wide epigenetic variance was higher in the ground control than in the flight subject during the 25 months of this study. Furthermore, the observed changes in metabolic levels in plasma returned to baseline postflight. The immune stress indicated by the transcriptional and proteomic data did not seem to impair recruitment of influenza-specific T cells, as evaluated by the response to the midflight vaccination, suggesting that primary immune functions, including chemotaxis, antigen distribution and trafficking, and presentation through the lymphatic system were maintained. Overall, these data show plasticity and resilience for many core genetic, epigenetic, transcriptional, cellular, and biological functions.

Telomere elongation

The spaceflight-specific telomere elongation observed in this study is consistent with similar findings in unrelated astronauts on shorter (~6 month) duration ISS missions, as well as in *Caenorhabditis elegans* flown on the ISS for 11 days (*53*). Although the underlying mechanisms and potential consequences of such transient telomere elongation are currently unknown, healthy lifestyle factors related to metabolic and nutritional status, physical activity, and weight loss have been associated with longer telomeres (*54*–*60*). Consistent with these studies, TW's reduced body mass and increased serum folate levels inflight correlated with telomere lengthening (fig. S15).

Microbiome changes

The GI microbiome can be expected to respond dynamically to changes in diet and other factors, and such variability over time was evident in both subjects. Although each subject maintained individual microbiome characteristics, more changes in microbial community composition and function were found during the flight period in TW than in the equivalent period in HR (Fig. 5). Given the number of significantly changed microbiome features inflight, it is likely that some microbiome changes observed are related to spaceflight. Inflight changes in small-molecule microbiome-derived metabolites (Fig. 5G) also suggest that the microbiome undergoes functional changes in response to spaceflight. Compared with the differences between individuals, the scale of microbiome changes in microbial diversity in TW during flight was relatively small and may be reflective of isolation and dietary change. This is consistent with ground-based studies of volunteers undergoing extended isolation (*61*, *62*). The flight subject showed a significant and spaceflight-specific increase in the F/B ratio; however, this ratio returned to preflight levels within weeks of landing, indicating a rebounding across the microbial ecosystem of the GI tract. Furthermore, the diversity of the microbiome, often considered an indication of microbiome health, was not decreased inflight. The health risks associated with these inflight changes are not known but may be minimal.

Associations with potential mid-level or unknown risk

Several features of long-duration spaceflight represent mid-level or unknown long-term risk, including collagen regulation, intravascular fluid management, and persistent telomere loss and/or critical shortening.

Collagen regulation

To our knowledge, spaceflight-related changes in urinary excretion of COL1A1 and COL3A1 have not previously been observed in astronauts. They are both more than twice the molecular weight of albumin, so whole collagen molecules would filter from blood into the urine poorly (*63*). They are present in the kidney in relatively low levels. Weightlessness alters loading on cartilage, bone, tendon, skin, vasculature, and the sclera, so these are other potential sources of increased urinary COL1A1 and COL3A1. TW had an increased internal jugular diameter and vascular remodeling of his carotid artery manifested as increased intima-media thickness. COL3A1 is a functionally important component of the vasculature, because defects in the *COL3A1* gene cause blood pooling in the legs and impaired blood pressure responses to standing. Changes in muscle, tendon, bone, and hydrostatic loading during weightlessness provide numerous sites where the body might undergo structural remodeling, leading to increased urinary excretion of COL1A1 and COL3A1.

Intravascular fluid management

Astronauts are at risk for dehydration, which can lead to increased renal stone risk (*47*). AQP2 controls water transport in the renal collecting duct epithelial cells and is regulated by vasopressin, which is released when the body is dehydrated. A decrease in both food and water intake might be linked to a decreased upper and lower GI motility associated with decreased gravitational force. The return to Earth usually leads to fluid retention and weight gain, and indeed, TW exhibited a modest weight gain in the days after landing. Our study provides evidence that an increase in urinary AQP2 manifests during spaceflight rather than being related to readaptation to the Earth environment and also correlates with serum sodium levels. It is thus likely that increased urine AQP2 was due to high plasma sodium stimulating vasopressin release. AQP2 is regulated by vasopressin, which elicits fluid reabsorption from the urine when activated (*64*). This renal water reabsorption protein was unable to fully compensate for decreased water intake, leading to an increased plasma sodium concentration and oncotic pressure during flight. TW's increased urine AQP2 may be the result of inflight dehydration or hypernatremia, as indicated by increased plasma sodium levels and measured by osmolality. For future missions, urine AQP2 levels should be monitored in crewmembers to identify who should be considered for potential therapeutic interventions to ameliorate the side effects and physiological complications of dehydration.

During spaceflight, 24-hour urine volumes are generally decreased, secondary to water intake and the low relative humidity onboard the ISS (*13*). Several of our findings may be associated with the reduced energy intake and weight loss observed in the flight subject, including telomere

Table 1. Spaceflight experience of study subjects. Summary of spaceflight missions (launch and landing dates) as well as durations for study subjects TW and HR.

Subject	Vehicle	Mission	Launch date	Landing date	Duration (days)
TW	Space shuttle	STS-103	12/19/99	12/27/99	8
	Space shuttle	STS-118	8/8/07	8/21/07	12.7
	International Space Station	Expedition 25/26	10/7/10	3/16/11	159
	International Space Station	Expedition 43/44/45/46	3/27/15	3/1/16	340
HR	Space shuttle	STS-108	12/5/01	12/17/01	11.8
	Space shuttle	STS-121	7/4/06	7/17/06	12.8
	Space shuttle	STS-124	5/31/14	6/14/14	13.8
	Space shuttle	STS-134	5/16/11	6/1/11	15.7

lengthening (56), decreased angiotensinogen (Fig. 8E), and decreased mitochondrial respiration (Fig. 6). Additionally, DNA methylation was altered inflight at genes enriched in the somatostatin pathway (Fig. 3D). Fasting is known to increase somatostatin transcription (65). Diminished caloric intake decreases many of the hormones related to blood pressure control and metabolism, generally lowering blood pressure and decreasing metabolic rate and muscle growth. TW had increased urine and plasma lactic acid levels inflight and an increased trend for TCA cycle intermediates (malic acid and citric acid), likely due to an intensive exercise regimen (Fig. 6F and fig. S12, D and E).

We also observed changes in urinary excretion of renin-angiotensin pathway proteins. In humans, renin and angiotensin II levels increase with upright posture, and high blood pressure is associated with higher urinary angiotensinogen (66, 67). Angiotensin II increases urinary angiotensinogen, probably because it stimulates production of angiotensinogen in the renal tubules. Astronauts are not "upright" in space, and an astronaut's blood pressure is lower in space (44). Indeed, we observed decreased angiotensinogen (fig. S5A) and lower blood pressure in TW inflight (table S7). The observed reduction in renin receptor protein in the urine during flight is likely due to a similar pathway that lowers angiotensinogen inflight.

Persistent telomere loss and/or critical shortening

The rapid (<48 hours) shortening of TW's telomeres upon return to Earth coincided with the extreme stresses associated with landing and a heightened inflammatory response, a well-established contributor to telomere shortening (68). The transient nature of spaceflight-induced telomere elongation was also apparent in TW's postflight telomere length distributions, which rapidly shifted back toward baseline upon return. However, there were substantial decreases in the number of telomeres detected, suggesting persistent telomere loss and/or increased numbers of critically short telomeres. Consistent with these observations, ISS astronauts in general tend to have significantly shorter telomeres after flight than before. The potential importance of such shifts in telomere length (elongation and accelerated shortening or loss) is underscored by accumulating evidence that supports telomere length not only as a robust biomarker of aging but also as a determinant of age-related diseases, such as cardiovascular disease and cancer (69). Because such metrics can inform overall health, monitoring telomere length dynamics represents an important element of evaluating health and potential long-term risk for future astronauts.

Associations with potentially high risk

Returning to Earth is an especially stressful event that represents one of the greatest physiological challenges of spaceflight. In the immediate post-landing period, manifestations of this include exaggerated or impaired cardiovascular, musculoskeletal, and stress and inflammatory responses (6, 11, 13, 70). Furthermore, there are concerns related to both the recovery period and to the long-term consequences of spaceflight with regard to cardiovascular, ocular, and cognitive systems, including the molecular features of astronauts' cells.

Spaceflight-associated neuro-ocular syndrome

As of May 2017, about 40% of astronauts have experienced one or more of the following ocular issues: optic disc edema, hyperopic shifts, globe flattening, cotton-wool spots, or choroidal folds (16). Multiple hypotheses have been proposed to explain the development of these symptoms, collectively referred to by NASA as SANS (16), including the spaceflight-induced cephalad fluid shift and associated adaptations. Distension of and increased pressure in the internal jugular vein were observed inflight in TW, at levels similar to those while supine on Earth. The result of this vascular engorgement may contribute to congestion of the vasculature supplying the retina, as suggested by the thickening of subfoveal choroid (14). Importantly, given that normal gravity and hydrostatic pressure gradients are not present onboard the ISS, there is no relief from the headward fluid shift as would be expected on Earth during normal postural changes. Indeed, clinical reports of optic disc edema from fundoscopy were confirmed by our optical coherence tomography measures of increased total peripapillary retinal thickness. Combined with worsening of choroidal folds from pre- to inflight, TW demonstrated symptoms that are consistent with SANS. Although some ocular changes recover in the postflight recovery period, such as choroidal congestion and retinal nerve fiber layer thickening, some ocular findings, including choroidal folds, may persist from a previous long-duration spaceflight mission (16) and worsen in a subsequent mission (71), as was observed in TW. By contrast, HR did not develop similar ocular findings across the measurements obtained during this study, despite participating in four previous short-duration space shuttle missions. Thus, any changes that HR might have experienced previously either did not manifest, despite HR expressing the same risk alleles as his twin brother, or had resolved since his last mission. These observations support the "multiple hit" hypothesis (72) that genetics presents a predisposing factor that manifests pathologically only when present in combination with one or more other physiological, biochemical, and/or environmental factors, including duration of continuous exposure (e.g., longer than a 2-week space shuttle flight).

Vascular physiology

The cephalad fluid shift that occurs when astronauts enter the weightless environment is hypothesized to be the initiating event associated with cardiovascular adaptations to spaceflight. Secondary to the loss of hydrostatic gradients due to weightlessness, about 2 liters of fluid move from the lower to the upper body (3, 7). Although some variability between crewmembers exists, this headward fluid shift is described as the appearance of a "puffy face" and "bird legs" in many crewmembers. Despite a relative decrease in plasma and blood volume (4, 5) and a reduction in blood pressure (44), stroke volume and cardiac output increase, and arteries and veins in the upper body are distended (73). Results from astronauts participating in 4- to 6-month missions reveal increased carotid intima-media thickness (45) and vascular stiffness (74) that are suggested to be related to increased oxidative stress, inflammation, and insulin resistance. Similar trends were observed in 10 astronauts completing 4- to 6-month missions, with carotid intima-media thickening observed early inflight that did not appear to increase further near the end of the mission (45). Consistent with these findings, similar adaptations developed in TW, as there was a rapid increase in carotid intima-media thickness after launch. However, the carotid intima-media layer did not continue to thicken during the latter half of the mission (from 6 to 12 months inflight). Whether the intima-media thickening is irreversible and represents an increased cardiovascular and cerebrovascular disease risk (75) across the lifetime of an astronaut is not yet known, especially because prediction of clinical events among otherwise healthy individuals is difficult. Similarly, we observed a pre- to inflight increase in the APOB/APOA1 ratio, specifically in the latter half of the mission, that might be suggestive of an increased cardiovascular disease risk in TW (76–78), but the long-term health consequences are as yet unknown. Measurements obtained during recovery from spaceflight in this subject, together with measurements taken from other astronauts in a companion study, will provide important information about the course of cardiovascular disease risk factors. Recent epidemiological studies suggest that astronauts do not have an increased cardiovascular morbidity (79) or mortality risk (80), but there is insufficient data to draw conclusions regarding astronauts who participate in long-duration missions; the vast majority of subjects in these investigations participated in short-duration missions.

Postflight stress and inflammatory response

The molecular features assessed in TW were consistent with a stress and inflammatory response in the days after landing. In particular, TW exhibited an increase in CRP from 1 to 19 mg/dl and increased levels of IL1RA (fig. S8, B and C, and table S8). TW's cytokine signature was also consistent with an inflammatory response upon return to Earth (Fig. 4A and fig. S8D). The stress and inflammatory response may have preceded the return phase of the mission as the increase in lysophospholipids containing proinflammatory fatty acids suggested a heightened inflammatory state during flight as well (Fig. 4B). Furthermore, TW's average urine sodium excretion from FD300 through FD334 was 147 mmol/day (table S8). On R+0, sodium excretion decreased to 47 mmol/day despite being given intravenous

saline, as is routine protocol at landing (81), as well as access to enough fluid intake to increase his urine volume from 1313 to 2999 ml. TW did not have blood volume measures until R+12; however, on the basis of previous data on crewmembers on long-duration spaceflight (5), TW's blood volume at R+0 was likely low. His plasma sodium concentration decreased from 146 to 138 mmol/liter on R+0 (table S8), consistent with urine sodium output not being decreased, likely owing to low plasma sodium. The observed two-thirds decrease in urine sodium excretion on landing, despite being provided intravenous saline, is a common response to volume depletion.

Genomic instability

Multiple lines of evidence revealed ongoing genome instability and rearrangement, potentially indicative of long-term molecular and/or adverse health effects of long-duration spaceflight. Notably, and consistent with reported space radiation exposure and inflight DNA damage responses, TW's chromosomal translocation and inversion frequencies were increased during flight and remained increased postflight. These findings are in agreement with reports of chromosomal translocations in individual astronauts (32), as well as with the proposal that inversions, together with their reciprocal counterpart small interstitial deletions, represent mutational signatures of radiation exposure (82). Furthermore, in vitro experiments have demonstrated that exposures to high-LET protons can evoke telomere lengthening (83), that low-LET gamma-ray exposures induce telomerase-dependent enrichment of putative stem and progenitor cell populations, and that low–dose rate irradiation of PBMCs shifts telomere length distributions toward cell populations with longer telomeres (24). Therefore, radiation- and DDR-induced changes in cell population dynamics, rather than telomere lengthening per se, may at least partially contribute to the telomere elongation observed during flight.

Dysregulated gene expression

Interestingly, the number of DEGs (table S2) in the 6- to 12-month inflight period was almost sixfold higher than in the 0- to 6-month inflight period in unsorted PBMCs (DEGs $q < 0.01$, DESeq2), indicating that the latter half of a year-long mission induces a far greater number of transcriptional changes. Furthermore, a distinct subset of genes did not return to preflight levels within 6 months of return to Earth (811 genes across different cell types), including genes related to immune function and DNA repair, representing candidate genes that may be altered for an extended period of time as a result of long-term spaceflight exposure.

Cognitive decline

Finally, our findings suggest that the cognitive performance effects of prolonging mission duration from 6 to 12 months may be limited to a few domains. However, this extended mission duration may negatively affect cognitive performance postflight, which could have implications for safe mission operations (e.g., after a landing on Mars). Automation of postflight operational procedures on future missions could help mitigate such risks. In addition to reexposure to Earth's gravity, the postflight period can be demanding for astronauts owing to participation in research studies and media events. It is unclear how strongly each of the above factors contributed to the observed decline in the flight subject's cognitive performance postflight.

Future missions and conclusions

This study has generated a unique, diverse biomedical dataset, despite the fact that studying the effects of space travel on the human body is challenging. Samples collected on the ISS were either frozen at −80°C and kept as such for the duration of the mission or returned under ambient conditions to Earth. Sample return from the ISS involved unavoidable transit times (~45 hours) through Earth's atmosphere and intercontinental travel, sometimes with unknown transit conditions (e.g., temperature and vibration). This resulted in significant changes, such as loss of telomerase activity. However, DNA integrity was intact and telomere length was unaffected (fig. S6, F to H).

Given our results, it is expected that astronauts conducting exploration-class missions could experience risks from mitochondrial dysfunction, immunological stress, vascular changes and fluid shifts, and cognitive performance decline, as well as alterations in telomere length, gene regulation, and genome integrity. Given the limitations in analyzing a single spaceflight subject, studies of additional astronauts on long-duration (≥12 month) missions are needed to confirm these findings and resolve outstanding questions. If confirmed, any biological, biophysical, or pharmacological countermeasures that reduce these risks should be considered for development and implementation. There is even less data, or no data, on astronauts who might be at increased risk owing to space radiation exposure associated with exploration missions beyond the protection afforded by Earth's magnetic field (84), including differences between a 1-year spaceflight in low Earth orbit and a 3-year Mars mission. Therefore, future studies with varying durations and longer periods of exposure (>1 year) will be required to determine the manner by which those risks will change (e.g., linear or exponential) and to establish appropriate safety thresholds.

These results represent an integrated portrait of molecular, physiological, and behavioral adaptations and challenges for the human body during extended spaceflight and are important to individual astronauts and to many groups at NASA (e.g., ISS Program, Space Medicine, and the Human Research Program) for planning other ISS missions. These data can be of immediate use by investigators and groups around the world planning future human spaceflight missions. Moreover, future year-long ISS missions would provide additional subjects and materials for subsequent studies and interpretation in support of future Mars missions. However, the opportunity to have an identical twin as a control for a spaceflight study is not currently planned nor expected. Thus, this study and its methodologies represent a uniquely controlled and integrated framework for comprehensively quantifying astronaut biology in space.

Materials and methods summary

The materials and methods are briefly summarized here; expanded materials and methods are included in the supplementary materials. Data were generated across human and microbial cells, including isolations of stool, saliva, skin, urine, blood, plasma, PBMCs, and immune cells that are CD4+, CD8+, and CD19+ enriched and lymphocyte-depleted (LD), from AutoMACS magnetic bead separation and validated by FACS (fig. S1). Molecular techniques included assessments of telomere length, telomerase activity, and chromosome aberration frequencies (qRT-PCR T:A, qRT-PCR TRAP, Telo-FISH, and dGH), WGBS, RNA-seq (polyA, riboRNA, and miRNA), mitochondrial quantification (qPCR and qRT-PCR), shotgun metagenome sequencing of fecal microbiome, targeted proteomics (LC-MS), untargeted proteomics (PECAN, MaxQuant for urine and SWATH-MS for plasma), targeted metabolomics (GC-MS), untargeted metabolomics (LC-MS), mitochondrial respiration (Seahorse XF), oxidative state measures (EPR), TCR and BCR (T cell and B cell receptor repertoire) profiling, 10 cognitive tests (motor praxis, visual object learning, fractal 2-back, abstract matching, line orientation, emotion recognition, matrix reasoning, digit symbol substitution, balloon analog risk, and psychomotor vigilance), vascular and ocular measures by ultrasound and optical coherence tomography, respectively, and a wide range of other biometrics (e.g., nutrition, height, and weight). Finally, a large set of biochemical profiles were measured pre-, in-, and postflight for both subjects: body mass, height, energy intake, vitamin levels (A, B6, B12, C, D, and E and 1-carbon metabolites), minerals (copper, ceruloplasmin, selenium, zinc, calcium, phosphorus, magnesium, and iodine), iron levels (ferritin, transferrin, transferrin receptors, Hgb, Hct, MCV, TIBC, and hepcidin), urine proteins (total, albumin, TTR, RBP, creatinine, metallothionein, 3-MH, nitrogen, and fibrinogen), bone markers (BSAP, PTH, OPG, RANKL, P1NP, sclerostin, and osteocalcin), collagen crosslinks (NTX, CTX, and DPD), oxidative stress and antioxidant capacity (8-OHdG, PGF2α, GPX, SOD, TAC, oxLDL, total lipid peroxides, heme, and glutathione), protein carbonyls (myeloperoxidase, lp-PLA2, neopterin, and beta-2 microglobulin), hormones and immune system markers (cytokines, testosterone, estradiol, DHEA/S, cortisol, IGF1, leptin, thyroid hormones, angiotensin, aldosterone, ANP, PRA, and insulin), and general urine chemistry (Na, K, and Cl ions; uric acid; cholesterol; triglyceride; HDL; LDL; phospholipids; renal stone risk; liver enzymes; hsCRP; NAD/P; and pH). Together, these data span 25 months for the flight subject twin (TW), who was compared with himself, either preflight, inflight, or postflight, and also with his twin control (HR) on Earth using generalized linear models (GLM), DESeq2, and

fuzzy *c*-means clustering for longitudinal trends. All *P* values were corrected for multiple testing using a FDR of 0.05 or 0.01, and *q* values are reported in all tables.

REFERENCES AND NOTES

1. M. Barratt, S. L. Pool, Eds., *Principles of Clinical Medicine for Space Flight* (Springer, 2008).
2. V. A. Convertino, "Exercise and adaptation to microgravity environments" in *Supplement 14: Handbook of Physiology, Environmental Physiology, Comprehensive Physiology* (Wiley, 2011), pp. 815–843.
3. W. E. Thornton, T. P. Moore, S. L. Pool, Fluid shifts in weightlessness. *Aviat. Space Environ. Med.* **58**, A86–A90 (1987). pmid: 3675511
4. C. S. Leach *et al*., Regulation of body fluid compartments during short-term spaceflight. *J. Appl. Physiol.* **81**, 105–116 (1996). doi: 10.1152/jappl.1996.81.1.105; pmid: 8828652
5. J. V. Meck, C. J. Reyes, S. A. Perez, A. L. Goldberger, M. G. Ziegler, Marked exacerbation of orthostatic intolerance after long- vs. short-duration spaceflight in veteran astronauts. *Psychosom. Med.* **63**, 865–873 (2001). doi: 10.1097/00006842-200111000-00003; pmid: 11719623
6. S. M. C. Lee, A. H. Feiveson, S. Stein, M. B. Stenger, S. H. Platts, Orthostatic intolerance after ISS and Space Shuttle missions. *Aerosp. Med. Hum. Perform.* **86** (suppl. 1), A54–A67 (2015). doi: 10.3357/AMHP.EC08.2015; pmid: 26630196
7. T. P. Moore, W. E. Thornton, Space shuttle inflight and postflight fluid shifts measured by leg volume changes. *Aviat. Space Environ. Med.* **58**, A91–A96 (1987). pmid: 3675513
8. M. A. Perhonen *et al*., Cardiac atrophy after bed rest and spaceflight. *J. Appl. Physiol.* **91**, 645–653 (2001). doi: 10.1152/jappl.2001.91.2.645; pmid: 11457776
9. H. Akima *et al*., Effect of short-duration spaceflight on thigh and leg muscle volume. *Med. Sci. Sports Exerc.* **32**, 1743–1747 (2000). doi: 10.1097/00005768-200010000-00013; pmid: 11039647
10. R. Gopalakrishnan *et al*., Muscle volume, strength, endurance, and exercise loads during 6-month missions in space. *Aviat. Space Environ. Med.* **81**, 91–104 (2010). doi: 10.3357/ASEM.2583.2010; pmid: 20131648
11. S. Trappe *et al*., Exercise in space: Human skeletal muscle after 6 months aboard the International Space Station. *J. Appl. Physiol.* **106**, 1159–1168 (2009). doi: 10.1152/japplphysiol.91578.2008; pmid: 19150852
12. J. C. Hayes, M. E. Guilliams, S. M. C. Lee, K. R. MacNeill, A. D. M. Jr, "Exercise: developing countermeasure systems for optimizing astronaut performance in space" in *Biomedical Results of the Space Shuttle Program*, D. Risin, P. C. Stepaniak, Eds. (NASA/SP-2013-607, NASA, Washington, DC, 2013), pp. 289–314.
13. S. M. Smith *et al*., Benefits for bone from resistance exercise and nutrition in long-duration spaceflight: Evidence from biochemistry and densitometry. *J. Bone Miner. Res.* **27**, 1896–1906 (2012). doi: 10.1002/jbmr.1647; pmid: 22549960
14. T. H. Mader *et al*., Optic disc edema, globe flattening, choroidal folds, and hyperopic shifts observed in astronauts after long-duration space flight. *Ophthalmology* **118**, 2058–2069 (2011). doi: 10.1016/j.ophtha.2011.06.021; pmid: 21849212
15. L. F. Zhang, A. R. Hargens, Spaceflight-induced intracranial hypertension and visual impairment: Pathophysiology and countermeasures. *Physiol. Rev.* **98**, 59–87 (2018). doi: 10.1152/physrev.00017.2016; pmid: 29167331
16. M. B. Stenger *et al*., "Evidence report: Risk of spaceflight associated neuro-ocular syndrome (SANS)" (NASA, Lyndon B. Johnson Space Center, Houston, 2018).
17. M. V. Carminati, D. Griffith, M. R. Campbell, Sub-orbital commercial human spaceflight and informed consent. *Aviat. Space Environ. Med.* **82**, 144–146 (2011). doi: 10.3357/ASEM.2846.2011; pmid: 21329032
18. K. Contrepois, L. Jiang, M. Snyder, Optimized analytical procedures for the untargeted metabolomic profiling of human urine and plasma by combining hydrophilic interaction (HILIC) and reverse-phase liquid chromatography (RPLC)-mass spectrometry. *Mol. Cell. Proteomics* **14**, 1684–1695 (2015). doi: 10.1074/mcp.M114.046508; pmid: 25787789
19. E. C. Borresen *et al*., A randomized controlled trial to increase navy bean or rice bran consumption in colorectal cancer survivors. *Nutr. Cancer* **68**, 1269–1280 (2016). doi: 10.1080/01635581.2016.1224370; pmid: 27689688
20. R. M. Cawthon, Telomere length measurement by a novel monochrome multiplex quantitative PCR method. *Nucleic Acids Res.* **37**, e21 (2009). doi: 10.1093/nar/gkn1027; pmid: 19129229
21. L. S. Honig *et al*., Heritability of telomere length in a study of long-lived families. *Neurobiol. Aging* **36**, 2785–2790 (2015). doi: 10.1016/j.neurobiolaging.2015.06.017; pmid: 26239175
22. J. Lin *et al*., Systematic and cell type-specific telomere length changes in subsets of lymphocytes. *J. Immunol. Res.* **2016**, 5371050 (2016). doi: 10.1155/2016/5371050; pmid: 26977417
23. P. M. Lansdorp *et al*., Heterogeneity in telomere length of human chromosomes. *Hum. Mol. Genet.* **5**, 685–691 (1996). doi: 10.1093/hmg/5.5.685; pmid: 8733138
24. B. J. Sishc *et al*., Telomeres and telomerase in the radiation response: Implications for instability, reprograming, and carcinogenesis. *Front. Oncol.* **5**, 257 (2015). doi: 10.3389/fonc.2015.00257; pmid: 26636039
25. C. W. Greider, E. H. Blackburn, Identification of a specific telomere terminal transferase activity in Tetrahymena extracts. *Cell* **43**, 405–413 (1985). doi: 10.1016/0092-8674(85)90170-9; pmid: 3907856
26. M. Hou, D. Xu, M. Björkholm, A. Gruber, Real-time quantitative telomeric repeat amplification protocol assay for the detection of telomerase activity. *Clin. Chem.* **47**, 519–524 (2001). pmid: 11238306
27. F. A. Cucinotta, Space radiation risks for astronauts on multiple International Space Station missions. *PLOS ONE* **9**, e96099 (2014). doi: 10.1371/journal.pone.0096099; pmid: 24759903
28. K. George, J. Rhone, A. Beitman, F. A. Cucinotta, Cytogenetic damage in the blood lymphocytes of astronauts: Effects of repeat long-duration space missions. *Mutat. Res.* **756**, 165–169 (2013). doi: 10.1016/j.mrgentox.2013.04.007; pmid: 23639573
29. F. A. Ray *et al*., Directional genomic hybridization for chromosomal inversion discovery and detection. *Chromosome Res.* **21**, 165–174 (2013). doi: 10.1007/s10577-013-9345-0; pmid: 23572395
30. F. A. Ray *et al*., Directional genomic hybridization: Inversions as a potential biodosimeter for retrospective radiation exposure. *Radiat. Environ. Biophys.* **53**, 255–263 (2014). doi: 10.1007/s00411-014-0513-1; pmid: 24477407
31. M. N. Cornforth, M. Durante, Radiation quality and intra-chromosomal aberrations: Size matters. *Mutat. Res.* **836** (part A), 28–35 (2018). doi: 10.1016/j.mrgentox.2018.05.002; pmid: 30389158
32. K. George, L. J. Chappell, F. A. Cucinotta, Persistence of space radiation induced cytogenetic damage in the blood lymphocytes of astronauts. *Mutat. Res.* **701**, 75–79 (2010). doi: 10.1016/j.mrgentox.2010.02.007; pmid: 20176126
33. G. Jenkinson, E. Pujadas, J. Goutsias, A. P. Feinberg, Potential energy landscapes identify the information-theoretic nature of the epigenome. *Nat. Genet.* **49**, 719–729 (2017). doi: 10.1038/ng.3811; pmid: 28346445
34. A. Koyanagi, C. Sekine, H. Yagita, Expression of Notch receptors and ligands on immature and mature T cells. *Biochem. Biophys. Res. Commun.* **418**, 799–805 (2012). doi: 10.1016/j.bbrc.2012.01.106; pmid: 22310713
35. M. Nakaya *et al*., Inflammatory T cell responses rely on amino acid transporter ASCT2 facilitation of glutamine uptake and mTORC1 kinase activation. *Immunity* **40**, 692–705 (2014). doi: 10.1016/j.immuni.2014.04.007; pmid: 24792914
36. J. E. Thaventhiran, D. T. Fearon, L. Gattinoni, Transcriptional regulation of effector and memory CD8$^+$ T cell fates. *Curr. Opin. Immunol.* **25**, 321–328 (2013). doi: 10.1016/j.coi.2013.05.010; pmid: 23747000
37. J. de Batlle *et al*., Association between Ω3 and Ω6 fatty acid intakes and serum inflammatory markers in COPD. *J. Nutr. Biochem.* **23**, 817–821 (2012). doi: 10.1016/j.jnutbio.2011.04.005; pmid: 21889886
38. P. C. Calder, Polyunsaturated fatty acids and inflammatory processes: New twists in an old tale. *Biochimie* **91**, 791–795 (2009). doi: 10.1016/j.biochi.2009.01.008; pmid: 19455748
39. Human Microbiome Project Consortium, Structure, function and diversity of the healthy human microbiome. *Nature* **486**, 207–214 (2012). doi: 10.1038/nature11234; pmid: 22699609
40. S. Li *et al*., Multi-platform assessment of transcriptome profiling using RNA-seq in the ABRF next-generation sequencing study. *Nat. Biotechnol.* **32**, 915–925 (2014). doi: 10.1038/nbt.2972; pmid: 25150835
41. SEQC/MAQC-III Consortium, A comprehensive assessment of RNA-seq accuracy, reproducibility and information content by the Sequencing Quality Control Consortium. *Nat. Biotechnol.* **32**, 903–914 (2014). doi: 10.1038/nbt.2957; pmid: 25150838
42. C. M. Gardiner, D. K. Finlay, What fuels natural killers? Metabolism and NK cell responses. *Front. Immunol.* **8**, 367 (2017). doi: 10.3389/fimmu.2017.00367; pmid: 28421073
43. A. Beheshti, E. Cekanaviciute, D. J. Smith, S. V. Costes, Global transcriptomic analysis suggests carbon dioxide as an environmental stressor in spaceflight: A systems biology GeneLab case study. *Sci. Rep.* **8**, 4191 (2018). doi: 10.1038/s41598-018-22613-1; pmid: 29520055
44. P. Norsk, A. Asmar, M. Damgaard, N. J. Christensen, Fluid shifts, vasodilatation and ambulatory blood pressure reduction during long duration spaceflight. *J. Physiol.* **593**, 573–584 (2015). doi: 10.1113/jphysiol.2014.284869; pmid: 25774397
45. P. Arbeille, R. Provost, K. Zuj, Carotid and femoral artery intima-media thickness during 6 months of spaceflight. *Aerosp. Med. Hum. Perform.* **87**, 449–453 (2016). doi: 10.3357/AMHP.4493.2016; pmid: 27099083
46. S. R. Zwart *et al*., Body mass changes during long-duration spaceflight. *Aviat. Space Environ. Med.* **85**, 897–904 (2014). doi: 10.3357/ASEM.3979.2014; pmid: 25197887
47. S. M. Smith *et al*., Bone metabolism and renal stone risk during International Space Station missions. *Bone* **81**, 712–720 (2015). doi: 10.1016/j.bone.2015.10.002; pmid: 26456109
48. S. M. Smith *et al*., Fifty years of human space travel: Implications for bone and calcium research. *Annu. Rev. Nutr.* **34**, 377–400 (2014). doi: 10.1146/annurev-nutr-071813-105440; pmid: 24995691
49. X. Wang *et al*., LRG1 promotes angiogenesis by modulating endothelial TGF-β signalling. *Nature* **499**, 306–311 (2013). doi: 10.1038/nature12345; pmid: 23868260
50. S. R. Zwart *et al*., Genotype, B-vitamin status, and androgens affect spaceflight-induced ophthalmic changes. *FASEB J.* **30**, 141–148 (2016). doi: 10.1096/fj.15-278457; pmid: 26316272
51. S. R. Zwart *et al*., Vision changes after spaceflight are related to alterations in folate- and vitamin B-12-dependent one-carbon metabolism. *J. Nutr.* **142**, 427–431 (2012). doi: 10.3945/jn.111.154245; pmid: 22298570
52. M. Basner *et al*., Development and validation of the cognition test battery for spaceflight. *Aerosp. Med. Hum. Perform.* **86**, 942–952 (2015). doi: 10.3357/AMHP.4343.2015; pmid: 26564759
53. Y. Zhao *et al*., A mutational analysis of *Caenorhabditis elegans* in space. *Mutat. Res.* **601**, 19–29 (2006). doi: 10.1016/j.mrfmmm.2006.05.001; pmid: 16765996
54. M. A. Shammas, Telomeres, lifestyle, cancer, and aging. *Curr. Opin. Clin. Nutr. Metab. Care* **14**, 28–34 (2011). doi: 10.1097/MCO.0b013e32834121b1; pmid: 21102320
55. W. R. Pendergrass, P. E. Penn, J. Li, N. S. Wolf, Age-related telomere shortening occurs in lens epithelium from old rats and is slowed by caloric restriction. *Exp. Eye Res.* **73**, 221–228 (2001). doi: 10.1006/exer.2001.1033; pmid: 11446772
56. M. Laimer *et al*., Telomere length increase after weight loss induced by bariatric surgery: Results from a 10 year prospective study. *Int. J. Obes.* **40**, 773–778 (2016). doi: 10.1038/ijo.2015.238; pmid: 26607038
57. L. F. Cherkas *et al*., The association between physical activity in leisure time and leukocyte telomere length. *Arch. Intern. Med.* **168**, 154–158 (2008). doi: 10.1001/archinternmed.2007.39; pmid: 18227361
58. L. Carulli *et al*., Telomere length elongation after weight loss intervention in obese adults. *Mol. Genet. Metab.* **118**, 138–142 (2016). doi: 10.1016/j.ymgme.2016.04.003; pmid: 27157420
59. V. Boccardi, G. Paolisso, P. Mecocci, Nutrition and lifestyle in healthy aging: The telomerase challenge. *Aging* **8**, 12–15 (2016). doi: 10.18632/aging.100886; pmid: 26826704
60. N. C. Arsenis, T. You, E. F. Ogawa, G. M. Tinsley, L. Zuo, Physical activity and telomere length: Impact of aging and potential mechanisms of action. *Oncotarget* **8**, 45008–45019 (2017). doi: 10.18632/oncotarget.16726; pmid: 28410238
61. S. Turroni *et al*., Temporal dynamics of the gut microbiota in people sharing a confined environment, a 520-day ground-based space simulation, MARS500. *Microbiome* **5**, 39 (2017). doi: 10.1186/s40168-017-0256-8; pmid: 28340597
62. A. V. Mardanov *et al*., Metagenomic analysis of the dynamic changes in the gut microbiome of the participants of the MARS-500 experiment, simulating long term space flight. *Acta Naturae* **5**, 116–125 (2013). pmid: 24303207
63. M. J. Mienaltowski, D. E. Birk, Structure, physiology, and biochemistry of collagens. *Adv. Exp. Med. Biol.* **802**, 5–29 (2014). doi: 10.1007/978-94-007-7893-1_2; pmid: 24443018
64. S. Sasaki, Aquaporin 2: From its discovery to molecular structure and medical implications. *Mol. Aspects Med.* **33**, 535–546 (2012). doi: 10.1016/j.mam.2012.03.004; pmid: 23078817

65. H. Yamada, D. Chen, H. J. Monstein, R. Håkanson, Effects of fasting on the expression of gastrin, cholecystokinin, and somatostatin genes and of various housekeeping genes in the pancreas and upper digestive tract of rats. *Biochem. Biophys. Res. Commun.* **231**, 835–838 (1997). doi: 10.1006/bbrc.1997.6198; pmid: 9070905
66. A. Nguyen Dinh Cat, R. M. Touyz, A new look at the renin-angiotensin system—Focusing on the vascular system. *Peptides* **32**, 2141–2150 (2011). doi: 10.1016/j.peptides.2011.09.010; pmid: 21945916
67. F. S. Michel *et al*., Urinary angiotensinogen excretion is associated with blood pressure independent of the circulating renin-angiotensin system in a group of African ancestry. *Hypertension* **64**, 149–156 (2014). doi: 10.1161/HYPERTENSIONAHA.114.03336; pmid: 24777983
68. J. Zhang *et al*., Ageing and the telomere connection: An intimate relationship with inflammation. *Ageing Res. Rev.* **25**, 55–69 (2016). doi: 10.1016/j.arr.2015.11.006; pmid: 26616852
69. R. C. Stone *et al*., Telomere length and the cancer-atherosclerosis trade-off. *PLOS Genet.* **12**, e1006144 (2016). doi: 10.1371/journal.pgen.1006144; pmid: 27386863
70. B. E. Crucian *et al*., Immune system dysregulation during spaceflight: Potential countermeasures for deep space exploration missions. *Front. Immunol.* **9**, 1437 (2018). doi: 10.3389/fimmu.2018.01437; pmid: 30018614
71. T. H. Mader *et al*., Optic disc edema in an astronaut after repeat long-duration space flight. *J. Neuroophthalmol.* **33**, 249–255 (2013). doi: 10.1097/WNO.0b013e31829b41a6; pmid: 23851997
72. S. R. Zwart *et al*., Astronaut ophthalmic syndrome. *FASEB J.* **31**, 3746–3756 (2017). doi: 10.1096/fj.201700294; pmid: 28546443
73. P. Arbeille, R. Provost, K. Zuj, N. Vincent, Measurements of jugular, portal, femoral, and calf vein cross-sectional area for the assessment of venous blood redistribution with long duration spaceflight (Vessel Imaging Experiment). *Eur. J. Appl. Physiol.* **115**, 2099–2106 (2015). doi: 10.1007/s00421-015-3189-6; pmid: 25991027
74. R. L. Hughson *et al*., Increased postflight carotid artery stiffness and inflight insulin resistance resulting from 6-mo spaceflight in male and female astronauts. *Am. J. Physiol. Heart Circ. Physiol.* **310**, H628–H638 (2016). doi: 10.1152/ajpheart.00802.2015; pmid: 26747504
75. M. W. Lorenz, H. S. Markus, M. L. Bots, M. Rosvall, M. Sitzer, Prediction of clinical cardiovascular events with carotid intima-media thickness: A systematic review and meta-analysis. *Circulation* **115**, 459–467 (2007). doi: 10.1161/CIRCULATIONAHA.106.628875; pmid: 17242284
76. G. Walldius, I. Jungner, The apoB/apoA-I ratio: A strong, new risk factor for cardiovascular disease and a target for lipid-lowering therapy—a review of the evidence. *J. Intern. Med.* **259**, 493–519 (2006). doi: 10.1111/j.1365-2796.2006.01643.x; pmid: 16629855
77. G. Florvall, S. Basu, A. Larsson, Apolipoprotein A1 is a stronger prognostic marker than are HDL and LDL cholesterol for cardiovascular disease and mortality in elderly men. *J. Gerontol. A Biol. Sci. Med. Sci.* **61**, 1262–1266 (2006). doi: 10.1093/gerona/61.12.1262; pmid: 17234819
78. M. Benn, B. G. Nordestgaard, G. B. Jensen, A. Tybjaerg-Hansen, Improving prediction of ischemic cardiovascular disease in the general population using apolipoprotein B: The Copenhagen City Heart Study. *Arterioscler. Thromb. Vasc. Biol.* **27**, 661–670 (2007). doi: 10.1161/01.ATV.0000255580.73689.8e; pmid: 17170368
79. C. J. Ade, R. M. Broxterman, J. M. Charvat, T. J. Barstow, Incidence rate of cardiovascular disease end points in the National Aeronautics and Space Administration Astronaut Corps. *J. Am. Heart Assoc.* **6**, e005564 (2017). doi: 10.1161/JAHA.117.005564; pmid: 28784652
80. R. J. Reynolds, S. M. Day, Mortality among U.S. astronauts: 1980–2009. *Aviat. Space Environ. Med.* **81**, 1024–1027 (2010). doi: 10.3357/ASEM.2847.2010; pmid: 21043299
81. A. P. Mulavara *et al*., Physiological and functional alterations after spaceflight and bed rest. *Med. Sci. Sports Exerc.* **50**, 1961–1980 (2018). doi: 10.1249/MSS.0000000000001615; pmid: 29620686
82. S. Behjati *et al*., Mutational signatures of ionizing radiation in second malignancies. *Nat. Commun.* **7**, 12605 (2016). doi: 10.1038/ncomms12605; pmid: 27615322
83. F. Berardinelli *et al*., The role of telomere length modulation in delayed chromosome instability induced by ionizing radiation in human primary fibroblasts. *Environ. Mol. Mutagen.* **54**, 172–179 (2013). doi: 10.1002/em.21761; pmid: 23401031
84. F. A. Cucinotta, N. Hamada, M. P. Little, No evidence for an increase in circulatory disease mortality in astronauts following space radiation exposures. *Life Sci. Space Res.* **10**, 53–56 (2016). doi: 10.1016/j.lssr.2016.08.002; pmid: 27662788

ACKNOWLEDGMENTS

The National Space Biomedical Research Institute partnered with NASA to support this study during the solicitation, design, implementation, and analysis phases via the provision of scientific expertise. We thank S. Horner and N. Gokhale from Duke University Medical Center (Durham, NC, USA) for mtRNA validation assistance, I. Tulchinsky, and the Genomics, Epigenomics, and Applied Bioinformatics Core Facilities at Weill Cornell Medicine for sequencing and data services. We thank the NASA JSC Nutritional Biochemistry Lab personnel, especially Y. Bourbeau, who led efforts on this project for project coordination, sample collection, processing, and analysis; the Cardiovascular and Vision Laboratory personnel for the collection and analysis of vascular, ocular, and fluid shifts data; the NASA Human Research Program's International Space Station Medical Project Team for their invaluable work to coordinate all of sample and data collection scheduling activities on the ground and during flight; D. Mollicone and C. Mott from Pulsar Informatics Inc., E. Hermosillo, and S. McGuire for support of the Cognition measures; Y.-R. Hasson from the Stanford Human Immune Monitoring Center for advice and support on cytokine profiling data; K. Bettinger from Stanford University for support with the Stanford Twins data repository; P. R. Kiela, D. Laubitz (University of Arizona), and E. Song (Northwestern University) for support of the Microbiome project sample collection; K. Kunstman (University of Illinois at Chicago) for shotgun metagenome library preparation and sequencing; S. Mehta (University of Illinois at Chicago) for help in statistical analysis; and J. Kim for laboratory support in targeted metabolomics. We thank the DRC Quantitative and Functional Proteomics Core and the UW Nutrition and Obesity Research Center for performing proteomics assays and New England Biolabs (NEB) for support. We thank J. X.-J. Yuan at the University of Arizona, Tuscon, for providing his support and laboratory for the Tucson sample collections. We thank J. Krauhs for her editorial assistance with the one-page summary. K.S. is also affiliated with the South Texas U.S. Department of Veterans Affairs as a staff physician. **Funding:** The study was supported by NASA: NNX14AH51G [all Twins Study principal investigators (PIs)]; NNX14AB02G (S.M.B.); NNX14AH27G/NCC 9-58 (M.B.); NN13AJ12G (A.R.H.); NNX14AN75G (S.M.C.L.); NNX17AB26G, NNX17AB26G, and TRISH: NNX16AO69A:0107 and NNX16AO69A:0061 (C.E.M.); NNX14AH52G (M.P.S.); and NNX14AH26G (F.W.T.). Additional support was provided by NIH grants AG035031, NIH/NIDDK P30 DK017047, and P30 DK035816 (K.S.); NSF grant CCF-1656201 (J.G.); and DLR space program grant 50WB1535 (M.H.), as well as the Bert L. and N. Kuggie Vallee Foundation, the WorldQuant Foundation, The Pershing Square Sohn Cancer Research Alliance, and the Bill and Melinda Gates Foundation (OPP1151054) for funding (C.E.M.). **Author contributions:** F.E.G.-B., M.D., S.J.G., R.C.G., L.L., B.R.M., M.J.M., C.M., T.M., J.N., B.D.P., L.F.R., K.S., J.H.S., L.T., and M.H.V. led the investigator teams across the study. *Conceptualization:* G.B.I.S., C.E.K., and J.B.C.; S.M.B. (Twins Study PI; Telomeres, Telomerase, DNA damage/cytogenetics); M.B. (Twins Study PI; Cognition); S.M.C.L. [Twins Study PI, Cardiovascular and Oxidative Stress (Cardio Ox); Twins Study co-investigator (Co-I), Fluid Shifts and Ocular]; S.M.S. and S.R.Z. (Biochem Profile); M.H. (Biochem Profile); A.P.F. (Twins Study PI; Epigenetics); M.B.S. (Fluid Shifts NASA site PI and Cardio Ox Co-I); B.R.M. (Fluids Shifts, Co-I); D.J.E. (Fluid Shifts, Co-I); B.K.R. (PI, Fluids Shifts and Co-I, Cardio Ox); I.D.V. (Co-I, Cardio Ox); D.D.S. (Co-I, Cardio Ox); K.S. (Co-I, Targeted Metabolomics, Cardio Ox); A.R.H. (Co-I, Fluid Shifts and Cardio Ox); V.Y.H.H. (Co-I, Fluid Shifts Proteomics); H.H.P., J.H.S., and J.M.S. (Fluid Shifts; Mitochondrial Function); T.V., A.N.H., and M.Af. (Targeted Urine Proteomics); M.P.S. (Twins Study PI; Untargeted Plasma Metabolomics and Proteomics, Plasma Cytokine Profiling, Integrative Analysis); T.M. (Untargeted Plasma Metabolomics and Proteomics, Plasma Cytokine Profiling, Integrative Analysis); B.D.P. (Integrative Analysis); S.J.G., A.K., F.W.T., and M.H.V. (Microbiome); C.E.M. (Twins study PI; Transcriptome, and Integration); and D.D.S. (Co-I, Cardio Ox). *Data Curation:* S.M.B. (Twins Study PI; Telomeres, Telomerase, DNA damage/cytogenetics); M.B. (Twins Study PI; Cognition); J.I.F. and L.F.R. (Epigenetics); S.R.Z. (Biochem Profile); R.P.H. (Immune Response); S.M.C.L. (Twins Study PI, Cardiovascular; Twins Study Co-I, Fluid Shifts and Ocular); S.S.L. (Fluids Shifts and Ocular, Co-I); B.R.M. (Fluids Shifts and Ocular, Co-I); D.J.E. (Fluid Shifts and Ocular, Co-I); B.K.R. (PI, Fluids Shifts and Ocular; Co-I, Cardio Ox); I.D.V. (Co-I, Cardio Ox); K.S. (Co-I, Cardio Ox); M.D. and R.S. (Targeted Metabolomics); J.H.S. and J.M.S. (Mitochondrial Function); D.N.S. (Integrative Analysis); G.E.C., S.J.G., P.J., M.G.M.-C., and M.H.V. (Microbiome); A.N.H. and T.V. (Urine Proteomics); T.M. (Untargeted Plasma Metabolomics and Proteomics, Plasma Cytokine Profiling, Integrative Analysis); S.A. (Untargeted Plasma Proteomics); K.C. (Untargeted Plasma Metabolomics); C.M. and C.E.M. (Twins study PI); E.A., D.B., F.E.G.-B., and M.M. (Transcriptome); B.D.P. (Integrative Analysis); and D.N.S. (Integrative Analysis). *Formal Analysis:* S.M.B. (Twins Study PI; Telomeres, Telomerase, DNA damage/cytogenetics), M.J.M. (Telomeres and Cytogenetics; FISH), L.T. (Telomeres and Telomerase; qRT-PCR); M.B. (Twins Study PI; Cognition); J.N. (Cognition); A.P.F., L.F.R., G.J., and J.G. (Epigenetics); R.P.H. (Immune Response); S.M.C.L. (Twins Study PI, Cardio Ox; Twins Study Co-I, Fluid Shifts and Ocular); S.M.S. and S.R.Z. (Biochem Profile); S.S.L. (Fluids Shifts and Ocular, Co-I); B.R.M. (Fluids Shifts and Ocular, Co-I); B.K.R. (PI, Fluids Shifts and Ocular; Co-I, Cardio Ox); M.G.Z. (Cardio Ox); I.D.V. (Co-I, Cardio Ox); D.D.S. (Co-I, Cardio Ox); K.S., M.D., and R.S. (Targeted Metabolomics); H.H.P., J.H.S., and J.M.S. (Mitochondrial Functional Assays); T.V. and A.N.H. (Urine Proteomics); T.M. (Untargeted Plasma Metabolomics and Proteomics, Plasma Cytokine Profiling, Integrative Analysis); S.A. (Untargeted Plasma Proteomics); K.C. (Untargeted Plasma Metabolomics); B.D.P. (Integrative Analysis); R.S. and M.D. (Metabolomics); P.J. (Microbiome); E.M., L.L., and A.A. (Vaccination study); and C.M., C.E.M., and A.M. (Transcriptome, Integrative Analysis). *Funding and Acquisition:* S.M.B. (Twins Study PI; Telomeres, Telomerase, DNA damage/cytogenetics); M.B. (Twins Study PI; Cognition); D.F.D. (Cognition); R.C.G. (Cognition); S.M.S. and S.R.Z. (Biochem Profile); M.H. (Biochem Profile); A.P.F. (Twins Study PI, Epigenetics); J.G. (Epigenetics); S.M.C.L. (Twins Study PI, Cardio Ox; Twins Study Co-I, Fluid Shifts and Ocular); M.B.S. (Fluid Shifts and Ocular NASA Site PI; Cardio Ox Co-I); B.R.M. (Fluids Shifts and Ocular; CardioOX, Co-I); D.J.E. (Fluid Shifts and Ocular, Co-I); B.K.R. (PI, Fluids Shifts and Ocular; UCSD Site PI, Cardio Ox); I.D.V. (Co-I, Cardio Ox); A.R.H. (Co-I, Fluid Shifts and Ocular; Cardio Ox); M.P.S. (Twins Study PI, Untargeted Plasma Metabolomics and Proteomics, Plasma Cytokine Profiling, Integrative Analysis); V.Y.H.H. (Co-I, Fluid Shifts); F.W.T. (PI), M.H.V. (Co-I) (Microbiome), C.E.M. (PI, Transcriptome), C.M., F.E.G.-B., and A.M.M. (Co-I, Transcriptome), G.S.G. (Co-I, Transcriptome); D.D.S. (Co-I, Cardio Ox); and B.R.M. (Co-I, Fluid Shifts and Ocular; Cardio Ox). *Investigation:* M.J.M. (Telomeres and Cytogenetics; FISH), L.T. (Telomeres and Telomerase; qRT-PCR); M.B. (Twins Study PI; Cognition); J.N. (Cognition); R.C.G. (Cognition); S.M.S. and S.R.Z. (Biochem Profile); L.F.R., R.T., C.M.C., and J.I.F. (Epigenetics); S.M.C.L. (Twins Study PI, Cardio Ox; Twins Study Co-I, Fluid Shifts and Ocular); M.B.S. (Fluid Shifts and Ocular; Cardio Ox, Co-I); S.S.L. (Fluids Shifts and Ocular, Co-I); B.R.M. (Fluids Shifts and Ocular, Co-I); D.J.E. (Fluid Shifts and Ocular, Co-I); B.K.R. (PI, Fluids Shifts and Ocular; Co-I, Cardio Ox); M.G.Z. (Cardio Ox); I.D.V. (Co-I, Cardio Ox); K.S., M.D., B.V.E. (Targeted Metabolomics); M.D. (Cardio Ox); B.V.E. (Cardio Ox); A.R.H. (Co-I, Fluid Shifts and Ocular; Cardio Ox); H.H.P., J.H.S., and J.M.S. (Mitochondrial Function Assays); Fluid Shifts); T.V. and A.N.H. (Urine Proteomics); T.M. (Untargeted Plasma Metabolomics and Proteomics, Plasma Cytokine Profiling, Integrative Analysis); B.D.P. (Integrative Analysis); S.A. (Untargeted Plasma Proteomics); V.R. (Plasma Cytokine Profiling); S.J.G. and P.J. (Microbiome); K.C., B.L.M., and S.C. (Untargeted Plasma Metabolomics); E.M., L.L., and A.A. (Vaccination study); and C.E.M., G.S.G., D.B., F.E.G.-B., and A.M.M. (Transcriptome, Integrative Analysis). *Methodology:* M.J.M. (Telomeres and Cytogenetics; FISH), L.T. (Telomeres and Telomerase; qRT-PCR); M.B. (Twins Study PI; Cognition); J.N. (Cognition); R.C.G.(Cognition); T.M.M. (Cognition); G.J., J.G., and J.I.F. (Epigenetics); S.M.C.L. (Twins Study PI, Cardio Ox; Twins Study Co-I, Fluid Shifts and Ocular); M.B.S. (NASA Site PI, Fluid Shifts and Ocular; Cardio Ox, Co-I); S.S.L. (Fluids Shifts and Ocular, Co-I); B.R.M. (Fluids Shifts and Ocular; Cardio Ox, Co-I); D.J.E. (Fluid Shifts and Ocular, Co-I); B.K.R. (PI, Fluids Shifts and Ocular; Co-I, Cardio Ox); M.G.Z. (Cardio Ox); I.D.V. and D.D.S. (Co-I, Cardio Ox); A.R.H. (Co-I, Fluid Shifts and Ocular; Cardio Ox, Co-I); H.H.P., J.H.S., and J.S. (Mitochondrial Function Assays); T.V., A.N.H., and M.Af. (Urine Proteomics); V.Y.H.H. (Proteomics); S.J.G., A.K., F.W.T., and M.H.V. (Microbiome); T.M. (Untargeted Plasma Metabolomics and Proteomics, Plasma Cytokine Profiling, Integrative Analysis); S.A. (Untargeted Plasma Proteomics); V.R. (Plasma Cytokine Profiling); K.C. (Untargeted Plasma Metabolomics); B.D.P. (Integrative Analysis); E.M., L.L., and A.A. (Vaccination study); C.M. (Transcriptome, Integrative Analysis); K.S. and M.D. (Targeted Metabolomics); S.M.S., S.R.Z., M.H., and B.E.C. (Biochem Profile blood and urine collection, processing, and analysis); S.S., S.Z., K.S., M.D., and D.D.S. (Urine collection and processing); A.M.K.C. and K.N. (Cell-free mtDNA); and L.L., A.F., J.I.F., C.K.S., and F.E.G.-B. (Blood Collection and Processing). *Project administration:* S.M.B. (Twins Study PI; Telomeres, Telomerase, DNA

damage/cytogenetics); M.B. (Twins Study PI; Cognition); L.F.R. (Epigenetics); R.P. (subject consent, scheduling, and sample logistics); S.M.C.L. (Twins Study PI, Cardio Ox; Twins Study Co-I, Fluid Shifts and Ocular); S.M.S. (Twins Study PI, Biochem Profile); M.B.S. (Fluid Shifts and Ocular, Co-I; Cardio Ox, Co-I); S.S.L. (Fluids Shifts and Ocular, Co-I); B.R.M. (Fluids Shifts and Ocular, Co-I); B.K.R. (PI, Fluids Shifts and Ocular; Co-I, Cardio Ox); M.P.S. (Twins study PI; Untargeted Plasma Metabolomics and Proteomics, Plasma Cytokine Profiling, Integrative Analysis); T.M. (Untargeted Plasma Metabolomics and Proteomics, Plasma Cytokine Profiling, Integrative Analysis); B.D.P. (Integrative Analysis); F.W.T. (Microbiome PI); M.H.V. (Microbiome Co-I); C.E.M. and F.E.G.-B. (Blood Collection and Processing and transcriptome studies); K.S. (Targeted Metabolomics); M.Ar.; S.L.; and M.C. *Resources:* S.M.B. (Twins Study PI; Telomeres, Telomerase, DNA damage/cytogenetics), K.G. (Telomeres; sample coordination, NASA IRB); M.B. (Twins Study PI; Cognition); S.M.S. (Biochem Profile); M.H. (Biochem Profile); B.E.C. (Biochem Profile); R.P. (laboratory facilities, materials, and instrumentation); S.M.C.L. (Twins Study PI, Cardio Ox; Twins Study Co-I, Fluid Shifts and Ocular); M.B.S. (Fluid Shifts and Ocular, Co-I; Cardio Ox, Co-I); B.K.R. (PI, Fluids Shifts and Ocular; Co-I, Cardio Ox); I.D.V. (Co-I, Cardio Ox); D.D.S. (Co-I, Cardio Ox); K.S. (Co-I, Cardio Ox); A.R.H. (Co-I, Fluid Shifts and Ocular; Cardio Ox); T.V. (Fluid Shifts and Ocular); A.N.H. (Fluid Shifts and Ocular); G.E.C., S.J.G., P.J., and M.G.M.-C. (Microbiome); M.P.S. (Twins study PI; Untargeted Plasma Metabolomics and Proteomics, Plasma Cytokine Profiling, Integrative Analysis); and D.S. (Data Storage Repository). *Software:* C.E.M. (Transcriptome); D.S. (Data Storage Repository); T.M. (Untargeted Plasma Metabolomics and Proteomics, Plasma Cytokine Profiling, Integrative Analysis); and B.D.P. (Integrative Analysis). *Supervision:* S.M.B. (Twins Study PI; Telomeres, Telomerase, DNA damage/cytogenetics); M.B. (Twins Study PI; Cognition); S.M.S. (Twins Study PI, Biochem Profile); A.P.F. (Twins Study PI); J.G. (Epigenetics); S.M.C.L. (Twins Study PI, Cardio Ox; Twins Study Co-I, Fluid Shifts and Ocular); M.B.S. (Fluid Shifts and Ocular, Co-I; Cardio Ox, Co-I); B.R.M. (Fluids Shifts and Ocular, Co-I); B.K.R. (PI, Fluids Shifts and Ocular; Co-I, Cardio Ox); I.D.V. (Co-I, Cardio Ox); D.D.S. (Co-I, Cardio Ox); K.S. (Co-I, Targeted Metabolomics); H.H.P. (Fluid Shifts and Ocular); J.M.S. (Fluid Shifts and Ocular); M.P.S. (Twins study PI; Untargeted Plasma Metabolomics and Proteomics, Plasma Cytokine Profiling, Integrative Analysis); S.J.G., A.K., F.W.T., and M.H.V. (Microbiome); K.C. (Untargeted Plasma Metabolomics); and C.E.M. and F.E.G.-B. (Blood Collection and Processing and transcriptome studies). *Validation:* M.J.M. (Telomeres and Cytogenetics; FISH), L.T. (Telomeres and Telomerase; qRT-PCR); C.E.M., A.C., K.N., N.S.G., and S.M.H. (mtDNA and mtRNA PCR); M.B. (Twins Study PI; Cognition); J.N. (Cognition); T.M.M. (Cognition); S.M.C.L. (Twins Study PI, Cardio Ox; Co-I, Fluid Shifts and Ocular), S.S.L. (Fluids Shifts and Ocular, Co-I); B.R.M. (Fluids Shifts and Ocular, Co-I); D.J.E. (Fluid Shifts and Ocular, Co-I); B.K.R. (PI, Fluids Shifts and Ocular; Co-I, Cardio Ox); S.M.S. and S.R.Z. (Biochem Profile); I.D.V. (Co-I, Cardio Ox PCR Based Telomere Length); K.S., M.D., and B.V.E. (Targeted Metabolomics); H.H.P. and J.M.S. (Proteomics); and L.L., F.E.G.-B., T.M., and C.M. (Ambient return controls). *Visualization:* S.M.B. (Twins Study PI; Telomeres, Telomerase, DNA damage/cytogenetics); M.J.M. (Telomeres and Cytogenetics; FISH), L.T. (Telomeres and Telomerase; qRT-PCR); M.B. (Twins Study PI; Cognition); J.N. (Cognition); L.F.R. (Epigenetics); S.R.Z. (Biochem Profile); S.M.C.L. (Twins Study PI, Cardio Ox; Twins Study Co-I, Fluid Shifts and Ocular); S.S.L. (Fluids Shifts and Ocular, Co-I); B.R.M. (Fluids Shifts and Ocular, Co-I); B.K.R. (PI, Fluids Shifts and Ocular; Co-I, Cardio Ox); H.H.P. (Fluid Shifts and Ocular); S.J.G., P.J., and M.G.M.-C. (Microbiome); M.M., C.E.M., and C.M. (Transcriptome, Integrative Analysis); and T.M. (Untargeted Plasma Metabolomics and Proteomics, Plasma Cytokine Profiling, Integrative Analysis). *Writing, original draft:* S.M.B. (Twins Study PI; Telomeres, Telomerase, DNA damage/cytogenetics); K.G. (Telomeres); M.B. (Twins Study PI; Cognition); L.F.R. (Epigenetics); S.M.C.L. (Twins Study PI, Cardiovascular; Twins Study Co-I, Fluid Shifts and Ocular); S.M.S. (Twins Study PI, Biochem Profile); S.R.Z. (Biochem Profile); S.S.L. (Fluids Shifts and Ocular, Co-I); B.R.M. (Fluids Shifts and Ocular, Co-I); D.J.E. (Fluid Shifts, Co-I); B.K.R. (PI, Fluids Shifts and Ocular; Co-I, Cardio Ox); M.G.Z. (Physiology and Proteomics); M.D. (Cardio Ox); T.M. (Untargeted Plasma Metabolomics and Proteomics, Plasma Cytokine Profiling, Integrative Analysis); S.J.G., P.J., A.K., F.W.T., and M.H.V. (Microbiome); H.H.P., J.M.S., and J.H.S. (Mitochondrial Function); C.E.M., C.M., F.E.G.-B., and M.M. (Twins Study PI, Transcriptome, Telomere Validation, Integration); D.D.S., K.S., and M.D. (Metabolomics); and A.H., T.V., and M.Af. (Urine Proteomics). *Editing and manuscript finalization:* F.E.G.-B., L.F.R., T.M., C.M., and C.E.M. *Writing, review and editing:* All authors reviewed and edited the manuscript. **Competing interests:** S.M.B. is a cofounder and scientific advisory board member of KromaTiD, Inc. C.E.M. is a cofounder and board member for Biotia, Inc., and Onegevity Health, Inc., as well as an advisor for Abbvie, Inc.; ArcBio; Daiichi Sankyo; DNA Genotek; Karius, Inc.; and Whole Biome, Inc. M.P.S. is a cofounder and scientific advisory board member of Personalis, SensOmics, Qbio, January, and Fitricine, and a scientific advisory board member of Genapsys, Epinomics, Jungla, and Jupyter. A.M.K.C. is a cofounder and stock holder and serves on the Scientific Advisory Board for Proterris, which develops therapeutic uses for carbon monoxide. A.M.K.C. also has a use patent on carbon monoxide. A.M.K.C. served as a consultant for TEVA Pharmaceuticals in July 2018. A.M.M. is a consultant for Janssen. **Data and materials availability:** The NASA Life Sciences Data Archive (LSDA) is the repository for all human and animal research data, including that associated with this study. LSDA has a public facing portal where data requests can be initiated (https://lsda.jsc.nasa.gov/Request/dataRequestFAQ). The LSDA team provides the appropriate processes, tools, and secure infrastructure for archival of experimental data and dissemination while complying with applicable rules, regulations, policies, and procedures governing the management and archival of sensitive data and information. The LSDA team enables data and information dissemination to the public or to authorized personnel either by providing public access to information or via an approved request process for information and data from the LSDA in accordance with NASA Human Research Program and JSC Institutional Review Board direction.

SUPPLEMENTARY MATERIALS

www.sciencemag.org/content/364/6436/eaau8650/suppl/DC1
Materials and Methods
Figs. S1 to S15
Tables S1 to S11
References (*85*–*156*)

24 July 2018; accepted 28 February 2019
10.1126/science.aau8650

RESEARCH ARTICLE SUMMARY

PLANT SCIENCE

Glycosidase and glycan polymorphism control hydrolytic release of immunogenic flagellin peptides

Pierre Buscaill, Balakumaran Chandrasekar, Nattapong Sanguankiattichai, Jiorgos Kourelis, Farnusch Kaschani, Emma L. Thomas, Kyoko Morimoto, Markus Kaiser, Gail M. Preston, Yuki Ichinose, Renier A. L. van der Hoorn†

INTRODUCTION: Immunogenic flagellin fragments are a signature of bacterial invasion in both plants and animals. Plants recognize flagellin fragments via flagellin sensitive 2 (FLS2), a model receptor kinase that is highly conserved among angiosperms. However, little is known about events upstream of flagellin perception by FLS2. The flagellin fragments recognized by FLS2 are buried in the flagellin polymer structure and require hydrolytic release before recognition can occur, yet the hydrolases releasing these elicitors remain to be identified. Uncovering their identity is a daunting task because the extracellular space of plants (the apoplast) contains hundreds of uncharacterized glycosidases and proteases.

RATIONALE: We reasoned that pathogenic bacteria would suppress plant hydrolases that are important for immunity. To identify suppressed hydrolases in the apoplast of infected plants, we applied activity-based protein profiling with the use of chemical probes that irreversibly label the active site of hydrolases. We applied this strategy to study the infection of the tobacco relative *Nicotiana benthamiana* with the bacterial pathogens *Pseudomonas syringae* pv. *tabaci* (*Pta*6605), *P. syringae* pv. *syringae* (*Psy*B728a), and a virulent mutant of *P. syringae* pv. *tomato* [*Pto*DC3000(Δ*hQ*)].

RESULTS: Glycosidase activity profiling of apoplastic fluids isolated from *Pto*DC3000 (Δ*hQ*)-infected plants revealed that the activity of β-galactosidase 1 (BGAL1) is suppressed in the apoplast during infection. BGAL1 suppression is caused by a heat-stable, basic, small inhibitor molecule that is produced by the bacteria under the control of *hrpR/S/L* virulence regulators. Null mutants of *N. benthamiana* lacking BGAL1 generated by genome editing have substantially reduced apoplastic β-galactosidase activity and are more susceptible to *Pto*DC3000 (Δ*hQ*), demonstrating that BGAL1 contributes to immunity. When investigating how BGAL1 functions in immunity, we discovered that treatment of *Pto*DC3000(Δ*hQ*) and *Pta6605* bacteria with apoplastic fluids containing BGAL1 results in the release of an elicitor that triggers a burst of reactive oxygen species in leaf discs, a signature immune response in plants. The released elicitor is flagellin derived because the triggered immune response requires both the FLS2 receptor in the plant and the flagellin-encoding *fliC* gene in the bacteria. More precisely, treatment of purified flagella with apoplastic fluids containing BGAL1 facilitates the release of immunogenic peptides from flagellin.

The flagellin polymer of both *Pto*DC3000 (Δ*hQ*) and *Pta6605* is O-glycosylated with glycans consisting of several rhamnose residues and a terminal modified viosamine (mVio). Mutant *Pta6605* bacteria carrying nonglycosylated flagellin, or carrying rhamnosylated flagellin lacking mVio, trigger the plant immune response when treated with apoplastic fluids, irrespective of BGAL1 presence, thus demonstrating that BGAL1 requires mVio for its function in immunity. Addition of a protease inhibitor cocktail to apoplastic fluids blocks the release of the flagellin elicitor from nonglycosylated flagellin, implicating apoplastic proteases in elicitor release acting downstream of BGAL1. Consistent with a specific role of BGAL1 in elicitor release, *bgal1* null mutants of *N. benthamiana* show increased susceptibility only to bacterial strains carrying mVio. Treatment of *Psy*B728a with apoplastic fluids containing BGAL1 does not facilitate release of the flagellin elicitor because its flagellin carries a different glycan moiety lacking mVio, thus providing protection against recognition.

CONCLUSION: Glycosidase BGAL1 acts upstream of proteases in the apoplast of *N. benthamiana* to release immunogenic peptides from glycosylated flagellin, but only on glycosylated flagellin containing mVio. *P. syringae* strains use both BGAL1 inhibitors and glycan polymorphism to suppress BGAL1 function and escape recognition. Glycan polymorphism is common to bacterial pathogens, indicating a general role for flagellin glycans in evading recognition of bacterial pathogens by both plants and animals. ■

ON OUR WEBSITE

Read the full article at http://dx.doi.org/10.1126/science.aav0748

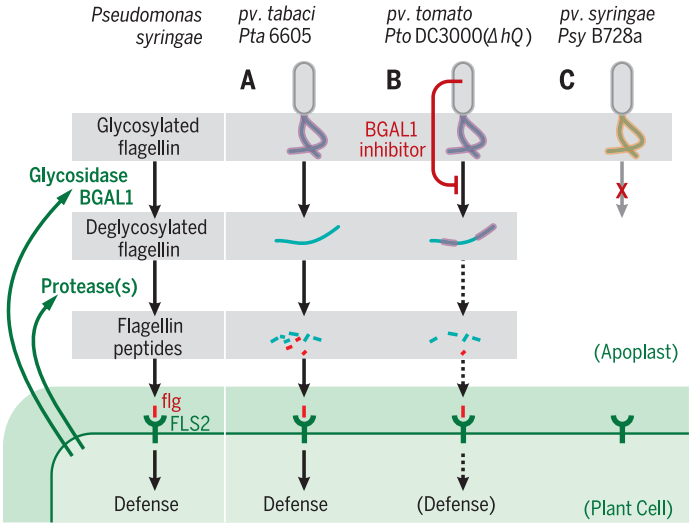

Control over hydrolytic release of immunogenic flagellin fragments. Secreted β-galactosidase BGAL1 and proteases contribute to immunity against bacteria with glycosylated flagellin carrying terminal mVio (purple) in both *Pta*6605 (**A**) and *Pto*DC3000(Δ*hQ*) (**B**) by releasing immunogenic peptides (flg, red) that are perceived by the FLS2 immune receptor. *Pto*DC3000(Δ*hQ*) (B) mitigates BGAL1 activity by the production of a BGAL1 inhibitor, whereas *Psy*B728a (**C**) produces BGAL1-insensitive glycans (orange) to escape recognition.

The list of author affiliations is available in the full article online.
†Corresponding author. Email: renier.vanderhoorn@plants.ox.ac.uk
Cite this article as P. Buscaill *et al.*, *Science* **364**, eaav0748 (2019). DOI: 10.1126/science.aav0748

RESEARCH ARTICLE

PLANT SCIENCE

Glycosidase and glycan polymorphism control hydrolytic release of immunogenic flagellin peptides

Pierre Buscaill[1], Balakumaran Chandrasekar[1]*, Nattapong Sanguankiattichai[1], Jiorgos Kourelis[1], Farnusch Kaschani[2], Emma L. Thomas[1], Kyoko Morimoto[1], Markus Kaiser[2], Gail M. Preston[1], Yuki Ichinose[3], Renier A. L. van der Hoorn[1]†

Plants and animals recognize conserved flagellin fragments as a signature of bacterial invasion. These immunogenic elicitor peptides are embedded in the flagellin polymer and require hydrolytic release before they can activate cell surface receptors. Although much of flagellin signaling is understood, little is known about the release of immunogenic fragments. We discovered that plant-secreted β-galactosidase 1 (BGAL1) of *Nicotiana benthamiana* promotes hydrolytic elicitor release and acts in immunity against pathogenic *Pseudomonas syringae* strains only when they carry a terminal modified viosamine (mVio) in the flagellin *O*-glycan. In counter defense, *P. syringae* pathovars evade host immunity by using BGAL1-resistant *O*-glycans or by producing a BGAL1 inhibitor. Polymorphic glycans on flagella are common to plant and animal pathogenic bacteria and represent an important determinant of host immunity to bacterial pathogens.

Plant pathogenic bacteria colonize the extracellular space within plant tissues (the apoplast) and manipulate their hosts with toxins and effector proteins delivered through the type III secretion system (T3SS) (*1*). Whereas these manipulation events inside the host cell are well studied, less is known about how bacteria manipulate the host apoplast.

One crucial aspect of plant–bacteria interactions is the recognition of extracellular pathogen-associated microbial patterns (PAMPs) that the plant can perceive, through pattern recognition receptors (PRRs), to mount PAMP-triggered immunity (PTI) (*2*). Most plants are able to recognize immunogenic peptides of bacterial flagellin through homologs of FLS2 (flagellin sensitive 2), a receptor kinase PRR (*2*, *3*). The 22–amino acid flagellin fragment flg22 has been intensively used to study receptor-like kinase (RLK) signaling and PTI in plants. Many T3SS-secreted effectors interfere in FLS2 signaling, underlining the important role of FLS2 signaling in immunity (*3*, *4*). However, although the release of immunogenic peptides like flg22 from the flagellin precursor protein has been anticipated, the mechanism by which this process occurs is unknown because these peptides are buried in the flagellin polymer structure (*5*). Identification of elicitor-releasing hydrolases is a daunting task because the plant apoplast contains hundreds of glycosidases, proteases, and other hydrolases (*6*, *7*).

We set out to discover the apoplastic hydrolases involved in immunity under the assumption that harmful host-secreted hydrolases will be suppressed by bacterial pathogens. To study apoplast manipulation, we investigated the interaction between *Nicotiana benthamiana* and the model bacterial pathogen *Pseudomonas syringae* pv. *tomato* DC3000 (*Pto*DC3000) (*8*). Whereas *Pto*DC3000 triggers nonhost resistance via recognition of the hopQ1-1 effector, the mutant lacking this type III effector [*Pto*DC3000 (Δ*hQ*)] is virulent on *N. benthamiana* (*8*).

Results

BGAL1 is inhibited during infection

To monitor the suppression of extracellular glycosidases, we applied glycosidase activity profiling on apoplastic fluids (AFs) isolated from infected plants and mock-inoculated control plants. Using the fluorescent activity–based probe JJB70, which labels the active site of glycosidases (*9*, *10*), we discovered a ~19-fold suppression of JJB70 labeling of a 45-kDa protein, previously identified as a putative β-galactosidase [BGAL1, NbS00024332g0007 (*10*)] (Fig. 1A). BGAL1 carries a signal peptide and is enriched in the apoplast (fig. S1). BGAL1 also accumulates in the apoplast when transiently overexpressed by infiltration of *N. benthamiana* with *Agrobacterium tumefaciens* (agroinfiltration) (Fig. 1B).

BGAL1 is a functional β-galactosidase because it can cleave galactose from FDG (fluorescein di-β-D-galactopyranoside) (fig. S2), and both JJB70 labeling and FDG hydrolysis by BGAL1 are blocked by the β-galactosidase inhibitor galactostatin (GSTN) (Fig. 1B). BGAL1 also selectively catalyzes hydrolyses of 4-nitrophenyl-β-galactopyranoside but not other monosaccharide conjugates (fig. S3). In contrast to active BGAL1, mutant BGAL1 protein carrying mutated catalytic residues [BGAL1^{E183A,E254A} (where E183A denotes Glu^{183}→Ala and E254A denotes Glu^{254}→Ala)] does not accumulate upon agroinfiltration (Fig. 1B). This nonaccumulating mutant BGAL1 is used as a "minus BGAL" (−BGAL1) control in follow-up experiments. Consistent with the strong suppression of JJB70 labeling in infected plants, FDG-hydrolyzing activity is reduced by a factor of ~30 in AFs upon infection (Fig. 1C).

Quantitative proteomic analysis indicated no change in the amounts of BGAL1 protein in AFs of infected plants (fig. S4), suggesting that BGAL1 is inactivated during infection. To test whether AFs of infected plants contain a BGAL1 inhibitor, we mixed AFs from infected and noninfected plants before and after JJB70 labeling, a method we term "convolution ABPP" [activity-based protein profiling (*11*)]. AFs from infected plants could suppress both JJB70 labeling (Fig. 1A) and FDG-hydrolyzing activity (Fig. 1C) present in AFs from the mock control, indicating that AFs from infected plants contain a BGAL1 inhibitor (Fig. 1D). The BGAL1 inhibitor is detected early during infection (fig. S6A) and also when *Pto*DC3000(Δ*hQ*) is grown in T3SS-inducing minimal media (fig. S5B). Inhibitor production is absent in Δ*hrpR*, Δ*hrpS*, and Δ*hrpL* mutants but present in Δ*hrpA* and Δ*hrcC* mutants of *Pto*DC3000, demonstrating that BGAL1 inhibitor production is controlled by virulence regulators but does not require the T3SS system (fig. S5B). The BGAL1 inhibitor is a heat-stable molecule of <3 kDa (fig. S6A) that is hydrophilic and basic (fig. S6, B and C). This BGAL1 inhibitor does not suppress the activity profiles of other hydrolases (fig. S6D) but remains to be identified.

BGAL1 contributes to immunity

We next investigated why *Pto*DC3000 inhibits BGAL1. BGAL1 is one of the 28 putative glycosyl hydrolases of family 35 (GH35) of *N. benthamiana* (fig. S7). *N. benthamiana* is an ancient alloploid, and BGAL1 has one putative homeolog, which has been pseudogenized (fig. S8A). Using genome editing with CRISPR-Cas9 (*12*), we generated two independent *BGAL1* null mutants: *bgal1-1* and *bgal1-2* (Fig. 2A and fig. S8). Both *bgal1* mutants contain frameshift mutations in the *BGAL1* open reading frame (fig. S8B), and BGAL1 depletion causes no major growth or developmental phenotypes (Fig. 2B). AFs from both *bgal1* mutants lack the JJB70 signal corresponding to BGAL1 (Fig. 2C) and have strongly reduced FDG hydrolyzing activity (Fig. 2D). Upon spray inoculation with *Pto*DC3000(Δ*hQ*), both *bgal1* mutants support enhanced bacterial growth (Fig. 2E) and develop more disease symptoms (Fig. 2F), confirming a role for BGAL1 in immunity. A similar increase in susceptibility was observed upon depletion of *BGAL1* transcripts by virus-induced gene silencing (VIGS) (fig. S9).

[1]Department of Plant Sciences, University of Oxford, Oxford, UK. [2]ZMB Chemical Biology, Faculty of Biology, University of Duisburg-Essen, Essen, Germany. [3]The Graduate School of Environmental and Life Science, Okayama University, Japan. *Present address: Institut für Pflanzliche Zellbiologie und Biotechnologie Heinrich-Heine-Universität, Düsseldorf, Germany. †Corresponding author. Email: renier.vanderhoorn@plants.ox.ac.uk

BGAL1 facilitates release of flagellin elicitor

We hypothesized that BGAL1 contributes to immunity by releasing an elicitor from bacteria that triggers a burst of reactive oxygen species (ROS), a signature immune response in plants. We therefore established an elicitor-release assay based on the incubation of bacteria with AFs and detection of released elicitors in a ROS burst assay using leaf discs of unchallenged plants (Fig. 3A). The ROS burst was induced in leaf discs of *N. benthamiana* when treated with bacteria that were incubated with AF from leaves overexpressing BGAL1 (Fig. 3B). The ROS burst was also absent when bacteria were omitted (fig. S10), indicating that the elicitor is derived from the bacteria. A similar BGAL1-dependent ROS burst was triggered in leaf discs of *Arabidopsis thaliana* (Fig. 3C), indicating that the BGAL1-released elicitor is recognized by different plant families.

We next found that *Arabidopsis* mutants lacking glycan receptors LORE or CERK1, or lacking both LYM1 and LYM3, still perceive the elicitor (fig. S11), indicating that the BGAL1-released elicitor is not related to lipopolysaccharide, chitin, or peptidoglycan, respectively (*13*–*15*). The ROS burst was also unaffected in leaf discs lacking SOBIR1 (fig. S11D) but was absent in leaf discs lacking BAK1 (Fig. 3D), indicating that elicitor perception involves a membrane-localized RLK but not a receptor-like protein (*3*). When testing BAK1-dependent immune RLKs, we discovered that leaf discs of the *Arabidopsis* mutant lacking FLS2, the RLK mediating flagellin recognition (*16*), are blind to the BGAL1-released elicitor (Fig. 3E). Likewise, *N. benthamiana* plants silenced for the *FLS2* ortholog [*NbFls2* (*17*)] were unable to sense the BGAL1-released elicitor (Fig. 3F). By contrast, an *Arabidopsis* mutant lacking EFR, the receptor for fragments of the bacterial EF-Tu protein, still perceives the BGAL1-released elicitor (fig. S11E).

Consistent with flagellin recognition via FLS2, BGAL1 treatment of mutant bacteria lacking flagellin [*Pto*DC3000(Δ*hQ*Δ*fliC* (*18*)] did not trigger the ROS burst in *Arabidopsis* (Fig. 3G) or *N. benthamiana* (Fig. 3H), indicating that the BGAL1-released elicitor is derived from flagellin. Indeed, treatment of purified flagellin with AFs containing BGAL1 also releases the elicitor (Fig. 3I), demonstrating that BGAL1 facilitates elicitor release directly from flagellin. Mass spectrometric analysis of peptides released from purified flagellin by AFs containing BGAL1 revealed several peptides known to trigger immunity (*19*) (fig. S12). These data demonstrate that BGAL1 controls the release of immunogenic peptides from flagellin.

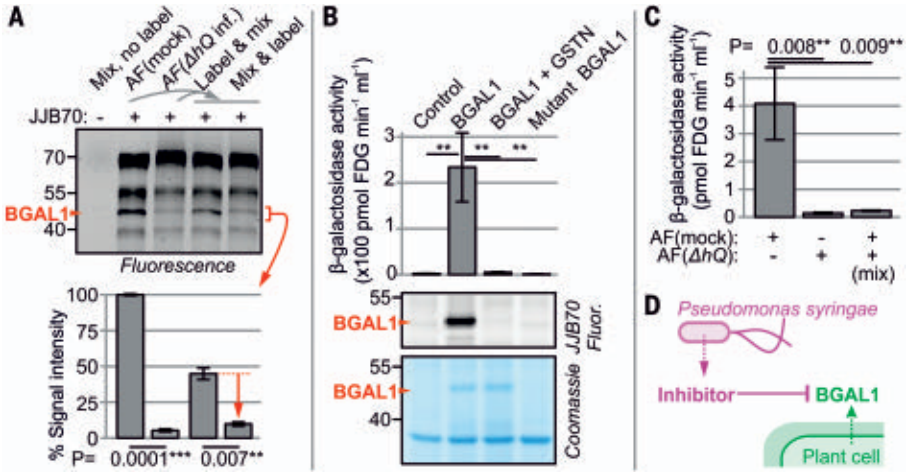

Fig. 1. BGAL1 is suppressed during bacterial infection. (**A**) BGAL1 labeling is suppressed in AFs of infected plants at 2 days postinfection (dpi). The two samples were also mixed in a 1:1 ratio before (mix and label) and after (label and mix) labeling with JJB70. The quantified fluorescence of the BGAL1 signal is plotted below. Error bars indicate mean ± SE of $n = 3$ replicates; t test was used to determine P values. (**B**) BGAL1 has β-galactosidase activity. FDG-hydrolyzing activity was measured on AFs isolated from leaves transiently expressing the silencing inhibitor P19 alone (control) or with BGAL1 (+) or mutant BGAL1 (−), pre-incubated with or without 10 μM galactostatin (GSTN). Error bars indicate mean ± SE of $n = 4$ replicates; Tukey HSD was used to determine P values. The samples were also labeled with JJB70 and stained with Coomassie. (**C**) Reduced β-galactosidase activity in AF from infected plants isolated at 2 dpi. The two samples were also mixed in a 1:1 ratio before FDG was added. Error bars indicate mean ± SE of $n = 5$ replicates; Tukey HSD was used to determine P values. (**D**) Schematic diagram showing BGAL1 and its inhibitor.

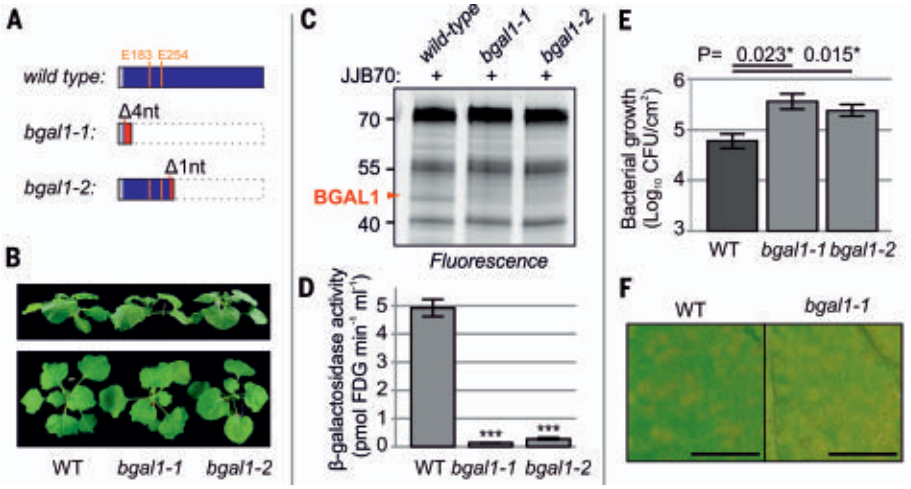

Fig. 2. BGAL1 contributes to immunity. (**A**) Open reading frames of wild type and two independent *bgal1* null mutants generated by genome editing (red, out-of-frame translation; orange, catalytic Glu residues). (**B**) Representative photos of 5-week-old plants. (**C**) Both *bgal1* null mutants lack the BGAL1 signal in the JJB70 labeling profile. (**D**) AF from both *bgal* mutants has reduced β-galactosidase activity. Error bars indicate mean ± SE of $n = 3$ replicates; Tukey HSD was used to determine ***P values < 0.001. (**E**) Compared with the wild type, both *bgal1* mutants are less resistant to *Pto*DC3000(Δ*hQ*). Bacterial growth of *Pto*DC3000(Δ*hQ*) upon spray inoculation was measured at 3 dpi. Error bars indicate mean ± SE of $n = 4$ replicates; t test was used to determine *P values. CFU, colony-forming units. (**F**) Representative photos of spray-infected leaves showing symptoms of bacterial spot disease at 6 dpi. Scale bars, 1 cm.

BGAL1 acts on glycosylated flagellin

A conserved fragment of 22 amino acid residues of flagellin (flg22) containing the immunogenic sequence KINSAKDDAAGLQ (K, Lys; I, Ile; N, Asn; S, Ser; D, Asp; G, Gly; L, Leu; Q, Gln) [flg15-Δ2 (*19*)] is universally recognized in angiosperms by orthologs of FLS2 (*19*–*22*). This immunogenic region resides inside the flagellin rod (Fig. 4 and fig. S13) and has to be unfolded and excised before it can interact with FLS2 (*5*, *23*). The solvent-exposed surface of flagella is covered with *O*-glycans linked to six serine residues located in the D2 and D3 domains of each flagellin protein (Fig. 4). The *O*-glycans of *Pto*DC3000 consist of two or three rhamnose residues and a terminal modified viosamine (mVio) (*24*, *25*) (Fig. 4).

The involvement of BGAL1 in the release of the flagellin elicitor suggests that BGAL1 acts on

glycosylated flagellin and that glycan removal exposes the flagellin protein to proteases that release the flagellin elicitor (Fig. 5). We tested this hypothesis using *P. syringae*. pv. *tabaci* 6605 (*Pta*6605), which is also pathogenic on *N. benthamiana* (*26*) and has been used as a model to elucidate the glycan structure on the flagellin. The *O*-glycans on the flagellin of *Pta*6605 are identical to those of *Pto*DC3000 (Fig. 6A) (*24*, *25*, *27*), but *Pta*6605 does not produce a BGAL1 inhibitor (fig. S14). As with *Pto*DC3000(Δ*hQ*), BGAL1-treatment of *Pta*6605 bacteria releases an elicitor detected in both *N. benthamiana* (Fig. 6B) and *Arabidopsis* (fig. S15A), and *Pta*6605 grows better on *N. benthamiana bgal1* mutants than on wild-type (WT) plants (Fig. 6C). The elicitor released by BGAL1 is derived from flagellin, as it is undetected in *N. benthamiana* and *Arabidopsis* lacking *Nb*FLS2 and FLS2, respectively (fig. S15, B and C), and the elicitor is not released from *Pta*6605(Δ*fliC*) lacking flagellin (fig. S15D).

Next, we took advantage of *Pta*6605 mutants that lack different enzymes involved in the *O*-glycan formation on flagellin. Incubation of *Pta*6605(Δ*fgt1*) bacteria, which carries unglycosylated flagellin (Fig. 6D) (*27*), with AFs releases the elicitor, irrespective of BGAL1 presence (Fig. 6E). Accordingly, *Pta*6605(Δ*fgt1*) bacteria grew less when compared with *Pta*6605(WT), and BGAL1 no longer contributed to immunity because Δ*fgt1* bacteria grew equally well on both WT plants and *bgal1* mutant plants (Fig. 6F). *Pta*6605 mutants producing flagella that lack one *O*-glycosylation site [S143A, S164A, S176A, S183A, S193A, and S201A mutants, respectively (*27*)] also released the elicitor when incubated with AFs, even in the absence of BGAL1 (fig. S16). Consistent with the implicated role of proteases in the release of flagellin fragments, elicitor release from *Pta*6605(Δ*fgt1*) bacteria and purified non-glycosylated flagellin was blocked with a protease inhibitor cocktail (fig. S17). These data demonstrate that *O*-glycans on flagellin provide protection against hydrolytic elicitor release and that BGAL1 overcomes this protection.

BGAL1's role is specific for mVio glycans

To further specify BGAL1 action, we tested the *Pta*6605 mVio transferase mutant Δ*vioT* and mVio biosynthesis mutants Δ*vioA* and Δ*vioB*, which all carry flagellin with rhamnose *O*-glycans that lack the terminal mVio residue (Fig. 6G) (*28*). Like the Δ*fgt1* mutant, incubation of Δ*vioT*, Δ*vioA*, and Δ*vioB* mutant bacteria with AFs released the flagellin elicitor irrespective of BGAL1 presence (Fig. 6H and fig. S18), and these mutant bacteria grew equally well on WT and *bgal1* mutant plants (Fig. 6I and fig. S18). These data demonstrate that rhamnosyl glycans on flagella do not prevent elicitor release in the apoplast and indicate that mVio protects against elicitor release. These data also show that BGAL1-mediated elicitor release and the role of BGAL1 in immunity requires mVio on the flagellin glycans.

All *P. syringae* bacteria produce O-glycosylated flagella but the structures of the *O*-glycans can differ between strains. For instance, *P. syringae* pv. *syringae* B728a (*Psy*B728a), which has been isolated from bean but is also pathogenic on *N. benthamiana* (*29*), does not carry a (1,3)-linked

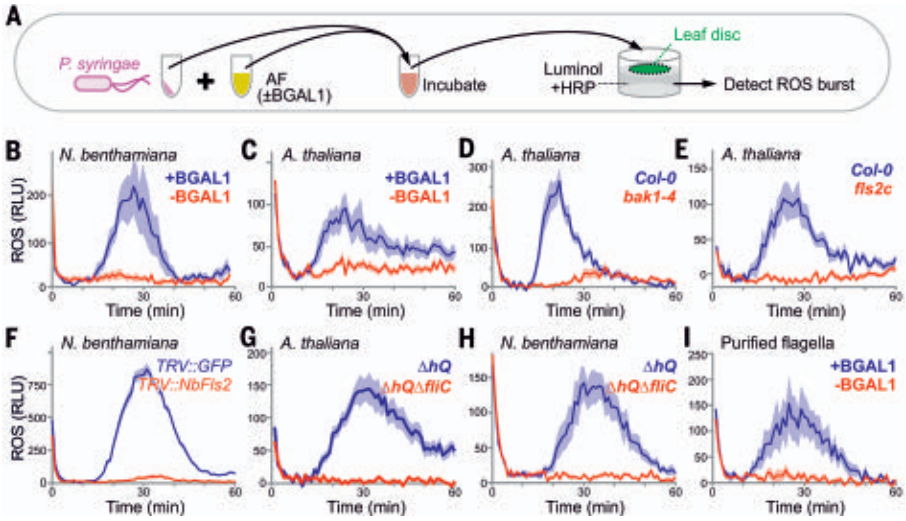

Fig. 3. BGAL1 controls the release of the flagellin elicitor. (**A**) Experimental procedure to detect BGAL1-released elicitors from bacteria. The pellet of a bacterial culture was resuspended and incubated with AF isolated from *N. benthamiana* leaves transiently overexpressing BGAL1 (+) or the minus BGAL control (−). The treated bacteria were added to leaf discs floating on a solution containing luminol and horseradish peroxidase (HRP), and ROS was detected over time by chemiluminescence. The ROS burst is triggered in leaf discs of *N. benthamiana* (**B**) and *Arabidopsis* (**C**) after pretreatment of bacteria with AFs from plants overexpressing BGAL1 (+BGAL1) but not the nonaccumulating mutant BGAL1 (−BGAL1). This ROS burst requires BAK1 (**D**) and FLS2 (**E**) and its ortholog NbFLS2 in *N. benthamiana* (**F**). The ROS burst also requires the flagellin-encoding *fliC* gene in *Pto*DC3000 in both *Arabidopsis* (**G**) and *N. benthamiana* (**H**), and is also induced in *N. benthamiana* by purified flagella treated with AF containing BGAL1 (**I**). Error intervals (shaded regions) indicate mean ± SE of n = 6 [(B) and (I)] or n = 12 [(C) to (H)] replicates. RLU, relative luminescence units.

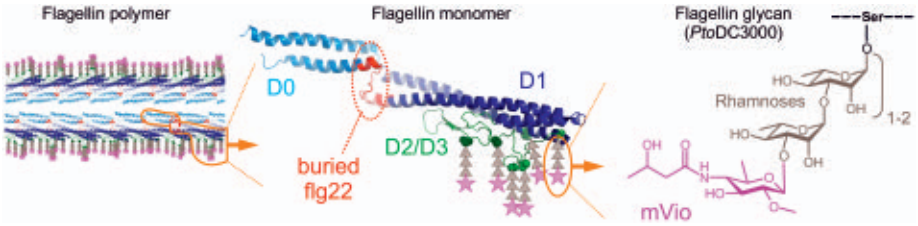

Fig. 4. Flagellin is a glycosylated protein polymer with a buried immunogenic sequence. Flagellin of *Pto*DC3000 was modeled on the basis of the flagellin polymer structure of *P. aeruginosa* (5wk5). Positions of O-glycosylated Ser residues (green) are distributed over the surface of the polymer.

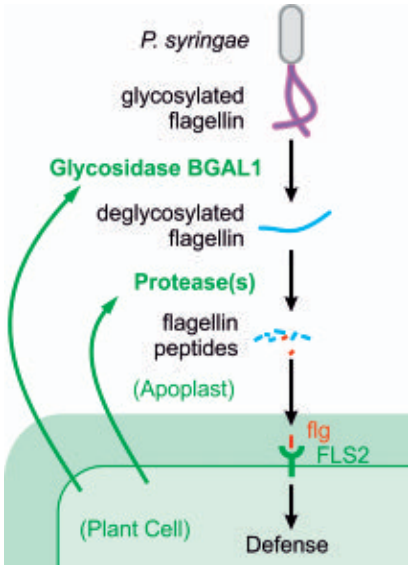

Fig. 5. Hydrolytic release of immunogenic peptides from flagellin. We hypothesize that BGAL1 controls the release of immunogenic flagellin elicitors (e.g., flg, red) from *P. syringae* by initiating the removal of the glycan protection layer from flagella. Proteases would then process flagellin to release the peptide elicitors, which are recognized by the FLS2 surface receptor.

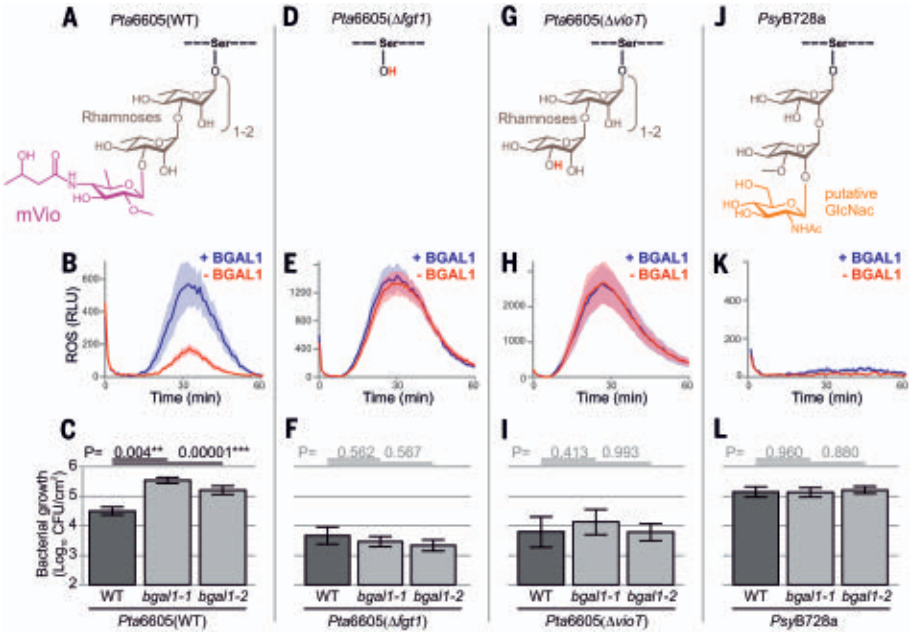

Fig. 6. BGAL1 acts in immunity only on bacteria carrying mVio on flagellin *O*-glycans. (**A** to **C**) BGAL1 also releases an elicitor from *Pta*6605. (**D** to **F**) BGAL1 is not required to release the flagellin elicitor from *Pta*6605(Δ*fgt1*) producing nonglycosylated flagellin. (**G** to **I**) BGAL1 is not required to release the flagellin elicitor from *Pta*6605(Δ*vioT*) lacking the terminal mVio. (**J** to **L**) BGAL1 does not release the flagellin elicitor from *Psy*B728a carrying a different flagellin glycan. (A, D, G, and J) Structures of flagellin *O*-glycans, determined previously. (B, E, H, and K) ROS burst assays of elicitor fractions from bacteria treated with AFs from plants overexpressing BGAL1 (+BGAL1) or mutant BGAL1 (-BGAL1). Error intervals (shaded regions) indicate mean ± SE of n = 12 replicates. (C, F, I, L) *Pta*6605 growth at 3 dpi on WT and *bgal1* mutant plants after spray inoculation. Error bars indicate mean ± SE of n = 3 (F), n = 6 (I), or n = 8 [(C) and (L)] replicates; t test was used to determine P values.

mVio but instead carries a putative (1,2)-linked terminal GlcNac [*N*-acetylglucosamine, Fig. 6J (*24*, *25*)]. Treatment of *Psy*B728a with AFs containing BGAL1 does not release the flagellin elicitor (Fig. 6K), and *Psy*B728a also grows equally well on WT and *bgal1* mutant plants (Fig. 6L). *Psy*B728a does not produce a BGAL1 inhibitor (fig. S14) and may suppress elicitor release through other mechanisms. These data indicate that the flagellin glycan of *Psy*B728a is protected against BGAL1 from *N. benthamiana*. However, plants silenced for NbFls2 are more susceptible to *Psy*B728a (*17*), which indicates that *N. benthamiana* has hydrolases that can release the flagellin elicitor from *Psy*B728a. We did not detect this activity in our elicitor-release assays, possibly because these hydrolases are not sufficiently present or active in the isolated AFs used. Overexpression of these hydrolases might overcome this limitation, as we discovered for BGAL1.

Discussion

Hydrolytic release of immunogenic peptides

We discovered that BGAL1 acts in immunity by controlling the release of immunogenic flagellin peptides and that bacteria counter the role of BGAL1 by producing a BGAL1 inhibitor or BGAL1-insensitive glycans. Our work also elucidates an important role for proteases in the release of immunogenic peptides. The *N. benthamiana* apoplast contains nearly 200 proteases that may act redundantly (*7*), and our strategy to identify hydrolases that are suppressed during infection may be useful for identifying the proteases that act in the release of the flagellin elicitor. We anticipate a similar important role for BGAL1 and other hydrolases in the release of different immunogenic flagellin fragments that are recognized in tomato and rice (*30*, *31*). Hydrolytic release of immunogenic peptides from precursors may also be required for peptide elicitors elf18, nlp24, and possibly pep13 from bacterial, fungal, and oomycete pathogens because these are also buried within folded protein structures (*32*–*36*). It will be interesting to determine whether the role of BGAL1 and proteases is conserved across plant species or whether host-specific hydrolytic processes dictate elicitor release and host specificity.

Glycan polymorphism as a common defense strategy

*Psy*B728a evades flagellin hydrolysis and recognition by the host, which suggests that polymorphic glycans on flagellin might help other plant-pathogenic bacteria evade recognition. Indeed, 2150-Da glycan moieties on flagellin in strain K1 of the bacterial rice pathogen *Acidovorax avenae* (*Ac*K1) prevent flagellin recognition in rice, whereas 1600-Da glycan moieties on flagellin from the related *Ac*N1141 strain do not prevent flagellin recognition (*37*). Likewise, despite being identical in protein sequence, the glycosylated flagellin of *P. syringae* pv. *glycinea* (*Psg*) triggers cell death in tobacco (*Nicotiana tabacum*) but the glycosylated flagellin of *Pta*6605 do not, probably owing to the distinctive *O*-glycan moieties (*38*, *39*). These observations indicate that polymorphic glycans are an important determinant in evading host immunity and that host plants secrete specialized glycosidases to release immunogenic flagellin fragments.

The role of flagellin glycans in host immunity evasion also extends to animal-pathogenic bacteria. Flagellin glycosylation mutants of *Pseudomonas aeruginosa*, for instance, are less virulent in wound infection assays in mice (*40*). Likewise, nonglycosylated flagellin proteins from the opportunistic human pathogen *Burkholderia cenocepacia* stimulate stronger TLR5-dependent immune responses in human cell lines when compared with glycosylated flagellin (*41*). Glycans on flagellin are also polymorphic in animal-pathogenic bacteria (*42*). For instance, *B. cenocepacia*, *Burkholderia pseudomallei*, and *Burkholderia thailandensis* carry different glycans that may provide different levels of protection against host hydrolases (*43*). These data indicate that polymorphic glycans on flagella are a common strategy to evade host immunity driven by host-specific hydrolases in both plants and animals.

Materials and methods

Plants

Nicotiana benthamiana plants were grown in a growth chamber at 21°C and ~60% relative humidity with a 12-hour photoperiod and a light intensity of 2000 cd·sr m^{-2}. *Arabidopsis* plants were grown in a Fitotron growth chamber (Weiss Gallenkamp, Loughborough, UK) at 21°C and ~60% relative humidity with a 12-hour photoperiod. *Arabidopsis* mutants used are all in *Col-0* background and are summarized in Table 1.

Bacterial strains

The *P. syringae* strains used in this study are listed in Table 2. *Pst*DC3000 strains were grown in Luria-Bertani (LB) medium with 50 μg/ml rifampicin at 28°C. *Pta*6605 strains were grown in King's B (KB) medium at 28°C. For the infection assays, bacteria were cultured in Luria-Bertani (LB) medium containing 10 mM $MgCl_2$ at 28°C.

Molecular cloning

All constructs were generated using standard molecular biology procedures. All new vectors are summarized in Table 3. All binary plasmids were transformed into *Agrobacterium tumefaciens* GV3101 (pMP90) by freeze-thawing and selected for kanamycin resistance.

The full-length *BGAL1* open reading frame and its catalytic mutant (*BGAL1*^{E183A,E254A}) were commercially synthesized without the sequence encoding the signal peptide (SeqA, Biomatik, Cambridge, Ontario, Canada). The synthetic sequence (SeqA) contained flanking *Xho*I/*Sal*I

and *Bam*HI restriction sites and a sequence encoding an *N*-terminal StrepII tag. The synthetic sequences were received in pBluescript (pBS) cloning vectors pBK23 and pBK25 for WT and mutant BGAL1, respectively. The open reading frame was cloned into the pRH509 binary vector (*44*) using *Sal*I and *Bam*H1 restriction sites, in between the *35S* promoter with a sequence encoding the PR1a signal peptide, and the *PI-II* terminator sites, resulting in binary vectors pBK26 (WT BGAL1) and pBK27 (mutant BGAL1), respectively.

The 281-bp fragment of *BGAL1* (SeqB) used for VIGS was commercially synthesized (Biomatik, Cambridge, Ontario, Canada) and was received in pBS vector pBK30. The fragment was cloned into binary TRV2 vector (*45*) using *Eco*R1 and *Bam*H1 restriction sites, resulting in binary vector pBK46.

The two CRISPR/Cas9 sgRNAs targeting BGAL were designed to minimize off-targets by using "CCTop - CRISPR/Cas9 target online predictor" (*46*), and their on-target activity was predicted according to Doench *et al.* (*47*). A CRISPR-Cas9 cloning vector (pL1V2-Kan-Cas9) was constructed by combining pAGM4723 [Addgene 48015 (*48*)] with pICH47742 [Addgene 49771 (*49*)], pICSL11017 (Addgene 51144) and pICH47761 [Addgene 48003 (*48*)] in a Golden Gate reaction with *Bpi*I, resulting in pJK236. Specific PCR products were generated by amplifying from the template for sgRNAs pICH86966 [Addgene 46966 (*12*)] using forward primers 5′-ttggtctcaattggccgtcaatgaccaacgccgttttagagctagaaatagcaag-3′ (for *sgRNA_147*/bgal1-1) or 5′-ttggtctcaattggccgaagttcgttccccggttttagagctagaaatagcaag-3′ (for *sgRNA_106/bgal1-2*) and reverse primer 5′-ttggtctcaagcgtaatgccaactttgtac-3′. The two PCR products were combined with pJK236 and the AtU6 promoter [pICSL01009, Addgene 46968 (*12*)] in a Golden Gate reaction with *Bsa*I to generate pBK13 (*for sgRNA_106/bgal1-2*) and pBK14 (*sgRNA_147/bgal1-1*), respectively.

SeqA (synthetic BGAL1-encoding sequence): **Bold underlined**: Codons encoding active site glutamates were mutated into *GCA* and *GCG* in the *BGAL1*^{E183A,E254A} catalytic mutant. Underlined: SeqB used for VIGS. **Bold**: Restriction sites. *Italic with asterisk above*: Two silent substitutions introduced to remove *Eco*RI sites.

5′-at**gtcgacctcgag**ctggtctcatcctcaatttgaaaagGCCAATGTGACGTATGATCACCGGGCGTTGGTCATTGACGGCCAGCGTAGAGTTCTCATCTCCGGCTCCATACATTACCCTCGTAGTACTCCTGATATGTGGCCAGACCTTATACAGAAATCTAAAGATGGAGGATTGGATGTACTAGAGACATATGTTTTCTGGAACATACATGAACCTGTTAGAAATCAGTATGATTTTGAAGGAAGGAAAGATTTGGTTAAATTTGTGAAGTTGGTGGGGAAAGCTGGCTTATATGCTCATATAAGGATCGGGCCTTATGTTTGTGCAGAATGGAACTATGGTGGGTTTCCTCTTTGGTTGCATTTCATTCCTGGAGTTGAATTTCGAACTGATAATGAACCATTCAAGGCAGAAATGAAGCGGTTTACAGCAAAAATTGTTGACATGCTCAAGCAAGAAAATCTTTATGCATCCCAAGGGGGACCGGTTATTTTGTCTCAGATAGAAAAT**GAA**TATGGCAATGGGGATATTGAGTCTCGTTATGGTCCTCGTGCCAAACCTTATGTCAACTGGGCAGCAAAAATGGCTACATCGTTGGATACAGGAGTGCCATGGGTTATGTGCCAGCAACCAGATGCCCCTGATCCCATAATAAACACTTGCAATGGATTCTATTGTGACCAATTCAAGCAGAAC*TCCGATAAGACACCCAAGATGTGGACG**GAG**AATTGGACTGGATGGTTTCTTTCTTTTGGTGGTGCTGTCCCTTACAGACCTGTGGAAGACATTGCTTTTTCTGTGGCTCGATTTTTCCAGCGAGGTGGAACCTTTCAGAACTATTACATGTACCACGGGGGAACGAACTTCGGCCGGACCAGTGGTGGGCCATTTATTTCAACTAGCTATGACTATGATGCTCCTTTAGATGAGTATGGCCTTATAAGACAACCAAAGTGGGGCCACTTGAAAGATCTCCATAAAGCCATAAAGCTGTGCGAGGCTGCAATGGTGGCAACTGATCCAACTATCACTTCTCCAGGATCTAACATAGAGGTCAGTGTTTATAAAACTGGATCGGTGTGTGCTGCATTTCTTGCCAATGTGGGTACACAGTCTGACGCAGCCGTGACTTTCAATGGAAATTCATATCATTTGCCTCCTTGGTCCGTGAGCATCTTACCTGATTGCAAAAATGTGGCATTTAGT-

Table 1. *Arabidopsis* mutants lines used in this study. NASC, Nottingham Arabidopsis Stock Centre.

Name	Locus	Origin	Reference	Provided by
sd1-29	At1g61380	SAIL_857_E06	(*13*)	NASC
cerk1-2	At3g21630	GABI_096F09	(*71*)	A. Gust, Thübingen
lym1-1/lym3-1	At1g21880/At1g77630	GABI_419G07 SALK_111212	(*15*)	A. Gust, Thübingen
bak1-4	At4g33430	SALK_116202C	(*72*)	NASC
sobir1-12	At2g31880	SALK_050715	(*73*)	M. Joosten, Wageningen
fls2c	At5g46330	SAIL_691C4	(*74*)	C. Zipfel, Norwich

Table 2. *P. syringae* strains used in this study. Rif, rifampicin; –, not applicable.

Strain	Selection	Reference
Pseudomonas syringae pv. *tomato* DC3000 Δ*hQ*	Rif	(*8*)
Pseudomonas syringae pv. *tomato* DC3000 Δ*hQ*Δ*fliC*	Rif	(*18*)
Pseudomonas syringae pv. *tomato* DC3000 Δ*hrpR*	Rif	(*75*)
Pseudomonas syringae pv. *tomato* DC3000 Δ*hrpS*	Rif	(*75*)
Pseudomonas syringae pv. *tomato* DC3000 Δ*hrpL*	Rif	(*75*)
Pseudomonas syringae pv. *tomato* DC3000 Δ*hrpA*	Rif	(*76*)
Pseudomonas syringae pv. *tomato* DC3000 Δ*hrcC*	Rif	(*76*)
Pseudomonas syringae pv. *tabaci* 6605	–	(*77*)
Pseudomonas syringae pv. *tabaci* 6605 Δ*fliC*	–	(*77*)
Pseudomonas syringae pv. *tabaci* 6605 Δ*fgt1*	–	(*27*)
Pseudomonas syringae pv. *tabaci* 6605 Δ*vioT*	–	(*28*)
Pseudomonas syringae pv. *tabaci* 6605 Δ*vioA*	–	(*28*)
Pseudomonas syringae pv. *tabaci* 6605 Δ*vioB*	–	(*28*)
Pseudomonas syringae pv. *tabaci* 6605 S143A	–	(*27*)
Pseudomonas syringae pv. *tabaci* 6605 S164A	–	(*27*)
Pseudomonas syringae pv. *tabaci* 6605 S176A	–	(*27*)
Pseudomonas syringae pv. *tabaci* 6605 S183A	–	(*27*)
Pseudomonas syringae pv. *tabaci* 6605 S193A	–	(*27*)
Pseudomonas syringae pv. *tabaci* 6605 S201A	–	(*27*)
Pseudomonas syringae pv. *syringae* B728a	–	(*78*)

Table 3. Binary vectors generated in this study. T-DNA, transferred DNA.

Name	Description
pBK26	Binary vector carrying *35S::BGAL1* (SeqA) and *NptII* on T-DNA
pBK27	Binary vector carrying *35S::BGAL1*^{E183A,E254A} and *NptII* on T-DNA
pBK13	Binary vector carrying *sgRNA_106*, *Cas9* and *NptII* on T-DNA, used to generate *bgal1-2*
pBK14	Binary vector carrying *sgRNA_147*, *Cas9* and *NptII* on T-DNA, used to generate *bgal1-1*
pBK46	Binary vector carrying TRV2 with 281-bp fragment (SeqB) of BGAL1 on T-DNA

ACTGCAAAGATTAACTCGATGTCAACAATCT-CAAAGTTTGTTACTCAGTCTACGGAAGCTG-ATGGTTCTGGCGCATCCTTGTCAGGTTGGAC-TTGGGTTAATGAGCCTGTAGGTATCTCAAGTG-ATAACGCGTTCACAAAAACGGGTTTGATGG-AGCAGATAAATACTACAGCAGATAAAAGTGA-TTATCTTTGGTACTCTCTGAGTGTTAATGTA-AAAAATGACGAGCCTTTCCTTCAAGATGGAT-CTCAAACAGTACTTCATGTGGAATCACTTGGC-CATGTTCTTCATGCTTTCATTAACGGAAAGCT-ATCAGGAAGTGGGAAAGGAAACAGTGGAAAT-TCTAAAGTTACAATTGATGTTCCTGTCACCCTT-GTACCTGGAGAAAACAAAATCGACCTGTTGA-GTGTGAATGTGGGGCTTCAGAACTATGGAGC-ATTCTTTGATCTTAAGGGAGCAGGTATTACCG-GTCCTGTGCAATTGAAAGGCTTCAAAAATGGC-TCTACTATTGATCTTTCGTCAAAGCAATGGA-CATATCAGGTTGGATTGAAAGGAGAAGAACT-GGGGTTATCTGATGGAAGTTCTTCGCTTTG-GAA$\overset{*}{C}$TCACAATCTGCATTGCCTACAAACCAAC-CATTAATTTGGTATAAGGCAAGTTTTGATG-CCCCTGCTGGAGATACCCCTCTTTCACTAG-ATTTTACTGGAATGGGAAAGGGTGAAGCA-TGGGTGAATGGACAAAGCATTGGCCGATTT-TGGCCTACCAATACTGCATCAAATGGAGGTT-GTACTGACTCCTGCAATTATAGAGGATCTTA-CAATTCTAACAAATGTCTTAAAAATTGTGGAA-AACCATCCCAGCTGCTATACCACGTTCCTCGT-TCATGGCTGCAATCCACGGGAAATGTCATAG-TGTTGTTTGAGGAAATGGGTGGGAATCCAAC-AAAGCTATCTTTTGCAACAAGAGAGACAAGT-AGTATATGCTCACGAGTTTCAGAGGCGCAT-CCACTTCCTATTGACAAGTGGACGTCGGATG-ACGATGCACGAAAGAAAGTAGGGCCAACTCT-GTCTCTTGAGTGCCCTCGTCCTGATCAAGTC-ATTTCTTCAATCAAATTTGCAAGCTTTGGC-ACTCCTCTTGGTGCATGTGGAAGCTTTA-GCCATGGTCGATGCACAAGCAACAATGCTCT-TTCCCATGTAAAGAAGGCTTGCATTGGATCG-AGACACTGTAGTGTTGGAGTTTCAATAGATG-TATTTGGTGATCCATGTATAGGAGTCACAA-AAAGTTTAGCCGTAGAAGCTTCCTGTTCG-**ggatcc**-3′

SeqB (fragment used for silencing BGAL1): **Bold**: Restriction sites.

5′-**gaattc**CTGTTAGAAATCAGTATGATTTTGAA-GGAAGGAAAGATTTGGTTAAATTTGTGAAGT-TGGTGGGGAAAGCTGGCTTATATGCTCATATA-AGGATCGGGCCTTATGTTTGTGCAGAATGGA-ACTATGGTGGGTTTCCTCTTTGGTTGCATTTC-ATTCCTGGAGTTGAATTTCGAACTGATAATGA-ACCATTCAAGGCAGAAATGAAGCGGTTTACA-GCAAAAATTGTTGACATGCTCAAGCAAGAAA-ATCTTTATGCATCCCAAGGGGGACCGGTTAT-TTTG**ggatcc**-3′

sgRNA_106 (for *bgal1-2*): Underlined: Spacer sequence.

5′-GGCCGAAGTTCGTTCCCCCGGTTTTAGAGC-TAGAAATAGCAAGTTAAAATAAGGCTAGTCC-GTTATCAACTTGAAAAAGTGGCACCGAGTCG-GTGCTTTTTTT-3′

sgRNA_147 (for *bgal1-1*): Underlined: Spacer sequence.

5′-GGCCGTCAATGACCAACGCCGTTTTAGAG-CTAGAAATAGCAAGTTAAAATAAGGCTAGTC-CGTTATCAACTTGAAAAAGTGGCACCGAGTC-GGTGCTTTTTTT-3′

Plant transformation

Agrobacterium mediated transformation of *N. benthamiana* was performed as described (*50*). Briefly, 4-week-old *N. benthamiana* plants were agroinfiltrated with *A. tumefaciens* strain GV3101 pMP90 carrying binary plasmids pBK13 (carrying sgRNA_106 for *bgal1-2*) and pBK14 (carrying sgRNA_147 for *bgal1-1*). At 3 days post-infiltration, the infiltrated leaves were cut into 1-cm^2 sections and were cultured under sterile conditions on shooting media [per liter: 4.3 g MS basal salts (1×), 30 g sucrose, 1× B5 vitamins, 0.1 mg naphthalene acetic acid (NAA), 0.59 g MES, pH 5.7 using KOH, 4 g Agargel, after autoclaving add 1 mg benzylaminopurine (BAP), 300 mg ticarcillin/clavulanic acid] for 3 days, and subsequently transferred to shooting media supplemented with 150 μg/ml kanamycin and cultured for approximately 2 to 3 weeks to select for stable transformants. Shoots were excised and transferred to rooting media [per liter: 2.15 g MS basal salts (0.5×), 5 g sucrose, 0.1 mg NAA stock, pH 5.8 with KOH, 2.5 g Gelrite, after autoclaving add 300 mg ticarcillin/clavulanic acid] supplemented with 150 μg/ml kanamycin and were further cultured until roots appeared, after which plantlets were transferred to soil and grown in the growth chamber. To identify stable *N. benthamiana* transformants carrying mutant *BGAL1* alleles, the targeted segment of the *BGAL1* gene was PCR amplified using primers for *bgal1-1* (forward primer: 5′- tctgcttctaagaacagat-3′; reverse primer: 5′-gtctctagtacatccaatcc-3′) and *bgal1-2* (forward primer: 5′-accatactcatctaaaggagca-3′; reverse primer: 5′-ggctcgatttttccagcgag-3′), and the PCR fragments were sequenced by Sanger sequencing to confirm mutations. Mutant lines were screened by ABPP using the JJB70 probe to confirm BGAL1 depletion in the T2 and T3 generations.

Virus-induced gene silencing (VIGS)

Agrobacterium cultures were grown overnight and resuspended in agroinfiltration buffer (10 mM $MgCl_2$, 10 mM MES pH 5.0, and 100 μM acetosyringone) at OD_{600} = 0.5. Bacteria containing pBK46 (*TRV::BGAL1)* or *TRV2::GFP* were mixed 1:1 with bacteria containing TRV1 (*45*). After incubation for 1 hour at room temperature, the mixed cultures were infiltrated into leaves of 10-day-old *N. benthamiana* plants. The infiltrated seedlings were grown for 3 to 4 weeks in a growth chamber until use.

Agroinfiltration

For transient expression of proteins in *N. benthamiana*, overnight cultures of *Agrobacterium* carrying binary vectors were harvested by centrifugation. Cells were resuspended in induction buffer (10 mM $MgCl_2$, 10 mM MES pH5.0, and 100 μM acetosyringone) at OD_{600} = 0.5. After 1 hour at 21°C, cells were infiltrated into leaves of 4-week-old *N. benthamiana*. Leaves were harvested and processed 4 days after agroinfiltration.

Isolation of apoplastic fluids

AFs were collected as described previously (*51*). Leaves from infected or agroinfiltrated plants were submerged in ice-cold water and infiltrated by applying vacuum for 5 min. The surface of water-infiltrated leaves were dried with absorbing paper and leaves were carefully mounted in an empty 20-ml syringe, placed in a 50-ml tube. AFs were collected by centrifugation at 2000*g* at 4°C for 20 min and used immediately.

In-solution digestion of apoplastic fluids for proteome analysis

AFs (500 μl) from *N. benthamiana* were isolated from 16 leaf discs. Proteins were reduced by incubation with dithiothreitol (DTT, final concentration 5 mM) for 30 min at room temperature. Samples were then alkylated with iodoacetamide (IAA, final concentration 20 mM) for 30 min at room temperature. Then the AFs were chloroform-methanol precipitated, and the precipitated proteins were dissolved in 100 μl of 6 M urea. 500-μl water was added and protein digestion was performed by adding 400 ng trypsin/LysC mix (Promega, Madison, WI, USA). Sample was incubated at 37°C for 18 hours. The protein digestion was stopped by adding formic acid (FA, final 1% v/v), and peptides were purified using the sep-paK C18 columns (Waters, Elstree, UK).

Proteome analysis of apoplastic fluids

Sample clean-up for LC-MS

Trypsin and LysC digested samples were desalted on homemade C18 StageTips as described (*52*). On each two-disc StageTip, peptides (~15 μg) were loaded (based on the initial protein concentration). After elution from the StageTips, samples were dried using a vacuum concentrator (Eppendorf) and the peptides were taken up into 10 μl of 0.1% formic acid solution. Samples for the analysis endogenously digested peptides in the AF were generated by supplementing the AF with four volumes of MS-grade acetone, followed by incubation on ice for 1 hour and centrifugation at 18,000*g* for 15 min. Four-fifths of the supernatants were then transferred to fresh Eppendorf tubes and the acetone evaporated by vacuum centrifugation. The dried peptide samples were then dissolved in 0.1% formic acid and immediately analyzed without further clean-up.

LC-MS/MS

Experiments were performed on an Orbitrap Elite instrument [Thermo Fisher Scientific, Waltham, MA, USA (*53*)] that was coupled to an EASY-nLC 1000 liquid chromatography (LC) system (Thermo Fisher Scientific, Waltham, MA, USA). The LC was operated in the one-column mode. For full AF analysis, the analytical column was a fused silica capillary (75 μm by 25 cm) with an integrated PicoFrit emitter (New Objective) packed in-house with Reprosil-Pur 120 C18-AQ 3-μm resin (Dr. Maisch). For analysis of endogenously digested peptides from the AF, the analytical column had a length of 35 cm and the resin was Reprosil-Pur 120 C18-AQ 1.9-μm resin (Dr. Maisch). The analytical column was encased by a column oven (Sonation) and attached to a nanospray flex ion source (Thermo Fisher Scientific, Waltham, MA, USA). The column oven temperature was adjusted

to 45°C during data acquisition. The LC was equipped with two mobile phases: solvent A (0.1% formic acid, FA, in water) and solvent B (0.1% FA in acetonitrile, ACN). All solvents were of UHPLC (ultra-high-performance liquid chromatography) grade (Sigma-Aldrich, Saint Louis, MO, USA). Peptides were directly loaded onto the analytical column with a maximum flow rate that would not exceed the set pressure limit of 980 bar (usually around 0.5 to 0.8 μl/min). Peptides were subsequently separated on the analytical column by running a 70- or 140-min gradient of solvent A and solvent B [start with 7% B; gradient 7% to 35% B for 60 (or 120 min); gradient 35% to 100% B for 5 min (or 10 min) and 100% B for 5 min (or 10 min)] at a flow rate of 300 nl/min. The mass spectrometer was operated using Xcalibur software (version 2.2 SP1.48). The mass spectrometer was set in the positive ion mode. Precursor ion scanning was performed in the Orbitrap analyzer (FTMS; Fourier transform mass spectrometry) in the scan range of m/z = 350 to 1800 and at a resolution of 60,000 with the internal lock mass option turned on [lock mass was 445.120025 m/z, polysiloxane (*54*)]. Product ion spectra were recorded in a data dependent fashion in the ion trap (ITMS; ion trap mass spectrometry) in a variable scan range and at a rapid scan rate. The ionization potential (spray voltage) was set to 1.8 to 2.0 kV. Peptides were analyzed using a repeating cycle consisting of a full precursor ion scan (1.0×10^6 ions or 30 ms) followed by 10 product ion scans (1.0×10^4 ions or 50 ms) where peptides are isolated based on their intensity in the full survey scan (threshold of 500 counts) for tandem mass spectrum (MS2) generation that permits peptide sequencing and identification. CID (collision-induced dissociation) collision energy was set to 35% for the generation of MS2 spectra. During MS2 data acquisition, dynamic ion exclusion was set to 60 s with a maximum list of excluded ions consisting of 500 members and a repeat count of one. Ion injection time prediction, preview mode for the FTMS, monoisotopic precursor selection and charge state screening were enabled. Only charge states >1 were considered for fragmentation.

Peptide and protein identification using MaxQuant

RAW spectra were submitted to an Andromeda (*55*) search in MaxQuant (version 1.5.3.30). For the analysis of trypsin/LysC digested samples, we used the following settings (*56*): Label-free quantification and match-between-runs was activated (*57*). MS/MS spectra data were searched against the ACE_0319_Niben_Final.fasta [*N. benthamiana*, 42853 entries (*6*)] and Uniprot reference database UP000002515_223283.fasta (*Pseudomonas syringae* pv. *tomato* (strain ATCC BAA-871/DC3000), 5431 entries) databases. All searches included also a contaminants database (as implemented in MaxQuant, 267 sequences). The contaminants database contains known MS contaminants and was included to estimate the level of contamination. Andromeda searches allowed oxidation of methionine residues (16 Da), acetylation of protein N terminus (42 Da) as dynamic modification, and the static modification of cysteine (57 Da, alkylation with IAM). Enzyme specificity was set to "Trypsin/P" with two missed cleavages allowed. The instrument type in Andromeda searches was set to Orbitrap and the precursor mass tolerance was set to ±20 ppm (first search) and ±4.5 ppm (main search). The MS/MS match tolerance was set to ±0.5 Da. The peptide spectrum match FDR and the protein FDR were set to 0.01 (based on target-decoy approach). Minimum peptide length was seven amino acids. For protein quantification, unique and razor peptides were allowed. Modified peptides were allowed for quantification. The minimum score for modified peptides was 40.

For the analysis of endogenously digested peptides in the AF, we used the following settings: Label-free quantification and match-between-runs was activated (*57*). MS/MS spectra data were searched against the p19_vector_proteins.fasta (two entries) and ACE_0383_SOI_v02.fasta (containing the sequence of flagellin and BGAL1). As above, all searches included also a contaminants database (as implemented in MaxQuant, 267 sequences). Andromeda searches allowed oxidation of methionine residues (16 Da) and acetylation of protein N terminus (42 Da) as dynamic modification. Enzyme specificity was set to "unspecific." The instrument type in Andromeda searches was set to Orbitrap and the precursor mass tolerance was set to ±20 ppm (first search) and ±4.5 ppm (main search). The MS/MS match tolerance was set to ±0.5 Da. The peptide spectrum match FDR and the protein FDR were set to 0.01 (based on target-decoy approach). Minimum peptide length was 8 amino acids and the maximum length 25. For protein quantification, unique and razor peptides were allowed. Modified peptides were allowed for quantification. The minimum score for modified peptides was 40.

Data analysis

Initial data analysis and filtering and statistical evaluation was performed by using the PERSEUS computational platform [version 1.5.5.3 (*58*)]. For data generated from trypsin/LysC digested samples, we performed the following manipulations: Briefly, only protein groups with at least two identified unique peptides over all runs were considered for further analysis. Non–*N. benthamiana* proteins and hits to the decoy database were removed. For quantification, we combined related biological replicates into categorical groups and investigated only those proteins that were found in all samples. Comparison of protein group quantities (relative quantification) between different MS runs is based solely on the LFQ's as calculated by MaxQuant [MaxLFQ algorithm (*57*)]. For the statistics, each biological replicate was used for a pairwise comparison. The identified proteins were plotted by the mean of the sum of Log_2(LFQ intensity) of the mock and Δ*hQ* samples against the mean of ratio(mock/Δ*hQ*) of four biological replicates. For the analysis of data generated from endogenously digested AF samples, we analyzed the peptide.txt output from MaxQuant. Peptide intensities were loaded into PERSEUS grouped into categorical groups (no_bGal or bGal) based on their treatment and normalized by subtraction from median. Missing values were then imputed and the categorical groups compared by performing a Student's *t* test (FDR 0.05; S0 0.1; number of randomizations 250). The output was visualized as volcano plot (+BGAL1 versus –BGAL1), annotated in PERSEUS and edited in CorelDraw.

TE versus AF proteomics

A comparison of an in-solution–digested *N. benthamiana* apoplastic proteome (AF) versus a leaf total extract (TE) was deposited recently (*6*). Contaminants, reverse proteins, and those only identified by matching were removed, and majority protein groups found in three out of four biological replicates of either AF or TE were retained. Log_2(sum LFQ intensity AF + TE) is plotted over the distribution (sum LFQ intensity AF)/(sum LFQ intensity AF + sum LFQ intensity TE). A ratio closer to 1 indicates predominant identification in the leaf apoplastic proteome, whereas a ratio closer to 0 indicates predominant identification in the total extract proteome.

Glycosidase activity profiling

AFs (50 μl) were incubated in 50 mM MES pH 5.0 with and without 1 μM JJB70 in the dark for 1 hour at room temperature. The labeling reaction was stopped by adding gel-loading buffer [200 mM Tris-HCl (pH 6.8), 400 mM DTT, 8% SDS, 0.4% bromophenol blue, 40% glycerol] and heating at 90°C for 5 min. The labeled proteins were separated on 10% gels at 200 volts for 1 hour.

Convolution ABPP

Two different samples were prepared for convolution ABPP. For the "label-and-mix" sample, AFs isolated from *Pto*DC3000(Δ*hQ*) infected plant (1×10^6 CFU/ml, 2 dpi), and the mock control samples (from water infiltrated plant) were first labeled individually with JJB70 for 1 hour at pH 5.0. After stopping the labeling reaction by boiling in gel-loading buffer, the labeled proteomes were mixed together in equal volumes. For the "mix-and-label" sample, equal volumes of AFs isolated from the *Pto*DC3000(Δ*hQ*)-infected and the mock control samples were first mixed, preincubated for 30 min and then labeled with JJB70 for 1 hour at pH 5.0. The labeling reaction was stopped by adding gel-loading buffer and heating at 95°C.

Detection of JJB70-labeled proteins

The fluorescently labeled proteins were detected from protein gels using the Amersham Typhoon 5 Biomolecular Imager (GE Healthcare Life Sciences, Little Chalfont, UK) using Cy2 settings (488-nm excitation and 525PB20 filter). The fluorescence was quantified using ImageQuant (GE Healthcare Life Sciences, Little Chalfont, UK).

Multiplex fluorescence ABPP

JJB70, JJB383, and FP-Tamra probes were prepared as 50 μM, 100 μM, and 10 μM stock solutions, respectively, in dimethyl sulfoxide. Labeling

was performed as described previously (10, 59). For fluorescence gel imaging, the AFs were incubated with 1 μM, 2 μM, and 0.2 μM probes, respectively, for 1 hour at room temperature in the dark at a 25-μl total reaction volume. The labeling reactions were stopped by adding 4× gel-loading buffer [200 mM Tris-HCl (pH 6.8), 400 mM DTT, 8% SDS, 0.4% bromophenol blue, 40% glycerol] and heating at 90°C for 5 min. The labeled proteins were separated on 10% protein gels at 200 volts for 1 hour. The fluorescently JJB70, JJB383, and FP-Tamra-labeled proteins were detected from protein gels using the Amersham Typhoon-5 Biomolecular Imager (GE Healthcare Life Sciences, Little Chalfont, UK) using Cy2 settings (488-nm excitation and 525PB20 filter), Cy5 settings (633-nm excitation and 670PB filter), or Cy3 settings (532-nm excitation and 610PB filter), respectively.

β-galactosidase activity assays

AF samples from *N. benthamiana* leaves were incubated at 25°C with 0.2 μM fluorescein di-β-D-galactopyranoside (FDG) (Marker Gene Technologies, Eugene, OR, USA) and 50 mM MES buffer pH5.0 in the total reaction volume of 100 μl. The fluorescence of fluorescein, a product of FDG hydrolysis by β-galactosidase, was measured over time using an Infinite M200 plate reader (Tecan, Mannedorf, Switzerland) with an excitation wavelength of 485 nm and emission wavelength of 535 nm.

Colorimetric assay for glycoside hydolase activities

4-Nitrophenyl conjugates of β-D-galactopyranoside, α-D-galactopyranoside, β-D-mannopyranoside, β-D-glucopyranoside, α-D-glucopyranoside, β-D-glucuronide, β-D-xylopyranoside, α-D-xylopyranoside, β-D-fucopyranoside, *N*-acetyl-β-D-glucosaminide, *N*-acetyl-α-D-glucosaminide, *N*-acetyl-β-D-galactosaminide, and *N*-acetyl-α-D-galactosaminide (Sigma-Aldrich, Saint Louis, MO, USA) were prepared as 10 mM stock solutions in water. AFs from agroinfiltrated plants were incubated with 1 mM of each 4-nitrophenyl conjugate of monosaccharide buffered with 50 mM MES at pH 5 for 10 min at 21°C. The reactions were stopped by adding 1 M Na_2CO_3, and the released 4-nitrophenol was measured by monitoring absorbance at 420 nm using an Infinite M200 plate reader (Tecan, Mannedorf, Switzerland).

Fractionation apoplastic proteomes

AFs isolated from *Pto*DC3000(Δ*hQ*) infected leaves were concentrated using Vivaspin 500 spin columns with 3000-Da MWCO filter (Sartorius Stedim Biotech, Göttingen, Germany) by centrifuging at 10,000*g*, 4°C for 60 min. The concentrate (>3 kDa) and filtrate (<3 kDa) were normalized to equal starting volumes and used for mixing and labeling assays.

Metabolite extraction

*Pto*DC3000(Δ*hQ*) was inoculated at OD_{600} = 0.5 and grown in mannitol-glutamate minimal medium supplemented with iron (60). The overnight grown bacterial culture was centrifuged and supernatant was collected. Chloroform-methanol precipitation was performed by adding 4 ml of extraction buffer (1:2.5:1 of chloroform-methanol-water) to 4 ml of supernatant or only the medium as control. The sample was vortexed and centrifuged. The upper hydrophilic (methanol:water) phase and the lower hydrophobic (chloroform) phase were collected and lyophilized. The lyophilized samples were dissolved in water and concentrated using ultrafiltration spin columns to remove the <3 kDa low–molecular weight compounds. The filtrate fractions were collected and treated with and without heating at 95°C for 5 min.

Bacterial growth upon spray inoculation

For spray inoculations, an overnight culture was washed and resuspended in sterile water to a density of 1×10^8 CFU/ml and sprayed onto leaf abaxial and adaxial surfaces of 3-week-old plants. Before inoculation, eight plants per genotype were incubated at 80% humidity for 1 day. Upon inoculation, plants were kept for 3 to 4 days in a growth cabinet at 21°C. Three leaf discs (1-cm diameter) were excised from infected leaves and each leaf disc (3.2-mm diameter) was soaked in 15% H_2O_2 for 1 min to sterilize leaf surfaces. Leaf discs were washed twice in sterile water and ground in sterile water for 5 min using the tissuelyser and metal beads (Biospec Products, Bartelsville, OK, USA). Serial dilutions of the homogenate were plated onto KB agar plates without selection for *Pta*6605 strains or containing 50 μg/ml rifampicin for *Pto*DC3000 strains. Colonies were counted after 36 hours of incubation at 28°C. The *P* value was calculated using the two-tailed Student *t* test to compare bacterial growth between WT and *BGAL1* mutant plants.

Bacterial growth assay in vitro

Bacteria were harvested from an overnight preculture in LB medium, washed with sterile water, and inoculated in 150 μl of the specified medium with the initial OD_{600} of 0.05. Bacterial growth was then monitored with the measurement of OD_{600} over time using Infinite M200 plate reader (Tecan, Mannedorf, Switzerland) at 28°C with shaking.

Isolation of flagellin proteins

Flagellin proteins were purified following the previously described procedure (27).

Oxidative burst assays

The generation of ROS was measured by a luminol-based assay on leaf discs adapted from (61). Luminol (Sigma-Aldrich, Saint Louis, MO, USA) was dissolved in dimethyl sulfoxide at a concentration of 10 mg/ml, and kept in the dark. Horseradish peroxidase (HRP) (Thermo Fisher Scientific, Waltham, MA, USA) was dissolved in water at a concentration of 10 mg/ml. Leaf discs (6-mm diameter) were incubated overnight in water in a 96-well plate. Bacterial pellets of an overnight culture were washed with sterile water and resuspended to an OD_{600} of 0.005 and 0.05 for *Pto*DC3000 and *Pta*6605 stains in 5 ml AF from leaves of *N. benthamiana* plants transiently expressing the indicated proteins. After 1 hour of incubation at 21°C, bacteria were centrifuged and resuspended in 2.5 ml of assay solution (water with 25 ng/μl luminol and 25 ng/μl HRP). For assays with purified flagellin, 10 ng/μl of flagellin were incubated in AF (ratio 1:15) from *N. benthamiana* leaves transiently expressing the indicated proteins for 1 hour and 30 min at RT on a rotor. After incubation, 25 ng/μl luminol and 25 ng/μl HRP were added to the AF. Before measurement, the water was removed from the 96-well plate, and 100 μl of assay solution was added to the leaf discs. Chemiluminescence was recorded immediately using an Infinite M200 plate reader (Tecan, Mannedorf, Switzerland) every minute for 1 hour. Standard errors were calculated at each time point and for each treatment. Experiments were repeated at least twice.

For protease inhibition experiments, AFs were first incubated with 1× Protease Inhibitor Cocktail (Sigma) for 1 hour at room temperature. An overnight culture of *Pta*6605(Δ*fgt1*) was pelleted and resuspended in sterile water. Bacteria were added to the AF mixture to a final OD_{600} of 0.5. Alternatively, flg22 peptide was added to a final concentration of 100 nM. After a 1-hour incubation at RT, luminol and HRP were added to the solution to final concentrations of 30 ng/μl and 20 ng/μl, respectively. ROS generation was then measured as described above.

Flagellin modelling

The *Pst*DC3000 FliC protein sequence was modeled on 5wk6 [cryo-EM structure of *P. aeruginosa* flagellar filaments G420A (62)] using SWISS MODEL (63) and visualized using PyMol. The best template (homo-41-mer of *P. aeruginosa* flagellin, 56.38% sequence identity) was identified with HHblits (64) and the model was built using ProMod3 version 1.1.0. The model quality parameters were: QMQE = 0.75 and QMEAN = −3.34.

RT-PCR

RNA was extracted by the addition of five volumes of Trizol and one volume of chloroform to ground tissue. After brief incubation on ice, samples were separated by centrifugation and the upper aqueous phase retained. RNA was pelleted by the addition of isopropanol and centrifugation at 12,000*g*. The pellet was washed in 70% ethanol, air dried, and then resuspended in RNase-free water. cDNA synthesis was performed using the Superscript II kit (Invitrogen, Carlsbad, CA, USA). The resulting cDNA was diluted 10 times and used as a template for PCR using the Mango Taq kit (Bioline, London, UK) with the primers for BGAL1 (5′atgtgacgtatgatcaccgggg-3′ and 5′-agctttccccaccaacttca-3′) and GAPDH [5′-agctcaagggaattctcgatg-3′ and 5′-aaccttaaccatgtcatctccc-3′ (65)]. cDNA was amplified with a T_m of 53°C for 38 cycles.

Phylogenetic analysis

Arabidopsis and tomato GH35-domain containing proteins (PF01301) were retrieved from GenBank

(*Arabidopsis* RefSeq proteins and NCBI *Solanum lycopersicum* annotation release 103). *N. benthamiana* GH35-domain containing proteins were extracted from the reannotated gene-models (*6*) and manually verified against the draft genome of *N. benthamiana* (*66*). Partial sequences and putative non-protein-encoding pseudogenes were cross-validated against the other available draft genomes (*67*). For putative pseudogenes, the closest BLAST hit in other *Nicotiana* species was used to visualize pseudogenization in the phylogenetic tree. Sequences were aligned with Clustal Omega (*68*), and the amino acid residues corresponding to BGAL1 (Nbv0.3scaffold63813_1713-9438) position 26-732 [lacking the signal peptide and the Gal-Lectin domain (PF02140)] were extracted and realigned using Clustal Omega. The evolutionary history was inferred by using the maximum likelihood method based on the Le_Gascuel_2008 model (*69*). The tree with the highest log likelihood (−36048.75) is shown. The percentage of trees in which the associated taxa clustered together in 1000 bootstrap repetitions is shown next to the branches. Initial tree(s) for the heuristic search were obtained automatically by applying Neighbor-Join and BioNJ algorithms to a matrix of pairwise distances estimated using a JTT model, and then selecting the topology with superior log likelihood value. A discrete Gamma distribution was used to model evolutionary rate differences among sites [five categories (+G, parameter = 1.0633)]. The rate variation model allowed for some sites to be evolutionarily invariable ([+I], 5.50% sites). The tree is drawn to scale, with branch lengths measured in the number of substitutions per site. The analysis involved 72 amino acid sequences. Evolutionary analyses were conducted in MEGA X (*70*).

Statistics

All values shown are mean values, and the error intervals shown represent standard error of the mean (SE), unless otherwise indicated. *P* values were calculated using two-tailed Student's *t* test or Tukey HSD test, as indicated. All experiments have been reproduced, and representative datasets are shown.

REFERENCES AND NOTES

1. M. Lindeberg, Genome-enabled perspectives on the composition, evolution, and expression of virulence determinants in bacterial plant pathogens. *Annu. Rev. Phytopathol.* **50**, 111–132 (2012). doi: 10.1146/annurev-phyto-081211-173022; pmid: 22559066
2. T. Boller, G. Felix, A renaissance of elicitors: Perception of microbe-associated molecular patterns and danger signals by pattern-recognition receptors. *Annu. Rev. Plant Biol.* **60**, 379–406 (2009). doi: 10.1146/annurev.arplant.57.032905.105346; pmid: 19400727
3. D. Couto, C. Zipfel, Regulation of pattern recognition receptor signalling in plants. *Nat. Rev. Immunol.* **16**, 537–552 (2016). doi: 10.1038/nri.2016.77; pmid: 27477127
4. H. Cui, T. Xiang, J. M. Zhou, Plant immunity: A lesson from pathogenic bacterial effector proteins. *Cell. Microbiol.* **11**, 1453–1461 (2009). doi: 10.1111/j.1462-5822.2009.01359.x; pmid: 19622098
5. J. Fliegmann, G. Felix, Immunity: Flagellin seen from all sides. *Nat. Plants* **2**, 16136 (2016). doi: 10.1038/nplants.2016.136; pmid: 27595659
6. J. Kourelis, F. Kaschani, F. M. Grosse-Holz, F. Homma, M. Kaiser, R. A. L. van der Hoorn, Re-annotated *Nicotiana benthamiana* gene models for enhanced proteomics and reverse genetics. bioRxiv 373506 [Preprint]. 27 July 2018. doi: 10.1101/373506
7. F. Grosse-Holz *et al*., The transcriptome, extracellular proteome and active secretome of agroinfiltrated *Nicotiana benthamiana* uncover a large, diverse protease repertoire. *Plant Biotechnol. J.* **16**, 1068–1084 (2018). doi: 10.1111/pbi.12852; pmid: 29055088
8. C. F. Wei *et al*., A *Pseudomonas syringae* pv. tomato DC3000 mutant lacking the type III effector HopQ1-1 is able to cause disease in the model plant *Nicotiana benthamiana*. *Plant J.* **51**, 32–46 (2007). doi: 10.1111/j.1365-313X.2007.03126.x; pmid: 17559511
9. W. W. Kallemeijn *et al*., Novel activity-based probes for broad-spectrum profiling of retaining β-exoglucosidases in situ and in vivo. *Angew. Chem. Int. Ed.* **51**, 12529–12533 (2012). doi: 10.1002/anie.201207771; pmid: 23139194
10. B. Chandrasekar *et al*., Broad-range glycosidase activity profiling. *Mol. Cell. Proteomics* **13**, 2787–2800 (2014). doi: 10.1074/mcp.O114.041616; pmid: 25056938
11. B. Chandrasekar, T. N. Hong, R. A. L. van der Hoorn, Inhibitor discovery by convolution ABPP. *Methods Mol. Biol.* **1491**, 47–56 (2017). doi: 10.1007/978-1-4939-6439-0_4; pmid: 27778280
12. V. Nekrasov, B. Staskawicz, D. Weigel, J. D. Jones, S. Kamoun, Targeted mutagenesis in the model plant *Nicotiana benthamiana* using Cas9 RNA-guided endonuclease. *Nat. Biotechnol.* **31**, 691–693 (2013). doi: 10.1038/nbt.2655; pmid: 23929340
13. S. Ranf *et al*., A lectin S-domain receptor kinase mediates lipopolysaccharide sensing in Arabidopsis thaliana. *Nat. Immunol.* **16**, 426–433 (2015). doi: 10.1038/ni.3124; pmid: 25729922
14. A. Miya *et al*., CERK1, a LysM receptor kinase, is essential for chitin elicitor signaling in Arabidopsis. *Proc. Natl. Acad. Sci. U.S.A.* **104**, 19613–19618 (2007). doi: 10.1073/pnas.0705147104; pmid: 18042724
15. R. Willmann *et al*., Arabidopsis lysin-motif proteins LYM1 LYM3 CERK1 mediate bacterial peptidoglycan sensing and immunity to bacterial infection. *Proc. Natl. Acad. Sci. U.S.A.* **108**, 19824–19829 (2011). doi: 10.1073/pnas.1112862108; pmid: 22106285
16. L. Gómez-Gómez, T. Boller, FLS2: An LRR receptor-like kinase involved in the perception of the bacterial elicitor flagellin in Arabidopsis. *Mol. Cell* **5**, 1003–1011 (2000). doi: 10.1016/S1097-2765(00)80265-8; pmid: 10911994
17. C. Segonzac *et al*., Hierarchy and roles of pathogen-associated molecular pattern-induced responses in *Nicotiana benthamiana*. *Plant Physiol.* **156**, 687–699 (2011). doi: 10.1104/pp.110.171249; pmid: 21478366
18. B. H. Kvitko *et al*., Deletions in the repertoire of *Pseudomonas syringae* pv. *tomato* DC3000 type III secretion effector genes reveal functional overlap among effectors. *PLOS Pathog.* **5**, e1000388 (2009). doi: 10.1371/journal.ppat.1000388; pmid: 19381254
19. G. Felix, J. D. Duran, S. Volko, T. Boller, Plants have a sensitive perception system for the most conserved domain of bacterial flagellin. *Plant J.* **18**, 265–276 (1999). doi: 10.1046/j.1365-313X.1999.00265.x; pmid: 10377992
20. S. Robatzek *et al*., Molecular identification and characterization of the tomato flagellin receptor LeFLS2, an orthologue of Arabidopsis FLS2 exhibiting characteristically different perception specificities. *Plant Mol. Biol.* **64**, 539–547 (2007). doi: 10.1007/s11103-007-9173-8; pmid: 17530419
21. D. R. Hann, J. P. Rathjen, Early events in the pathogenicity of Pseudomonas syringae on Nicotiana benthamiana. *Plant J.* **49**, 607–618 (2007). doi: 10.1111/j.1365-313X.2006.02981.x; pmid: 17217460
22. R. Takai, A. Isogai, S. Takayama, F. S. Che, Analysis of flagellin perception mediated by flg22 receptor OsFLS2 in rice. *Mol. Plant Microbe Interact.* **21**, 1635–1642 (2008). doi: 10.1094/MPMI-21-12-1635; pmid: 18986259
23. Y. Rossez, E. B. Wolfson, A. Holmes, D. L. Gally, N. J. Holden, Bacterial flagella: Twist and stick, or dodge across the kingdoms. *PLOS Pathog.* **11**, e1004483 (2015). doi: 10.1371/journal.ppat.1004483; pmid: 25590430
24. K. Chiku *et al*., Comparative analysis of flagellin glycans among pathovars of phytopathogenic Pseudomonas syringae. *Carbohydr. Res.* **375**, 100–104 (2013). doi: 10.1016/j.carres.2013.04.018; pmid: 23694710
25. M. Yamamoto *et al*., Identification of genes involved in the glycosylation of modified viosamine of flagellins in Pseudomonas syringae by Mass Spectrometry. *Genes* **2**, 788–803 (2011). doi: 10.3390/genes2040788; pmid: 24710292
26. S. Lee, D. S. Yang, S. R. Uppalapati, L. W. Sumner, K. S. Mysore, Suppression of plant defense responses by extracellular metabolites from *Pseudomonas syringae* pv. *tabaci* in *Nicotiana benthamiana*. *BMC Plant Biol.* **13**, 65 (2013). doi: 10.1186/1471-2229-13-65; pmid: 23597256
27. F. Taguchi *et al*., Identification of glycosylation genes and glycosylated amino acids of flagellin in *Pseudomonas syringae* pv. *tabaci*. *Cell. Microbiol.* **8**, 923–938 (2006). doi: 10.1111/j.1462-5822.2005.00674.x; pmid: 16681835
28. L. C. Nguyen *et al*., Genetic analysis of genes involved in synthesis of modified 4-amino-4,6-dideoxyglucose in flagellin of *Pseudomonas syringae* pv. *tabaci*. *Mol. Genet. Genomics* **282**, 595–605 (2009). doi: 10.1007/s00438-009-0489-8; pmid: 19787374
29. B. A. Vinatzer *et al*., The type III effector repertoire of *Pseudomonas syringae* pv. *syringae* B728a and its role in survival and disease on host and non-host plants. *Mol. Microbiol.* **62**, 26–44 (2006). doi: 10.1111/j.1365-2958.2006.05350.x; pmid: 16942603
30. S. R. Hind *et al*., Tomato receptor FLAGELLIN-SENSING 3 binds flgII-28 and activates the plant immune system. *Nat. Plants* **2**, 16128 (2016). doi: 10.1038/nplants.2016.128; pmid: 27548463
31. Y. Katsuragi *et al*., CD2-1, the C-terminal region of flagellin, modulates the induction of immune repsonses in rice. *Mol. Plant Microbe Interact.* **28**, 648–658 (2015). doi: 10.1094/MPMI-11-14-0372-R; pmid: 25625819
32. F. Brunner *et al*., Pep-13, a plant defense-inducing pathogen-associated pattern from Phytophthora transglutaminases. *EMBO J.* **21**, 6681–6688 (2002). doi: 10.1093/emboj/cdf667; pmid: 12485989
33. S. Oome *et al*., Nep1-like proteins from three kingdoms of life act as a microbe-associated molecular pattern in Arabidopsis. *Proc. Natl. Acad. Sci. U.S.A.* **111**, 16955–16960 (2014). doi: 10.1073/pnas.1410031111; pmid: 25368167
34. C. Ottmann *et al*., A common toxin fold mediates microbial attack and plant defense. *Proc. Natl. Acad. Sci. U.S.A.* **106**, 10359–10364 (2009). doi: 10.1073/pnas.0902362106; pmid: 19520828
35. K. Reiss *et al*., Structural and phylogenetic analyses of the GP42 transglutaminase from *Phytophthora sojae* reveal an evolutionary relationship between oomycetes and marine Vibrio bacteria. *J. Biol. Chem.* **286**, 42585–42593 (2011). doi: 10.1074/jbc.M111.290544; pmid: 21994936
36. H. Böhm *et al*., A conserved peptide pattern from a widespread microbial virulence factor triggers pattern-induced immunity in Arabidopsis. *PLOS Pathog.* **10**, e1004491 (2014). doi: 10.1371/journal.ppat.1004491; pmid: 25375108
37. H. Hirai *et al*., Glycan moiety of flagellin in *Acidovorax avenae* K1 prevents the recognition by rice that causes the induction of immune responses. *Plant Signal. Behav.* **9**, e972782 (2014). doi: 10.4161/psb.29933; pmid: 25482815
38. F. Taguchi *et al*., Post-translational modification of flagellin determines the specificity of HR induction. *Plant Cell Physiol.* **44**, 342–349 (2003). doi: 10.1093/pcp/pcg042; pmid: 12668781
39. K. Takeuchi *et al*., Flagellin glycans from two pathovars of *Pseudomonas syringae* contain rhamnose in D and L configurations in different ratios and modified 4-amino-4,6-dideoxyglucose. *J. Bacteriol.* **189**, 6945–6956 (2007). doi: 10.1128/JB.00500-07; pmid: 17644592
40. S. K. Arora, A. N. Neely, B. Blair, S. Lory, R. Ramphal, Role of motility and flagellin glycosylation in the pathogenesis of *Pseudomonas aeruginosa* burn wound infections. *Infect. Immun.* **73**, 4395–4398 (2005). doi: 10.1128/IAI.73.7.4395-4398.2005; pmid: 15972536
41. A. Hanuszkiewicz *et al*., Identification of the flagellin glycosylation system in *Burkholderia cenocepacia* and the contribution of glycosylated flagellin to evasion of human innate immune responses. *J. Biol. Chem.* **289**, 19231–19244 (2014). doi: 10.1074/jbc.M114.562603; pmid: 24841205
42. C. Schäffer, P. Messner, Emerging facets of prokaryotic glycosylation. *FEMS Microbiol. Rev.* **41**, 49–91 (2017). doi: 10.1093/femsre/fuw036; pmid: 27566466
43. A. E. Scott *et al*., Flagellar glycosylation in *Burkholderia pseudomallei* and *Burkholderia thailandensis*. *J. Bacteriol.* **193**, 3577–3587 (2011). doi: 10.1128/JB.01385-10; pmid: 21602339
44. R. A. L. Van Der Hoorn, S. Rivas, B. B. Wulff, J. D. Jones, M. H. Joosten, Rapid migration in gel filtration of the Cf-4 and Cf-9 resistance proteins is an intrinsic property of Cf proteins and not because of their association with high-molecular-

weight proteins. *Plant J.* **35**, 305–315 (2003). doi: 10.1046/j.1365-313X.2003.01803.x; pmid: 12887582
45. Y. Liu, M. Schiff, R. Marathe, S. P. Dinesh-Kumar, Tobacco Rar1, EDS1 and *NPR1/NIM1* like genes are required for *N*-mediated resistance to tobacco mosaic virus. *Plant J.* **30**, 415–429 (2002). doi: 10.1046/j.1365-313X.2002.01297.x; pmid: 12028572
46. M. Stemmer, T. Thumberger, M. Del Sol Keyer, J. Wittbrodt, J. L. Mateo, CCTop: An intuitive, flexible and reliable CRISPR/Cas9 target prediction tool. *PLOS ONE* **10**, e0124633 (2015). doi: 10.1371/journal.pone.0124633; pmid: 25909470
47. J. G. Doench *et al*., Optimized sgRNA design to maximize activity and minimize off-target effects of CRISPR-Cas9. *Nat. Biotechnol.* **34**, 184–191 (2016). doi: 10.1038/nbt.3437; pmid: 26780180
48. E. Weber, C. Engler, R. Gruetzner, S. Werner, S. Marillonnet, A modular cloning system for standardized assembly of multigene constructs. *PLOS ONE* **6**, e16765 (2011). doi: 10.1371/journal.pone.0016765; pmid: 21364738
49. K. Belhaj, A. Chaparro-Garcia, S. Kamoun, V. Nekrasov, Plant genome editing made easy: Targeted mutagenesis in model and crop plants using the CRISPR/Cas system. *Plant Methods* **9**, 39 (2013). doi: 10.1186/1746-4811-9-39; pmid: 24112467
50. I. A. Sparkes, J. Runions, A. Kearns, C. Hawes, Rapid, transient expression of fluorescent fusion proteins in tobacco plants and generation of stably transformed plants. *Nat. Protoc.* **1**, 2019–2025 (2006). doi: 10.1038/nprot.2006.286; pmid: 17487191
51. F. Grosse-Holz *et al*., Three unrelated protease inhibitors enhance accumulation of pharmaceutical recombinant proteins in *Nicotiana benthamiana*. *Plant Biotechnol. J.* **16**, 1797–1810 (2018). doi: 10.1111/pbi.12916; pmid: 29509983
52. J. Rappsilber, M. Mann, Y. Ishihama, Protocol for micro-purification, enrichment, pre-fractionation and storage of peptides for proteomics using StageTips. *Nat. Protoc.* **2**, 1896–1906 (2007). doi: 10.1038/nprot.2007.261; pmid: 17703201
53. A. Michalski *et al*., Ultra high resolution linear ion trap Orbitrap mass spectrometer (Orbitrap Elite) facilitates top down LC MS/MS and versatile peptide fragmentation modes. *Mol. Cell. Proteomics* **11**, 013698 (2012). doi: 10.1074/mcp.O111.013698; pmid: 22159718
54. J. V. Olsen *et al*., Parts per million mass accuracy on an Orbitrap mass spectrometer via lock mass injection into a C-trap. *Mol. Cell. Proteomics* **4**, 2010–2021 (2005). doi: 10.1074/mcp.T500030-MCP200; pmid: 16249172
55. J. Cox *et al*., Andromeda: A peptide search engine integrated into the MaxQuant environment. *J. Proteome Res.* **10**, 1794–1805 (2011). doi: 10.1021/pr101065j; pmid: 21254760
56. J. Cox, M. Mann, MaxQuant enables high peptide identification rates, individualized p.p.b.-range mass accuracies and proteome-wide protein quantification. *Nat. Biotechnol.* **26**, 1367–1372 (2008). doi: 10.1038/nbt.1511; pmid: 19029910
57. J. Cox *et al*., Accurate proteome-wide label-free quantification by delayed normalization and maximal peptide ratio extraction, termed MaxLFQ. *Mol. Cell. Proteomics* **13**, 2513–2526 (2014). doi: 10.1074/mcp.M113.031591; pmid: 24942700
58. S. Tyanova *et al*., The Perseus computational platform for comprehensive analysis of (prote)omics data. *Nat. Methods* **13**, 731–740 (2016). doi: 10.1038/nmeth.3901; pmid: 27348712
59. A. M. Husaini *et al*., Multiplex fluorescent, activity-based protein profiling identifies active α-glycosidases and other hydrolases in plants. *Plant Physiol.* **177**, 24–37 (2018). pmid: 29555787
60. P. A. Bronstein *et al*., Global transcriptional responses of Pseudomonas syringae DC3000 to changes in iron bioavailability in vitro. *BMC Microbiol.* **8**, 209 (2008). doi: 10.1186/1471-2180-8-209; pmid: 19055731
61. J. M. Smith, A. Heese, Rapid bioassay to measure early reactive oxygen species production in Arabidopsis leave tissue in response to living *Pseudomonas syringae*. *Plant Methods* **10**, 6 (2014). doi: 10.1186/1746-4811-10-6; pmid: 24571722
62. F. Wang *et al*., A structural model of flagellar filament switching across multiple bacterial species. *Nat. Commun.* **8**, 960 (2017). doi: 10.1038/s41467-017-01075-5; pmid: 29038601
63. A. Waterhouse *et al*., SWISS-MODEL: Homology modelling of protein structures and complexes. *Nucleic Acids Res.* **46**, W296–W303 (2018). doi: 10.1093/nar/gky427; pmid: 29788355
64. M. Remmert, A. Biegert, A. Hauser, J. Söding, HHblits: Lightning-fast iterative protein sequence searching by HMM-HMM alignment. *Nat. Methods* **9**, 173–175 (2011). doi: 10.1038/nmeth.1818; pmid: 22198341
65. D. Liu *et al*., Validation of reference genes for gene expression studies in virus-infected *Nicotiana benthamiana* using quantitative real-time PCR. *PLOS ONE* **7**, e46451 (2012). doi: 10.1371/journal.pone.0046451; pmid: 23029521
66. A. Bombarely *et al*., A draft genome sequence of *Nicotiana benthamiana* to enhance molecular plant-microbe biology research. *Mol. Plant Microbe Interact.* **25**, 1523–1530 (2012). doi: 10.1094/MPMI-06-12-0148-TA; pmid: 22876960
67. F. Naim *et al*., Advanced engineering of lipid metabolism in *Nicotiana benthamiana* using a draft genome and the V2 viral silencing-suppressor protein. *PLOS ONE* **7**, e52717 (2012). doi: 10.1371/journal.pone.0052717; pmid: 23300750
68. F. Sievers *et al*., Fast, scalable generation of high-quality protein multiple sequence alignments using Clustal Omega. *Mol. Syst. Biol.* **7**, 539 (2011). doi: 10.1038/msb.2011.75; pmid: 21988835
69. S. Q. Le, O. Gascuel, An improved general amino acid replacement matrix. *Mol. Biol. Evol.* **25**, 1307–1320 (2008). doi: 10.1093/molbev/msn067; pmid: 18367465
70. S. Kumar, G. Stecher, M. Li, C. Knyaz, K. Tamura, MEGA X: Molecular evolutionary genetics analysis across computing platforms. *Mol. Biol. Evol.* **35**, 1547–1549 (2018). doi: 10.1093/molbev/msy096; pmid: 29722887
71. S. Gimenez-Ibanez *et al*., AvrPtoB targets the LysM receptor kinase CERK1 to promote bacterial virulence on plants. *Curr. Biol.* **19**, 423–429 (2009). doi: 10.1016/j.cub.2009.01.054; pmid: 19249211
72. A. Heese *et al*., The receptor-like kinase SERK3/BAK1 is a central regulator of innate immunity in plants. *Proc. Natl. Acad. Sci. U.S.A.* **104**, 12217–12222 (2007). doi: 10.1073/pnas.0705306104; pmid: 17626179
73. M. Gao *et al*., Regulation of cell death and innate immunity by two receptor-like kinases in Arabidopsis. *Cell Host Microbe* **6**, 34–44 (2009). doi: 10.1016/j.chom.2009.05.019; pmid: 19616764
74. C. Zipfel *et al*., Bacterial disease resistance in Arabidopsis through flagellin perception. *Nature* **428**, 764–767 (2004). doi: 10.1038/nature02485; pmid: 15085136
75. C. Waite, J. Schumacher, M. Jovanovic, M. Bennett, M. Buck, Negative autogenous control of the master type III secretion system regulator hrpL in *Pseudomonas syringae*. *mBio* **8**, e02273-16 (2017). doi: 10.1128/mBio.02273-16; pmid: 28119474
76. W. Wei *et al*., The gene coding for the Hrp pilus structural protein is required for type III secretion of Hrp and Avr proteins in *Pseudomonas syringae* pv. *tomato*. *Proc. Natl. Acad. Sci. U.S.A.* **97**, 2247–2252 (2000). doi: 10.1073/pnas.040570097; pmid: 10681465
77. R. Shimizu *et al*., The DeltafliD mutant of *Pseudomonas syringae* pv. *tabaci*, which secretes flagellin monomers, induces a strong hypersensitive reaction (HR) in non-host tomato cells. *Mol. Genet. Genomics* **269**, 21–30 (2003). pmid: 12715150
78. H. Feil *et al*., Comparison of the complete genome sequences of *Pseudomonas syringae* pv. *syringae* B728a and pv. *tomato* DC3000. *Proc. Natl. Acad. Sci. U.S.A.* **102**, 11064–11069 (2005). doi: 10.1073/pnas.0504930102; pmid: 16043691

ACKNOWLEDGMENTS

We thank M. Joosten and A. Gust for providing seeds of *Arabidopsis* mutants; H. Overkleeft for providing glycosidase probes; I. Somssich for providing flg22; C. Zipfel for helpful strategic suggestions and providing *fls2c* seeds; A. Collmer for providing *Pto*DC3000 mutants; U. Pyzio for plant care; J. Baker for photography; J. Jones, S. Kamoun, and S. Marillonnet for providing plasmids via AddGene; and R. Tóth and D. Sueldo for critically reading the manuscript. **Funding:** This work was supported by ERC Consolidator grant 616449 "GreenProteases" (to P.B., K.M., R.A.L.v.d.H.), BBSRC grant BB/R017913/1 (to P.B., R.A.L.v.d.H.), a Royal Thai Government Scholarship (to N.S.), the Clarendon Foundation (to J.K.), and the Oxford Interdisciplinary Bioscience DTP (BB/M011224/1 to N.S., E.L.T., G.M.P.). **Author contributions:** P.B., B.C., N.S., G.M.P., and R.A.L.v.d.H. conceived of the project; P.B., B.C., N.S., E.L.T., and K.M. performed experiments; J.K. performed bioinformatic analysis; F.K. and M.K. performed proteomic analysis; Y.I. provided materials; and R.A.L.v.d.H. wrote the manuscript with input from all authors. **Competing interests:** The authors declare no competing interests. **Data and materials availability:** All data are available in the manuscript, supplementary materials, and cited references. The proteomics data have been deposited to the ProteomeXchange Consortium via the PRIDE partner repository (www.ebi.ac.uk/pride/archive/) with dataset identifiers PXD010461 and PXD011823.

SUPPLEMENTARY MATERIALS

www.sciencemag.org/content/364/6436/eaav0748/suppl/DC1
Figs. S1 to S18
Reference (*79*)

13 August 2018; accepted 12 February 2019
10.1126/science.aav0748

RESEARCH ARTICLE SUMMARY

NEUROSCIENCE

Ultrapotent chemogenetics for research and potential clinical applications

Christopher J. Magnus*, Peter H. Lee*, Jordi Bonaventura, Roland Zemla, Juan L. Gomez, Melissa H. Ramirez, Xing Hu, Adriana Galvan, Jayeeta Basu, Michael Michaelides, Scott M. Sternson†

INTRODUCTION: Localized control of neuron activity is important for both brain research and therapy. Chemogenetics is a method to control cellular activity by targeting defined cell populations with an exogenous receptor that is engineered to respond selectively to a small-molecule agonist. The approach is generalizable because a receptor-agonist combination can be used to activate or inhibit different neural populations in any brain region. Moreover, using agonists that are selective for the chemogenetic receptor allows cell type–specific modulation, in contrast to traditional pharmacology. Chemogenetic tools have achieved widespread utility in animal models, and there is growing interest in developing chemogenetic systems that are suitable for human therapeutic applications.

RATIONALE: Optimally, a chemogenetic system should have several characteristics for use in the nervous system: (i) The introduced receptor should be activated by low agonist doses; (ii) human use would be facilitated by a chemogenetic agonist that is already a safe and well-tolerated clinically approved drug that crosses the blood-brain barrier, whereas for research applications the agonist should be highly selective for the chemogenetic receptor over endogenous targets; (iii) chemogenetic receptors should be inert in the absence of the drug, lacking constitutive activity or responsiveness to endogenous ligands; (iv) the receptors should activate or inhibit neurons efficaciously, durably, and reversibly; and (v) the site and level of expression of the chemogenetic receptor should be measurable noninvasively. Existing chemogenetic systems did not fulfill all these criteria.

RESULTS: We identified mutations of the ligand-binding domain of the α7 nicotinic acetylcholine receptor that conferred potent activity to the FDA-approved smoking cessation drug varenicline. We created chimeric ligand-gated ion channels by combining these modified ligand-binding domains with ion pore domains from either the glycine receptor or the serotonin 3 receptor, which conduct chloride or cations, respectively. These two types of chemogenetic channels inhibit or activate neurons upon binding varenicline at concentrations below those used clinically to treat nicotine addiction. Varenicline is especially attractive for potential therapeutic applications because it shows limited metabolism, durable pharmacokinetics, and high oral and brain bioavailability. Chemogenetic inhibition or activation was sustained for at least 2 to 3 weeks of continual exposure to varenicline, indicating suitability for chronic use. Expression of the chemogenetic ion channels was visualized in animals by positron emission tomography, enabling noninvasive measurement of the expression and anatomic site of chemogenetic receptors. We showed robust responses to chemogenetic silencing of neurons using low doses of varenicline in mice and one monkey. Finally, we synthesized brain-penetrant analogs of varenicline with subnanomolar potency and with greatly enhanced selectivity for the chemogenetic receptors that were effective for modulation of neural activity in mice.

CONCLUSION: We developed a toolbox of modular ion channels and selective, ultrapotent agonists that can be used for targeted control of brain activity in rodent and primate models. Additional studies will be needed to establish long-term safety and efficacy with chemogenetic receptors for therapeutic applications, but this is facilitated by using varenicline. These chemogenetic technologies can advance research into neural circuit disorders while enabling extension to human therapies. ■

ON OUR WEBSITE

Read the full article at http://dx.doi.org/10.1126/science.aav5282

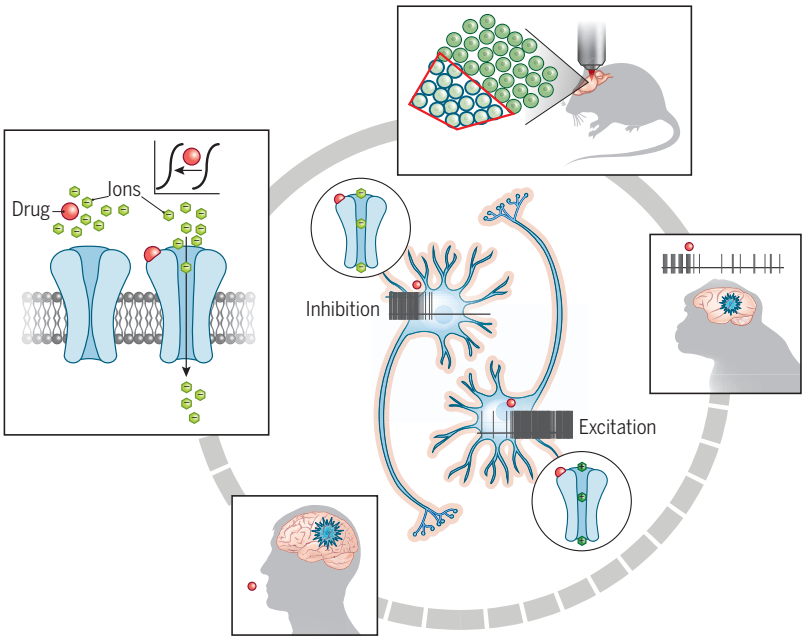

Chemogenetics for mice, monkeys, and potential therapy in humans. Modular ion channels were engineered to be activated by ultrapotent agonists, which selectively inhibit or excite activity in neurons expressing the chemogenetic receptors (blue). Neuron modulation was characterized by calcium imaging, electrophysiology, and behavior in mice and a monkey. These chemogenetic receptors and their FDA-approved agonists may facilitate translation of chemogenetics to therapies for human neurological diseases.

The list of author affiliations is available in the full article online.
*These authors contributed equally to this work.
†Corresponding author. Email: sternsons@janelia.hhmi.org
Cite this article as C. J. Magnus *et al.*, *Science* 364, eaav5282 (2019). DOI: 10.1126/science.aav5282

RESEARCH ARTICLE

NEUROSCIENCE

Ultrapotent chemogenetics for research and potential clinical applications

Christopher J. Magnus[1]*, Peter H. Lee[1]*, Jordi Bonaventura[2], Roland Zemla[3,4], Juan L. Gomez[2], Melissa H. Ramirez[1], Xing Hu[5], Adriana Galvan[5], Jayeeta Basu[3,6], Michael Michaelides[2,7], Scott M. Sternson[1]†

Chemogenetics enables noninvasive chemical control over cell populations in behaving animals. However, existing small-molecule agonists show insufficient potency or selectivity. There is also a need for chemogenetic systems compatible with both research and human therapeutic applications. We developed a new ion channel–based platform for cell activation and silencing that is controlled by low doses of the smoking cessation drug varenicline. We then synthesized subnanomolar-potency agonists, called uPSEMs, with high selectivity for the chemogenetic receptors. uPSEMs and their receptors were characterized in brains of mice and a rhesus monkey by in vivo electrophysiology, calcium imaging, positron emission tomography, behavioral efficacy testing, and receptor counterscreening. This platform of receptors and selective ultrapotent agonists enables potential research and clinical applications of chemogenetics.

Chemogenetics (*1*) targets an exogenous receptor to a specific cell population to control cellular activity only when engaged by a selective agonist. The approach is generalizable because the same receptor and agonist combination is used for different cell types. Chemogenetic tools have widespread utility in animal models (*2*) and for therapeutic applications (*3*, *4*). However, there are fundamental shortcomings of the small-molecule agonists for research purposes (*5*–*7*). Moreover, human therapies would be facilitated by chemogenetic receptors that are potently activated by existing clinically approved drugs.

Chemogenetic systems (table S1) based on engineered G protein–coupled receptors (GPCRs) called DREADDs have been used with the agonist clozapine-*N*-oxide (CNO) (*8*, *9*), but CNO is a substrate for the P-glycoprotein efflux pump (PgP) and is metabolically converted to clozapine, which is the active agent in the brain (*5*, *6*, *10*). Clozapine binds with high affinity to many receptors and has side effects such as behavioral inhibition (*7*) and potentially fatal agranulocytosis (*11*). Chemogenetic GPCR tools often rely on GPCR overexpression (*12*) to achieve high-potency responses, and effects on cell electrical activity are variable as a result of indirect coupling to ion channels. Engineered ligand-gated ion channels (LGICs) enable direct control over cellular activity by a small molecule. However, despite decades of development, chemogenetic tools have been hindered by limitations of the small-molecule agonists.

Pharmacologically selective actuator modules (PSAMs) are a modular chemogenetic platform based on modified α7 nicotinic acetylcholine receptor (nAChR) ligand-binding domains that are engineered to selectively interact with brain-penetrating synthetic agonists called pharmacologically selective effector molecules (PSEMs). PSAMs can be combined with various ion pore domains (IPDs) from different ion channels, such as serotonin receptor 3 (5HT3) or glycine receptor (GlyR), to produce chimeric LGICs with common pharmacology but distinct functional properties (Fig. 1A). PSAM-5HT3 chimeric channels are cation-selective and PSAM-GlyR channels are chloride-selective, leading to neuron activation or silencing, respectively, in response to PSEM agonists (Fig. 1A) (*13*). Engineered chimeric channels have been used to investigate the involvement of specific neuron populations in multiple functions (*2*). The primary limitations of PSEMs are short clearance times (30 to 60 min) and low-micromolar potency (*13*), which are not ideal for in vivo applications. In addition, the sensitivity of PSAMs to clinically approved drugs is unknown. We combined structure-guided ion channel engineering with synthetic chemistry and testing by in vivo imaging, electrophysiology, and behavioral perturbation to develop an ultrapotent chemogenetic system for research and potential clinical applications.

Engineering channel sensitivity to clinically used drugs

We examined 44 clinically used drugs with chemical similarity to nicotinic receptor agonists in a membrane potential screen against a panel of 41 chimeric channels with mutant α7 nAChR ligand-binding domains spliced onto the 5HT3 IPD (α7-5HT3) (*13*) (Fig. 1B). The membrane potential assay yields dose responses that reflect sustained channel activation, which is most relevant for chemogenetic applications (fig. S1) (*13*).

The anti-emetic drug granisetron (Fig. 1C), which has no agonist activity at α7 nAChR, activated $\alpha7^{W77F}$-5HT3 [membrane potential median effective concentration ($EC50_{MP}$) = 1.2 μM] and $\alpha7^{W77Y}$-5HT3 ($EC50_{MP}$ = 1.1 μM) as well as the $\alpha7^{W77F}$-GlyR chloride-selective chimeric channel ($EC50_{MP}$ = 0.60 ± 0.07 μM; mean ± SEM) (Fig. 1D). Thus, Trp^{77} in the ligand-binding domain controls off-target selectivity of granisetron at α7 nAChR.

Another anti-emetic drug, tropisetron, and the smoking cessation drug varenicline activated many of the mutant channels (Fig. 1, B and C, and fig. S2, A and B), consistent with the established α7 nAChR agonist activity of these molecules (*14*, *15*). Mutation at Gln^{79} → Gly (Q79G) enhanced the activity of tropisetron by a factor of 4 ($EC50_{MP}$ = 38 ± 3 nM) (Fig. 1E) as well as the potency of additional α7 nAChR agonists (fig. S2). Varenicline agonist activity was slightly improved relative to α7-5HT3 with mutations at Gln^{79} → Ser ($EC50_{MP}$ = 470 ± 70 nM) or Gln^{139} → Leu ($EC50_{MP}$ = 300 nM) (fig. S2B).

Ultrapotent chemogenetic receptor for varenicline

Varenicline is an especially attractive molecule for chemogenetic applications in the central nervous system because (i) it is well-tolerated by patients at low doses (*16*, *17*), (ii) it has excellent brain penetrance (*18*), (iii) it is not a PgP substrate (*19*), (iv) it has low binding to plasma proteins, and (v) it has long-lived pharmacology in monkeys and humans (half-life $t_{1/2}$ >17 hours) and acceptable half-life in mice and rats ($t_{1/2}$ = 1.4 hours and 4 hours, respectively) (*20*). Anti-smoking activity is reportedly due to α4β2 nAChR partial agonism, but varenicline has off-target agonist activity at 5HT3-R (*21*) and at α7 nAChR (*15*), and it is the latter activity that we exploited for chemogenetic applications. Comparison of crystal structures of ACh-binding proteins complexed with varenicline or tropisetron showed distinct binding poses of the two molecules (Fig. 2A) (*22*, *23*). The tropisetron indole substituent is positioned at the binding pocket entrance, near Gln^{79}, consistent with the potency-enhancing effect of mutating Gln^{79} to smaller amino acid residues for tropisetron and other tropane and quinuclidine α7 nAChR agonists (fig. S2, C and D). In contrast, varenicline binds in an orientation

[1]Janelia Research Campus, Howard Hughes Medical Institute, Ashburn, VA 20147, USA. [2]Biobehavioral Imaging and Molecular Neuropsychopharmacology Unit, National Institute on Drug Abuse Intramural Research Program, Baltimore, MD 21224, USA. [3]Neuroscience Institute, New York University, New York, NY 10016, USA. [4]Medical Scientist Training Program, New York University School of Medicine, New York, NY 10016, USA. [5]Yerkes National Primate Research Center and Department of Neurology, Emory University, Atlanta, GA 30329, USA. [6]Department of Neuroscience and Physiology, New York University Langone Medical Center, New York, NY 10016, USA. [7]Department of Psychiatry & Behavioral Sciences, Johns Hopkins University School of Medicine, Baltimore, MD 21205, USA.
*These authors contributed equally to this work.
†Corresponding author. Email: sternsons@janelia.hhmi.org

that directs its quinoxaline ring system toward the interior of the ligand-binding domain, near Val^{106}, which is equivalent to amino acid Leu^{131} in the α7 nAChR ligand-binding domain (Fig. 2A), and this binding pose may explain the limited potency enhancement of varenicline observed for our initial panel of 41 mutant channels (fig. S2B). This amino acid residue had not been investigated previously, so we examined the influence of mutations at Leu^{131} on agonist potency.

Replacement of Leu^{131} with smaller amino acid residues markedly increased the potency of varenicline, tropisetron, and several other synthetic agonists while reducing the potency of the canonical agonists ACh and nicotine (Fig. 2B and fig. S3A). $\alpha7^{L131G}$-GlyR showed a factor of 17 potency enhancement for varenicline ($EC50_{MP}$ = 37 ± 26 nM) but only a factor of 3 improvement for tropisetron (Fig. 2B), which is consistent with their orthogonal binding orientations (Fig. 2A). On the basis of secondary screening results (fig. S2B), we combined additional mutations with Leu^{131} → Gly to further improve varenicline potency. In most cases, better varenicline potency was accompanied by an unwanted increase in ACh sensitivity (fig. S3, B and C). Nonetheless, for varenicline but not for tropisetron, some combinations were selective for agonist type: Gln^{139} → Leu and Tyr^{217} → Phe reduced ACh potency and enhanced varenicline potency (fig. S3D). The triple mutant $\alpha7^{L131G,Q139L,Y217F}$-GlyR markedly improved varenicline potency ($EC50_{MP}$ = 1.6 ± 0.1 nM), which is more potent than at the parent α7-GlyR channel by a factor of 390 (Fig. 2C). Competition binding by displacement of the selective α7 nAChR antagonist [^{3}H]-ASEM (*24*) with varenicline showed inhibitory binding constant K_i = 1.3 ± 0.4 nM at $\alpha7^{L131G,Q139L,Y217F}$-GlyR (fig. S4A), which is lower than the reported K_i of varenicline at α7 nAChR by a factor of 475 (*25*). In electrophysiological recordings from human embryonic kidney (HEK)–293 cells expressing $\alpha7^{L131G,Q139L,Y217F}$-GlyR, varenicline was a strong agonist (fig. S4, B and C, I_{VAR}/I_{ACh} = 1.9 ± 0.2, n = 13) that produced a slowly activating response, with a sustained window current balancing channel activation and inactivation, as well as a slow ligand off-rate due to the high-affinity interaction (Fig. 2D and fig. S4D). Similar response properties were also observed in an immune cell line (fig. S4, E and F), demonstrating that channel function is comparable in another cell type. The agonist selectivity of varenicline at $\alpha7^{L131G,Q139L,Y217F}$-GlyR over the drug's clinical target, α4β2 nAChR, was greater by a factor of 160 (fig. S4G), and it was more potent than at 5HT3-R by a factor of 880 (fig. S4H), indicating a good window for selective chemogenetic agonism with this drug.

The ACh potency of the $\alpha7^{L131G,Q139L,Y217F}$-GlyR chimeric channel was also reduced by a factor of 13 ($EC50_{MP}$ = 83 ± 20 μM), which is higher than basal mouse brain ACh levels (0.9 nM) by nearly five orders of magnitude (*26*). This is higher than measurements of transient ACh rises in the brain, which reach 1 to 2 μM (*27*) and do not activate the channel (fig. S4, I and J). The remarkably slow activation of α7-GlyR chimeric channels (*28*) (fig. S4I) serves as a temporal filter for fast ACh transients. Choline responsiveness was also low ($EC50_{MP}$ = 128 ± 32 μM) (fig. S4, K to M), requiring concentrations substantially higher than brain or circulating plasma levels (0.54 to 7.8 μM) (*29*, *30*).

The agonist potency of $\alpha7^{L131G,Q139L,Y217F}$-GlyR was enhanced for only a subset of α7 nAChR agonists but was reduced for others (Fig. 2B), indicating that the ligand-binding domain modifications are selective for particular chemical structures, instead of displaying a nonspecific reduction in channel activation energy. Blocking $\alpha7^{L131G,Q139L,Y217F}$-GlyR with the noncompetitive ion pore antagonist picrotoxin (PTX) did not affect the voltage clamp holding current (fig. S5A), demonstrating the absence of ligand-independent leak conductance (fig. S5B). This contrasts with other channel variants that we made based on different designs that showed enhanced potency but also constitutive conductance (fig. S6). In addition, $\alpha7^{L131G,Q139L,Y217F}$-GlyR did not respond to glycine, nor did it inhibit endogenous glycine-gated GlyR currents (fig. S5, C to E). Because of its high potency, selectivity, and lack of constitutive activity, the $\alpha7^{L131G,Q139L,Y217F}$ ligand-binding domain was selected as a chemogenetic tool that is activated by varenicline and is named PSAM[4].

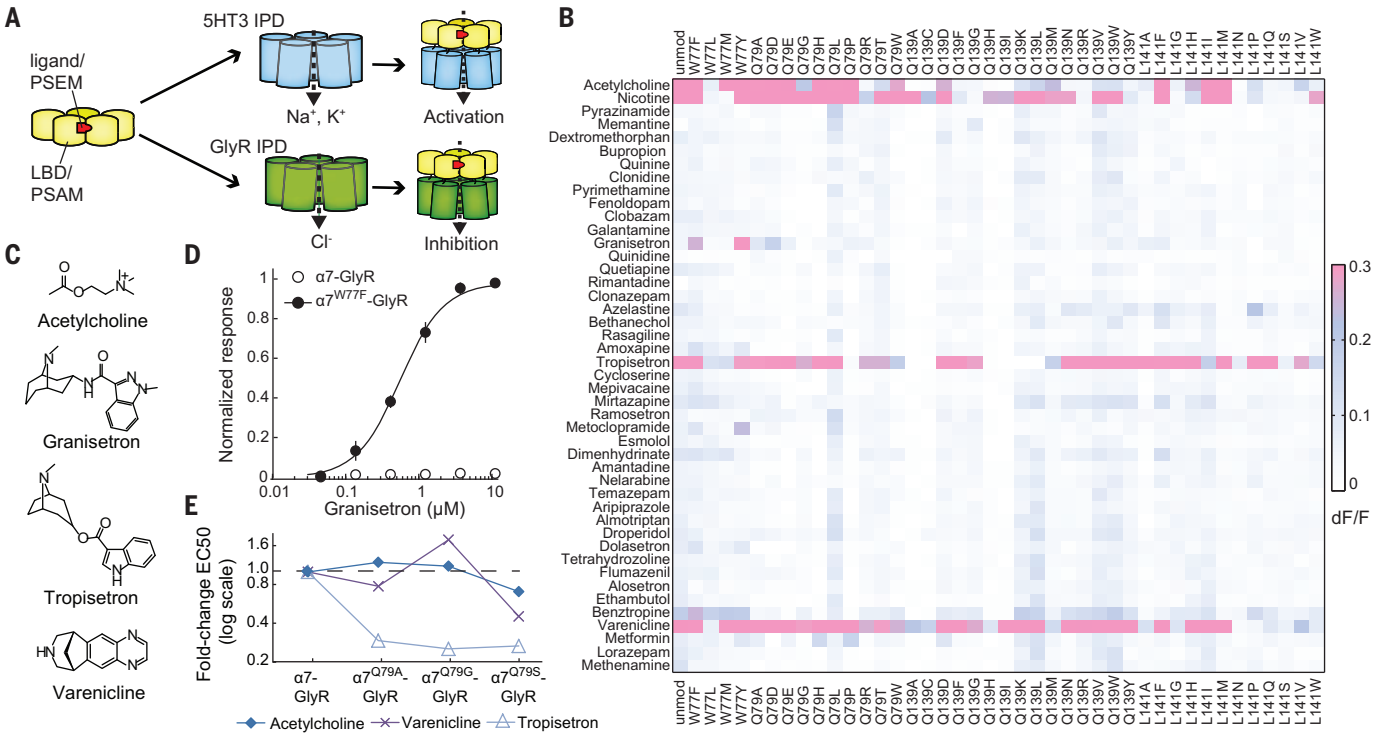

Fig. 1. Screen of mutant α7 nAChR ligand-binding domain ion channel activity against clinically used drugs. (**A**) Schematic of modular PSAM-IPD chimeric channels for cell activation and inhibition. (**B**) Screen of 41 α7-5HT3 channels with mutant ligand-binding domains against 44 clinically used drugs. (**C**) Key molecules. (**D**) Granisetron sensitivity conferred by Trp^{77} → Phe (W77F) mutation. (**E**) Tropisetron potency improved by Gln^{79} (Q79) mutations.

Neuron silencing and activation ex vivo

To test PSAM^4-GlyR as a neuronal silencer, we used in utero electroporation in mice to coexpress the chemogenetic channel and enhanced green fluorescent protein (EGFP) in layer 2/3 cortical neurons (Fig. 2E). PSAM^4-GlyR–expressing neuron properties in acute brain slices were similar to those of nearby untransfected control cells (fig. S4M). Varenicline (10 to 16 nM) strongly suppressed firing (Fig. 2F) as a result of electrical shunting that, on average, reduced the input resistance by a factor of 3 (Fig. 2G) and increased the current amplitude required to fire an action potential by a factor of 6 (rheobase) (Fig. 2H), with multiple neurons not firing even with 500 pA depolarizing current. Silencing was reversible upon ligand washout, although not all cells fully recovered during the recording because of the slow off-rate of varenicline from PSAM^4-GlyR (Fig. 2D). We examined the durability of continuous silencing in cultured hippocampal neurons expressing PSAM^4-GlyR under constant exposure to 15 nM varenicline for 3 to 18 days, which maintained elevated rheobase that reversed on washout and could be resilenced by reapplication of varenicline (fig. S5, F to I). These low concentrations of varenicline for silencing are less than the estimated range of steady-state brain concentrations of varenicline in humans from a twice-daily 1-mg dose by a factor of 2 to 13 (*18*). This raises the possibility that varenicline can be used for chemogenetic applications at doses below those that are effective for anti-nicotine therapy.

For chemogenetic activation, we generated PSAM^4-5HT3 (*13*), which has the cation-selective conductance properties of the 5HT3 receptor. Varenicline was a partial agonist (fig. S7, A and B, I_{VAR}/I_{ACh} = 0.17 ± 0.08) that activated long-lasting currents (Fig. 2I) with high potency ($EC50_{MP}$ = 4 ± 2 nM; Fig. 2I and fig. S7C) and slow off-rates ($t\text{-off}_{1/2}$ = 3.2 ± 1.3 min). In contrast, the endogenous ligands ACh and choline had low potencies at PSAM^4-5HT3 (fig. S7, D and E). This ion channel–ligand combination can be used to gate a constant depolarizing current in cells. Sustained depolarization of cultured hippocampal neurons by PSAM^4-5HT3 was durable for at least 14 to 22 days of continuous varenicline (15 nM) exposure (fig. S7, F and G). We also made a high-conductance channel variant, PSAM^4-5HT3 HC (*13*), and layer 2/3 cortical neurons expressing the channel (Fig. 2J) showed membrane properties similar to those of intermingled nontransfected neurons (fig. S7H). Varenicline depolarized PSAM^4-5HT3 HC–expressing cells (+17.2 ± 2.4 mV) (Fig. 2K) and led to action potential firing (Fig. 2L).

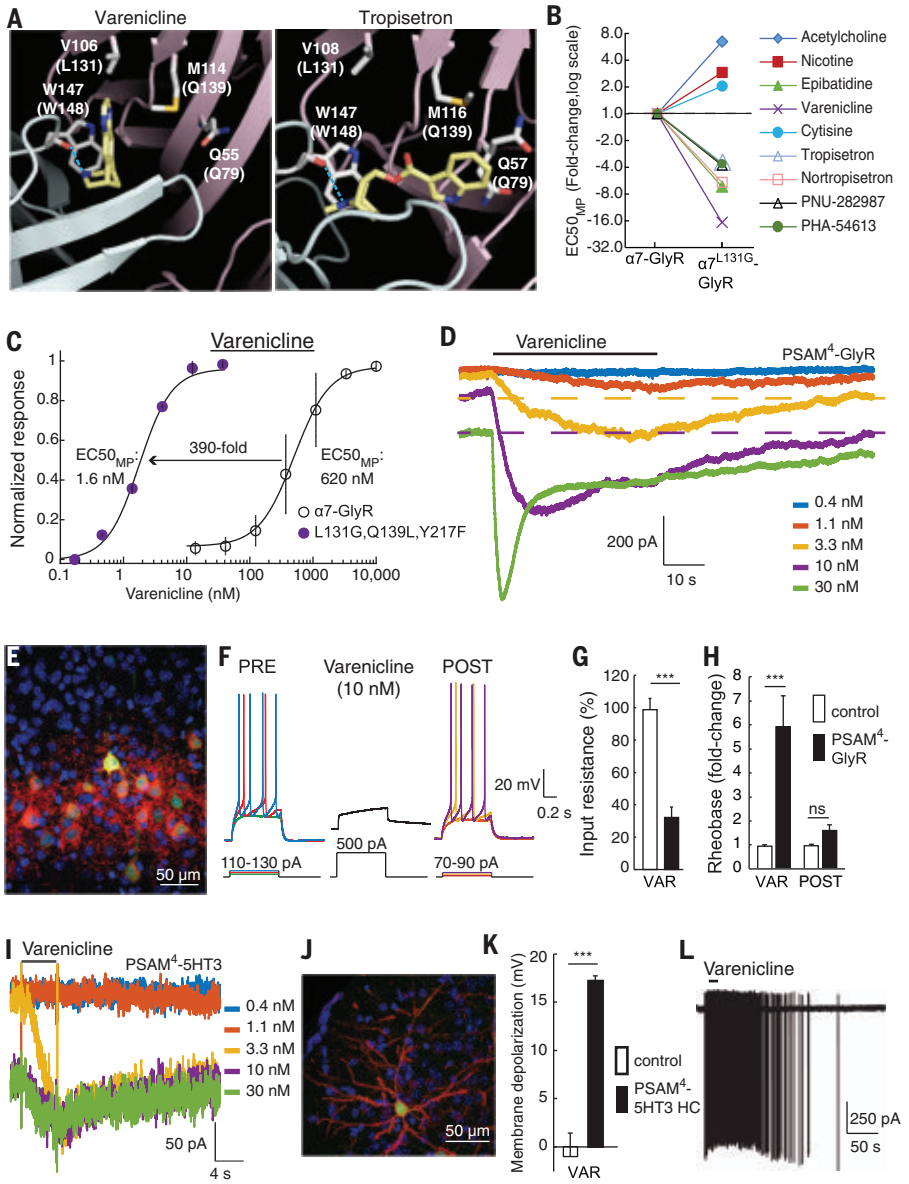

Fig. 2. Development of an ultrapotent PSAM for varenicline. (**A**) Varenicline (left) and tropisetron (right) bind ACh-binding proteins in distinct orientations. Dashed line denotes H bond with Trp^{147}; homologous α7 nAChR pre-protein numbering is in parentheses. L, Leu; M, Met; Q, Gln; V, Val; W, Trp. (**B**) Leu^{131} → Gly oppositely affects potency for varenicline, ACh, and other α7 nAChR agonists. (**C**) Potency enhancement of varenicline for α7^{L131G,Q139L,Y217F}-GlyR. (**D**) Varenicline whole-cell voltage clamp response at α7^{L131G,Q139L,Y217F}-GlyR. Baseline shifts reflect slow washout (dashed lines). (**E**) Cortical layer 2/3 neurons expressing EGFP and PSAM^4-GlyR with nonpermeabilized cell surface labeling by α-bungarotoxin–Alexa594 (αBgt-594). (**F** to **H**) Action potential firing was strongly suppressed by varenicline in neurons expressing PSAM^4-GlyR (F) as a result of reduced input resistance (G) and elevated rheobase (H). (**I**) Varenicline binding to PSAM^4-5HT3 elicits a weakly desensitizing current with high potency. Baseline shifts reflect slow washout. (**J**) αBgt-594 labeling of PSAM^4-5HT3 HC (red) on cell surface of a cortical layer 2/3 neuron coexpressing EGFP. (**K** and **L**) Varenicline (15 nM) depolarizes (K) and elicits action potentials (L) in neurons expressing PSAM^4-5HT3 HC. Error bars are SEM. ***P < 0.001 (Mann-Whitney U test); n.s., not significant (P > 0.05).

Chemogenetic silencing in mice and monkey

In vivo chemogenetic efficacy was tested with PSAM^4-GlyR in mice by targeting *Slc32a1* (*vesicular GABA transporter*)-expressing GABAergic neurons in the substantia nigra reticulata (SNr) (Fig. 3A). Unilateral silencing of SNr neurons by intracranial microinjection of the GABA receptor agonist muscimol results in rotation contraversive to the inhibited side (*31*). For chemogenetic silencing, the SNr was transduced with PSAM^4-GlyR by injection of recombinant adeno-associated virus *rAAV1-Syn::FLEX-rev-PSAM^4-GlyR–IRES–EGFP*. The dose response of varenicline-mediated PSAM^4-GlyR silencing was established by monitoring mouse rotation in the presence of low-dose amphetamine (3 mg/kg) to increase overall activity. The lowest effective dose (LED) for onset of rotation activity in PSAM^4-GlyR mice after

intraperitoneal varenicline delivery was 0.1 mg/kg (Fig. 3B and movie S1). Subsequent varenicline readministration after 5 hours reactivated rotation activity without tachyphylaxis of the chemogenetic response (Fig. 3C). Behavioral effects of silencing were evident within 20 min, and rotation activity returned nearly to baseline after 4 hours (Fig. 3D), consistent with reported varenicline half-life (*20*). These low doses of varenicline are an order of magnitude lower than those required for mice to recognize varenicline as a replacement for nicotine (*32*, *33*) or for other reported behavioral consequences in mice (*34*). In addition, oral delivery of varenicline (5 μg/ml) also elicited circling (fig. S5K).

We also tested PSAM^4-GlyR for silencing activity in a rhesus monkey in the globus pallidus internal region (GPi) (Fig. 3E). GPi was transduced with PSAM^4-GlyR by electrophysiologically guided injection of *rAAV8-Syn::PSAM^4-GlyR–IRES–EGFP* (Fig. 3, F to H). The GPi neuron firing rate and burst firing rate were significantly inhibited by subcutaneous varenicline (0.1 mg/kg) delivery relative to GPi activity in the presence of varenicline prior to AAV transduction (Fig. 3, I and J). Neither the regularity of firing (coefficient of variation for interspike interval) nor burst probability was affected by chemogenetic silencing (Fig. 3, K and L). This dose is lower than the dose required for varenicline to serve as a nicotine-substituting discriminative stimulus in monkeys by a factor of 5 (*35*).

Highly potent and selective chemogenetic agonists

Chemogenetic agonists for research applications should balance requirements for high potency, selectivity, and brain bioavailability along with pharmacodynamic responses of hours. We set out to make molecules that retained the high potency of varenicline at PSAM^4 but improved selectivity over varenicline's endogenous targets. We synthesized 30 varenicline analogs (Fig. 4A and table S2) modified at the quinoxaline portion of the molecule because of its proximity to the "hole" predicted by the Leu^{131} → Gly mutation (Fig. 2A). We chose modifications that kept structural elements and physicochemical properties within ranges associated with brain bioavailability and low PgP substrate activity (*36*). Thirteen molecules had potency below 10 nM at PSAM^4-GlyR or PSAM^4-5HT3 and had high selectivity for PSAM^4-GlyR with reduced agonist activity at the three endogenous targets of varenicline (α4β2 nAChR, α7 nAChR, and 5HT3-R) (table S2).

We focused on four molecules that had high potency in mice (Fig. 4B, table S2, and below). Quinoxalone derivative 792 (Fig. 4A, pathway e) had subnanomolar affinity for PSAM^4-GlyR (K_i = 0.7 ± 0.1 nM) (Fig. 4, C and D) and was an ultrapotent PSEM (uPSEM) agonist for PSAM^4-GlyR and PSAM^4-5HT3 (Fig. 4, B and E, and fig. S8, A and B). uPSEM^{792} showed agonist selectivity for PSAM^4-GlyR and PSAM^4-5HT3 relative to α7-GlyR, α7-5HT3, and 5HT3-R by more than four orders of magnitude (Fig. 4, B and E, and fig. S8C). At α4β2 nAChRs, uPSEM^{792} was a very weak partial agonist (10 ± 0.4%) (figs. S8D and S9A) with selectivity for PSAM^4-GlyR by a factor of 230 (Fig. 4, B and E). Thus, uPSEM^{792} retained the potency of varenicline for PSAM^4-GlyR with enhanced chemogenetic selectivity.

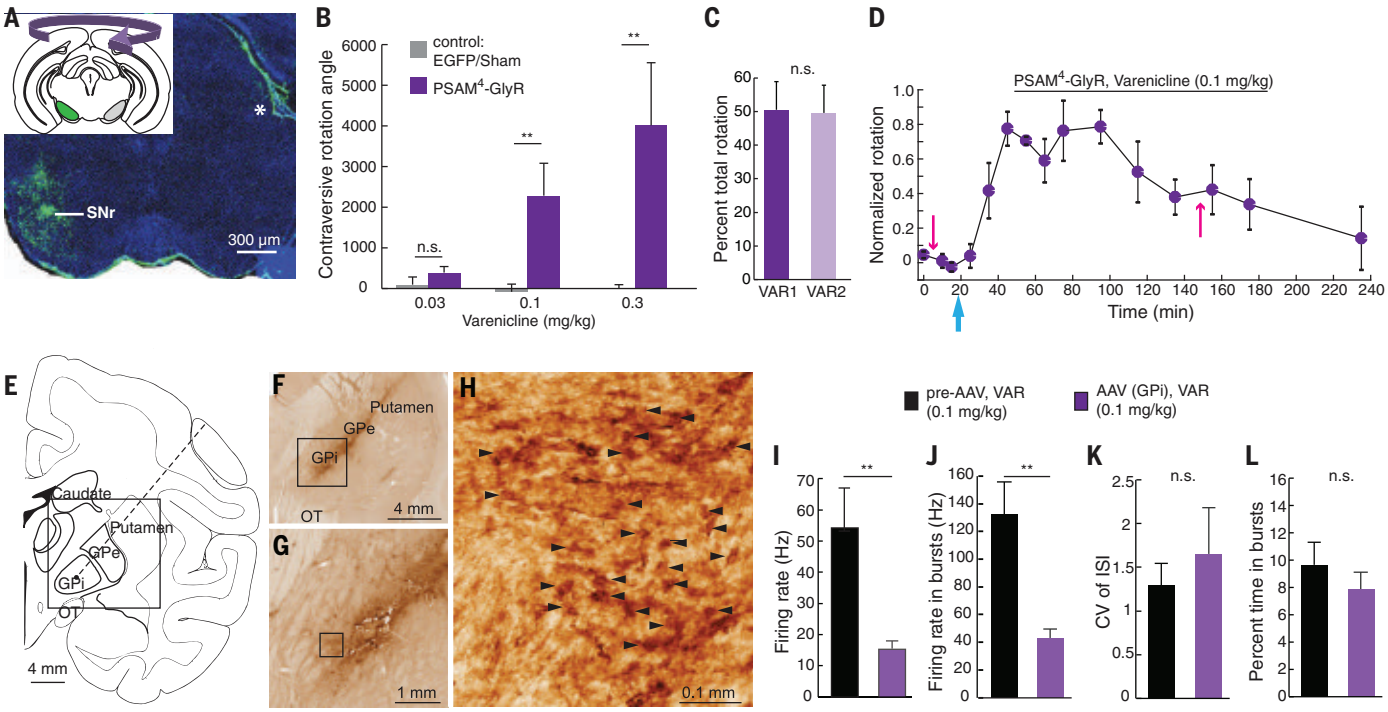

Fig. 3. PSAM^4-GlyR neuron silencing in mice and a monkey. (**A**) PSAM^4-GlyR–IRES–EGFP targeted unilaterally to the SNr. Inset: Schematic of unilateral SNr transduction and contralateral rotation. Asterisk denotes nonspecific immunofluorescence. (**B**) Low doses of intraperitoneal varenicline elicit contraversive rotation for mice expressing PSAM^4-GlyR (n = 9 mice) but not mice that were sham-operated or expressed EGFP alone (n = 6 mice). (**C**) Two doses of varenicline separated by 5 hours gave similar proportions of total rotation (n = 4 mice). (**D**) Time course of rotation response normalized to maximum rotation for each mouse (n = 4 mice). Magenta arrows, amphetamine injections; cyan arrow, varenicline injection. (**E**) Coronal diagram of rhesus macaque brain showing location of GPi targeted for AAV injection and in vivo electrophysiological recordings along trajectory shown by dashed line. Box denotes area of interest for (F). OT, optic tract; GPe, external globus pallidus. (**F** to **H**) EGFP marker gene expression near injection site. Boxes denote area of interest for subsequent panel; arrowheads (H) indicate EGFP-positive neuronal profiles visualized by 3,3′-diaminobenzidine polymerization. (**I** to **L**) In one monkey, electrophysiological reduction of overall neuronal firing rate (I) and burst firing rate (J) in GPi after peripheral varenicline injection. Coefficient of variation of interspike interval (CV of ISI) (K) and percent time in burst firing (L) were not affected (pre-AAV, n = 8 neurons; post-PSAM^4-GlyR AAV, n = 10 neurons). Error bars are SEM. **P < 0.01 (Mann-Whitney U test).

Alkoxy substitution of varenicline (Fig. 4A, pathway d) resulted in subnanomolar PSAM^4-GlyR and PSAM^4-5HT3 affinities and potencies (Fig. 4B and fig. S8, E, G, and I). The highest-affinity PSAM^4-GlyR agonist, uPSEM^{817} (K_i = 0.15 ± 0.02 nM) (Fig. 4C), was generated by propoxy substitution of varenicline and had remarkable potency ($EC50_{MP}$ = 0.3 ± 0.4 nM), which makes uPSEM^{817} one of the most potent LGIC agonists ever reported. uPSEM^{817} agonist selectivity was also excellent, with selectivity for PSAM^4-GlyR over α7-GlyR, α7-5HT3, and 5HT3-R by factors of 5000 to 10,000 (Fig. 4B). uPSEM^{815} and uPSEM^{817} did not show evident α4β2 nAChR agonism up to 30 μM (fig. S9B), and uPSEMs 793 and 815 had selectivity for PSAM^4-GlyR over 5HT3-R by a factor of >2000 (Fig. 4B and fig. S8, F and H). α7 nAChR agonism was not detected for any of the uPSEMs at 1000 times their PSAM^4-GlyR EC50 values (fig. S9, C and D).

To test for binding to a larger range of molecular targets, we used radioligand displacement against functionally important endogenous receptors and transporters (*37*). This showed no significant binding at 30 to 100 times the PSAM^4-GlyR EC50 values of the uPSEMs at 48 of 52 targets, including serotonin, GABA, adrenergic, muscarinic, dopamine, and histamine receptors (tables S3 and S4). [^{3}H]-ASEM radioligand displacement from rat forebrain tissue α7 nAChRs by uPSEMs showed high K_i values of 0.3 to 8 μM (fig. S9E). The molecules retained binding to β2-containing nAChRs, with highest affinity for α4β2 nAChR (fig. S9E and tables S3 and S4). However, for uPSEM^{792}, functional measurements of α4β2 channel activation by 1 μM ACh (a low but physiologically relevant concentration) did not show inhibitory consequences of uPSEM^{792} before the higher concentrations at which uPSEM^{792} elicited weak α4β2 agonist activity (fig. S9A), and the IC50 for uPSEM^{817} at α4β2 nAChRs was higher than its EC50 for PSAM^4-GlyR by two orders of magnitude (Fig. 4, B and F).

uPSEMs 792, 793, 815, and 817 strongly suppressed layer 2/3 cortical neurons expressing PSAM^4-GlyR in brain slices at low concentrations ranging from 1 to 15 nM (Fig. 4G and fig. S9, G to K). In addition, all uPSEMs were soluble in water. We tested the most selective uPSEMs 792 and 817 for P-glycoprotein pump efflux. They were not PgP substrates (efflux ratio < 2; Fig. 4I and table S5), indicating that they are suitable candidates for in vivo applications in the brain.

Imaging chemogenetic receptors in vivo

Delivery of chemogenetic receptors to the brain can be variable; thus, it is desirable to noninvasively monitor chemogenetic receptor expression and anatomical distribution in the brain. To noninvasively measure the distribution of PSAM^4-GlyR in vivo as well as accessibility and binding of uPSEMs in the mouse brain, we used positron emission tomography (PET). PSAM^4-GlyR expressed unilaterally in the cortex potently bound the radiolabeled α7 nAChR antagonist [^{18}F]-ASEM (*38*) at this location in vivo (Fig. 4, J and K). Receptor localization could be readily visualized against endogenous ligand binding, even with extremely low doses of the tracer. The distribution of PSAM^4-GlyR can thus be determined noninvasively with a PET ligand that has been used in humans and is suitable for both research and clinical applications.

To establish uPSEM binding to PSAM^4-GlyR in brain tissue, we used radioligand displacement. PSAM^4-GlyR–IRES–EGFP was expressed in the left dorsal striatum and EGFP alone was expressed in the right striatum. We performed autoradiography with [^{3}H]-ASEM bound to PSAM^4-GlyR in striatal brain slices to confirm ligand displacement ex vivo (fig. S9, M to O), and the radioactivity corresponded to the location of PSAM^4-GlyR–IRES–EGFP expression (fig. S9P). Next, we established brain penetrance and receptor binding of uPSEMs in vivo using PET by competition of [^{18}F]-ASEM binding with intraperitoneal (i.p.) injection of uPSEM agonists (Fig. 4L). [^{18}F]-ASEM binding in the left dorsal striatum (Fig. 4M) was eliminated by injection of these agonists (Fig. 4N). The in vivo [^{18}F]-ASEM localization matched ex vivo expression of PSAM^4-GlyR–IRES–EGFP established by post hoc fluorescence microscopy (Fig. 4O) as well as [^{3}H]-ASEM autoradiography (Fig. 4P) in the same tissue sections, but binding was not observed in the right striatum, which expressed EGFP alone.

Potent uPSEM neuron silencing in vivo

To directly monitor uPSEM^{792}-mediated neuronal silencing in vivo, we recorded calcium dynamics of hippocampal neurons in area CA1 by two-photon imaging in head-fixed mice running on a treadmill marked with texture cues (Fig. 5A). In a *Thy1::GCaMP6f* transgenic mouse, PSAM^4-GlyR was expressed in hippocampal pyramidal cells by injection of *rAAV1-CamkII::PSAM^4-GlyR–IRES–EGFP* (Fig. 5A). The field of view contained distinct domains of neurons densely and sparsely transduced with PSAM^4-GlyR–IRES–EGFP (Fig. 5B). In stationary and running behavioral epochs, which elicit different levels of CA1 activity, both domains showed similar baseline activity, indicating that expression of PSAM^4-GlyR did not perturb basal activity (Fig. 5, C and D). After intraperitoneal injection of uPSEM^{792} (3 mg/kg), the densely transduced CA1 hippocampal domains were strongly silenced, while the sparsely transduced domain showed a modest reduction in activity (Fig. 5, C and D). In mice not expressing PSAM^4-GlyR, we found no significant difference in calcium activity of CA1 pyramidal neurons after administration of uPSEM^{792} at 3 mg/kg (P = 0.9515, n = 265 neurons, 3 mice, 93.5% of median baseline activity, signed rank test). Place cells, which fire as a result of powerful circuit and cell-autonomous conductances, were also silenced by PSAM^4-GlyR and uPSEM^{792} (Fig. 5E).

Finally, to determine dose responses for uPSEMs in vivo, we used behavioral assays by measuring contralateral rotation in mice with the unilateral SNr silencing assay. The potency in mice was exceptional for uPSEM^{793} (LED = 0.03 mg/kg) (Fig. 5, F and G), which is an improvement on first-generation PSEMs by three orders of magnitude (movie S2). One of the most selective agonists, uPSEM^{792}, was active at a LED of 1 mg/kg in vivo (Fig. 5, H and I, and movie S2). uPSEM^{817} also has a favorable selectivity profile and the same LED (0.1 mg/kg) as varenicline (fig. S10 and movie S2). These low doses reflect the most selective silencing regime for these molecules. All molecules elicited durable responses of 3 to 4 hours in mice with acute intraperitoneal dosing (Fig. 5, G and I, and fig. S10), which was comparable to varenicline. To examine potential off-target behavioral effects of uPSEMs, we monitored food intake, which is sensitive to off-target 5HT3-R activation. Food consumption was not significantly altered by uPSEMs at 3 times the lowest effective doses determined in the SNr silencing assay, although food intake was reduced with elevated varenicline doses, highlighting the superior selectivity of uPSEMs (fig. S11).

Discussion

Chemogenetics permits targeted, noninvasive, and reversible perturbations of cellular function. Here, we developed a set of modular ion channels and selective, exceptionally potent agonists that are effective in the brain for rodent and primate models. Chemogenetic agonists were derived from the clinically approved drug varenicline and required optimization to balance competing needs for potency, selectivity, brain penetrance, and response times of hours. We determined the lowest effective doses of the uPSEMs and varenicline in vivo to achieve the optimal balance of efficacy and selectivity. Note that varenicline can also be used for chemogenetics at lower concentrations than those associated with antinicotine clinical applications (*18*).

The effectiveness, ease of use, and targeted nature of chemogenetics have made clinical applications attractive (*3*, *4*, *39*). Chemogenetics uses a limited repertoire of drug/receptor pairs but achieves diverse therapeutic effects by targeting the receptors via gene transfer to distinct regions. This offers a model for therapy that circumvents the pharmacological complexity of protein target identification followed by drug development for each new target. Our engineered ion channel technology facilitates chemogenetic therapies because it uses a well-tolerated approved drug that can potentially be used at or below doses for which it is currently approved. Clinical applications of chemogenetics are well suited for conditions that can be ameliorated by modulating cellular activity at localized sites to which the chemogenetic receptor can be delivered in the course of standard surgical procedures, such as pharmacotherapy-refractory localized pain, focal epilepsy, and some movement disorders (*4*, *39*, *40*). Our own work has revealed chemogenetic perturbations in two nodes of the basal ganglia that are associated with invasive Parkinson's disease deep brain stimulation therapies. Additional studies will be needed to establish long-term safety and efficacy with chemogenetic receptors for therapeutic applications, but this is facilitated by the current clinical

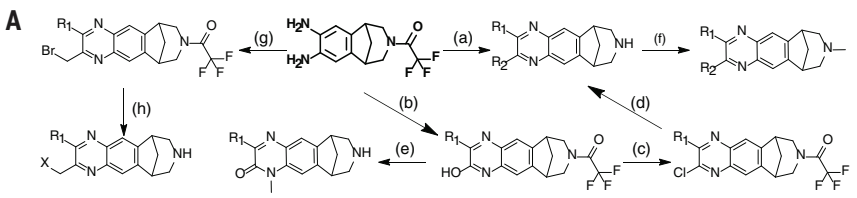

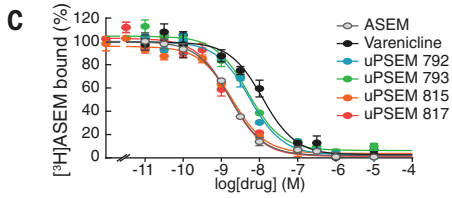

B

	α7 nAChR	α7-GlyR	α7-5HT3	PSAM^4-GlyR	PSAM^4-5HT3	α4β2 agonist	h5HT3-R agonist	α4β2 ant. 1 μM ACh	LED in vivo
varenicline	not determined	620 (200) **390-fold**	920 (150) **230-fold**	1.6 (0.1)	4 (2)	250 (60) **160-fold**	1,400 (400) **880-fold**	3 **2-fold**	0.1 mg/kg
792	**>1,000-fold**	>30,000 **>10,000-fold**	>30,000 **>10,000-fold**	2.3 (0.3)	1.6 (0.2)	520 (100) **230-fold**	40,500 (500) **>10,000-fold**	(agonist)	1 mg/kg
793	**>1,000-fold**	31,000 (17,000) **>10,000-fold**	26,000 (4,200) **>10,000-fold**	0.6 (0.4)	0.9 (0.4)	610 (250) **1,000-fold**	1,300 (0) **2,200-fold**	23 (5) **38-fold**	0.03 mg/kg
815	**>1,000-fold**	>100,000 **>10,000-fold**	>100,000 **>10,000-fold**	0.5 (1)	0.8 (0.4)	>30 **>10,000-fold**	1,200 (100) **3,000-fold**	21 (4) **42-fold**	0.1 mg/kg
817	**>1,000-fold**	>100,000 **>10,000-fold**	>100,000 **>10,000-fold**	0.3 (0.4)	0.5 (0.2)	>30 **>10,000-fold**	1,500 (100) **5,000-fold**	31 (10) **100-fold**	0.1 mg/kg

D

(nM)	VAR	792	793	815	817	ASEM
PSAM^4-GlyR	1.3 (0.4)	0.70 (0.10)	0.66 (0.07)	0.21 (0.01)	0.15 (0.02)	0.26 (0.03)

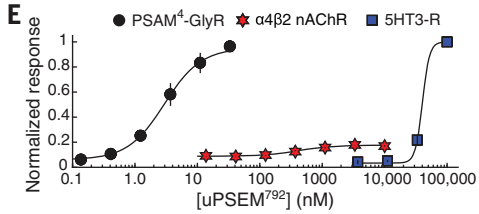

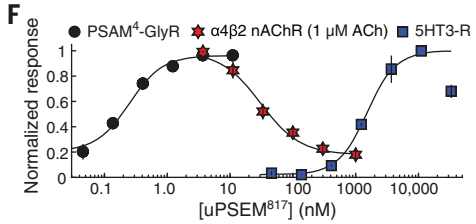

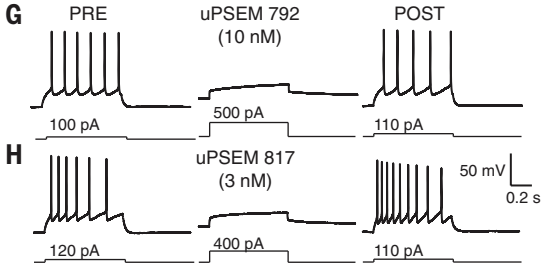

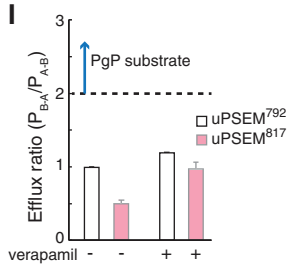

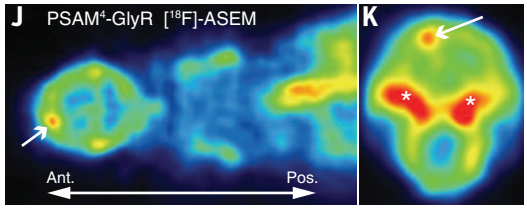

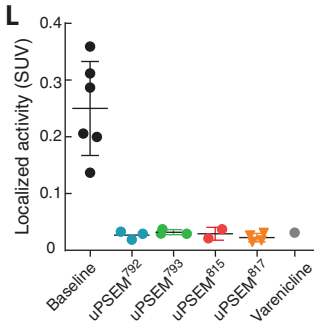

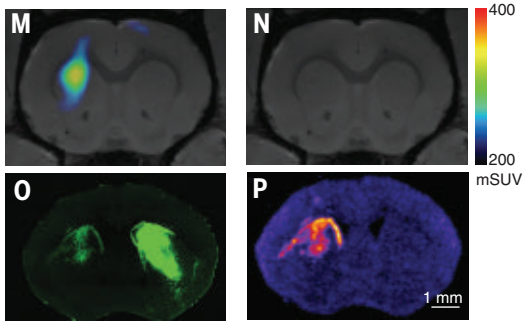

Fig. 4. Highly selective chemogenetic agonists. (**A**) Synthetic pathways (letters) for uPSEM agonists (see supplementary materials). (**B**) Comparison of uPSEM agonist EC50s at PSAM^4 channels and endogenous varenicline targets, as well as IC50 for α4β2 nAChR with 1 μM ACh. LED, lowest effective dose for mice in SNr rotation assay. Units are nM; parentheses denote SEM. Selectivity relative to PSAM^4-GlyR is shown in boldface. (**C** and **D**) Displacement of [^{3}H]-ASEM at PSAM^4-GlyR by uPSEMs (C) and K_i values (D). Parentheses denote SEM. (**E** and **F**) Dose response curves for PSAM^4-GlyR, α4β2 nAChR, and 5HT3-R. uPSEM^{792} (E) is a 10% partial agonist of α4β2 nAChR; uPSEM^{817} (F) inhibits α4β2 nAChR. (**G** and **H**) uPSEM^{792} (G) and uPSEM^{817} (H) strongly suppress firing in neurons expressing PSAM^4-GlyR. (**I**) Efflux ratio < 2, indicating that uPSEM^{792} and uPSEM^{817} are not PgP substrates. P_{B-A} and P_{A-B} are basal and apical permeability, respectively, across the Caco-2 cell line monolayer (n = 2 replicates). (**J** and **K**) In vivo PET imaging after [^{18}F]-ASEM injection, showing cortical localization of PSAM^4-GlyR in horizontal view through head and upper torso (J) and coronal view of the head (K). Arrow shows site of PSAM^4-GlyR expression; asterisks show accumulation of [^{18}F] outside the brain. (**L**) [^{18}F]-ASEM binding to PSAM^4-GlyR under baseline conditions and with competition by uPSEMs (uPSEM^{792}, 1 mg/kg; uPSEM^{793}, uPSEM^{815}, and uPSEM^{817}, 0.3 mg/kg) and varenicline (0.3 mg/kg). (**M**) Tomographic plane showing [^{18}F]-ASEM binding to PSAM^4-GlyR in vivo. (**N**) Competition of [^{18}F]-ASEM binding by intraperitoneally administered uPSEM^{792}. (**O** and **P**) Ex vivo fluorescence image (O) and autoradiographic image of [^{3}H]-ASEM binding (P) of corresponding brain slice expressing PSAM^4-GlyR–IRES–EGFP in left dorsal striatum. Right striatum was injected with virus expressing EGFP alone. Error bars are SEM.

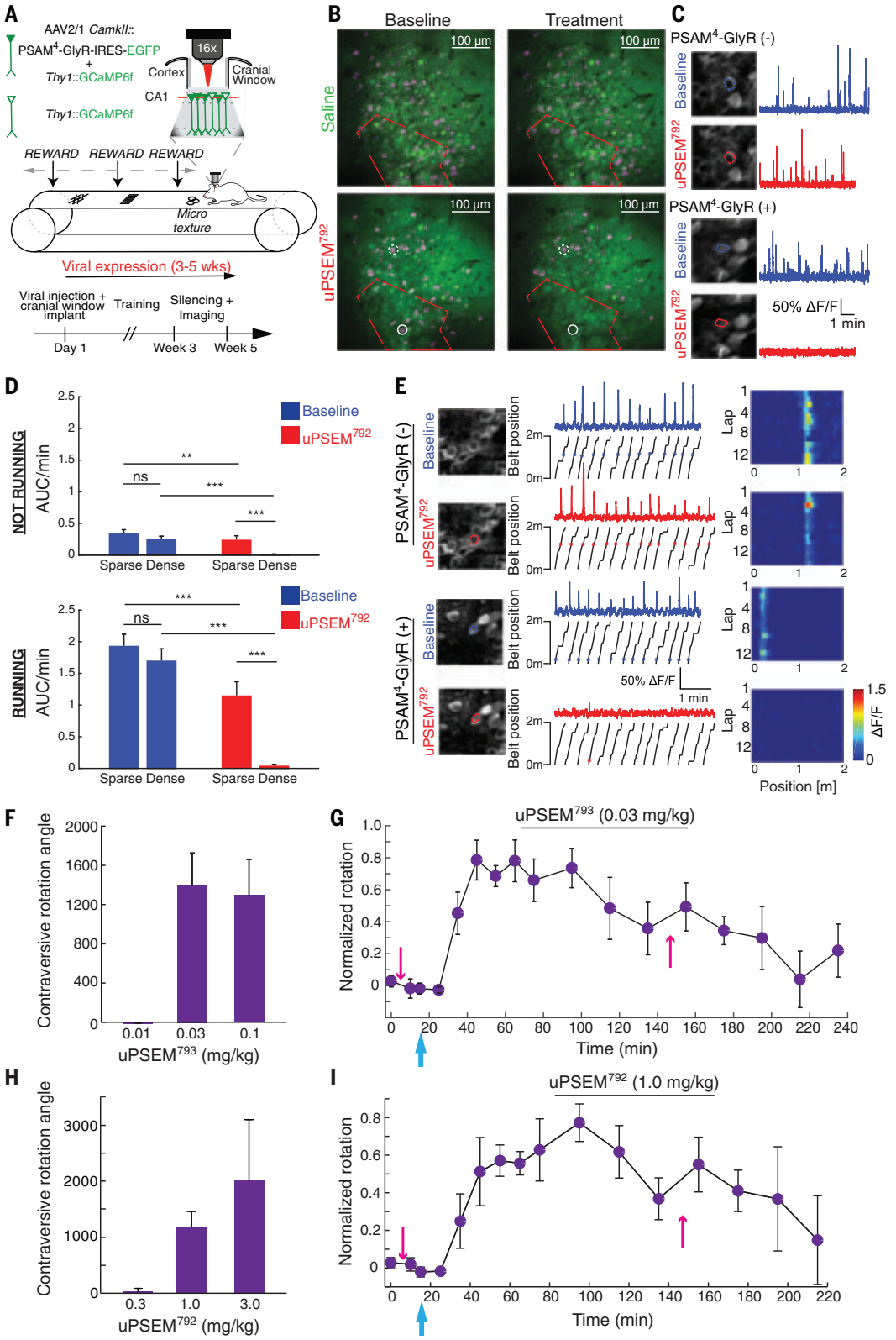

Fig. 5. Neuron silencing with uPSEMs and PSAM^4-GlyR in vivo. (**A**) Experimental design for monitoring hippocampal CA1 neuron silencing with PSAM^4-GlyR and uPSEM^{792} using in vivo two-photon Ca^{2+} imaging in head-fixed mice running on a treadmill with textural landmarks. PSAM^4-GlyR–IRES–EGFP was virally expressed in hippocampal CA1 pyramidal neurons in Thy1-GCaMP6f mice. Neurons coexpressing GCaMP6f and viral PSAM^4-GlyR–IRES–EGFP are solid green; neurons expressing only GCaMP6f are green outline. (**B**) Z-stack projections (green) overlaid with maximum-intensity projections of GCaMP6f fluorescence in time (magenta). Example images from a saline-treated (top) and uPSEM^{792}-treated (bottom) mouse. Red outline encloses densely transduced region, which also shows strong uPSEM^{792}-mediated reduction of neuron activity (reduced magenta signals). Outside the red boundary is the sparsely transduced region. Neurons depicted in (C) are circled. [dashed, PSAM^4-GlyR(−); solid, PSAM^4-GlyR(+)]. (**C**) Representative regions of interest (ROIs, left) and somatic Ca^{2+} traces (right). Transduced PSAM^4-GlyR(+) pyramidal neurons are identified by EGFP-filled somata, whereas PSAM^4-GlyR(−) cells have only cytoplasmic GCaMP6f fluorescence. (**D**) Activity rate [area under $\Delta F/F$ trace of Ca^{2+} transients divided by epoch duration (AUC/min)] for episodes in which mice were running and not running on the treadmill. Densely transduced: run, n = 68 neurons, no-run, n = 58 neurons from 2 mice; sparsely transduced: run, n = 103 neurons, no-run, n = 96 neurons from 2 mice. $^{**}P < 0.01$, $^{***}P < 0.001$ (Mann-Whitney U test and signed rank test with Holm-Sidak correction). (**E**) Place field activity after uPSEM^{792} administration. Shown are somatic ROI outlines before and after treatment (left), $\Delta F/F$ activity (center top) with associated position of the mouse on the belt (center bottom), and raster plots with mean $\Delta F/F$ activity in each 2-cm spatial bin across laps (right). Asterisks denote the location of significant running calcium transients along the belt. (**F** to **I**) In vivo uPSEM dose responses for mice (n = 4) expressing PSAM^4-GlyR unilaterally in SNr. Behavioral response and time course for uPSEM^{793} [(F) and (G)] and uPSEM^{792} [(H) and (I)] are shown. Time course of rotation response is normalized to maximum rotation for each mouse. Magenta arrows, amphetamine injections; cyan arrows, uPSEM injection. Error bars are SEM.

use of varenicline. These chemogenetic technologies offer opportunities in basic research and the capability for extending findings to potential therapeutic applications.

REFERENCES AND NOTES

1. S. M. Sternson, B. L. Roth, Chemogenetic tools to interrogate brain functions. *Annu. Rev. Neurosci.* **37**, 387–407 (2014). doi: 10.1146/annurev-neuro-071013-014048; pmid: 25002280
2. D. Atasoy, S. M. Sternson, Chemogenetic Tools for Causal Cellular and Neuronal Biology. *Physiol. Rev.* **98**, 391–418 (2018). doi: 10.1152/physrev.00009.2017; pmid: 29351511
3. J. G. English, B. L. Roth, Chemogenetics—A Transformational and Translational Platform. *JAMA Neurol.* **72**, 1361–1366 (2015). doi: 10.1001/jamaneurol.2015.1921; pmid: 26409113
4. D. Kätzel, E. Nicholson, S. Schorge, M. C. Walker, D. M. Kullmann, Chemical-genetic attenuation of focal neocortical seizures. *Nat. Commun.* **5**, 3847 (2014). doi: 10.1038/ncomms4847; pmid: 24866701
5. J. L. Gomez *et al*., Chemogenetics revealed: DREADD occupancy and activation via converted clozapine. *Science* **357**, 503–507 (2017). doi: 10.1126/science.aan2475; pmid: 28774929
6. J. Raper *et al*., Metabolism and Distribution of Clozapine-N-oxide: Implications for Nonhuman Primate Chemogenetics. *ACS Chem. Neurosci.* **8**, 1570–1576 (2017). doi: 10.1021/acschemneuro.7b00079; pmid: 28324647
7. D. A. A. MacLaren *et al*., Clozapine-n-oxide administration produces behavioral effects in Long-Evans rats—implications for designing DREADD experiments. *eNeuro* **3**, 0219-16 (2016). doi: 10.1126/science.aan2475; pmid: 28774929
8. G. M. Alexander *et al*., Remote control of neuronal activity in transgenic mice expressing evolved G protein-coupled receptors. *Neuron* **63**, 27–39 (2009). doi: 10.1016/j.neuron.2009.06.014; pmid: 19607790
9. B. N. Armbruster, X. Li, M. H. Pausch, S. Herlitze, B. L. Roth, Evolving the lock to fit the key to create a family of G protein-coupled receptors potently activated by an inert ligand. *Proc. Natl. Acad. Sci. U.S.A.* **104**, 5163–5168 (2007). doi: 10.1073/pnas.0700293104; pmid: 17360345
10. M. W. Jann, Y. W. Lam, W. H. Chang, Rapid formation of clozapine in guinea-pigs and man following clozapine-N-oxide administration. *Arch. Int. Pharmacodyn. Ther.* **328**, 243–250 (1994). pmid: 7710309
11. C. J. Wenthur, C. W. Lindsley, Classics in chemical neuroscience: Clozapine. *ACS Chem. Neurosci.* **4**, 1018–1025 (2013). doi: 10.1021/cn400121z; pmid: 24047509
12. B. L. Roth, DREADDs for Neuroscientists. *Neuron* **89**, 683–694 (2016). doi: 10.1016/j.neuron.2016.01.040; pmid: 26889809
13. C. J. Magnus *et al*., Chemical and genetic engineering of selective ion channel-ligand interactions. *Science* **333**, 1292–1296 (2011). doi: 10.1126/science.1206606; pmid: 21885782
14. J. E. Macor *et al*., The 5-HT3 antagonist tropisetron (ICS 205-930) is a potent and selective α7 nicotinic receptor partial agonist. *Bioorg. Med. Chem. Lett.* **11**, 319–321 (2001). doi: 10.1016/S0960-894X(00)00670-3; pmid: 11212100
15. K. B. Mihalak, F. I. Carroll, C. W. Luetje, Varenicline is a partial agonist at α4β2 and a full agonist at α7 neuronal nicotinic receptors. *Mol. Pharmacol.* **70**, 801–805 (2006). doi: 10.1124/mol.106.025130; pmid: 16766716
16. M. Nakamura *et al*., Efficacy and tolerability of varenicline, an α4β2 nicotinic acetylcholine receptor partial agonist, in a 12-week, randomized, placebo-controlled, dose-response study with 40-week follow-up for smoking cessation in Japanese smokers. *Clin. Ther.* **29**, 1040–1056 (2007). doi: 10.1016/j.clinthera.2007.06.012; pmid: 17692720
17. K. Kaur, S. Kaushal, S. C. Chopra, Varenicline for smoking cessation: A review of the literature. *Curr. Ther. Res. Clin. Exp.* **70**, 35–54 (2009). doi: 10.1016/j.curtheres.2009.02.004; pmid: 24692831
18. H. Rollema *et al*., Pre-clinical properties of the α4β2 nicotinic acetylcholine receptor partial agonists varenicline, cytisine and dianicline translate to clinical efficacy for nicotine dependence. *Br. J. Pharmacol.* **160**, 334–345 (2010). doi: 10.1111/j.1476-5381.2010.00682.x; pmid: 20331614
19. H. M. Faessel *et al*., Lack of a pharmacokinetic interaction between a new smoking cessation therapy, varenicline, and digoxin in adult smokers. *Eur. J. Clin. Pharmacol.* **64**, 1101–1109 (2008). doi: 10.1007/s00228-008-0530-6; pmid: 18661125
20. R. S. Obach *et al*., Metabolism and disposition of varenicline, a selective α4β2 acetylcholine receptor partial agonist, in vivo and in vitro. *Drug Metab. Dispos.* **34**, 121–130 (2006). doi: 10.1124/dmd.105.006767; pmid: 16221753
21. S. C. Lummis, A. J. Thompson, M. Bencherif, H. A. Lester, Varenicline is a potent agonist of the human 5-hydroxytryptamine3 receptor. *J. Pharmacol. Exp. Ther.* **339**, 125–131 (2011). doi: 10.1124/jpet.111.185306; pmid: 21775477
22. P. Rucktooa *et al*., Structural characterization of binding mode of smoking cessation drugs to nicotinic acetylcholine receptors through study of ligand complexes with acetylcholine-binding protein. *J. Biol. Chem.* **287**, 23283–23293 (2012). doi: 10.1074/jbc.M112.360347; pmid: 22553201
23. R. E. Hibbs *et al*., Structural determinants for interaction of partial agonists with acetylcholine binding protein and neuronal α7 nicotinic acetylcholine receptor. *EMBO J.* **28**, 3040–3051 (2009). doi: 10.1038/emboj.2009.227; pmid: 19696737
24. A. G. Horti *et al*., ^{18}F-ASEM, a radiolabeled antagonist for imaging the α7-nicotinic acetylcholine receptor with PET. *J. Nucl. Med.* **55**, 672–677 (2014). doi: 10.2967/jnumed.113.132068; pmid: 24556591
25. J. W. Coe *et al*., 3,5-Bicyclic aryl piperidines: A novel class of α4β2 neuronal nicotinic receptor partial agonists for smoking cessation. *Bioorg. Med. Chem. Lett.* **15**, 4889–4897 (2005). doi: 10.1016/j.bmcl.2005.08.035; pmid: 16171993
26. P. Uutela, R. Reinilä, P. Piepponen, R. A. Ketola, R. Kostiainen, Analysis of acetylcholine and choline in microdialysis samples by liquid chromatography/tandem mass spectrometry. *Rapid Commun. Mass Spectrom.* **19**, 2950–2956 (2005). doi: 10.1002/rcm.2160; pmid: 16180202
27. V. Parikh, R. Kozak, V. Martinez, M. Sarter, Prefrontal acetylcholine release controls cue detection on multiple timescales. *Neuron* **56**, 141–154 (2007). doi: 10.1016/j.neuron.2007.08.025; pmid: 17920021
28. T. Grutter *et al*., Molecular tuning of fast gating in pentameric ligand-gated ion channels. *Proc. Natl. Acad. Sci. U.S.A.* **102**, 18207–18212 (2005). doi: 10.1073/pnas.0509024102; pmid: 16319224
29. C. A. Griffith, L. J. Owen, R. Body, G. McDowell, B. G. Keevil, Development of a method to measure plasma and whole blood choline by liquid chromatography tandem mass spectrometry. *Ann. Clin. Biochem.* **47**, 56–61 (2010). doi: 10.1258/acb.2009.008191; pmid: 19837724
30. B. Yue *et al*., Choline in whole blood and plasma: Sample preparation and stability. *Clin. Chem.* **54**, 590–593 (2008). doi: 10.1373/clinchem.2007.094201; pmid: 18310145
31. J. Scheel-Krüger, J. Arnt, G. Magelund, Behavioural stimulation induced by muscimol and other GABA agonists injected into the substantia nigra. *Neurosci. Lett.* **4**, 351–356 (1977). doi: 10.1016/0304-3940(77)90183-5; pmid: 19556189
32. C. S. Cunningham, L. R. McMahon, Multiple nicotine training doses in mice as a basis for differentiating the effects of smoking cessation aids. *Psychopharmacology* **228**, 321–333 (2013). doi: 10.1007/s00213-013-3037-5; pmid: 23494230
33. F. B. de Moura, L. R. McMahon, The contribution of α4β2 and non-α4β2 nicotinic acetylcholine receptors to the discriminative stimulus effects of nicotine and varenicline in mice. *Psychopharmacology* **234**, 781–792 (2017). doi: 10.1007/s00213-016-4514-4; pmid: 28028600
34. N. C. Ortiz, H. C. O'Neill, M. J. Marks, S. R. Grady, Varenicline blocks β2*-nAChR-mediated response and activates β4*-nAChR-mediated responses in mice in vivo. *Nicotine Tobacco Res.* **14**, 711–719 (2012). doi: 10.1124/jpet.112.193078; pmid: 22438471
35. C. S. Cunningham, M. A. Javors, L. R. McMahon, Pharmacologic characterization of a nicotine-discriminative stimulus in rhesus monkeys. *J. Pharmacol. Exp. Ther.* **341**, 840–849 (2012). doi: 10.1124/jpet.112.193078; pmid: 22438471
36. S. A. Hitchcock, Structural modifications that alter the P-glycoprotein efflux properties of compounds. *J. Med. Chem.* **55**, 4877–4895 (2012). doi: 10.1021/jm201136z; pmid: 22506484
37. J. Besnard *et al*., Automated design of ligands to polypharmacological profiles. *Nature* **492**, 215–220 (2012). doi: 10.1038/nature11691; pmid: 23235874
38. D. F. Wong *et al*., Human brain imaging of α7 nAChR with [^{18}F]ASEM: A new PET radiotracer for neuropsychiatry and determination of drug occupancy. *Mol. Imaging Biol.* **16**, 730–738 (2014). doi: 10.1124/jpet.112.193078; pmid: 22438471
39. G. A. Weir *et al*., Using an engineered glutamate-gated chloride channel to silence sensory neurons and treat neuropathic pain at the source. *Brain* **140**, 2570–2585 (2017). doi: 10.1093/brain/awx201; pmid: 28969375
40. S. Hirschberg, Y. Li, A. Randall, E. J. Kremer, A. E. Pickering, Functional dichotomy in spinal- vs prefrontal-projecting locus coeruleus modules splits descending noradrenergic analgesia from ascending aversion and anxiety in rats. *eLife* **6**, e29808 (2017). doi: 10.7554/eLife.29808; pmid: 29027903

ACKNOWLEDGMENTS

We thank J. Lindstrom for providing stable cell lines expressing human α4β2 nAChR or α7 nAChR. Receptor counter-screening and associated K_i determinations were generously provided by the National Institute of Mental Health's Psychoactive Drug Screening Program, contract HHSN-271-2013-00017-C (NIMH PDSP). We are grateful for support from Janelia core facility staff; S. Lindo performed in utero electroporations. **Funding:** Supported by HHMI (S.M.S., C.J.M., P.H.L., and M.H.R.); NIH grant ORIP OD P51-OD011132 to the Yerkes National Primate Research Center (X.H. and A.G.); the Alfred P. Sloan Foundation, Klingenstein-Simons Foundation, NIH grant NINDS 1R01 NS109362-01, and Whitehall Foundation (J.Ba.); and National Institute for Drug Abuse Intramural Research Program ZIA000069 with support via the Resource for Molecular Imaging Agents in Precision Medicine (P41EB024495) at JHU (M.M.). **Author contributions:** C.J.M. performed ex vivo electrophysiology and SNr silencing behavioral experiments; P.H.L. developed and synthesized uPSEMs and performed dose response assays with C.J.M.; M.H.R. made ion channel constructs; J.Bo., J.L.G., and M.M. performed PET imaging and radioligand displacement at PSAM^4-GlyR and α7 nAChR; X.H. and A.G. performed rhesus macaque experiments; R.Z. and J.Ba. performed in vivo calcium imaging; and S.M.S. conceived the project, designed experiments, and wrote the paper with input from all the authors. **Competing interests:** S.M.S., C.J.M., and P.H.L. have pending patents on this technology and own stock in Redpin Therapeutics Inc., which is a biotech company focusing on therapeutic applications of chemogenetics. S.M.S. is a cofounder and consultant for Redpin Therapeutics Inc. M.M. is a cofounder and owns stock in Metis Laboratories Inc. **Data and materials availability:** All data to support the conclusions of this manuscript are included in the main text and supplementary materials. Plasmids and AAV vectors are available from www.addgene.org/browse/article/28196963/. Accession numbers are PSAM^4-GlyR (MK492109), PSAM^4-5HT3 (MK492107), PSAM^4-5HT3 HC (MK492108). uPSEM^{792} and uPSEM^{817} are available from Tocris. DNA constructs and viral vectors for PSAMs and uPSEMs are available from S.M.S. under a material agreement with the Howard Hughes Medical Institute.

SUPPLEMENTARY MATERIALS

www.sciencemag.org/content/364/6436/eaav5282/suppl/DC1
Materials and Methods
Figs. S1 to S11
Tables S1 to S6
Movies S1 and S2
References (*41*–*78*)

30 September 2018; accepted 15 February 2019
Published online 14 March 2019
10.1126/science.aav5282

RESEARCH ARTICLE SUMMARY

NEUROSCIENCE

Sustained rescue of prefrontal circuit dysfunction by antidepressant-induced spine formation

R. N. Moda-Sava*, M. H. Murdock*, P. K. Parekh*, R. N. Fetcho, B. S. Huang, T. N. Huynh, J. Witztum, D. C. Shaver, D. L. Rosenthal, E. J. Alway, K. Lopez, Y. Meng, L. Nellissen, L. Grosenick, T. A. Milner, K. Deisseroth, H. Bito, H. Kasai, C. Liston†

INTRODUCTION: Depression is an episodic form of mental illness, yet the circuit-level mechanisms driving the induction, remission, and recurrence of depressive episodes over time are not well understood. Ketamine relieves depressive symptoms rapidly, providing an opportunity to study the neurobiological substrates of transitions from depression to remission and to test whether mechanisms that induce antidepressant effects acutely are distinct from those that sustain them.

RATIONALE: Contrasting changes in dendritic spine density in prefrontal cortical pyramidal cells have been associated with the emergence of depression-related behaviors in chronic stress models and with ketamine's antidepressant effects. But whether and how dendritic spine remodeling is causally involved, or whether it is merely correlated with these effects, is unclear. To answer these questions, we used two-photon imaging to study how chronic stress and ketamine affect dendritic spine remodeling and neuronal activity dynamics in the living prefrontal cortex (PFC), as well as a recently developed optogenetic tool to manipulate the survival of newly formed spines after ketamine treatment.

RESULTS: The induction of depression-related behavior in multiple chronic stress models was associated with targeted, branch-specific elimination of postsynaptic dendritic spines and a loss of correlated multicellular ensemble activity in PFC projection neurons. Antidepressant-dose ketamine reversed these effects by selectively rescuing eliminated spines and restoring coordinated activity in multicellular ensembles that predicted motivated escape behavior. Unexpectedly, ketamine's effects on behavior and ensemble activity preceded its effects on spine formation, indicating that spine formation was not required for inducing these effects acutely. However, individual differences in the restoration of lost spines were correlated with behavior 2 to 7 days after treatment, suggesting that spinogenesis may be important for the long-term maintenance of these effects. To test this, we used a photoactivatable probe to selectively reverse the effects of ketamine on spine formation in the PFC and found that the newly formed spines play a necessary and specific role in sustaining ketamine's antidepressant effects on motivated escape behavior. By contrast, optically deleting a random subset of spines unrelated to ketamine treatment had no effect on behavior.

CONCLUSION: Prefrontal cortical spine formation sustains the remission of specific depression-related behaviors after ketamine treatment by restoring lost spines and rescuing coordinated ensemble activity in PFC microcircuits. Pharmacological and neurostimulatory interventions for enhancing and preserving the rescue of lost synapses may therefore be useful for promoting sustained remission. ■

ON OUR WEBSITE

Read the full article at http://dx.doi.org/10.1126/science.aat8078

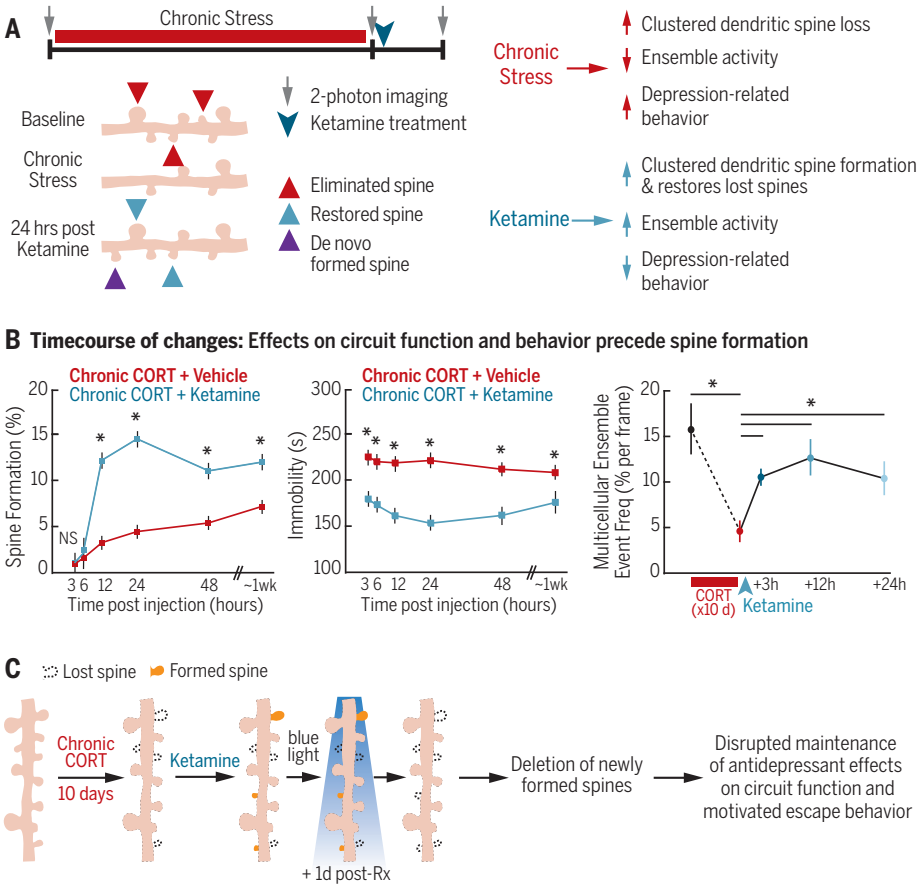

Prefrontal spinogenesis is required for sustaining—but not inducing—ketamine's effects on behavior and circuit function. (**A**) Complementary effects of stress and ketamine on spine remodeling, circuit function, and behavior. (**B**) The time course of changes indicates that spine formation is not required for inducing these effects initially. * indicates significantly different post hoc contrast, Holm-Bonferroni corrected ($P < 0.002$, $P < 0.0006$, and $P < 0.05$ for spine formation, immobility, and ensemble event frequency, respectively). NS, not significant. Error bars indicate SEM. (**C**) Optogenetic deletion of newly formed spines interferes with the long-term maintenance of these effects. Rx, treatment.

*These authors contributed equally to this work.
The list of author affiliations is available in the full article online.
†Corresponding author. Email: col2004@med.cornell.edu
Cite this article as R. N. Moda-Sava *et al.*, *Science* 364, eaat8078 (2019). DOI: 10.1126/science.aat8078

RESEARCH ARTICLE

NEUROSCIENCE

Sustained rescue of prefrontal circuit dysfunction by antidepressant-induced spine formation

R. N. Moda-Sava[1]*, M. H. Murdock[1]*, P. K. Parekh[1]*, R. N. Fetcho[1], B. S. Huang[1], T. N. Huynh[1], J. Witztum[1], D. C. Shaver[1], D. L. Rosenthal[1], E. J. Alway[1], K. Lopez[1], Y. Meng[1], L. Nellissen[1], L. Grosenick[1,2], T. A. Milner[1], K. Deisseroth[2], H. Bito[3], H. Kasai[4,5], C. Liston[1]†

The neurobiological mechanisms underlying the induction and remission of depressive episodes over time are not well understood. Through repeated longitudinal imaging of medial prefrontal microcircuits in the living brain, we found that prefrontal spinogenesis plays a critical role in sustaining specific antidepressant behavioral effects and maintaining long-term behavioral remission. Depression-related behavior was associated with targeted, branch-specific elimination of postsynaptic dendritic spines on prefrontal projection neurons. Antidepressant-dose ketamine reversed these effects by selectively rescuing eliminated spines and restoring coordinated activity in multicellular ensembles that predict motivated escape behavior. Prefrontal spinogenesis was required for the long-term maintenance of antidepressant effects on motivated escape behavior but not for their initial induction.

Depression is an episodic form of mental illness featuring discrete symptomatic periods interposed between periods of apparent wellness. The circuit-level mechanisms driving the induction, remission, and recurrence of depressive episodes over time are not well understood. Ketamine, a rapidly acting antidepressant, relieves depressive symptoms within hours (*1*–*3*), providing an experimentally tractable opportunity to study the mechanisms that underlie transitions from depression to remission and recurrence.

Sustaining remission after ketamine treatment is a particular challenge. Antidepressant effects of a single dose of ketamine eventually dissipate, and the long-term safety and efficacy of repeated dosing are not well understood. Whether the antidepressant effects that emerge hours after ketamine treatment are driven by mechanisms distinct from those that sustain the effects in the days after treatment is also unclear. Increasing evidence suggests that signaling pathways (*4*–*6*) may converge to increase spine density in prefrontal cortical pyramidal cells (*4*, *7*, *8*), potentially accelerating remission by directly and selectively reversing prefrontal cortical synapse loss, a putative neurobiological substrate of depression that occurs in multiple chronic stress models of depression-related behavior (*9*–*12*). Alternatively, ketamine may indirectly compensate for synapse loss by inducing synapse formation nonspecifically.

Until recently, it has been difficult to investigate how spine remodeling contributes to transitions between depression-like behavioral states, because of technical obstacles in quantifying synaptic remodeling longitudinally in the living prefrontal cortex (PFC). Using recently developed technologies for obtaining high-resolution optical access to deep brain structures in vivo (*13*–*16*), quantifying neocortical activity dynamics in awake, behaving animals (*17*–*19*), and optically manipulating the survival of newly formed synapses (*20*), we tested the hypothesis that ketamine accelerates the remission of a depression-like behavioral state by restoring lost spines in the PFC.

Results

Targeted, branch-specific spine remodeling underlies behavioral state transitions

We began by testing whether the induction of depression-related behavior in chronic stress models is associated with targeted effects on specific dendritic spine populations. To this end, we imaged the PFC through a prism (*13*, *16*) chronically implanted in the contralateral hemisphere (Fig. 1A). Using two-photon (2P) laser-scanning microscopy, we obtained high-resolution images of the apical dendrites of yellow fluorescent protein (YFP)–expressing projection neurons in the medial PFC (mPFC) [in Thy1/YFP-H mice (Jackson Labs)] before and after 21 days of exposure to corticosterone (CORT) (0.10 mg/ml in the drinking water) (*21*), the principal murine stress hormone (Fig. 1A). CORT is a critical mediator of chronic stress effects on behavior, and chronic CORT treatment recapitulates important aspects of the neuroendocrine response to chronic stress (*21*–*26*). The prism implantation procedure elicits a reactive gliosis limited to a volume of up to 50 μm from the face of the prism, whereas at distances of >50 μm, there is no evidence of gliosis or effects on spine remodeling (*13*, *16*). Therefore, we limited our analysis to distances of >50 μm from the prism face.

Chronic CORT recapitulated established depression- and anxiety-related behaviors (*27*–*31*), including increased immobility on the tail suspension test (TST), decreased sucrose preference, and decreased open-arm exploration in an elevated plus maze (fig. S1). Chronic CORT also increased spine elimination rates (Fig. 1B) and decreased spine formation rates (Fig. 1C). To assess the time course and stability of these changes, we quantified spine remodeling in mice imaged after both 10 and 21 days of CORT exposure (fig. S2). Similar effects were observed at the 10-day time point, and the vast majority (88.8%) of spines that were eliminated after 10 days did not recur spontaneously at the 21-day time point. To test whether these effects generalized to other forms of chronic stress, we repeated these experiments in mice exposed to 21 days of repeated restraint stress, a commonly used psychosocial stress paradigm, and found comparable effects on both behavior (fig. S3, A to D) and spine remodeling (fig. S3, E and F).

Stress-induced dendritic atrophy is limited to specific prefrontal projections (*32*), and functionally homogeneous synaptic inputs cluster on individual branch segments of the apical dendritic arbor in cortical pyramidal cells (*33*–*40*). We therefore examined the spatial distribution of stress-related spine elimination in order to assess whether spine loss occurred randomly throughout the apical dendritic tree or targeted specific dendritic branch segments. Eliminated spines were not randomly distributed. Whereas most dendritic branches exhibited spine elimination rates comparable to those observed in controls, spine elimination rates were two to four times as high (~35 to 40%) in a subset of branches, yielding a bimodal distribution across dendritic branch segments (Fig. 1D). Furthermore, within individual branches, spine loss was strongly spatially clustered to a significantly greater degree than would be expected by chance, given the observed rates of spine loss (Fig. 1E). Similar, spatially clustered effects were also observed after repeated restraint stress (fig. S3G), indicating that the emergence

[1]Brain and Mind Research Institute, Department of Psychiatry, and Sackler Institute for Developmental Psychobiology, Weill Cornell Medicine, New York, NY 10021, USA. [2]Departments of Bioengineering and of Psychiatry and Behavioral Sciences, Stanford University, Stanford, CA 94305, USA. [3]Department of Neurochemistry, Graduate School of Medicine, The University of Tokyo, 7-3-1 Hongo, Bunkyo-ku, Tokyo 113-0033, Japan. [4]Laboratory of Structural Physiology, Center for Disease Biology and Integrative Medicine, Faculty of Medicine, The University of Tokyo, Bunkyo-ku, Tokyo 113-0033, Japan. [5]International Research Center for Neurointelligence (WPI-IRCN), UTIAS, The University of Tokyo, Bunkyo-ku, Tokyo 113-0033, Japan.
*These authors contributed equally to this work.
†Corresponding author. Email: col2004@med.cornell.edu

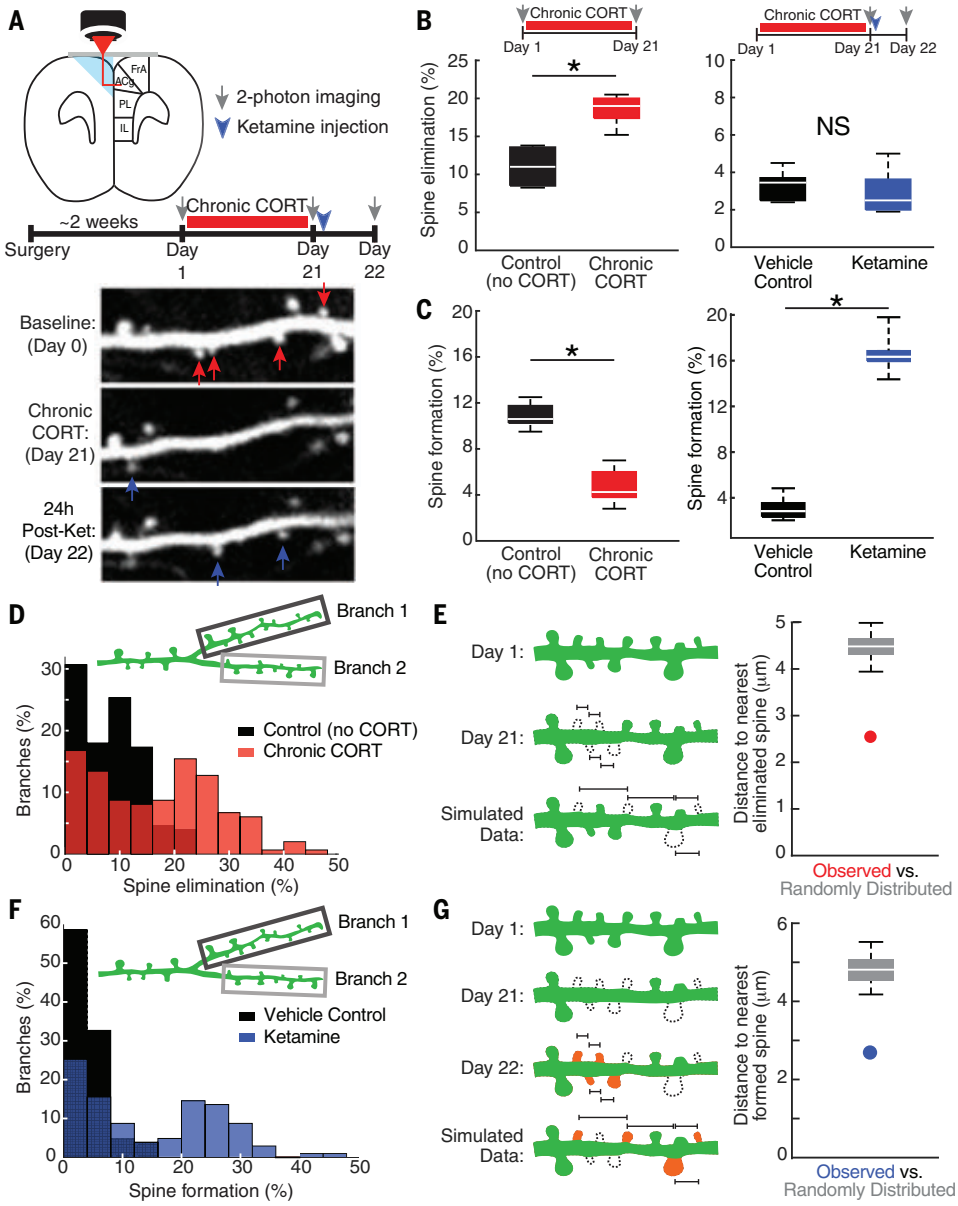

Fig. 1. Targeted, branch-specific spine remodeling underlies behavioral state transitions. (**A**) 2P spine imaging of YFP-expressing neurons through a microprism implanted across the midline in the mPFC before and after 21 days of chronic CORT exposure and after antidepressant-dose ketamine (post-ket) (10 mg/kg ip). Red and blue arrows indicate eliminated and formed spines, respectively. FrA, frontal association cortex; ACg, anterior cingulate cortex; PL, prelimbic cortex; IL, infralimbic cortex. (**B**) Spine elimination increased (*P = 0.0043, Wilcoxon W = 15.0) after 21 days of chronic CORT (n = 6 mice) compared with that in controls (n = 5 mice), whereas ketamine had no effect on spine elimination (n = 7 mice) compared with that in vehicle-treated controls (n = 6 mice). Throughout, box plots depict the median, interquartile range, and minimum and maximum excluding outliers, and outliers are plotted individually. NS, not significant. (**C**) Spine formation decreased (*P = 0.0087, Wilcoxon W = 44.5) after 21 days of chronic CORT, whereas ketamine increased spine formation. (**D**) Spine elimination per dendritic branch segment was significantly elevated (t = 8.05, df = 297, $P = 1.9 \times 10^{-14}$) and bimodally distributed in the chronic CORT–exposed group (n = 149 branches from 5 mice) compared with that in controls (n = 150 branches from 6 mice), such that 39.6% of dendritic branch segments in the chronic CORT–exposed group exhibited spine elimination rates that were >2 standard deviations above the mean for controls. (**E**) Spatially clustered spine elimination after chronic CORT exposure. The average distance between an eliminated spine and its nearest eliminated neighbor (2.5 μm) (red circle) was significantly reduced (P < 0.001), relative to what would be expected by chance given the observed rate of spine elimination, in simulations denoted by the box plot (see supplementary materials). (**F**) Spine formation per dendritic branch segment was significantly elevated (t = 9.48, df = 205, $P = 6.7 \times 10^{-18}$) and bimodally distributed in the ketamine-treated group (n = 103 branches from 7 mice) compared with that in vehicle-treated controls (n = 104 branches from 7 mice), such that 51.5% of dendritic branch segments in the ketamine-treated group exhibited spine formation rates that were highly elevated compared with those in vehicle-treated controls. (**G**) The average distance between a newly formed spine and its nearest eliminated neighbor (2.8 μm) (blue circle) was significantly reduced (P < 0.001) relative to what would be expected by chance given the observed rate of spine formation, as estimated in simulated data.

of depression-related behavior in multiple models is associated with spatially clustered, branch-specific spine loss.

Next, we tested whether the remission of depression-related behavior after ketamine treatment was associated with a targeted reversal of stress-induced spine loss. We used 2P imaging to visualize dendritic spine remodeling before and after chronic CORT exposure and again 24 hours after a single subanesthetic, antidepressant dose of ketamine [10 mg per kilogram of body weight, intraperitoneally (ip)] (Fig. 1A). Ketamine had rapid effects on depression-related behavior, reversing CORT effects on immobility in the TST, open-arm exploration in an elevated plus maze, and sucrose preference, relative to those in vehicle-treated controls (fig. S4) (*4*–*6*). Ketamine also increased spine formation rates to 16.8% over 24 hours but did not significantly alter spine elimination rates (Fig. 1, B and C). Newly formed spines were also clustered and branch specific. Ketamine effects on spine formation were bimodally distributed across individual dendritic branches and driven by a subset of branches (51.5%) for which spine formation rates were 5 to 10 times as high as the mean formation rate in vehicle-treated controls (Fig. 1F). Likewise, ketamine's effects on spine formation were spatially clustered relative to controls and to a significantly greater degree than would be expected by chance given the observed rates of spine formation (Fig. 1G and fig. S3, H to J).

Antidepressant-dose ketamine selectively restores lost spines

Rather than compensating for stress-related synapse loss by increasing spine formation indiscriminately, ketamine may instead restore precisely the same synaptic connections lost

during chronic CORT exposure. To test this, we began by assessing whether spines formed after ketamine treatment appeared in the same dendritic location as spines lost during chronic CORT exposure (Fig. 2A). Of the newly formed spines, 47.7% were located <2 μm from a spine lost during chronic CORT exposure, a proportion significantly greater than the 14.5% observed in vehicle-treated controls (Fig. 2B), as well as the 17.0% expected by chance if new spines were randomly distributed (Fig. 2C), given the observed rates of CORT-induced spine elimination and ketamine-induced spine formation. These selective reversal effects were not observed in vehicle-treated controls (Fig. 2B) or in CORT-treated mice imaged repeatedly after 10 and 21 days of exposure (fig. S2), indicating that the observed rescue of eliminated spines was not attributable to technical obstacles in resolving spines at a single time point. At the same time, whereas spinogenesis after ketamine treatment fully reversed the effects of CORT on spine density (Fig. 2D), many of these newly formed spines appeared in new positions where a spine did not previously exist (Fig. 2A, de novo formed spines). This meant that a majority (mean = 51.7%) of spines lost during chronic CORT exposure were not restored by ketamine treatment (Fig. 2E). Thus, these longitudinal imaging experiments reveal that ketamine only partially restores the baseline configuration of spines on PFC projection neurons and that substantial CORT-induced spine loss persists after treatment, despite the normalization of depression-related behaviors tested at the same time point (fig. S4).

Two additional experiments revealed that ketamine not only restored lost spines but also generated functional synapses. First, motivated by prior work showing that essentially all new spines that persist for at least 4 days contain functional synapses (*41*, *42*), we imaged the same dendritic segments 4 days later (fig. S5A). Ketamine increased the formation of these long-lasting spines (fig. S5B), which are highly likely to contain functional synapses. Furthermore, restored spines (those that formed <2 μm from a previously lost spine) were significantly more likely to persist than de novo formed spines (fig. S5C). On the basis of these data, we estimate that ketamine restored 20.4 to 31.0% of lost synapses in their original positions after 4 days, versus the restoration of 0 to 2.4% in vehicle-treated controls (fig. S5D). Second, we tested for corresponding changes in spine density in fixed tissue and synapse density as quantified by immunofluorescence labeling of the postsynaptic density protein PSD-95. Chronic CORT treatment decreased both PSD-95 density and dendritic spine density throughout the PFC, including the anterior cingulate, prelimbic, and infralimbic subregions, whereas ketamine had the opposite effect (Fig. 2, F and G and fig. S6).

Ketamine rescues PFC microcircuit dysfunction

How CORT- and ketamine-induced spine remodeling relates to prefrontal microcircuit function is not well understood. We hypothesized that the CORT-induced elimination of excitatory synapses within dendritic spines would be associated with a loss of functional coupling between PFC neurons. We therefore used 2P calcium imaging to characterize functional connectivity in PFC microcircuits before and after 10 days of chronic CORT exposure and again 24 hours after ketamine treatment (Fig. 3, A to C). Using vascular landmarks, the contours of the prism,

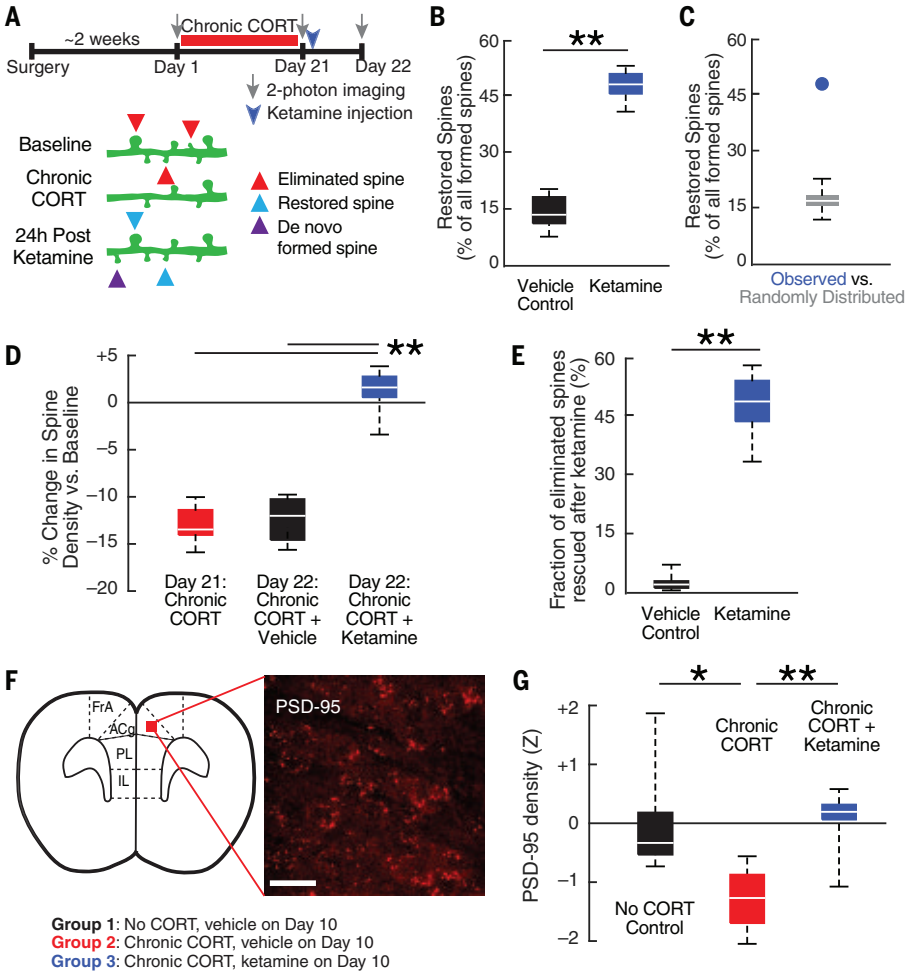

Fig. 2. Ketamine selectively restores spines lost during chronic CORT exposure. (**A**) Experimental timeline (identical to that in Fig. 1A). Restored spines (blue) were defined as spines that formed in the 24-hour period after ketamine treatment in a position <2 μm from a previously eliminated spine. (**B**) Of newly formed spines, 47.7% were located <2 μm from a spine lost during chronic CORT exposure (n = 7 mice), a proportion significantly greater than the 14.5% observed in vehicle-treated controls (n = 6 mice; *P = 0.0012, Wilcoxon W = 21.0). (**C**) The observed fraction of restored spines (blue circle) was significantly (P < 0.001) greater than expected by chance given the observed rate of spine formation in simulated data in which formed spines were randomly distributed (box plot) (see supplementary materials). (**D**) The change in spine density from day 1 (baseline) to day 21 (post–chronic CORT) or day 22 (postketamine) was quantified by subtracting the spine elimination rate from the spine formation rate during the specified imaging interval. Ketamine reversed chronic CORT effects on spine density [Kruskal-Wallis analysis of variance (ANOVA), **$P = 5.6 \times 10^{-4}$, $\chi^2 = 14.96$]. (**E**) Of spines lost during chronic CORT, 48.3% were restored after ketamine treatment (n = 7 mice) versus 3.3% in vehicle-treated controls (n = 6 mice; **P = 0.0012, Wilcoxon W = 21.0). (**F**) Representative confocal image of PSD-95 immunofluorescence in the mPFC. Scale bar, 30 μm. (**G**) PSD-95 density (z-scored with respect to the mean density in controls; N = 18 samples from n = 6 subjects per group) varied by experimental condition (mixed-effects ANOVA, $F_{2,45}$ = 10.39, P = 0.0019). In the dorsal mPFC, PSD-95 density was significantly lower in the chronic CORT–treated group than in untreated controls (t_{10} = 2.43, *P = 0.035). Ketamine reversed this effect (t_{10}= 4.15, **P = 0.002). (For other PFC subregions, see fig. S6.)

and measurements of depth from the cortical surface, we were able to record activity repeatedly from the same PFC cell populations, which were stably expressing a genetically encoded calcium sensor (GCaMP6s) (17) over this 11-day period. We selected this interval to avoid the potentially toxic accumulation of GCaMP that can occur after prolonged, virally driven expression and on the basis of spine imaging experiments showing comparable effects at 10 and 21 days (fig. S2). We tested for CORT- and ketamine-induced changes in functional connectivity between PFC neurons, as indexed by correlation matrices quantifying correlated activity across all cells in a field of view (Fig. 3D).

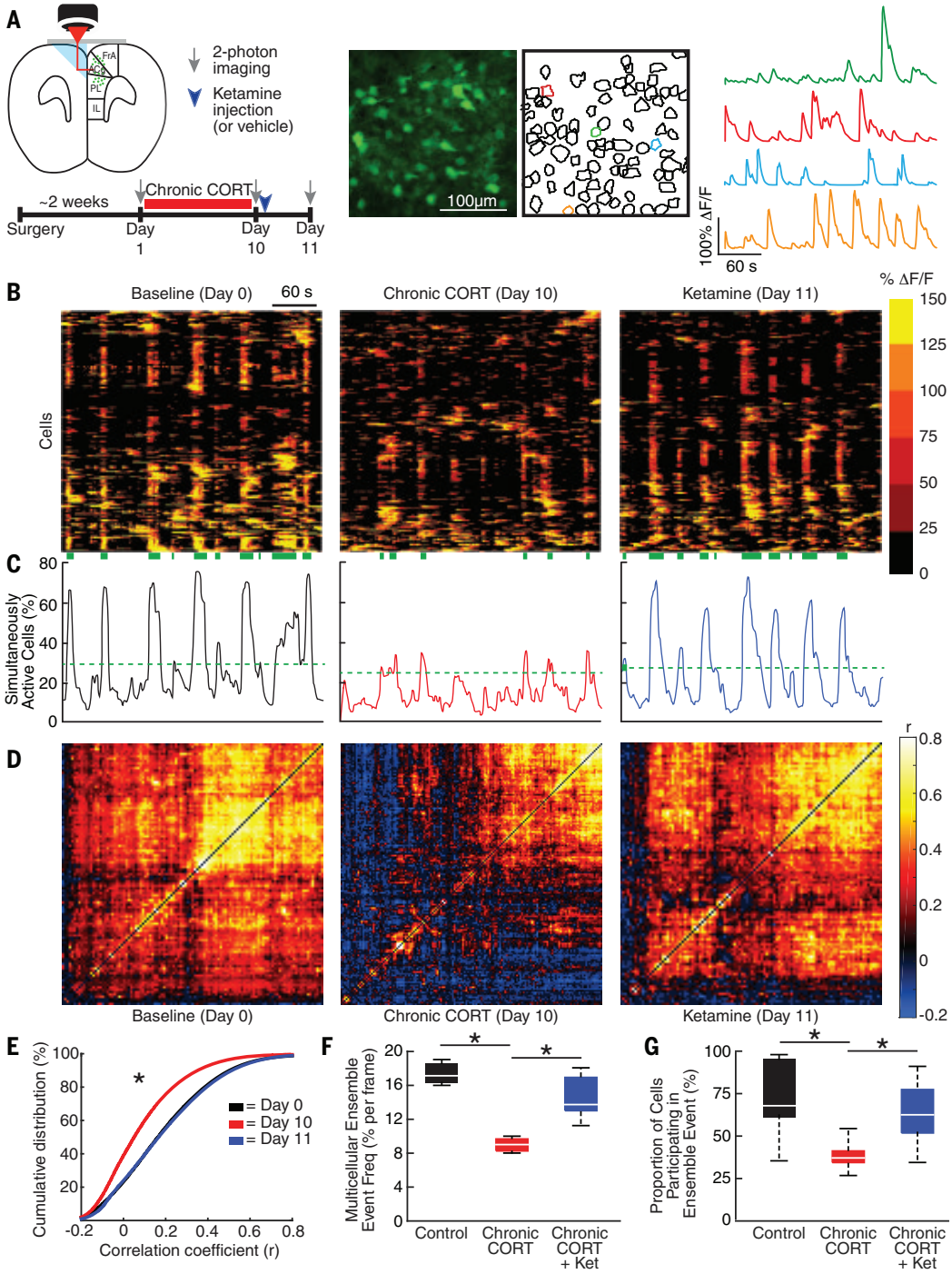

Fig. 3. Ketamine rescues CORT-induced microcircuit dysfunction. (**A**) 2P calcium imaging of GCaMP6s-expressing neurons through a microprism implanted across the midline in the mPFCs of head-fixed, awake mice. Calcium imaging occurred before and after 10 days of chronic CORT treatment and 24 hours after ketamine treatment (10 mg/kg ip). (**B**) Raster plots depicting changes in activity ($\Delta F/F$) over time for a representative neuronal population before and after chronic CORT and 1 day after ketamine treatment. Each row represents a single cell. Green bands below denote statistically significant multicellular ensemble events. (**C**) Representative traces depicting the proportion of simultaneously active cells over time for the neuronal population depicted in (B). The green dashed line delineates the upper end of a 99.9% confidence interval for the proportion of simultaneously active cells in shuffled data (see supplementary materials). (**D**) Representative correlation matrices quantifying functional connectivity between each cell and every other cell. (**E**) Cumulative distribution plot of cell-cell correlations for all cells across all animals in each condition (N = 98,878 correlations at baseline, N = 145,467 after chronic CORT, N = 114,593 after ketamine from n = 3 mice). Mixed-effects ANOVA (subject = random effect) showed that the distribution shifted left (decreased) after chronic CORT (mean correlation coefficient r = 0.084 versus 0.188 at baseline; t = 3.02; P = 0.0025 for the difference between chronic CORT and baseline), and ketamine rescued this effect (mean r = 0.187; t = 0.39; P = 0.698 for the difference between ketamine and baseline). (**F**) The frequency of multicellular ensemble events (expressed as the probability of an ensemble event occurring in any given time frame) decreased after chronic CORT (median, 8.4% versus 17.4% at baseline) and was rescued after ketamine treatment (chronic CORT + Ket) (median, 14.7%; mixed-effects ANOVA, $F_{2,15}$ = 17.1, P = 0.00013 for main effect of group; N = 8 observations per experimental condition). (**G**) The proportion of cells participating in a multicellular ensemble event also decreased after chronic CORT (mean = 37.7% versus 74.1% at baseline for N = 39 and N = 28 multicellular ensemble events in n = 3 mice) and was rescued after ketamine treatment (mean = 63.8% for N = 35 events; mixed-effects ANOVA, $F_{2,93}$ = 10.8, P = 0.024). By contrast, in untreated controls, no significant changes occurred over time in any of the measures in (E) to (G) (fig. S5). *P < 0.05 (significantly different post hoc contrast, Holm-Bonferroni corrected).

Chronic CORT significantly reduced functional connectivity within PFC microcircuits (Fig. 3, D and E). At baseline, most activity in a given field of view occurred at discrete time points involving many simultaneously active cells (Fig. 3, B and C), reminiscent of the multicellular ensemble activity that has been implicated in pattern formation and stimulus encoding and is disrupted in animal models of neuropsychiatric disease (43–45). After chronic CORT exposure, the frequency of these multicellular ensemble events (see supplementary materials) was significantly reduced (Fig. 3F), and they tended to involve significantly fewer cells (Fig. 3G). Ketamine rescued both effects 24 hours after treatment (Fig. 3, E to G). By contrast, the correlated activity and multicellular ensemble events were stable over time in untreated controls (fig. S7).

To better understand how ketamine's effects on spine formation and microcircuit activity relate to its antidepressant behavioral effects,

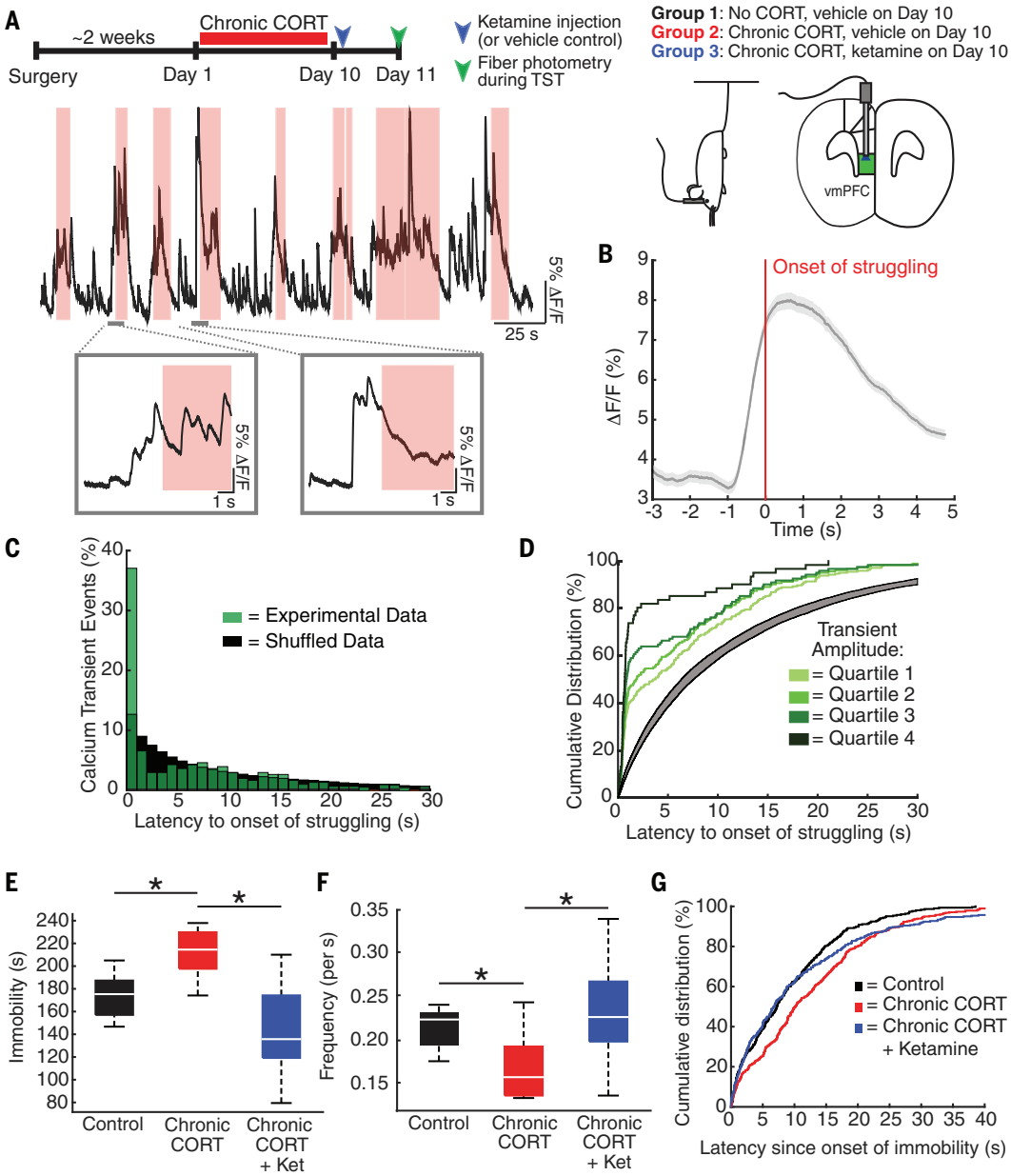

Fig. 4. Ketamine rescues CORT effects on coordinated PFC activity and active avoidance behavior. (**A**) (Top) Experimental timeline and schematic showing optical fiber placement in the vmPFC and representative fiber photometry recording of GCaMP6s-expressing neurons during tail suspension. (Bottom) A representative photometry trace in which pink bands indicate periods of struggling to escape. Insets show representative examples of GCaMP6s activity increasing before the onset of struggling. (**B**) Mean vmPFC activity ($\Delta F/F$) ± SEM (gray band) time locked to the onset of struggling (time = 0), averaged over all bouts of struggling across all mice. Increased vmPFC activity preceded the onset of struggling by ~1 s. (**C**) Distribution of calcium-transient events during bouts of immobility by latency to the onset of the next bout of struggling. Monte Carlo simulation showed that during bouts of immobility, calcium transients predicted the onset of struggling: The median latency to the onset of struggling (4.0 s) was significantly shorter than would be expected by chance (7.0 s) in randomly shuffled data ($P < 0.0001$ across 10,000 iterations), and 37.1% of all transients occurred <1 s before the onset of struggling. (**D**) Cumulative distribution of calcium transients by latency to the onset of struggling, grouped by transient amplitude. Linear mixed-effects modeling showed that latency to the onset of struggling varied with transient amplitude ($t_{303} = 3.84$, $P = 0.0015$), such that larger transients predicted shorter latencies. The gray band denotes the 99% confidence interval for the median latency in shuffled data. The median latency for transients in all four groups was less than that expected by chance in shuffled data, with the largest effects occurring for transients in the upper quartile (median latency = 0.69 s). (**E**) Chronic CORT increased the total duration of immobility during tail suspension, whereas ketamine rescued this effect [$n = 8$ control mice, $n = 10$ chronic CORT–treated mice, $n = 14$ chronic CORT–plus–ketamine (CORT+ket)–treated mice; Kruskal-Wallis ANOVA, $^*P = 0.0003$, $\chi^2 = 15.93$]. (**F**) Chronic CORT significantly reduced the frequency of vmPFC calcium transients during tail suspension, and ketamine rescued this effect ($n = 8$ control mice, $n = 10$ chronic CORT–treated mice, $n = 11$ ketamine-treated mice; Kruskal-Wallis ANOVA, $^*P = 0.0083$, $\chi^2 = 9.59$). (**G**) Cumulative distribution of calcium transients by latency since the onset of immobility showing the accumulation of transients over time, sorted by experimental condition. Linear mixed-effects modeling showed that vmPFC activity accumulated more slowly over time after chronic CORT exposure (median latency, 10.2 s for $n = 378$ transients versus 7.2 s for $n = 305$ transients in controls), and ketamine rescued this effect (median latency, 6.8 s for $n = 378$ transients; $t_{983} = 2.21$).

we used fiber photometry (18, 19) to record the activity of GCaMP6s-expressing neurons in the ventromedial PFC (vmPFC) during tail suspension (Fig. 4A and fig. S8). The vmPFC has been implicated in driving motivated escape behavior during similar behavioral challenge assays (46) in which mice alternate between periods of passive immobility and active struggling to escape. Prolonged immobility is a consistent finding in chronic stress models (47), and antidepressants tend to reverse this behavior (48, 49). PFC activity was significantly elevated during periods of struggling (fig. S9), an effect that was likely driven in part by differences in locomotor activity (46). However, we also found that increased PFC activity preceded the onset of struggling, predicting the shift from immobility to struggling behavior within ~1 s on average (Fig. 4B). This effect was not due to systematic delays in recording the onset of struggling (fig. S10). PFC activity during bouts of immobility tended to occur at the end of a bout (<1 s before struggling) and predicted a significantly shorter latency to the onset of struggling than randomly shuffled data (Fig. 4C). Larger calcium transients predicted progressively shorter latencies to struggling, such that the largest PFC activity events predicted a shift from immobility to struggling within <1 s >80% of the time (Fig. 4D).

Chronic CORT exposure significantly reduced the frequency of calcium transients during the TST (Fig. 4F). Calcium transients also accumulated more slowly over time during bouts of immobility and were associated with longer immobility periods and increased immobility overall (Fig. 4, E and G). Ketamine reversed these deficits.

Prefrontal spinogenesis sustains the remission of depression-related behavior over time

Lastly, we investigated whether PFC spinogenesis is required for—or merely correlated with—changes in behavior and circuit function after antidepressant treatment. We began by characterizing the time course of these changes in the hours and days after ketamine treatment. As in (5), we observed rapid effects on motivated avoidance behavior in the TST, beginning just 3 hours after ketamine treatment (10 mg/kg ip), peaking 24 hours postinjection, and persisting for up to a week (Fig. 5, A and B). However, ketamine effects on spine formation were slower: Formation rates were not significantly altered at 3 to 6 hours posttreatment but were markedly elevated at 12 to 24 hours (Fig. 5C). Increased spine formation in Thy1/YFP–expressing projection neurons is thus not required for the induction of ketamine's acute effects on immobility behavior 3 to 6 hours after treatment. In accordance with this interpretation, we found no association between spine formation and immobility in the first day after treatment (fig. S11). By contrast, individual differences in the restoration of spines lost during chronic CORT exposure were correlated with immobility behavior 2 to 7 days after treatment (Fig. 5D).

To investigate the temporal relationship between spinogenesis and ketamine's effects on PFC microcircuit dynamics, we repeated the 2P calcium imaging experiment in Fig. 3, imaging before and after chronic CORT exposure and 3, 12, and 24 hours after ketamine treatment (Fig. 5E). As in Fig. 3, chronic CORT interfered with correlated activity, reduced the frequency of multicellular ensemble events, and decreased the proportion of cells participating in these events (Fig. 5, F to K). Ketamine reversed all three effects within 3 hours of treatment (Fig. 5, I to K, and fig. S12), ~9 hours before effects on spine formation were detectable in Fig. 5C. This suggests that ketamine-induced spine remodeling may be an activity-dependent consequence, rather than a cause of changes in circuit function. In conjunction with the data in Fig. 5D, these results indicate that prefrontal spinogenesis is not required for inducing ketamine's effects on circuit function and behavior, but it may be important for sustaining these effects over time.

To test this hypothesis, we used a photoactivatable probe—activated synapse–targeting photoactivatable Rac1 (AS-PaRac1)—to optically manipulate the survival of newly formed spines (20). This construct is selectively expressed in newly formed and recently potentiated synapses, and upon prolonged photoactivation by blue light, it causes spine shrinkage and collapse (20). To validate this tool for manipulating the survival of spines formed after ketamine treatment, we injected a viral vector driving AS-PaRac1 expression (AAV1-SARE-Arc-PSDdelta1.2-mVenus-PARac1) into the mPFC and implanted a microprism for visualizing changes in AS-PaRac1 expression over time. As in (20), AS-PaRac1 expression was sparse and punctate in the mPFC (fig. S13, A to C) and increased significantly 1 day after ketamine treatment [mean increase in AS-PaRac1-positive (AS-PaRac1$^+$) puncta = 92.3%] (fig. S13, D and E). Furthermore, ketamine induced a spatially clustered pattern of AS-PaRac1 expression (fig. S13, F to H) that resembled its spatially clustered effects on spine formation, with 41.4% of AS-PaRac1$^+$ puncta occurring in spatially clustered pairs or triplets, versus <5% in simulated data in which an equal number of puncta were randomly distributed throughout an equivalent imaging volume (fig. S13, I and J) (see Materials and methods for details).

To test whether prefrontal spinogenesis is required for maintaining ketamine's effects on PFC circuit function and behavior, we injected viral vectors driving AS-PaRac1 and GCaMP6s expression bilaterally in the mPFC, implanted dual-core optical fibers, and treated the mice with CORT for 10 days, followed by ketamine on day 11, photoactivation (20-mW, 150-ms pulses at 1 Hz for 1 hour) 1 day after ketamine treatment, and behavioral testing 2 days after ketamine treatment (Fig. 6A). To validate this strategy for deleting newly formed spines, a separate cohort of Thy1/YFP-H transgenic mice was injected with AS-PaRac1 but not GCaMP6s.

Photoactivating AS-PaRac1 increased spine elimination and blocked the effects of ketamine on spine formation (Fig. 6B) relative to spine elimination and spine formation in controls exposed to the same ketamine and photoactivation paradigm but not expressing AS-PaRac1. Behavioral testing 2 days after ketamine treatment showed that deleting newly formed spines by photoactivating AS-PaRac1 blocked the long-term effects of ketamine on PFC activity events (calcium transients) and on motivated avoidance behavior in the TST (Fig. 6, C and D), a behavior that is linked specifically to PFC function (Fig. 4) (46). This effect on behavior was selective: Ketamine's long-term effect on sucrose preference was preserved (Fig. 6E), indicating that spine remodeling in other brain regions or spine-independent processes may be involved in sustaining ketamine's effects on other depression-related behaviors. To evaluate the effect of eliminating a random subset of spines unrelated to ketamine treatment, we also tested mice after activating AS-PaRac1 3 hours after ketamine treatment—before the onset of ketamine-induced spine formation. This manipulation had no effect on immobility behavior at 2 days after treatment (Fig. 6F).

Discussion

A growing body of work has begun to elucidate the molecular mechanisms underlying stress and antidepressant effects on depression-related behavior, including neurotrophic factors, inflammatory signals, and regulators of neuronal excitability (4, 5, 50–59). By contrast, the circuit-level mechanisms mediating transitions between depression-related behavioral states over time are not well understood. Our findings delineate one such mechanism. The emergence of depression-related behavior in multiple chronic stress models was associated with spatially clustered spine loss and a loss of functional connectivity within PFC microcircuits, driven in part by the disruption of coordinated activity in multicellular ensembles, which play an important role in multiple computational processes (43–45). Ketamine facilitated the transition to recovery by rescuing these effects in both stress models. Varying stress mediators (60–66) and circuit-level mechanisms (51, 67–76) may contribute to model-specific stress effects on behavior and circuit function. Synaptic remodeling in PFC projection neurons may also influence depression-related behavior indirectly, through effects on social hierarchical interactions, which are modulated by synaptic efficacy and thalamocortical inputs to the PFC (77–79). Distinct processes may also be involved in sustaining the long-term effects of conventional antidepressants. These caveats notwithstanding, our convergent findings implicate complementary effects on spine remodeling and multicellular ensemble activity in the induction and remission of a depression-related behavioral state.

Both CORT and ketamine are well positioned to regulate dendritic spine remodeling at a molecular level. Circadian oscillations in glucocorticoid

activity have been implicated in balancing spine formation and elimination through both transcription-dependent processes and rapid, nongenomic mechanisms converging on the regulation of actin cytoskeletal remodeling by LIM kinase 1 and its substrate cofilin (*80*). Chronic excessive CORT exposure disrupts this balance, leading to widespread spine loss (*80*, *81*). Stress effects on microglial activation may also be involved (*82*–*86*). Ketamine is well positioned to regulate spine density through the activation of brain-derived neurotrophic factor (BDNF)–TrkB and mammalian target of rapamycin complex 1 (mTORC1) signaling (*4*, *5*, *50*). BDNF-dependent signaling may also be involved in

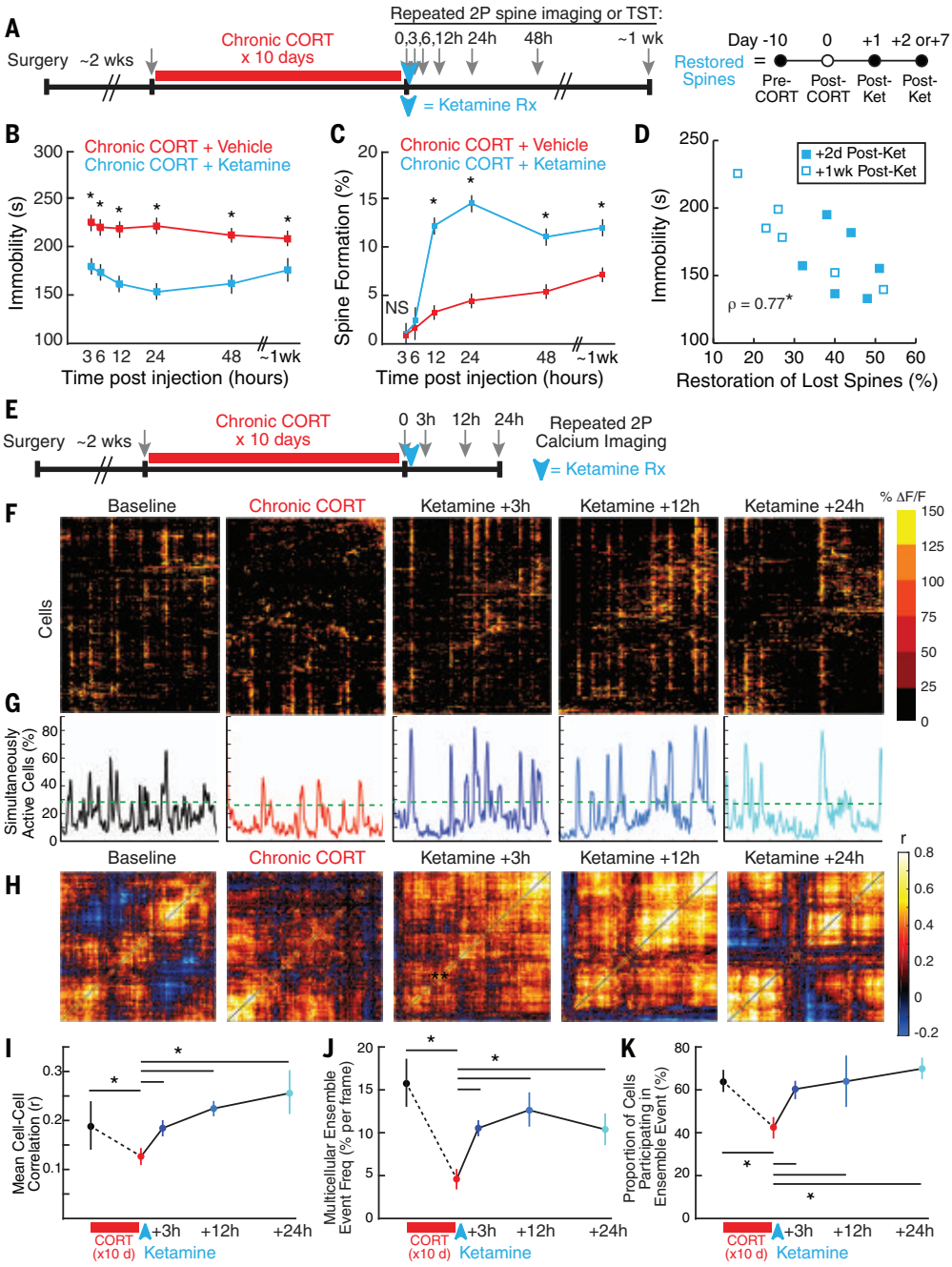

Fig. 5. Prefrontal spinogenesis is not required for inducing ketamine's effects on behavior or circuit function. (**A**) Experimental timeline for data in (B) to (D). To avoid habituation in the TST due to repeated testing on the same day, each subject in (B) was tested only once in this assay (between-subjects design; N = 12 subjects per time point per group). For 2P imaging in (C), each subject was assessed repeatedly at each specified time point (within-subjects design; N = 12 subjects per group). (**B**) Rapid effect of ketamine on immobility in the TST (main effect of treatment, $F_{1,132}$ = 149.1, P < 0.0001; main effect of time, $F_{5,132}$ = 1.20, P = 0.314; interaction, $F_{5,132}$ = 1.24, P = 0.295). *P < 0.002 (significant post hoc linear contrast). (**C**) Delayed effect of ketamine on spine formation (main effect of treatment, $F_{1,108}$ = 145.7, P < 0.0001; main effect of time, $F_{5,108}$ = 81.6, P < 0.0001; interaction, $F_{5,108}$ = 17.4, P < 0.0001). *P < 0.0006 (significant post hoc linear contrast). NS, not significant. (**D**) The survival of restored spines (the percentage of spines lost after chronic CORT and restored after ketamine) was significantly correlated with immobility behavior 2 to 7 days after treatment (Spearman's rho = 0.770, P = 0.0034). (**E**) Experimental timeline for data in (F) to (K). To test whether ketamine effects on microcircuit activity preceded or followed effects on spines, 2P calcium imaging was performed before and after chronic CORT and 3, 12, and 24 hours after ketamine treatment (within-subjects design). (**F**) Raster plots depicting changes in activity ($\Delta F/F$) over time for a representative neuronal population before and after chronic CORT and 1 day after ketamine treatment, as in Fig. 3B. (**G**) Representative traces depicting the proportion of simultaneously active cells over time for the neuronal population depicted in (F). The green dashed line delineates the upper end of a 99.9% confidence interval for the proportion of simultaneously active cells in shuffled data (see supplementary materials). (**H**) Representative correlation matrices quantifying functional connectivity between each cell and every other cell. (**I**) There was a reduction in functional connectivity (mean correlation) after chronic CORT, and ketamine rescued this effect within 3 hours of treatment (N = 5 to 8 samples per condition from n = 3 subjects; mixed-effects ANOVA, subject = random effect; main effect of time, $F_{4,32}$ = 3.05, P = 0.032). For cumulative distribution functions for all correlation coefficients, see fig. S12. (**J**) The frequency of multicellular ensemble events (expressed as the probability of an ensemble event occurring in any given time frame) decreased after chronic CORT and was rescued within 3 hours of ketamine treatment (mixed-effects ANOVA; main effect of time, $F_{4,32}$ = 9.28, P = 4.27 × 10^{-5}). (**K**) The proportion of cells participating in a multicellular ensemble event also decreased after chronic CORT and was rescued within 3 hours of ketamine treatment (mixed-effects ANOVA; main effect of time, $F_{4,341}$ = 7.65, P = 6.55 × 10^{-6}). For (I) to (K), *P < 0.05 (significantly different post hoc contrast, Holm-Bonferroni corrected).

facilitating clustered spine restoration after ketamine treatment. Activity-dependent BDNF signaling at existing spines can "prime" neighboring dendritic sites for structural plasticity by activating a tripartite signaling mechanism involving Cdc42, Rac1, and RhoA (*87*).

Our results also define a specific causal role for PFC spinogenesis in mediating transitions among a depression-related behavioral state, behavioral remission, and spontaneous recurrence. Ketamine's acute effects on depression-related behavior and circuit function occur rapidly and precede the onset of spine formation, which in turn suggests that spine remodeling may be an activity-dependent adaptation to changes in circuit function (*83*, *88*) and is consistent with theoretical models implicating synaptic homeostasis mechanisms in depression and the stress response (*89*, *90*). Although not required for inducing ketamine's effects acutely, these newly formed spines are critical for sustaining the antidepressant effect over time. Of note, interfering with ketamine-induced spine formation blocked its effects on motivated escape behavior but not on sucrose preference, indicating a specific role for prefrontal spinogenesis in sustaining some but not all antidepressant behavioral changes. Spine remodeling in the hippocampus, amygdala, nucleus accumbens, and other structures may support other behaviors, and some behavioral changes may be sustained by other mechanisms (*5*, *89*, *91*–*95*).

By monitoring spine remodeling longitudinally, our experiments also reveal that although ketamine reverses chronic CORT effects on spine density and behavior, this apparent normalization

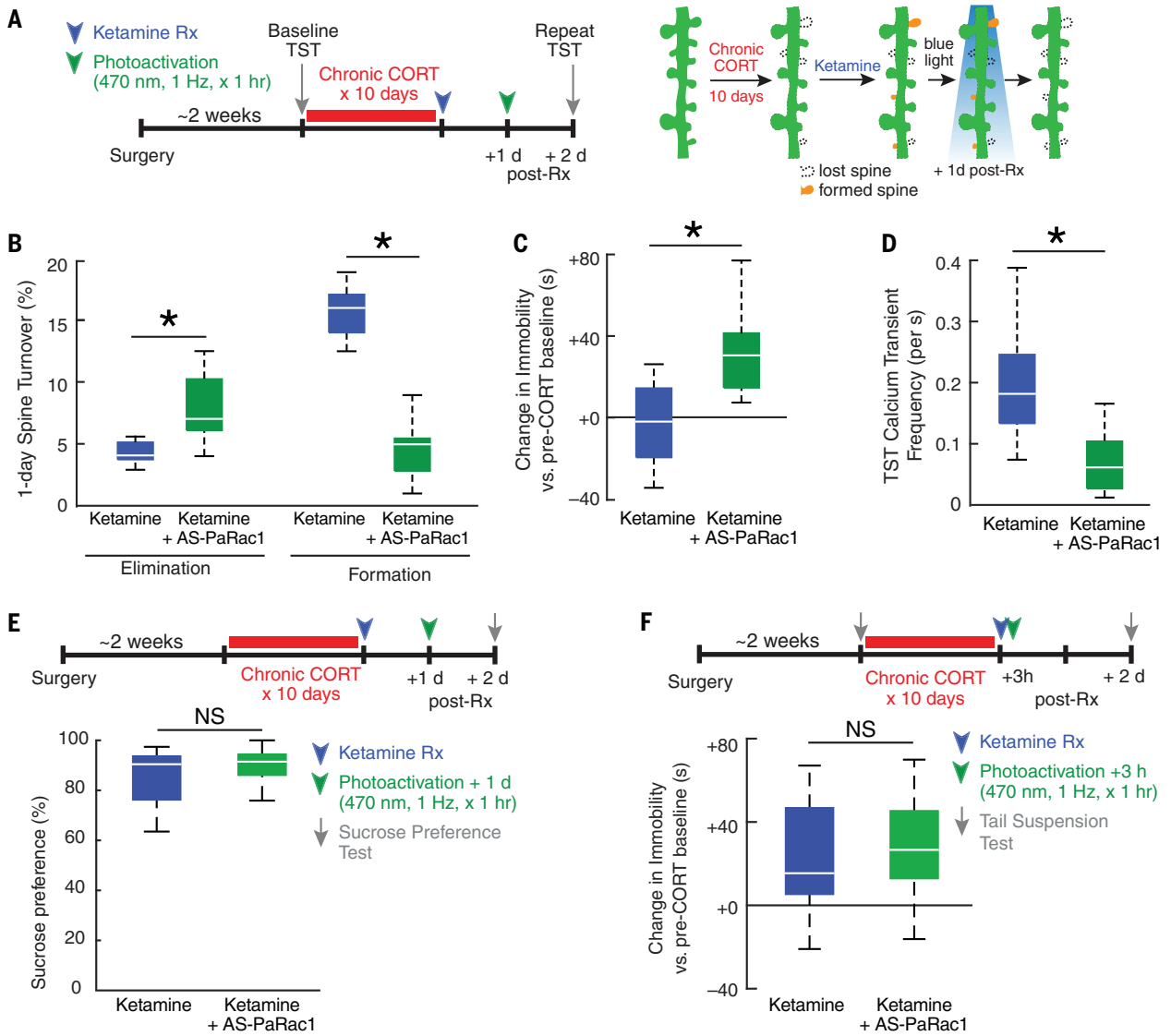

Fig. 6. Prefrontal spinogenesis sustains antidepressant-induced behavioral recovery over time. (**A**) Experimental time course schematic. To control for individual differences in TST behavior as in a recently published report (*72*), we tested subjects before chronic CORT exposure and again 2 days after ketamine treatment (Rx) to determine whether ketamine reversed CORT effects on immobility and whether maintaining this effect required spine formation. (**B**) Photoactivating AS-PaRac1 (N = 7 mice) blocked ketamine effects on spine formation (Wilcoxon W = 50.0, *P = 0.0025) (right) and increased spine elimination (Wilcoxon W = 18.0, *P = 0.0177) (left) compared with that in controls not expressing AS-PaRac1 (N = 5 mice). (**C**) Photoactivating AS-PaRac1 interfered with the maintenance of ketamine's effects on immobility behavior ($F_{1,17}$ = 9.96, *P = 0.0058) and (**D**) calcium-transient frequency ($F_{1,17}$ = 16.6, *P = 0.019) during tail suspension 2 days after treatment. (**E**) No effect of photoactivating AS-PaRac1 on sucrose preference behavior 2 days after ketamine treatment (N = 8 mice per group; Wilcoxon W = 63.0, P = 0.645). (**F**) Photoactivating AS-PaRac1 3 hours after ketamine treatment (before the onset of ketamine's effects on spine formation) had no effect on TST behavior 2 days after treatment ($F_{1,17}$ = 0.201, P = 0.660, N = 10 AsPaRac1 mice and N = 9 controls). NS, not significant.

belies the facts that most lost spines are not restored in their original positions and the baseline configuration of prefrontal spines is persistently altered. Whereas ~45% of new spines persisted for at least 4 days after ketamine treatment—indicating a high likelihood that they contain functional synapses—the remaining ~55% were quickly lost. Together, the failure to fully restore the baseline configuration of PFC synapses immediately after ketamine treatment and the subsequent loss of at least half of these newly formed spines may act as substrates for the spontaneous recurrence of depression-related behaviors—a common finding in clinical studies 1 week after treatment (*1–3*). Pharmacological and neurostimulatory interventions for enhancing and preserving the rescue of lost synapses may therefore be useful for promoting sustained remission.

Materials and methods summary

For additional details on each section below, as well as information on stress paradigms, ketamine treatment, stereotaxic coordinates, behavioral assays, immunohistochemistry, histological verification, and statistical analyses and other information, see the supplementary materials.

Animals

Young adult (aged 9 to 20 weeks) male Thy1/YFP-H transgenic mice and C57BL/6J mice were used for spine imaging and other experiments, respectively. Animals were group-housed under a 12-hour–12-hour light-dark cycle and provided ad libitum access to food and water (except during restraint stress). Sample sizes for each experiment were determined by using G*Power analysis software, on the basis of anticipated effect sizes that were estimated from previously published reports whenever they were available, and were powered to detect moderate, biologically meaningful effect sizes. All studies were approved by the Weill Cornell Institutional Animal Care and Use Committee.

Surgery

Stereotactic injections were performed under anesthesia to introduce viral vectors. AAV1-hSyn-GCaMP6s was injected into the PFC for calcium imaging and fiber photometry experiments. AAV1-SARE-Arc-PSDelta1.2-mVenus-PARac1 was expressed in the mPFC for spine deletion experiments. For prism implantations, 4-mm-diameter circular craniotomies were centered over the midline, and 1.5-mm right-angle borosilicate glass prisms were implanted in the mPFC contralateral to the viral injection site by using a digital micromanipulator. For fiber photometry experiments, a smaller craniotomy was opened, and 400-um-diameter multimodal optical fibers or custom dual-core implantable fiber optic cannulas were implanted above the injection sites.

Data acquisition summary

All in vivo images were acquired by using a 2P laser-scanning microscope (Olympus RS) with a Mai Tai DeepSee laser tuned to 920 nm and a 25×, 1.0NA water-immersion objective (4-mm working distance). For calcium imaging experiments, time-lapse images were acquired at ~1 frame per second in awake mice. *Z*-stacks through up to 250-μm depths were acquired for spine and AS-PaRac1 experiments. Fiber photometry was conducted during tail suspension behavior. GCaMP6s was excited with a 470-nm light-emitting diode (LED) through an optical fiber patch cord (modulated at a frequency of 521 Hz). Calcium signals were aligned to behavioral measures via transistor-to-transistor logic (TTL) pulses.

Data analysis summary

All data were analyzed by investigators who were blind to the experimental condition. Dendritic spine remodeling was assessed in ImageJ in Thy1/YFP mice on randomly selected dendritic branch segments containing clearly distinguishable spines. Formed and eliminated spines were identified in pairs of images obtained from the same areas over given intervals, and rates were quantified as a proportion of the total number of spines evaluated. Calcium imaging data preprocessing and cell segmentation were performed by using established methods (*90–92*) instantiated in MATLAB scripts. Fluorescence signal time series [the change in fluorescence divided by the baseline fluorescence ($\Delta F/F$)] were calculated for each neuron relative to a 40-s sliding window baseline. Photometry data were acquired continuously during tail suspension behavior and analyzed by using MATLAB scripts to normalize fluorescence signals and identify the onset and termination of calcium transients. For details on the analysis of clustered spine remodeling, calcium imaging (correlated activity and ensemble events), and photometry data (predicting TST behavior), see the supplementary materials.

REFERENCES AND NOTES

1. R. M. Berman *et al*., Antidepressant effects of ketamine in depressed patients. *Biol. Psychiatry* **47**, 351–354 (2000). doi: 10.1016/S0006-3223(99)00230-9; pmid: 10686270
2. C. A. Zarate Jr., *et al*., A randomized trial of an *N*-methyl-D-aspartate antagonist in treatment-resistant major depression. *Arch. Gen. Psychiatry* **63**, 856–864 (2006). doi: 10.1001/archpsyc.63.8.856; pmid: 16894061
3. L. Ibrahim *et al*., Course of improvement in depressive symptoms to a single intravenous infusion of ketamine vs add-on riluzole: Results from a 4-week, double-blind, placebo-controlled study. *Neuropsychopharmacology* **37**, 1526–1533 (2012). doi: 10.1038/npp.2011.338; pmid: 22298121
4. N. Li *et al*., mTOR-dependent synapse formation underlies the rapid antidepressant effects of NMDA antagonists. *Science* **329**, 959–964 (2010). doi: 10.1126/science.1190287; pmid: 20724638
5. A. E. Autry *et al*., NMDA receptor blockade at rest triggers rapid behavioural antidepressant responses. *Nature* **475**, 91–95 (2011). doi: 10.1038/nature10130; pmid: 21677641
6. P. Zanos *et al*., NMDAR inhibition-independent antidepressant actions of ketamine metabolites. *Nature* **533**, 481–486 (2016). doi: 10.1038/nature17998; pmid: 27144355
7. V. Phoumthipphavong, F. Barthas, S. Hassett, A. C. Kwan, Longitudinal effects of ketamine on dendritic architecture in vivo in the mouse medial frontal cortex. *eNeuro* **3**, ENEURO.0133-15.2016 (2016). doi: 10.1523/ENEURO.0133-15.2016; pmid: 27066532
8. R. S. Duman, J. Malberg, J. Thome, Neural plasticity to stress and antidepressant treatment. *Biol. Psychiatry* **46**, 1181–1191 (1999). doi: 10.1016/S0006-3223(99)00177-8; pmid: 10560024
9. J. J. Radley *et al*., Repeated stress induces dendritic spine loss in the rat medial prefrontal cortex. *Cereb. Cortex* **16**, 313–320 (2006). doi: 10.1093/cercor/bhi104; pmid: 15901656
10. S. C. Cook, C. L. Wellman, Chronic stress alters dendritic morphology in rat medial prefrontal cortex. *J. Neurobiol.* **60**, 236–248 (2004). doi: 10.1002/neu.20025; pmid: 15266654
11. C. Liston *et al*., Stress-induced alterations in prefrontal cortical dendritic morphology predict selective impairments in perceptual attentional set-shifting. *J. Neurosci.* **26**, 7870–7874 (2006). doi: 10.1523/JNEUROSCI.1184-06.2006; pmid: 16870732
12. S. L. Gourley, A. M. Swanson, A. J. Koleske, Corticosteroid-induced neural remodeling predicts behavioral vulnerability and resilience. *J. Neurosci.* **33**, 3107–3112 (2013). doi: 10.1523/JNEUROSCI.2138-12.2013; pmid: 23407965
13. S. S. Pattwell *et al*., Dynamic changes in neural circuitry during adolescence are associated with persistent attenuation of fear memories. *Nat. Commun.* **7**, 11475 (2016). doi: 10.1038/ncomms11475; pmid: 27215672
14. T. H. Chia, M. J. Levene, Microprisms for in vivo multilayer cortical imaging. *J. Neurophysiol.* **102**, 1310–1314 (2009). doi: 10.1152/jn.91208.2008; pmid: 19494189
15. M. L. Andermann *et al*., Chronic cellular imaging of entire cortical columns in awake mice using microprisms. *Neuron* **80**, 900–913 (2013). doi: 10.1016/j.neuron.2013.07.052; pmid: 24139817
16. R. J. Low, Y. Gu, D. W. Tank, Cellular resolution optical access to brain regions in fissures: Imaging medial prefrontal cortex and grid cells in entorhinal cortex. *Proc. Natl. Acad. Sci. U.S.A.* **111**, 18739–18744 (2014). doi: 10.1073/pnas.1421753111; pmid: 25503366
17. T.-W. Chen *et al*., Ultrasensitive fluorescent proteins for imaging neuronal activity. *Nature* **499**, 295–300 (2013). doi: 10.1038/nature12354; pmid: 23868258
18. L. A. Gunaydin *et al*., Natural neural projection dynamics underlying social behavior. *Cell* **157**, 1535–1551 (2014). doi: 10.1016/j.cell.2014.05.017; pmid: 24949967
19. G. Cui *et al*., Concurrent activation of striatal direct and indirect pathways during action initiation. *Nature* **494**, 238–242 (2013). doi: 10.1038/nature11846; pmid: 23354054
20. A. Hayashi-Takagi *et al*., Labelling and optical erasure of synaptic memory traces in the motor cortex. *Nature* **525**, 333–338 (2015). doi: 10.1038/nature15257; pmid: 26352471
21. I. N. Karatsoreos *et al*., Endocrine and physiological changes in response to chronic corticosterone: A potential model of the metabolic syndrome in mouse. *Endocrinology* **151**, 2117–2127 (2010). doi: 10.1210/en.2009-1436; pmid: 20211972
22. S. R. Bodnoff *et al*., Enduring effects of chronic corticosterone treatment on spatial learning, synaptic plasticity, and hippocampal neuropathology in young and mid-aged rats. *J. Neurosci.* **15**, 61–69 (1995). doi: 10.1523/JNEUROSCI.15-01-00061.1995; pmid: 7823152
23. V. N. Luine, R. L. Spencer, B. S. McEwen, Effects of chronic corticosterone ingestion on spatial memory performance and hippocampal serotonergic function. *Brain Res.* **616**, 65–70 (1993). doi: 10.1016/0006-8993(93)90193-Q; pmid: 7689414
24. R. N. McLay, S. M. Freeman, J. E. Zadina, Chronic corticosterone impairs memory performance in the Barnes maze. *Physiol. Behav.* **63**, 933–937 (1998). doi: 10.1016/S0031-9384(97)00529-5; pmid: 9618019
25. J. Radley, D. Morilak, V. Viau, S. Campeau, Chronic stress and brain plasticity: Mechanisms underlying adaptive and maladaptive changes and implications for stress-related CNS disorders. *Neurosci. Biobehav. Rev.* **58**, 79–91 (2015). doi: 10.1016/j.neubiorev.2015.06.018; pmid: 26116544
26. I. N. Karatsoreos, S. Bhagat, E. B. Bloss, J. H. Morrison, B. S. McEwen, Disruption of circadian clocks has ramifications for metabolism, brain, and behavior. *Proc. Natl. Acad. Sci. U.S.A.* **108**, 1657–1662 (2011). doi: 10.1073/pnas.1018375108; pmid: 21220317
27. Y. Zhao *et al*., A mouse model of depression induced by repeated corticosterone injections. *Eur. J. Pharmacol.* **581**, 113–120 (2008). doi: 10.1016/j.ejphar.2007.12.005; pmid: 18184609
28. S. L. Gourley *et al*., Regionally specific regulation of ERK MAP kinase in a model of antidepressant-sensitive chronic depression. *Biol. Psychiatry* **63**, 353–359 (2008). doi: 10.1016/j.biopsych.2007.07.016; pmid: 17889834
29. R. Mitra, R. M. Sapolsky, Acute corticosterone treatment is sufficient to induce anxiety and amygdaloid dendritic hypertrophy. *Proc. Natl. Acad. Sci. U.S.A.* **105**, 5573–5578 (2008). doi: 10.1073/pnas.0705615105; pmid: 18391224

30. T. Strekalova, R. Spanagel, D. Bartsch, F. A. Henn, P. Gass, Stress-induced anhedonia in mice is associated with deficits in forced swimming and exploration. *Neuropsychopharmacology* **29**, 2007–2017 (2004). doi: 10.1038/sj.npp.1300532; pmid: 15266352
31. S. L. Gourley, J. R. Taylor, Recapitulation and reversal of a persistent depression-like syndrome in rodents. *Curr. Protoc. Neurosci.* **Chapter 9**, 32 (2009). doi: 10.1002/0471142301.ns0932s49; pmid: 19802817
32. R. M. Shansky, C. Hamo, P. R. Hof, B. S. McEwen, J. H. Morrison, Stress-induced dendritic remodeling in the prefrontal cortex is circuit specific. *Cereb. Cortex* **19**, 2479–2484 (2009). doi: 10.1093/cercor/bhp003; pmid: 19193712
33. H. Kasai, M. Fukuda, S. Watanabe, A. Hayashi-Takagi, J. Noguchi, Structural dynamics of dendritic spines in memory and cognition. *Trends Neurosci.* **33**, 121–129 (2010). doi: 10.1016/j.tins.2010.01.001; pmid: 20138375
34. O. Gökçe, T. Bonhoeffer, V. Scheuss, Clusters of synaptic inputs on dendrites of layer 5 pyramidal cells in mouse visual cortex. *eLife* **5**, e09222 (2016). doi: 10.7554/eLife.09222; pmid: 27431612
35. T. Kleindienst, J. Winnubst, C. Roth-Alpermann, T. Bonhoeffer, C. Lohmann, Activity-dependent clustering of functional synaptic inputs on developing hippocampal dendrites. *Neuron* **72**, 1012–1024 (2011). doi: 10.1016/j.neuron.2011.10.015; pmid: 22196336
36. N. Takahashi *et al*., Locally synchronized synaptic inputs. *Science* **335**, 353–356 (2012). doi: 10.1126/science.1210362; pmid: 22267814
37. H. Makino, R. Malinow, Compartmentalized versus global synaptic plasticity on dendrites controlled by experience. *Neuron* **72**, 1001–1011 (2011). doi: 10.1016/j.neuron.2011.09.036; pmid: 22196335
38. T. J. McBride, A. Rodriguez-Contreras, A. Trinh, R. Bailey, W. M. Debello, Learning drives differential clustering of axodendritic contacts in the barn owl auditory system. *J. Neurosci.* **28**, 6960–6973 (2008). doi: 10.1523/JNEUROSCI.1352-08.2008; pmid: 18596170
39. S. Druckmann *et al*., Structured synaptic connectivity between hippocampal regions. *Neuron* **81**, 629–640 (2014). doi: 10.1016/j.neuron.2013.11.026; pmid: 24412418
40. J.-C. Rah *et al*., Thalamocortical input onto layer 5 pyramidal neurons measured using quantitative large-scale array tomography. *Front. Neural Circuits* **7**, 177 (2013). doi: 10.3389/fncir.2013.00177; pmid: 24273494
41. G. W. Knott, A. Holtmaat, L. Wilbrecht, E. Welker, K. Svoboda, Spine growth precedes synapse formation in the adult neocortex in vivo. *Nat. Neurosci.* **9**, 1117–1124 (2006). doi: 10.1038/nn1747; pmid: 16892056
42. C. Lohmann, T. Bonhoeffer, A role for local calcium signaling in rapid synaptic partner selection by dendritic filopodia. *Neuron* **59**, 253–260 (2008). doi: 10.1016/j.neuron.2008.05.025; pmid: 18667153
43. L. Carrillo-Reid, W. Yang, Y. Bando, D. S. Peterka, R. Yuste, Imprinting and recalling cortical ensembles. *Science* **353**, 691–694 (2016). doi: 10.1126/science.aaf7560; pmid: 27516599
44. J. E. Miller, I. Ayzenshtat, L. Carrillo-Reid, R. Yuste, Visual stimuli recruit intrinsically generated cortical ensembles. *Proc. Natl. Acad. Sci. U.S.A.* **111**, E4053–E4061 (2014). doi: 10.1073/pnas.1406077111; pmid: 25201983
45. J. P. Hamm, D. S. Peterka, J. A. Gogos, R. Yuste, Altered cortical ensembles in mouse models of schizophrenia. *Neuron* **94**, 153–167.e8 (2017). doi: 10.1016/j.neuron.2017.03.019; pmid: 28384469
46. M. R. Warden *et al*., A prefrontal cortex-brainstem neuronal projection that controls response to behavioural challenge. *Nature* **492**, 428–432 (2012). doi: 10.1038/nature11617; pmid: 23160494
47. J. F. Cryan, C. Mombereau, A. Vassout, The tail suspension test as a model for assessing antidepressant activity: Review of pharmacological and genetic studies in mice. *Neurosci. Biobehav. Rev.* **29**, 571–625 (2005). doi: 10.1016/j.neubiorev.2005.03.009; pmid: 15890404
48. X.-C. Ma *et al*., Long-lasting antidepressant action of ketamine, but not glycogen synthase kinase-3 inhibitor SB216763, in the chronic mild stress model of mice. *PLOS ONE* **8**, e56053 (2013). doi: 10.1371/journal.pone.0056053; pmid: 23390559
49. C. Yang *et al*., R-ketamine: A rapid-onset and sustained antidepressant without psychotomimetic side effects. *Transl. Psychiatry* **5**, e632 (2015). doi: 10.1038/tp.2015.136; pmid: 26327690
50. R. S. Duman, G. K. Aghajanian, G. Sanacora, J. H. Krystal, Synaptic plasticity and depression: New insights from stress and rapid-acting antidepressants. *Nat. Med.* **22**, 238–249 (2016). doi: 10.1038/nm.4050; pmid: 26937618
51. V. Krishnan *et al*., Molecular adaptations underlying susceptibility and resistance to social defeat in brain reward regions. *Cell* **131**, 391–404 (2007). doi: 10.1016/j.cell.2007.09.018; pmid: 17956738
52. E. Castrén, R. Hen, Neuronal plasticity and antidepressant actions. *Trends Neurosci.* **36**, 259–267 (2013). doi: 10.1016/j.tins.2012.12.010; pmid: 23380665
53. M. Popoli, Z. Yan, B. S. McEwen, G. Sanacora, The stressed synapse: The impact of stress and glucocorticoids on glutamate transmission. *Nat. Rev. Neurosci.* **13**, 22–37 (2011). doi: 10.1038/nrn3138; pmid: 22127301
54. K. T. Ota *et al*., REDD1 is essential for stress-induced synaptic loss and depressive behavior. *Nat. Med.* **20**, 531–535 (2014). doi: 10.1038/nm.3513; pmid: 24728411
55. R. S. Duman, L. M. Monteggia, A neurotrophic model for stress-related mood disorders. *Biol. Psychiatry* **59**, 1116–1127 (2006). doi: 10.1016/j.biopsych.2006.02.013; pmid: 16631126
56. O. Berton *et al*., Essential role of BDNF in the mesolimbic dopamine pathway in social defeat stress. *Science* **311**, 864–868 (2006). doi: 10.1126/science.1120972; pmid: 16469931
57. G. E. Hodes *et al*., Individual differences in the peripheral immune system promote resilience versus susceptibility to social stress. *Proc. Natl. Acad. Sci. U.S.A.* **111**, 16136–16141 (2014). doi: 10.1073/pnas.1415191111; pmid: 25331895
58. G. E. Hodes, V. Kana, C. Menard, M. Merad, S. J. Russo, Neuroimmune mechanisms of depression. *Nat. Neurosci.* **18**, 1386–1393 (2015). doi: 10.1038/nn.4113; pmid: 26404713
59. A. H. Miller, V. Maletic, C. L. Raison, Inflammation and its discontents: The role of cytokines in the pathophysiology of major depression. *Biol. Psychiatry* **65**, 732–741 (2009). doi: 10.1016/j.biopsych.2008.11.029; pmid: 19150053
60. S. Vijayraghavan, M. Wang, S. G. Birnbaum, G. V. Williams, A. F. T. Arnsten, Inverted-U dopamine D1 receptor actions on prefrontal neurons engaged in working memory. *Nat. Neurosci.* **10**, 376–384 (2007). doi: 10.1038/nn1846; pmid: 17277774
61. A. F. T. Arnsten, Stress signalling pathways that impair prefrontal cortex structure and function. *Nat. Rev. Neurosci.* **10**, 410–422 (2009). doi: 10.1038/nrn2648; pmid: 19455173
62. S. G. Birnbaum *et al*., Protein kinase C overactivity impairs prefrontal cortical regulation of working memory. *Science* **306**, 882–884 (2004). doi: 10.1126/science.1100021; pmid: 15514161
63. M. Joëls, T. Z. Baram, The neuro-symphony of stress. *Nat. Rev. Neurosci.* **10**, 459–466 (2009). doi: 10.1038/nrn2632; pmid: 19339973
64. Y. Chen *et al*., Correlated memory defects and hippocampal dendritic spine loss after acute stress involve corticotropin-releasing hormone signaling. *Proc. Natl. Acad. Sci. U.S.A.* **107**, 13123–13128 (2010). doi: 10.1073/pnas.1003825107; pmid: 20615973
65. E. Y. Yuen *et al*., Repeated stress causes cognitive impairment by suppressing glutamate receptor expression and function in prefrontal cortex. *Neuron* **73**, 962–977 (2012). doi: 10.1016/j.neuron.2011.12.033; pmid: 22405206
66. E. Y. Yuen *et al*., Acute stress enhances glutamatergic transmission in prefrontal cortex and facilitates working memory. *Proc. Natl. Acad. Sci. U.S.A.* **106**, 14075–14079 (2009). doi: 10.1073/pnas.0906791106; pmid: 19666502
67. E. Dias-Ferreira *et al*., Chronic stress causes frontostriatal reorganization and affects decision-making. *Science* **325**, 621–625 (2009). doi: 10.1126/science.1171203; pmid: 19644122
68. D. Chaudhury *et al*., Rapid regulation of depression-related behaviours by control of midbrain dopamine neurons. *Nature* **493**, 532–536 (2013). doi: 10.1038/nature11713; pmid: 23235832
69. A. Friedman, Jump-starting natural resilience reverses stress susceptibility. *Science* **346**, 555 (2014). doi: 10.1126/science.1260781; pmid: 25359955
70. B. Li *et al*., Synaptic potentiation onto habenula neurons in the learned helplessness model of depression. *Nature* **470**, 535–539 (2011). doi: 10.1038/nature09742; pmid: 21350486
71. O. Hikosaka, The habenula: From stress evasion to value-based decision-making. *Nat. Rev. Neurosci.* **11**, 503–513 (2010). doi: 10.1038/nrn2866; pmid: 20559337
72. C. D. Proulx, O. Hikosaka, R. Malinow, Reward processing by the lateral habenula in normal and depressive behaviors. *Nat. Neurosci.* **17**, 1146–1152 (2014). doi: 10.1038/nn.3779; pmid: 25157511
73. S. Lammel *et al*., Input-specific control of reward and aversion in the ventral tegmental area. *Nature* **491**, 212–217 (2012). doi: 10.1038/nature11527; pmid: 23064228
74. B. K. Lim, K. W. Huang, B. A. Grueter, P. E. Rothwell, R. C. Malenka, Anhedonia requires MC4R-mediated synaptic adaptations in nucleus accumbens. *Nature* **487**, 183–189 (2012). doi: 10.1038/nature11160; pmid: 22785313
75. A. McGirr, J. LeDue, A. W. Chan, Y. Xie, T. H. Murphy, Cortical functional hyperconnectivity in a mouse model of depression and selective network effects of ketamine. *Brain* **140**, 2210–2225 (2017). doi: 10.1093/brain/awx142; pmid: 28899017
76. R. Hultman *et al*., Brain-wide electrical spatiotemporal dynamics encode depression vulnerability. *Cell* **173**, 166–180.e14 (2018). doi: 10.1016/j.cell.2018.02.012; pmid: 29502969
77. T. Zhou *et al*., History of winning remodels thalamo-PFC circuit to reinforce social dominance. *Science* **357**, 162–168 (2017). doi: 10.1126/science.aak9726; pmid: 28706064
78. F. Wang *et al*., Bidirectional control of social hierarchy by synaptic efficacy in medial prefrontal cortex. *Science* **334**, 693–697 (2011). doi: 10.1126/science.1209951; pmid: 21960531
79. R. C. Bagot *et al*., Ventral hippocampal afferents to the nucleus accumbens regulate susceptibility to depression. *Nat. Commun.* **6**, 7062 (2015). doi: 10.1038/ncomms8062; pmid: 25952660
80. C. Liston *et al*., Circadian glucocorticoid oscillations promote learning-dependent synapse formation and maintenance. *Nat. Neurosci.* **16**, 698–705 (2013). doi: 10.1038/nn.3387; pmid: 23624512
81. C. Liston, W.-B. Gan, Glucocorticoids are critical regulators of dendritic spine development and plasticity in vivo. *Proc. Natl. Acad. Sci. U.S.A.* **108**, 16074–16079 (2011). doi: 10.1073/pnas.1110444108; pmid: 21911374
82. A. H. Stephan, B. A. Barres, B. Stevens, The complement system: An unexpected role in synaptic pruning during development and disease. *Annu. Rev. Neurosci.* **35**, 369–389 (2012). doi: 10.1146/annurev-neuro-061010-113810; pmid: 22715882
83. D. Stellwagen, R. C. Malenka, Synaptic scaling mediated by glial TNF-alpha. *Nature* **440**, 1054–1059 (2006). doi: 10.1038/nature04671; pmid: 16547515
84. R. C. Paolicelli *et al*., Synaptic pruning by microglia is necessary for normal brain development. *Science* **333**, 1456–1458 (2011). doi: 10.1126/science.1202529; pmid: 21778362
85. D. P. Schafer *et al*., Microglia sculpt postnatal neural circuits in an activity and complement-dependent manner. *Neuron* **74**, 691–705 (2012). doi: 10.1016/j.neuron.2012.03.026; pmid: 22632727
86. E. S. Wohleb, T. Franklin, M. Iwata, R. S. Duman, Integrating neuroimmune systems in the neurobiology of depression. *Nat. Rev. Neurosci.* **17**, 497–511 (2016). doi: 10.1038/nrn.2016.69; pmid: 27277867
87. N. G. Hedrick *et al*., Rho GTPase complementation underlies BDNF-dependent homo- and heterosynaptic plasticity. *Nature* **538**, 104–108 (2016). doi: 10.1038/nature19784; pmid: 27680697
88. G. G. Turrigiano, The self-tuning neuron: Synaptic scaling of excitatory synapses. *Cell* **135**, 422–435 (2008). doi: 10.1016/j.cell.2008.10.008; pmid: 18984155
89. R. S. Duman, G. K. Aghajanian, Synaptic dysfunction in depression: Potential therapeutic targets. *Science* **338**, 68–72 (2012). doi: 10.1126/science.1222939; pmid: 23042884
90. E. T. Kavalali, L. M. Monteggia, Synaptic mechanisms underlying rapid antidepressant action of ketamine. *Am. J. Psychiatry* **169**, 1150–1156 (2012). doi: 10.1176/appi.ajp.2012.12040531; pmid: 23534055
91. S. J. Russo, E. J. Nestler, The brain reward circuitry in mood disorders. *Nat. Rev. Neurosci.* **14**, 609–625 (2013). doi: 10.1038/nrn3381; pmid: 23942470
92. Q. LaPlant *et al*., Dnmt3a regulates emotional behavior and spine plasticity in the nucleus accumbens. *Nat. Neurosci.* **13**, 1137–1143 (2010). doi: 10.1038/nn.2619; pmid: 20729844
93. R. Mitra, S. Jadhav, B. S. McEwen, A. Vyas, S. Chattarji, Stress duration modulates the spatiotemporal patterns of spine formation in the basolateral amygdala. *Proc. Natl. Acad. Sci. U.S.A.* **102**, 9371–9376 (2005). doi: 10.1073/pnas.0504011102; pmid: 15967994
94. Y. Yang *et al*., Ketamine blocks bursting in the lateral habenula to rapidly relieve depression. *Nature* **554**, 317–322 (2018). doi: 10.1038/nature25509; pmid: 29446381
95. T. A. LeGates *et al*., Reward behaviour is regulated by the strength of hippocampus-nucleus accumbens synapses. *Nature* **564**, 258–262 (2018). doi: 10.1038/s41586-018-0740-8; pmid: 30478293

ACKNOWLEDGMENTS
We thank all members of the Liston lab for helpful discussions. **Funding:** This work was supported by funds from the Whitehall Foundation, Hartwell Foundation, One Mind Institute, Rita Allen Foundation, and National Institute of Mental Health (R00 MH097822, R01 MH109685, and R01 MH118451) and by a Klingenstein-Simons Fellowship in Brain Science. R.N.M.-S. was supported by a fellowship from the NSF. H.B. was supported by KAKENHI grant 17H06312. H.K. was supported by CREST (JPMJCR1652) from JST, SRPBS (17dm0107120h002) from AMED, and a grant-in-aid (26221001) and WPI from MEXT of Japan. D.C.S. and R.N.F. were supported by a Medical Scientist Training Program grant from the National Institute of General Medical Sciences of the National Institutes of Health under award T32GM007739 to the Weill Cornell/Rockefeller/Sloan Kettering Tri-Institutional MD-PhD Program. R.N.F. was supported by a fellowship from the NIH (F30 MH115622). L.G. was supported by Simons Foundation award 429965. T.A.M. was supported by NIH grants R01 DA08259 and HL136520. **Author contributions:** R.N.M.-S., M.H.M., P.K.P., and C.L. designed experiments. R.N.M.-S., M.H.M., P.K.P., R.N.F., B.S.H., T.N.H., J.W., D.C.S., E.J.A., D.L.R., K.L., Y.M., L.N., T.A.M., and C.L. carried out experiments and analyzed data. L.G. and K.D. developed the fiber photometry technology, advised on its implementation in the lab, and consulted on the design and analysis of the photometry experiments. H.B. and H.K. developed the AS-PaRac1 technology, shared critical reagents, and consulted on the design and analysis of the AS-PaRac1 experiments. R.N.M.-S., M.H.M., P.K.P., and C.L. wrote the manuscript. **Competing interests:** The authors declare no competing interests. **Data and materials availability:** AAV1-SARE-Arc-PSDdelta1.2-mVenus-PARac1 is available upon request from H.K. (hkasai@m.u-tokyo.ac.jp) and H.B. (hbito@m.u-tokyo.ac.jp) under a material transfer agreement with the University of Tokyo. All other materials are commercially available. All data needed to evaluate the conclusions in the paper are present in the paper or the supplementary materials.

SUPPLEMENTARY MATERIALS

www.sciencemag.org/content/364/6436/eaat8078/suppl/DC1
Materials and Methods
Figs. S1 to S13

7 May 2018; accepted 18 February 2019
10.1126/science.aat8078

Robotics for Science, Science for **Robotics**

Transforming the Future of Robotics in Research !

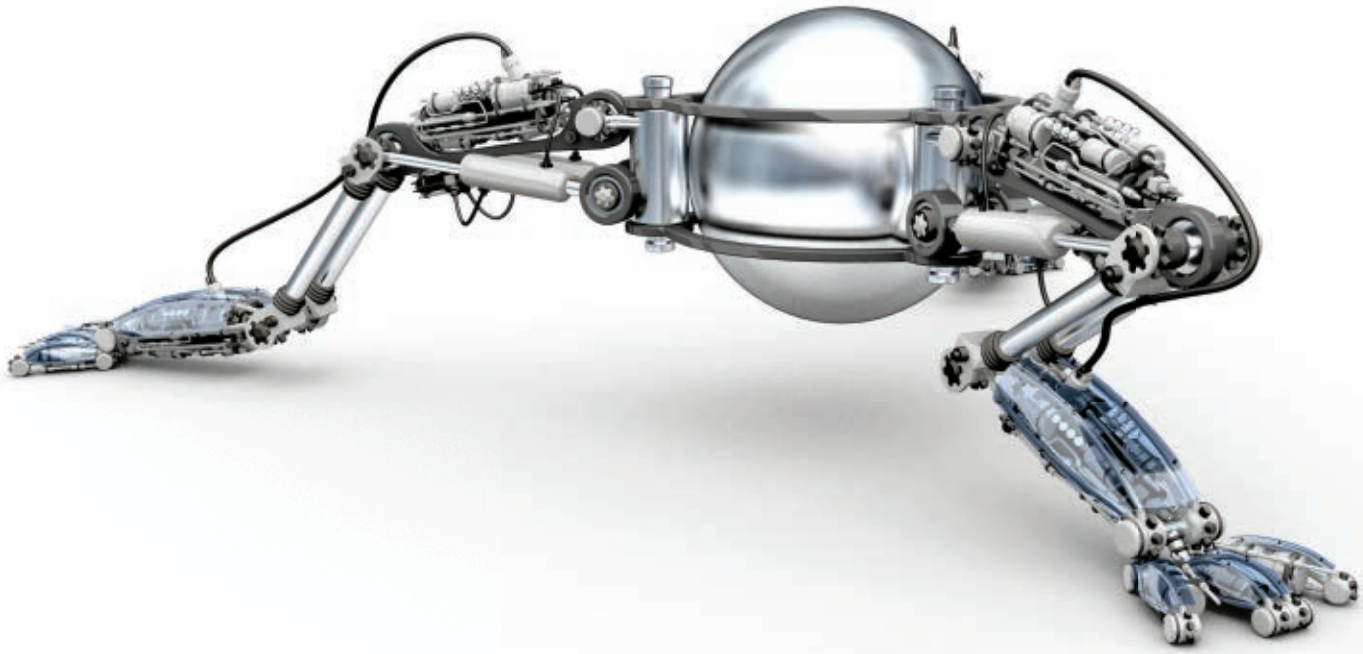

As a multidisciplinary online-only journal, *Science Robotics* publishes original, peer-reviewed, science or engineering-based research articles that advance the field of robotics. The journal provides a central forum for communication of new ideas, general principles, and original developments in research and field applications of robotics for all environments.

Submit your research today!

Learn more at: **ScienceRobotics.org**

Science Robotics | AAAS

RESEARCH ARTICLE

STRUCTURAL BIOLOGY

Structure and dynamics of the active human parathyroid hormone receptor-1

Li-Hua Zhao[1]*, Shanshan Ma[1,2]*, Ieva Sutkeviciute[3]*, Dan-Dan Shen[4]*, X. Edward Zhou[5], Parker W. de Waal[5], Chen-Yao Li[1,2], Yanyong Kang[1], Lisa J. Clark[3,6], Frederic G. Jean-Alphonse[3], Alex D. White[3,7], Dehua Yang[1], Antao Dai[1], Xiaoqing Cai[1], Jian Chen[8], Cong Li[8], Yi Jiang[1], Tomoyuki Watanabe[9]†, Thomas J. Gardella[9], Karsten Melcher[5], Ming-Wei Wang[1,8]‡, Jean-Pierre Vilardaga[3]‡, H. Eric Xu[1,5]‡, Yan Zhang[4]‡

The parathyroid hormone receptor-1 (PTH1R) is a class B G protein–coupled receptor central to calcium homeostasis and a therapeutic target for osteoporosis and hypoparathyroidism. Here we report the cryo–electron microscopy structure of human PTH1R bound to a long-acting PTH analog and the stimulatory G protein. The bound peptide adopts an extended helix with its amino terminus inserted deeply into the receptor transmembrane domain (TMD), which leads to partial unwinding of the carboxyl terminus of transmembrane helix 6 and induces a sharp kink at the middle of this helix to allow the receptor to couple with G protein. In contrast to a single TMD structure state, the extracellular domain adopts multiple conformations. These results provide insights into the structural basis and dynamics of PTH binding and receptor activation.

Parathyroid hormone (PTH) and PTH-related peptide (PTHrP) are two endogenous ligands that play critical and distinct roles in skeletal development, calcium homeostasis, and bone turnover (*1*). Analogs of both PTH and PTHrP have been developed into therapeutic agents for osteoporosis, and PTH is used to treat hypoparathyroidism. In addition, tumor-produced PTHrP is a key factor driving cancer-associated hypercalcemia and cachexia (*2*), which is associated with weight loss disorder and is frequently the actual cause of death in cancer patients. Thus, modulating the PTH-PTHrP signaling axis is important for the development of treatments for a number of diseases, including osteoporosis and cancer.

The pleiotropic functions of PTH and PTHrP are mediated primarily through their binding and activation of the PTH type 1 receptor (PTH1R), a member of the class B G protein–coupled receptor (GPCR) subfamily, which also includes receptors for glucagon, glucagon-like peptides (GLPs), calcitonin, calcitonin gene–related peptide (CGRP), and other therapeutically important peptide hormones. The PTH1R couples primarily to stimulatory G protein (G_s), which is considered the major mediator of bone turnover and calcium homeostasis in response to PTH.

PTH1R contains two modular domains: a relatively large N-terminal extracellular domain (ECD) and a transmembrane domain (TMD). Activation of PTH1R is initiated by a rapid binding of the C-terminal region of peptide hormones to the receptor ECD, followed by a slow insertion of the N-terminal region of the peptide into the receptor's TMD (*3*). Peptide hormone binding triggers the conformational changes in the TMD that mediate receptor activation. Previous crystal structures of the isolated PTH1R ECD bound to the C-terminal fragments of PTH and PTHrP have revealed that the peptides dock as amphipathic helices into a central groove formed by a three-layer α-β-βα fold in the ECD to resemble a "hot dog in a bun" configuration (*4*, *5*). However, the structural basis by which the full-length PTH1R interacts with a functional peptide hormone and couples to downstream G protein remains unknown, and this is an obstacle to the development of clinically relevant PTH analogs and to understanding the fundamental mechanisms of GPCR signaling.

Recent technological advances in cryo–electron microscopy (cryo-EM) have revolutionized the progress in GPCR structural biology, resulting in a series of breakthrough structures, including several class A and class B GPCRs in complex with G proteins (*6*–*13*). In particular, cryo-EM structures of the glucagon-like peptide-1 receptor (GLP-1R) bound to GLP-1 (*10*) or a G_s-biased peptide Exendin-P5 (*13*) demonstrate that both peptides adopt a single continuous α helix, with their N termini pointing toward TM6, which induces a sharp kink at the middle of TM6 and an opening of the receptor's cytoplasmic face to accommodate the α5 helix of the Ras-like domain of $G\alpha_s$. The TM6 outward movement in G_s-bound GLP-1R has been observed in all other available class B GPCR–G_s complex structures. Nevertheless, the amino acid sequences of the class B GPCRs and their peptide ligands diverge considerably within the subfamily (*3*), such that the basis for ligand-binding specificity remains unknown.

We have reported previously that class B GPCRs vary widely in their requirement of the ECD for activation. For example, the ECD is not required for PTH1R activation when the peptide hormone is fused directly to the N-terminal end of its TMD (*14*, *15*). In contrast, the ECD of GLP-1R is required for TMD activation even when the peptide ligand is covalently linked to the TMD or the receptor is activated by small molecules that interact with the intracellular side of TM6 (*14*, *15*). To understand the specificity of peptide hormone recognition and receptor activation, we used single-particle cryo-EM to determine the structure of human PTH1R in complex with a long-acting PTH (LA-PTH) analog and G_s protein.

Structure determination of the LA-PTH–PTH1R–G_s complex

To prepare a stable PTH1R–G_s complex for cryo-EM studies, we had to overcome several technical obstacles associated with low expression levels of the human PTH1R and the instability of the receptor–G_s complex. The expression level of PTH1R was increased by using a double tag of maltose binding protein at the receptor C terminus (fig. S1A). The stability of the receptor–G_s complex was achieved through coexpression of the receptor with a dominant negative form of the heterotrimeric G_s protein (*13*) and the use of the Gα- and Gβ-binding nanobody Nb35 (*16*) (fig. S1, B to D). The activation of the receptor was achieved, and the receptor–G_s complex was further stabilized by LA-PTH (*17*), a modified PTH/PTHrP chimera that activates the receptor with 10- to 100-fold higher potency than endogenous PTH or PTHrP, in both G protein–free and G protein–bound states (*18*, *19*). The use of LA-PTH was particularly important for the stability of the receptor–G_s complex because it has a much longer residence time on the receptor compared with PTH (fig. S2A). This peptide induced sustained receptor signaling via adenosine

[1]The CAS Key Laboratory of Receptor Research, Shanghai Institute of Materia Medica, Chinese Academy of Sciences, Shanghai 201203, China. [2]University of Chinese Academy of Sciences, Beijing 100049, China. [3]Laboratory for GPCR Biology, Department of Pharmacology and Chemical Biology, University of Pittsburgh School of Medicine, University of Pittsburgh, Pittsburgh, PA 15261, USA. [4]Department of Pathology of Sir Run Run Shaw Hospital and Department of Biophysics, Zhejiang University School of Medicine, Hangzhou 310058, China. [5]Center for Cancer and Cell Biology, Innovation and Integration Program, Van Andel Research Institute, Grand Rapids, MI 49503, USA. [6]Graduate Program in Molecular Biophysics and Structural Biology, University of Pittsburgh School of Medicine, University of Pittsburgh, Pittsburgh, PA 15261, USA. [7]Graduate Program in Molecular Pharmacology, University of Pittsburgh School of Medicine, University of Pittsburgh, Pittsburgh, PA 15261, USA. [8]School of Pharmacy, Fudan University, Shanghai 201203, China. [9]Endocrine Unit, Massachusetts General Hospital and Harvard Medical School, Boston, MA 02114, USA.
*These authors contributed equally to this work. †Present address: Chugai Pharmaceutical Co., Ltd., Tokyo 103-8324, Japan.
‡Corresponding author. Email: eric.xu@vai.org (H.E.X.); mwwang@simm.ac.cn (M.-W.W.); jpv@pitt.edu (J.-P.V.); zhang_yan@zju.edu.cn (Y.Z.)

3′,5′-monophosphate (cAMP) (fig. S2B) derived from stable PTH1R–G_s complexes within endosomes (*20*). The PTH1R (residues 27 to 502) used in this study can be bound and activated by both PTH and LA-PTH almost equally as the full-length receptor (residues 27 to 593) (fig. S1, E to H).

A large dataset of 1.4 million particles was collected from vitrified samples of LA-PTH–bound receptor-G_s complex. After 2D averaging analysis and global 3D sorting on the whole complex, about 40% of the particle projections out of the semi-autopicked particle repertoire were subjected to the reconstruction and yielded a high-resolution cryo-EM density map at a nominal resolution of 3.0 Å. Further consecutive classification on the peptide-receptor region resulted in three distinct conformational states of the PTH1R–G_s signaling complex, designated state 1, state 2, and state 3, respectively (figs. S3 and S4). The interaction analysis is based on state 1 unless noted otherwise. The overall structure was built on the basis of the GLP-1R–G_s complex (*13*), and the ECD region was fitted into the map as a rigid body using the available PTHrP-PTH1R ECD crystal structure (*4*). Apart from the α-helical domain of $G\alpha_s$, which is poorly resolved in most cryo-EM GPCR–G protein complex structures, the presence of the bound LA-PTH, the receptor, and G_s in the isolated complex was clearly visible in the EM map (Fig. 1A and fig. S5). Side chains of the majority of amino acid residues are well defined in all protein components. The final models contain 34 of the 36 LA-PTH residues, the Gαβγ subunits of G_s, and the PTH1R residues from $V31^{ECD}$ to $F483^{8.67b}$ (class B GPCR numbering in superscript) (*21*), the very last residue of helix 8, with a few missing residues in the extracellular loop 1 (ECL1; residues 251 to 272) and the intracellular loop 3 (ICL3; residues 394 to 398). Thus, the structure provides a detailed model of intermolecular interactions of the receptor with LA-PTH and G_s.

The EM maps also show that the lipid-modified moieties of $G\alpha_s$ and Gβγ were inserted into the disc-shaped detergent micelle (Fig. 1A and fig. S3), which has a diameter of 12 nm as indicated by the 2D class averages, mimicking well the morphology of the lipid bilayer. We also observed that the $G\alpha_s$ αN helix is almost parallel to the micelle (Fig. 1A). Unlike many GPCR cryo-EM structures, an ordered annular lipid belt wrapping the periphery of the receptor TMD is clearly discernible in the cryo-EM map, among which several cholesterol molecules were built (Fig. 1B). These structural lipids possibly constrain the mobility of the TMD and thus contribute to the stability of the receptor in its active state.

Molecular recognition of LA-PTH by PTH1R

The overall structure of the LA-PTH–bound PTH1R in complex with G_s is organized into three layers: the top layer is the receptor ECD, the middle layer is the receptor TMD embedded in a large disc-shaped micelle, and the bottom layer is the G_s protein (Fig. 1A). In the complex, LA-PTH adopts a single continuous helix that anchors the top ECD layer with the middle TMD layer, with the orientation of the LA-PTH helix and the ECD nearly perpendicular to the horizontal membrane (Figs. 1A and 2A). The structure of the receptor ECD and the C-terminal half of LA-PTH helix (hereafter referred to as $LA\text{-}PTH^C$) closely resembles the crystal structure of a PTHrP fragment bound to the PTH1R ECD (*4*) (fig. S6), which is expected given that LA-PTH is a PTH/PTHrP chimera whose C-terminal fragment (residues 16 to 34) corresponds to the PTHrP sequence (fig. S2C). The N-terminal half of the LA-PTH helix (hereafter referred to as $LA\text{-}PTH^N$; residues 1 to 16) adopts four helical turns and is inserted deeply into the TMD core. It is directly surrounded by TM1, TM2, TM3, TM5, TM6, and TM7. TM4 is the only transmembrane helix that does not contact the LA-PTH helix (Figs. 1B and 2). The EM map is very clear for the LA-PTH helix and the surrounding TM helices, allowing unambiguous assignment of most side chains of the bound LA-PTH and its binding pocket in the TMD core (figs. S3 and S5).

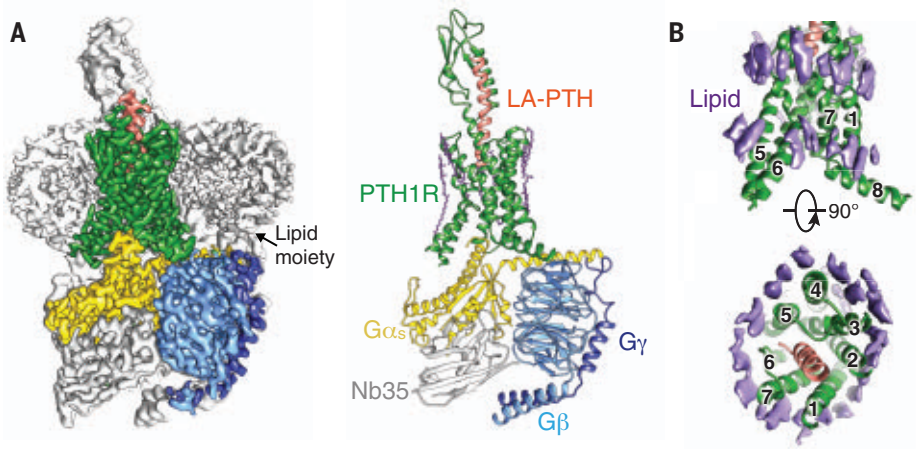

Fig. 1. Cryo-EM structure of LA-PTH–bound human PTH1R in complex with G_s. (**A**) (Left) Cut-through view of cryo-EM density map that illustrates the LA-PTH–PTH1R–G_s complex and the disc-shaped micelle. The unsharpened cryo-EM density map at the 0.01 threshold shown as light gray surface indicates a micelle diameter of 12 nm. The colored cryo-EM density map is shown at 0.026 threshold. (Right) Cartoon representation of the LA-PTH–PTH1R–G_s complex is shown with annular lipids in purple stick representation. Green, PTH1R; orange, LA-PTH; gold, G_s Ras-like domain; light blue, Gβ; medium blue, Gγ; gray, Nb35. (**B**) Cryo-EM density of the ordered annular lipid layer around the receptor TMD shown in purple; numbers 1 through 7 represent TM1 to TM7; receptor ECD and G protein are omitted.

The binding of LA-PTH to PTH1R buries a total surface area of 3809 $Å^2$, with the interaction of $LA\text{-}PTH^N$ with the TMD core contributing >60% of the buried surface, suggesting that interactions in this region provide the major binding energy for the formation of the complex. The stability of the interface between $LA\text{-}PTH^N$ and the TMD is well supported by an extensive network of complementary polar and nonpolar interactions between the bound peptide ligand and the TMD (table S1 and Fig. 2, B and C), with details described in the supplementary text.

Interactions between LA-PTH and PTH1R help rationalize numerous studies on receptor structure-activity relationship for PTH and PTH1R that have been reviewed in (*1*) and also point toward residues that are possible determinants for the mechanism of prolonged cAMP signaling. Originally designed to place the optimal signaling domain of PTH (residues 1 to 14) with the optimal binding domain of PTHrP (residues 15 to 36) (*22*), LA-PTH displays markedly enhanced affinity for the PTH1R when coupled to G proteins (*17*). This enhanced affinity is accompanied not only by prolonged endosomal cAMP production in cells but also by prolonged calcemic responses in mice and primates that are independent of the ligand half-life in the circulation (*17*). Specifically, LA-PTH has four major amino acid changes at positions 10, 11, 12, and 14 from PTH (fig. S2C). These changes make either additional hydrophobic contacts [Gly^{12}→Ala (G12A) and H14W] or additional hydrogen bonds (N10Q and L11R) (table S1), thus increasing the binding affinity of LA-PTH to the receptor TMD and accounting for the long-acting property of LA-PTH.

The structure further unveils the complex network of interactions formed by the first four residues of LA-PTH. Consistent with a critical role for these residues in activating the receptor, an N-terminally truncated $LA\text{-}PTH_{(5\text{-}36)}$ peptide is a potent antagonist of PTH1R (fig. S7). Competition-binding isotherms indicated that this truncated peptide maintains most of the stabilizing interactions used by LA-PTH (fig. S7A) and is thus only missing the signaling interactions that permit G_s coupling and activation (fig. S7, B to E). Together with earlier studies on class B chimeric GPCRs and hybrid peptides (*23–25*), these results support the model that peptide ligands of class B GPCRs are composed of two independent domains,

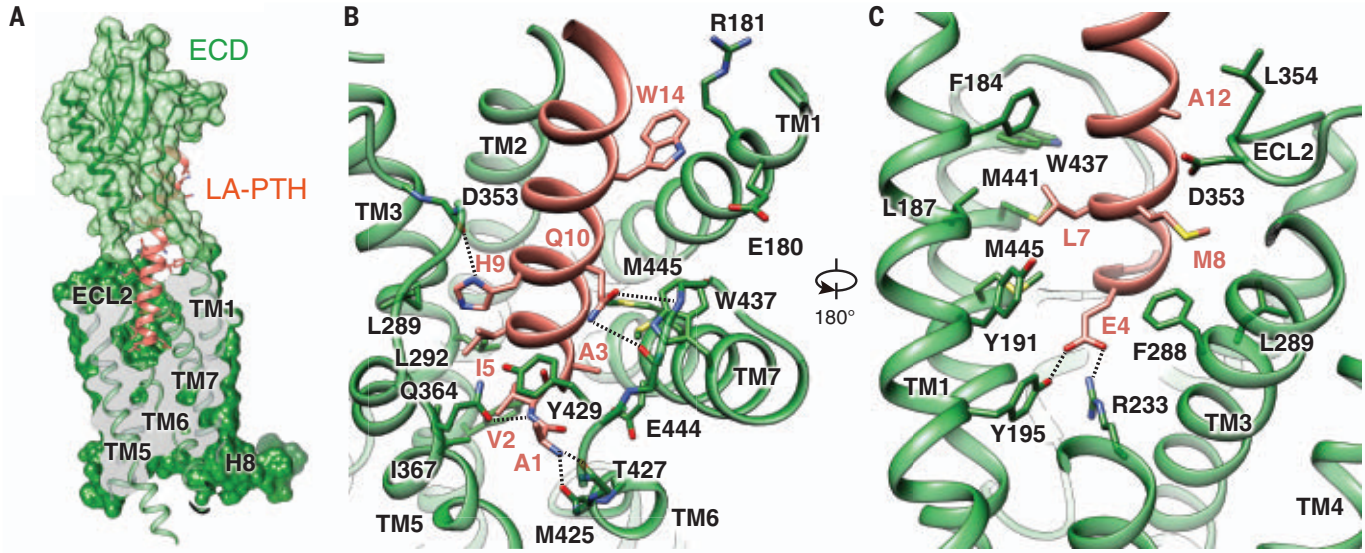

Fig. 2. Molecular recognition of LA-PTH by PTH1R. (**A**) The binding mode of LA-PTH with PTH1R, showing that LA-PTH^N (ribbon and stick representation, orange) penetrates into a pocket formed by all TM helices except TM4, and by ECL2 and ECL3 whereas its C-terminal half is recognized by the ECD (ribbon in transparent surface, green). Single-letter abbreviations for the amino acid residues are as follows: A, Ala; C, Cys; D, Asp; E, Glu; F, Phe; G, Gly; H, His; I, Ile; K, Lys; L, Leu; M, Met; N, Asn; P, Pro; Q, Gln; R, Arg; S, Ser; T, Thr; V, Val; W, Trp; and Y, Tyr. (**B** and **C**) Detailed interactions of LA-PTH with the PTH1R TMD pocket with hydrogen bonds shown as dotted lines.

with the C-terminal residues contributing to peptide binding selectivity, whereas N-terminal residues switch on receptor activation.

Conformational dynamics of the PTH1R–G_s complex

The relatively weak density for the ECD in the initial EM map suggests that multiple conformations are present simultaneously in the active PTH1R–G_s complex. To address the dynamic agonist recognition by the PTH1R, we employed extensive particle classifications that yielded three distinct subclasses and revealed the position of the ECD in three different conformational states relative to the TMD core, with nominal global resolutions of 3.0, 3.5, and 4.0 Å, respectively. In contrast, a single homogeneous conformation of the receptor TMD and TMD-bound LA-PTH^N was evident throughout all three major conformational states (Fig. 3 and figs. S4 and S8).

The first two conformational states are very similar, with the ECD and LA-PTH^C rotated about 15° against each other (Fig. 3 and fig. S8A). In the third conformation, the LA-PTH^C is bent, resulting in a loss of the interaction of LA-PTH^C with the ECD and, thereby, a largely unresolved ECD density in the EM map compared with the other two conformational states (Fig. 3 and fig. S8B). However, the distinctive conformation of LA-PTH^N among all three conformational states implies that stable interactions between LA-PTH^N and the TMD core likely provide the driving energy that induces receptor activation, an observation consistent with previous studies (*14*). Molecular dynamics (MD) simulation results corroborate the EM structures, revealing that the LA-PTH^N and the TMD core are in a single dominant conformational state in the simulation, whereas the ECD can twist around the LA-PTH helix (Fig. 3 and movie S1). Flexibility of the ECD might be required for initial binding of the peptide to the receptor, which is the first step in the two-step/two-domain model of ligand binding and receptor activation (*26*, *27*). The third conformational state also implies that the separation of the LA-PTH^C from ECD is likely the first step of the receptor–ligand dissociation process.

Basis of peptide hormone specificity

Peptide ligands of class B GPCRs vary greatly in their amino acid sequences (Fig. 4), which contribute to the specificity of ligand recognition by each receptor. Comparison of the LA-PTH–PTH1R–G_s complex with three other distinct class B GPCR–G_s complexes shows the underlying structural features that determine receptor–ligand specificity. The major difference among receptors lies in the position and orientation of their ECDs (Fig. 4A), which hold the corresponding peptide ligands in different conformations and orientations. The specificity of interaction between the ECD and the C-terminal half of the peptide ligand resembles what has been observed in the previously reported crystal structures of ECD-peptide complexes (*4*, *5*) (fig. S6). Here we focus on differences in the N-terminal halves of the peptide helices in the TMD cores. Figure 4B illustrates shapes and sizes of the TMD pockets and the N-terminal halves of their corresponding peptide ligands. The TMD pockets of class B GPCRs typically range in size from 3300 to 3700 Å^3, and only 32 to 61% of the pocket space is occupied by a peptide ligand. Despite a common structural packing of TM helices that construct the pocket, the pocket shape is unique for each receptor, owing to low conservation of the side chains lining it (fig. S9); thus, each pocket is capable of accommodating specific residues of a particular peptide ligand. In addition, different positions of the ECD among PTH1R, GLP-1R, and CGRP receptors help tweak the peptide helices differently into the TMD pocket (Fig. 4B), thereby contributing additional specificity to ligand binding.

The ECD of class B GPCRs displays a broad spectrum of relative stability, ranging from the poorly resolved calcitonin receptor (CTR) ECD to the resolved CTR ECD to the CGRP receptor (CGRPR) ECD whose mobility is restricted by interactions with RAMP1 (*11*, *12*). Of the class B GPCR complex structures resolved to date, the orientation of the ECDs of PTH1R and GLP-1R is partially limited by the extended peptide α helix that extends from the ECD to the receptor TMD. One notable difference between the active-state structures of PTH1R and GLP-1R is in the ECL1 region, which is unstructured in PTH1R but has a helical extension in GLP-1R (left and middle panels in Fig. 4A) that forms several additional direct contacts with the C-terminal portion of the bound GLP-1 helix. The ECL1 in both rat and human GLP-1R is in a position close enough to form van der Waals interactions with the first two helical turns of the N-terminal helix of the ECD, whereas there is no interaction between PTH1R ECD and its TMD. The differences mentioned above likely contribute to the greater mobility of the PTH1R ECD compared with that of GLP-1R, resulting in the unwinding of LA-PTH from the active state of the PTH1R complex. In contrast, the occupancy of the LA-PTH^N ligand in the TMD pocket is much higher than that of GLP-1 (63 versus 38%), suggesting substantially tighter binding and thus providing the potential structural

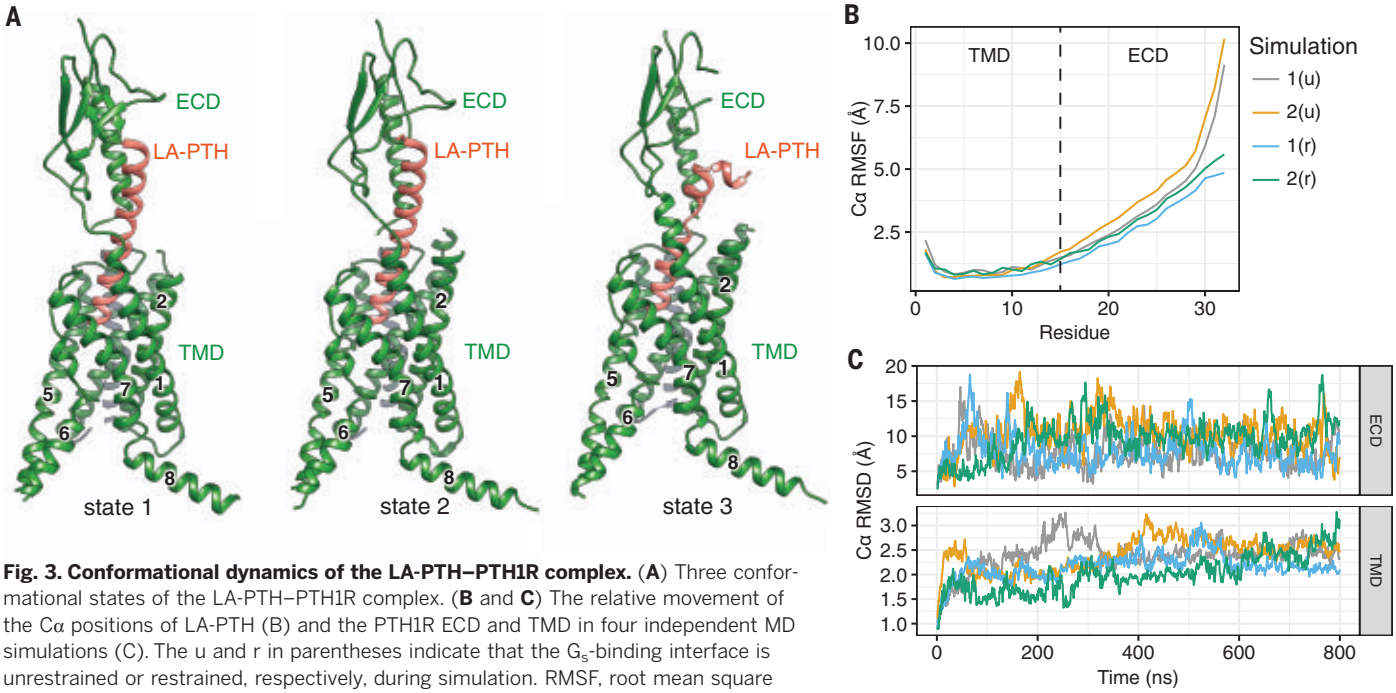

Fig. 3. Conformational dynamics of the LA-PTH–PTH1R complex. (**A**) Three conformational states of the LA-PTH–PTH1R complex. (**B** and **C**) The relative movement of the Cα positions of LA-PTH (B) and the PTH1R ECD and TMD in four independent MD simulations (C). The u and r in parentheses indicate that the G_s-binding interface is unrestrained or restrained, respectively, during simulation. RMSF, root mean square fluctuation; RMSD, root mean square deviation.

basis for the high potency of LA-PTH that sustains cAMP responses after receptor internalization to endosomes. $PTH_{(1-14)}$ peptide analogs that contain the same or a very similar set of six substitutions that are incorporated into the N-terminal portion of LA-PTH exhibit much greater potency on a PTH1R TMD construct than the unmodified $PTH_{(1-14)}$ peptide (*28*). Together, these observations provide a rationale for the fact that ECD is required for GLP-1R activation but dispensable for PTH1R activation (*14*, *26*).

Toward a common mechanism of class B GPCR activation and G_s coupling

Despite the different conformations and orientations of LA-PTH, GLP-1, and CGRP, the first residue at the N-terminal helical end of each peptide is located at the same relative position near TM6 in the TMD pocket of the cognate receptor (Fig. 4, A and B). Both LA-PTH and GLP-1 have one additional N-terminal residue before the N-terminal helical end. CGRP has five additional N-terminal residues, which structurally turn away from the bottom of the agonist-binding pocket (*12*) (Fig. 4C). These extra residues also point toward TM6, pushing the C-terminal half of TM6 outward and partially unwinding this portion of the TM6 helix. There is also a similar outward movement of this region in TM7 (Figs. 4A and 5A). A near-80° sharp kink is seen between $P415^{6.47b}$ and $G418^{6.50b}$ in the middle of TM6, which is stabilized by $H420^{6.52b}$, $Q451^{7.49b}$, and $N374^{5.50b}$ that form capping interactions with the three backbone carbonyls from the broken helix residues 415 to 417 at the kink (Fig. 5B). $N374^{5.50b}$, $P415^{6.47b}$, $G418^{6.50b}$, $H420^{6.52b}$, and $Q451^{7.49b}$ (NPGHQ motif) are conserved across the class B GPCRs, with the only exception being $H^{7.49b}$ (fig. S9). Thus, despite different shapes and sizes of the TM pockets and the different peptide sequences, class B GPCRs share a common mechanism of ligand-mediated receptor activation through key conserved residues that stabilize the sharp kink at the middle of TM6.

This sharp kink results in a pronounced outward movement of the cytoplasmic end of the TM6 helix. This outward movement is also accompanied by a 90° rotation of the helical wheel at the $T410^{6.42b}$ position (fig. S10), which normally forms a conserved polar core with residues in TM2, TM3, and TM7 in the inactive GLP-1R structure (fig. S9). Rearrangement of this polar core has been proposed as a conserved mechanism for constitutively active class B GPCR mutants (*29*, *30*), and it is consistent with the constitutively active PTH1R mutant $H223R^{2.50b}$, which causes Jansen-type metaphyseal chondrodysplasia (*31*). Thus, the structure and sequence analyses indicate that the key residues that keep the receptors in an inactive state and the key residues that are involved in receptor activation are highly conserved among class B GPCRs.

The outward movement of TM6 leads to a large opening of the cytoplasmic cavity for coupling G_s. Compared with typical class A GPCRs, which undergo rapid deactivation (*32*, *33*), PTH1R can remain activated long after peptide dissociation (*34*), a phenomenon that was considered as a possible "molecular memory" of the active PTH1R state. Given the large degree of conformational changes between the active and inactive states of TM6, and prolonged signaling of PTH1R, we reason that the transition between these two states is separated by a high-energy barrier, which may explain slow kinetics of receptor activation and deactivation. A similar phenomenon of molecular memory and mechanism remains to be seen for other class B GPCRs.

The overall assembly of the receptor–G_s complex is remarkably similar among class B GPCR structures solved to date (*10*–*13*). This outward movement of TM6 and the resulting cavity formed on the cytoplasmic surface were not present in the recent crystal structure of an engineered PTH1R in complex with a PTH peptide, likely because of the TMD mutations that were introduced for thermal stability, as these mutations prevented activation and signaling (*35*). In the current structure, the main PTH1R–G_s complex is anchored by the α5 helix of $G\alpha_s$, which fits snugly into the cytoplasmic cavity of the TMD (Fig. 5, C and D). Additional contacts are observed between the extended helix 8 of the receptor and the Gβ subunit (Figs. 1 and 5F). The PTH1R residues that interface with the G_s protein are highly conserved across class B GPCRs (fig. S9). Structure comparison of PTH1R–G_s complexes with other class B GPCR–G_s complexes reveals substantial similarity in the G protein–binding interface, consistent with a common mechanism of G_s protein engagement (*36*). The only major difference is in the ICL2 conformation, in which PTH1R and GLP-1R are most similar to each other but different from CTR and CGRPR. In this conformation, the CGRPR F246 from ICL2 and corresponding F253 residue in CTR make much closer contacts with the αN helix and α5 helix of the $G\alpha_s$ than the corresponding residue in PTH1R and GLP-1R.

Outlook

We used cryo-EM to solve the near-atomic resolution structure of the LA-PTH–bound PTH1R in complex with G_s. This structure provides a

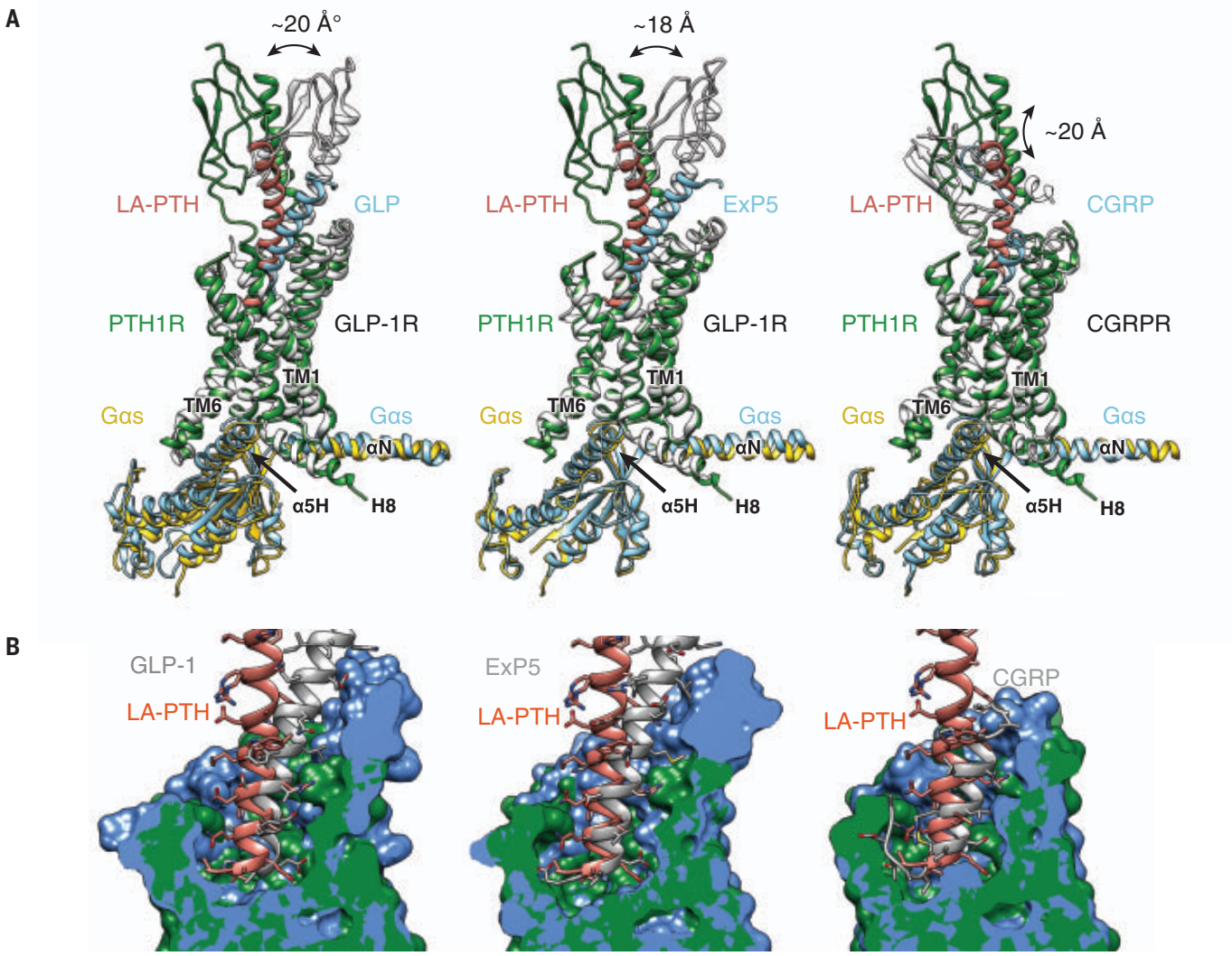

C

```
Glucagon-like
       PTH .....SVSEIQLMHNLGKHLNSMERVEWLRKKLQDVHN
     PTHrP .....AVSEHQLLHDKGKSIQDLRRRFFLHHLIAEIHT
   LA-PTH .....AVAEIQLMHQRAKWIQDARRRAFLHKLIAEIHT
      GLP1 ......HAEGTFTSDVSSYLEGQAAKEFIAWLVKGRG.
      GLP2 ......HADGSFSDEMNTILDNLAARDFINWLIQTKIT
  Glucagon ......HSQGTFTSDYSKYLDSRRAQDFVQWLMNT...
 Secretin ......HSDGTFTSELSRLREGARLQRLLQGLV.....
       GIP ......YAEGTFISDYSIAMDKIHQQDFVNWLLAQKGK
   PACAP27 ......HSDGIFTDSYSRYRKQMAVKKYLAAVLGKRYK
       VIP ......HSDAVFTDNYTRLRKQMAVKKYLNSILN....
     TIP39 ...SLALADDAAFRERARLLAALERRHWLNSYMHKLLV

Calcitonin-like
 Calcitonin CGNLSTCMLGTYTQDFNKFHTFPQTAIGVGAP.....
       CGRP ACDTATCVTHRLAGLLSRSGGVVKNNFVPTNVGSKAF.
     Amylin KCNTATCATQRLANFLVHSSNNFGAILSSTNVGSNTY.
Adrenomedullin GCRFGTCTVQKLAHQIYQFTDKDKDNVAPRSKISPQGY
```

D

	PTH1R	GLP1R[a]	GLP1R[b]	CGRPR
Receptor-peptide interface (Å^2)	3545	3465	2876	3841
ECD-peptide interface (Å^2)	1240	1170	884	1425
TMD-peptide interface (Å^2)	2305	2295	1983	2417
Pocket Volume (Å^3)	3581	3693	3663	3527
Peptide Occupied Volume (Å^3)	1839	1174	1188	1511
Peptide Pocket Occupancy (%)	51	32	32	42

Fig. 4. Basis of peptide hormone specificity. (**A**) Pairwise comparison of the LA-PTH bound to PTH1R with GLP-1, Exendin-P5 (ExP5), and CGRP in complex with their corresponding receptors, showing the relative positions of peptide ligands and their receptor ECDs. The RAMP1 component was omitted from the CGRPR figure for clarity. (**B**) Pairwise comparison of the PTH1R structure with GLP-1R bound to GLP-1, ExP5, and CGRPR, showing the pocket shapes accommodating respective peptide ligands. (**C**) Sequence alignment of class B GPCR peptide ligands. (**D**) Pocket size and occupancy of peptide ligands in class B GPCR structures. GLP-1R[a] is a GLP-1–bound GLP-1R structure, and GLP-1R[b] is an ExP5–bound GLP-1R structure.

comprehensive understanding of how PTH1R interacts with an agonist peptide ligand and couples to G_s and further reveals the prolonged active state of PTH1R that sustains endosomal cAMP signaling. Structural comparison with other class B GPCRs provides the basis of peptide binding specificity as well as the common mechanism of ligand-induced receptor activation and coupling to downstream G_s protein. Given the relatively conserved complex assembly and key structural components, the principles derived from these structural observations should be applicable to the entire family of class B GPCRs. Moreover, PTH is a classic endocrine hormone identified more than 80 years ago, with a rich history of physiological and pharmacological studies. The structure reported in this paper provides a foundation to systematically rationalize the extensive

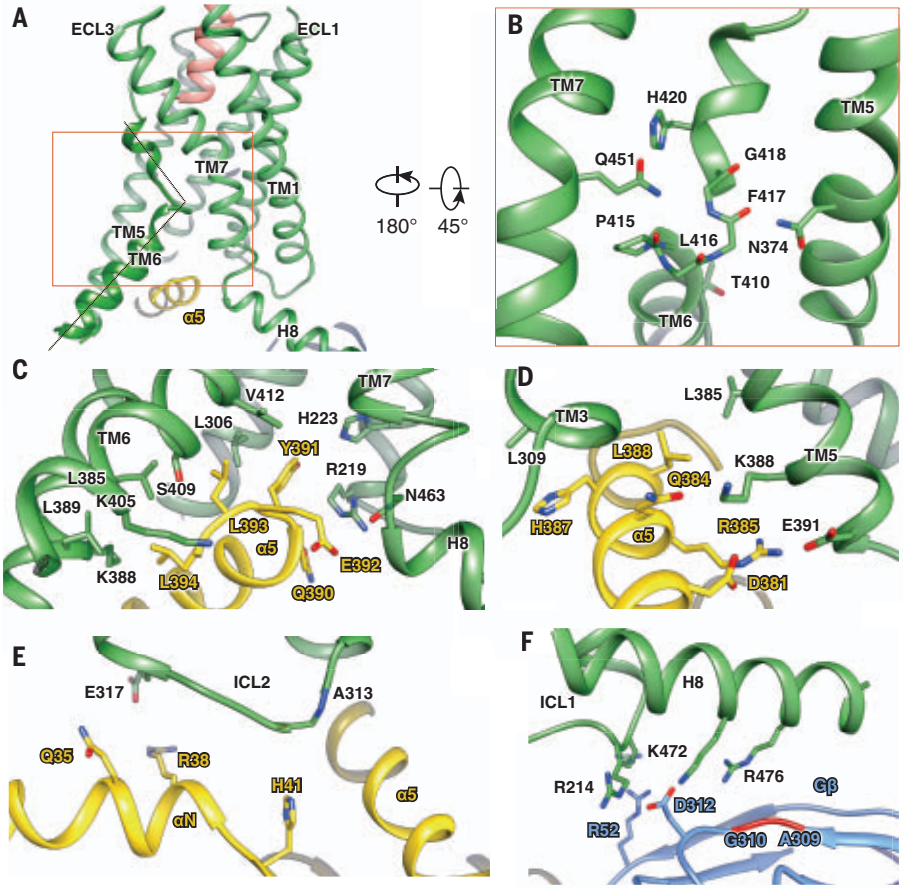

Fig. 5. Common mechanism of class B GPCR activation and G_s coupling. (**A**) The relative position of the LA-PTH N terminus (orange) toward the sharp kink of TM6 (green). (**B**) The kink and helix capping at TM6 are stabilized by conserved interactions with residues from TM5 ($N374^{5.50b}$) and TM7 ($Q451^{7.49b}$). (**C** to **F**) The PTH1R–G_s interface, including $G\alpha_s$ α5-PTH1R helix 8 interface (C); $G\alpha_s$ α5-PTH1R TM3/TM5 interface (D); PTH1R ICL2-$G\alpha_s$ αN helix interface (E); and helix 8–Gβ interface (F). PTH1R, green; $G\alpha_s$, yellow; and Gβ, cyan.

body of biochemical and mutational data developed for the PTH1R and from which to move toward new treatments of bone and mineral diseases, such as osteoporosis and cancer cachexia. In addition, the extensive ordered lipids around the PTH1R TMD provide a structural template for studying membrane protein–lipid interactions.

REFERENCES AND NOTES

1. T. J. Gardella, J. P. Vilardaga, *Pharmacol. Rev.* **67**, 310–337 (2015).
2. S. Kir *et al.*, *Nature* **513**, 100–104 (2014).
3. K. Pal, K. Melcher, H. E. Xu, *Acta Pharmacol. Sin.* **33**, 300–311 (2012).
4. A. A. Pioszak, N. R. Parker, T. J. Gardella, H. E. Xu, *J. Biol. Chem.* **284**, 28382–28391 (2009).
5. A. A. Pioszak, H. E. Xu, *Proc. Natl. Acad. Sci. U.S.A.* **105**, 5034–5039 (2008).
6. Y. Kang *et al.*, *Nature* **558**, 553–558 (2018).
7. A. Koehl *et al.*, *Nature* **558**, 547–552 (2018).
8. C. J. Draper-Joyce *et al.*, *Nature* **558**, 559–563 (2018).
9. J. García-Nafría, R. Nehmé, P. C. Edwards, C. G. Tate, *Nature* **558**, 620–623 (2018).
10. Y. Zhang *et al.*, *Nature* **546**, 248–253 (2017).
11. Y. L. Liang *et al.*, *Nature* **546**, 118–123 (2017).
12. Y. L. Liang *et al.*, *Nature* **561**, 492–497 (2018).
13. Y. L. Liang *et al.*, *Nature* **555**, 121–125 (2018).
14. L. H. Zhao *et al.*, *J. Biol. Chem.* **291**, 15119–15130 (2016).
15. Y. Yin *et al.*, *Cell Discov.* **2**, 16042 (2016).
16. S. G. Rasmussen *et al.*, *Nature* **477**, 549–555 (2011).
17. M. Shimizu *et al.*, *J. Bone Miner. Res.* **31**, 1405–1412 (2016).
18. G. Hattersley, T. Dean, B. A. Corbin, H. Bahar, T. J. Gardella, *Endocrinology* **157**, 141–149 (2016).
19. A. Maeda *et al.*, *Proc. Natl. Acad. Sci. U.S.A.* **110**, 5864–5869 (2013).
20. J. P. Vilardaga, F. G. Jean-Alphonse, T. J. Gardella, *Nat. Chem. Biol.* **10**, 700–706 (2014).
21. D. Wootten, J. Simms, L. J. Miller, A. Christopoulos, P. M. Sexton, *Proc. Natl. Acad. Sci. U.S.A.* **110**, 5211–5216 (2013).
22. T. J. Gardella *et al.*, *J. Biol. Chem.* **270**, 6584–6588 (1995).
23. C. Bergwitz *et al.*, *J. Biol. Chem.* **271**, 26469–26472 (1996).
24. J. P. Vilardaga, I. Lin, R. A. Nissenson, *Mol. Endocrinol.* **15**, 1186–1199 (2001).
25. P. Gourlet *et al.*, *Eur. J. Biochem.* **239**, 349–355 (1996).
26. M. D. Luck, P. H. Carter, T. J. Gardella, *Mol. Endocrinol.* **13**, 670–680 (1999).
27. T. Dean, A. Khatri, Z. Potetinova, G. E. Willick, T. J. Gardella, *J. Biol. Chem.* **281**, 32485–32495 (2006).
28. N. Shimizu, J. Guo, T. J. Gardella, *J. Biol. Chem.* **276**, 49003–49012 (2001).
29. Y. Yin *et al.*, *J. Biol. Chem.* **292**, 9865–9881 (2017).
30. X. E. Zhou, K. Melcher, H. E. Xu, *Protein Sci.* **28**, 487–501 (2018).
31. E. Schipani, K. Kruse, H. Jüppner, *Science* **268**, 98–100 (1995).
32. R. O. Dror *et al.*, *Proc. Natl. Acad. Sci. U.S.A.* **108**, 18684–18689 (2011).
33. K. J. Kohlhoff *et al.*, *Nat. Chem.* **6**, 15–21 (2014).
34. S. Ferrandon *et al.*, *Nat. Chem. Biol.* **5**, 734–742 (2009).
35. J. Ehrenmann *et al.*, *Nat. Struct. Mol. Biol.* **25**, 1086–1092 (2018).
36. A. Glukhova *et al.*, *ACS Pharmacol. Transl. Sci.* **1**, 73–83 (2018).

ACKNOWLEDGMENTS

The cryo-EM data were collected at the Center of Cryo-Electron Microscopy, Zhejiang University, with the assistance of S. Chang and X. Zhang. **Funding:** This work was partially supported by National Key Basic Research Program of China (2018YFC1003600 to Y.Z.); Zhejiang Province Science Fund for Distinguished Young Scholars (LR19H310001 to Y.Z.); Shanghai Science and Technology Development Fund (18ZR1447800 to L.-H.Z. and 16ZR1407100 to A.D.); the Young Innovator Association of CAS (2018325 to L.-H.Z.); SA-SIBS Scholarship Program (L.-H.Z. and D.Y.); the Fudan-SIMM Joint Research Fund (FU-SIMM-20174003 to L.-H.Z. and M.-W.W.); National Key R&D Program of China grant (2018YFA0507000 to M.-W.W.); National Science & Technology Major Project "Key New Drug Creation and Manufacturing Program," China (2018ZX09711002-002-005 to D.Y. and 2018ZX09735-001 to M.-W.W.); the National Natural Science Foundation of China (31300245 to L.-H.Z.; 81573479 and 81773792 to D.Y.); Ministry of Science and Technology (China) grants 2012ZX09301001, 2012CB910403, 2013CB910600, XDB08020303, and 2013ZX09507001 (to H.E.X.); Novo Nordisk-CAS Research Fund (NNCAS-2017-1-CC to D.Y.); the Jay and Betty Van Andel Foundation (H.E.X.); National Institutes of Health grants (GM127710 to H.E.X.; R01-DK102495, R01-DK111427, and R01-DK116780 to J.-P.V.; DK11794 to T.J.G.; and T32-GM008424 to A.D.W.); and the Cotswold Foundation Fellowship Awards (to F.G. J.-A. and A.D.W.). **Author contributions:** L.-H.Z. designed the expression constructs, purified the LA-PTH1R–G_s complex, prepared the final samples for negative stain and data collection toward the structures, and participated in figure and manuscript preparation. S.M. designed the expression constructs and purified the LA-PTH1R–G_s complex for initial negative stain EM. D.-D.S. performed specimen screening by negative-stain EM, cryo-EM grid preparation, cryo-EM data collection, and map calculations and prepared the bulk of figures. C.-Y.L. assisted in construct preparation, protein expression, and purification. M.-W.W. conceived of the study design, analyzed the data, and edited the manuscript. I.S., with the help of L.J.C., optimized the expression, purification, and assembly of the PTH1R in complex with LA-PTH and G_s and participated in manuscript editing. F.G.J.-A., A.D.W., A.D., X.C., J.C., and C.L. performed ligand-binding and signaling experiments. J.-P.V. independently conceived of the project; supervised the work of I.S., L.J.C., F.G.J.-A., and A.D.W.; and participated in manuscript writing. X.E.Z. built and refined the structure models and participated in manuscript writing. Y.K. performed initial negative stain EM screening. P.W.d.W. performed structural analysis, MD simulations, and figure preparation and participated in manuscript writing. D.Y., Y.J., and K.M. participated in data analysis and manuscript editing. H.E.X. conceived of the project; initiated collaborations with Y.Z., M.-W.W., and J.P.V.; supervised L.-H.Z., S.M., X.E.Z., P.W.d.W., and Y.K.; analyzed the structures; and wrote the manuscript. Y.Z. supervised the overall structural studies and participated in manuscript writing. **Competing interests:** The authors declare no competing interests. **Data and materials availability:** Density maps and structure coordinates have been deposited to the Electron Microscopy Database and the Protein Data Bank with accession numbers EMD-0410 and PDB ID 6NBF for conformation state 1, EMD-0411 and PDB ID 6NBH for conformation state 2, and EMD-0412 and PDB ID 6NBI for conformation state 3.

SUPPLEMENTARY MATERIALS

www.sciencemag.org/content/364/6436/148/suppl/DC1
Materials and Methods
Supplementary Text
Figs. S1 to S10
Tables S1 and S2
References (*37*–*58*)
Movie S1

20 October 2018; accepted 8 March 2019
10.1126/science.aav7942

REPORTS

PHYSICS

Electron-phonon instability in graphene revealed by global and local noise probes

Trond I. Andersen[1]*, Bo L. Dwyer[1]*, Javier D. Sanchez-Yamagishi[2]*, Joaquin F. Rodriguez-Nieva[1], Kartiek Agarwal[3], Kenji Watanabe[4], Takashi Taniguchi[4], Eugene A. Demler[1], Philip Kim[1,5], Hongkun Park[1,6], Mikhail D. Lukin[1]†

Understanding and controlling nonequilibrium electronic phenomena is an outstanding challenge in science and engineering. By electrically driving ultraclean graphene devices out of equilibrium, we observe an instability that is manifested as substantially enhanced current fluctuations and suppressed conductivity at microwave frequencies. Spatial mapping of the nonequilibrium current fluctuations using nanoscale magnetic field sensors reveals that the fluctuations grow exponentially along the direction of carrier flow. Our observations, including the dependence on density and temperature, are consistently explained by the emergence of an electron-phonon Cerenkov instability at supersonic drift velocities. These results offer the opportunity for tunable terahertz generation and active phononic devices based on two-dimensional materials.

Nonequilibrium phenomena in driven electronic and optical systems display rich dynamics that can be harnessed for applications such as Gunn diodes and lasers. Two-dimensional (2D) materials (*1*) constitute a new platform for exploring such nonequilibrium phenomena. In particular, modern ultraclean graphene devices exhibit high mobilities (*2*) and can be driven to high electronic drift velocities where instabilities have been predicted to occur. Examples include hydrodynamic instabilities (*3*) in electronic fluids (*4*, *5*), as well as Dyakonov-Shur instabilities, where plasmons are amplified by driven electrons (*6*, *7*). In addition to the potential use for high-frequency signal generation, understanding nonequilibrium dynamics is vital for many technological applications of graphene, including high-frequency transistors (*8*), ultrafast incandescent light sources (*9*), and flexible transparent interconnects (*10*). In practice, such electronic instabilities are difficult to realize owing to increased phonon scattering at high drift velocities. Although phonon scattering is typically an irreversible loss channel, long-lived phonons can themselves act as a source of instabilities. Specifically, when the electronic drift velocity (v_D) exceeds the sound velocity (v_s), stimulated phonon emission can dominate over absorption (Fig. 1B), resulting in exponential growth of the phonon population known as phonon Cerenkov amplification (*11*, *12*). This phenomenon has long been theoretically explored as a method to produce high-frequency acoustic waves (*13*, *14*), with experimental evidence found in bulk systems and semiconductor superlattices via acoustic and optical measurements (*15*–*18*).

Our experiments make use of electrically gated graphene devices encapsulated in hexagonal boron nitride (hBN) (Fig. 1A) and are conducted at cryogenic temperatures (T = 10 to 80 K). Figure 1C presents the low-bias transport properties of the ultraclean graphene system, with a mobility of 20 to 40 $m^2/V{\cdot}s$ at a carrier density, n, of 2×10^{12} cm^{-2}, corresponding to nearly ballistic transport (*19*). Due to the high mobility, carriers can be accelerated by an electric field to high drift velocities ($v_D \gg v_s = 21$ km/s), where a nonlinear current response is observed (Fig. 1D, blue). By contrast, a disordered device shows linear ohmic behavior (Fig. 1D, black).

We first study the nonequilibrium behavior by measuring the global noise in the source-drain current with a spectrum analyzer (noise power spectral density, PSD, averaged over 0.1 to 0.3 GHz), while varying the applied bias power, P. The noise observed in disordered devices (Fig. 1E, black) is in good agreement with increased thermal noise due to Joule heating and shows a characteristic $P^{1/3}$-dependence (*19*, *20*). Different behavior is observed in clean (hBN-encapsulated) devices, where the noise grows superlinearly with drive power and reaches values that are inconsistent with thermal noise. In particular, at higher biases, the noise increases to values equivalent to the thermal noise expected for a sample at 10,000 K (*19*). This behavior, observed consistently in 12 devices (*19*), stands in stark contrast to that of more disordered (not hBN-encapsulated) devices studied here and elsewhere (*20*, *21*), indicating a new noise source in driven graphene devices with low disorder.

To gain insights into the origin of this anomalous noise, we perform spatially resolved noise measurements by fabricating graphene devices on diamond substrates that contain shallow nitrogen-vacancy (NV) color-center impurities (40 to 60 nm depth) (*19*, *22*). These atomlike spin qubits can be individually measured using confocal microscopy and can probe nanoscale current noise by measuring the resulting magnetic fields (*23*–*25*). The locally probed noise under a driven clean graphene device exhibits similar superlinear behavior as global measurements (Fig. 1F).

We probe the spatial dependence of the anomalous noise by optically addressing single NV centers along the device (Fig. 2A) and measuring their spin relaxation rate (Fig. 2B), which is determined by the local noise at 2.87 GHz (*23*). Far from the midpoint of the device, the noise exhibits a clear asymmetry with current direction (Fig. 2C), with nearly an order of magnitude difference when the current is reversed. This is surprising given that the global noise and transport properties are independent of current direction (*19*). Using the device gate, we invert the sign of the charge carriers and find that the asymmetric pattern also inverts, indicating that the local noise signal depends on the flow direction of momentum, not charge. Figure 2D shows the local noise profile along the source-drain direction when $v_D = 5.8v_s$. We observe that the noise is small at the carrier entry point but then grows exponentially as the carriers flow down the 17-μm-long device. The noise profile inverts when the current direction is reversed and flips back when the carrier sign is also switched (Fig. 2E).

To explore the underlying dynamics, we measure the spectrum of the global current noise. When driven, the disordered graphene samples show $1/f$ noise and white thermal noise (Fig. 3A, black curve), consistent with previous studies (*20*, *26*). Clean devices, on the other hand, exhibit a peaked spectrum with a roll-off at ~1.5 GHz. The ac differential conductivity is suppressed at similar frequencies (Fig. 3B). These gigahertz features are in stark contrast to the equilibrium graphene Drude spectrum, which is featureless up to terahertz frequencies (*27*, *28*), thus indicating time scales much longer than the typical electronic lifetime. The frequencies of these nonequilibrium features are independent of drive voltage, doping, and temperature (*19*), but they are upshifted in a shorter device (Fig. 3, C and D).

The observed spectrum, spatial dependence, and scale of the anomalous noise are inconsistent

[1]Department of Physics, Harvard University, Cambridge, MA 02138, USA. [2]Department of Physics and Astronomy, University of California, Irvine, Irvine, CA 92697, USA. [3]Department of Physics, McGill University, Montréal, Québec H3A 2T8, Canada. [4]National Institute for Materials Science, Namiki 1-1, Tsukuba, Ibaraki 305-0044, Japan. [5]John A. Paulson School of Engineering and Applied Sciences, Harvard University, Cambridge, MA 02138, USA. [6]Department of Chemistry and Chemical Biology, Harvard University, Cambridge, MA 02138, USA.
*These authors contributed equally to this work.
†Corresponding author. Email: lukin@physics.harvard.edu

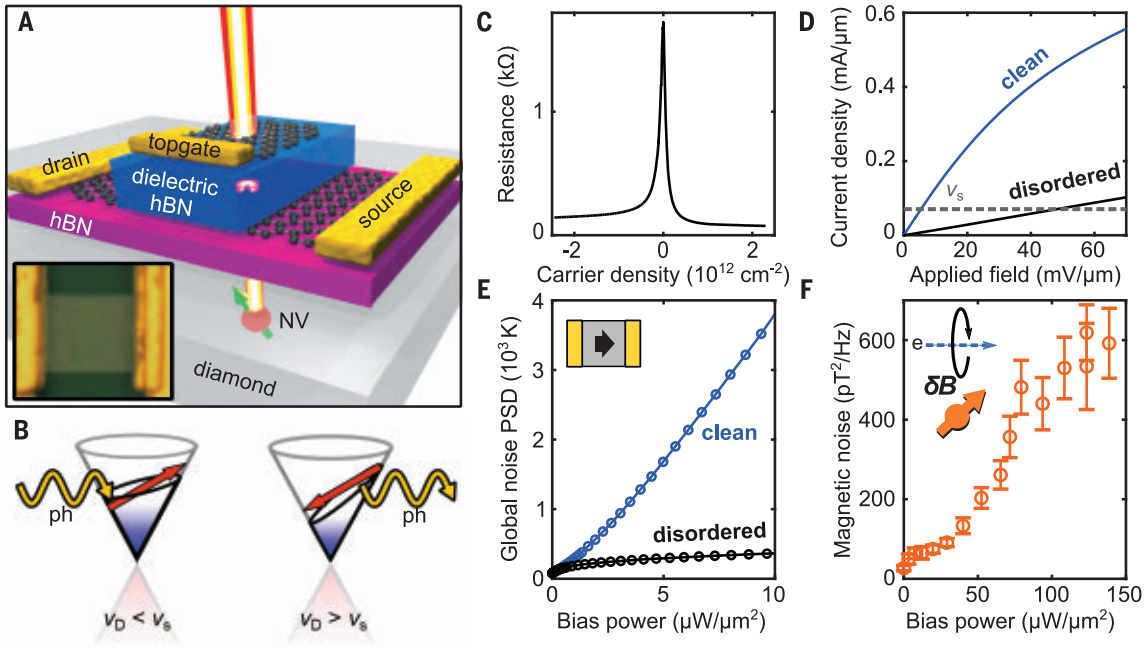

Fig. 1. Nonequilibrium dynamics in graphene, probed both globally and locally. (**A**) Device schematic: hBN-encapsulated graphene device on diamond substrate containing NV centers for nanomagnetometry. (Inset) Optical image of clean hBN-encapsulated device A1 (6 μm by 5.4 μm). (**B**) Condition for Cerenkov emission of phonons: when $v_D > v_s$, stimulated phonon (ph) emission dominates over absorption (right). (**C**) Two-probe resistance versus carrier density of device A1 (T = 10 K). (**D**) Current density as a function of applied electric field (T = 80 K) in clean device A1 (blue) and disordered device B1 (7 μm by 18 μm, black). The gray dashed line indicates where $v_D = v_s$ for the longitudinal acoustic mode. (**E**) Global electronic noise PSD (averaged over 100 to 300 MHz) as a function of bias power in devices A1 (blue) and B1 (black). Blue curve satisfies $v_D > v_s$ for P > 0.12 μW/μm^2. (**F**) Local magnetic noise (measured by NV nanomagnetometry) versus applied bias power in clean device C1 on diamond substrate. Error bars represent 95% confidence intervals.

with conventional noise sources (such as $1/f$ or white thermal/shot noise) (*29*). Our observations, especially the slow time scales and their independence on electronic parameters, are incompatible with many purely electronic mechanisms for ac signal generation (*3*, *6*, *19*, *30*) and suggest that other, longer-lived excitations play a role. In particular, the time scales match well with the time it takes for acoustic phonons to traverse the device. Furthermore, the anomalous effects occur only when the electronic drift velocity is higher than the speed of sound, but emerge at energies that are too low to excite optical phonons and plasmons ($2\hbar k_F v_D$, $k_B T <$ 20 meV, where $\hbar$ is the reduced Planck constant, k_F is the Fermi wavevector, and k_B is the Boltzmann constant) (*19*).

All of our observations are consistently explained as an electron-phonon Cerenkov instability. The key insight is that when the electronic drift velocity exceeds the speed of sound, a cone of forward-moving acoustic phonon modes experiences a faster rate of stimulated emission ($\gamma_{\mathbf{q}}^{\mathrm{em}}$) than absorption ($\gamma_{\mathbf{q}}^{\mathrm{abs}}$) (*11*–*14*). For the emitted phonons to amplify, $\gamma_{\mathbf{q}}^{\mathrm{em}}$ must exceed the loss rate due to absorption and other decay sources. Pristine graphene exhibits long acoustic phonon lifetimes ($\tau_{\mathbf{q}}$) (*31*), thus an emitted phonon can stimulate the emission of more phonons, leading to exponential growth (Fig. 3G). This process is seeded by a wide spectrum of spontaneously emitted and thermal phonons and is therefore expected to have limited coherence. Stochastic electronic scattering with the growing phonon population is expected to reduce the conductivity and increase noise.

To model these effects, we analyze the coupled electron-phonon dynamics by including the influence of the phonons on the electronic scattering rate, Γ_e (*19*)

$$\partial_t \mathbf{j}(\mathbf{r},t) = D\mathbf{E}(\mathbf{r},t) - \Gamma_e(\{n_{\mathbf{q}}\})\mathbf{j}(\mathbf{r},t) \qquad (1)$$

$$\partial_t n_{\mathbf{q}} = -\frac{(n_{\mathbf{q}} - n_{\mathbf{q},0})}{\tau_{\mathbf{q}}} + \gamma_{\mathbf{q}}^{\mathrm{em}}(\mathbf{j})(n_{\mathbf{q}}+1) - \gamma_{\mathbf{q}}^{\mathrm{abs}}(\mathbf{j})n_{\mathbf{q}} - v_s\hat{\mathbf{q}}\cdot\nabla n_{\mathbf{q}} \qquad (2)$$

Here, $D = 2e^2 v_F k_F/h$ is the Drude weight of graphene, $\mathbf{E}(\mathbf{r},t)$ is the electric field, $n_{\mathbf{q}}$ is the phonon occupation at wavevector $\mathbf{q}$, $n_{\mathbf{q},0}$ is the equilibrium phonon occupation when the current density, $\mathbf{j}$, is zero, and $\tau_{\mathbf{q}}^{-1}$ is assumed to be dominated by anharmonic interactions. Although we describe the phonon population using second quantization, the results can also be obtained through a semiclassical treatment. Using known constants for the electron-phonon coupling and anharmonic decay, we find that phonon amplification ($\Gamma_{\mathbf{q}}^{\mathrm{amp}} = \gamma_{\mathbf{q}}^{\mathrm{em}} - \gamma_{\mathbf{q}}^{\mathrm{abs}} - \tau_{\mathbf{q}}^{-1} >$ 0) can be easily achieved for a wide range of parameters (*19*). For instance, the parameters used in Fig. 2D ($v_D = 5.8 v_s$) give a maximum $\gamma_{\mathbf{q}}^{\mathrm{em}} - \gamma_{\mathbf{q}}^{\mathrm{abs}} = 11\,\mathrm{GHz}$ at $q \sim 2\pi/(25\,\mathrm{nm})$, where $\tau_{\mathbf{q}}^{-1} = 0.02\,\mathrm{GHz}$. The amplification of stochastically emitted phonons is expected to cause large fluctuations in the local electronic scattering rate, thus generating current noise. Due to the Poissonian nature of phonon emission, the fluctuations are expected to scale with the mean emission rate, which is proportional to $n_{\mathbf{q}}$. We thus plot the spatial profile of the excess phonon population ($\sim e^{\Gamma^{\mathrm{amp}} x/v_s} - 1$) associated with $\Gamma^{\mathrm{amp}} = 11\,\mathrm{GHz}$ (dashed black curve) along with the noise profile in Fig. 2D, and find good agreement with our experimental results. Integrating over more modes gives a similar profile, indicating the dominance of the most-amplified modes (*19*). This amplification behavior is also consistent with our global measurements, where the anomalous noise increases with device length (*19*).

The model also predicts that the electron-phonon Cerenkov instability gives rise to a conductivity spectrum of the form

$$\sigma(\omega) = \frac{\sigma^{\mathrm{Drude}}(0)}{1 - \frac{iK}{\omega t_T}(1 - e^{-i\omega t_T})} \qquad (3)$$

where $\sigma^{\mathrm{Drude}}(0) = D/\Gamma_e$ is the usual dc Drude conductivity and K is an increasing function of $\Gamma_{\mathbf{q}}^{\mathrm{amp}}$ (*19*). Importantly, $\sigma(\omega)$ depends on the sample traversal time for phonons, $t_T = L/v_s$, where L

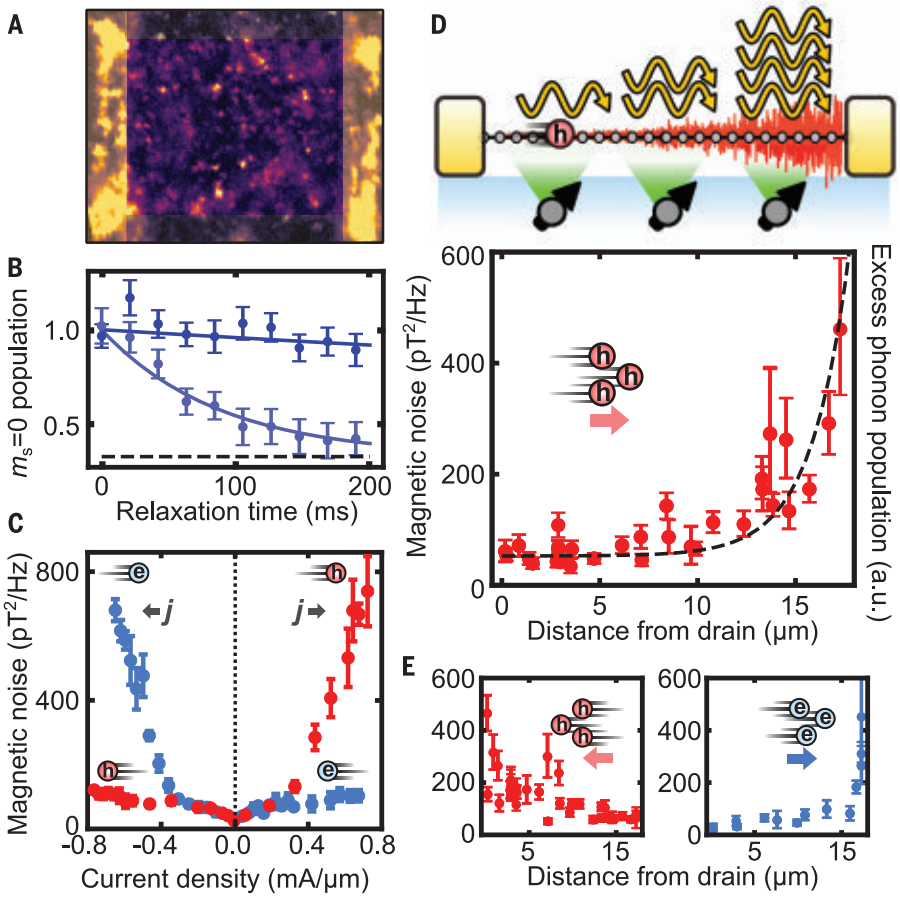

Fig. 2. Spatially resolved local noise measurements with NV magnetometry. (**A**) Fluorescence image of NV centers underneath device C2, with false-colored contacts and borders added. (**B**) NV spin relaxation from polarized to thermal state (dashed line), when current densities j = 0 mA/μm (dark blue) and j = −0.19 mA/μm (light blue) are passed through the device. Solid lines are fits. m_s, spin quantum number. (**C**) Local magnetic noise near drain contact as a function of graphene current density (device C1) in electron (e)– and hole (h)–doped regime (blue and red, respectively). (**D**) Spatial map of the local magnetic noise (device C2) at j = 0.18 mA/μm and $n = 0.92 \times 10^{12}$ cm^{-2}. The spatial profile is consistent with the exponential growth of phonons due to Cerenkov amplification (cartoon, top). Dashed black curve shows the theoretically predicted excess phonon population (offset to account for background noise). a.u., arbitrary units. (**E**) The growth direction is reversed by changing the current direction (left) or the charge carrier sign (right). Error bars represent 95% confidence intervals.

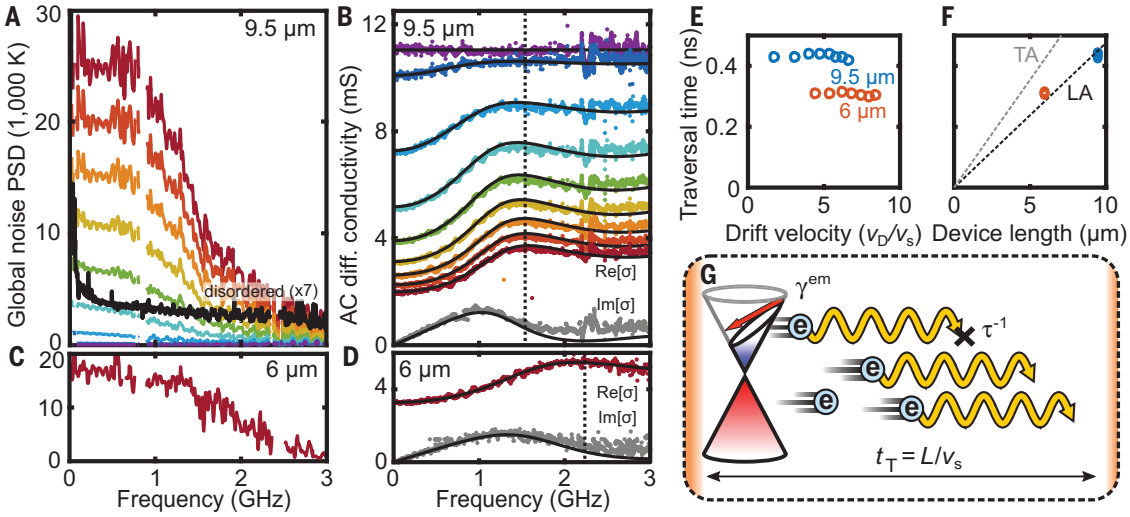

Fig. 3. Slow dynamics in global electronic measurements. (**A**) Global noise spectra at $n = 2 \times 10^{12}$ cm^{-2}. Colored curves: clean device A2 (9.5 μm by 11 μm) at bias ranging from 0 to 0.8 V (bottom to top). Black curve: disordered device B1 at maximum power applied to device A2 (scaled 7×). (**B**) Ac differential conductivity spectra (excitation: −20 dBm) (*19*) with biases 0 to 0.8 V [top to bottom, colors same as in (A)]. The real (Re) component is suppressed at low frequencies. Gray curve: imaginary (Im) component at 0.8 V. Black curves are fits. (**C** and **D**) Features in noise and conductivity spectra shift to higher frequencies in a shorter (6-μm) device (device A1) under similar electric field as maximum in (A) and (B). (**E** and **F**) Extracted traversal time from (B) and (D) as a function of drift velocity and device length. Dashed curves correspond to speed of sound in graphene [light gray, transverse acoustic (TA); dark gray, longitudinal acoustic (LA)]. (**G**) Cartoon of important rates in the driven electron-phonon system. During Cerenkov amplification, the correlation time observed in electronic measurements is limited by the phonon traversal time, $t_T = L/v_s$.

is the device length. When Cerenkov amplification occurs, the correlation time probed in conductivity measurements is no longer limited by the individual electron and phonon lifetimes but by the traversal time, because the memory of an emission event is amplified until the phonons reach the edge (reflected, backward-moving modes are no longer amplified). To account for the variation in t_T with phonon emission angle, we sum over a cone in phonon phase space in our fits (*19*). Our model gives excellent agreement with the observed conductivity spectra (Fig. 3, B and D, black curves) and even predicts the slight oscillatory behavior due to the sharp transit time cutoff. The extracted traversal time is

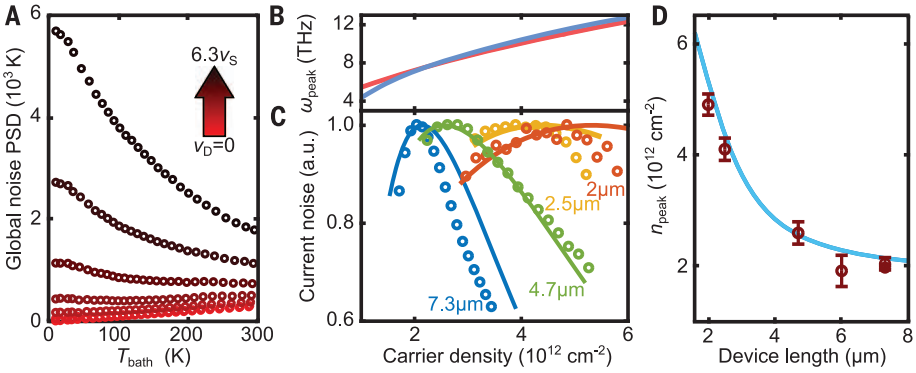

Fig. 4. Dependence on bath temperature and charge density. (**A**) Global noise PSD as a function of bath temperature at constant drift velocities and $n = 2 \times 10^{12}$ cm^{-2}. (**B**) Calculated peak phonon emission frequency, which can be tuned via the graphene carrier density (blue: T_e = 0 K; red: T_e = 320 K). (**C**) Normalized global current noise as a function of carrier density for different device lengths (j = 0.6 mA/μm). Solid curves show predicted total phonon emission. (**D**) The charge density at which the noise peaks (n_{peak}) for a wider variety of samples than in (C), with fit (blue). Error bars represent sampling spacing of carrier densities.

independent of drift velocity (Fig. 3E), and the corresponding speed matches that of the longitudinal acoustic mode in graphene (Fig. 3F) (*32*).

The extension of the correlation time is expected to also cause noise in the same low-frequency range, consistent with our observations (Fig. 3, A and C). Whereas the stochastic emission of a phonon normally causes a small drop in current that only lasts for $1/\Gamma_e \sim$ picoseconds, Cerenkov amplification both prolongs and magnifies the effect. The emitted phonon stimulates cascading emission of subsequent phonons, causing the current to continue decreasing until the phonon packet reaches the device edge. This should give strong current correlations $\langle \delta j(t) \delta j(t+\tau) \rangle$ for long τ (up to $t_T \sim 100$ ps) and thus noise at low frequencies $\lesssim 1/t_T$.

Cerenkov amplification is sensitive to the phonon lifetime, and the effect is therefore expected to intensify at lower temperatures because of slower anharmonic decay (*33*). We observe a strong increase in noise as the temperature is reduced from 300 to 10 K (Fig. 4A), in clear contrast to the decreasing thermal noise observed at low drives ($v_D \lesssim v_s$). This suggests that the amplification process is limited by scattering with thermally occupied modes at energies similar to that of the amplified mode (7 THz ~ 50 K at $n = 2 \times 10^{12}$ cm^{-2}).

Another important aspect of Cerenkov amplification in graphene is that the peak emission frequency is tunable via the carrier density, n (Fig. 4B). This peak occurs just below the upper limit $\omega \sim 2 v_s k_F$, corresponding to transitions across the entire Fermi surface. The frequency tunability manifests as a nonmonotonic dependence of the global current noise on n (Fig. 4C) (*19*). Initially, the noise increases with n, because the larger Fermi surface permits emission of more (and higher-energy) modes. In other words, increasing n broadens $\Gamma_{\mathbf{q}}^{amp}$. However, its maximum value decreases at constant current because $v_D = j/ne$, eventually causing a downturn in noise.

The crossover density, n_{peak}, is determined by the relative importance of the width and maximum of $\Gamma_{\mathbf{q}}^{amp}$, which depends on the device length. Analogously to an active filter, the amplification process narrows the excess phonon distribution $n_{\mathbf{q}}(x) \sim e^{\Gamma_{\mathbf{q}}^{amp} x / v_s}$ as it traverses the device. In longer devices, the noise therefore depends more on the maximum of $\Gamma_{\mathbf{q}}^{amp}$ than its width, causing a smaller n_{peak}. We observe such a length dependence, shown in Fig. 4, C and D in terms of current noise to facilitate comparison with the model. Plotting the predicted total phonon emission along with the data, we find that our model reproduces both the peak shift and narrowing well (*19*).

These considerations show that our observations are well explained as an electron-phonon Cerenkov instability in a 2D material. This driven electron-phonon system shows rich nonequilibrium dynamics that merit further exploration, potentially by developing new techniques to directly characterize the phonon spectrum. Prior theoretical work predicts that the amplified phonons in graphene have frequencies as high as 10 THz (*14*), substantially higher than those observed in other materials (*15*, *16*, *18*). Moreover, this system can offer purely electrical generation and amplification of phonons in a single micrometer-scale device, with wide frequency tunability. Future work could explore coupling to a mechanical cavity to develop a phononic laser, as well as outcoupling of the amplified sound waves to far-field terahertz radiation. Our results represent a promising step toward a new generation of active phononic and photonic devices based on 2D materials.

REFERENCES AND NOTES

1. K. S. Novoselov, A. Mishchenko, A. Carvalho, A. H. Castro Neto, *Science* **353**, aac9439 (2016).
2. L. Wang *et al.*, *Science* **342**, 614–617 (2013).
3. M. Mendoza, H. J. Herrmann, S. Succi, *Phys. Rev. Lett.* **106**, 156601 (2011).
4. R. Krishna Kumar *et al.*, *Nat. Phys.* **13**, 1182–1185 (2017).
5. J. Crossno *et al.*, *Science* **351**, 1058–1061 (2016).
6. M. Dyakonov, M. Shur, *Phys. Rev. Lett.* **71**, 2465–2468 (1993).
7. A. Tomadin, M. Polini, *Phys. Rev. B* **88**, 205426 (2013).
8. Y.-M. Lin *et al.*, *Science* **327**, 662 (2010).
9. Y. D. Kim *et al.*, *Nano Lett.* **18**, 934–940 (2018).
10. R.-H. Kim *et al.*, *Nano Lett.* **11**, 3881–3886 (2011).
11. A. Pippard, *Philos. Mag.* **8**, 161–165 (1963).
12. H. N. Spector, *Phys. Rev.* **127**, 1084–1090 (1962).
13. S. M. Komirenko, K. W. Kim, A. A. Demidenko, V. A. Kochelap, M. A. Stroscio, *Phys. Rev. B* **62**, 7459–7469 (2000).
14. C. X. Zhao, W. Xu, F. M. Peeters, *Appl. Phys. Lett.* **102**, 222101 (2013).
15. A. R. Hutson, J. H. McFee, D. L. White, *Phys. Rev. Lett.* **7**, 237–239 (1961).
16. M. Pomerantz, *Phys. Rev. Lett.* **13**, 308–310 (1964).
17. M. Eizenberg, B. Fisher, *J. Appl. Phys.* **49**, 5260–5269 (1978).
18. K. Shinokita *et al.*, *Phys. Rev. Lett.* **116**, 075504 (2016).
19. See supplementary materials.
20. A. Betz *et al.*, *Nat. Phys.* **9**, 109–112 (2013).
21. W. Yang *et al.*, *Nat. Nanotechnol.* **13**, 47–52 (2018).
22. J. R. Maze *et al.*, *Nature* **455**, 644–647 (2008).
23. S. Kolkowitz *et al.*, *Science* **347**, 1129–1132 (2015).
24. K. Agarwal *et al.*, *Phys. Rev. B* **95**, 155107 (2017).
25. F. Casola, T. van der Sar, A. Yacoby, *Nat. Rev. Mater.* **3**, 17088 (2018).
26. A. A. Balandin, *Nat. Nanotechnol.* **8**, 549–555 (2013).
27. J. Horng *et al.*, *Phys. Rev. B* **83**, 165113 (2011).
28. S. Awan *et al.*, *2D Mater.* **3**, 015010 (2016).
29. H. L. Hartnagel, R. Katilius, A. Matulionis, *Microwave Noise in Semiconductor Devices* (Wiley, 2001).
30. S. A. Mikhailov, *Phys. Rev. B* **87**, 115405 (2013).
31. D. L. Nika, E. P. Pokatilov, A. S. Askerov, A. A. Balandin, *Phys. Rev. B* **79**, 155413 (2009).
32. K. Kaasbjerg, K. S. Thygesen, K. W. Jacobsen, *Phys. Rev. B* **85**, 165440 (2012).
33. P. Klemens, D. Pedraza, *Carbon* **32**, 735–741 (1994).

ACKNOWLEDGMENTS

We thank J. Waissman, A. Talanov, B. Halperin, L. Levitov, D. Ham, K. de Greve, A. Safira, and K. C. Fong for helpful discussions. **Funding:** T.I.A., B.L.D., J.D.S.-Y., and M.D.L. acknowledge financial support from the Center for Ultracold Atoms, the National Science Foundation (NSF), the Department of Defense Vannevar Bush Faculty Fellowship, and the Gordon and Betty Moore Foundation. All fabrication was performed at the Center for Nanoscale Systems (CNS), a member of the National Nanotechnology Coordinated Infrastructure Network (NNCI), which is supported by the National Science Foundation under NSF award 1541959. CNS is part of Harvard University. K.A. acknowledges support from the UK Foundation. K.W. and T.T. acknowledge support from the Elemental Strategy Initiative conducted by the MEXT, Japan and the CREST (JPMJCR15F3), JST. P.K. acknowledges support from ARO (W911NF-17-1-0574). **Author contributions:** T.I.A., B.L.D., J.D.S.-Y., and K.A. conceived of the project. T.I.A., B.L.D., and J.D.S.-Y. designed and performed the experiments, fabricated the devices, analyzed the data, and wrote the manuscript. T.I.A., K.A., and J.F.R.-N. developed the theoretical model. T.T. and K.W. grew the hBN crystals. E.A.D., P.K., H.P., and M.D.L. supervised the project. **Competing interests:** The authors declare no competing interests. **Data and materials availability:** All data needed to evaluate the conclusions in the paper are present in the paper and the supplementary materials.

SUPPLEMENTARY MATERIALS

www.sciencemag.org/content/364/6436/154/suppl/DC1
Materials and Methods
Supplementary Text
Figs. S1 to S26
Table S1
References (*34*–*60*)

28 November 2018; accepted 14 March 2019
10.1126/science.aaw2104

GRAPHENE

Quantum-critical conductivity of the Dirac fluid in graphene

Patrick Gallagher[1,2], Chan-Shan Yang[1,3], Tairu Lyu[1], Fanglin Tian[1,4], Rai Kou[1], Hai Zhang[1,5], Kenji Watanabe[6], Takashi Taniguchi[6], Feng Wang[1,2,7]*

Graphene near charge neutrality is expected to behave like a quantum-critical, relativistic plasma—the "Dirac fluid"—in which massless electrons and holes collide at a rapid rate. We used on-chip terahertz spectroscopy to measure the frequency-dependent optical conductivity of clean, micrometer-scale graphene at electron temperatures between 77 and 300 kelvin. At charge neutrality, we observed the quantum-critical scattering rate characteristic of the Dirac fluid. At higher doping, we detected two distinct current-carrying modes with zero and nonzero total momenta, a manifestation of relativistic hydrodynamics. Our work reveals the quantum criticality and unusual dynamic excitations near charge neutrality in graphene.

Landau's theory of the Fermi liquid describes the interacting electrons of a typical metal as an ideal gas of noninteracting quasiparticles (*1*). This description is expected to fail in monolayer graphene (*2*): Owing to its linearly dispersing bands and minimally screened Coulomb interactions, graphene near charge neutrality should host a "Dirac fluid" (*3*–*8*)—a quantum-critical (*3*, *9*, *10*) plasma of electrons and holes governed by relativistic hydrodynamics (*11*–*13*).

A surprising consequence of relativistic hydrodynamics is that in lightly doped graphene, current should be carried by two distinct modes with zero and nonzero total momenta (*11*–*13*), sometimes referred to as energy waves and plasmons (*8*). The zero-momentum mode (Fig. 1A, left), which characterizes transport in the pure Dirac fluid at charge neutrality, consists of counterpropagating populations of thermally excited electrons and holes with equal but opposite net momenta. This current can be relaxed by charge carrier collisions, predicted to occur at the quantum-critical rate ~$k_B T/\hbar$, where k_B is the Boltzmann constant, T is absolute temperature, and $\hbar$ is the Planck constant divided by 2π (*9*). The finite-momentum mode (Fig. 1A, right), which emerges upon doping, can be pictured as a fluid of co-propagating electrons and holes. Unbalanced charge in this moving fluid produces an electrical current that cannot be relaxed by the momentum-conserving interactions between charge carriers, as in a Fermi liquid (*12*). As doping increases, the weight of the zero-momentum mode should decrease while that of the finite-momentum mode increases, smoothly crossing over from Dirac fluid to Fermi liquid behavior (*8*, *12*). The coexistence of these two modes—relaxed by entirely different mechanisms—leads to transport beyond the standard Drude picture.

Recent experiments on clean monolayer graphene have observed low-frequency transport phenomena consistent with the hydrodynamic description, including a violation of the Wiedemann-Franz law predicted for the Dirac fluid (*4*) and viscous flow of electrons (*14*, *15*). Electron-hole collisions have also been shown to limit conductivity in charge-neutral bilayer graphene (*16*). Yet direct observation of the quantum-critical conductivity of the Dirac fluid has remained elusive. Time-domain terahertz spectroscopy (*17*) is an ideal probe of the dynamic response over a broad frequency range, but the mismatch between the ~300-μm photon wavelength and ~10-μm lateral size of clean (*18*) graphene samples has limited its use to lower-quality, large-area films (*19*–*25*) in which Dirac fluid physics is obscured (*7*). Our study leverages the subwavelength confinement of a coplanar waveguide (*26*) to measure the terahertz optical

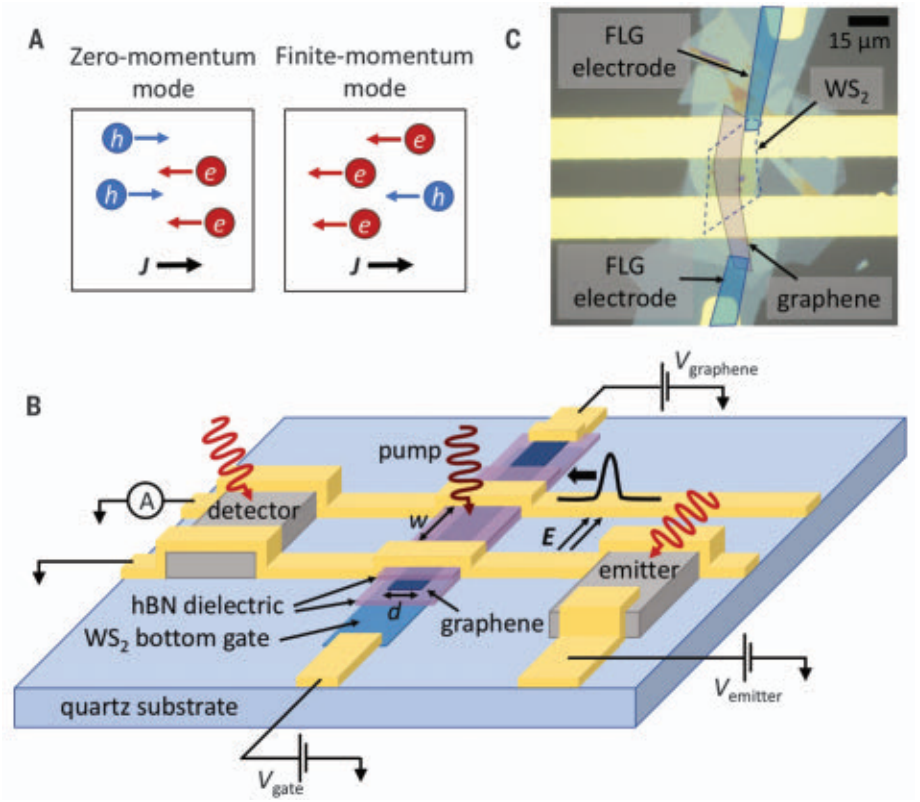

Fig. 1. Using on-chip terahertz spectroscopy to probe the electrodynamics of graphene. (**A**) Current-carrying modes of a graphene sheet. The zero-momentum mode corresponds to a plasma of counterpropagating electrons and holes, and can be relaxed by electron-hole interactions. The finite-momentum mode corresponds to a fluid of co-propagating electrons or holes with nonzero net charge, and cannot be relaxed by charge carrier interactions. The vector J denotes the net current flow. (**B**) Cartoon of our sample. Photoconductive switches ("emitter" and "detector") triggered by a pulsed laser emit and detect terahertz pulses (electric field E) within the waveguide. The transmitted pulse is reconstructed by measuring the current collected by the preamplifier ("A") as a function of delay between laser pulse trains illuminating the emitter and detector. The graphene is optionally excited by a separate pulsed beam ("pump") to heat the electron system. (**C**) Photograph of the heterostructure embedded in the waveguide. Few-layer graphene (FLG) electrodes make contact to the monolayer graphene sheet under study and the WS_2 gate electrode. Scale bar, 15 μm.

conductivity of 10-μm–scale graphene encapsulated (*18*) in hexagonal boron nitride (hBN). The measured conductivity at electron temperatures T_e between 77 and 300 K confirms the quantum-critical scattering rate near charge neutrality, as well as the coexistence of the zero- and finite-momentum modes at nonzero doping.

Our waveguide (Fig. 1B) consists of two parallel gold traces 16 μm wide and 200 nm thick, separated by 14 μm and extending 8 mm on a fused quartz substrate. Centered beneath the waveguide is the heterostructure under study (Fig. 1C), which from top to bottom consists of a 48-nm hBN flake, monolayer graphene, a 32-nm hBN flake, and a few-layer WS_2 gate electrode, chosen for its minimal terahertz absorption (see fig. S2 for sample cross section). The graphene within the w = 14 μm waveguide gap is d = 9 μm wide. Both graphene and WS_2 are isolated at dc from the waveguide traces by the hBN flakes, whose impedances at microwave frequencies are small.

Emission and detection of terahertz pulses is accomplished using photoconductive switches (*17*) made of semiconducting GaAs with a carrier lifetime of ~1 ps. The emitter switch contacts the lower waveguide trace (Fig. 1B) and is biased with a dc voltage. When triggered by a laser pulse (pulse width 150 fs, center wavelength 800 nm, repetition rate 80 MHz), the biased emitter becomes highly conductive for ~1 ps and injects a current pulse into the coplanar waveguide, exciting a quasi-TEM (transverse electromagnetic) mode whose field distribution resembles an electric dipole with opposite charges on each trace (*27*). The pulse travels with minimal dispersion (*26*) along the waveguide, interacting with graphene before reaching a detector switch spanning both traces. When the detector is triggered by a laser pulse, a current proportional to the instantaneous local voltage between waveguide traces flows into the upper trace and is collected by a current preamplifier. Recording the current as a function of time delay between laser pulse trains triggering the emitter and detector measures the time-domain profile of the transmitted voltage pulse, $V(t)$. In practice, we achieve lower noise by modulating the optical path length and detecting the resulting modulation in current with a lock-in amplifier, effectively measuring dV/dt (*27*).

All measurements are performed at a lattice temperature of 77 K unless noted otherwise. We use a separate optical pump pulse (*27*) (Fig. 1B) to independently heat the electron system as follows. After absorption, the electron system rapidly (~150 fs) thermalizes to a high temperature T_e and equilibrates with a bath of strongly coupled optical phonons (*28*, *29*). These phonons decay over 1 to 2 ps (*30*, *31*), returning the lattice to near-equilibrium and lowering T_e below the threshold for optical phonon emission. After this rapid cooling, a period of much slower (tens of picoseconds) cooling ensues (*32*–*34*); we study different values of T_e by timing our probing terahertz pulse to arrive at the sample at different times during that slow-cooling period (*32*–*34*). In conjunction with ac modulation techniques, our optical heating approach enables us to isolate the terahertz response of graphene from that of other materials in the waveguide (*27*). Optical heating also reduces phonon contributions to the observed scattering rate because the lattice remains near 77 K.

We first investigated the optical conductivity of the Fermi liquid at 77 K. The transmitted waveforms contain sharp, subpicosecond features that evolve with gate voltage (Fig. 2A, inset), with maximum transmission at charge neutrality (*27*). To extract the optical conductivity from the time-domain data, we model our device as an infinite, lossless transmission line containing a short segment with conductance G (graphene) between the conductors; this approach is justified by finite-element simulations (*27*). A wave mechanics calculation (*27*) yields $G = 2Z_0^{-1}(\tilde{V}_0/\tilde{V} - 1)$, where Z_0 = 133 ohms is the waveguide impedance determined from simulations, $\tilde{V}$ is the Fourier transform of the measured time-domain pulse transmitted through graphene, and $\tilde{V}_0$ is the Fourier transform of the transmitted pulse in the absence of graphene. Because we cannot measure $\tilde{V}_0$, we approximate it by the transmission at charge neutrality, incurring small, correctable errors (*27*). In all measurements, we heavily dope the graphene beneath the waveguide traces to minimize its impedance, so that $G = (d/w)\sigma$ measures the conductance of the $d \times w$ graphene region of conductivity σ between the traces. [At large ε_F, however, corrections stemming from graphene beneath the traces must still be applied to obtain σ (*27*).]

The extracted optical conductivities $\sigma = \sigma' + i\sigma''$ at various values of $\varepsilon_F \geq 46$ meV (Fig. 2, A and B) clearly follow the Drude form, $\sigma = D_{gr}\pi^{-1}(\tau^{-1} - i\omega)^{-1}$. Using the chemical potential μ determined from the gate capacitance [32 nm hBN, ε = 3 along the c axis (*35*)] and the known Drude weight of graphene, $D_{gr} = 2(e/\hbar)^2 k_B T_e \log\{2\cosh[\mu(2k_B T_e)^{-1}]\}$ (*24*), Drude fits match the data well with only τ^{-1} as a free parameter. The extracted scattering rates at 77 K fall between 0.5 and 1 THz (Fig. 2B, inset), indicative of infrequent scattering by disorder and phonons, and consistent with transport studies of similar heterostructures at comparable doping (*18*). These results confirm the anticipated Fermi liquid behavior.

We probed transport at charge neutrality by observing the change in terahertz transmission ΔV upon optically heating the electron system from T_0 = 77 K to different electron temperatures T_e, varied by adjusting the delay between optical pump and terahertz probe pulses. The transmission line model yields (*27*) the corresponding conductivity change $\Delta\sigma = (w/d)\Delta G = -2(w/d)Z_0^{-1}\Delta\tilde{V}/\tilde{V}$ (Fig. 3, A and B); although this model becomes less accurate as σ decreases, simulations confirm that it introduces only minor errors in our analysis (*27*). Current in charge-neutral graphene should be carried by the zero-momentum mode (Fig. 1A, left), which is relaxed primarily by electron-electron scattering at a rate τ_{ee}^{-1}, but also by disorder/phonon scattering at a rate τ_d^{-1}. Using a relaxation-time approximation, both scattering mechanisms can be captured by the sum $\tau^{-1} = \tau_{ee}^{-1} + \tau_d^{-1}$ so that

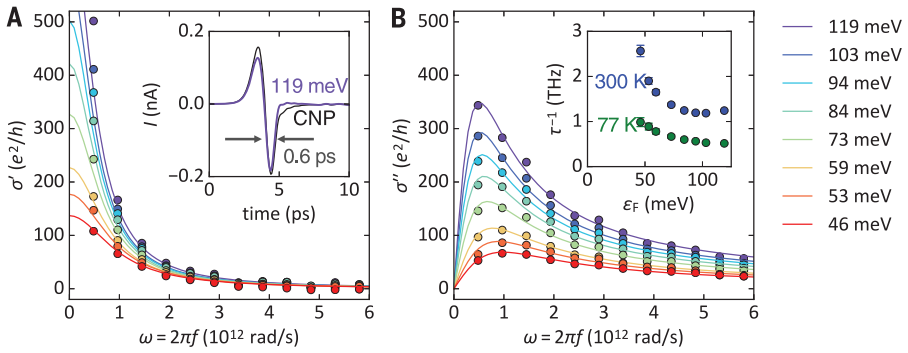

Fig. 2. Frequency-dependent optical conductivity of graphene in the Fermi liquid regime. (**A** and **B**) Real (A) and imaginary (B) parts of the extracted optical conductivity for several Fermi energies between 46 and 119 meV (electron doping) at 77 K. Solid curves are Drude fits using only the scattering rate τ^{-1} as a free fitting parameter for each curve. Inset in (A) shows an example of the time-domain current data used to extract conductivity in the frequency domain; the purple trace shows the transmitted waveform at 119 meV, and the black trace shows the transmitted waveform at the charge neutrality point (CNP), which is used as a reference. Fast Fourier transforms of these traces are shown in fig. S3. Inset in (B) shows the extracted τ^{-1} at lattice temperatures of 77 K and 300 K.

[1]Department of Physics, University of California, Berkeley, CA 94720, USA. [2]Kavli Energy NanoScience Institute, University of California, and Lawrence Berkeley National Laboratory, Berkeley, CA 94720, USA. [3]Institute of Electro-Optical Science and Technology, National Taiwan Normal University, Taipei 11677, Taiwan. [4]School of Physics, Nankai University, Tianjin 300071, China. [5]School of Information Engineering, Nanchang Institute of Technology, Nanchang 330099, China. [6]National Institute for Materials Science, 1-1 Namiki, Tsukuba 305-0044, Japan. [7]Materials Sciences Division, Lawrence Berkeley National Laboratory, Berkeley, CA 94720, USA.
***Corresponding author. Email: fengwang76@berkeley.edu (F.W.)**

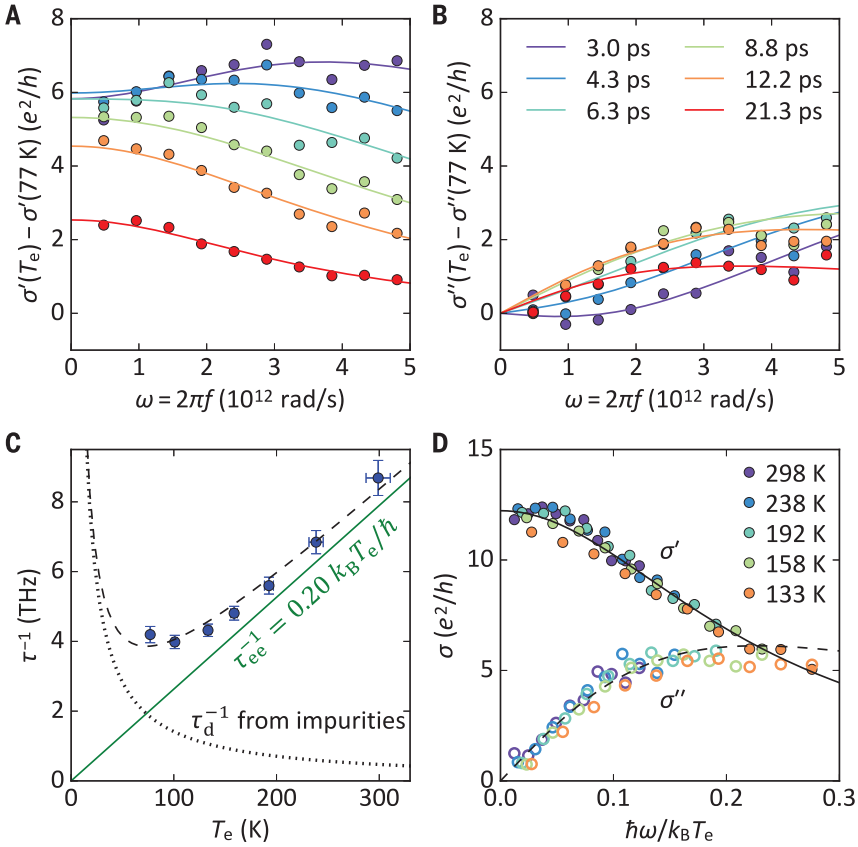

Fig. 3. Quantum-critical scattering rate of the Dirac fluid. (**A** and **B**) Real (A) and imaginary (B) parts of the change in optical conductivity at charge neutrality upon optically heating the electron system to a temperature T_e above the equilibrium temperature T_0 = 77 K. Each curve corresponds to a different delay between the optical pump pulse (fluence 21 nJ cm^{-2}) and the terahertz probe pulse; see legend in (B). Solid curves are fits to a difference between Drude functions at T_e and T_0, using T_e and the scattering rate $\tau^{-1}(T_e)$ as free fit parameters for each pair of curves of the complex conductivity. (**C**) Blue markers indicate the scattering rates and electron temperatures extracted from the fits shown in (A) and (B); error bars indicate SE in the fits. The experimental scattering rate follows $\tau^{-1} = \tau_{ee}^{-1} + \tau_d^{-1}$ (dashed curve), where $\tau_{ee}^{-1} = 0.20 k_B T_e/\hbar$ (green line) is the scattering rate due to charge carrier interactions, and $\tau_d^{-1} \propto n_{imp} T_e^{-1}$ (dotted curve) is the scattering rate due to unscreened, singly charged impurities with density $n_{imp} = 2.1 \times 10^9$ cm^{-2}. (**D**) Real and imaginary parts (open and solid circles, respectively) of σ at different values of T_e (i.e., different optical pump delays), replotted as a function of $\hbar\omega/k_B T_e$. The data for T_e = 100 K (21.3 ps delay) do not collapse and are omitted. Solid and dashed curves are fits to the real and imaginary parts of the universal function σ_U; the fits yield C = 0.23 (see text).

the conductivity follows the simple Drude form $D_{gr}^{\mu=0}\pi^{-1}(\tau^{-1} - i\omega)^{-1}$, where $D_{gr}^{\mu=0} \propto T_e$ is the Drude weight for graphene evaluated at μ = 0 (*9*, *12*, *13*). Although not exact, this Drude form is qualitatively reasonable. We thus fit Δσ to a difference between Drude functions at T_e and T_0: $\Delta\sigma = D_{gr}^{\mu=0}(T_e)\pi^{-1}(\tau^{-1} - i\omega)^{-1} - D_{gr}^{\mu=0}(T_0)\pi^{-1}(\tau_0^{-1} - i\omega)^{-1}$. For each optical pump delay, T_e and the associated scattering rate τ^{-1} are unknown fit parameters, whereas τ_0^{-1}, the scattering rate at T_0 = 77 K, is a global fit parameter for all curves.

The data are well described by the difference in Drude functions (Fig. 3, A and B, solid curves), providing precise estimates of τ^{-1} as a function of T_e (Fig. 3C). For T_e > 130 K, τ^{-1} grows almost linearly with T_e up to the highest accessible temperature, T_e = 299 ± 12 K. This linear evolution is a key signature of charge carrier interactions in the quantum-critical Dirac fluid, which are expected to scale as $\tau_{ee}^{-1} = Ck_B T_e/\hbar$, where C is a dimensionless constant (*9*). Below 130 K, τ^{-1} deviates from the linear τ_{ee}^{-1}, likely because of charged impurities, which contribute a scattering rate $\tau_d^{-1} \propto n_{imp} T_e^{-1}$ for a density n_{imp} of unscreened impurities (*27*). Using the fitted value $n_{imp} = 2.1 \times 10^9$ cm^{-2}, the experimental τ^{-1} is quantitatively explained by the sum $\tau^{-1} = \tau_{ee}^{-1} + \tau_d^{-1}$ (Fig. 3C, dashed curve). Phonon scattering appears to be unimportant, consistent with expected phonon scattering rates for a phonon bath near T_0 = 77 K [~0.6 THz for T_e = 300 K, and much smaller scattering rates for lower T_e (*7*, *36*)].

The quantum-critical scattering at charge neutrality can be separately visualized in a plot of the conductivity σ as a function of $\hbar\omega/k_B T_e$: In the limit $\tau_{ee}^{-1} = Ck_B T_e/\hbar \gg \tau_d^{-1}$, the conductivity should approach the universal curve $\sigma_U = 4\log(2)\, e^2/h\, (C + i\hbar\omega/k_B T_e)^{-1}$. We retrieve σ by summing the measured Δσ (Fig. 3, A and B) and the Drude conductivity at T_0 (determined by the fit parameter τ_0^{-1}). Above 130 K, σ indeed collapses onto a single curve (Fig. 3D). The best fit to the universal curve σ_U yields C = 0.23, in approximate agreement with the value C = 0.20 obtained by fitting directly to $\tau^{-1}(T_e)$ (Fig. 3C).

The experimental value C = 0.20 aligns with theoretical expectations. Following the quantum Boltzmann theory of (*9*), C determines the fine-structure constant of graphene as $\alpha = \sqrt{C/3.646} = 0.23$. This value of α compares favorably with theory: Assuming an effective dielectric constant ε = 4 for interactions between carriers in hBN-encapsulated graphene, an unscreened picture finds $\alpha_0 \approx 300/(137\varepsilon) = 0.55$ (we assume a Fermi velocity $v_F = 10^6$ m/s), whereas accounting for screening via the random phase approximation (RPA) (*9*, *37*) gives $\alpha_{RPA} = \alpha_0[1 + (\pi\alpha_0/2)]^{-1} = 0.29$. Similar values of α have also been inferred from measurements of plasmons in hBN-encapsulated graphene (*38*). In total, our results validate the predicted quantum-critical scattering of the zero-momentum mode at charge neutrality.

Away from charge neutrality, current should be carried by both zero- and finite-momentum modes (Fig. 1A). The latter corresponds to a fluid of co-propagating electrons and holes with a net charge; because the total momentum is conserved by charge carrier collisions, this mode is only relaxed by disorder and phonon scattering events occurring with frequency $\tau_d^{-1} \ll \tau_{ee}^{-1}$. The two-component conductivity can be written as

$$\sigma = D_Z\pi^{-1}(\tau_{ee}^{-1} + \tau_d^{-1} - i\omega)^{-1} + D_F\pi^{-1}(\tau_d^{-1} - i\omega)^{-1} \quad (1)$$

(*8*), where D_Z and D_F are the Drude weights of the zero- and finite-momentum modes, respectively, and are known functions of μ and T_e (*27*). For a given $\varepsilon_F \neq 0$, the finite-momentum mode carries all of the Drude weight at T_e = 0, whereas at high temperatures, μ tends to zero and D_Z dominates (Fig. 4A).

We recorded the complex conductivity change $\Delta\sigma = \sigma(\varepsilon_F = 33\ \text{meV}, T_e) - \sigma(0, T_0)$ upon simultaneously doping from ε_F = 0 to 33 meV and heating from T_0 = 77 K to $T_e \approx 300$ K (Fig. 4, B and C). The real part, Δσ′, reveals two distinct Drude components: a narrow peak of

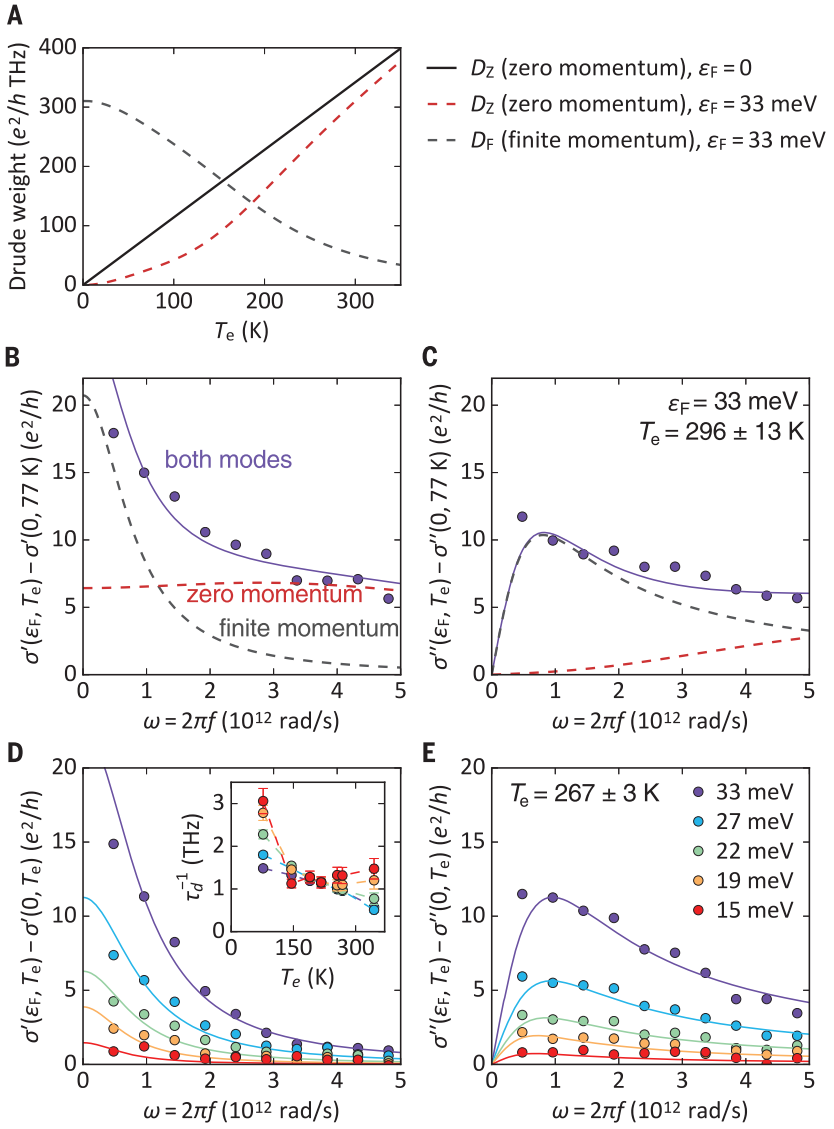

Fig. 4. Coexistence of zero- and finite-momentum modes at low doping. (**A**) Calculated Drude weights D_Z and D_F of the zero- and finite-momentum modes (*27*) in lightly electron-doped (ε_F = 33 meV) and undoped graphene. (**B** and **C**) Real (B) and imaginary (C) parts of the measured change in optical conductivity when charge-neutral graphene in equilibrium (T_0 = 77 K) is simultaneously heated to an electron temperature T_e (optical pump delay 3 ps, fluence 21 nJ cm^{-2}) and doped to ε_F = 33 meV. Solid curves show fits using the function described in the text, which sums the changes (dashed curves) in zero- and finite-momentum mode conductivities between (ε_F = 33 meV, T_e) and (ε_F = 0, T_0). (**D** and **E**) Real (D) and imaginary (E) parts of the measured change in optical conductivity when charge-neutral graphene at an electron temperature T_e (optical pump delay 4 ps, fluence 20 nJ cm^{-2}) is doped to various values of ε_F. Data at each doping are well fit by a single Drude function (solid curves) describing the conductivity of the finite-momentum mode with free fit parameters T_e = 267 ± 3 K and $\tau_d^{-1}(\varepsilon_F)$ ~ 1 THz. Inset in (D) shows the scattering rate for the finite-momentum mode τ_d^{-1} versus T_e extracted from fits at varying T_e; colors indicate ε_F as in (D) and (E).

width $\Delta\omega < 1 \times 10^{12}$ rad/s and a slowly varying background on the order of $7e^2/h$. We attribute these features to the conductivity changes of the finite- and zero-momentum modes, respectively. A numerical fit to the expression $\Delta\sigma = \sigma(\varepsilon_F = 33\text{ meV}, T_e) - \sigma(0, T_0)$, with σ described by Eq. 1 and $\sigma(0, T_0)$ already known (Fig. 3), confirms our qualitative assignments (Fig. 4, B and C, dashed curves). The fit yields $T_e = 296 \pm 13$ K, $\tau_{ee}^{-1} = 6.6 \pm 0.3$ THz, and $\tau_d^{-1} = 0.8 \pm 0.1$ THz.

As further evidence of two-mode conductivity, we isolated the contribution from the finite-momentum mode and showed that it behaves as a single Drude peak with the predicted Drude weight D_F. More specifically, we measured the conductivity change $\Delta\sigma = \sigma(\varepsilon_F, T_e) - \sigma(0, T_e)$ upon light doping under fixed optical pumping conditions (i.e., for T_e nearly constant). For sufficiently large T_e, $\Delta\sigma$ should approximate the conductivity of the finite-momentum mode at ε_F: Although light doping away from charge neutrality changes D_F and D_Z by similar amounts (Fig. 4A), the zero-momentum contribution to $\Delta\sigma$ is greatly spread out in frequency because $\tau_{ee}^{-1} \sim 10\tau_d^{-1}$. Using optical pumping conditions that produce $T_e \approx 250$ K at charge neutrality, the measured values of $\Delta\sigma$ at varying ε_F indeed behave like Drude functions (Fig. 4, D and E). The data are well fit by the expression $D_F\pi^{-1}(\tau_d^{-1} - i\omega)^{-1}$ (Fig. 4, D and E, solid curves), where the only free fitting parameters are τ_d^{-1} for each ε_F and the shared value of T_e, which enters the fit implicitly through D_F. The fits yield $T_e = 267 \pm 3$ K and $\tau_d^{-1} \sim 1$ THz for all values of ε_F.

To highlight the very different scattering mechanisms of the conducting modes, we collected $\Delta\sigma = \sigma(\varepsilon_F, T_e) - \sigma(0, T_e)$ for different doping levels and pumping conditions (i.e., varying both ε_F and T_e) and fit all data using Eq. 1 for σ. We assert that $\tau_{ee}^{-1} = 0.20k_BT_e/\hbar$ does not vary with ε_F; this approximate assignment leaves only T_e and τ_d^{-1} as free fitting parameters. The extracted values of τ_d^{-1} for the finite-momentum mode (Fig. 4D, inset) generally decrease with increasing T_e within our temperature window, in sharp contrast to the scattering rate for the zero-momentum mode, which increases approximately linearly with T_e.

The quantitative agreement between our experimental results and the relativistic hydrodynamic theory of the Dirac fluid implies that graphene should host relativistic phenomena not seen in typical electron systems, where relativistic hydrodynamics does not apply. For example, electronic sound waves in conventional metals either morph into plasmons or are destroyed by momentum relaxation, but such waves can exist in charge-neutral graphene owing to low disorder and zero coupling to plasmon modes (*39*). At high temperatures, graphene is also expected to display a collective cyclotron resonance that is primarily damped by collisions between charge carriers, rather than by disorder (*13*).

REFERENCES AND NOTES

1. D. Pines, P. Nozières, *The Theory of Quantum Liquids* (Addison-Wesley, 1989).
2. A. H. Castro Neto, F. Guinea, N. M. R. Peres, K. S. Novoselov, A. K. Geim, *Rev. Mod. Phys.* **81**, 109–162 (2009).
3. D. E. Sheehy, J. Schmalian, *Phys. Rev. Lett.* **99**, 226803 (2007).
4. J. Crossno *et al.*, *Science* **351**, 1058–1061 (2016).
5. A. Lucas, J. Crossno, K. C. Fong, P. Kim, S. Sachdev, *Phys. Rev. B* **93**, 075426 (2016).
6. B. N. Narozhny, I. V. Gornyi, A. D. Mirlin, J. Schmalian, *Ann. Phys.* **529**, 1700043 (2017).
7. D. Y. H. Ho, I. Yudhistira, N. Chakraborty, S. Adam, *Phys. Rev. B* **97**, 121404 (2018).
8. Z. Sun, D. N. Basov, M. M. Fogler, *Proc. Natl. Acad. Sci. U.S.A.* **115**, 3285–3289 (2018).
9. L. Fritz, J. Schmalian, M. Müller, S. Sachdev, *Phys. Rev. B* **78**, 085416 (2008).
10. D. T. Son, *Phys. Rev. B* **75**, 235423 (2007).
11. S. A. Hartnoll, P. K. Kovtun, M. Müller, S. Sachdev, *Phys. Rev. B* **76**, 144502 (2007).

12. M. Müller, L. Fritz, S. Sachdev, *Phys. Rev. B* **78**, 115406 (2008).
13. M. Müller, S. Sachdev, *Phys. Rev. B* **78**, 115419 (2008).
14. D. A. Bandurin *et al.*, *Science* **351**, 1055–1058 (2016).
15. R. Krishna Kumar *et al.*, *Nat. Phys.* **13**, 1182–1185 (2017).
16. Y. Nam, D.-K. Ki, D. Soler-Delgado, A. F. Morpurgo, *Nat. Phys.* **13**, 1207–1214 (2017).
17. M. C. Nuss, J. Orenstein, in *Millimeter and Submillimeter Wave Spectroscopy of Solids* (Springer, 1998), vol. 12, pp. 7–50.
18. L. Wang *et al.*, *Science* **342**, 614–617 (2013).
19. W. Liu, R. Valdés Aguilar, Y. Hao, R. S. Ruoff, N. P. Armitage, *J. Appl. Phys.* **110**, 083510 (2011).
20. L. Ren *et al.*, *Nano Lett.* **12**, 3711–3715 (2012).
21. G. Jnawali, Y. Rao, H. Yan, T. F. Heinz, *Nano Lett.* **13**, 524–530 (2013).
22. K. J. Tielrooij *et al.*, *Nat. Phys.* **9**, 248–252 (2013).
23. S.-F. Shi *et al.*, *Nano Lett.* **14**, 1578–1582 (2014).
24. A. J. Frenzel, C. H. Lui, Y. C. Shin, J. Kong, N. Gedik, *Phys. Rev. Lett.* **113**, 056602 (2014).
25. S. Kar, D. R. Mohapatra, E. Freysz, A. K. Sood, *Phys. Rev. B* **90**, 165420 (2014).
26. D. R. Grischkowsky, *IEEE J. Sel. Top. Quantum Electron.* **6**, 1122–1135 (2000).
27. See supplementary materials.
28. C. H. Lui, K. F. Mak, J. Shan, T. F. Heinz, *Phys. Rev. Lett.* **105**, 127404 (2010).
29. I. Gierz *et al.*, *Nat. Mater.* **12**, 1119–1124 (2013).
30. H. Yan *et al.*, *Phys. Rev. B* **80**, 121403 (2009).
31. K. Kang, D. Abdula, D. G. Cahill, M. Shim, *Phys. Rev. B* **81**, 165405 (2010).
32. J. H. Strait *et al.*, *Nano Lett.* **11**, 4902–4906 (2011).
33. M. W. Graham, S.-F. Shi, D. C. Ralph, J. Park, P. L. McEuen, *Nat. Phys.* **9**, 103–108 (2012).
34. J. C. W. Song, L. S. Levitov, *J. Phys. Condens. Matter* **27**, 164201 (2015).
35. A. F. Young *et al.*, *Phys. Rev. B* **85**, 235458 (2012).
36. T. Sohier *et al.*, *Phys. Rev. B* **90**, 125414 (2014).
37. R. R. Biswas, S. Sachdev, D. T. Son, *Phys. Rev. B* **76**, 205122 (2007).
38. G. X. Ni *et al.*, *Nat. Photonics* **10**, 244–247 (2016).
39. T. V. Phan, J. C. W. Song, L. S. Levitov, arXiv 1306.4972 [cond-mat.mes-hall]. 20 June 2013.
40. P. Gallagher, Data for: Quantum-critical conductivity of the Dirac fluid in graphene. Zenodo (2019). http://doi.org/10.5281/zenodo.2552519.

ACKNOWLEDGMENTS

Funding: Terahertz measurements were primarily supported by the Office of Naval Research under award N00014-15-1-2651. Sample fabrication was supported by the U.S. Department of Energy, Office of Science, Basic Energy Sciences, Materials Sciences and Engineering Division under contract DE-AC02-05-CH11231 (van der Waals heterostructures program, KCWF16). P.G. was supported by the Heising-Simons Junior Fellowship program of the Kavli ENSI at Berkeley. C.-S.Y. was supported by the Ministry of Science and Technology under grant 105-2917-I-564-026. R.K. was supported by the JSPS Overseas Research Fellowship program. Growth of hexagonal boron nitride crystals (K.W., T.T.) was supported by the Elemental Strategy Initiative conducted by the MEXT, Japan, and the CREST (JPMJCR15F3), JST. **Author contributions:** P.G. and C.-S.Y. built the optical apparatus and collected the data; P.G. performed the data analysis with input from all authors; P.G., C.-S.Y., F.T., and R.K. fabricated the samples; T.L. and H.Z. performed the waveguide simulations; P.G., C.-S.Y., and F.W. designed the experiment; P.G. wrote the manuscript with input from all authors; and K.W. and T.T. grew the hBN crystals. **Competing interests:** Authors declare no competing interests. **Data and materials availability:** All data necessary to understand and assess this manuscript are shown in the main text and supplementary materials. Data shown in the main text are also available in tabular form through Zenodo (*40*).

SUPPLEMENTARY MATERIALS

www.sciencemag.org/content/364/6436/158/suppl/DC1
Materials and Methods
Supplementary Text
Figs. S1 to S17
References (*41*, *42*)

13 April 2018; accepted 6 February 2019
Published online 28 February 2019
10.1126/science.aat8687

GRAPHENE

Measuring Hall viscosity of graphene's electron fluid

A. I. Berdyugin[1]*, S. G. Xu[1,2]*, F. M. D. Pellegrino[3,4], R. Krishna Kumar[1,2], A. Principi[1], I. Torre[5], M. Ben Shalom[1,2], T. Taniguchi[6], K. Watanabe[6], I. V. Grigorieva[1], M. Polini[7,1], A. K. Geim[1,2]†, D. A. Bandurin[1]†

An electrical conductor subjected to a magnetic field exhibits the Hall effect in the presence of current flow. Here, we report a qualitative deviation from the standard behavior in electron systems with high viscosity. We found that the viscous electron fluid in graphene responds to nonquantizing magnetic fields by producing an electric field opposite to that generated by the ordinary Hall effect. The viscous contribution is substantial and identified by studying local voltages that arise in the vicinity of current-injecting contacts. We analyzed the anomaly over a wide range of temperatures and carrier densities and extracted the Hall viscosity, a dissipationless transport coefficient that was long identified theoretically but remained elusive in experiments.

Electron transport in metallic systems is routinely described in terms of classical charges that whizz through the bulk and scatter at various defects, such as impurities, edges, or lattice vibrations. This semiclassical picture does not hold, however, for materials in which defects are scarce, and electron-electron collisions provide the shortest scattering length. In the latter case, electrons respond to external fields collectively so that their transport resembles a classical fluid flow (*1*–*3*). The studies of electron hydrodynamics have been hampered by the scarcity of experimental systems in which both impurity and electron-phonon scattering—which do not conserve the electron momentum—are weak so that electron-electron collisions become the dominant source of scattering. The situation has changed recently owing to improvements in materials quality (*4*, *5*), including high-quality graphene with its exceptionally weak electron-phonon coupling (*6*–*8*). Transport experiments have provided clear evidence for a fluid-like behavior of charge carriers in graphene, which reveals itself in, for example, negative vicinity resistance (*6*, *7*) and superballistic transport (*8*). Good agreement between the experiments and theory indicates that electron transport in high-quality graphene at temperatures (T) above 100 K is consistent with the hydrodynamics description (*7*, *9*–*13*).

[1]School of Physics and Astronomy, University of Manchester, Manchester M13 9PL, UK. [2]National Graphene Institute, University of Manchester, Manchester M13 9PL, UK. [3]Dipartimento di Fisica e Astronomia, Università di Catania, Via S. Sofia, 64, I-95123 Catania, Italy. [4]Istituto Nazionale di Fisica Nucleare, Sez. Catania, I-95123 Catania, Italy. [5]ICFO–Institut de Ciències Fotòniques, Barcelona Institute of Science and Technology, 08860 Castelldefels (Barcelona), Spain. [6]National Institute for Materials Science, 1-1 Namiki, Tsukuba, 305-0044 Japan. [7]Istituto Italiano di Tecnologia, Graphene Labs, Via Morego 30, 16163 Genova, Italy.
*These authors contributed equally to this work.
†Corresponding author. Email: geim@manchester.ac.uk (A.K.G.); bandurin.d@gmail.com (D.A.B.)

So far, studies of electron hydrodynamics focused on zero magnetic field B. On the other hand, the finite B regime described by a combination of the Navier-Stokes and Maxwell's equations is relevant for many research fields, ranging from astrophysics to plasma physics to geophysics and engineering. For static B, the viscous response of a charged fluid is described by a tensor in the Navier-Stokes equation that contains a dissipationless, off-diagonal coefficient called Hall or odd viscosity ν_H (*14*–*17*). To get some qualitative insight into the behavior of a two-dimensional (2D) electron fluid subjected to a nonquantizing magnetic field, we plotted the calculated electric potential distribution $\phi(\boldsymbol{r})$ expected near a narrow current injector in zero (Fig. 1A) and finite B (Fig. 1B). The injected current I entrains adjacent fluid regions, which results in negative lobes of the potential near the injector (*18*, *19*). In zero B (Fig. 1A), the lobes are symmetric with respect to the injection direction and, for restricted geometries, can be accompanied by whirlpools of electric current (*18*–*22*). Finite B induces considerable asymmetry in $\phi(\boldsymbol{r})$ (Fig. 1B), which involves the following three contributions. First, the ordinary Hall effect (HE) causes the well-known potential difference $V_H = IB/ne$ between the left and right sides of the half-plane (Fig. 1C), where n is the carrier density and e is the elementary charge. The second contribution comes from the longitudinal viscosity $\nu(B)$ and, in small B, is practically indistinguishable from that shown in Fig. 1A for zero B. The third contribution arises from Hall viscosity, the main subject of our interest here. The ν_H contribution (Fig. 1D) is opposite in sign to the classical HE (Fig. 1C); ν_H suppresses the normal Hall response, but this influence rapidly decays away from the injector region (Fig. 1D). The latter feature makes it difficult to observe the Hall viscosity by using conventional devices and measurement geometries such as the standard Hall bar configuration

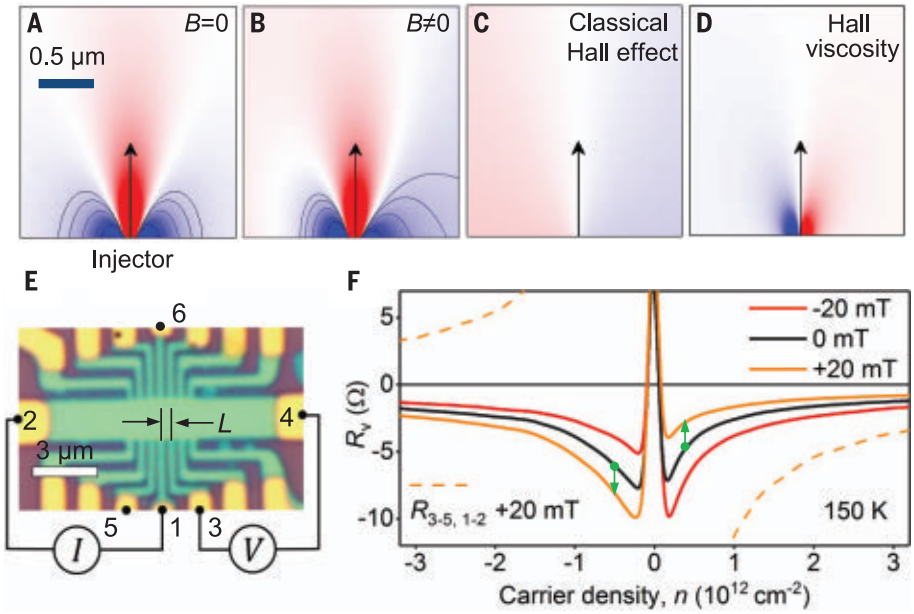

Fig. 1. Effect of magnetic field on viscous electron flow. (**A** and **B**) Electric potential distribution $\phi(\boldsymbol{r})$ expected in graphene's electron fluid near a current injector in zero B and 50 mT, respectively. The calculations were based on equations C15 and C16 of (*16*) by using characteristic zero-field viscosity $\nu_0 = 0.1$ m^2/s, found in our experiments; $n = 2 \times 10^{12}$ cm^{-2}; and $\tau = 2$ ps. Solid curves indicate equipotentials. (**C**) Contribution from the ordinary HE toward the map in (B). (**D**) Contribution that comes from ν_H. Color scale in (A) to (D) is dark blue to dark red and reflects −2.5 to +2.5 of the potential induced by the ordinary HE in (C). (**E**) Optical micrograph of one of our devices, along with the schematic of the vicinity geometry from which R_v is obtained. (**F**) Examples of the vicinity resistance for different B (solid curves); $L \approx 1$ μm. Dashed lines indicate Local Hall resistance measured by using voltage probes 3 and 5 close to the current injector (*22*).

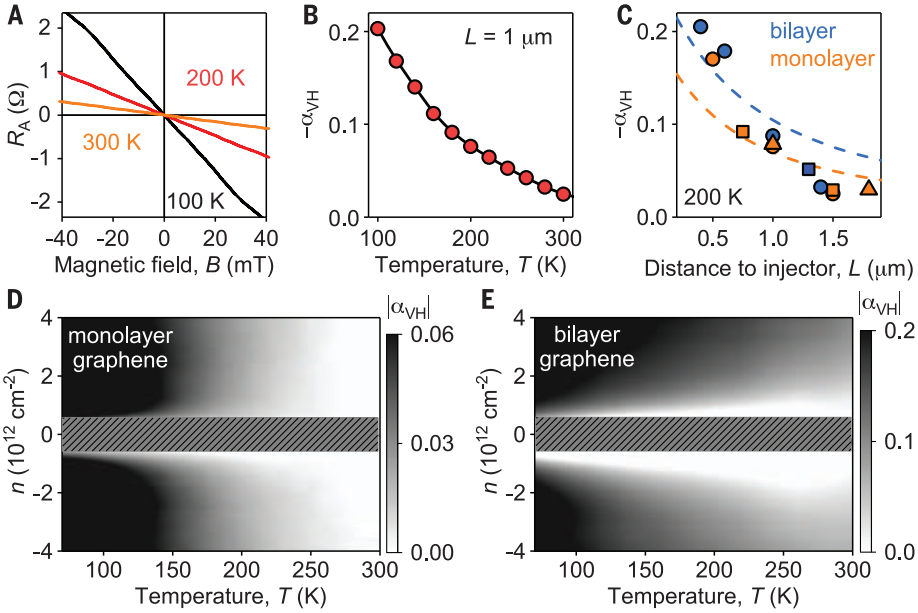

Fig. 2. Viscous Hall effect. (**A**) $R_A(B)$ for one of our MLG devices at $L \approx 1$ μm for three different temperatures. (**B**) The dimensionless viscous coefficient $\alpha_{VH}(T)$ (symbols). Reproducibility is provided in fig. S2C. (**C**) $\alpha_{VH}(L)$ found for five different devices indicated with different symbols, whereas the color refers to MLG and BLG. $n = 2 \times 10^{12}$ cm^{-2} for (A) to (C), which corresponds to the Fermi energy of ~165 and ~70 meV for MLG and BLG, respectively. Dashed lines in (C) indicate dependences from Eq. 2 with no fitting parameters; $\sigma_0(T)$ is determined as described in (*22*), section 1, and $\nu_0(T)$ is taken from experiment (*6*). (**D** and **E**) Maps of $|\alpha_{VH}|$ in MLG and BLG devices for $L \approx 1.5$ μm and 0.7 μm, respectively; $B = 40$ mT. Shaded areas indicate omitted analysis because the cyclotron diameter becomes comparable with the device width (*23*).

(*15*, *16*). As shown below, the vicinity geometry (Fig. 1E) allows us to distinguish between the ordinary HE and the anomalous one caused by ν_H.

Our devices were multiterminal Hall bars such as shown in Fig. 1E and fig. S1, A and B. They were made from graphene encapsulated between hexagonal boron-nitride crystals (*22*). The Hall bars had typical widths of 2 to 4 μm and were endowed with narrow (~0.3 μm) and closely spaced (~0.5 μm) voltage probes (Fig. 1E). Such submicrometer probes are essential for detection of viscous effects as seen from the spatial scale of Fig. 1, A to D. Several devices made from mono- and bilayer graphene (MLG and BLG, respectively) were studied, all exhibiting similar behavior. The data reported below are from three MLG and two BLG devices that were studied in great detail. They had typical mobilities exceeding ~100,000 cm^2 V^{-1} s^{-1} at all temperature (T) up to 300 K (*22*), which ensured micrometer-scale transport with respect to momentum-nonconserving scattering over the entire T range explored in the experiments (fig. S1); for comparison, the electron-electron mean free path at representative $n = 10^{12}$ cm^{-2} and $T = 150$ K is ~0.4 μm, shorter than a typical distance of ~1 μm, at which the viscous contribution was probed (*8*, *11*).

In the vicinity geometry, the current I was injected through a narrow contact (for example, Fig. 1E, probe 1) into a wide graphene channel, and the local potential ϕ was measured by using probe 3 positioned at the distance L from the injector. Contacts 2 and 4 (chosen sufficiently far away from the injection region) complete the electric circuit, serving as the drain and reference-voltage contacts, respectively. The vicinity resistance is defined as $R_v = R_{34,12} = V_{34}/I_{12}$, where V_{34} is the voltage drop between 3 and 4. As per Fig. 1, A to D, R_v is expected to be sensitive to viscous effects (*6*, *7*, *18*, *22*). According to the previous experiments and theory (*6*, *7*, *12*, *18*), R_v is a nonmonotonic

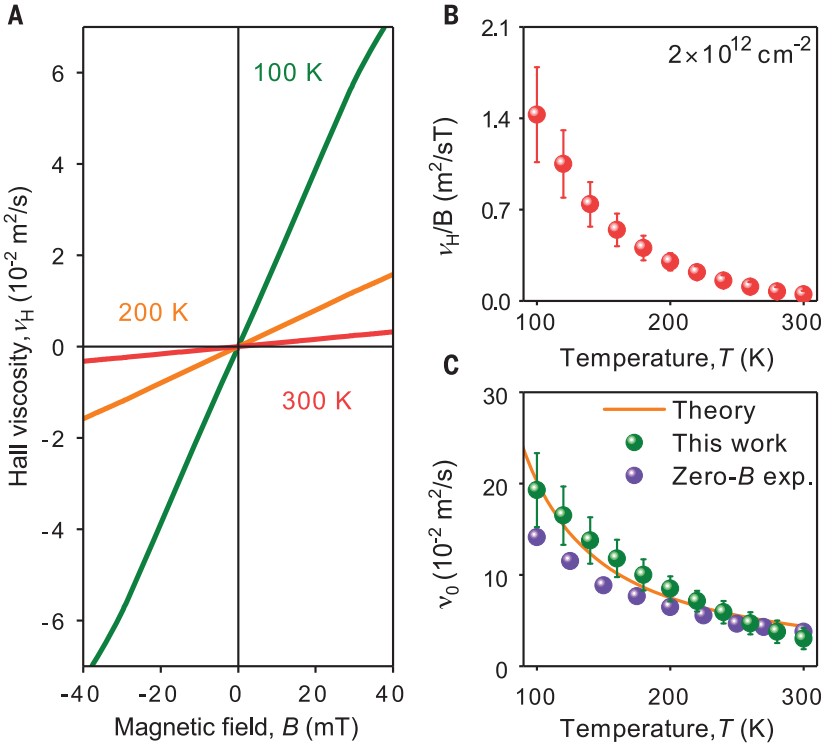

Fig. 3. Hall viscosity in graphene. (**A**) Examples of ν_H extracted by using data from Fig. 2A. (**B**) ν_H/B as a function of T. (**C**) Zero-field viscosity ν_0 extracted from our $R_A(B)$ measurements (green). Solid curve indicates theory (*11*). Purple symbols indicate previous experiments (*8*). For (A) to (C), MLG at $n = 2 \times 10^{12}$ cm^{-2}. No fitting parameters were used for the theory curve in (C). Error bars in (B) and (C) represent the scatter for measurements by using different L. The notable increase of the error below 150 K indicates that the electron system starts exiting the hydrodynamic regime (*7*, *12*).

function of T so that R_v is positive in the ballistic regime at low T, changes its sign to negative with increasing T, passes through a minimum, and then starts growing. The negative sign of R_v is a clear indicator that electron-electron scattering strongly affects ballistic transport (*6*, *7*, *12*, *18*, *22*), whereas the turning point marks the onset of the regime in which the hydrodynamics approach becomes applicable (*6*, *7*).

For the purpose of this Report, we focus on the latter regime, which in our devices starts above 100 to 150 K, depending on n (fig. S2A). In addition, we set several other constraints on variables used in the experiments. First, we limited ourselves to $B < 40$ mT so that the cyclotron radius always exceeded our devices' width. This was to avoid hydrodynamics effects being obscured by those caused by Landau quantization and electron focusing (*23*). In addition, such small B are not expected to affect the longitudinal viscosity ν. Second, to avoid unrelated effects stemming from thermal excitations and charge inhomogeneity, we carried out experiments away from the charge neutrality point, at n of the order of 10^{12} cm^{-2}. Last, we used small $I \leq 1$ μA so as to stay in the linear response regime and avoid nonlinear effects, including electron heating (*2*, *6*).

Examples of $R_v(n)$ in the hydrodynamic regime are shown in Fig. 1F for one of our MLG devices. In agreement with the previous studies (*6*, *7*), R_v in zero B is negative for all n away from the charge neutrality and is practically symmetric for electron and hole doping (positive and negative n, respectively). The small positive field of 20 mT shifts the R_v curves in opposite directions for electrons and holes, as indicated by the green arrows in Fig. 1F. The shifts are opposite for negative B. This behavior implies a contribution that is antisymmetric with respect to B and n, similar to the ordinary HE. However, the latter cannot possibly explain the observed shifts because in the vicinity, geometry voltage probes are placed on the same side of the current path, which cancels the ordinary HE contribution to the measured voltages. A formal proof of this can be found in (*16*). Experimentally, we have also checked that there is no ordinary HE contribution for the vicinity geometry by using similar graphene devices but exhibiting low mobility (fig. S2, D to F). Furthermore, it is important to compare the sign of the R_v changes induced by B with the sign of the ordinary HE. To keep the same sign convention for B and n, it is instructive to measure the local Hall resistance $R_{35,12}$ (Fig. 1E and fig. S6) instead of using the standard Hall geometry. In this case, we used contact 5 instead of 4 and kept all the other contacts same as in the R_v measurements. This swap placed the voltage probes at the opposite sides of the current path, which gave rise to the voltage drop V_H owing to the ordinary HE. The antisymmetric-in-B part of $R_{35,12}$ (to avoid a contribution from longitudinal resistivity) is plotted in Fig. 1F (dashed lines). It shows that the ordinary HE induces ϕ of the opposite polarity with respect to those causing the B shifts in R_v. Indeed, the vicinity curve in Fig. 1F is shifted, for example, upward for hole doping and positive B, whereas the ordinary HE would shift it downward [(*22*), section 6]. This behavior agrees well with the opposite signs of the contributions expected from V_H and ν_H toward R_v, as shown in theoretical Fig. 1, C and D.

For further analysis, we define the Hall (odd) component of the vicinity resistance as $R_A(B) = [R_v(B) - R_v(-B)]/2$. The antisymmetrization removes the contributions that are symmetric in B and caused by the longitudinal viscosity ν and the Ohmic flow (*6*, *16*). Examples of the $R_A(B)$ curves for MLG and BLG devices are shown in Fig. 2A and fig. S3A, respectively. Within the ranges of T and B used in our experiment, the dependences are linear in B for all the studied devices and for all L. By analogy with the conventional Hall coefficient, where $\alpha_H = R_H ne/B \equiv 1$, it is instructive to introduce the viscous Hall coefficient, $\alpha_{VH} = R_A ne/B$ (*22*). In this form, the antisymmetric contribution R_A is effectively normalized by the ordinary HE, which provides a sense of the magnitude for the observed viscous effects.

Shown in Fig. 2B is the T dependence of α_{VH} obtained by using data such as those in Fig. 2A. Above 100 K, at which the hydrodynamic regime becomes fully developed (*6*, *7*, *10*, *12*), the viscous contribution reaches 20% of the ordinary HE and has the opposite sign (Fig. 2B). $|\alpha_{VH}|$ decreases with increasing T and eventually disappears below noise above room T. This T dependence was found to be universal for all the studied devices (fig. S2C). The observed behavior is detailed in Fig. 2, D and E, by plotting $\alpha_{VH}(T, n)$ for MLG and BLG. The maps are somewhat different because of different viscosities of the two graphene systems (*6*, *10*, *11*)

but show similar trends as functions of n and T. We have also studied how α_{VH} depends on L and found that it decreases with increasing L, practically disappearing if the voltage probe is placed further than ~2 μm from the current-injecting contact (Fig. 2C). The latter highlights the importance of the vicinity geometry to detect viscous effects.

The anomalous viscous contribution to the HE, which is found by using the vicinity geometry, is fully consistent with our measurements of a local Hall resistance [(*22*), section 6]. To this end, we again used voltage contacts close to the current injector (for example, using $R_{35,16}$) and compared those measurements with the standard HE geometry ($R_{42,16} \equiv R_{16,42}$). The latter exhibited the ordinary HE with $\alpha_H = 1$, as expected. By contrast, the local Hall resistance was notably suppressed in the hydrodynamic regime (fig. S6) and agreed quantitatively with the behavior of α_{VH} reported above.

Here, we turn to theory. In the linear-response and steady-state regimes, 2D viscous transport in the presence of a perpendicular field B (in the z direction) is described by the Navier-Stokes equation

$$\frac{\sigma_0}{ne}\nabla\phi(\boldsymbol{r}) = (1 - D_\nu^2\nabla^2)\boldsymbol{v}(\boldsymbol{r}) + \omega_c\tau(1 + D_H^2\nabla^2)\boldsymbol{v}(\boldsymbol{r}) \times \hat{\boldsymbol{z}} \quad (1)$$

in conjunction with the continuity equation and no-slip boundary conditions (*16*, *22*). Here, $\boldsymbol{v}(\boldsymbol{r})$ is the local fluid velocity, $\omega_c = eB/m$ is the cyclotron frequency for electrons with the effective mass m, $\sigma_0 = ne^2\tau/m$ is the Drude conductivity, and τ is the transport time with respect to momentum-nonconserving collisions, such as scattering on phonons. The right-hand side of Eq. 1 contains two terms. The first describes the electric current and viscous friction parameterized through the diffusion constant, $D_\nu = \sqrt{\nu\tau}$. The second term arises from the Lorentz force $\boldsymbol{F}_L = -(\omega_c m)\boldsymbol{v}(\boldsymbol{r}) \times \hat{\boldsymbol{z}}$ and its viscous counterpart that depends on ν_H and is parameterized through another diffusion constant, $D_H = \sqrt{\nu_H/\omega_c}$. The Hall friction acts against $\boldsymbol{F}_L$, which also means that ν_H does not perform any work on the electron fluid and, therefore, is a dissipationless coefficient.

For the half-plane geometry (fair approximation for our devices) and close to the injection point, the above equation can be solved analytically (*16*), yielding $\phi(\boldsymbol{r})$ shown in Fig. 1, A to D (examples of the potential and current maps calculated taking into account the finite device width are provided in fig. S4). The Hall contribution to the vicinity resistance can be written as

$$R_A = -\sigma_0^{-1}\xi\left(\frac{L}{D_\nu}\right)\frac{\nu_H}{\nu} \quad (2)$$

where $\xi(x) = [L_1(x) - I_1(x)]/2x$, and $L_1(x)$ and $I_1(x)$ are the modified Struve and Bessel functions, respectively (*16*). The function $\xi(L/D_\nu)$ decreases monotonically with increasing L, behaving as $D_\nu/\pi L$ for $L \gg D_\nu$. The L dependence expected for our devices by using Eq. 2 is plotted in Fig. 2C, showing reasonable agreement with the experiment (especially in terms of the absolute values), even without taking into account the finite width (~0.3 μm) of our current and voltage contacts.

The measured $R_A(B)$ such as shown in Fig. 2A can be used to extract v_H. To this end, we rewrite Eq. 2 as $\nu_H = -R_A\sigma_0\nu/\xi(L/\sqrt{\nu\tau})$, where σ_0 and τ can be deduced from standard longitudinal resistivity measurements (*6*, *8*). The longitudinal viscosity $\nu(B)$ can be approximated by using the semiclassical expression $\nu(B) = \nu_0\frac{B_0^2}{B^2+B_0^2}$, where ν_0 is the kinematic viscosity in zero B, and $B_0 = \hbar v_F k_F/(8e\nu_0)$ is the characteristic magnetic field expressed through the Fermi wave number k_F, the Fermi velocity v_F, and the reduced Planck constant $\hbar$ (*16*, *24*, *25*). For the reported range of n and T, B_0 is much larger than the fields in our experiments. Accordingly, we can assume $\nu \approx \nu_0$ in Eq. 2 and then use ν_0 found experimentally in (*8*). Using the above protocol, it is straightforward to calculate ν_H and its B and T dependences. Examples are shown in Fig. 3, A and B. One can see that the Hall viscosity is linear in B and rapidly decreases with increasing T.

For consistency, we cross-checked the above analysis against the results obtained previously (*8*) for zero-field viscosity ν_0. To this end, the field dependence of $R_A = R_A[\nu_H(B), \nu(B)]$ originates from changes in both longitudinal and Hall viscosities. The full formula for $\nu(B)$ is given above, whereas the same semiclassical consideration (*16*, *24*) for the Hall viscosity yields $\nu_H(B) = \nu_0\frac{BB_0}{B^2+B_0^2}$. This allows us to redefine the anomalous Hall contribution as $R_A[\nu_0, B]$ and calculate ν_0 from the measured $R_A(B)$ dependences, such as in Fig. 2A. ν_0 extracted by using this procedure is compared in Fig. 3C with the values found independently in (*8*). The figure shows good agreement between the two analyses and with the viscosity expected theoretically (*11*).

Last, the above hydrodynamic description is also consistent with the large negative magnetoresistance observed in our graphene devices at elevated T by using the standard longitudinal geometry (*22*). The magnetoresistance can be described accurately, without any fitting parameters (fig. S5), by using the same viscosity values as found experimentally in Fig. 3C. Similar magnetoresistance was reported in other high-quality 2D systems and attributed to ballistic transport affected by electron-electron interactions (*26*, *27*). Only recently has it been realized that the anomalous negative magnetoresistance at elevated T may signify the presence of a viscous flow and can also be described by the hydrodynamic approach (*15*, *24*), which is consistent with our work (*22*). It would be interesting to expand studies of the Hall viscosity into the quantum HE regime, which attracts considerable theory interest (*28*–*30*), but unfortunately, no experimental procedure has so far been suggested to probe this regime.

REFERENCES AND NOTES

1. R. N. Gurzhi, *Sov. Phys. Usp.* **11**, 255–270 (1968).
2. M. J. M. de Jong, L. W. Molenkamp, *Phys. Rev. B* **51**, 13389–13402 (1995).
3. A. O. Govorov, J. J. Heremans, *Phys. Rev. Lett.* **92**, 026803 (2004).
4. P. J. W. Moll, P. Kushwaha, N. Nandi, B. Schmidt, A. P. Mackenzie, *Science* **351**, 1061–1064 (2016).
5. J. Gooth *et al.*, *Nat. Commun.* **9**, 4093 (2018).
6. D. A. Bandurin *et al.*, *Science* **351**, 1055–1058 (2016).
7. D. A. Bandurin *et al.*, *Nat. Commun.* **9**, 4533 (2018).
8. R. Krishna Kumar *et al.*, *Nat. Phys.* **13**, 1182–1185 (2017).
9. A. Lucas, K. C. Fong, *J. Phys. Condens. Matter* **30**, 053001 (2018).
10. D. Y. H. Ho, I. Yudhistira, N. Chakraborty, S. Adam, *Phys. Rev. B* **97**, 121404 (2018).
11. A. Principi, G. Vignale, M. Carrega, M. Polini, *Phys. Rev. B* **93**, 125410 (2016).
12. A. Shytov, J. F. Kong, G. Falkovich, L. Levitov, *Phys. Rev. Lett.* **121**, 176805 (2018).
13. J. Crossno *et al.*, *Science* **351**, 1058–1061 (2016).
14. J. E. Avron, *J. Stat. Phys.* **92**, 543–557 (1998).
15. T. Scaffidi, N. Nandi, B. Schmidt, A. P. Mackenzie, J. E. Moore, *Phys. Rev. Lett.* **118**, 226601 (2017).
16. F. M. D. Pellegrino, I. Torre, M. Polini, *Phys. Rev. B* **96**, 195401 (2017).
17. L. V. Delacrétaz, A. Gromov, *Phys. Rev. Lett.* **119**, 226602 (2017).
18. I. Torre, A. Tomadin, A. K. Geim, M. Polini, *Phys. Rev. B* **92**, 165433 (2015).
19. L. Levitov, G. Falkovich, *Nat. Phys.* **12**, 672–676 (2016).
20. G. Falkovich, L. Levitov, *Phys. Rev. Lett.* **119**, 066601 (2017).
21. F. M. D. Pellegrino, I. Torre, A. K. Geim, M. Polini, *Phys. Rev. B* **94**, 155414 (2016).
22. Materials and methods are available as supplementary materials.
23. C. W. J. Beenakker, H. van Houten, *Solid State Phys.* **44**, 1–228 (1991).
24. P. S. Alekseev, *Phys. Rev. Lett.* **117**, 166601 (2016).
25. M. S. Steinberg, *Phys. Rev.* **109**, 1486–1492 (1958).
26. Q. Shi *et al.*, *Phys. Rev. B* **89**, 201301 (2014).
27. V. T. Renard *et al.*, *Phys. Rev. Lett.* **100**, 186801 (2008).
28. J. E. Avron, R. Seiler, P. G. Zograf, *Phys. Rev. Lett.* **75**, 697–700 (1995).
29. I. V. Tokatly, G. Vignale, *Phys. Rev. B* **76**, 161305 (2007).
30. F. D. M. Haldane, *Phys. Rev. Lett.* **107**, 116801 (2011).
31. A. I. Berdyugin *et al.*, Measuring Hall viscosity of graphene's electron fluid. Zenodo (2019); doi:10.5281/zenodo.2562181.

ACKNOWLEDGMENTS

Funding: This work was supported by the European Research Council, the Graphene Flagship, and Lloyd's Register Foundation. D.A.B. acknowledges the financial support from Leverhulme Trust, and R.K.K. acknowledges that from the EPSRC. **Author contributions:** D.A.B. and A.K.G. designed and supervised the project. A.I.B. and D.A.B. performed electrical measurements. S.G.X. and M.B.S. fabricated devices. A.I.B. and D.A.B. analyzed the data with input from R.K.K. and A.K.G.; F.M.D.P., A.P., I.T., and M.P. provided theoretical support. T.T. and K.W. provided hBN crystals. D.A.B. and A.I.B. wrote the manuscript with help from A.K.G. All the authors contributed to discussions. **Competing interests:** The authors declare no competing interests. **Data and materials availability:** The data reported in this work are archived at Zenodo (*31*).

SUPPLEMENTARY MATERIALS

www.sciencemag.org/content/364/6436/162/suppl/DC1
Supplementary Text
Figs. S1 to S6
References (*32*–*40*)

4 May 2018; accepted 19 February 2019
Published online 28 February 2019
10.1126/science.aau0685

THIN FILMS

Spin coating epitaxial films

Meagan V. Kelso[1], Naveen K. Mahenderkar[1]*, Qingzhi Chen[2], John Z. Tubbesing[2], Jay A. Switzer[2]†

Spin-coated films, such as photoresists for lithography or perovskite films for solar cells, are either amorphous or polycrystalline. We show that epitaxial films of inorganic materials such as cesium lead bromide ($CsPbBr_3$), lead(II) iodide (PbI_2), zinc oxide (ZnO), and sodium chloride (NaCl) can be deposited onto a variety of single-crystal and single-crystal–like substrates by simply spin coating either solutions of the material or precursors to the material. The out-of-plane and in-plane orientations of the spin-coated films are determined by the substrate. The thin stagnant layer of supersaturated solution produced during spin coating promotes heterogeneous nucleation of the material onto the single-crystal substrate over homogeneous nucleation in the bulk solution, and ordered anion adlayers may lower the activation energy for nucleation on the surface. The method can be used to produce functional materials such as inorganic semiconductors or to deposit water-soluble materials such as NaCl that can serve as growth templates.

Epitaxy is the growth of crystals whose orientation is determined by their crystalline substrate (*1*, *2*). Epitaxy can produce thin films with atomic perfection that rivals that of single crystals as well as metastable phases (such as body-centered cubic Ni on Fe and face-centered cubic Fe on Cu), superlattices, quantum wells, and strained-layer architectures with tunable properties (*2*). Although epitaxial growth is usually constrained to ultrahigh vacuum or high temperatures by techniques such as molecular beam epitaxy, chemical vapor deposition, and liquid-phase epitaxy, it was first demonstrated in aqueous solution in 1836 when Frankenheim showed that sodium nitrate crystals could be grown epitaxially on a freshly cleaved calcite substrate (*3*). In 1950, Johnson also used aqueous solution to grow NaCl crystals epitaxially on single-crystal Ag (*4*). Other examples of solution-based deposition of epitaxial films are hydrothermal processing (*5*), chemical bath deposition (*6*–*8*), and electrodeposition (*9*–*11*).

Each of these solution methods has limitations. Hydrothermal processing requires high temperature and pressure, chemical bath deposition requires specific reactions to occur at the substrate surface, and electrodeposition requires conducting or semiconducting substrates. Here, we show that epitaxial films can be deposited by a simple, rapid, and inexpensive spin-coating method directly from solution precursors. We demonstrate the epitaxial growth of a diverse array of inorganic materials such as $CsPbBr_3$, PbI_2, NaCl, and ZnO onto a variety of single-crystal and single-crystal–like substrates such as Au, Ag, $SrTiO_3$, and mica by spin coating with low-temperature in situ heating.

Spin coating is used commercially to deposit polymer films for lithography. It has also been used to deposit organic semiconductor films (*12*, *13*) and has become the preferred deposition method for perovskite materials such as $CH_3NH_3PbI_3$ and $CsPbBr_3$ for use in solar cells, photodetectors, and light-emitting diodes (LEDs) (*14*–*19*). For example, dense and uniform films of $CH_3NH_3PbI_{3-x}Br_x$ have been spin coated by engineering the solvent mix (*17*), and $CH_3NH_3PbI_{3-x}Cl_x$ films with millimeter-scale crystal grains have been spin coated by dispensing the precursor solution onto a heated substrate (*16*). However, the substrates in this earlier work were polycrystalline or amorphous, so the films were not epitaxial. Ji *et al.* have spin coated $CH_3NH_3PbI_3$ onto single-crystal KCl and crystallized the as-deposited amorphous material into an epitaxial film with a final annealing step (*19*). There has also been previous work on the spin coating of amorphous sol-gel precursors for oxides onto single-crystal surfaces that were then converted into epitaxial films by a high-temperature burn off of organics (*20*–*22*). In the present work, the epitaxial films were directly spin coated from solution precursors without the need for postannealing or a high-temperature conversion step.

We propose that the very thin supersaturated solution layer that is formed in spin coating serves to promote heterogeneous nucleation of the material onto the single-crystal substrate over homogeneous nucleation in the bulk solution

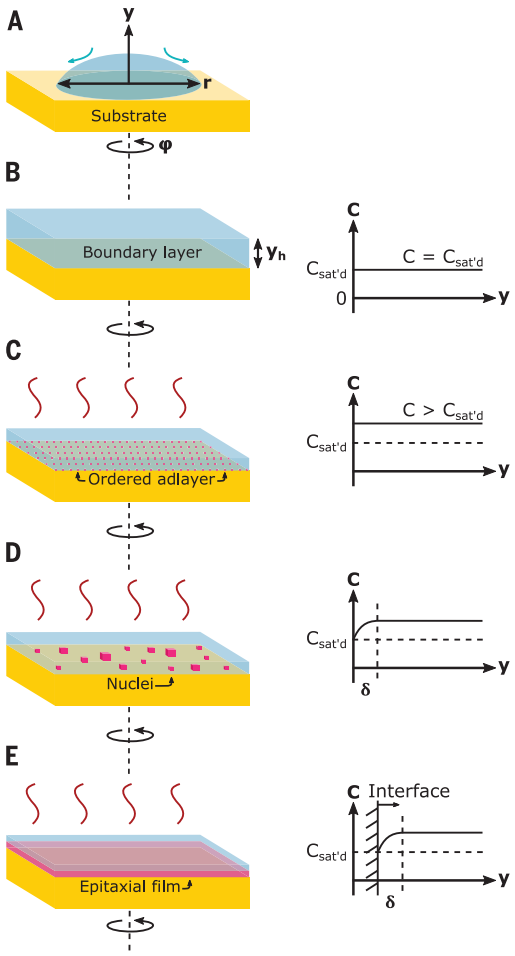

Fig. 1. Epitaxial spin coating schematic. (**A**) Each precursor solution is dispensed on a room temperature or preheated single-crystal or single-crystal–like substrate as it begins to spin. y, cylindrical axis; r, radius; ϕ, azimuthal angle. (**B**) When the solution reaches the spin speed of the sample, a hydrodynamic boundary layer forms with thickness y_h. (**C**) An ordered anion adlayer forms at the substrate-solution interface, and the solution concentration reaches supersaturation owing to evaporation. (**D**) Nucleation occurs at the solution-substrate interface, and a concentration gradient and diffusion layer form with thickness δ. (**E**) The nuclei grow into a film, and the interface between solution and substrate continues to shift until solvent evaporation is complete.

[1]Department of Materials Science and Engineering and Graduate Center for Materials Research, Missouri University of Science and Technology, Rolla, MO 65409-1170, USA.
[2]Department of Chemistry and Graduate Center for Materials Research, Missouri University of Science and Technology, Rolla, MO 65409-1170, USA.
*Present address: Lam Research Corporation, 4650 Cushing Parkway, Fremont, CA 94538, USA.
†Corresponding author. Email: jswitzer@mst.edu

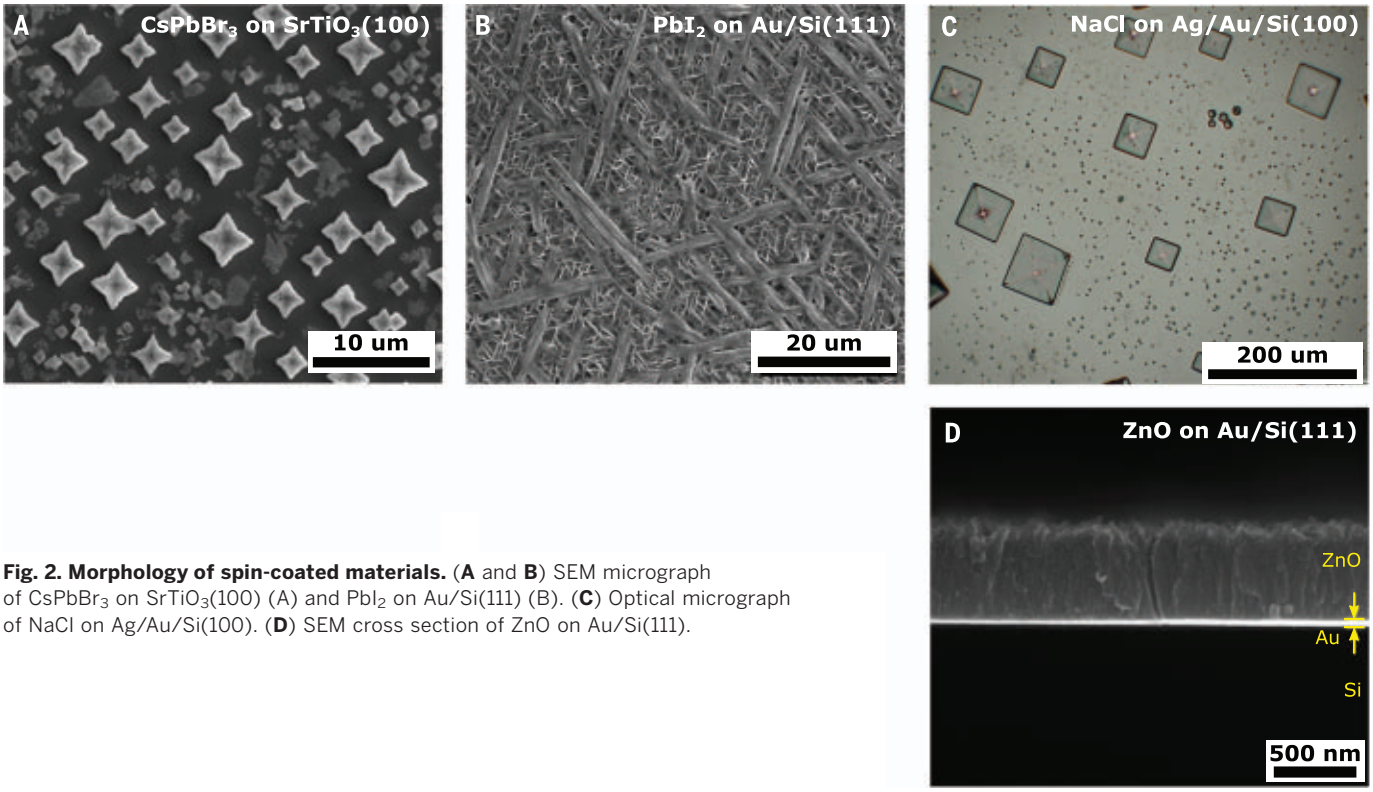

Fig. 2. Morphology of spin-coated materials. (**A** and **B**) SEM micrograph of $CsPbBr_3$ on $SrTiO_3$(100) (A) and PbI_2 on Au/Si(111) (B). (**C**) Optical micrograph of NaCl on Ag/Au/Si(100). (**D**) SEM cross section of ZnO on Au/Si(111).

that would occur during crystallization by conventional solvent evaporation methods. The activation energy for nucleation on the single-crystal surface may also be lowered by the production of ordered adlayers of anions on the surface. Anions specifically adsorb on single-crystal metal surfaces to form monolayer or submonolayer adlayers (*23*). For example, I^- forms a (√3 by √3)R30° adlayer on Au(111), and Cl^- forms a c(2 by 2) adlayer on Ag(100). These anion adlayers could mimic the anion-terminated surfaces of compounds to serve as seed crystals for the nucleation of the spin-coated material.

The general mechanism for epitaxial spin coating that we outline in Fig. 1 assumes that the formation of a hydrodynamic boundary layer and the subsequent evaporation of the solvent occur in steps, as opposed to more rigorous models in which the two processes occur simultaneously (*24*, *25*). A drop of solution containing dissolved material or precursors is dispensed onto the rotating substrate (Fig. 1A). After spinning, the solution forms a stagnant hydrodynamic boundary layer (Fig. 1B) whose thickness, y_h, is determined by the kinematic viscosity, v, of the solution and the rotation rate, ω (in terms of angular frequency of rotation, measured in s^{-1}), of the substrate (*26*):

$$y_h = 3.6\left(\frac{v}{\omega}\right)^{1/2} \quad (1)$$

For example, a rotation rate of 3000 rpm and a kinematic viscosity of 0.01 $cm^2\ s^{-1}$ will generate a boundary layer ~200 μm thick. An ordered adlayer that lowers the activation energy for nucleation also forms at this stage (Fig. 1C). Because of the in situ heating and the spinning of the substrate, the solvent evaporates and the solution reaches supersaturation (Fig. 1C). Once the supersaturation reaches the critical value for nucleation, the nuclei form on the substrate, and the concentration at the solid-liquid interface is reduced to the saturation concentration of the solution, $c_{sat'd}$. A concentration gradient is then established that serves as the driving force for the ion or molecule diffusion (Fig. 1D). The diffusion layer thickness, δ, is given by Eq. 2, where D is the diffusion coefficient of dissolved species ($cm^2\ s^{-1}$) (*26*):

$$\delta = 1.61 D^{1/3} \omega^{-1/2} v^{1/6} \quad (2)$$

For a rotation rate of 3000 rpm and a diffusion coefficient of $1 \times 10^{-6}\ cm^2\ s^{-1}$, the diffusion layer would be ~4 μm thick. An epitaxial film continues to grow until the solvent completely evaporates (Fig. 1E). A similar model is observed in chemical vapor deposition and liquid phase epitaxy, in which film growth occurs by mass transport across a diffusion layer (*1*).

The spin coating of epitaxial films requires either that the material to be spin coated is soluble or that a soluble precursor to the material is available that can be converted to the material after drying at slightly increased temperatures. For the first case, we have spin coated PbI_2 from *N*,*N*-dimethylformamide (DMF) solution, $CsPbBr_3$ from dimethyl sulfoxide (DMSO) solution, and NaCl from aqueous solution. For the second case, we have spin coated ZnO from an aqueous ammonia solution of Zn(II) (*27*). In the ZnO case, the NH_3 evolved during the spin-coating process. The concentrations and conditions for spin coating are given in the supplementary materials. The substrates used for spin coating were either single crystals such as $SrTiO_3$ and mica or proxies for single crystals that were thin epitaxial films of Au or Ag that were electrodeposited onto single-crystal Si wafers (*11*, *28*, *29*). PbI_2, $CsPbBr_3$, and ZnO are all functional materials that can serve as semiconductors in solar cells and LEDs (*9*, *15*, *27*, *30*). Epitaxial NaCl can serve as a water-soluble template for large-scale epitaxial lift-off of flexible single-crystal–like materials for electronics, solar cells, and displays (*31*).

The in-plane order of the spin-coated materials can be seen in the scanning electron micrographs (SEMs) and optical micrographs in Fig. 2. $CsPbBr_3$ deposited with a diamond-like morphology on single-crystal $SrTiO_3$ (Fig. 2A). Although the $CsPbBr_3$ typically deposited as islands, it may be possible to produce dense films by multiple spin-coating applications or by using additives such as HBr or solvent mixtures (*17*, *32*). PbI_2, NaCl, and ZnO were all deposited onto epitaxial films of either Au or Ag on single-crystal Si. PbI_2 showed a mesh-like morphology with the expected threefold symmetry of the Au(111) surface (Fig. 2B). NaCl deposited as perfectly aligned cubes on the surface of Ag(100) (Fig. 2C). Optical micrographs of NaCl on Ag(111) and Ag(110) are shown in fig. S1. The plan view of ZnO on Au(111) was featureless (fig. S2), so the SEM in Fig. 2D

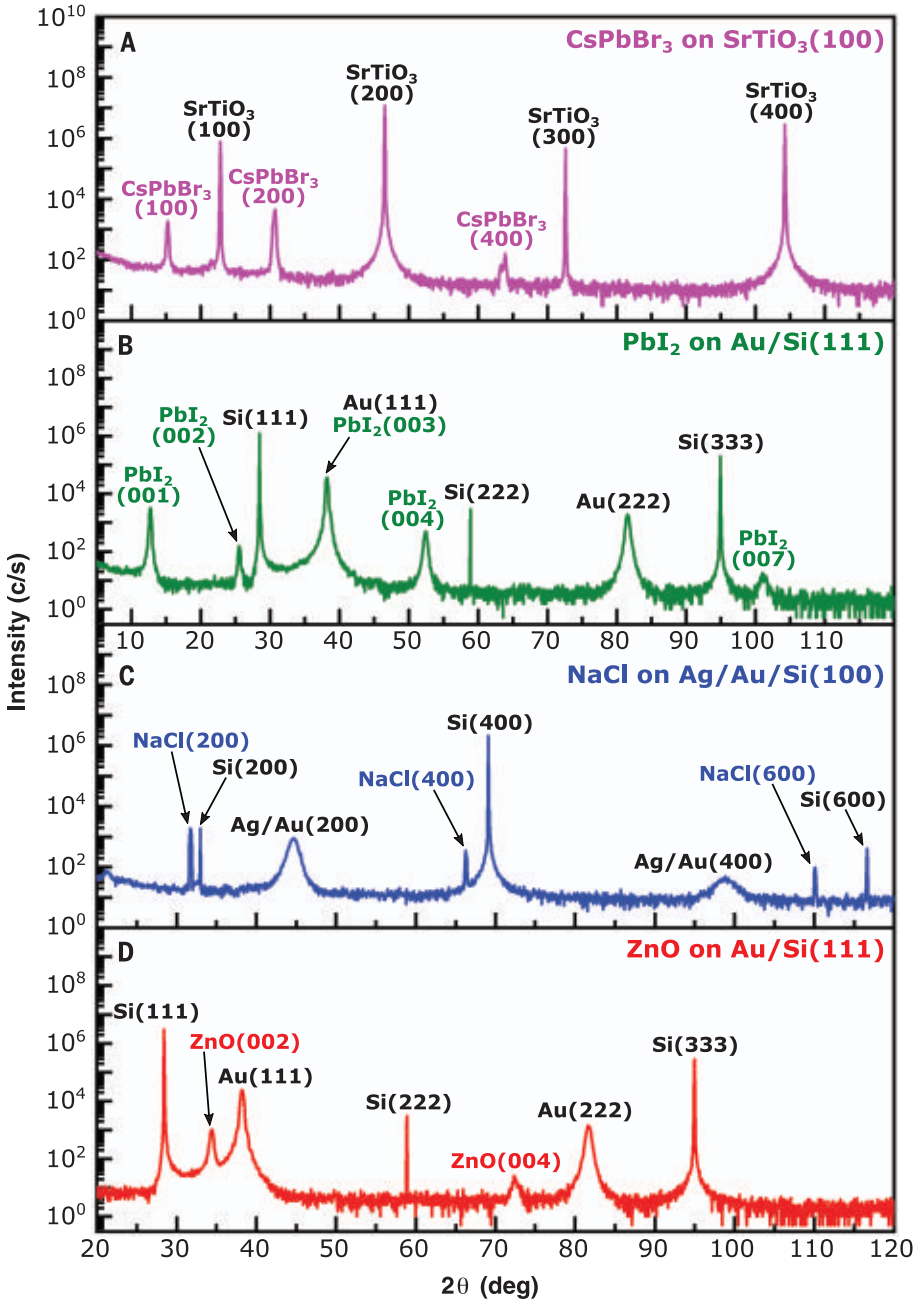

Fig. 3. Out-of-plane orientation by x-ray diffraction. (**A** to **D**) 2θ scans of $CsPbBr_3$ on single crystal $SrTiO_3$(100) (A), PbI_2 on Au/Si(111) (B), NaCl on Ag/Au/Si(100) (C), and ZnO on Au/Si(111) (D). c/s, counts per second.

is a cross-sectional view of the ~500-nm-thick ZnO film.

The crystallographic orientation of the spin-coated materials relative to the single-crystal and single-crystal–like substrates was determined by x-ray diffraction. The single-crystal–like substrates were thin epitaxial layers of Au or Ag that were electrochemically deposited onto single-crystal Si to serve as large-area, inexpensive proxies for a single-crystal surface (*29*). The out-of-plane orientation of the deposits was determined by x-ray 2θ scans using $CuK\alpha_1$ radiation. Figure 3A shows the 2θ scan of $CsPbBr_3$ on single-crystal $SrTiO_3$. Only the {100} family of peaks was observed for the cubic material, consistent with a [100] preferred out-of-plane orientation. The 2θ scans of $CsPbBr_3$ on Mica(001), Au(100)/Si(100), and Au(111)/Si(111) are shown in fig. S3. In all cases, the out-of-plane orientation of the $CsPbBr_3$ was determined by the substrate. Figure 3B shows the 2θ scan of PbI_2 on Au(111)/Si(111). Only the {001} family of peaks was observed for the material, consistent with a [001] orientation for the material. The triclinic PbI_2 grew with the (001) basal plane parallel with the Au(111) surface. Similarly, Fig. 3C shows that cubic NaCl grew with a [100] orientation on Ag(100)/Au(100)/Si(100), and Fig. 3D shows that hexagonal ZnO grew with a [001] orientation on Au(111)/Si(111).

The in-plane orientation of the deposits relative to the substrate was determined by x-ray pole figures. In these measurements, the 2θ value was fixed for either the film or the substrate, and the sample was rotated azimuthally from 0° to 360° at a series of tilt angles from 0° to 90°. Discrete spots in the pole figures instead of rings indicate that the material had both out-of-plane and in-plane order. Figure 4 shows pole figures for both films and substrates for $CsPbBr_3$ on $SrTiO_3$(100), PbI_2 on Au(111)/Si(111), NaCl on Ag(111)/Au(111)/Si(111), and ZnO on Au(111)/Si(111). Figure 4A shows a (220) pole figure of $CsPbBr_3$, and Fig. 4B shows a (110) pole figure of $SrTiO_3$, both with four spots separated azimuthally by 90° at a tilt angle of 45°, corresponding to the fourfold symmetry of the (100) plane. The tilt angle of 45° corresponds to the angle between the (100) and (220) planes in a cubic system. The pole figure of the $CsPbBr_3$ was rotated 45° in-plane in relation to $SrTiO_3$. This rotation could be explained with the lower mismatch caused by the rotation, as shown in interface models in fig. S4. The epitaxial relation is given by $CsPbBr_3(100)[011] \parallel SrTiO_3(100)[001]$.

Figure 4C shows a (102) pole figure of PbI_2 on the Au(111)/Si(111) substrate. The pole figure showed six spots separated azimuthally by 60° at a tilt angle of 42°, corresponding to two domains of threefold symmetry for trigonal PbI_2. The presence of the second domain is caused by the second in-plane domain in the epitaxial Au(111) film on Si(111) substrate, as previously studied (*29*) and shown in the Au substrate (200) pole figure in Fig. 4D. The tilt angle of 42° corresponds to the angle between (001) and (102) planes in a trigonal system. The Au pole figure shows six spots (two domains with three spots) separated azimuthally by 60° at a tilt angle of 55°, corresponding to the threefold symmetry of the cubic (111) plane. There is also a minor set of six spots corresponding to the (103) pole of PbI_2, which had a 2θ close enough to the (200) pole of Au to appear in the same projection. Comparing the Au and PbI_2 pole figures showed that PbI_2 was rotated 30° in-plane in relation to its Au substrate. The epitaxial relation is given by $PbI_2(001)[100] \parallel Au(111)[10\bar{1}] \parallel Si(111)[10\bar{1}]$.

Unlike $CsPbBr_3$ and PbI_2, there is no in-plane rotation between the spin-coated material and substrate for NaCl and ZnO. The (422) pole figure of NaCl is shown in Fig. 4E, and the (422) pole figure for the Si(100) substrate is shown in Fig. 4F. Both pole figures showed four spots separated azimuthally by 90° at a tilt angle of 35° and eight spots (four sets separated 53° azimuthally of two spots separated 37° azimuthally) at a tilt angle of 66°, corresponding to the fourfold symmetry of the (100) plane. All of the spots

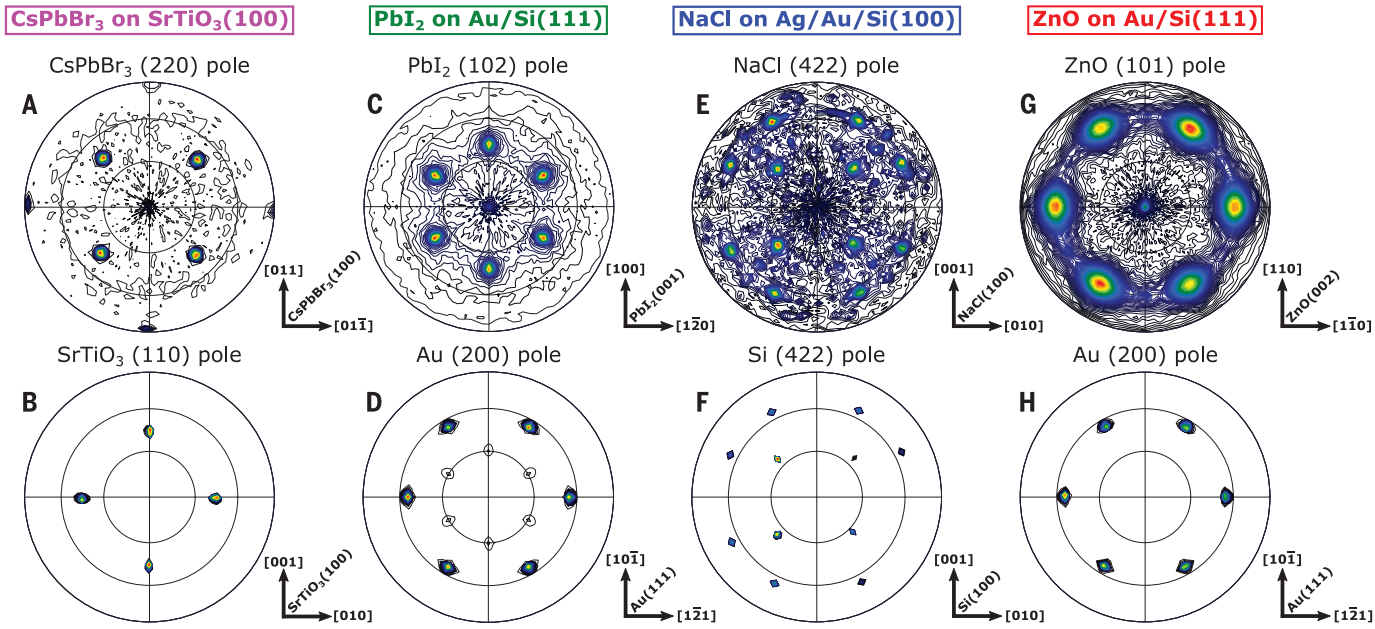

Fig. 4. In-plane orientation by x-ray pole figures. (**A** and **B**) (220) pole figure of $CsPbBr_3$ (A) and (110) pole figure of $SrTiO_3$(100) (B) substrate show that $CsPbBr_3$ is epitaxial with a 45° in-plane rotation from $SrTiO_3$. (**C** and **D**) (102) pole figure of PbI_2 (C) and (200) pole figure of Au(111) (D) film show that PbI_2 is epitaxial with a 30° in-plane rotation from Au. (**E** and **F**) (422) pole of NaCl (E) and (422) pole of Si(100) (F) substrate show that NaCl is epitaxial with no in-plane rotation. (**G** and **H**) (101) pole of ZnO (G) and (200) pole of Au(111) (H) film show that ZnO is epitaxial with no in-plane rotation. The radial grid lines represent 30° increments of the tilt angle.

corresponded to the angle between the (100) and (422) planes in a cubic system. The epitaxial relation is given by NaCl(100)[001] || Ag(100)[001] || Au(100)[001] || Si(100)[001].

Similarly, the in-plane order of ZnO is indicated by the (101) pole figure in Fig. 4G and Au substrate pole figure in Fig. 4H. The ZnO pole figure showed six spots, separated azimuthally by 60° at a tilt angle of 62°, corresponding to the angle between (001) and (101) and the sixfold symmetry in the hexagonal system. The Au substrate pole figure again showed six spots separated azimuthally by 60° at a tilt angle of 55°, corresponding to two in-plane domains of the threefold symmetric cubic (111) plane. The epitaxial relation is given by ZnO(001)[110] || Au(111)[10$\bar{1}$] || Si(111)[10$\bar{1}$].

The spin coating of epitaxial films offers an inexpensive and readily accessible route to single-crystal–like materials that should exhibit superior electronic and optical properties owing to the absence of high-angle grain boundaries. A wide range of materials can be deposited onto a variety of wafer-sized substrates with unprecedented simplicity. The films were deposited from solutions of the material or from precursors of the material that readily converted to the final product with only volatile side products. The precursor route used for depositing ZnO from an ammine complex should be applicable to other metal oxides. Spin coating also offers two avenues to highly-ordered semiconductors for flexible electronics, displays, and solar cells. The materials can be spin coated onto flexible single-crystal–like metal foils (*11*, *33*), or they can be deposited by more conventional vapor deposition techniques onto spin-coated water-soluble salts such as NaCl that serve as sacrificial templates for epitaxial lift-off of free-standing semiconductor foils (*31*).

REFERENCES AND NOTES

1. G. B. Stringfellow, *Rep. Prog. Phys.* **45**, 469–525 (1982).
2. E. G. Bauer *et al.*, *J. Mater. Res.* **5**, 852–894 (1990).
3. M. L. Frankenheim, *Ann. Phys.* **113**, 516–522 (1836).
4. G. W. Johnson, *J. Appl. Phys.* **21**, 1057–1062 (1950).
5. D. Andeen, L. Loeffler, N. Padture, F. F. Lange, *J. Cryst. Growth* **259**, 103–109 (2003).
6. M. Froment, M. C. Bernard, R. Cortès, B. Mokili, D. Lincot, *J. Electrochem. Soc.* **142**, 2642–2649 (1995).
7. S. Sengupta *et al.*, *J. Mater. Chem. C Mater. Opt. Electron. Devices* **4**, 1996–2002 (2016).
8. O. Friedman, D. Korn, V. Ezersky, Y. Golan, *CrystEngComm* **19**, 5381–5389 (2017).
9. R. Liu, A. A. Vertegel, E. W. Bohannan, T. A. Sorenson, J. A. Switzer, *Chem. Mater.* **13**, 508–512 (2001).
10. R. Liu, F. Oba, E. W. Bohannan, F. Ernst, J. A. Switzer, *Chem. Mater.* **15**, 4882–4885 (2003).
11. N. K. Mahenderkar *et al.*, *Science* **355**, 1203–1206 (2017).
12. F. Zhang *et al.*, *Adv. Mater.* **25**, 1401–1407 (2013).
13. Y. Yuan *et al.*, *Nat. Commun.* **5**, 3005 (2014).
14. C. Liu *et al.*, *J. Am. Chem. Soc.* **140**, 3825–3828 (2018).
15. J. Li *et al.*, *J. Phys. Chem. Lett.* **7**, 4059–4066 (2016).
16. W. Nie *et al.*, *Science* **347**, 522–525 (2015).
17. N. J. Jeon *et al.*, *Nat. Mater.* **13**, 897–903 (2014).
18. J. Burschka *et al.*, *Nature* **499**, 316–319 (2013).
19. L. Ji, H.-Y. Hsu, J. C. Lee, A. J. Bard, E. T. Yu, *Nano Lett.* **18**, 994–1000 (2018).
20. A. Seifert, F. F. Lange, J. S. Speck, *J. Mater. Res.* **10**, 680–691 (1995).
21. F. Rivadulla *et al.*, *Chem. Mater.* **25**, 55–58 (2013).
22. Y. Kokubun, Y. Amano, Y. Meguro, S. Nakagomi, *Thin Solid Films* **601**, 76–79 (2016).
23. O. M. Magnussen, *Chem. Rev.* **102**, 679–725 (2002).
24. W. W. Flack, D. S. Soong, A. T. Bell, D. W. Hess, *J. Appl. Phys.* **56**, 1199–1206 (1984).
25. C. J. Lawrence, *Phys. Fluids* **31**, 2786–2795 (1988).
26. A. J. Bard, L. R. Faulkner, *Electrochemical Methods: Fundamentals and Applications* (Wiley, ed. 2, 2001), chap. 9.
27. S. Y. Park *et al.*, *RSC Advances* **4**, 11295–11299 (2014).
28. P. Prod'homme, F. Maroun, R. Cortès, P. Allongue, *Appl. Phys. Lett.* **93**, 171901 (2008).
29. J. A. Switzer, J. C. Hill, N. K. Mahenderkar, Y.-C. Liu, *ACS Appl. Mater. Interfaces* **8**, 15828–15837 (2016).
30. A. Janotti, C. G. Van de Walle, *Rep. Prog. Phys.* **72**, 126501 (2009).
31. D. K. Lee *et al.*, *Sci. Rep.* **7**, 8716 (2017).
32. J. H. Heo, D. H. Song, S. H. Im, *Adv. Mater.* **26**, 8179–8183 (2014).
33. C. M. Hull, J. A. Switzer, *ACS Appl. Mater. Interfaces* **10**, 38596–38602 (2018).

ACKNOWLEDGMENTS

Funding: The material is based on work supported by the U.S. Department of Energy, Office of Basic Sciences, Division of Materials Sciences and Engineering, under grant DE-FG02-08ER46518. **Author contributions:** M.V.K. and J.A.S. wrote the article with input, edits, and approval from all the authors. N.K.M. and J.Z.T. deposited and characterized PbI_2 and perovskite films, Q.C. deposited and characterized NaCl films, and M.V.K. deposited and characterized ZnO films. The idea was conceived and the research was directed by J.A.S. **Competing interests:** The authors declare no competing interests. **Data and materials availability:** All data are presented in the main paper and supplementary materials.

SUPPLEMENTARY MATERIALS

www.sciencemag.org/content/364/6436/166/suppl/DC1
Materials and Methods
Figs. S1 to S4
Table S1

9 January 2019; accepted 13 March 2019
10.1126/science.aaw6184

PHYSICS

Anti–parity-time symmetry in diffusive systems

Ying Li[1]*, Yu-Gui Peng[1,2]*, Lei Han[1,3]*, Mohammad-Ali Miri[4,5], Wei Li[6], Meng Xiao[6,7], Xue-Feng Zhu[2]†, Jianlin Zhao[3], Andrea Alù[4,8,9,10], Shanhui Fan[6]†, Cheng-Wei Qiu[1]†

Various concepts related to parity-time symmetry, including anti–parity-time symmetry, have found broad applications in wave physics. Wave systems are fundamentally described by Hermitian operators, whereas their unusual properties are introduced by incorporation of gain and loss. We propose that the related physics need not be restricted to wave dynamics, and we consider systems described by diffusive dynamics. We study the heat transfer in two countermoving media and show that this system exhibits anti–parity-time symmetry. The spontaneous symmetry breaking results in a phase transition from motionless temperature profiles, despite the mechanical motion of the background, to moving temperature profiles. Our results extend the concepts of parity-time symmetry beyond wave physics and may offer opportunities to manipulate heat and mass transport.

Quantum physics has shown that a non-Hermitian Hamiltonian operator can exhibit entirely real spectra (*1*, *2*) when parity-time (PT) symmetry is preserved. The studies on this concept are especially fruitful in classical wave systems (*3*–*7*), where PT symmetry is manifested as balanced gain and loss. Spontaneous symmetry breaking happens when the system is tuned across an exceptional point (EP) (*8*–*11*), and this is related to many intriguing phenomena (*12*–*19*). Recently, anti-PT (APT) symmetric systems also have been of interest (*20*–*25*). The Hamiltonian H of such a system is mapped to its opposite by parity ($\mathcal{P}$) and time-reversal ($\mathcal{T}$) operators. Such systems are known to exhibit noteworthy effects, such as energy difference–conserving dynamics (*23*), coherent switch (*24*), and constant refraction (*25*).

Earlier work on PT and/or APT symmetry was carried out in wave systems whose underlying physics is described by a Hermitian operator. Non-hermiticity then emerges by introducing gain or loss [dissipation with a negative or positive decay rate (blue dots in Fig. 1A)]. Because non-Hermitian physics is closely related to dissipation, one should be able to explore it in processes that are intrinsically dissipative as well, such as heat or mass transfer described by the diffusion equation. To date, studies of PT-related physics in diffusion are lacking. Here, we introduce a route to explore APT symmetry in heat transfer. Starting from purely dissipative heat conduction, we then introduce oscillatory (Hermitian) components to achieve the required symmetry (red dots in Fig. 1A). This idea motivates us to use heat convection (*26*) in moving media. Mechanical motion generally "drags" waves (*27*, *28*) or heat (*29*, *30*). Notably, we found that for heat convection, the temperature profile can stay still ($v_{\mathrm{Temp}} = 0$) despite the flow ($v > 0$) in the APT symmetric phase. In the symmetry-broken phase, the temperature profile can either follow the flow ($v_{\mathrm{Temp}} > 0$) or even move against it ($v_{\mathrm{Temp}} < 0$). Therefore, all three scenarios in Fig. 1B are possible.

We consider heat convection in two channels with opposite background velocities that are coupled by heat conduction (Fig. 1C) [three-dimensional (3D) version in Fig. 1D]. We denote the temperature field in the upper (or lower) channel with velocity v (or $-v$) as T_1 (or T_2). Consider a simple model of these temperature fields (*26*)

$$\frac{\partial T_1}{\partial t} = D\frac{\partial^2 T_1}{\partial x^2} - v\frac{\partial T_1}{\partial x} + h(T_2 - T_1)$$
$$\frac{\partial T_2}{\partial t} = D\frac{\partial^2 T_2}{\partial x^2} + v\frac{\partial T_2}{\partial x} + h(T_1 - T_2) \qquad (1)$$

where D is the diffusivity, h is the rate of heat exchange between the two channels, t is the time, and x is the position. Using plane-wave solutions, Eq. 1 is reduced to an eigenvalue problem for the

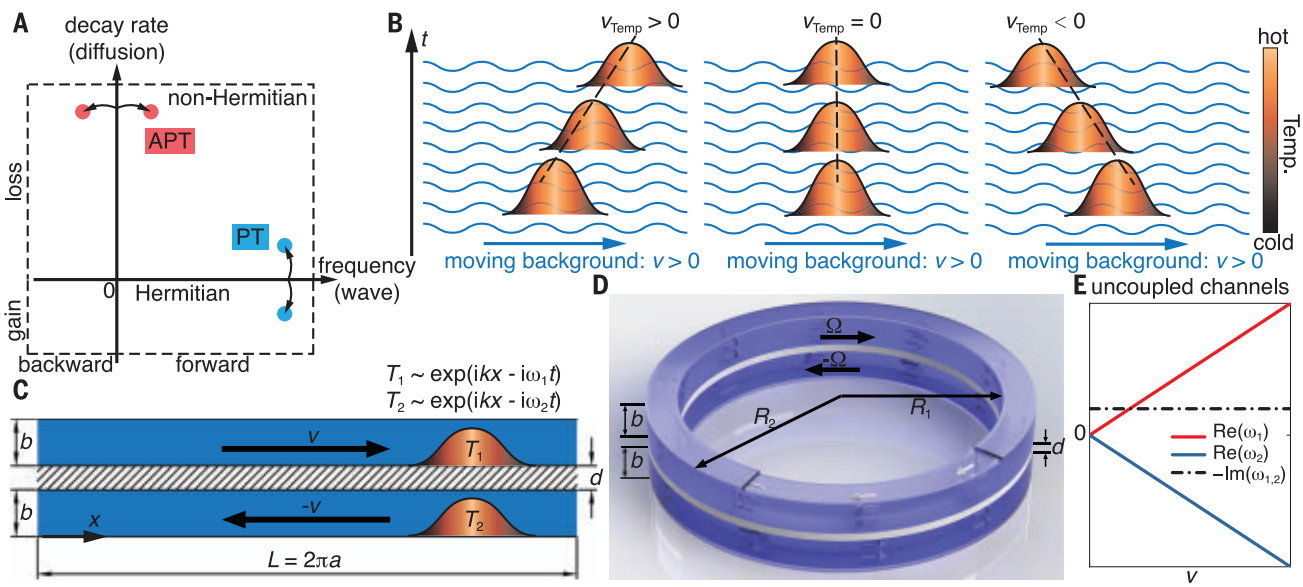

Fig. 1. APT symmetric diffusive system. (**A**) Two routes to explore non-Hermitian physics: from a wave system with zero decay rate (the abscissa) or from a diffusive system with zero frequency (the ordinate). (**B**) For heat convection, the temperature profile can follow, remain motionless, or move against the moving background. (**C**) A 2D model of an APT symmetric system. b, channel width; d, thickness. (**D**) A 3D model. R_1, interior ring radius; R_2, exterior ring radius. (**E**) The eigenfrequency of heat convection in the uncoupled limit. Re, real; Im, imaginary.

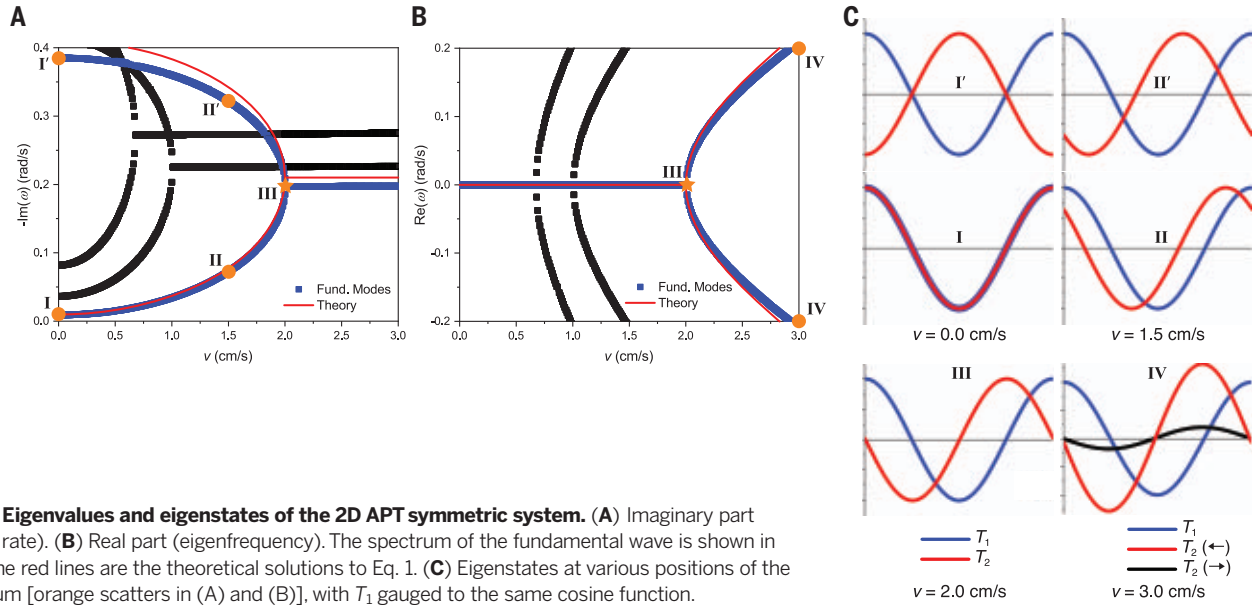

Fig. 2. Eigenvalues and eigenstates of the 2D APT symmetric system. (**A**) Imaginary part (decay rate). (**B**) Real part (eigenfrequency). The spectrum of the fundamental wave is shown in blue. The red lines are the theoretical solutions to Eq. 1. (**C**) Eigenstates at various positions of the spectrum [orange scatters in (A) and (B)], with T_1 gauged to the same cosine function.

effective Hamiltonian H, which is APT symmetric (materials and methods S1),

$$H = \begin{pmatrix} -i(k^2D+h)+kv & ih \\ ih & -i(k^2D+h)-kv \end{pmatrix} \quad (2)$$

where k is the wave number. The eigenvalue can be solved as

$$\omega_{\pm} = -i\left[(k^2D+h) \pm \sqrt{h^2-k^2v^2}\right] \quad (3)$$

In the uncoupled limit with $h = 0$, the system exhibits only a single phase, in which the eigenvalues always have a nonzero real part at $v \neq 0$ (Fig. 1E). When $h \neq 0$, this system exhibits two phases as v varies. For small v, the system is in the symmetric phase with purely imaginary eigenvalues. The corresponding eigenstates preserve APT symmetry. With large v, the system is in the symmetry-broken phase, where the eigenvalues have nonzero real parts (materials and methods S1). The transition between the two phases occurs at the EP, $k^2v_{\mathrm{EP}}^2 = h^2$, where v_{EP} is the critical velocity, which depends on k (supplementary text S1 and figs. S1 and S2).

We study the eigenvalue ω of the system in Fig. 1C with finite element simulations (materials and methods S2). Periodic boundary conditions are applied on the channels with length L, which only allows for discrete wave number $k = n/a$ (where n is an integer and $a = L/2\pi$). As v increases, the two branches of −Im(ω) coalesce at the EP, and then nonzero Re(ω) appears, as well described by the analytical model in Eq. 3

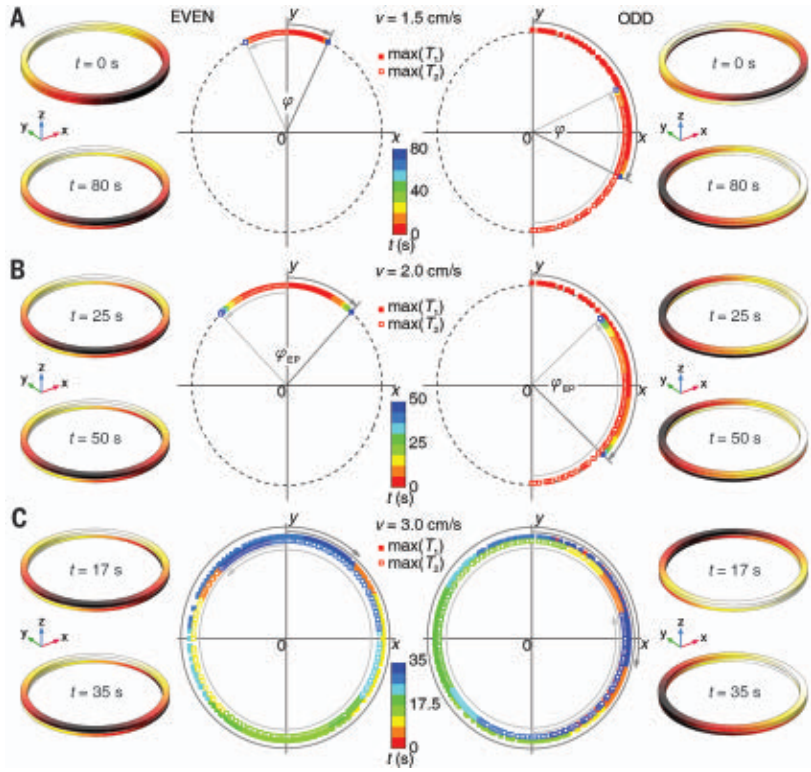

Fig. 3. Transient evolution of temperature profiles in the 3D APT symmetric system. Profiles for three velocities v are shown: 1.5 cm/s (**A**), 2.0 cm/s (**B**), and 3.0 cm/s (**C**). Snapshots of the temperature profiles are shown at the left and right sides, where the bright (dark) color represents hot (cold). In the center, we plot the trajectories of max(T_1) and max(T_2) along the interior edges of the rings (dashed circles), with scatters colored according to the time.

[1]Department of Electrical and Computer Engineering, National University of Singapore, Singapore 117583, Singapore. [2]School of Physics and Innovation Institute, Huazhong University of Science and Technology, Wuhan 430074, China. [3]MOE Key Laboratory of Material Physics and Chemistry under Extraordinary Conditions and Shaanxi Key Laboratory of Optical Information Technology, School of Natural and Applied Sciences, Northwestern Polytechnical University, Xi'an 710072, China. [4]Department of Electrical and Computer Engineering, The University of Texas at Austin, Austin, TX 78712, USA. [5]Department of Physics, Queens College, City University of New York, Queens, NY 11367, USA. [6]Department of Electrical Engineering, Ginzton Laboratory, Stanford University, Stanford, CA 94305, USA. [7]School of Physics and Technology, Wuhan University, Wuhan 430072, China. [8]Photonics Initiative, Advanced Science Research Center, City University of New York, New York, NY 10031, USA. [9]Physics Program, Graduate Center, City University of New York, New York, NY 10026, USA. [10]Department of Electrical Engineering, City College of New York, New York, NY 10031, USA.
*These authors contributed equally to this work.
†Corresponding author. Email: xfzhu@hust.edu.cn (X.-F.Z.); shanhui@stanford.edu (S.F.); chengwei.qiu@nus.edu.sg (C.-W.Q.)

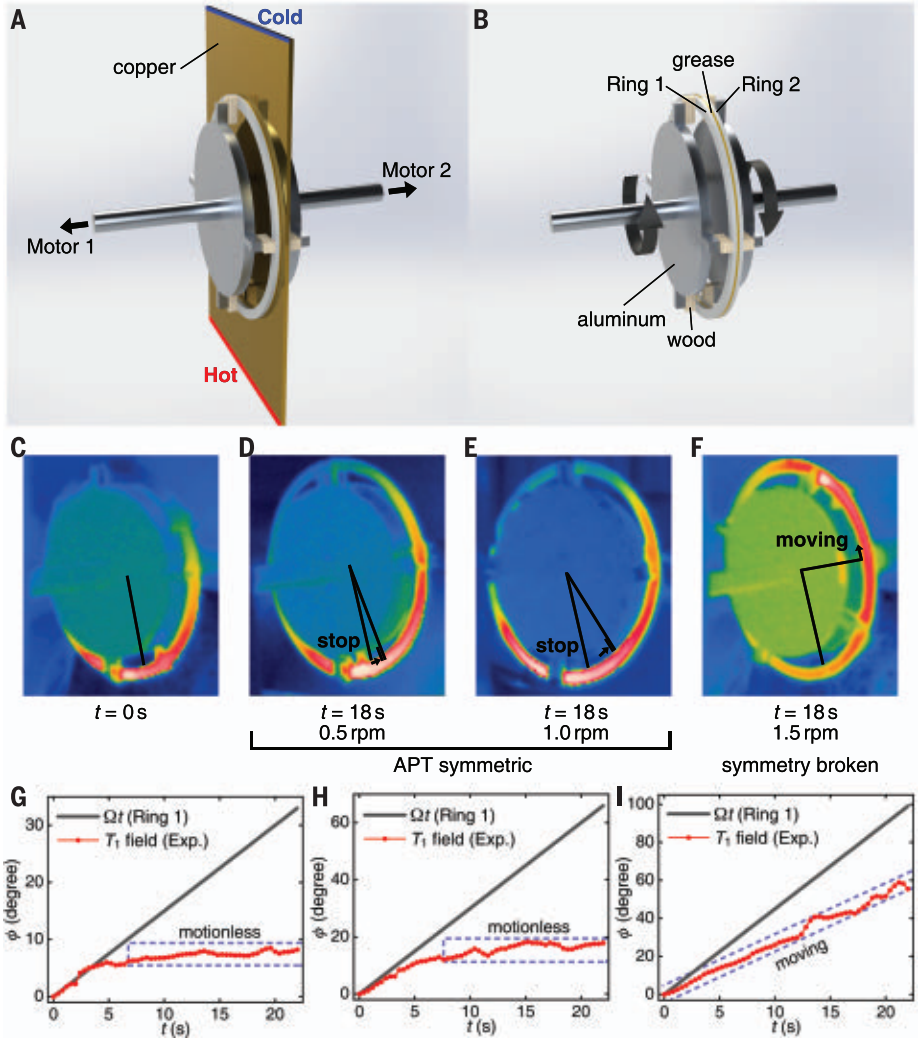

Fig. 4. Experimental setup and results for the APT symmetric and symmetry-broken phases. (**A** and **B**) Schematic graphs of the experimental setup for generating the initial temperature gradient (A) and performing transient measurements (B). (**C** to **F**) Infrared images of the temperature profiles on ring 1. (C) Snapshot taken at t = 0 s when the motors were just turned on. (D to F) Snapshots taken at t = 18 s for rings rotating at 0.5 rpm (D), 1.0 rpm (E), and 1.5 rpm (F). The colors from dark blue to red represent low to high temperatures, respectively. (**G** to **I**) Evolution of the temperature field T_1, represented as the rotation angle ϕ of the temperature dipole from the initial state, with a rotation speed Ω of 0.5 rpm (G), 1.0 rpm (H), and 1.5 rpm (I). The dark gray lines represent the rotation angles of ring 1.

(Fig. 2, A and B). Next, we focus on the fundamental modes with $\pm k_0 = \pm a^{-1}$ and track the eigenstates by looking at the temperature profiles along the upper and lower boundaries of the system, representing T_1 and T_2, respectively. The changes of profiles exactly follow the theoretical prediction (Fig. 2C). At v = 0 cm/s, the two eigenstates have even and odd symmetries with respect to the mirror plane between the channels. As v increases, T_2 gradually accumulates a negative (positive) phase along the lower (upper) branch of eigenvalues. At v_{EP} = 2 cm/s, the two profiles of T_2 coincide with one another, with $\pi/2$ phase behind T_1. For $v > v_{EP}$, the profiles start moving, because the system acquires nonzero eigenfrequency. At v = 3.0 cm/s, the amplitude of the forward wave ($+x$) is 0.38, whereas that of the backward wave ($-x$) is 1/0.38 = 2.61. These values agree well with the theoretical requirement.

The phase transition of temperature profiles across the EP can also be observed directly in the transient behavior. To do so, we numerically simulate a 3D system of two ring-shaped channels packed vertically (Fig. 1D). We define T_1 and T_2 as the temperatures along the upper and lower interior edges of the rings (interior radius $R_1 = a$). To induce the fundamental modes, we set the initial states as the eigenstates at v = 0 cm/s, namely, the same (even) or opposite (odd) temperature gradients along y in the two rings (materials and methods S3). With the same wave number $\pm k_0$, the initial states are expected to evolve to the fundamental modes for nonzero v.

One way to follow the evolution of the profiles of T_1 and T_2 is to follow their maximum points. The trajectories of max(T_1) and max(T_2) are shown with snapshots of the temperature profiles in the left and right panels of Fig. 3, A to C. At low speeds, the maximum points move from their initial positions to certain positions and stops (Fig. 3A). The temperature profile remains motionless thereafter for both initial conditions. For the even initial condition, the temperature profile directly evolves into the eigenstate illustrated in II of Fig. 2C, with T_1 ahead of T_2 for a phase ϕ that is less than $\pi/2$. For the odd initial condition, the temperature profile also eventually evolves into the same state as for the even initial condition. This is due to the typical nonorthogonality of the two eigenstates at different branches (*2*), so an odd initial condition also can evolve to the eigenstate at the lower branch of Fig. 2A, which decays much slower than the other eigenstate and eventually becomes the observed one.

At the EP when v = 2.0 cm/s, the motions are almost the same as when v is lower. Only the accumulated phase difference ϕ_{EP} is larger (Fig. 3B). This phase is found numerically to be $\phi_{EP} = 0.48\pi$, close to the analytically predicted $\pi/2$. At v > 2.0 cm/s, the temperature profiles are always in motion (scatters in Fig. 3C). The profile in each channel follows the background velocity direction, due to the broken APT symmetry of the state with complex eigenvalue.

The finite eigenfrequency indicates a moving temperature profile, but its direction does not necessarily have to follow that of the background. In fact, details of the symmetry-broken states depend on the initial condition. Numerical simulations reveal that the symmetry-broken phase can exhibit temperature flow opposite to the background motion, when an asymmetric initial condition is used (supplementary text S2 and fig. S3).

To observe the phenomena predicted in Fig. 3, we propose the experimental setup in Fig. 4, A and B (see also materials and methods S4 and fig. S4). The system consists of two plastic rings rotated by motors. The two solid rings exchange heat through a layer of lubricating grease. The heat exchange rate h of the grease layer can be estimated as 0.13 s^{-1}, which gives a critical rotation speed of ≈1.27 rpm. We first vertically place a copper plate, whose bottom (top) end is in a hot (cold) bath. The two rings are then brought in contact with the copper plate to achieve the vertical temperature gradient (Fig. 4A). After reaching steady state, we quickly remove the copper plate, make the two rings contact, and turn on the two motors so that the rings rotate in opposite directions with the same rotation speed Ω (Fig. 4B). An infrared camera is used to observe and record the evolution of the temperature field during the whole process (movies S1 to S3).

A snapshot of the temperature profiles on ring 1 at 0 s (when the motors were turned on) is shown in Fig. 4C, and snapshots at 18 s are shown in Fig. 4, D to F. At slower rotation speeds (0.5 and 1.0 rpm), the high-temperature regions are fixed after a small rotation from the initial place (Fig. 4, D and E), demonstrating the symmetric phase. On the contrary, at a faster rotation speed of 1.5 rpm, the high-temperature region is continuously moving (Fig. 4F), demonstrating the symmetry-broken phase. To further calibrate this rotation of temperature field, we postprocess the infrared images to calculate a "temperature dipole" $\mathbf{p}_T$ (materials and methods S4). The angle $\phi(t)$ between $\mathbf{p}_T(t)$ and $\mathbf{p}_T(0)$ is plotted in Fig. 4, G to I. Its rotation again confirms the phase transition.

This work reveals that APT symmetry can be realized with common materials in diffusion, which is outside wave physics. What establishes the symmetry is the opposite velocities of the two channels; this is different from previous systems that require opposite signs in material parameters (*3*–*6*) or require rescaling (*10*, *16*). Our findings open opportunities for using diffusive dynamics to study PT-related physics and provide insight into the development of control mechanisms in the broad area of nonequilibrium mass or energy transport.

REFERENCES AND NOTES

1. C. M. Bender, S. Boettcher, *Phys. Rev. Lett.* **80**, 5243–5246 (1998).
2. C. M. Bender, *Rep. Prog. Phys.* **70**, 947–1018 (2007).
3. K. G. Makris, R. El-Ganainy, D. N. Christodoulides, Z. H. Musslimani, *Phys. Rev. Lett.* **100**, 103904 (2008).
4. C. E. Rüter *et al.*, *Nat. Phys.* **6**, 192–195 (2010).
5. B. Peng *et al.*, *Nat. Phys.* **10**, 394–398 (2014).
6. X. Zhu, H. Ramezani, C. Shi, J. Zhu, X. Zhang, *Phys. Rev. X* **4**, 031042 (2014).
7. R. El-Ganainy *et al.*, *Nat. Phys.* **14**, 11–19 (2018).
8. W. D. Heiss, *J. Phys. Math. Gen.* **45**, 444016 (2012).
9. B. Peng *et al.*, *Science* **346**, 328–332 (2014).
10. A. Guo *et al.*, *Phys. Rev. Lett.* **103**, 093902 (2009).
11. L. Chang *et al.*, *Nat. Photonics* **8**, 524–529 (2014).
12. Z. Lin *et al.*, *Phys. Rev. Lett.* **106**, 213901 (2011).
13. A. Regensburger *et al.*, *Nature* **488**, 167–171 (2012).
14. L. Feng *et al.*, *Nat. Mater.* **12**, 108–113 (2013).
15. Z. J. Wong *et al.*, *Nat. Photonics* **10**, 796–801 (2016).
16. L. Feng, Z. J. Wong, R.-M. Ma, Y. Wang, X. Zhang, *Science* **346**, 972–975 (2014).
17. H. Hodaei, M.-A. Miri, M. Heinrich, D. N. Christodoulides, M. Khajavikhan, *Science* **346**, 975–978 (2014).
18. S. Assawaworrarit, X. Yu, S. Fan, *Nature* **546**, 387–390 (2017).
19. M.-A. Miri, A. Alù, *Science* **363**, eaar7709 (2019).
20. J.-H. Wu, M. Artoni, G. C. La Rocca, *Phys. Rev. Lett.* **113**, 123004 (2014).
21. J.-H. Wu, M. Artoni, G. C. La Rocca, *Phys. Rev. A* **91**, 033811 (2015).
22. P. Peng *et al.*, *Nat. Phys.* **12**, 1139–1145 (2016).
23. Y. Choi, C. Hahn, J. W. Yoon, S. H. Song, *Nat. Commun.* **9**, 2182 (2018).
24. V. V. Konotop, D. A. Zezyulin, *Phys. Rev. Lett.* **120**, 123902 (2018).
25. F. Yang, Y.-C. Liu, L. You, *Phys. Rev. A* **96**, 053845 (2017).
26. A. Bejan, *Convection Heat Transfer* (Wiley, 2013).
27. S. Franke-Arnold, G. Gibson, R. W. Boyd, M. J. Padgett, *Science* **333**, 65–67 (2011).
28. R. Fleury, D. L. Sounas, C. F. Sieck, M. R. Haberman, A. Alù, *Science* **343**, 516–519 (2014).
29. D. Torrent, O. Poncelet, J.-C. Batsale, *Phys. Rev. Lett.* **120**, 125501 (2018).
30. Y. Li *et al.*, *Nat. Mater.* **18**, 48–54 (2019).

ACKNOWLEDGMENTS

Funding: C.-W.Q. acknowledges financial support from the Ministry of Education, Singapore (project R-263-000-C05-112). X.-F.Z. and Y.-G.P. acknowledge the financial support of the National Natural Science Foundation of China (grants 11674119, 11690030, and 11690032) and the Bird Nest Plan of HUST. W.L. and S.F. acknowledge the support of U.S. Department of Energy grant DE-FG-07ER46426. **Author contributions:** Y.L. and C.-W.Q. conceived the concept. Y.L., S.F., and C.-W.Q. designed the model. Y.L. performed the numerical simulations. Y.L., M.-A.M., W.L., J.Z., A.A., and C.-W.Q. discussed the theoretical results and analyzed the model. Y.L., Y.-G.P., and L.H. prepared the samples and performed the experiments. X.-F.Z., S.F., and C.-W.Q. supervised the research. All authors discussed and contributed to the manuscript. **Competing interests:** The authors declare no competing interests. **Data and materials availability:** All data are available in the main text or the supplementary materials.

SUPPLEMENTARY MATERIALS

www.sciencemag.org/content/364/6436/170/suppl/DC1
Materials and Methods
Supplementary Text
Figs. S1 to S4
References (*31*–*40*)
Movies S1 to S3

10 January 2019; accepted 14 March 2019
10.1126/science.aaw6259

TROPHIC CASCADES

Cascading impacts of large-carnivore extirpation in an African ecosystem

Justine L. Atkins[1]*, Ryan A. Long[2], Johan Pansu[1,3,4], Joshua H. Daskin[1]†, Arjun B. Potter[1], Marc E. Stalmans[5], Corina E. Tarnita[1], Robert M. Pringle[1]*

Populations of the world's largest carnivores are declining and now occupy mere fractions of their historical ranges. Theory predicts that when apex predators disappear, large herbivores become less fearful, occupy new habitats, and modify those habitats by eating new food plants. Yet experimental support for this prediction has been difficult to obtain in large-mammal systems. After the extirpation of leopards and African wild dogs from Mozambique's Gorongosa National Park, forest-dwelling antelopes [bushbuck (*Tragelaphus sylvaticus*)] expanded into treeless floodplains, where they consumed novel diets and suppressed a common food plant [waterwort (*Bergia mossambicensis*)]. By experimentally simulating predation risk, we demonstrate that this behavior was reversible. Thus, whereas anthropogenic predator extinction disrupted a trophic cascade by enabling rapid differentiation of prey behavior, carnivore restoration may just as rapidly reestablish that cascade.

The worldwide decline in populations of large mammalian carnivores is a major environmental concern (*1*, *2*), in part because apex predators can exert a defining influence on ecosystems via trophic cascades (*3*). A trophic cascade occurs when predators indirectly affect plants through either of two mechanisms: by consumptively reducing prey abundance (*4*) or by imposing "landscapes of fear" in which prey modify their behavior to reduce predation risk. In landscapes of fear, prey are expected to forego foraging opportunities in resource-rich habitats that are risky, thereby creating spaces where palatable food plants can thrive (*5*, *6*). Accordingly, the extirpation of top carnivores should create "landscapes of fearlessness" where large herbivores seek out the nutritional benefits of previously risky habitats, suppressing food-plant abundance in the process (*5*); conversely, the reestablishment of real or perceived predation risk should reverse this behavior (*7*). Although behaviorally mediated trophic cascades have been documented frequently for relatively small consumer species (*8*–*10*), there are few unequivocal examples involving large mammalian carnivores and herbivores (*11*–*13*). This gap reflects the difficulty of experimentally manipulating predation risk and quantifying its downstream effects at scales relevant to large mammals. Correlative and comparative analyses generally cannot rule out potentially confounding factors, which has fueled debates (*14*–*18*) and prompted calls for stronger mechanistic inference in the study of megafaunal trophic cascades (*19*).

Ecosystems in which top predators have been extirpated present valuable opportunities to test predictions of trophic-cascade theory (*4*, *14*, *20*). In Mozambique's Gorongosa National Park, large-mammal populations were severely reduced during the Mozambican Civil War (1977 to 1992),

[1]Department of Ecology and Evolutionary Biology, Princeton University, Princeton, NJ, USA. [2]Department of Fish and Wildlife Sciences, University of Idaho, Moscow, ID, USA. [3]Station Biologique de Roscoff, UMR 7144 CNRS-Sorbonne Université, 29688 Roscoff, France. [4]CSIRO Ocean and Atmosphere, Lucas Heights, NSW 2234, Australia. [5]Department of Scientific Services, Parque Nacional da Gorongosa, Sofala, Mozambique.
***Corresponding author. Email: jlatkins@princeton.edu (J.L.A.); rpringle@princeton.edu (R.M.P.)**
†Present address: Department of Ecology and Evolutionary Biology, Yale University, New Haven, CT, USA.

with >90% declines across all monitored species (*21–23*). Large-herbivore populations have subsequently increased, but leopards (*Panthera pardus*), wild dogs (*Lycaon pictus*), and hyenas (*Crocuta crocuta*) were extirpated, while lions (*P. leo*) persisted at low abundance (*23*, *24*) (table S1). In this carnivore-depleted system, we evaluated evidence for a behaviorally mediated trophic cascade by using field manipulations of predator cues and herbivory, GPS telemetry of herbivore movements, spatially explicit wildlife-count data, DNA-based diet analysis, and body-condition measurements.

Gorongosa's central valley (Fig. 1, A and B) encompasses the ~750-km^2 Lake Urema floodplain and surrounding savanna woodlands (*25*). During the dry season (May to November), the floodplain is a flat, largely treeless landscape, dominated by grasses and forbs and dotted with leguminous subshrubs. Such open habitat is typically avoided by herbivores that rely on crypsis, tree cover, and known escape trails to avoid detection and capture by predators. One such herbivore species is bushbuck (*Tragelaphus sylvaticus*). This midsized antelope is a closed-habitat specialist that is "dependent on thick cover" (*26*) and "concealment to avoid predators" (*27*) and "is not found on open plains or anywhere without sufficient cover to conceal it" (*28*) from key predators such as leopards and wild dogs (*29*). Previous studies of African ungulates have emphasized the comparative safety of open areas with high visibility (*11*, *13*). For secretive forest browsers such as bushbuck, however, treeless areas should be riskier, and relaxation of predation pressure might embolden individuals to exploit what would otherwise be prohibitively dangerous open habitat. Bushbuck in Gorongosa were historically confined to woodland and thicket habitat (*30*), but in the largely predator-free contemporary environment, we have observed them venturing into the open Urema floodplain.

We quantified these initial observations by fitting GPS collars to 11 bushbuck in 2015 and collecting hourly locations for up to 8 months.

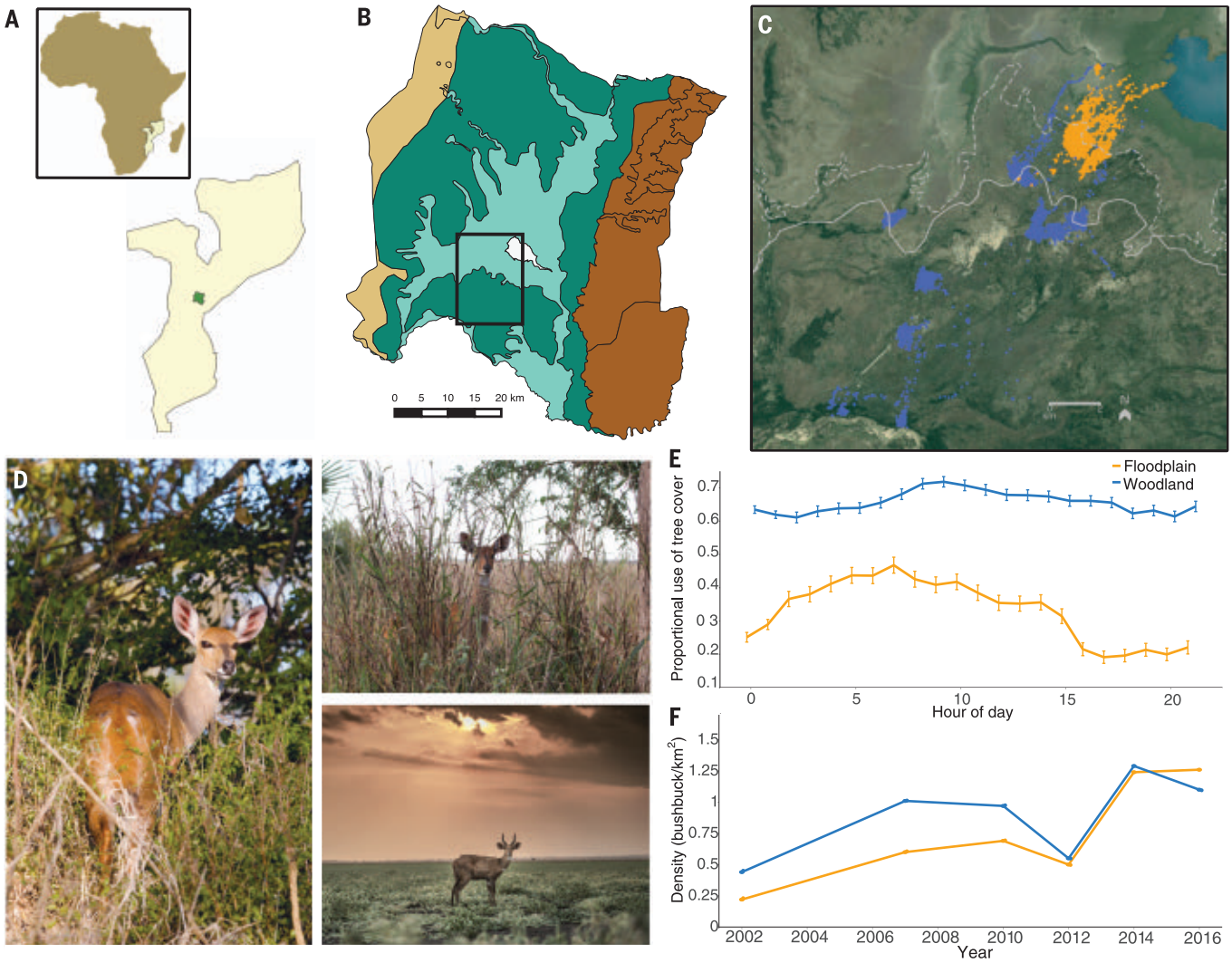

PHOTOS (CLOCKWISE FROM TOP RIGHT): J. H. DASKIN, B. KUXHAUSEN, R. M. PRINGLE

Fig. 1. Differential habitat use by bushbuck. (**A**) Map of Africa and Mozambique, showing the location of Gorongosa National Park (**B**) with its major habitat zones (*25*), from left: the western escarpment, savanna woodland (dark green), floodplain (light green), Lake Urema (white), and eastern escarpment. The boxed area indicates the region shown in the satellite image in (C). (**C**) GPS-collar locations from 11 individuals, three in the floodplain (orange) and eight in the adjoining woodland (blue), from June 2015 to March 2016. The solid line distinguishes the boundary between the floodplain and dense woodland; the dashed line distinguishes the boundary between the sparsely wooded floodplain margin and the treeless floodplain (*25*). (**D**) Bushbuck in woodland (left), the floodplain margin (top right), and the open floodplain (bottom right). (**E**) Use of woody cover by the bushbuck in (C), measured as the proportion of locations falling within a pixel classified as containing tree cover (*32*); error bars show ±1 SE. (**F**) Bushbuck densities in the floodplain and woodland, 2002 to 2016, determined via six aerial helicopter counts (*32*); here, "floodplain" refers conservatively to the treeless area surrounding Lake Urema [dashed line in (C)].

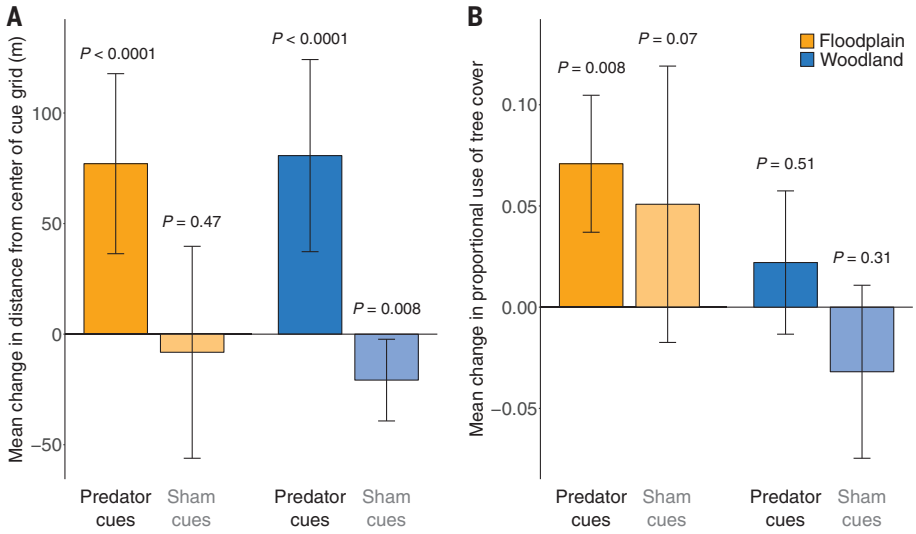

Fig. 2. Responses of floodplain and woodland bushbuck to simulated-predator and procedural-control cues. Average changes in (**A**) the distance from cues (avoidance) and (**B**) the proportional use of tree cover for bushbuck in woodland (n = 5) and floodplain (n = 7) habitats at night. Each bar (colored by habitat affiliation) represents the average difference between the 48-hour pre-cue period and the 48-hour post-cue period across all collared individuals in each category; error bars show ±1 SE. Shading indicates experimental treatment, with darker bars for the predator cues and lighter bars for the sham cues (see x-axis labels). P values from generalized linear mixed models are shown above each bar, indicating whether each response differed significantly from zero (see full model results in table S2).

The data revealed two broad patterns in habitat use. One subset of individuals was largely confined to densely wooded home ranges; another occupied the sparsely wooded floodplain margin and routinely forayed into treeless floodplain habitat, both at night and throughout the day (Fig. 1, C to E)—behavior never documented prior to predator extirpation (*30*). All available evidence indicates that this habitat shift cannot be explained by competitive interactions. In principle, carnivore extirpation might have increased woodland bushbuck densities, prompting individuals to move into the floodplain to mitigate intraspecific competition, as predicted by ideal free distribution theory (*31*). We explored this possibility by using data from six helicopter counts conducted between 2002 and 2016, when all ungulate populations were recovering from similarly severe war-induced declines (*21*–*23*, *30*). If competition caused the habitat shift, then we would expect floodplain bushbuck densities to be negligible during the earliest counts, to increase only after woodland densities reached some threshold, and to remain lower than woodland densities throughout. To the contrary, floodplain bushbuck density was already ~50% of woodland bushbuck density in 2002, and by 2016, density was ~15% higher in the floodplain (Fig. 1F). Moreover, densities of other ungulates were also highest in the floodplain (*21*). Thus, the observed habitat shift cannot obviously be explained by either intra- or interspecific competition.

To directly test the hypothesis that predator extirpation has promoted the use of open habitat by bushbuck, we experimentally assessed the responses of GPS-collared floodplain (n = 7) and woodland (n = 5) bushbuck to simulated predator presence in August and September 2016. Habitat affiliations were determined on the basis of capture location and were subsequently verified with reference to GPS-collar locations and diet composition data (figs. S1 and S2). We exposed each individual to both predator and procedural-control cues in separate trials (in randomized order), with collars recording locations every 15 min (*32*). Treatments comprised both auditory and scent cues within the home range of each collared individual (fig. S3). Because both felids and canids prey on bushbuck, we aimed to create generalized hot spots of perceived predation risk by deploying several cues that collectively simulated multiple predator species. Playbacks of leopard vocalizations, artificial lion scat, and generic carnivore urine (*32*) were used to mimic predator presence; white noise, locally collected herbivore dung, and saline solution were used as sham cues in procedural-control trials (*12*, *33*). We restricted our analyses to data collected between 17:00 and 06:00, the period encompassing peak bushbuck activity (*32*). For each individual, we quantified two response variables in the 48 hours immediately before and after cue deployment. First, we measured the avoidance of predator and control cues by calculating the distance between each bushbuck GPS point and the sound-cue location. Second, we measured whether simulated risk caused floodplain individuals to increase their use of tree cover (i.e., shift back toward a more "typical" bushbuck habitat).

Bushbuck strongly avoided predator cues in both habitats but did not avoid sham cues in either habitat (Fig. 2A and table S2). Moreover, predator cues caused a significant increase in the use of tree cover by floodplain but not woodland bushbuck, whereas sham cues did not significantly alter tree-cover use in either habitat (Fig. 2B and table S2). We evaluated the statistical significance of these responses by using mixed-effects models with random intercepts for individuals (table S2). These results were robust to both GPS and habitat classification error (*32*) (figs. S4 and S5 and table S3). That floodplain bushbuck exhibited more cautious behavior in response to even a brief exposure to simulated risk suggests that some fear of predators has been retained and is primed in more risky open habitats (*7*, *12*). Our design does not enable us to distinguish the roles of specific predator cues in generating these responses, but future studies could test sound and scent cues separately.

Theory often assumes a nutritional opportunity cost of risk avoidance (*5*). We therefore hypothesized that floodplain bushbuck would consume higher-quality diets and exhibit greater size and body condition. We analyzed bushbuck diet composition by using DNA metabarcoding of fecal samples (*32*, *34*). We also quantified the digestible-energy and digestible-protein contents of foliage from Gorongosa's most common browse plants. Of the 51 molecular operational taxonomic units (mOTUs) identified in bushbuck diets, 22 matched plant species for which we had nutritional-quality data, and those 22 species accounted for >83% of total diet [measured as the relative read abundance (RRA) of those mOTUs across all samples (*32*)]. We calculated weighted averages of digestible energy and protein in the diet of each sampled bushbuck, using the RRA of each plant species as the weighting factor. We quantified the body condition of captured individuals by using principal components analysis to reduce multiple measurements of bushbuck morphology (e.g., body mass, body length, fat and muscle thickness, and standardized palpation scores) to two indices of condition: body size and body fat (*32*) (fig. S6 and tables S4 and S5).

We found pronounced differences in diet composition between floodplain and woodland bushbuck (Fig. 3A and fig. S2). The diets of floodplain bushbuck (21 mOTUs) were dominated by the leguminous shrub *Mimosa pigra* (mean RRA = 74% ± 11%) (Fig. 3B and fig. S2), with the forbs *Bergia mossambicensis* (Elatinaceae; syn. *B. salaria*) and *Ludwigia adscendens* (Onagraceae; syn. *L. stolonifera*) accounting for an additional 11 and 3% of RRA, respectively. These plants had relatively high crude-protein and digestible-energy contents (fig. S2, C and D). The diets of woodland bushbuck (36 mOTUs) had greater evenness: Two tree species, *Berchemia discolor* and *Diospyros* sp., together accounted for 44% of RRA (Fig. 3B), and both species had lower crude protein and

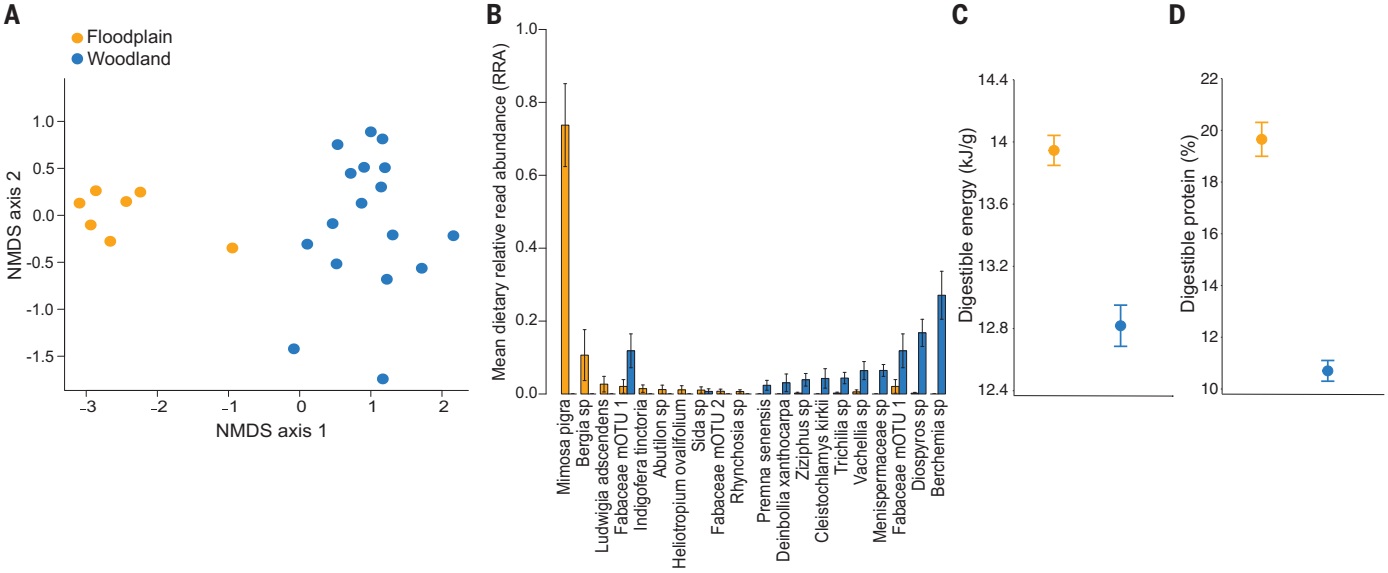

Fig. 3. Differences in composition and nutritional quality of bushbuck diets across habitats. (**A**) Nonmetric multidimensional scaling (NMDS) ordination, based on Bray-Curtis dissimilarities from DNA-metabarcoding data, showing that bushbuck diets clustered within each habitat and diverged between them. The distance between points (n = 7 floodplain fecal samples; n = 17 woodland fecal samples) reflects compositional dissimilarity. (**B**) The 10 most abundant food-plant taxa for bushbuck in the floodplain (orange bars) and woodland (blue bars). (**C**) Mean digestible energy and (**D**) protein contents of bushbuck diets, revealing higher diet quality in floodplain individuals (Wilcoxon rank sum tests; energy, W = 76, n = 18 individuals, P = 0.0001; protein, W = 77, n = 18 individuals, P < 0.0001). Error bars show ±1 SE.

digestible energy than *M. pigra* and most other floodplain food plants (fig. S2, C and D). Overall, floodplain bushbuck diets were 8.8 and 83.6% richer in digestible energy and protein, respectively, than woodland bushbuck diets (Fig. 3, C and D). Consistent with these differences in diet quality, floodplain bushbuck were in better condition than woodland bushbuck, with significantly higher scores for the body size [principal component 1 (PC1)] index (table S6). The nutritional value of the most heavily utilized plant, *M. pigra*, may help to promote floodplain use by bushbuck, but this factor alone does not provide a plausible alternative explanation for the long-term shift in habitat use. *M. pigra* was also present on the floodplain before predator extirpation (*30*), with availability similar to that at the time of this study; if this plant drove habitat use independently of predation risk, then bushbuck should have been using the floodplain during the prewar era as well. The relative influences of risk and resource quality on bushbuck habitat use could in principle be quantified by removing *M. pigra* at large scales; we hypothesize that this would reduce carrying capacity but not expel bushbuck from these areas.

In a final experiment, we tested whether the expansion of bushbuck into the floodplain has measurable effects on floodplain plants. Plant community responses to herbivory can be tested by using exclosures, but it would be impossible to parse the effects of bushbuck relative to those of other floodplain ungulates with overlapping diets. Thus, to isolate the effects of bushbuck, we used our diet analysis to identify an indicator plant species consumed almost exclusively by bushbuck. The waterwort *B. mossambicensis* was the second most abundant taxon in the diets of floodplain bushbuck but was negligible (≤1% RRA) in the diets of all other floodplain herbivores (Fig. 4A). We constructed wire-mesh herbivore exclosures around *Bergia* plants in a randomized, paired caged-uncaged design (fig. S7) at two different floodplain sites (with 15 total pairs) (*32*). Before the experiment, and again after a minimum of 16 days, we measured the dimensions of each plant and counted all leaves, flowers, and browsed stems. The percentage of browsed stems per plant increased in uncaged plants during the experiment but did not change in caged plants (Fig. 4B and table S7). Similarly, the mean number of leaves increased in caged plants but decreased in uncaged plants (Fig. 4C). The mean number of flowers, height, and canopy area at the conclusion of the experiment were all significantly greater in caged plants (Fig. 4 and table S7). Thus, the expansion of bushbuck into open habitats was accompanied by strong suppression of growth and reproduction in *Bergia*. Although other floodplain herbivores may have contributed somewhat to this effect, only bushbuck consumed substantial quantities of *Bergia* (Fig. 4A), suggesting that this plant would otherwise find refuge from large-mammal herbivory in the floodplain.

Altogether, our results provide evidence that the extirpation of large carnivores in the wake of the Mozambican Civil War has disrupted a behaviorally mediated trophic cascade. In the absence of apex predators such as leopards and wild dogs, a common ungulate prey species rapidly expanded into a high-risk, high-reward habitat, with concomitant shifts in diet composition and quality, body size and condition, and the performance of a key food plant. Despite the multidecadal absence of several apex predators in Gorongosa, we found that bushbuck retained a fear of these carnivores (*7*, *12*): Experimental imposition of risk cues over just 48 hours shifted habitat use toward patterns that prevailed before carnivore loss (*30*). The next phase of trophic rewilding in Gorongosa involves carnivore reintroductions (*23*), beginning in 2018 with 14 wild dogs, which should eventually enable tests of our prediction that bushbuck will vacate the floodplain. Notably, the relaxation of risk after carnivore extirpation differentially affected individual behavior within a population, leading to bimodality in habitat use and perhaps some degree of reproductive separation, which could amplify preexisting individual variation (*35*). The influence of carnivores on behavioral variation within ungulate populations, and its potential evolutionary significance, remains largely unexplored.

Our study supports the general hypothesis that the loss of top carnivores can convert landscapes of fear into landscapes of fearlessness for large mammalian herbivores, with far-reaching consequences for prey and plant populations (*6*). It further shows that the effects of fear depend on the social, foraging, and antipredator behaviors of the species involved. Whereas recent work has shown that gregarious, flight-dependent grazers and mixed feeders use open, high-visibility habitat for risk avoidance (*11*, *13*), our study of a solitary, crypsis-dependent browser reveals an opposing pattern. This distinction was appreciated by early naturalists [(*36*), pp. 32–33]:

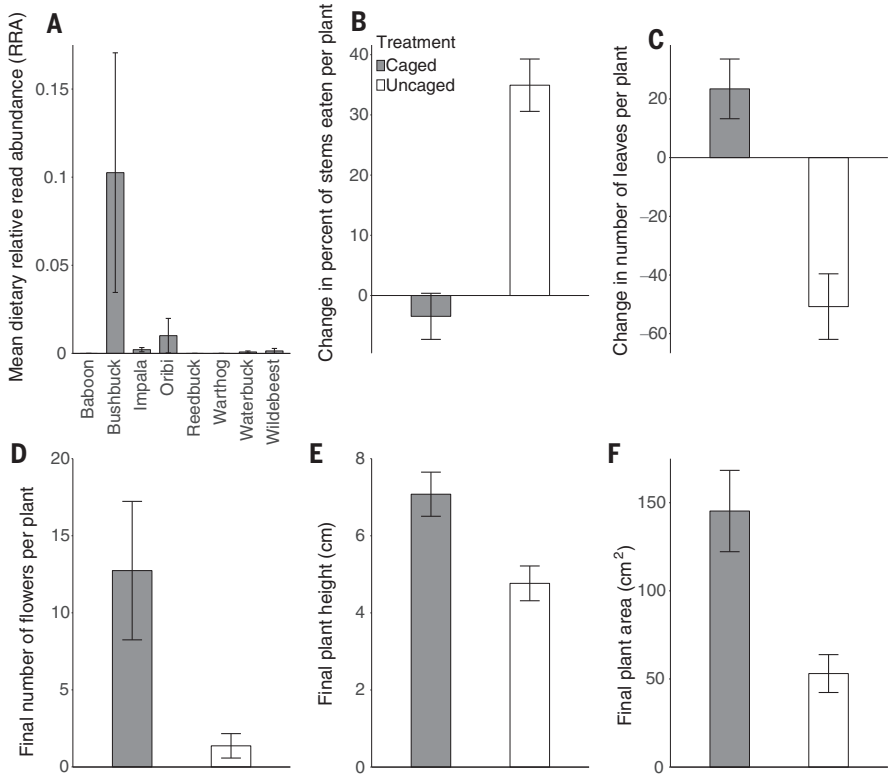

Fig. 4. Large herbivores suppress *Bergia mossambicensis*, a common floodplain plant. (**A**) Among all floodplain herbivore species in Gorongosa, only bushbuck consumed substantial quantities of *Bergia*. Shown are the mean changes in (**B**) the percentage of stems browsed and (**C**) the number of leaves per plant on caged versus uncaged *Bergia* plants over a minimum of 16 days (maximum of 18 days). Herbivores also reduced (**D**) the mean number of flowers per plant, (**E**) mean height, and (**F**) mean canopy area at the conclusion of the experiment. For (D) to (F), there was no significant difference in the initial values between caged and uncaged treatment groups. Model results of the effects of herbivore exclusion on each response variable are presented in table S7. Error bars show ±1 SE.

> It is curious to note the different ideas of safety entertained respectively by the plain and the bush dweller. Let us say a Grant's gazelle and a bushbuck are grazing near each other on the edge of a plain when something occurs to alarm them. The bushbuck lopes quickly back into the bush, sure that in this lies his only chance of safety. The Grant's turns and gallops from the bush as if it were some deadly thing ….

Thus, although generalizations about trophic cascades involving particular species and food chains may be possible on the basis of characteristics such as herbivore size, behavior (*37*, *38*), and predator hunting mode (*39*), we suggest that community-wide cascades may be dampened in diverse African large-mammal assemblages because of the orthogonal responses of different herbivore species to predation risk (*40*).

REFERENCES AND NOTES

1. J. A. Estes *et al.*, *Science* **333**, 301–306 (2011).
2. W. J. Ripple *et al.*, *Science* **343**, 1241484 (2014).
3. J. Terborgh, J. A. Estes, Eds., *Trophic Cascades: Predators, Prey and the Changing Dynamics of Nature* (Island Press, 2010).
4. J. A. Estes, J. F. Palmisano, *Science* **185**, 1058–1060 (1974).
5. J. S. Brown, J. W. Laundre, M. Gurung, *J. Mammal.* **80**, 385–399 (1999).
6. J. W. Laundré, L. Hernandez, W. J. Ripple, *Open Ecol. J.* **3**, 1–7 (2010).
7. J. Berger, J. E. Swenson, I. L. Persson, *Science* **291**, 1036–1039 (2001).
8. B. L. Peckarsky *et al.*, *Ecology* **89**, 2416–2425 (2008).
9. G. C. Trussell, P. J. Ewanchuk, C. M. Matassa, *Ecology* **87**, 2979–2984 (2006).
10. O. J. Schmitz, V. Krivan, O. Ovadia, *Ecol. Lett.* **7**, 153–163 (2004).
11. A. T. Ford *et al.*, *Science* **346**, 346–349 (2014).
12. J. P. Suraci, M. Clinchy, L. M. Dill, D. Roberts, L. Y. Zanette, *Nat. Commun.* **7**, 10698 (2016).
13. E. le Roux, G. I. H. Kerley, J. P. G. M. Cromsigt, *Curr. Biol.* **28**, 2493–2499.e3 (2018).
14. W. J. Ripple, E. J. Larsen, R. A. Renkin, D. W. Smith, *Biol. Conserv.* **102**, 227–234 (2001).
15. D. Fortin *et al.*, *Ecology* **86**, 1320–1330 (2005).
16. M. J. Kauffman, J. F. Brodie, E. S. Jules, *Ecology* **91**, 2742–2755 (2010).
17. B. L. Allen *et al.*, *Biol. Conserv.* **159**, 158–174 (2013).
18. J. Winnie Jr., S. Creel, *Food Webs* **12**, 88–94 (2017).
19. A. T. Ford, J. R. Goheen, *Trends Ecol. Evol.* **30**, 725–735 (2015).
20. J. Terborgh *et al.*, *Science* **294**, 1923–1926 (2001).
21. M. E. Stalmans, T. J. Massad, M. J. S. Peel, C. E. Tarnita, R. M. Pringle, *PLOS ONE* **14**, e0212864 (2019).
22. J. H. Daskin, M. Stalmans, R. M. Pringle, *J. Ecol.* **104**, 79–89 (2016).
23. R. M. Pringle, *Nature* **546**, 91–99 (2017).
24. P. Bouley, M. Poulos, R. Branco, N. H. Carter, *Biol. Conserv.* **227**, 233–242 (2018).
25. M. Stalmans, R. Beilfuss, "Landscapes of the Gorongosa National Park" (Gorongosa National Park, 2008).
26. J. Kingdon, *The Kingdon Field Guide to African Mammals* (Bloomsbury, ed. 2, 2015).
27. R. D. Estes, *The Safari Companion: A Guide to Watching African Mammals* (Chelsea Green, ed. 2, 1999).
28. R. D. Estes, *The Behavior Guide to African Mammals* (Univ. of California Press, 1991).
29. F. G. T. Radloff, J. T. Du Toit, *J. Anim. Ecol.* **73**, 410–423 (2004).
30. K. L. Tinley, thesis, University of Pretoria, Pretoria, South Africa (1977).
31. S. D. Fretwell, H. L. J. Lucas Jr., *Acta Biotheor.* **19**, 16–36 (1969).
32. Materials and methods are available as supplementary materials.
33. A. T. Ford, J. R. Goheen, *J. Mammal.* **96**, 918–926 (2015).
34. J. Pansu *et al.*, *J. Ecol.* 10.1111/1365-2745.13113 (2018).
35. D. I. Bolnick *et al.*, *Am. Nat.* **161**, 1–28 (2003).
36. C. H. Stigand, *The Game of British East Africa* (Horace Cox, 1909).
37. P. J. Jarman, *Behaviour* **48**, 215–267 (1974).
38. K. P. Dial, E. Greene, D. J. Irschick, *Trends Ecol. Evol.* **23**, 394–401 (2008).
39. O. J. Schmitz, *Science* **319**, 952–954 (2008).
40. N. Owen-Smith, *Oikos* **124**, 1417–1426 (2015).
41. J. L. Atkins, R. A. Long, J. Pansu, J. H. Daskin, A. B. Potter, M. E. Stalmans, C. E. Tarnita, R. M. Pringle, Data for "Cascading impacts of large-carnivore extirpation in an African ecosystem," Dryad (2019); https://doi.org/10.5061/dryad.h4r1003.

ACKNOWLEDGMENTS

We thank J. Guyton, G. Gibbons, M. Demmel, A. Becker, P. Bouley, R. Branco, L. Van Wyk, P. Tonecas, C. Lencastro, the Gorongosa park staff, the Republic of Mozambique, and five reviewers. **Funding:** We acknowledge support from the U.S. National Science Foundation (IOS-1656527 and IOS-1656642), Cameron Schrier Foundation, Greg Carr Foundation, Parque Nacional da Gorongosa, and Princeton University. **Author contributions:** J.L.A., R.A.L., C.E.T., and R.M.P. conceived and designed the study; J.L.A., R.A.L., J.P., A.B.P., M.E.S, and R.M.P. collected data; J.L.A. performed and analyzed the field experiments; J.P. analyzed diet data; J.H.D. performed satellite image classification; and J.L.A., R.A.L., C.E.T., and R.M.P. wrote the manuscript with input from all authors. **Competing interests:** R.M.P. serves as an unpaid member of the Board of Directors of the Gorongosa Project, a U.S. 501(c)(3) nonprofit organization that oversees conservation and restoration activities in Gorongosa National Park. **Data and materials availability:** Data are archived in Dryad (*41*).

SUPPLEMENTARY MATERIALS

www.sciencemag.org/content/364/6436/173/suppl/DC1
Materials and Methods
Figs. S1 to S7
Tables S1 to S8
References (*42*–*85*)

2 June 2018; accepted 22 February 2019
Published online 7 March 2019
10.1126/science.aau3561

PLANT SCIENCE

Bacterial medium-chain 3-hydroxy fatty acid metabolites trigger immunity in *Arabidopsis* plants

Alexander Kutschera[1]*, Corinna Dawid[2]*, Nicolas Gisch[3], Christian Schmid[2], Lars Raasch[1], Tim Gerster[1], Milena Schäffer[1], Elwira Smakowska-Luzan[4], Youssef Belkhadir[4], A. Corina Vlot[5], Courtney E. Chandler[6], Romain Schellenberger[7], Dominik Schwudke[3], Robert K. Ernst[6], Stéphan Dorey[7], Ralph Hückelhoven[1], Thomas Hofmann[2], Stefanie Ranf[1]†

In plants, cell-surface immune receptors sense molecular non–self-signatures. Lipid A of Gram-negative bacterial lipopolysaccharide is considered such a non–self-signature. The receptor kinase LIPOOLIGOSACCHARIDE-SPECIFIC REDUCED ELICITATION (LORE) mediates plant immune responses to *Pseudomonas* and *Xanthomonas* but not enterobacterial lipid A or lipopolysaccharide preparations. Here, we demonstrate that synthetic and bacterial lipopolysaccharide-copurified medium-chain 3-hydroxy fatty acid (mc-3-OH-FA) metabolites elicit LORE-dependent immunity. The mc-3-OH-FAs are sensed in a chain length– and hydroxylation-specific manner, with free (*R*)-3-hydroxydecanoic acid [(*R*)-3-OH-C10:0] representing the strongest immune elicitor. By contrast, bacterial compounds comprising mc-3-OH-acyl building blocks but devoid of free mc-3-OH-FAs—including lipid A or lipopolysaccharide, rhamnolipids, lipopeptides, and acyl-homoserine-lactones—do not trigger LORE-dependent responses. Hence, plants sense low-complexity bacterial metabolites to trigger immune responses.

Plant cell–surface pattern recognition receptors sense characteristic microbe- or pathogen-associated molecular patterns (MAMPs or PAMPs) and host-derived damage-associated patterns (DAMPs) and activate pattern-triggered immunity (*1*). Lipopolysaccharide, a glycolipid consisting of lipid A, core oligosaccharide, and O-polysaccharide, is the major outer membrane component of most Gram-negative bacteria (*2*). In humans and mammals, lipid A triggers inflammation and pyroptosis, potentially culminating in life-threatening sepsis (*2*, *3*). Lipopolysaccharide also elicits defense responses in various plant species (*4*). In *Arabidopsis thaliana* (hereafter *Arabidopsis*) and other crucifers, lipopolysaccharide preparations from *Pseudomonas* spp. and *Xanthomonas campestris*, but not from *Escherichia coli*, *Salmonella enterica*, or *Burkholderia* spp., activate characteristic immune responses through the plant-specific bulb-type lectin receptor kinase LIPOOLIGOSACCHARIDE-SPECIFIC REDUCED ELICITATION/S-DOMAIN-1-29 (LORE/SD1-29) (*5*). *Pseudomonas aeruginosa* lipid A is sufficient to trigger immunity, whereas removal of the ester-linked acyl chains from lipid A abolishes its activity (*5*). Thus, lipid A with a distinctive acylation pattern appeared to be critical for immune sensing in *Arabidopsis*.

To decipher the structural features of LORE-dependent lipid A sensing, we screened lipopolysaccharide with different acylation patterns from various bacterial species and *P. aeruginosa* lipid A biosynthesis mutants for activation of cytosolic calcium ($[Ca^{2+}]_{cyt}$) signaling as an indicator of immune response in *Arabidopsis* (table S1 and figs. S1 to S4). Structurally, all tested, elicitor-active lipopolysaccharide preparations comprise a medium-length acyl chain, mostly 3-OH-decanoyl, at positions C-3 and/or C-3′ of lipid A, whereas lipopolysaccharide with 3-OH-tetradecanoyl chains at these positions was inactive. This suggests that a 3-OH-decanoyl chain is a key structural feature for LORE-dependent lipopolysaccharide sensing.

Therefore, synthetic 3-OH-FAs of varying chain length (table S2) were tested for activation of *Arabidopsis* immune responses. Free synthetic 3-OH-C10:0 (**1**; see table S2 for assignment of compound numbers; Fig. 1A) elicits increases in $[Ca^{2+}]_{cyt}$ comparable to those of *Pseudomonas* lipopolysaccharide preparations (Fig. 1B and fig. S5A). Medium-chain (mc)-3-OH-FAs (bearing 8 to 12 carbon atoms, **1** to **5**), particularly 3-OH-C10:0 (**1**), but not long-chain (lc)-3-OH-FAs (13 to 16 carbon atoms, **6** to **8**) activated LORE-dependent $[Ca^{2+}]_{cyt}$ signaling, biphasic production of reactive oxygen species (ROS), transcript accumulation of defense-related genes, and phosphorylation of mitogen-activated protein kinases (Fig. 1, C and D, and fig. S5, B to F). In plants, local MAMP application induces systemic resistance to pathogen infection (*6*). Wild-type *Arabidopsis* plants pretreated with 3-OH-C10:0 (**1**) were more resistant to *P. syringae* infection, but this systemic resistance was not activated in *Arabidopsis lore*-1 mutants or when 3-OH-C14:0 (**7**) was used (Fig. 1E and fig. S5G). Solanaceous *Nicotiana benthamiana* plants are insensitive to *Pseudomonas* lipopolysaccharide preparations but gain responsiveness upon transient expression of a LORE–green fluorescent protein (GFP) fusion (*5*). mc-3-OH-FAs (but not lc-3-OH-FAs) also induced ROS production in *N. benthamiana* leaves expressing LORE-GFP but not leaves expressing a kinase-inactive control (Fig. 1F and fig. S5H). LORE ectodomain expressed and purified from insect cells directly binds 3-OH-C10:0 (**1**) in vitro. Under these conditions, the observed binding affinity was relatively low, however (Fig. 1G and fig. S6). Taken together, this supports that LORE is a receptor for mc-3-OH-FAs.

Next, we tested whether a 3-hydroxyl and/or a carboxyl group are molecular determinants for activating LORE-mediated immunity (Fig. 2). Compared with mc-3-OH-FAs (**1** to **5**), mc-2-OH-FAs (**11** to **13**) and nonhydroxylated mc-FAs (**15** to **17**) induced only limited immune responses in *Arabidopsis* and LORE-GFP-expressing *N. benthamiana* (Fig. 2, A and B, and fig. S7, A to E). Nonhydroxylated or Δ^2-unsaturated (**19**,**20**) mc-FAs induced weak LORE-independent responses (Fig. 2, A and B, and fig. S7, A to F). The 4-OH-C10:0 (**21**) and 5-OH-C10:0 (**22**) did not elicit LORE-dependent ROS production (Fig. 2C and fig. S7G). The 3-oxodecanoic acid (3-oxo-C10:0, **23**), or its keto-enol tautomer 3-OH-decenoic acid, induced a moderate LORE-dependent $[Ca^{2+}]_{cyt}$ response (Fig. 2D and fig. S7H). Modification of the 3-hydroxyl group of 3-OH-C10:0 (**1**) with a methyl ether (**24**) or acetyl ester (**25**) or substitution with chlorine (**27**) abolished elicitor activity (Fig. 2, D and E, and fig. S7, H and J). The synthetic 3-OH-FAs used here are racemates, but *Pseudomonas* lipopolysaccharide comprises typically (*R*)-3-OH-decanoyl as primary ester-linked acyl chains (*7*) (table S1 and figs. S1 and S2). (*R*)-3-OH-C10:0 (**28**) induced stronger immune signaling than (*S*)-3-OH-C10:0 did (**29**) (Fig. 2F and fig. S8). Collectively, a free 3-hydroxyl group, preferably in the (*R*)-configuration, is critical for LORE-mediated immune sensing. 3-Decanol (**31**) or 1,3-decandiol (**32**) was inactive (Fig. 2G and fig. S9, A and B), indicating that the carboxyl function is also required for activating LORE-mediated immunity. Ester- or amide-linked moieties at the carboxyl group of 3-OH-C10:0 (**26**, **33** to **43**) gradually impaired elicitor activity with increasing hydrophobicity and size, with bulky moieties, such as *tert*-butyl (**35**) or glucosamine (**43**), rendering the 3-OH-C10:0 derivatives inactive (Fig. 2, H to J, and fig. S9, B to E). Thus, mc-3-OH-FAs

[1]Chair of Phytopathology, TUM School of Life Sciences Weihenstephan, Technical University of Munich, 85354 Freising-Weihenstephan, Germany. [2]Chair of Food Chemistry and Molecular Sensory Science, TUM School of Life Sciences Weihenstephan, Technical University of Munich, 85354 Freising-Weihenstephan, Germany. [3]Division of Bioanalytical Chemistry, Priority Area Infections, Research Center Borstel, Leibniz Lung Center, Parkallee 1-40, 23845 Borstel, Germany. [4]Gregor Mendel Institute, Austrian Academy of Sciences, Vienna Biocenter, 1030 Vienna, Austria. [5]Helmholtz Zentrum Muenchen, Department of Environmental Science, Institute of Biochemical Plant Pathology, 85764 Neuherberg, Germany. [6]Department of Microbial Pathogenesis, University of Maryland School of Dentistry, Baltimore, MD 21201, USA. [7]RIBP-EA 4707, SFR Condorcet-FR CNRS 3417, University of Reims Champagne-Ardenne, 51100 Reims, France.
*These authors contributed equally to this work.
†Corresponding author. Email: ranf@wzw.tum.de

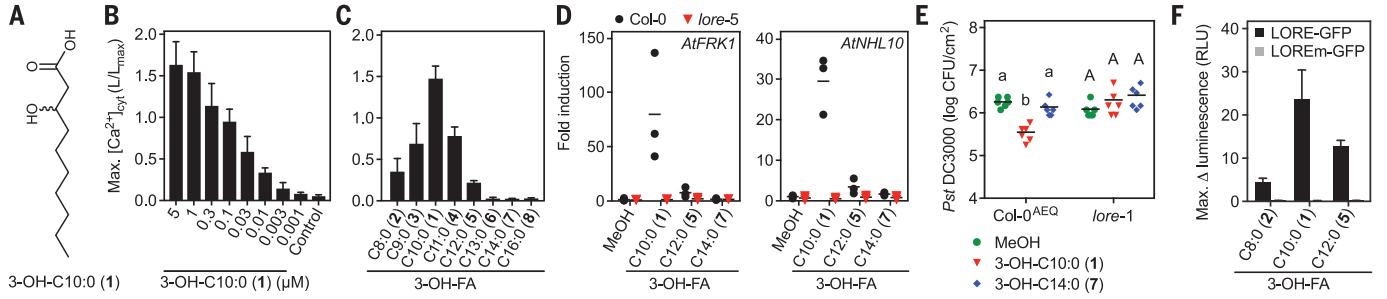

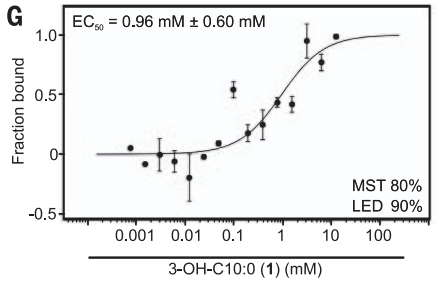

Fig. 1. The 3-OH-FAs trigger LORE-dependent immune responses in a chain length–specific manner. (**A**) Chemical structure of 3-OH-C10:0 (**1**). (**B** and **C**) Maximum (Max.) increases in $[Ca^{2+}]_{cyt}$ in *Arabidopsis* Col-0^{AEQ} seedlings treated with different concentrations of 3-OH-C10:0 (**1**, stock concentration determined by quantitative nuclear magnetic resonance spectroscopy) or (C) 1 μM 3-OH-FAs of various chain length [mean ± SD, n = 12 (B), n = 3 (C)]. Kinetics are shown in fig. S5, A and B. (**D**) Defense gene expression in *Arabidopsis* seedlings 4 hours after elicitation with 3-OH-FAs (1 μM) relative to Col-0 MeOH control. Individual data (symbols) and means (bars) of three experiments are shown. (**E**) *Pst* DC3000 titer 4 days after infection in *Arabidopsis* plants pretreated with 10 μM 3-OH-FAs or MeOH for 3 days before infection. Individual data (symbols) and means (bars) of two experiments are shown (n = 6). Different letters indicate significant differences [one-way analysis of variance (ANOVA) with Tukey's post hoc test applied separately to Col-0^{AEQ} (small letters) and *lore*-1 (capitals), $P < 0.01$]. Similar results occur with 2 days of pretreatment (fig. S5G). CFU, colony-forming units. (**F**) Maximum ROS accumulation in leaf disks from *N. benthamiana* transiently expressing LORE-GFP or kinase-inactive LOREm-GFP elicited with 1 μM 3-OH-FAs (mean ± SE, n = 8). LOREm, kinase-inactive LORE variant (Lys^{516} mutated to Ala); RLU, relative light units. (**G**) Quantification of binding between 3-OH-C10:0 (**1**) and fluorescently His-tag-labeled LORE ectodomain by microscale thermophoresis (MST). Measurements were performed at a light-emitting diode (LED) power of 90% and MST power of 80%. Data points indicate the fraction of labeled LORE ectodomain bound to 3-OH-C10:0 (**1**) (mean ± SE, n = 4). EC_{50}, half-maximal effective concentration. Full figures including controls and additional data with alternatively labeled LORE ectodomain are provided in fig. S6. Experiments were repeated two (F and G), three (B), or four times (C) with similar results.

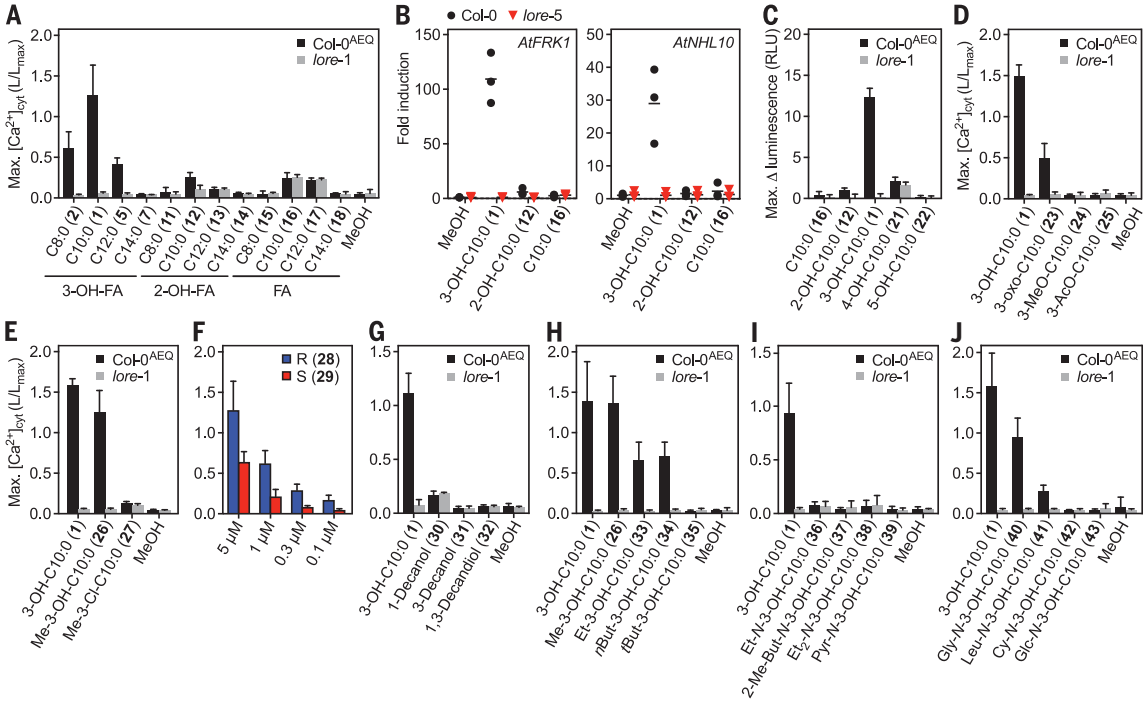

Fig. 2. The 3-OH-FAs in their free form show the strongest elicitor activity in *Arabidopsis*. (**A**) Maximum increases in $[Ca^{2+}]_{cyt}$ in *Arabidopsis* seedlings treated with FAs (5 μM) or MeOH (mean ± SD, n = 6). (**B**) Defense gene expression in *Arabidopsis* seedlings 4 hours after elicitation with FAs (1 μM) relative to Col-0 MeOH control. Individual data (symbols) and means (bars) of three experiments are shown. (**C**) Maximum ROS accumulation in *Arabidopsis* leaf disks treated with the indicated compounds (5 μM; mean ± SE, n = 8). (**D**, **E**, and **G** to **J**) Maximum increases in $[Ca^{2+}]_{cyt}$ in *Arabidopsis* seedlings treated with the indicated compounds (5 μM) or MeOH [mean ± SD, n = 6 (D and G to J), n = 3 (E)]. (**F**) Maximum increases in $[Ca^{2+}]_{cyt}$ in *Arabidopsis* seedlings treated with different concentrations of (*R*)-3-OH-C10:0 (**28**) or (*S*)-3-OH-C10:0 (**29**) (mean ± SD, n = 6). (A, C to J) Kinetics are shown in figs. S7 to S9. Experiments were repeated two (A, C, and G to J), three (D and E), or four times (F) with similar results.

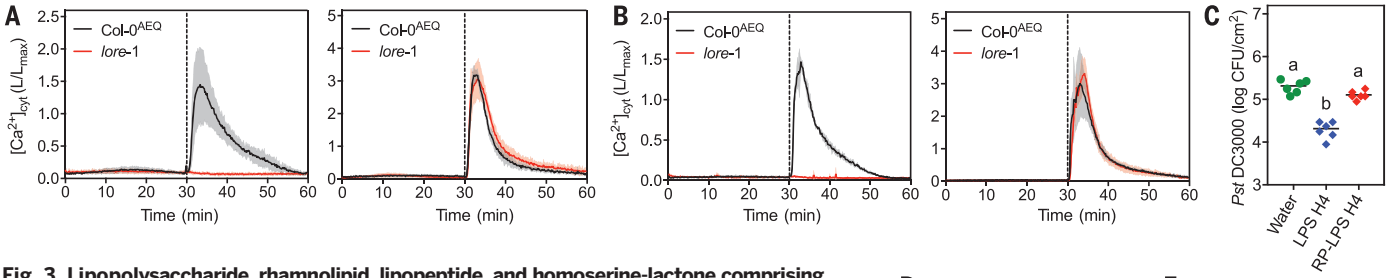

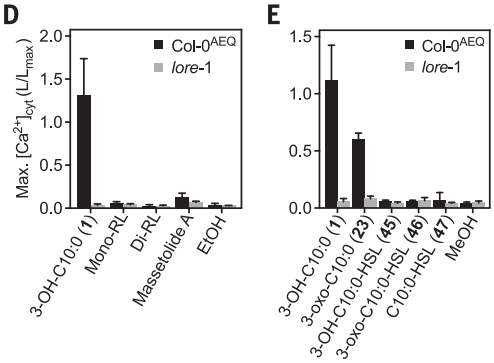

Fig. 3. Lipopolysaccharide, rhamnolipid, lipopeptide, and homoserine-lactone comprising 3-OH-acyl building blocks but devoid of free 3-OH-C10:0 (1) do not activate LORE-mediated immune signaling. (**A** and **B**) $[Ca^{2+}]_{cyt}$ kinetics in *Arabidopsis* seedlings treated with (A) *P. cichorii* S400/S200 lipopolysaccharide (50 μg/ml; repurified by gel permeation chromatography using a desoxycholate-containing buffer (DOC-GPC), pool 3; table S3 and figs. S10 and S11, A to C) or (B) heat-detergent-repurified *P. aeruginosa* H4 lipopolysaccharide (100 μg/ml; table S3 and figs. S10 and S11D). After 30 min, synthetic 3-OH-C10:0 (**1**) (left) or flg22 (right) was added and measurements continued for 30 min (mean ± SD, $n = 3$ each). Full figures including controls and additional repurified lipopolysaccharide pools are provided in figs. S12 and S13, A and B. (**C**) *Pst* DC3000 titer 4 days after infection in *Arabidopsis* plants pretreated with *P. aeruginosa* H4 (25 μg/ml; LPS H4), heat-detergent-repurified *P. aeruginosa* H4 lipopolysaccharide (25 μg/ml; RP-LPS H4; table S3 and fig. S11D), or water for 3 days before infection. Individual data (symbols) and means (bars) of two experiments are shown ($n = 6$). Different letters indicate significant differences (one-way ANOVA with Tukey's post hoc test, $P < 0.01$). (**D** and **E**) Maximum increases in $[Ca^{2+}]_{cyt}$ in *Arabidopsis* seedlings treated with the indicated compounds (5 μM; table S3) or solvent control (mean ± SD, $n = 6$). Kinetics are shown in fig. S14. EtOH, ethanol; HSL, homoserine-lactone; RL, rhamnolipid. Experiments were repeated two (D and E) or three times (A and B) with similar results.

are the minimal motif for LORE-mediated immune activation, with free (*R*)-3-OH-C10:0 (**28**) showing the strongest activity in *Arabidopsis*.

The latter indicates that free mc-3-OH-FAs are sensed by *Arabidopsis* rather than lipid A–bound mc-3-OH-acyl chains. Indeed, unbound 3-OH-C10:0 (**1**) was detected and quantified by means of stable isotope dilution analysis combined with ultrahigh-performance liquid chromatography–mass spectrometry (SIDA-UHPLC-MS/MS) in all lipopolysaccharide and lipid A preparations that activated LORE-dependent immunity (table S3 and fig. S10). As this includes samples from different sources, including commercial suppliers, or isolated by different multistep procedures (table S3), mc-3-OH-FAs appear to copurify with lipopolysaccharide and lipid A. Detergent-based repurification depleted unbound mc-3-OH-FAs from lipopolysaccharide samples (table S3 and figs. S10 and S11). mc-3-OH-FA–depleted lipopolysaccharide samples did not activate immune signaling, whereas typical responses were induced by subsequent application of synthetic 3-OH-C10:0 (**1**) or the peptide MAMP flg22 (*8*) (Fig. 3, A and B, and figs. S12 and S13). mc-3-OH-FA–depleted lipopolysaccharide samples also did not induce systemic resistance to *P. syringae* infection in *Arabidopsis* (Fig. 3C). This hints at a separate source of free, elicitor-active mc-3-OH-FAs in bacteria rather than rapid release of mc-3-OH-FAs from lipopolysaccharide in the plant apoplast.

Several bacterial compounds, such as polyhydroxyalkanoates (*9*), rhamnolipids (*10*), lipopeptides (*11*), and *N*-acyl-homoserine-lactones (*12*), comprise 3-OH-acyl moieties, in *Pseudomonas* commonly 3-OH-decanoyl moieties (*11*, *12*). The 3-OH-decanoyl-comprising rhamnolipids (*13*) or synthetic 3-OH-C10:0- (**45**) and 3-oxo-C10:0-homoserine-lactones (**46**) did not activate LORE-mediated immune signaling in *Arabidopsis* (Fig. 3, D and E, and fig. S14). Massetolide A, a 3-OH-decanoyl-containing lipopeptide (*14*), triggered LORE-independent ROS production and a weak LORE-dependent increase in $[Ca^{2+}]_{cyt}$ (Fig. 3D and fig. S14, A and B), most likely caused by the 3-OH-C10:0 (**1**) contamination detected in this sample (table S3 and fig. S10). Taken together, this suggests that the receptor kinase LORE senses mc-3-OH-FAs in their free form but not 3-OH-decanoyl-comprising bacterial compounds.

Pseudomonas releases free (*R*)-3-OH-C10:0 (**28**) during synthesis of penta-acylated lipid A through PagL-catalyzed (*R*)-3-OH-C10:0 removal from hexa-acylated lipid A in the outer membrane (*15*, *16*). However, lipopolysaccharide preparations from *Pseudomonas* Δ*pagL* mutants still contain free 3-OH-C10:0 (**1**) and activate LORE-mediated immunity (tables S1 and S3 and figs. S3 and S4, F and G), indicating additional sources of free mc-3-OH-FAs in bacteria. Acyl carrier protein (ACP)– and coenzyme A (CoA)–bound mc-3-OH-FAs are intermediates of fatty acid metabolism. Free mc-3-OH-FAs may be released from ACP and CoA precursors through thioesterase activities (*17*) or nonenzymatically upon cell lysis in bacteria as well as in plants. In crucifers, mc-3-OH-FAs released upon tissue damage could function as DAMPs. Outer membrane vesicles, constantly released by bacteria (*18*), may deliver membrane-located or intracellular mc-3-OH-FAs. Firmicutes (*19*), honey bees (*20*), and leafcutter ants (*21*) also produce free mc-3-OH-FAs. Thus, mc-3-OH-FAs could be delivered through multiple metabolic sources. We propose that plants evolved to sense a ubiquitous low-complexity metabolite instead of different, complex microbial end products.

Humans, animals, and fungi sense metabolites, including various hydroxy fatty acids, through G protein–coupled receptors (*22*–*24*). The proinflammatory receptor GPR84 expressed in leukocytes senses mc-FAs and their 2- or 3-hydroxylated forms (*22*, *25*). GPR84 may sense mc-FAs and mc-2/3-OH-FAs of pathogenic or commensal bacteria in addition to endogenous metabolites. Therefore, our finding that lipopolysaccharide, rhamnolipid, and lipopeptide preparations from certain bacterial species may contain free mc-3-OH-FAs (table S3) is relevant to immune studies in humans and mammals, as complete removal of highly elicitor-active compounds from such biological samples is difficult (*26*, *27*). In conclusion, both plants and animals may monitor their microbial environments by sensing low-complexity microbial metabolites through cell-surface receptors (*22*, *23*, *28*).

REFERENCES AND NOTES

1. S. Ranf, *Curr. Opin. Plant Biol.* **38**, 68–77 (2017).
2. C. Alexander, E. T. Rietschel, *J. Endotoxin Res.* **7**, 167–202 (2001).
3. K. J. Kieser, J. C. Kagan, *Nat. Rev. Immunol.* **17**, 376–390 (2017).
4. S. Ranf, *PLOS Pathog.* **12**, e1005596 (2016).
5. S. Ranf *et al.*, *Nat. Immunol.* **16**, 426–433 (2015).
6. T. E. Mishina, J. Zeier, *Plant J.* **50**, 500–513 (2007).
7. U. Zähringer, B. Lindner, E. T. Rietschel, *Adv. Carbohydr. Chem. Biochem.* **50**, 211–276 (1994).
8. G. Felix, J. D. Duran, S. Volko, T. Boller, *Plant J.* **18**, 265–276 (1999).
9. R. A. Verlinden, D. J. Hill, M. A. Kenward, C. D. Williams, I. Radecka, *J. Appl. Microbiol.* **102**, 1437–1449 (2007).
10. A. M. Abdel-Mawgoud, F. Lépine, E. Déziel, *Appl. Microbiol. Biotechnol.* **86**, 1323–1336 (2010).
11. J. M. Raaijmakers, I. de Bruijn, M. J. D. de Kock, *Mol. Plant Microbe Interact.* **19**, 699–710 (2006).
12. J. M. Raaijmakers, I. de Bruijn, O. Nybroe, M. Ongena, *FEMS Microbiol. Rev.* **34**, 1037–1062 (2010).
13. A.-L. Varnier *et al.*, *Plant Cell Environ.* **32**, 178–193 (2009).

14. J. T. de Souza, M. de Boer, P. de Waard, T. A. van Beek, J. M. Raaijmakers, *Appl. Environ. Microbiol.* **69**, 7161–7172 (2003).
15. R. K. Ernst *et al.*, *J. Bacteriol.* **188**, 191–201 (2006).
16. J. Geurtsen, L. Steeghs, J. T. Hove, P. van der Ley, J. Tommassen, *J. Biol. Chem.* **280**, 8248–8259 (2005).
17. Z. Zheng *et al.*, *Appl. Environ. Microbiol.* **70**, 3807–3813 (2004).
18. L. Katsir, O. Bahar, *PLOS Pathog.* **13**, e1006306 (2017).
19. J. Sjögren, J. Magnusson, A. Broberg, J. Schnürer, L. Kenne, *Appl. Environ. Microbiol.* **69**, 7554–7557 (2003).
20. N. Weaver, N. C. Johnston, R. Benjamin, J. H. Law, *Lipids* **3**, 535–538 (1968).
21. H. Schildknecht, K. Koob, *Angew. Chem. Int. Ed. Engl.* **10**, 124–125 (1971).
22. C. C. Blad, C. Tang, S. Offermanns, *Nat. Rev. Drug Discov.* **11**, 603–619 (2012).
23. C. D. Hanlon, D. J. Andrew, *J. Cell Sci.* **128**, 3533–3542 (2015).
24. C. Braunsdorf, D. Mailänder-Sánchez, M. Schaller, *Cell. Microbiol.* **18**, 1188–1200 (2016).
25. M. Suzuki *et al.*, *J. Biol. Chem.* **288**, 10684–10691 (2013).
26. M. Hirschfeld, Y. Ma, J. H. Weis, S. N. Vogel, J. J. Weis, *J. Immunol.* **165**, 618–622 (2000).
27. S. Ranf, D. Scheel, J. Lee, *Mol. Plant Pathol.* **17**, 1165–1169 (2016).
28. F. Boutrot, C. Zipfel, *Annu. Rev. Phytopathol.* **55**, 257–286 (2017).

ACKNOWLEDGMENTS

We thank W. Bitter, B. A. Dmitriev, K. Kawahara, U. Mamat, K. Rudolph, S. N. Senchenkova, C. Galanos, M. Ongena, J. M. Raaijmakers, J. Hubert, J. H. Renault, A. Collmer, M. Knight, and the University of Oxford for providing material. We thank B. Buske, B. Kunz, U. Schombel, M. Wenig, D. Günzkofer, and K. Mühlenkamp for technical assistance and I. Hang (Vienna Biocenter Protein Technologies Facility) for help with protein purification. **Funding:** This work was supported by the German Research Foundation (SFB924/TP-B10 to S.R. and TP-B06 to A.C.V. and Emmy Noether program RA2541/1 to S.R.); grant Rhamnoprot, Région Grand-Est and FEDER (R.S.); Vienna Science and Technology Fund (WWTF) project LS17-047 and grants from the Austrian Academy of Science through the Gregor Mendel Institute (Y.B.). E.S.-L is supported by a Hertha Firnberg Programme postdoctoral fellowship (T-947) from the FWF Austrian Science Fund. **Author contributions:** S.R. initiated and managed the project and designed plant experiments. C.D., C.S., and T.H. designed chemical syntheses and analytics. C.D. and C.S. performed chemical syntheses and analytics. A.K., N.G., T.G., C.E.C., R.K.E., and S.R. prepared lipopolysaccharide. N.G., D.S., C.E.C., and R.K.E. performed structural analysis of lipopolysaccharide and lipid A samples. N.G., A.K., and S.R. designed lipopolysaccharide repurification approaches. R.S. and S.D. initiated rhamnolipid and lipopeptide experiments and prepared rhamnolipid samples. A.C.V., M.S., A.K., and S.R. designed infection experiments. A.C.V., A.K., and M.S. performed infection experiments. A.K. performed and analyzed calcium, ROS, and peroxidase assays. L.R. performed and analyzed MAPK activation and gene expression experiments. E.S.-L., Y.B., and S.R. designed binding assays. E.S.-L. performed protein expression and binding assays. A.K., C.D., C.S., N.G., L.R., A.C.V., E.S.-L., Y.B., and S.R. analyzed the data. S.R. drafted the manuscript. A.K., C.D., N.G., C.S., L.R., T.G., E.S.-L., and A.C.V. contributed methods sections. A.K., C.D., N.G., S.D., Y.B., R.H., T.H., and S.R. contributed ideas, interpreted results, and critically revised the manuscript. All authors discussed the results and approved the manuscript. **Competing interests:** The Technical University of Munich has filed a patent application with inventors A.K., C.D., L.R., M.S, R.H., T.H., and S.R. The authors declare no conflicts of interest in relation to this work. **Data and materials availability:** All data are available in the manuscript or the supplementary material. *A. thaliana* Col-0 expressing pCaMV35S-apoaequorin in the cytosol (Col-0^{AEQ}) can be requested from Marc Knight (Department of Biosciences, Durham University) under a material transfer agreement with Durham University.

SUPPLEMENTARY MATERIALS

www.sciencemag.org/content/364/6436/178/suppl/DC1
Materials and Methods
Figs. S1 to S14
Tables S1 to S3
References (*29–89*)

9 May 2018; resubmitted 2 January 2019
Accepted 12 March 2019
10.1126/science.aau1279

GLACIAL CYCLES

Arc-continent collisions in the tropics set Earth's climate state

Francis A. Macdonald[1]*, Nicholas L. Swanson-Hysell[2], Yuem Park[2], Lorraine Lisiecki[1], Oliver Jagoutz[3]

On multimillion-year time scales, Earth has experienced warm ice-free and cold glacial climates, but it is unknown whether transitions between these background climate states were the result of changes in carbon dioxide sources or sinks. Low-latitude arc-continent collisions are hypothesized to drive cooling by exhuming and eroding mafic and ultramafic rocks in the warm, wet tropics, thereby increasing Earth's potential to sequester carbon through chemical weathering. To better constrain global weatherability through time, the paleogeographic position of all major Phanerozoic arc-continent collisions was reconstructed and compared to the latitudinal distribution of ice sheets. This analysis reveals a strong correlation between the extent of glaciation and arc-continent collisions in the tropics. Earth's climate state is set primarily by global weatherability, which changes with the latitudinal distribution of arc-continent collisions.

Over geological history, Earth's climate has varied between warm ice-free climate states, and cold glacial climate states in which polar continents were covered in ice (*1*, *2*). Through the Phanerozoic Eon [past 540 million years (Ma)], Earth's climate has been predominantly nonglacial (~75%), with relatively brief, ~3- to 60-Ma intervals of glacial climate (*1*, *3*). Similarly, aside from Snowball Earth events, much of the preceding Proterozoic Eon was also characterized by a nonglacial climate state (*3*). Given that a warm, nonglacial climate is the most common climate state for Earth, what processes have caused cooling trends on million-year time scales resulting in glacial climate states, like that observed today?

Earth's climate state is set by the balance between geological sources and sinks of carbon to the ocean-atmosphere system, but their relative importance is uncertain (*4*–*8*). On long time scales, CO_2 is emitted primarily by volcanism and consumed primarily by chemical weathering of silicate rocks, which delivers alkalinity through rivers to the ocean and sequesters carbon via the precipitation of carbonate rocks. Prolonged imbalances between the magnitude of the sources and sinks would catastrophically manifest in either the onset of a Snowball Earth or a runaway greenhouse (*7*). The relative clemency of Phanerozoic climate requires that CO_2 sinks scale with changes in the sources, which can be explained through the silicate weathering feedback where increased CO_2 leads to higher temperatures and invigorated hydrological cycling that enhances chemical weathering and vice versa (*4*). Because of the silicate weathering feedback, a decrease in the CO_2 flux to the atmosphere leads to decreased weathering until a new steady state is achieved at lower CO_2 concentrations in the atmosphere (*4*, *7*). CO_2 levels also vary as a result of changes in global weatherability—the cumulative factors that affect chemical weathering aside from climate (*8*). Global weatherability is the product of variables such as lithology, topography, and paleolatitude (*8*, *9*). An increase in global weatherability also results in cooling as the consumption of carbon through silicate weathering will match that of volcanic input at lower concentrations of atmospheric CO_2.

Present-day global CO_2-consumption estimates emphasize the importance of highly weatherable areas: ~10 to 20% of land area is responsible for ~50 to 75% of CO_2 consumption through silicate weathering (*10*, *11*). These highly weatherable areas, e.g., Southeast Asia, are mainly situated in the warm, wet tropics with substantial topographic relief and are composed of Ca- and Mg-rich mafic and ultramafic rocks, which have faster dissolution rates than felsic rocks (*8*–*12*). In general, basaltic watersheds in the tropical rain belt have about two-orders-of-magnitude higher CO_2-consumption rates than granitic watersheds outside of the tropics (*13*).

In the modern climate, the annual migration of the intertropical convergence zone results in a tropical rain belt within 10° to 20° of the equator (fig. S5). The tropical rain belt is below the ascending branch of the Hadley circulation, which has been confined to low-latitude throughout Earth's history (*14*). Thus, geological data coupled with paleogeographic reconstructions can be used to estimate changes in topography and lithology within the tropical rain belt through time. Notably, as climate warms or cools, the tropics remain relatively warm and wet with high

[1]Department of Earth Science, University of California, Santa Barbara, CA 93106, USA. [2]Department of Earth and Planetary Science, University of California, Berkeley, CA 94720, USA. [3]Department of Earth, Atmospheric, and Planetary Sciences, Massachusetts Institute of Technology, Cambridge, MA 02139, USA.
***Corresponding author. Email: francism@ucsb.edu**

weathering rates such that global weatherability is particularly sensitive to paleogeographic changes in the tropics (*15–17*).

Phanerozoic cooling trends have been previously attributed to a decrease in CO_2 output from volcanism (*6*, *18*), or an increase in global weatherability through mountain building (*2*, *5*, *8*), or the drift of mafic rocks associated with large igneous provinces (LIPs) through the tropics (*15*). Recently, it was proposed that low-latitude arc-continent collisions combine these processes by terminating subduction-related volcanic CO_2 outgassing along the collided segment, while also increasing global weatherability by actively exhuming volcanic arcs in the warm, wet tropics (*19*).

During arc-continent collisions volcanic arcs are obducted onto continents, creating ophiolites, which are preserved along suture zones and mark the position of former oceans. Arcs and ophiolites are composed predominantly of basalt and ultramafic rocks that are Ca- and Mg-rich and effective at consuming CO_2 through silicate weathering (*8–13*, *20*). Ophiolites in collisional belts can extend tens of thousands of kilometers along strike and be progressively exhumed as they are thrust over a continental margin. The combination of high chemical weathering rates in the tropics and the generation of topography during exhumation makes low-latitude arc-continent collisions particularly effective at liberating the large quantities of cations in arcs to the ocean, thereby increasing global weatherability and driving global cooling (*19*).

The process of arc-continent collision in the tropics has been invoked to explain specific cooling episodes during the Ordovician and Late Cretaceous to Oligocene (*19*, *21*), but are intervals of extensive tropical suture length specifically associated with intervals of cool climate? To test this hypothesis, we created a database of Phanerozoic ophiolite-bearing sutures associated with arc-continent collisions that we reconstructed with paleogeographic models (*22*). These geological reconstructions (Fig. 1, fig. S1, and movie S1) provide a framework for analyzing the relationships between the latitudinal distribution of highly weatherable lithologies and Phanerozoic climate change. Particularly, we compare the length of active sutures in the tropics through time with the Phanerozoic record of glaciation (Fig. 2 and fig. S2). Ophiolite obduction along a suture was deemed active from the time of the first evidence of arc exhumation, such as the appearance of ophiolite detritus in the foreland, to the age of the final collision, preferably defined by the cessation of foreland deposition.

Our results show that global active suture zone length varied through the Phanerozoic between 0 and 30,000 km. Peaks in total suture length (between 10,000 and 30,000 km) are associated with major tectonic events such as the Taconic (~465 to 440 Ma), early Uralian (~375 to 358 Ma), Hercynian (~340 to 300 Ma), Central Asian (~250 to 220 Ma), Himalayan (~50 to 0 Ma), and Indonesian (~20 to 0 Ma) orogenies (Fig. 2A). Some of these orogenic events resulted in extensive ophiolite obduction within the tropics (Fig. 2B) as these collisions occurred at low latitude in roughly east-west oriented orogenic belts. Because of their geometry, the Taconic, Hercynian, Himalayan, and Indonesian orogenies had 5000- to 15,000-km-long sutures that were within 15° of the equator. By contrast, the early Uralian and Central Asian orogenies occurred at mid- to high latitudes, with less than 3000-km suture length exposed in the tropics (Fig. 2B).

To characterize Earth's climate state through the Phanerozoic, we use the latitudinal extent of continental ice sheets, which were compiled with updated age constraints (Fig. 2C and table S3). Although extent of glaciation is an imperfect proxy for global climate, Phanerozoic pCO_2 (partial pressure of CO_2) estimates are very uncertain (*23*). Over the Phanerozoic, there have been three major glacial intervals, in the Late Ordovician (~455 to 440 Ma), Permo-Carboniferous (~335 to 280 Ma), and the Cenozoic (~35 to 0 Ma), with a smaller glacial advance in the Late Devonian (~360 Ma). Similarly, the major peaks in the record of suture length in the tropics are in the Late Ordovician, the Permian-Carboniferous, and the Cenozoic (Fig. 2B). Notably, there are no major tropical suture length peaks during extended periods of nonglacial climate (e.g., the Mesozoic; 250 to 65 Ma).

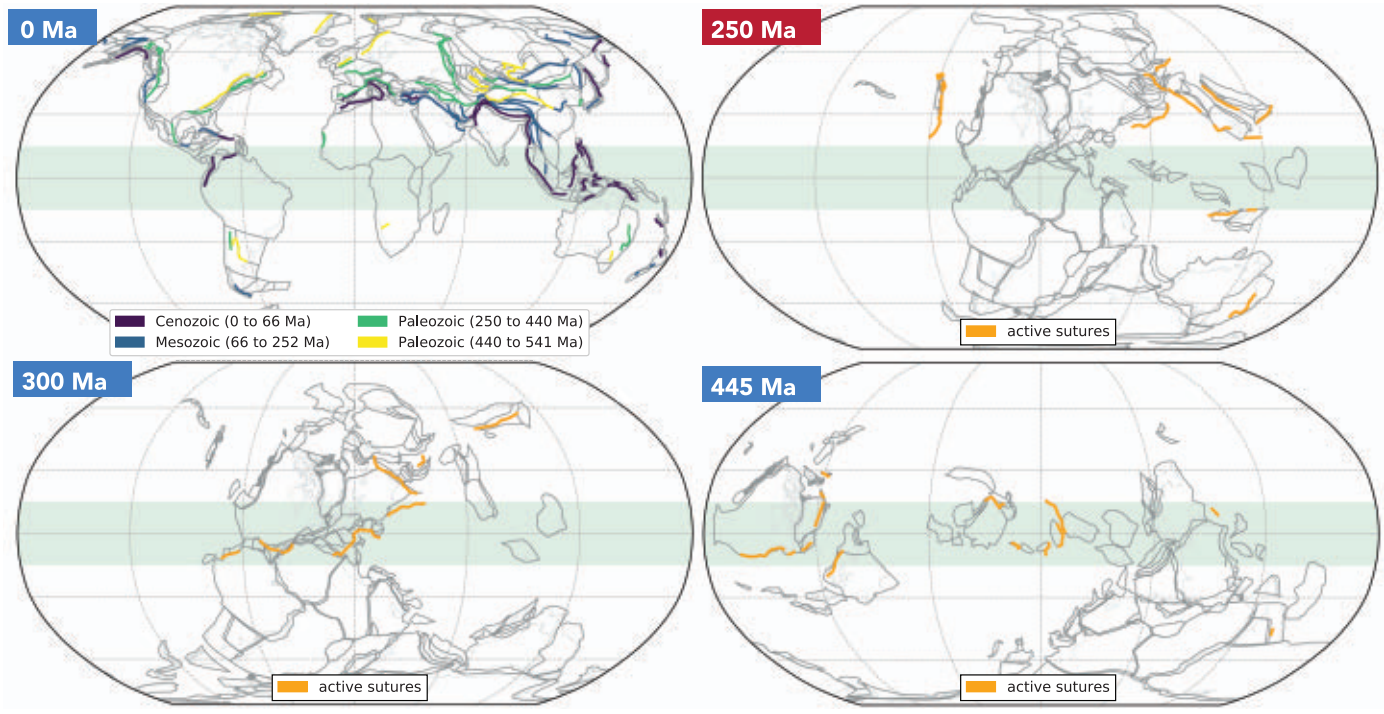

Fig. 1. Reconstructions of ophiolite-bearing sutures. All sutures within the compilation are shown in present-day coordinates in the 0 Ma map and are color-coded by age. The tropical rain belt is shaded green. Continental outlines shown are tectonic units of Torsvik and Cocks (*30*). Paleogeographic reconstructions of these tectonic units and actively exhuming sutures are shown at the times of peaks in total suture length (Fig. 2). The Triassic (250 Ma) peak in total suture length is at a nonglacial interval (red) with minimal suture length in the tropics. The Carboniferous (300 Ma) and Ordovician (445 Ma) peaks are both during glacial intervals (blue) and have extensive suture length in the tropics.

To provide a statistical test of the correlation between arc-continent collisions in the tropics and glaciation, we evaluated whether suture length (*22*) correlates better with the real ice-extent record than with randomly generated synthetic records of ice extent (i.e., simulating the null hypothesis that ice extent is independent of the proposed forcing). Synthetic ice-extent records with 5-Ma resolution were generated by randomly varying the timing of four glacial episodes (Late Ordovician, Late Devonian, Permo-Carboniferous, and Cenozoic) over the past 520 Ma (fig. S6). We also compared the percent of overlap between records, i.e., time steps containing both glaciation and significant suture length (fig. S7). This analysis reveals that ice extent correlates strongly with tropical (r = 0.66 to 0.59) and total (r = 0.57) suture length, with statistical significance relative to the null-hypothesis (p < 0.01), and that ice extent lacks correlation with high-latitude sutures (r = −0.06, p = 0.55) (fig. S8 and table S4). The strongest correlation is between ice extent and sutures <20° of latitude (r = 0.66), where under the null hypothesis, only 0.002% of the random simulations of ice extent correlate as well as the observed data (table S4); results are similar for sutures within 15° of the equator. Correlations were found to be relatively insensitive to age uncertainties when age errors in aggregate suture length were simulated by using a random walk scaled to a maximum of 5 or 10 Ma (fig. S8).

The peaks in suture length within the tropics that correspond with the three major glacial intervals are each ~10,000 km. This is approximately the length of present-day sutures in the tropics in the Indonesian orogenic system, including New Guinea and the Philippines. Currently, this region, which includes two of the three largest ophiolites on Earth (*24*), is estimated to account for ~9 to 14% of the modern global carbon sink (*10*, *11*). We propose that the increasing exhumation of the ophiolite-bearing sutures in Indonesia and New Guinea has been a major factor in Middle Miocene to present cooling by increasing global weatherability.

From the present maximum in suture length in the tropics, there is a local minimum in active sutures at ~25 Ma (Fig. 2B). This minimum broadly coincides with the Late Oligocene to Middle Miocene warm interval. A second Cenozoic peak in suture length in the tropics occurs during the Eocene leading up to the initiation of Antarctic glaciation. The two-pronged cooling trend from the Late Cretaceous to Eocene (*25*) has been attributed to low-latitude arc-continent collision (*19*) and corresponds with local maxima in suture length in the tropics (Fig. 2B).

The Permo-Carboniferous glaciations have classically been related to an increase in carbon storage on land (*26*). Recently, it was proposed that the low-latitude Hercynian orogeny was sufficient to initiate glaciation (*17*). Our data broadly support the latter hypothesis but highlight the importance of a specific phase of mountain building, that is, the exhumation of ophiolites in the tropics. Our results also confirm that Late Ordovician glaciation was coincident with low-latitude arc-continent collision in the Taconic orogeny (*21*), Kazakh terranes, Tarim, and North China (*27*).

Like the Eocene, the Early Ordovician increase in suture length in the tropics precedes glaciation by ~10 Ma. This lag may be due to warm background climate states and low global weatherability during the early Cenozoic and early Paleozoic, such that substantial and prolonged increases in global weatherability were necessary to drive cooling and initiate glaciation. Indeed, oxygen isotope records from both the Eocene and Ordovician demonstrate long-term cooling trends prior to glaciation (*21*, *25*).

The Cenozoic seawater rise in radiogenic Sr and Os isotopes appears inconsistent with our hypothesis, as arcs contain relatively unradiogenic Sr and Os. However, these trends can be attributed to the differential exhumation of Greater and Lesser Himalayan lithologies (*28*). That isotopically distinct source rocks can drive seawater Sr and Os isotope records complicates their use as a global radiogenic to juvenile weathering proxy.

The hypothesis evaluated here, that Earth's climate state is set by the presence or absence of arc-continent collisions in the tropics, is analogous to proposals that have linked the drift of LIPs into the tropics as a driver for Cenozoic (*15*) and Neoproterozoic cooling (*16*). We have performed a similar analysis of the paleolatitude of LIPs through time (figs. S3 and S4), in which we imposed two postemplacement scenarios, one with exponential decay of LIP areas with a 120-Ma

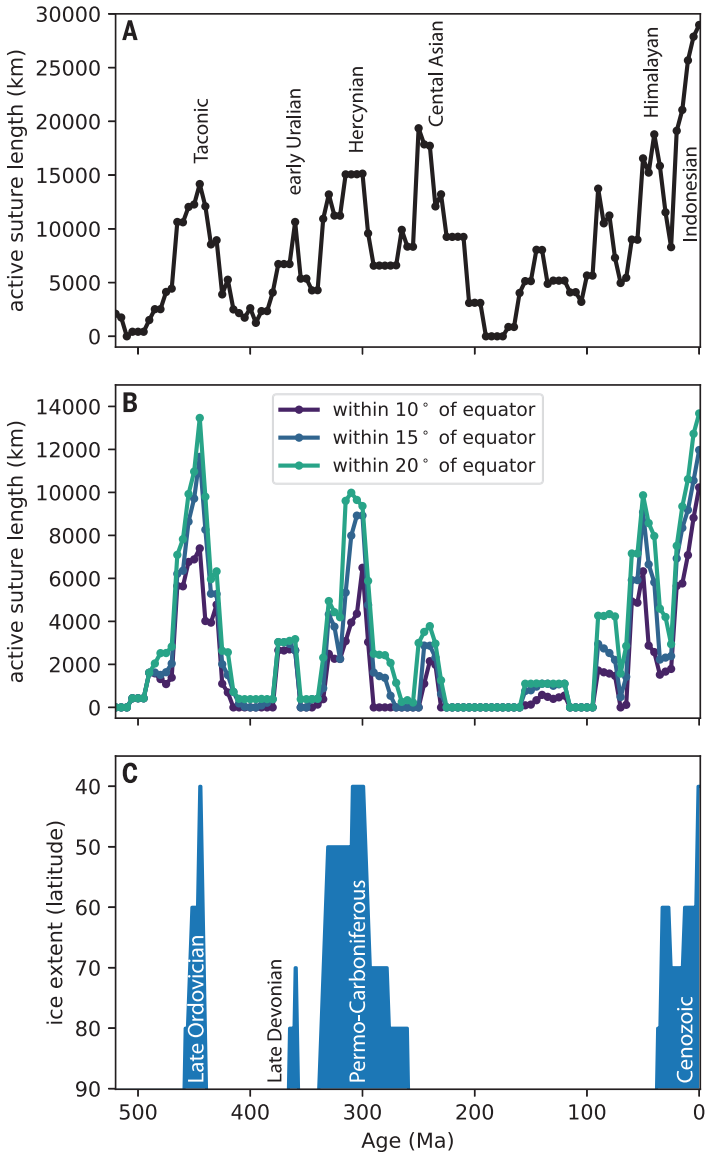

Fig. 2. Phanerozoic suture length in the tropics compared to the latitudinal extent of continental glaciation. (**A**) Total length of active suture length. (**B**) Total length of active sutures that are reconstructed to be within 10°, 15°, and 20° of the equator over the past 520 million years. (**C**) Blue marks the latitudinal extent of continental ice sheets, excluding Alpine glaciers (table S3).

half-life, and a second in which there is also burial of LIPs associated with rifting and subsidence (*22*). In both scenarios, area of total LIPs at all latitudes and LIPs above and below 15° have a weakly negative to zero correlation with ice extent, with the exception of the decay plus burial scenario at <15°, which has a weakly positive correlation coefficient of $r = 0.10$ (fig. S9 and table S4). The lack of a clear relationship between LIP area and climate state (fig. S4) may be due to regolith development and soil shielding in the absence of active exhumation (*10*). By contrast, arc-continent collisions create active topography, limiting the effect of shielding and facilitating high local weathering rates.

Because arc-continent collisions terminate subduction-related volcanism along the collided segment, cooling may also be due to reduced volcanic activity and CO_2 output (*19*). However, the high total suture length related to the Central Asian and the early Uralian orogenies during nonglacial intervals demonstrate that reduction in arc length and volcanic CO_2 output alone are not sufficient to push the global climate into a glacial climate state. These results indicate that changes in chemical weatherability due to low latitude arc-continent collision and associated ophiolite obduction are the primary driver of global cooling trends, and reduction in volcanic CO_2 output is of secondary importance.

Alternatively, it has been proposed that the extent of continental arc-volcanism is responsible for long-term climate change by modulating CO_2 outgassing (*18*, *29*). To quantify the strength of this proposed correlation, Phanerozoic ice extent was compared to a compilation of continental arc length (*29*). A Mesozoic peak and Cenozoic low in continental arc length results in a significantly weaker correlation with arc length ($r = 0.38$) than that for the suture records (<15° $r = 0.64$, <20° $r = 0.66$) (fig. S9 and table S4).

Although we acknowledge that volcanic outgassing must have changed through time and that organic carbon burial also had an impact on long-term climate, our analysis suggests that global weatherability has provided the first-order control on Earth's climate state. Particularly, arc-continent collisions in the tropics, such as the Indonesian orogenic system today, are ephemeral on geological time scales, and when they drift out of the tropics or exhumation ceases and topography is eroded away, Earth returns to a nonglacial climate state. Thus, our model accounts for both the initiation and termination of ice ages. This pattern has repeated at least three times throughout the Phanerozoic—when there have been abundant tracts of ophiolites being exhumed and eroded in the tropics, Earth has been in a glacial climate state, and when not, Earth has been in a nonglacial climate state.

REFERENCES AND NOTES

1. C. E. P. Brooks, *Climate Through the Ages. A Study of the Climate Factors and Their Variations* (Coleman, New York, 1926).
2. T. C. Chamberlin, *J. Geol.* **7**, 545–584 (1899).
3. P. F. Hoffman, *Geol. Today* **25**, 100–107 (2009).
4. J. C. G. Walker, P. B. Hays, J. F. Kasting, *Geophys. Res. Lett.* **86**, 9776–9782 (1981).
5. M. E. Raymo, *Geology* **19**, 344–347 (1991).
6. R. A. Berner, *Am. J. Sci.* **294**, 56–91 (1994).
7. R. A. Berner, K. Caldeira, *Geology* **25**, 955–956 (1997).
8. L. R. Kump, M. A. Arthur, in *Tectonic Uplift and Climate Change* (Springer, 1997), pp. 399–426.
9. J. Gaillardet, B. Dupré, P. Louvat, C. Allegre, *Chem. Geol.* **159**, 3–30 (1999).
10. J. Hartmann, N. Moosdorf, R. Lauerwald, M. Hinderer, A. J. West, *Chem. Geol.* **363**, 145–163 (2014).
11. C. Dessert, B. Dupré, J. Gaillardet, L. M. François, C. J. Allegre, *Chem. Geol.* **202**, 257–273 (2003).
12. K. Lackner, C. Wendt, D. Butt, E. Joyce Jr., D. Sharp, *Energy* **20**, 1153–1170 (1995).
13. C. Dessert *et al*., *Earth Planet. Sci. Lett.* **188**, 459–474 (2001).
14. D. A. Evans, *Nature* **444**, 51–55 (2006).
15. D. V. Kent, G. Muttoni, *Clim. Past* **9**, 525–546 (2013).
16. Y. Goddéris *et al*., *Earth Planet. Sci. Lett.* **211**, 1–12 (2003).
17. Y. Goddéris *et al*., *Nat. Geosci.* **10**, 382–386 (2017).
18. N. R. McKenzie *et al*., *Science* **352**, 444–447 (2016).
19. O. Jagoutz, F. A. Macdonald, L. Royden, *Proc. Natl. Acad. Sci. U.S.A.* **113**, 4935–4940 (2016).
20. H. Schopka, L. Derry, C. Arcilla, *Geochim. Cosmochim. Acta* **75**, 978–1002 (2011).
21. N. L. Swanson-Hysell, F. A. Macdonald, *Geology* **45**, 719–722 (2017).
22. See online supplementary materials.
23. G. L. Foster, D. L. Royer, D. J. Lunt, *Nat. Commun.* **8**, 14845 (2017).
24. C. Monnier, J. Girardeau, R. C. Maury, J. Cotten, *Geology* **23**, 851–854 (1995).
25. B. Cramer, K. Miller, P. Barrett, J. Wright, *J. Geophys. Res. Oceans* **116**, C12023 (2011).
26. R. A. Berner, *Science* **276**, 544–546 (1997).
27. M. Domeier, *Geoscience Frontiers* **9**, 789–862 (2018).
28. C. L. Colleps *et al*., *Geochem. Geophys. Geosyst.* **19**, 257–271 (2018).
29. W. Cao, C.-T. A. Lee, J. S. Lackey, *Earth Planet. Sci. Lett.* **461**, 85–95 (2017).
30. T. H. Torsvik, L. R. M. Cocks, *Earth History and Palaeogeography*. (Cambridge Univ. Press, 2017).

ACKNOWLEDGMENTS

R. Ernst provided GIS shapefiles of original LIP extent used in the analysis. **Funding:** F.A.M., N.L.S.-H., and Y.P. were partially supported by NSF grant EAR-1547434. **Author contributions:** F.A.M. and N.L.S.-H. designed the study. F.A.M. and O.J. constructed the ophiolite database. N.L.S.-H. and Y.P. conducted the paleogeographic analysis and associated calculations. L.E.L. performed the statistical analysis. F.A.M., N.L.S.-H., and O.J. wrote the manuscript with input from Y.P. and L.E.L. **Competing interests:** None declared. **Data and materials availability:** A summary of the suture database is available in table S1 with the ice latitude compilation provided in table S3. The full suture database as well as the code associated with paleogeographic and statistical analysis is available at: https://github.com/Swanson-Hysell-Group/Arc_Continent_Analysis.

SUPPLEMENTARY MATERIALS

www.sciencemag.org/content/364/6436/181/suppl/DC1
Materials and Methods
Figs. S1 to S9
Tables S1 to S4
References (*31*–*218*)
Movie S1

25 September 2018; accepted 26 February 2019
Published online 14 March 2019
10.1126/science.aav5300

HEART REGENERATION

Evidence for hormonal control of heart regenerative capacity during endothermy acquisition

Kentaro Hirose[1,2]*, Alexander Y. Payumo[1,2]*, Stephen Cutie[1,2], Alison Hoang[1,2], Hao Zhang[3], Romain Guyot[4], Dominic Lunn[1,2], Rachel B. Bigley[1,2], Hongyao Yu[5], Jiajia Wang[5], Megan Smith[6], Ellen Gillett[7], Sandra E. Muroy[8], Tobias Schmid[9], Emily Wilson[3], Kenneth A. Field[10], DeeAnn M. Reeder[10], Malcom Maden[11], Michael M. Yartsev[9], Michael J. Wolfgang[12], Frank Grützner[7], Thomas S. Scanlan[13], Luke I. Szweda[14], Rochelle Buffenstein[6], Guang Hu[5], Frederic Flamant[4], Jeffrey E. Olgin[1,3], Guo N. Huang[1,2]†

Tissue regenerative potential displays striking divergence across phylogeny and ontogeny, but the underlying mechanisms remain enigmatic. Loss of mammalian cardiac regenerative potential correlates with cardiomyocyte cell-cycle arrest and polyploidization as well as the development of postnatal endothermy. We reveal that diploid cardiomyocyte abundance across 41 species conforms to Kleiber's law—the ¾-power law scaling of metabolism with bodyweight—and inversely correlates with standard metabolic rate, body temperature, and serum thyroxine level. Inactivation of thyroid hormone signaling reduces mouse cardiomyocyte polyploidization, delays cell-cycle exit, and retains cardiac regenerative potential in adults. Conversely, exogenous thyroid hormones inhibit zebrafish heart regeneration. Thus, our findings suggest that loss of heart regenerative capacity in adult mammals is triggered by increasing thyroid hormones and may be a trade-off for the acquisition of endothermy.

In adult zebrafish and neonatal mice, heart regeneration occurs primarily through proliferation of preexisting cardiomyocytes (*1*, *2*). Most mammalian cardiomyocytes undergo polyploidization and permanently withdraw from the cell-cycle postnatally, whereas lower vertebrates, such as newts and zebrafish, generally maintain >95% diploid mononucleated cardiomyocytes even as adults (*1*, *2*). Recent studies in both mice and zebrafish further substantiate the positive correlation between diploid mononucleated cardiomyocyte abundance and heart

regenerative capacity (*3*, *4*). We therefore exploited cardiomyocyte ploidy as a proxy for heart regenerative potential and analyzed its variability across vertebrate species (Fig. 1A and tables S1 and S2).

Our phylogenetic analysis confirmed that cardiomyocytes from adult fish, amphibians, and reptiles are mostly (98.3 to 77.1%) mononucleated and diploid (Fig. 1B), which is consistent with their high proliferative and regenerative capacities (fig. S1) (*5*, *6*). Certain monotreme, edentate, cetacean, and chiropteran species retained high percentages of mononucleated diploid cardiomyocytes in the adult heart. In particular, the short-beaked echidna (*Tachyglossus aculeatus*), platypus (*Ornithorhynchus anatinus*), lesser anteater (*Tamandua tetradactyla*), bowhead whale (*Balaena mysticetus*), little brown bat (*Myotis lucifugus*), and Egyptian fruit bat (*Rousettus aegyptiacus*) possessed 59.3 to 34.1% diploid cardiomyocytes as compared with 9.4% observed in mice (Fig. 1B, fig. S2, and table S2).

Diploid cardiomyocyte abundance did not significantly correlate with bodyweight, heart rate, or blood pressure (fig. S3A and table S3). However, it displayed a robust inverse correlation with standard metabolic rate (Fig. 2A and fig. S3B). According to Kleiber's law (*7*), basal metabolic rate (MR) scales with body mass (M) as $MR = MR_0M^{0.75}$, in which MR_0 is the standard metabolic rate. Ectothermic animals have a distinct MR_0 value from that of endothermic animals: The average value of MR_0 is 0.21 W kg$^{-0.75}$ for fish, amphibians, and reptiles (*8*), an order of magnitude less than that observed in endothermic eutherians (3.35 W kg$^{-0.75}$) (*9*). The change of cardiomyocyte ploidy in vertebrates seemingly occurred in parallel with the major metabolic transition from ectotherms to endotherms (Fig. 2A).

[1]Cardiovascular Research Institute and Department of Physiology, University of California, San Francisco, San Francisco, CA 94158, USA. [2]Eli and Edythe Broad Center for Regeneration Medicine and Stem Cell Research, University of California, San Francisco, San Francisco, CA 94158, USA. [3]Department of Medicine, Division of Cardiology, University of California San Francisco, San Francisco, CA 94158, USA. [4]Department of Internal Medicine, Institut de Génomique Fonctionnelle de Lyon, Institut National de la Recherche Agronomique, Université Lyon 1, CNRS, École Normale Superieure de Lyon, 69 007 France. [5]Epigenetics and Stem Cell Biology Laboratory, National Institute of Environmental Health Sciences, Research Triangle Park, NC 27709, USA. [6]Calico Life Sciences, 1170 Veterans Boulevard, South San Francisco, CA 94080, USA. [7]School of Biological Sciences, University of Adelaide, South Australia, Adelaide 5005, Australia. [8]Department of Molecular and Cell Biology, University of California, Berkeley, Berkeley, CA 94708, USA. [9]Helen Wills Neuroscience Institute and Department of Bioengineering, University of California, Berkeley, Berkeley, CA 94708, USA. [10]Department of Biology, Bucknell University, Lewisburg, PA 17837, USA. [11]Department of Biology and UF Genetics Institute, University of Florida, Gainesville, FL 32611, USA. [12]Department of Biological Chemistry, Johns Hopkins University School of Medicine, Baltimore, MD 21205, USA. [13]Department of Physiology and Pharmacology, Oregon Health & Science University, 3181 SW Sam Jackson Park Road, Portland, OR 97239, USA. [14]Division of Cardiology, University of Texas Southwestern Medical Center, Dallas, TX 75390-8573, USA.
*These authors contributed equally to this work.
†Corresponding author. Email: guo.huang@ucsf.edu

In addition to mass, another key determinant of metabolic rate is temperature. Standard metabolic rate MR_0 is proportional to biochemical reaction rates and therefore varies with temperature as $MR_0 \sim e^{-E/kT}$, where E represents the average activation energy for the reactions, k is the Boltzmann constant, and T is the absolute temperature (*10*). Data collected from microbes, plants, and animals confirm a universal inverse relationship between MR_0 and $e^{-1000/T}$ (*10*). We evaluated cardiomyocyte nucleation as a function of $e^{-1000/T}$—particularly among mammalian species, for which T is stable throughout most of their lives—and found a strong inverse correlation (fig. S3C). In mammals, T is a simple function of body temperature (T_b) as $T = T_b + 273$. In the physiological range of mammalian T_b (30 to 39°C), $e^{-1000/T}$ displays a

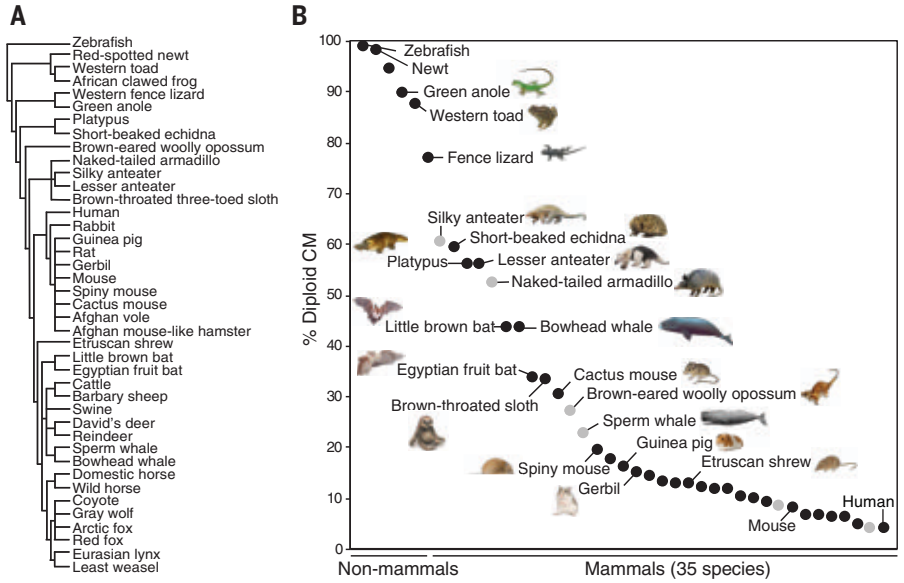

Fig. 1. Phylogenetic analysis of vertebrate cardiomyocyte (CM) nucleation and ploidy. (**A**) Cladogram of species examined here. (**B**) Percentages of mononucleated diploid CMs. Each dot represents the value from the adult heart(s) of one species. Black, multiple samples were quantified; gray, only a single specimen was collected and analyzed. The data are listed from left to right according to the value of diploid CMs. Each new species analyzed in the current study is marked with an animal symbol next to it. Unlabeled dots represent species with previously reported CM ploidy values. All data are presented in table S2. Mammalian species with >30% mononucleated (diploid) CMs are first identified in this study.

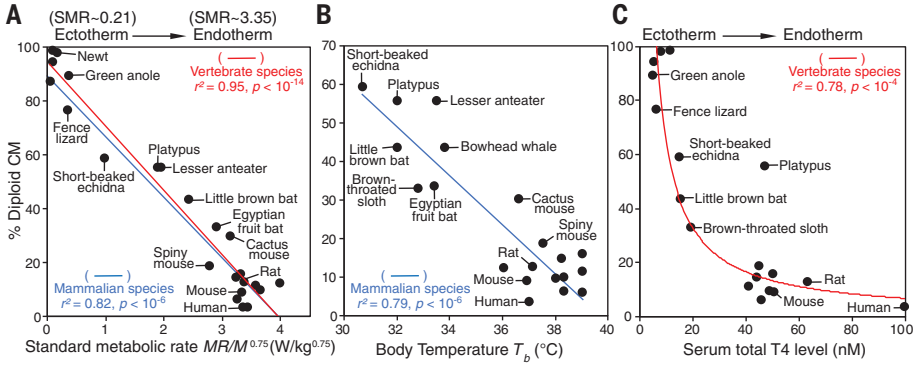

Fig. 2. The percentage of diploid CM inversely correlates with standard metabolic rate, body temperature, and plasma total T_4 levels. (**A**) Effect of standard metabolic rate (SMR, in W/kg$^{0.75}$) on the content of diploid CMs. SMR is defined as $MR/M^{0.75}$ (MR, metabolic rate; M, body mass). The data are fit by regression lines (red for vertebrate species and blue for mammalian species). (**B**) Effect of body temperature (T_b, in degrees celsius) on the percentage of diploid CMs. (**C**) Effect of plasma T_4 levels on the frequency of diploid CMs. In (A) to (C), analyses include all species that have published physiological data to our knowledge. r^2 denotes the coefficient of determination. For visual clarity, only a subset of ectodermic and endothermic species are labeled. All data are presented in tables S2 to S4.

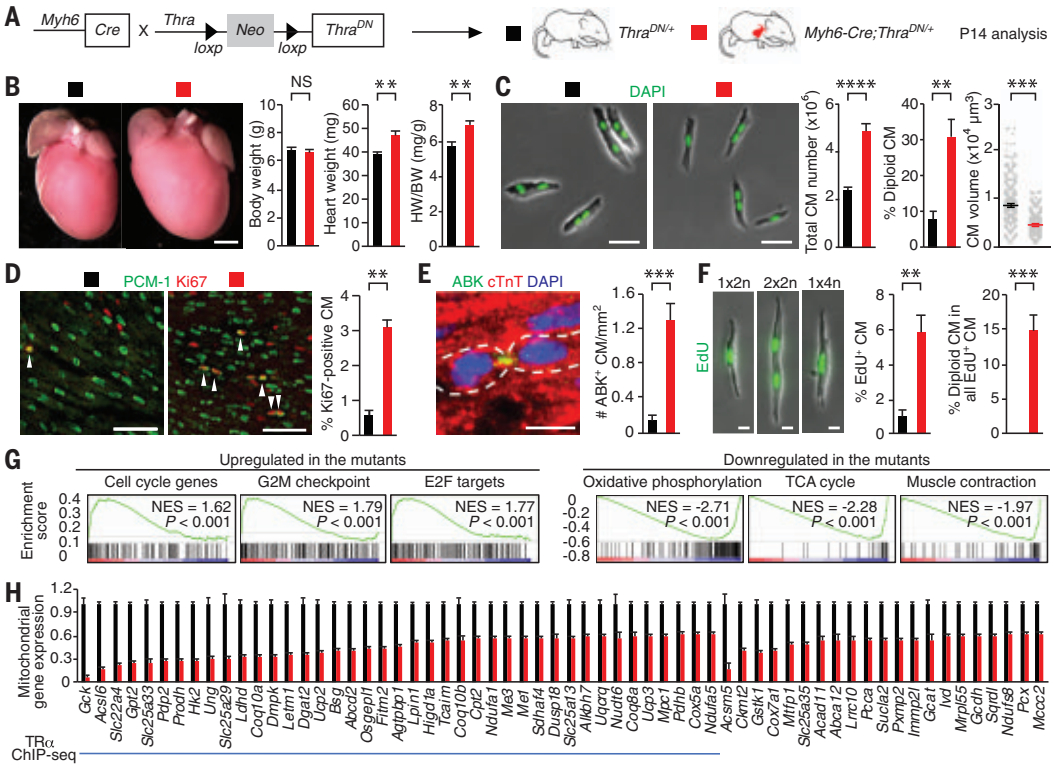

Fig. 3. CM-specific inactivation thyroid hormone receptor enhances CM proliferation in neonatal mice. (**A**) Schematic for generating *Myh6-Cre;Thra*$^{DN/+}$ mice with CM-restricted expression of a dominant negative (DN) TRα and analyzing phenotypes at P14. (**B**) Measurement of the bodyweight (BW) and heart weight (HW) (n = 4 mice). (**C**) Ventricular CM number, ploidy, and size analysis (n = 3 to 7 mice). (**D** to **F**) CM proliferative activity analysis. Representative images and quantifications of (D) proliferating CMs that stained positive for Ki67, (E) Aurora B kinase (ABK) localization at the cleavage furrow, and (F) EdU (n = 4 animals). Arrowheads indicate proliferating CM. In (E), cardiomyocytes undergoing cytokinesis are outlined. In (F), EdU was analyzed in dissociated CMs at P14 from mice injected with EdU at P12 and P13. 1x2n, 2x2n, and 1x4n denote CMs with one diploid nucleus, two diploid nuclei, and one tetraploid nucleus, respectively. (**G**) Expression profiling. Gene set enrichment analysis of up-regulated and down-regulated pathways in the mutant heart based on the RNA-seq analysis. (**H**) RNA-seq and ChIP-seq analysis. Mitochondrial genes whose expression is significantly down-regulated in the mutant hearts are shown (n = 3 hearts). The blue line marks mitochondrial genes directly targeted by TRα. Values are reported as mean ± SEM. NS, not significant. **P < 0.01, ***P < 0.001, ****P < 0.0001. Scale bars, (B) 1 mm; (C) 50 μm; (D) 100 μm; (E) and (F) 20 μm.

linear relationship with T (fig. S3D). Indeed, when we plotted mammalian diploid cardiomyocyte percentages against their respective body temperatures, a linear relationship was observed (Fig. 2B and figs. S3E and S4).

As the major regulators of energy metabolism and thermogenesis (fig. S5) (*11*), thyroid hormones are hypothesized to drive the ectotherm-to-endotherm transition (*12*). We analyzed the relationship between previously reported thyroid hormone levels on cardiomyocyte nucleation and uncovered an inverse correlation between plasma thyroxine (T_4) levels and diploid cardiomyocyte content (Fig. 2C and table S4). Altogether, our analyses implicate that animals with lower standard metabolic rates, body temperatures, and serum T_4 levels may have more abundant diploid cardiomyocytes.

The level of circulating thyroid hormones rises >50-fold in newborn mice shortly after birth (fig. S6A) (*13*), which coincides with cardiomyocyte cell-cycle exit, binucleation, and loss of regenerative capacity (*1*). The physiological role of thyroid hormones in cardiomyocyte proliferation has not been established. Thyroid hormones have been reported to either inhibit (*14*, *15*), enhance (*16*), or have no effect on (*17*) cardiomyocyte proliferation. We found no effect of exogenous triiodothyronine (T_3) on cardiomyocyte proliferation in vitro (fig. S6B). In addition, thyroid hormones were recently proposed to promote a burst of mouse cardiomyocyte division at postnatal day 15 (P15) (*18*); however, others have found no evidence of cardiomyocyte expansion at this stage (*19*, *20*).

To determine the role of thyroid hormones in the regulation of cardiomyocyte proliferation in vivo, we injected mice daily with NH3, a specific inhibitor of thyroid hormone receptors (fig. S7A) (*21*). Cardiomyocytes were identified by means of perinuclear staining of pericentriolar material 1 (PCM1) protein, and proliferation was assessed at P14, when cardiomyocyte binucleation and cell-cycle arrest are largely completed (*1*). Our results demonstrate that treatment with NH3 enhanced myocyte proliferation by approximately fourfold (fig. S7, B to D), whereas chemical inhibition of other pathways documented to change during the perinatal window did not significantly affect cardiomyocyte proliferation in our assay (fig. S7B and table S5). We further validated the role of thyroid hormone signaling in promoting myocyte postnatal cell-cycle exit by blocking thyroid hormone synthesis with propylthiouracil (PTU) and analyzing mutant mice with global expression of dominant negative (DN) thyroid hormone receptor–α (TRα) (fig. S8) (*22*). Both conditions similarly resulted in approximately threefold increases in proliferating and diploid cardiomyocytes.

We next generated mutant mice with cardiomyocyte-specific expression of dominant negative TRα (*Myh6-Cre;Thra*$^{DN/+}$) (Fig. 3A). Despite a normal bodyweight at P14, the heart weight of *Myh6-Cre;Thra*$^{DN/+}$ mice increased by 21% (Fig. 3B and fig. S9B). We also observed a ~2.3-fold increase in total cardiomyocyte numbers as estimated with dissociation (Fig. 3C) and stereological approaches (fig. S9D), retention of ~30% diploid cardiomyocytes (Fig. 3C), and a 47% reduction in myocyte size in mutant hearts (Fig. 3C and fig. S9C). Furthermore, increased numbers of mutant cardiomyocytes expressed proliferation markers Ki67 (3.5-fold), phospho-histone 3 ser10 (pHH3) (twofold), and cleavage furrow-localized Aurora B kinase (8.8-fold) (Fig. 3, D and E, and fig. S9E). Furthermore, EdU incorporation assays from P12 through P14 revealed that thyroid hormone mutants possessed increased numbers of EdU-positive diploid cardiomyocytes, whereas in control mice, all EdU-positive cardiomyocytes were polyploid (Fig. 3F and fig. S9F). Furthermore, we generated *Myh6-merCremer;Thra*$^{DN/+}$ mice and induced DN-TRα expression around the perinatal window (fig. S10). Increased prevalence of diploid proliferative cardiomyocytes was also observed in these mutants (fig. S10). Taken together, these data demonstrate that perinatal thyroid hormone signaling has an

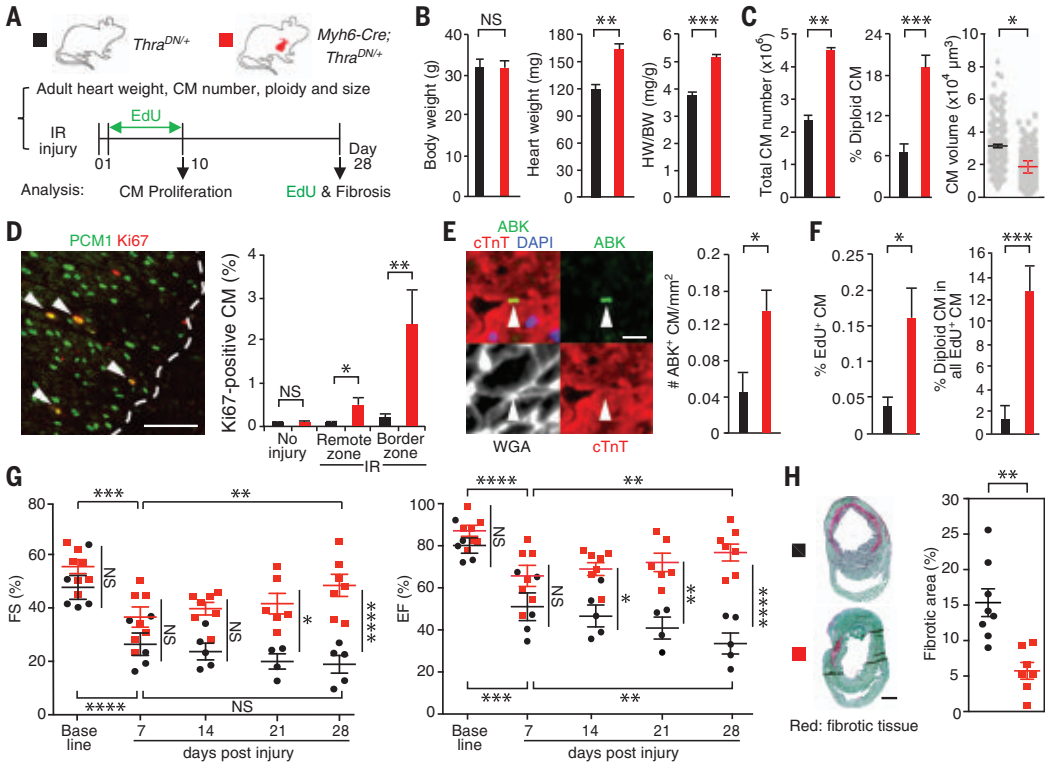

Fig. 4. CMs deficient in thyroid hormone signaling retain significant regenerative potential in adult mice. (**A**) Schematic of the experimental plan to analyze adult hearts and assess regenerative response after myocardial ischemia-reperfusion (IR) injury. (**B**) Measurement of the body-weight (BW) and heart weight (HW) (n = 5 mice). (**C**) Analysis of ventricular CM number, ploidy, and cell size in adult mice (n = 3 animals). (**D** and **E**) CM proliferation analysis 10 days after injury. Quantification and representative images of CMs that are stained positive for Ki67 and Aurora B kinase (ABK) localization at the cleavage furrow in the hearts with no injury (n = 3 or 4 animals) or the hearts after IR injury (n = 4 or 5 animals). Dash lines mark the border of injury, whereas arrowheads show proliferating CMs. (**F**) Analysis of the number and ploidy of EdU-incorporated CMs. EdU is injected daily in the first 10 days after injury. Dissociated CMs are analyzed 28 days after IR (n = 4 animals). (**G**) Measurement of cardiac functions by means of echocardiography. The fraction shortening (FS) and ejection faction (EF) data of individual animals are presented (n = 5 to 7 animals). (**H**) Fibrosis analysis 28 days after injury (n = 7 or 8 animals). Values are reported as mean ± SEM. NS, not significant, *P < 0.05, **P < 0.01, ***P < 0.001, ****P < 0.0001. Scale bars, (D) 100 μm; (E) 20 μm; (H) 1 mm.

intrinsic role in cardiomyocyte cell-cycle arrest and polyploidization.

To identify transcripts regulated by thyroid hormone signaling, we next performed RNA sequencing (RNA-seq) analyses of P14 control and *Myh6-Cre;Thra*$^{DN/+}$ hearts. Gene-set enrichment analyses revealed that cell-cycle, E2F target, and G2M checkpoint genes were significantly upregulated (Fig. 3G and fig. S11). In genes downregulated in thyroid hormone mutant hearts, we found an enrichment of components involved in oxidative phosphorylation, citrate (TCA) cycle, and cardiac muscle contraction (Fig. 3G and fig. S11). The expression levels of many mitochondrial genes were reduced (Fig. 3H). To identify TRα direct gene targets, we generated a mouse strain termed *ThraTAG* in which the coding sequence for protein G–tagged TRα1 receptor is knocked into the endogenous *Thra* locus, allowing for Cre-dependent expression. Chromatin immunoprecipitation-sequencing (ChIP-seq) analyses suggest that a majority of down-regulated mitochondrial genes are direct targets of TRα (Fig. 3H and fig. S12). One of these targets is *carnitine palmitoyltransferase 2* (*Cpt2*), which encodes an enzyme essential for β oxidation of long-chain fatty acids in the mitochondria (*23*). Both *Cpt2* mRNA and protein levels were partially (~40%) depleted in the hearts of *Myh6-Cre;Thra*$^{DN/+}$ mice (fig. S13). We further showed that partial depletion of *Cpt2* in *Myh6-Cre;Cpt2*$^{fl/+}$ heterozygous mutant mice resulted in enhanced cardiomyocyte proliferation (fig. S14) without increased heart size, which is in contrast to the severe pathological hypertrophy observed in homozygous mutants (*24*). Thus, our findings suggest that reduction of *Cpt2*, at least in part, contributes to the increased cardiomyocyte proliferation observed in thyroid hormone mutants.

Consistent with reduced expression of many mitochondrial genes, *Myh6-Cre;Thra*$^{DN/+}$ mutant hearts have less mitochondrial DNA, an increased ratio of reduced to oxidized glutathione, and diminished levels of reactive oxygen species (fig. S15). Previous studies have implicated that increasing reactive oxygen species in the postnatal heart, associated with mitochondrial biogenesis, is a major inhibitor of cardiomyocyte proliferation and heart regeneration (*25*, *26*). Thus, our results identify thyroid hormone signaling as an upstream regulator of this pathway.

We next characterized the hearts of adult *Myh6-Cre;Thra*$^{DN/+}$ mutant mice and their regenerative capacity (Fig. 4A). Adult thyroid hormone mutant hearts were 37% larger than controls (Fig. 4B and fig. S16) and contained an increased number (approximately twofold) of cardiomyocytes as shown with both dissociation (Fig. 4C) and stereological methods (fig. S16). Mutant cardiomyocytes are smaller, and ~19% of them remain diploid (Fig. 4C). To assess the cardiac regenerative potential of these adult mutants, we performed cardiac surgery to induce ischemia reperfusion (IR) injury. First, cardiomyocyte viability was assessed, and no significant difference was found between the mutant and control hearts 24 hours after ischemia (fig. S17). Second, cardiomyocyte proliferation was examined 10 days after injury. Mutant mice possess a 3- to 10-fold increase in proliferating cardiomyocytes after cardiac injury (Fig. 4, D and E, and fig. S18). Injection of EdU during the first 10 days after injury revealed a 10-fold increase in EdU-positive diploid cardiomyocytes 28 days after injury, further suggesting that complete cardiomyocyte division is increased in thyroid hormone mutant hearts (Fig. 4F and fig. S18). Third, cardiac functions were evaluated by means of echocardiography, which revealed that mutant mice exhibited significant improvement of systolic functions after injury by 11%, whereas control mice did not (Fig. 4G and fig. S19A). Last, analysis of cardiac fibrosis 1 month after injury revealed a ~62% reduction of scar area in mutant hearts (Fig. 4H and fig. S19B). Taken together, these results show that adult cardiomyocytes with defects in thyroid hormone receptor activation retain significant proliferative and regenerative potential.

Adult zebrafish possess the ability to completely regenerate their hearts (*5*); thus, we investigated how exogenous thyroid hormones could affect zebrafish cardiomyocyte proliferation and regeneration. T_3 treatment resulted

in a 45% reduction in cardiomyocyte proliferation, impaired regeneration accompanied with prominent scars, and a fivefold increase of cardiomyocyte binucleation (fig. S20). These results demonstrate that exogenous thyroid hormones inhibit zebrafish cardiomyocyte proliferation and regeneration after myocardial injury and implicate an evolutionarily conserved function of thyroid hormone in regulating cardiomyocyte proliferation.

Our findings support a model (fig. S21) in which loss of cardiac regenerative capacity is driven by increasing levels of circulating thyroid hormones. This process coincides with the metabolic increase and thermogenesis that occurs during the ectotherm-to-endotherm transition in both phylogeny (Fig. 2) and ontogeny. Newborn mice, like many other mammalian neonates, are poikilothermic at birth and later increase heat production to regulate body temperature (*27*), coinciding with increasing levels of thyroid hormones in circulation. The essential role of thyroid hormones in driving thermogenesis is evident in adult mice devoid of thyroid hormone receptors (*28*) or those treated with thyroid hormone synthesis inhibitor PTU (fig. S22), which have dramatically decreased basal body temperatures compared with those observed in monotremes. Elevated metabolic rate and the evolution of endothermy likely offered early mammals survival advantages as they inhabited a temporally wide nocturnal niche and expanded into regions of colder climates previously unexplored by reptiles. Altogether, our study suggests that loss of mammalian cardiac regenerative potential may be a trade-off for thyroid hormone-dependent acquisition of endothermy during animal development and evolution. It will be of key importance to identify other pathways, in addition to thyroid hormone signaling, regulating the logic of regenerative diversity to further understand why this capacity is lost in adult mammals.

REFERENCES AND NOTES

1. M. Xin, E. N. Olson, R. Bassel-Duby, *Nat. Rev. Mol. Cell Biol.* **14**, 529–541 (2013).
2. G. Matrone, C. S. Tucker, M. A. Denvir, *Cell. Mol. Life Sci.* **74**, 1367–1378 (2017).
3. M. Patterson *et al.*, *Nat. Genet.* **49**, 1346–1353 (2017).
4. J. M. González-Rosa *et al.*, *Dev. Cell* **44**, 433–446.e7 (2018).
5. K. D. Poss, L. G. Wilson, M. T. Keating, *Science* **298**, 2188–2190 (2002).
6. P. P. Rumyantsev, *Growth and Hyperplasia of Cardiac Muscle Cells*, B. M. Carlson, Ed. (Harwood, 1991).
7. M. Kleiber, *Hilgardia* **6**, 315–353 (1932).
8. A. M. Makarieva *et al.*, *Proc. Natl. Acad. Sci. U.S.A.* **105**, 16994–16999 (2008).
9. K. Schmidt-Nielsen, L. Bolis, C. R. Taylor, Eds., *Comparative Physiology: Primitive Mammals* (Cambridge Univ. Press, 1980).
10. J. F. Gillooly, J. H. Brown, G. B. West, V. M. Savage, E. L. Charnov, *Science* **293**, 2248–2251 (2001).
11. A. J. Hulbert, *Biol. Rev. Camb. Philos. Soc.* **75**, 519–631 (2000).
12. A. G. Little, F. Seebacher, *J. Exp. Biol.* **217**, 1642–1648 (2014).
13. S. Friedrichsen *et al.*, *Endocrinology* **144**, 777–784 (2003).
14. N. N. Chattergoon, G. D. Giraud, K. L. Thornburg, *J. Endocrinol.* **192**, R1–R8 (2007).
15. X. Yang *et al.*, *J. Mol. Cell. Cardiol.* **72**, 296–304 (2014).
16. J. L. Segar, K. A. Volk, M. H. Lipman, T. D. Scholz, *Exp. Physiol.* **98**, 722–733 (2013).
17. A. C. Svensson Holm, I. Lindgren, H. Osterman, J. Altimiras, *Physiol. Rep.* **2**, e12182 (2014).
18. N. Naqvi *et al.*, *Cell* **157**, 795–807 (2014).
19. M. H. Soonpaa *et al.*, *Cell* **163**, 781–782 (2015).
20. K. Alkass *et al.*, *Cell* **163**, 1026–1036 (2015).
21. N. H. Nguyen *et al.*, *J. Med. Chem.* **45**, 3310–3320 (2002).
22. L. Quignodon, S. Vincent, H. Winter, J. Samarut, F. Flamant, *Mol. Endocrinol.* **21**, 2350–2360 (2007).
23. S. M. Ceccarelli, O. Chomienne, M. Gubler, A. Arduini, *J. Med. Chem.* **54**, 3109–3152 (2011).
24. A. S. Pereyra *et al.*, *J. Biol. Chem.* **292**, 18443–18456 (2017).
25. B. N. Puente *et al.*, *Cell* **157**, 565–579 (2014).
26. G. Tao *et al.*, *Nature* **534**, 119–123 (2016).
27. K. Lagerspetz, *Helgol. Wiss. Meeresunters.* **14**, 559–571 (1966).
28. K. Gauthier *et al.*, *Mol. Cell. Biol.* **21**, 4748–4760 (2001).

ACKNOWLEDGMENTS

We thank D. Julius, B. Black, and J. Chen for discussions and suggestions. We also thank Huang laboratory members for data analyses; C. White for the contribution of the original concept and initial nucleation analyses; B. Gillet and S. Hughes of the PSI deep-sequencing facility for their help in ChIP-seq; R. Gibeaux and R. Heald for providing the hearts of African clawed frogs; J. Wilson-Rawls, K. Kusumi, and C. Xu for providing the hearts of green anoles; S. Ray, N. Pak, M. Brecht, S. Erdman, and E. Boyden for providing the hearts of Etruscan shrew; the Museum of Vertebrate Zoology, University of California, Berkeley for various mammalian, reptilian, and amphibian tissues (MVZ:Mamm:155186, MVZ:Mamm:155186, MVZ:Mamm:157801, MVZ:Mamm:190247, MVZ:Mamm:193692, MVZ:Herp:142847, MVZ:Herp:107011, MVZ:Herp:265556, and MVZ:Herp:265557); and the Museum of Southwestern Biology (MSB:Mamm:140338 and MSB:Mamm:211353) and the Museum of the North, University of Alaska for the toad and whale samples (UAM:Mamm:53932, UAM:Mamm:66458, UAM:Mamm:97497, UAM:Mamm:115643, UAM:Herp:14, and UAM:Herp:9). **Funding:** This work is supported by JSPS Overseas Research Fellowships (to K.H.), a UCSF-IRACDA postdoctoral fellowship (to A.P.), a NIGMS IMSD fellowship and Hillblom fellowship (to S.C.), an ARC fellowship (to F.G.), the Agence Nationale de Recherche Thyromut2 program, ANR-15-CE14-0011-01 (to F.F.), Intramural Research Program of the NIH, National Institute of Environmental Health Sciences 1ZIAES102745 (to G. H.), NIH (R01HL13845) Pathway to Independence Award (R00HL114738), Edward Mallinckrodt Jr. Foundation, March of Dimes Basil O'Conner Scholar Award, American Heart Association Beginning Grant-in-Aid, American Federation for Aging Research, Life Sciences Research Foundation, Program for Breakthrough Biomedical Research, UCSF Eli and Edythe Broad Center of Regeneration Medicine and Stem Cell Research Seed Grant, UCSF Academic Senate Committee on Research, REAC Award (Harris Fund), Department of Defense, and Cardiovascular Research Institute (to G.N.H.). **Author contributions:** K.H., A.Y.P, S.C., A.H., H.Z., D.L., R.B.B., H.Y., J.W., E.W., L.I.S., and G.H. performed experiments. K.H, A.Y.P, S.C., A.H., D.L., and G.N.H. analyzed data. R.G., M.S., E.G., S.E.M., T.S., K.A.F., D.M.R., M.M., M.M.Y., M.J.W., F.G., T.S.S., L.I.S., R.B., G.H., F.F., and J.E.O provided reagents and contributed to discussions. K.H., A.Y.P, and G.N.H. designed experiments and wrote the manuscript. **Competing interests:** The authors declare no competing interests. **Data and materials availability:** RNA-seq and ChIP-seq datasets were deposited in the Gene Expression Omnibus (GEO) database under accession nos. GSE125596 and GSE125414, respectively. All other data are available in the manuscript or supplementary materials.

SUPPLEMENTARY MATERIALS

www.sciencemag.org/content/364/6436/184/suppl/DC1
Materials and Methods
Figs. S1 to S22
Tables S1 to S7
References (*29*–*65*)

13 October 2017; resubmitted 15 November 2018
Accepted 21 February 2019
Published online 7 March 2019
10.1126/science.aar2038

SIGNAL TRANSDUCTION

Deubiquitinase USP10 regulates Notch signaling in the endothelium

R. Lim[1]*, T. Sugino[1]*, H. Nolte[2], J. Andrade[1], B. Zimmermann[1], C. Shi[1], A. Doddaballapur[1], Y. T. Ong[1], K. Wilhelm[1], J. W. D. Fasse[1], A. Ernst[3,4], M. Kaulich[3], K. Husnjak[3], T. Boettger[5], S. Guenther[5], T. Braun[5], M. Krüger[2], R. Benedito[6], I. Dikic[3,7], M. Potente[1,8,9]†

Notch signaling is a core patterning module for vascular morphogenesis that codetermines the sprouting behavior of endothelial cells (ECs). Tight quantitative and temporal control of Notch activity is essential for vascular development, yet the details of Notch regulation in ECs are incompletely understood. We found that ubiquitin-specific peptidase 10 (USP10) interacted with the NOTCH1 intracellular domain (NICD1) to slow the ubiquitin-dependent turnover of this short-lived form of the activated NOTCH1 receptor. Accordingly, inactivation of USP10 reduced NICD1 abundance and stability and diminished Notch-induced target gene expression in ECs. In mice, the loss of endothelial *Usp10* increased vessel sprouting and partially restored the patterning defects caused by ectopic expression of NICD1. Thus, USP10 functions as an NICD1 deubiquitinase that fine-tunes endothelial Notch responses during angiogenic sprouting.

To add new vessel sprouts to an existing vascular network, endothelial cells (ECs) specialize into leading tip cells and following stalk cells (*1*), which dynamically interchange positions (*2*). Signaling by the Delta-like 4 (DLL4) ligand and NOTCH1 receptor helps to coordinate these processes. Inhibition of signaling causes excessive sprouting and vessel overgrowth, whereas forced activation leads to vascular rarefaction (*3*–*10*). DLL4 induces the cleavage of NOTCH1 by the γ-secretase protease, which releases the NOTCH1 intracellular domain (NICD1). This fragment forms a ternary complex with the DNA binding protein recombining binding protein suppressor of hairless (RBPJ) and the coactivators mastermind-like proteins 1 to 3 (MAML1

to -3) to drive the transcription of Notch target genes (*11–13*). In many cellular contexts, the half-life of NICD1 is short because NICD1 undergoes rapid proteasomal degradation mediated by ubiquitin ligases, such as SCF^{FBXW7} [the SKP1–CUL1–F-box protein complex (SCF) containing the substrate recognition component F-box– and Trp-Asp (WD) repeat domain–containing protein 7 (FBXW7)] (*14–16*). Inactivation of FBXW7 increases the abundance of NICD1 levels and causes severe defects in vascular sprouting (*17–19*). Having the right amount of NICD1 at the right time is thus critical for the cooperative behavior of ECs.

To identify regulators of NICD1, we examined the NICD1 interactome in human embryonic kidney (HEK) 293T cells by using stable isotope labeling with amino acids in cell culture (SILAC)–based quantitative proteomics (fig. S1A). Liquid chromatography–tandem mass spectrometry (MS/MS) analysis revealed that NICD1 interacted with core components of the Notch transcription complex, including RBPJ and MAML1 (Fig. 1A). Ubiquitin-specific peptidase 10 (USP10), a deubiquitinase that removes ubiquitin modifications from its protein targets, was also among the NICD1-immunoprecipitated proteins (Fig. 1, A and B). To confirm this, we used primary ECs, in which USP10 is an abundant nucleocytoplasmic protein (Fig. 1, C and D, and fig. S1, B to D). We immunoprecipitated NICD1 from cultured human umbilical vein ECs (HUVECs) that expressed a V5 epitope–tagged NICD1 ($NICD1^{V5}$). Immunoblotting for USP10 demonstrated that endogenous USP10 associated with $NICD1^{V5}$, as did the ternary complex factors RBPJ and MAML1 (Fig. 1E). This interaction also occurred when endogenous NICD1 was immunoprecipitated from HUVECs, as demonstrated by a DLL4-inducible NICD1-USP10 protein complex that was enriched in the nuclear fraction (Fig. 1F and fig. S1E). Together, these findings suggest that USP10 interacts with NICD1 in ECs.

To investigate the role of USP10 in endothelial Notch signaling, we performed knockdown experiments in HUVECs by using small interfering RNAs (siRNAs) and assayed Notch signaling with various Notch-responsive luciferase (luc) reporters. Treatment of scrambled control siRNA (siCtrl)–transfected HUVECs with DLL4 induced a γ-secretase inhibitor [dibenzazepine (DBZ)]–sensitive and RBPJ-dependent increase in Notch reporter gene activity (Fig. 2, A and B, and fig. S2B). Depletion of USP10 with USP10 siRNA (si*USP10*) did not affect the baseline activity of the reporters but reduced the DLL4-induced increase in Notch activity (Fig. 2, A and B, and fig. S2, A and B), suggesting that USP10 regulates canonical Notch responses in ECs. These findings were corroborated by a genome-wide transcriptomic analysis of siCtrl- and si*USP10*-transfected HUVECs stimulated with DLL4 or unstimulated for 24 hours, which revealed that depletion of USP10 reduced the expression of canonical Notch target genes, such as *HEY1* [encoding Hes-related family basic helix-loop-helix (BHLH) transcription factor with YRPW (Tyr-Arg-Pro-Trp) motif 1], *HEY2*, *HES1* (encoding Hes family BHLH transcription factor 1), and *NRARP* (encoding Notch-regulated ankyrin repeat protein), as well as other genes that are regulated by DLL4-Notch (*20*) (Fig. 2C and fig. S2C). Quantitative real-time polymerase chain reaction (qRT-PCR) analysis confirmed this finding (fig. S2, D and E).

Loss of USP10 did not lead to compensatory expression changes of other deubiquitinases (fig. S2A), nor did we detect expression changes in core Notch signaling components in unstimulated HUVECs that might explain the reduction in pathway activity (fig. S2F). We surmised that USP10 regulates Notch signaling posttranscriptionally and focused on the short-lived NICD1 protein. Immunoblot analysis showed that the NICD1 protein concentration was low under basal conditions but that the protein became abundant in response to short (6-hour) or prolonged (24-hour) stimulation with DLL4 (Fig. 2D and fig. S3A). Inactivation of USP10 by siRNA or CRISPR-Cas9 gene editing reduced the abundance

[1]Angiogenesis and Metabolism Laboratory, Max Planck Institute for Heart and Lung Research, D-61231 Bad Nauheim, Germany. [2]Institute for Genetics and Excellence Cluster on Cellular Stress Responses in Aging-Associated Diseases (CECAD), University of Cologne, D-50931 Cologne, Germany. [3]Institute of Biochemistry II, Faculty of Medicine, Goethe University, D-60590 Frankfurt am Main, Germany. [4]Fraunhofer Institute for Molecular Biology and Applied Ecology IME, Project Group Translational Medicine and Pharmacology TMP, D-60590 Frankfurt am Main, Germany. [5]Department of Cardiac Development and Remodeling, Max Planck Institute for Heart and Lung Research, D-61231 Bad Nauheim, Germany. [6]Molecular Genetics of Angiogenesis Laboratory, Centro Nacional de Investigaciones Cardiovasculares (CNIC), 28029 Madrid, Spain. [7]Buchmann Institute for Molecular Life Sciences, Goethe University, D-60438 Frankfurt am Main, Germany. [8]DZHK (German Center for Cardiovascular Research), partner site Frankfurt Rhine-Main, D-13347 Berlin, Germany. [9]International Institute of Molecular and Cell Biology, 02-109 Warsaw, Poland.
*These authors contributed equally to this work.
†Corresponding author. Email: michael.potente@mpi-bn.mpg.de

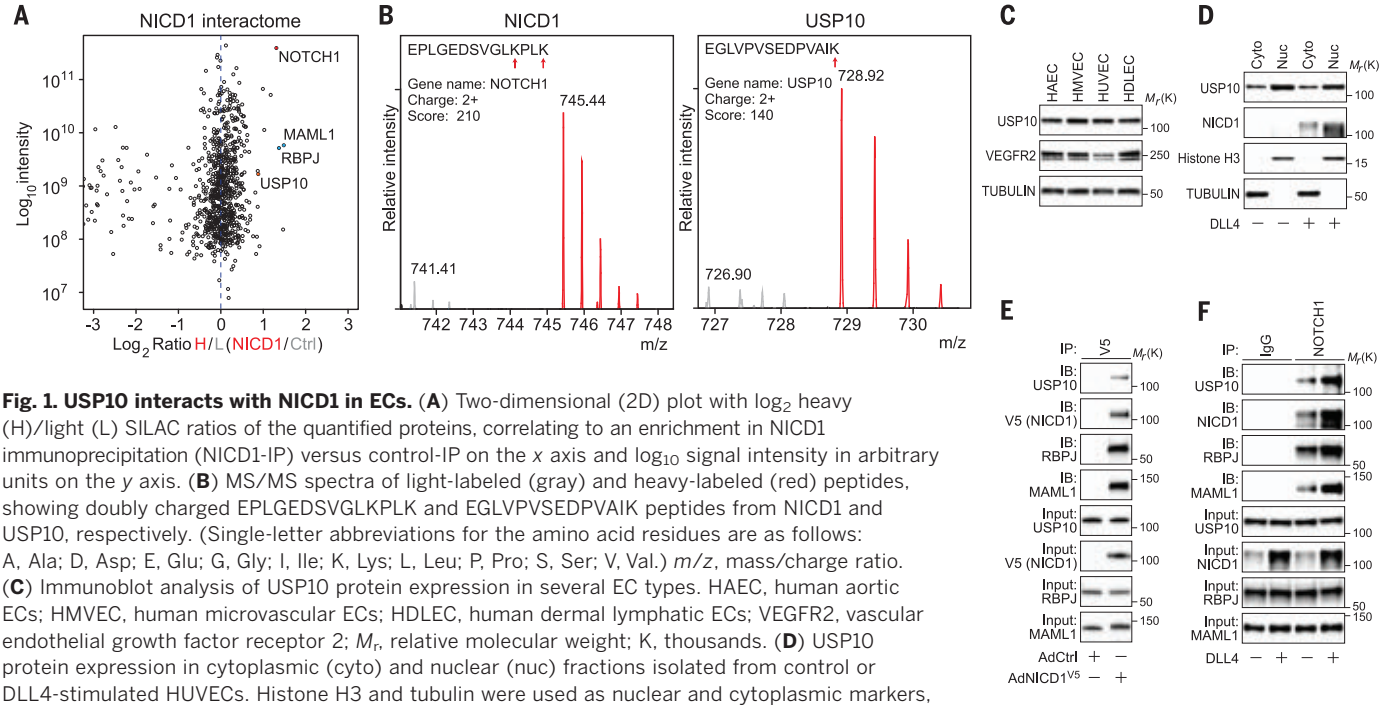

Fig. 1. USP10 interacts with NICD1 in ECs. (**A**) Two-dimensional (2D) plot with log_2 heavy (H)/light (L) SILAC ratios of the quantified proteins, correlating to an enrichment in NICD1 immunoprecipitation (NICD1-IP) versus control-IP on the *x* axis and log_{10} signal intensity in arbitrary units on the *y* axis. (**B**) MS/MS spectra of light-labeled (gray) and heavy-labeled (red) peptides, showing doubly charged EPLGEDSVGLKPLK and EGLVPVSEDPVAIK peptides from NICD1 and USP10, respectively. (Single-letter abbreviations for the amino acid residues are as follows: A, Ala; D, Asp; E, Glu; G, Gly; I, Ile; K, Lys; L, Leu; P, Pro; S, Ser; V, Val.) *m/z*, mass/charge ratio. (**C**) Immunoblot analysis of USP10 protein expression in several EC types. HAEC, human aortic ECs; HMVEC, human microvascular ECs; HDLEC, human dermal lymphatic ECs; VEGFR2, vascular endothelial growth factor receptor 2; M_r, relative molecular weight; K, thousands. (**D**) USP10 protein expression in cytoplasmic (cyto) and nuclear (nuc) fractions isolated from control or DLL4-stimulated HUVECs. Histone H3 and tubulin were used as nuclear and cytoplasmic markers, respectively. (**E**) Coimmunoprecipitation of adenovirus-delivered $NICD1^{V5}$ ($AdNICD1^{V5}$) and endogenous USP10, MAML1, and RBPJ from HUVECs. AdCtrl, control adenovirus; IB, immunoblotting. (**F**) Coimmunoprecipitation of NICD1 and USP10 from HUVECs treated with or without DLL4 for 24 hours. Endogenous NICD1 was immunoprecipitated by anti-NOTCH1 antibody. IgG, immunoglobulin G.

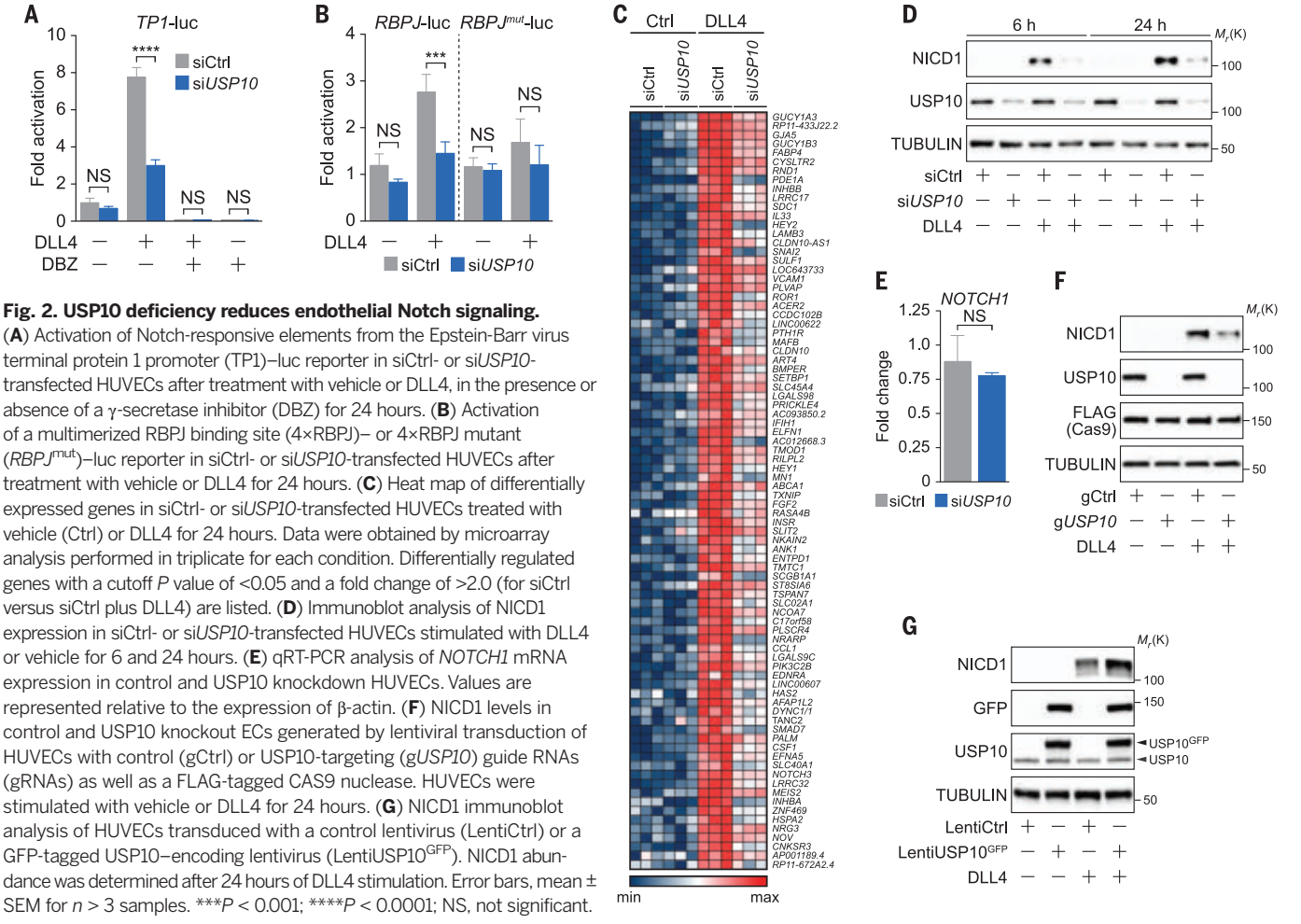

Fig. 2. USP10 deficiency reduces endothelial Notch signaling. (**A**) Activation of Notch-responsive elements from the Epstein-Barr virus terminal protein 1 promoter (TP1)–luc reporter in siCtrl- or si*USP10*-transfected HUVECs after treatment with vehicle or DLL4, in the presence or absence of a γ-secretase inhibitor (DBZ) for 24 hours. (**B**) Activation of a multimerized RBPJ binding site (4×RBPJ)– or 4×RBPJ mutant (*RBPJ*^{mut})–luc reporter in siCtrl- or si*USP10*-transfected HUVECs after treatment with vehicle or DLL4 for 24 hours. (**C**) Heat map of differentially expressed genes in siCtrl- or si*USP10*-transfected HUVECs treated with vehicle (Ctrl) or DLL4 for 24 hours. Data were obtained by microarray analysis performed in triplicate for each condition. Differentially regulated genes with a cutoff *P* value of <0.05 and a fold change of >2.0 (for siCtrl versus siCtrl plus DLL4) are listed. (**D**) Immunoblot analysis of NICD1 expression in siCtrl- or si*USP10*-transfected HUVECs stimulated with DLL4 or vehicle for 6 and 24 hours. (**E**) qRT-PCR analysis of *NOTCH1* mRNA expression in control and USP10 knockdown HUVECs. Values are represented relative to the expression of β-actin. (**F**) NICD1 levels in control and USP10 knockout ECs generated by lentiviral transduction of HUVECs with control (gCtrl) or USP10-targeting (g*USP10*) guide RNAs (gRNAs) as well as a FLAG-tagged CAS9 nuclease. HUVECs were stimulated with vehicle or DLL4 for 24 hours. (**G**) NICD1 immunoblot analysis of HUVECs transduced with a control lentivirus (LentiCtrl) or a GFP-tagged USP10–encoding lentivirus (LentiUSP10^{GFP}). NICD1 abundance was determined after 24 hours of DLL4 stimulation. Error bars, mean ± SEM for *n* > 3 samples. ***$P < 0.001$; ****$P < 0.0001$; NS, not significant.

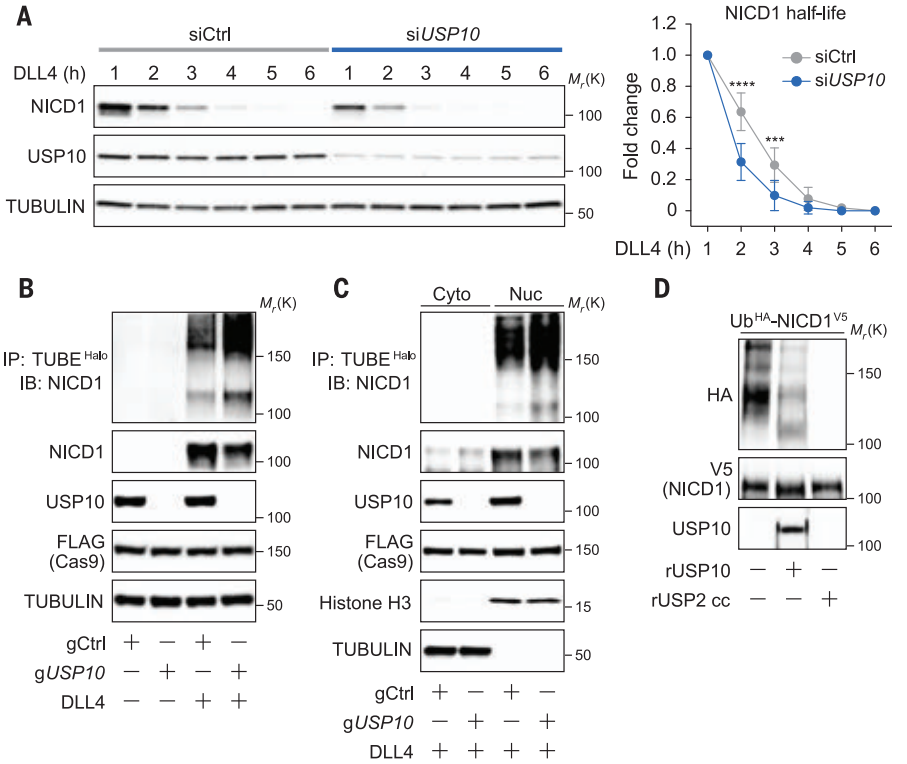

Fig. 3. USP10 regulates NICD1 stability by altering its ubiquitin-dependent turnover. (**A**) NICD1 abundance in HUVECs transfected with siCtrl or si*USP10*. After 24 hours, cells were stimulated with DLL4 after pretreatment with cycloheximide. ECs were collected at 1-hour intervals, and NICD1 protein levels were analyzed by immunoblotting. The fold change in NICD1 levels is shown on the right. (**B**) NICD1 ubiquitination pattern in control (gCtrl) or USP10 knockout (g*USP10*) HUVECs stimulated with vehicle or DLL4 for 24 hours. Cell lysates were incubated with TUBE^{Halo} to enrich ubiquitinated proteins. Ubiquitinated NICD1 was detected by immunoblotting using an NICD1-specific antibody. (**C**) Endogenous NICD1 ubiquitination in cytoplasmic (Cyto) and nuclear (Nuc) fractions derived from control (gCtrl) or USP10 knockout (g*USP10*) HUVECs stimulated with vehicle or DLL4 for 24 hours. (**D**) Ubiquitinated NICD^{V5} was purified by anti-V5 immunoaffinity chromatography from HEK293T cells transfected with NICD1^{V5}, FBXW7^{FLAG}, and Ub^{HA} and then incubated in vitro with vehicle, recombinant USP10 (rUSP10), or the recombinant catalytic core of USP2 (rUSP2 cc). Levels of NICD1 ubiquitination were determined by immunoblotting for HA. Error bars, mean ± SEM for *n* > 3 samples. ***$P < 0.001$; ****$P < 0.0001$.

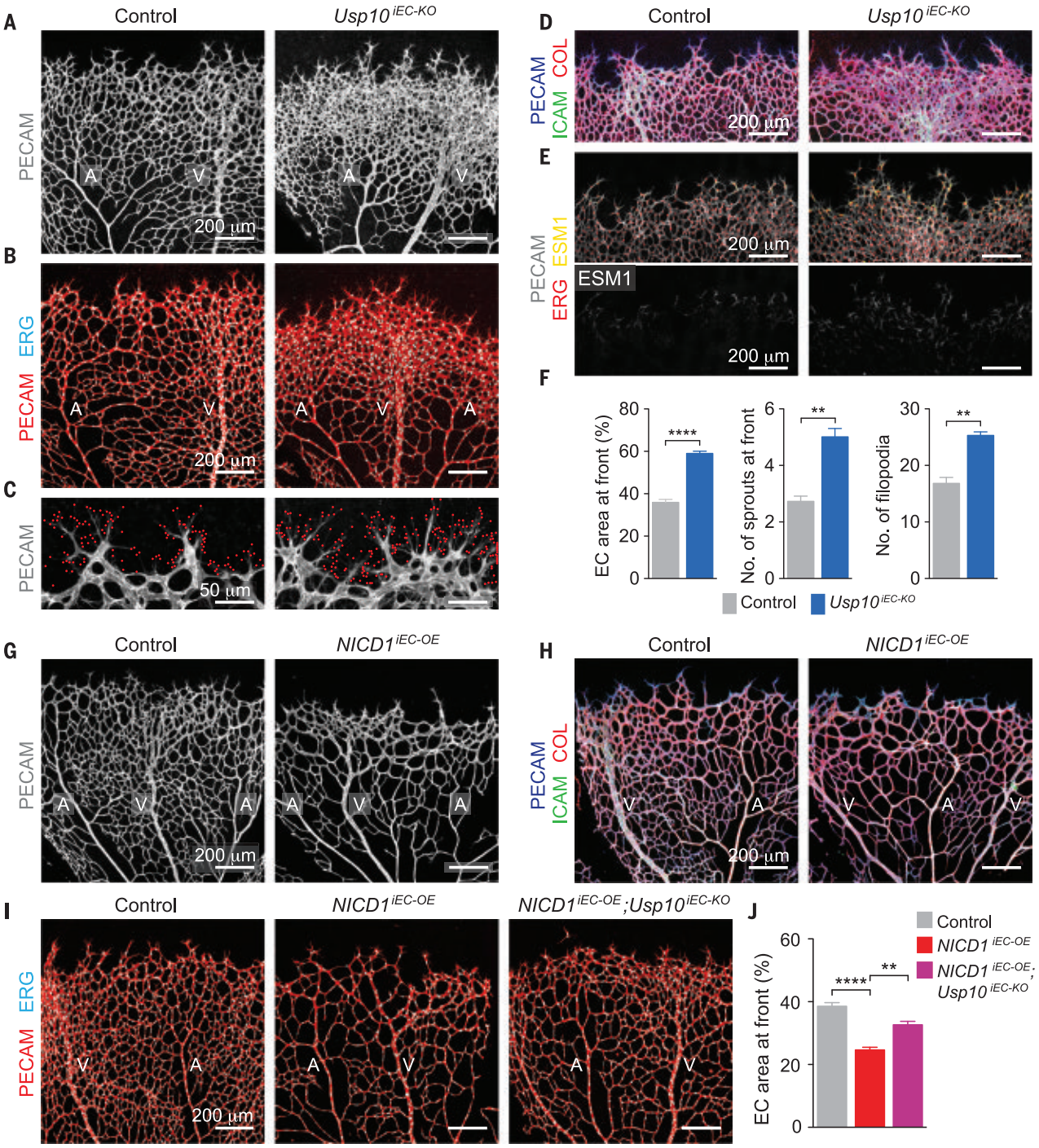

Fig. 4. Deletion of Usp10 in ECs increases angiogenic sprouting and partially restores vascular defects caused by forced NICD1 expression. (**A**) Immunofluorescence staining for platelet EC adhesion molecule (PECAM) in P7 mouse retinas of 4-OHT–injected control (*Usp10*$^{fl/fl}$) and *Usp10*^{iECKO} (*Pdgfb-creERT2;Usp10*$^{fl/fl}$) mice. A, artery; V, vein. (**B**) Images of PECAM (red)– and erythroblast transformation–specific–related gene (ERG) (cyan)–stained P7 retinas of control and *Usp10*$^{iEC-KO}$ mutants showing clustering of ECs at the angiogenic front. (**C**) Higher-magnification confocal images of PECAM-labeled P7 retinas isolated from control and *Usp10*$^{iEC-KO}$ mice. Endothelial filopodia are denoted by the small red dots. (**D**) PECAM (blue), intracellular adhesion molecule 2 (ICAM) (green), and collagen IV (COL) (red) labeling of control and *Usp10*$^{iEC-KO}$ retinas at P7. The vasculature at the angiogenic front is shown. (**E**) Confocal images showing PECAM (gray), ERG (red), and ESM1 (yellow) immunostaining of the retinal vasculature in control and *Usp10*$^{iEC-KO}$ mutants at P7. ESM1 immunostaining behind the angiogenic front was enhanced in *Usp10*$^{iEC-KO}$ mice. (**F**) Quantifications of vascular parameters at the angiogenic front in P7 control and mutant retinas as indicated. (**G**) Confocal images of PECAM-labeled (gray) P6 retinas in control and *NICD1*$^{iEC-OE}$ mice. (**H**) Immunofluorescence staining for PECAM (blue), ICAM2 (green), and collagen IV (COL) (red) in P6 retinas from 4-OHT–injected control and *NICD1*$^{iEC-OE}$ mice. (**I** and **J**) Confocal images (I) of PECAM (red)– and ERG (cyan)–labeled retinas in control mice, *NICD1*$^{iEC-OE}$ mice, and *NICD1*$^{iEC-OE}$; *Usp10*$^{iEC-KO}$ double mutants. The quantification (J) of the endothelial coverage at the angiogenic front in the respective genotypes is shown. Error bars, mean ± SEM for $n > 3$ samples. $^{**}P < 0.01$; $^{****}P < 0.0001$.

of NICD1 in response to DLL4 stimulation without affecting basal *NOTCH1* mRNA expression (Fig. 2, D to F, and fig. S3, A to D). Similar results were obtained with the Notch ligands Delta-like 1 (DLL1) and Jagged 1 (JAG1), which trigger distinct Notch responses and signaling dynamics (*8*, *21*). However, DLL1 and JAG1 were weaker NOTCH1 agonists than DLL4 in HUVECs, and higher concentrations were needed for receptor activation (fig. S3, E to G). Depletion of USP7, USP11, or USP15, three USP family members that associate with NICD1 in cancer cells (*22*), did not change NICD1 protein expression (fig. S4A). Thus, USP10 regulates endothelial Notch signaling by controlling NICD1 abundance, though we cannot exclude the possibility that alternative mechanisms may contribute to the observed effects on the Notch pathway.

This regulation appears to occur at the level of the NICD1 (downstream of γ-secretase cleavage) because the amounts of ectopically expressed $NICD1^{V5}$ were also reduced in USP10-deficient ECs (fig. S4B). Overexpression of USP10, on the other hand, enhanced the abundance of NICD1 in HUVECs (Fig. 2G and fig. S4C). Because USP10 is a deubiquitinase, we tested whether USP10 interferes with NICD1 protein degradation. Treatment of ECs with the proteasome inhibitor MG132 or depletion of FBXW7 increased the abundance of NICD1 protein in USP10-deficient HUVECs (fig. S5, A and B). Moreover, measurement of the rate of NICD1 decay in cycloheximide-treated cells showed that the half-life of endogenous NICD1 protein was decreased upon depletion of USP10 (Fig. 3A). Depletion of endothelial USP10 did not alter the abundance of cellular tumor antigen p53 or sirtuin 6 (SIRT6) (fig. S5C), two substrates of USP10 in tumor cells (*23*, *24*), suggesting that the signaling context in primary ECs differs from that in cancer cell lines.

To test whether USP10 modulates NICD1 ubiquitination in ECs, we captured ubiquitinated proteins from HUVECs by using Halo-tagged tandem ubiquitin binding entities ($TUBE^{Halo}$) (*25*) followed by immunoblotting with an NICD1 antibody. This analysis revealed a high-molecular-size ubiquitin smear in DLL4-stimulated ECs that was enhanced by MG132 treatment (fig. S5D). Coexpression of USP10 decreased this ubiquitin signal (fig. S5E), suggesting that USP10 can deubiquitinate NICD1. Consistent with these data, the depletion of USP10 in DLL4-stimulated HUVECs enhanced the endogenous ubiquitination of NICD1 (Fig. 3B). This increase in NICD1 ubiquitination was observed in the nuclear fraction of HUVECs (Fig. 3C), where NICD1 is targeted by ubiquitin ligases such as SCF^{FBXW7} (*14*–*16*) and where NICD1 and USP10 interact. To finally assess whether USP10 deubiquitinates NICD1, we purified ubiquitinated NICD1 from HEK293T cells that were cotransfected with $NICD1^{V5}$, hemagglutinin (HA)-tagged ubiquitin (Ub^{HA}), and FLAG-tagged FBXW7 ($FBXW7^{FLAG}$) (fig. S5F). Incubation of ubiquitinated NICD1 with recombinant USP10 under conditions allowing NICD1 deubiquitination by the promiscuous catalytic core of USP2 led to decreased polyubiquitination of NICD1 (Fig. 3D), suggesting that USP10 functions as an NICD1 deubiquitinase.

To understand the physiological role of USP10 in the regulation of Notch signaling, we generated mice in which exons 7 and 8 of *Usp10* were flanked by *loxP* sites ($Usp10^{fl/fl}$ mice) (fig. S6A). Germline deletion of *Usp10* (yielding the genotype $Usp10^{-/-}$) caused perinatal lethality (fig. S6B) (*26*). To bypass lethality, we crossed $Usp10^{fl/fl}$ mice with mice expressing a tamoxifen-inducible *cre* deleter (*creERT2*) that is driven by the EC-selective platelet-derived growth factor subunit B (*Pdgfb*) promoter (*Pdgfb-creERT2* deleter mice) and assessed vascular phenotypes in the retinas of the resulting mutants ($Usp10^{iEC\text{-}KO}$). The mouse retina is a well-established model of Notch-dependent angiogenesis. We injected 4-hydroxytamoxifen (4-OHT) from postnatal day 1 (P1) to P4 and analyzed retinal angiogenesis at P7 (fig. S6C). Endothelially restricted deletion of *Usp10* increased EC density and sprouting at the angiogenic front but had little effect or even opposite effects in the central parts of the retinal vasculature (Fig. 4, A and B). At the front, $Usp10^{iEC\text{-}KO}$ retinas displayed increased numbers of endothelial sprouts and filopodia (Fig. 4, C, D, and F) and showed enhanced immunostaining for EC-specific molecule 1 (ESM1) (Fig. 4E and fig. S6D), a tip cell marker that is suppressed by DLL4-Notch signaling (fig. S2C) (*9*, *27*). In *Usp10* mutant mice, ECs accumulated in veins and perivenous capillaries and veins were enlarged (fig. S6, D and E). Together, these phenotypes resemble aspects of reduced DLL4-NOTCH1 signaling in the retinal endothelium (*3*, *5*, *6*, *9*) and indicate that USP10 deficiency reduces Notch responses in vivo.

We tested whether USP10 inactivation would restore endothelial sprouting behavior when Notch signaling was aberrantly activated. We used a Cre-inducible Notch gain-of-function mouse model in which NICD1 is expressed from the ubiquitously active cytomegalovirus early enhancer–chicken β-actin (*CAG*) promoter (fig. S7A). The expression of NICD1 [as well as those of membrane-targeted Tomato and nucleus-targeted green fluorescent protein (GFP)] is controlled by a floxed stop cassette, which can be removed by Cre-mediated excision (yielding $Rosa26^{NICD1}$) (fig. S7, A and B). *Pdgfb-creERT2*–mediated recombination in $Rosa26^{NICD1}$ ($NICD1^{iEC\text{-}OE}$) mice led to severe retinal vascular defects, which correlated with the expression of the fluorescent reporters (Fig. 4, G and H, and fig. S7B). The vascular network in $NICD1^{iEC\text{-}OE}$ mutant mice was sparse and had fewer vessel sprouts (Fig. 4, G and H, and fig. S7, C and D), a phenotype that is consistent with increased endothelial Notch activity (*9*, *19*). We also combined $Rosa26^{NICD1}$, $Usp10^{flox}$, and *Pdgfb-creERT2* alleles ($NICD1^{iEC\text{-}OE}$;$Usp10^{iEC\text{-}KO}$) to generate compound mutants. Deletion of *Usp10* reduced the sprouting defects caused by forced endothelial expression of NICD1 (Fig. 4, I and J). Compared with the $NICD1^{iEC\text{-}OE}$ mice, $NICD1^{iEC\text{-}OE}$; $Usp10^{iEC\text{-}KO}$ double mutants had an increased number of vessel sprouts and branches, giving rise to a more dense vascular network at the angiogenic front (Fig. 4, I and J). Thus, USP10 deficiency can, at least in part, restore vessel density under conditions of enhanced NICD1 signaling, suggesting that USP10 is a regulator of Notch-dependent vascular morphogenesis in vivo.

In summary, we identify USP10-mediated deubiquitination of NICD1 as a mechanism to delay the rate of NICD1 degradation, which prolongs cellular Notch responses. Such regulation appears to be particularly relevant for angiogenic sprouting, during which dynamic changes in Notch activity determine the specification and position of tip and stalk cells (*28*). USP10 is itself a regulated protein, and recent studies reported that adenosine monophosphate (AMP)–activated kinase (AMPK)–mediated phosphorylation activates the enzyme (*29*). Because AMPK senses cellular energy levels and is activated by hypoxia and nutrient limitation, USP10 may be particularly active in ECs that face oxygen and nutrient deprivation, as they do when invading avascular tissues. We observed increased USP10 activity in ECs that were cultured in hypoxic or nutrient-starved conditions (fig. S8, A and B). These considerations could explain why the loss of USP10 in mice causes Notch loss-of-function phenotypes only at the sprouting front and not in the central plexus, where ECs are exposed to physiological oxygen and nutrient levels. Further studies on the regulation of USP10 may reveal in which other cell types and (patho)physiological contexts the USP10-dependent modulation of Notch signaling is at play (*30*).

REFERENCES AND NOTES

1. M. Potente, H. Gerhardt, P. Carmeliet, *Cell* **146**, 873–887 (2011).
2. L. Jakobsson *et al.*, *Nat. Cell Biol.* **12**, 943–953 (2010).
3. M. Hellström *et al.*, *Nature* **445**, 776–780 (2007).
4. A. F. Siekmann, N. D. Lawson, *Nature* **445**, 781–784 (2007).
5. S. Suchting *et al.*, *Proc. Natl. Acad. Sci. U.S.A.* **104**, 3225–3230 (2007).
6. I. B. Lobov *et al.*, *Proc. Natl. Acad. Sci. U.S.A.* **104**, 3219–3224 (2007).
7. J. D. Leslie *et al.*, *Development* **134**, 839–844 (2007).
8. R. Benedito *et al.*, *Cell* **137**, 1124–1135 (2009).
9. M. E. Pitulescu *et al.*, *Nat. Cell Biol.* **19**, 915–927 (2017).
10. S. S. Hasan *et al.*, *Nat. Cell Biol.* **19**, 928–940 (2017).
11. C. Siebel, U. Lendahl, *Physiol. Rev.* **97**, 1235–1294 (2017).
12. S. J. Bray, *Nat. Rev. Mol. Cell Biol.* **17**, 722–735 (2016).
13. R. Kopan, M. X. Ilagan, *Cell* **137**, 216–233 (2009).
14. C. Öberg *et al.*, *J. Biol. Chem.* **276**, 35847–35853 (2001).
15. C. J. Fryer, J. B. White, K. A. Jones, *Mol. Cell* **16**, 509–520 (2004).
16. J. O'Neil *et al.*, *J. Exp. Med.* **204**, 1813–1824 (2007).
17. M. T. Tetzlaff *et al.*, *Proc. Natl. Acad. Sci. U.S.A.* **101**, 3338–3345 (2004).
18. R. Tsunematsu *et al.*, *J. Biol. Chem.* **279**, 9417–9423 (2004).
19. N. Izumi *et al.*, *PLOS ONE* **7**, e41116 (2012).
20. L. S. Harrington *et al.*, *Microvasc. Res.* **75**, 144–154 (2008).
21. N. Nandagopal *et al.*, *Cell* **172**, 869–880.e19 (2018).
22. A. Yatim *et al.*, *Mol. Cell* **48**, 445–458 (2012).
23. J. Yuan, K. Luo, L. Zhang, J. C. Cheville, Z. Lou, *Cell* **140**, 384–396 (2010).
24. Z. Lin *et al.*, *Cell Rep.* **5**, 1639–1649 (2013).
25. R. Hjerpe *et al.*, *EMBO Rep.* **10**, 1250–1258 (2009).
26. M. Higuchi *et al.*, *Stem Cell Rep.* **7**, 1116–1129 (2016).
27. S. F. Rocha *et al.*, *Circ. Res.* **115**, 581–590 (2014).
28. B. Ubezio *et al.*, *eLife* **5**, e12167 (2016).
29. M. Deng *et al.*, *Mol. Cell* **61**, 614–624 (2016).
30. J. Zhang, M. Liu, Y. Su, J. Du, A. J. Zhu, *G3* **2**, 1563–1575 (2012).

ACKNOWLEDGMENTS

We thank J. Yuan, Z. Lou, and N. Popov for expression plasmids and M. Gyrd-Hansen for advice on the TUBE assays. **Funding:** This work is supported by the Max Planck Society, European Research Council (ERC) starting grant ANGIOMET (311546), ERC consolidator grant EMERGE (773047), the Deutsche Forschungsgemeinschaft (SFB 834), the Excellence Cluster Cardiopulmonary System (EXC 147/1), LOEWE grant Ub-Net, the DZHK (German Center for Cardiovascular Research), the Stiftung Charité, the Cardio-Pulmonary Institute (EXC 2026

project ID 390649896), and the European Molecular Biology Organization (EMBO) Young Investigator Programme. **Author contributions:** R.L., T.S., H.N., J.A., B.Z., C.S., A.D., Y.T.O., K.W., J.W.D.F., A.E., M.Ka., K.H., T.Bo., and S.G. performed experiments. R.L., T.S., H.N., J.A., B.Z., C.S., A.D., Y.T.O., K.W., J.W.D.F., A.E., M.Ka., K.H., T.Bo., S.G., and M.P. analyzed data. A.E., M.Ka., K.H., T.Br., M.Kr., R.B., and I.D. provided essential reagents and protocols. M.P. supervised the study. R.L., T.S., I.D., and M.P. wrote the paper. All authors discussed the results and commented on the manuscript. **Competing interests:** The authors declare no competing financial interests. **Data and materials availability:** The Rosa26NICD1 mice are available from R.B. under a material agreement with the CNIC. The proteomics data have been deposited to the ProteomeXchange Consortium via the PRIDE partner repository under accession number PXD013192. The microarray data have been deposited in the ArrayExpress repository under accession number E-MTAB-7774. Data from the RNA sequencing analysis have been deposited in NCBI Gene Expression Omnibus under accession numberGSE128179.

SUPPLEMENTARY MATERIALS
www.sciencemag.org/content/364/6436/188/suppl/DC1
Materials and Methods
Figs. S1 to S8
References (*31*–*43*)

25 January 2018; accepted 14 March 2019
10.1126/science.aat0778

EVOLUTIONARY BIOLOGY

Rapid plant evolution driven by the interaction of pollination and herbivory

Sergio E. Ramos and Florian P. Schiestl*

Pollination and herbivory are both key drivers of plant diversity but are traditionally studied in isolation from each other. We investigated real-time evolutionary changes in plant traits over six generations by using fast-cycling *Brassica rapa* plants and manipulating the presence and absence of bumble bee pollinators and leaf herbivores. We found that plants under selection by bee pollinators evolved increased floral attractiveness, but this process was compromised by the presence of herbivores. Plants under selection from both bee pollinators and herbivores evolved higher degrees of self-compatibility and autonomous selfing, as well as reduced spatial separation of sexual organs (herkogamy). Overall, the evolution of most traits was affected by the interaction of bee pollination and herbivory, emphasizing the importance of the cross-talk between both types of interactions for plant evolution.

Insects and plants have been interacting since their origins, with these interactions driving the evolution of their notable diversity (*1*). Insects impose strong selection on plants—for example, as pollinators selecting for floral traits and mating systems (*2*, *3*) or as herbivores selecting for defense traits (*4*, *5*). Because floral and defense traits are not independent but rather connected through ecological and physiological mechanisms, the effects of pollination and herbivory on plant evolution are also linked to some degree (*6*–*8*). For example, whereas plants profit from showy flowers that attract pollinators, such attractive signals sometimes bring in herbivores as well, imposing an ecological trade-off on the evolution of such signals (*9*, *10*). As another mechanism, plant investment in defense, such as the production of toxic metabolites, may compromise pollinator attraction by drawing resources from flower tissues or increasing the toxicity of rewards such as nectar (*11*), thereby causing physiological trade-offs (*12*). Nevertheless, pollination and herbivory have traditionally been studied in isolation from each other, and the combined effects of both factors remain a major gap in our understanding of plant evolution (*6*). Given the commonness of insect pollination and herbivory in angiosperms, it is surprising how little we know about the effects of herbivores on the evolution of pollinator-attracting signals or the combined effects of herbivores and pollinators on the balance between self-pollination and outcrossing (*6*, *9*, *13*).

Most studies of plant evolution are limited to hypothesizing or predicting evolutionary trajectories for species and traits, because they either use a comparative approach or study factors relevant for evolution (e.g., selection) within a single plant generation. Experimental evolution under controlled conditions can close this gap by directly demonstrating the (short-term) evolutionary consequences of ecological interactions. Although experimental evolution studies have traditionally focused on organisms with very short generation times, a few recent studies have dealt with plants and interacting insects by using either pollinators (*3*, *14*, *15*) or herbivores (*4*, *5*) as selective agents, but no real-time evolution study so far has included the combined effects of both.

Department of Systematic and Evolutionary Botany, University of Zurich, Zollikerstrasse 107, CH-8008 Zürich, Switzerland.
***Corresponding author. Email: florian.schiestl@systbot.uzh.ch**

Table 1. The effects of bee pollination, herbivory, and their interaction on the evolution of floral traits, nectar and leaf glucosinolates, and the mating system. Values in parentheses are sample sizes. All traits with a significant effect (indicated by Y for "yes") of either bee pollination, herbivory, or their interaction are shown (see table S2 for full statistical values). (+) indicates a positive effect (increase) whereas (−) indicates a negative effect (decrease) of either bee pollination or herbivory (see table S1 for exact values). N, no significant effect.

Trait	Bee pollination	Herbivory	Interaction of bee pollination and herbivory
Morphology			
Sepal length (391)	Y(+)	N	Y
Petal width (391)	Y(+)	N	N
Pistil length (391)	N	Y(−)	N
Floral volatiles			
Z-3-Hexenyl acetate (344)	N	N	Y
Phenylacetaldehyde (344)	Y(+)	Y(+)	Y
Benzyl nitrile (344)	Y(+)	Y(+)	Y
p-Anisaldehyde (344)	Y(+)	N	Y
(*E*,*E*)-α-Farnesene (344)	N	N	Y
Total volatile emission (344)	N	N	Y
Floral nectar glucosinolates			
Gluconapin (123)	N	N	Y
Glucoraphanin (123)	N	N	Y
Leaf glucosinolates			
Hydroxyglucobrassicin (253)	N	Y(+)	Y
Methoxyglucobrassicin (253)	N	Y(+)	Y
Mating system			
Self-compatibility (384)	N	N	Y
Autonomous selfing (384)	N	N	Y
Herkogamy (391)	N	Y(−)	N

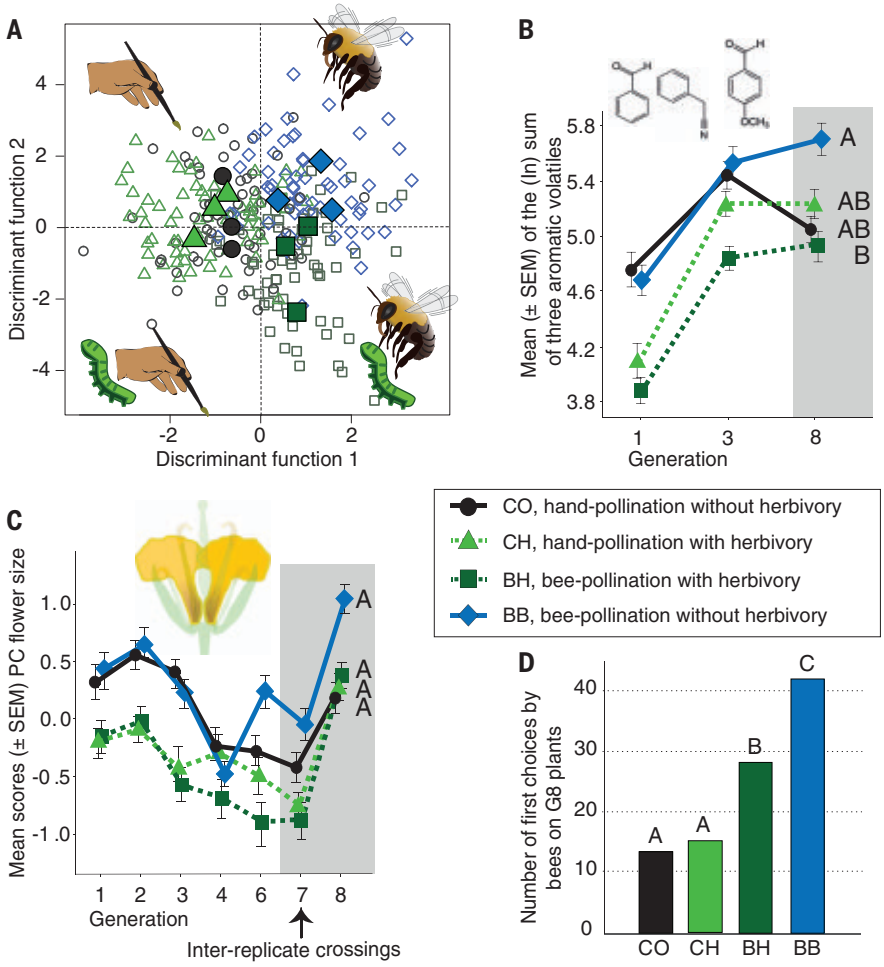

Fig. 1. Evolutionary changes in floral traits and bee preferences. (**A**) Multivariate analysis (linear discriminant function analysis; N = 257 samples) used to examine differences among replicates of the different treatment groups. Enlarged filled symbols depict the group centroid per replicate. In the analysis, only the replicate, not the treatment group, was predefined. For statistical values, see (*16*). (**B** and **C**) Changes in floral traits during experimental evolution. Trait differences among treatments with and without herbivory in the first generations are due to phenotypic plasticity; the shaded areas indicate generations where insects were no longer applied. Trends toward decreased size common to all treatment groups likely show the effects of inbreeding. (B) Sum of data for three aromatic floral volatiles (benzaldehyde, benzyl nitrile, and *p*-anisaldehyde) that showed a trend or significant increase in the BB treatment group (GLMM; N = 344 samples; different letters refer to $P < 0.05$). (C) Principal component (PC) representing petal length and width (N = 391 samples). Data for generation 5 were not available. (**D**) Bioassays testing the preferences (first choices) of bumble bees for plants of different treatment groups at generation 8 (G8). Bees significantly preferred plants that evolved under bee pollination without herbivory (GLMM; N = 80 bees and 320 plants; different letters refer to $P < 0.05$). For statistical details, see (*16*).

For these reasons, mechanisms of plant evolution driven by different interacting organisms are little understood. Our study addresses this topic with experimental evolution using fast-cycling *Brassica rapa* plants and combined pollination by bumble bees and herbivory by caterpillars as selective agents. We studied the evolution of floral traits (i.e., morphology and scent), the mating system (self-compatibility and autonomous selfing), and plant defense (glucosinolates). In our greenhouse experiment, plants from the source population were split into four treatment groups, varying in the type of pollination and the presence or absence of herbivores (*Pieris brassicae* larvae on leaves) (*16*): (i) hand pollination without herbivory (control); (ii) hand pollination with herbivory; (iii) bee pollination with herbivory; and (iv) bee pollination without herbivory (fig. S1). We replicated each treatment three times with 36 plants each, and each replicate evolved independently during six consecutive plant generations. At generations 7 and 8, all plants were grown without insects to reduce maternal effects caused by herbivory; plants of generation 7 were manually crossed between replicates (but only within the treatment groups) to restore heterozygosity and reduce inbreeding effects (*17*). Plants were phenotyped to detect consistent evolutionary divergence between treatment groups. In our analysis, we focused on the following questions: How do floral traits and attractiveness, defense, and mating systems evolve with different pollination and herbivory treatments? Does the interaction between bee pollination and herbivory lead to distinct evolutionary trajectories in experimental plants?

Using a multivariate analysis including 19 floral traits, we showed that plants in our treatment groups differed significantly at generation 8, demonstrating divergent trait evolution during our experiment (Fig. 1A). As expected, bee pollination caused more intensive evolutionary changes in plant traits than leaf herbivory alone, compared with traits in control plants, but the presence of herbivores changed the evolutionary outcome of bee pollination to some degree (Fig. 1A). In more detail, bumble bee-pollinated plants without herbivory evolved more fragrant flowers, which tended to be larger (Fig. 1, B and C, and table S1). Bumble bees clearly preferred those flowers over the flowers of all other treatment groups at generation 8 (Fig. 1D), showing that the plants had adapted to the bees' preferences during the experiment (*3*). With the addition of herbivores, plants with bumble bee pollination did not evolve a detectable increase in floral signals (Fig. 1, B and C) and the flowers of these plants were less attractive to bumblebees (Fig. 1D) than the flowers of plants that evolved with bumble bees only, but they were still more attractive than flowers of plants that evolved with hand pollination (Fig. 1D). These results show that herbivory compromised the evolution of attractive flowers. This was likely caused by resource reallocation, as plants assigned more resources to defense at the cost of investment in reproductive tissues and floral signals, manifesting a physiological trade-off (*8*, *18*). Consistently, we found that defense traits were influenced by the mode of pollination in our experiment. Although only one glucosinolate compound increased in plants with hand pollination and herbivory (table S1), we detected a significant interactive effect of herbivory and bee pollination for two leaf and two nectar glucosinolates (Table 1). Although the physiological link between defense compounds, floral signals, and reward needs more in-depth investigation, we show here that the evolution of both glucosinolate defense and floral attractiveness is influenced by the combined effects of pollination and herbivory.

Besides influencing the evolution of floral traits and plant defense, pollination and herbivory

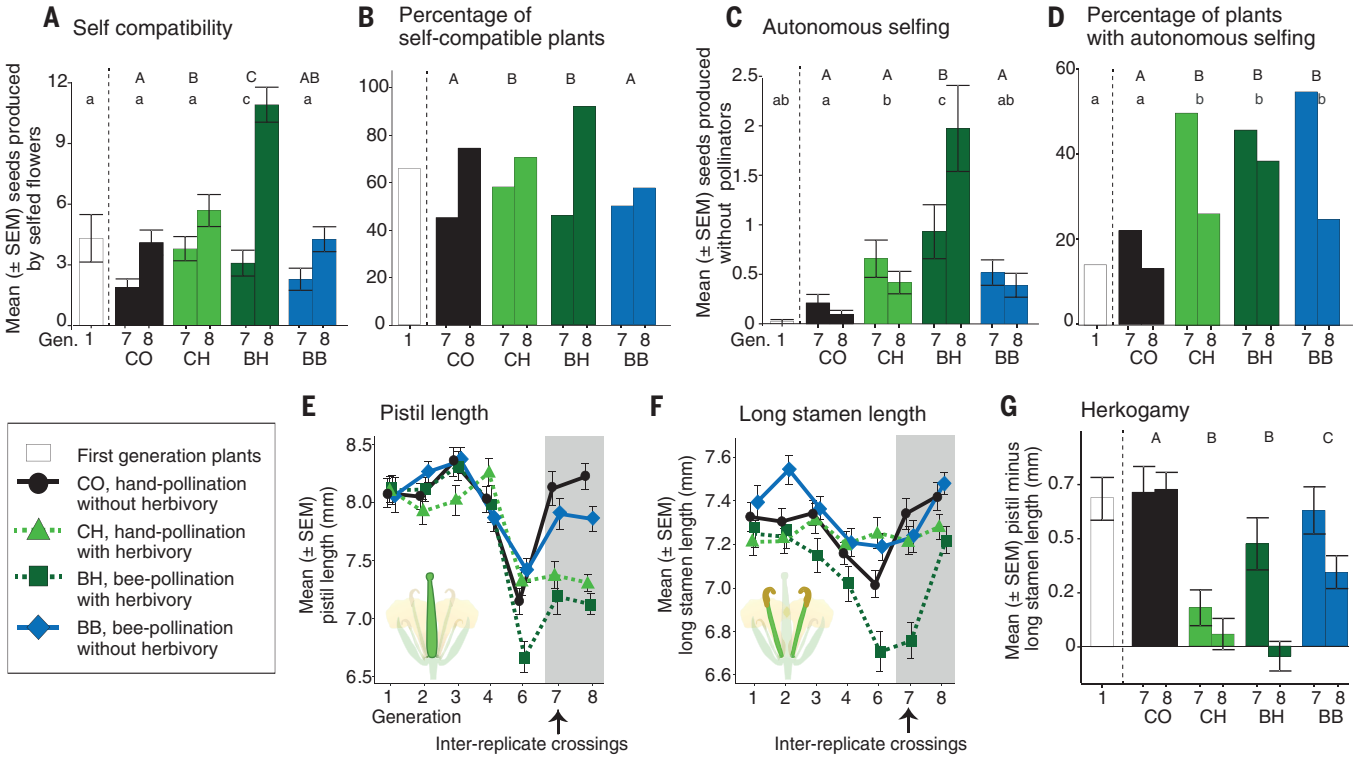

Fig. 2. Evolutionary changes in mating system and flower morphology in experimental plants. (**A**) Self-compatibility (measured as seeds produced by manually self-pollinated flowers) and (**B**) the percentage of plants with at least one seed formed after manual self-pollination were higher in bee-pollinated plants with herbivory (BH) (GLMM; N = 35 samples for generation 1 and 63 to 91 samples per generation and treatment group for generations 7 and 8; different uppercase letters refer to $P < 0.05$ between treatment groups, and different lowercase letters refer to $P < 0.05$ between plants of generation 1 and treatment groups with generations 7 and 8 pooled). The factor "generation x treatment" was not significant in any GLMM, except for the percentage of self-compatible plants (see tables S3 and S4 for statistical values). Gen., generation. (**C**) Autonomous selfing (measured as seeds produced by flowers without access to any pollinators) was elevated in bee-pollinated plants with herbivory (BH) and found with greater frequency in plants of generation 7 or 8 than in plants of generation 1 (**D**). (**E** and **F**) Evolutionary change in pistil (E) and long stamen (F) lengths throughout the experiment (without generation 5). Shaded areas represent plants grown without insects. (**G**) Herkogamy (the spatial separation of sexual organs in a flower) was reduced in both treatment groups that experienced herbivory (CH and BH) (GLMM, N = 50 to 104 samples per generation and treatment group).

are also key factors determining mating system evolution (*13*, *19*). A common switch in plant mating systems is the change from primarily outcrossing to self-pollination (*20*), which is thought to be driven predominantly by pollen limitation (*21*). Although the combined effects of pollination and herbivory on mating system evolution are little understood, the usually detrimental effects of herbivory on pollinator attraction and therefore pollen income (*8*, *22*, *23*) led to the idea that herbivory may indirectly promote selfing or mixed mating through increased pollen limitation (*13*). We found that herbivory in bee-pollinated plants led to an increase in self-compatibility (Fig. 2, A and B, and tables S3 and S4) and autonomous selfing (Fig. 2, C and D, and tables S3 and S4) compared with these traits in the control group and plants of the first generation. Moreover, we found that both self-compatibility and autonomous selfing were affected by the interaction between bee pollination and herbivory (Table 1). These results may have been caused by a change in bee behavior triggered by herbivore-induced phenotypic changes in flowers. In agreement with earlier studies (*24*), we showed that bees spent less time on herbivore-infested plants than on plants without herbivory [measured only in generation 1; mean ± SD, 78.80 ± 117.09 s and 96.45 ± 108.07 s; generalized linear mixed model (GLMM), N = 101 samples; estimate = 1.557, z-score = 2.43, P = 0.015]. As a consequence, shorter bee visits to herbivore-infested plants may have increased pollen limitation, thus selecting for enhanced selfing (*2*, *3*). In this way, herbivore-induced changes, although a form of phenotypic plasticity and not evolution, can affect evolutionary change by altering pollinator behavior and hence selection on plant traits.

Autonomous selfing depends on self-compatibility and flower morphology that permits self-pollen to be deposited on stigmas (*25*). One mechanism that modulates the potentially detrimental deposition of self-pollen is herkogamy, the spatial separation between sexual organs in a flower (*20*). In our starting population, herkogamy was evident in pistils being longer than the long stamen (see illustrations in Fig. 2, E and F). At the end of our experiment, herkogamy remained unchanged in hand-pollinated plants without herbivory, whereas in plants with herbivory (independent of pollination), it evolved to be reduced so that sexual organs overlapped (Fig. 2G and table S3). This overlap of the sexual organs was mediated by a reduction in pistil length rather than an elongation of the long stamen (Fig. 2, E and F).

Reduced herkogamy likely facilitated autonomous selfing in our experimental plants and may have evolved under selection for reproductive assurance (*2*). We found negative selection on herkogamy in plants with bee pollination and herbivory (table S5), suggesting pollen limitation as a selective factor. On the other hand, plants with hand pollination and herbivory also evolved reduced herkogamy but not via direct selection, because in these plants the degree of pollen limitation was obviously not influenced by the presence or absence of herbivory. Alternatively, reduced herkogamy may be modulated by pleiotropy or genetic correlation with signaling by jasmonate, a plant hormone involved

both in defense responses against herbivores and in flower development (*26*, *27*). Such a physiological link between defense and traits involved in mating systems may be adaptive, especially in annual plants, where the time available for outcrossing is limited and fitness under herbivore attack is optimized with selfing.

In conclusion, we have demonstrated rapid evolutionary changes in plants driven by mutualists and antagonists. We found that nonadditive interactions between pollinators and herbivores shape the evolution of the majority of traits with very different yet physiologically and ecologically linked functions, such as pollinator attraction, defense, and mating (Table 1). The importance of such interactive effects points out the need for more integrative studies to better understand how interactions shape the evolution of diversity. Understanding mechanisms of evolution has never been more relevant as in contemporary times, where human-altered environments change evolutionary fates of a multitude of organisms, with consequences for ecosystem functioning, biodiversity loss, and food security (*28*).

REFERENCES AND NOTES

1. P. R. Guimarães Jr., M. M. Pires, P. Jordano, J. Bascompte, J. N. Thompson, *Nature* **550**, 511–514 (2017).
2. S. Kalisz, D. W. Vogler, K. M. Hanley, *Nature* **430**, 884–887 (2004).
3. D. D. L. Gervasi, F. P. Schiestl, *Nat. Commun.* **8**, 14691 (2017).
4. A. A. Agrawal, A. P. Hastings, M. T. J. Johnson, J. L. Maron, J.-P. Salminen, *Science* **338**, 113–116 (2012).
5. T. Züst *et al.*, *Science* **338**, 116–119 (2012).
6. D. Lucas-Barbosa, *Trends Plant Sci.* **21**, 125–133 (2016).
7. C. M. Herrera *et al.*, *Proc. Natl. Acad. Sci. U.S.A.* **99**, 16823–16828 (2002).
8. S. Y. Strauss, J. K. Conner, S. L. Rush, *Am. Nat.* **147**, 1098–1107 (1996).
9. N. Theis, L. S. Adler, *Ecology* **93**, 430–435 (2012).
10. A. Knauer, F. Schiestl, *Evol. Ecol.* **31**, 285–304 (2017).
11. L. S. Adler, M. Wink, M. Distl, A. J. Lentz, *Ecol. Lett.* **9**, 960–967 (2006).
12. J. D. Hare, E. Elle, N. M. van Dam, *Evolution* **57**, 793–805 (2003).
13. M. T. J. Johnson, S. A. Campbell, S. C. H. Barrett, *Annu. Rev. Ecol. Evol. Syst.* **46**, 191–213 (2015).
14. S. A. Bodbyl Roels, J. K. Kelly, *Evolution* **65**, 2541–2552 (2011).
15. F. P. Schiestl, A. Balmer, D. D. Gervasi, *Evolution* **72**, 2653–2668 (2018).
16. Materials and methods are available as supplementary materials.
17. T. J. Kawecki *et al.*, *Trends Ecol. Evol.* **27**, 547–560 (2012).
18. S. Y. Strauss, R. E. Irwin, V. M. Lambrix, *J. Ecol.* **92**, 132–141 (2004).
19. C. T. Ivey, D. E. Carr, *Am. J. Bot.* **92**, 1641–1649 (2005).
20. S. C. H. Barrett, *Nat. Rev. Genet.* **3**, 274–284 (2002).
21. D. G. Lloyd, *N.Z. J. Bot.* **17**, 595–606 (1979).
22. A. Kessler, R. Halitschke, K. Poveda, *Ecology* **92**, 1769–1780 (2011).
23. F. P. Schiestl, H. Kirk, L. Bigler, S. Cozzolino, G. A. Desurmont, *New Phytol.* **203**, 257–266 (2014).
24. M. Bruinsma *et al.*, *J. Chem. Ecol.* **40**, 39–49 (2014).
25. A. Sicard *et al.*, *Proc. Natl. Acad. Sci. U.S.A.* **113**, 13911–13916 (2016).
26. Z. Yuan, D. Zhang, *Curr. Opin. Plant Biol.* **27**, 44–51 (2015).
27. L. T. S. Chrétien *et al.*, *New Phytol.* **217**, 1279–1291 (2018).
28. M. Galetti *et al.*, *Science* **340**, 1086–1090 (2013).

ACKNOWLEDGMENTS

We thank A. Balmer for her help in data collection, R. Jonas and M. Meierhofer for taking care of the plants during the experiment, T. Christoffel for insect rearing, F. Huber for help with gas chromatographic analyses, and L. Bigler for advice in glucosinolate analysis; the seed families used in this study were kindly provided by D. D. Gervasi. **Funding:** The research was funded by grants to F.P.S. from the European Union's Seventh Framework Program (FP7/2007-2013, FP7/2007-2011) under grant agreement 281093 and by a full graduate fellowship to S.E.R. funded by the Consejo de Ciencia y Tecnología CONACYT-México (CVU-346745). **Author contributions:** F.P.S. and S.E.R. planned and designed the study and developed the methodology; S.E.R. performed the investigations; S.E.R. and F.P.S. wrote the manuscript. **Competing interests:** The authors declare no competing interests. **Data and materials availability:** All data are available in the text and supplementary materials of this paper.

SUPPLEMENTARY MATERIALS

www.sciencemag.org/content/364/6436/193/suppl/DC1
Materials and Methods
Figs. S1 and S2
Tables S1 to S7
References (*29*–*33*)

16 October 2018; resubmitted 20 December 2018
Accepted 28 February 2019
10.1126/science.aav6962

High-Speed Microscope Autofocus
PureFocus 850 from Prior Scientific is a fast, accurate focusing system designed to fit both upright and inverted microscopes using infinity-corrected optics. Easy to use and quick to set up, the system provides a real-time focus for a range of sample types, saving the user from spending time finding and maintaining focus on the sample, thus preventing focus drift. It reliably focuses on slides, well plates, chamber slides, and Petri dishes, while maintaining clear images for long-term studies. PureFocus 850 also works on samples with reflective surfaces, including metallurgical, semiconductors, and liquid-crystal displays (LCDs). It is also ideal for high-speed slide scanning. A stand-alone system with no PC required during operation, PureFocus 850 is fully controllable via keyboard option, and further optional PC control can be made via USB.
Prior Scientific
For info: +44-(0)-1223-881711
www.prior.com/product/purefocus850

Anti-Eculizumab Antibodies
Bio-Rad Laboratories offers a range of recombinant monoclonal anti-idiotypic antibodies that inhibit the binding of eculizumab (Soliris) to its target, complement C5 protein. This new range of antibodies comprises four inhibitory antibodies that are highly specific for the humanized IgG2/4 kappa monoclonal antibody drug eculizumab, a biotherapeutic used to treat paroxysmal nocturnal hemoglobinuria and atypical hemolytic uremic syndrome. The anti-eculizumab inhibitory antibodies can be used to quantify the level of eculizumab in patient samples, and may also be used in bioanalytical assays for biosimilar development. An antibody pair is suitable for the development of a pharmacokinetic (PK) bridging ELISA, and antibodies of high, medium, and low affinity can be used as a positive control or calibrator in an antidrug antibody assay.
Bio-Rad
For info: 919-878-7978
www.bio-rad-antibodies.com/anti-eculizumab-antibody-soliris.html

Cloud-Connected Pipette
Gilson Connect is a cloud-connected platform that powers smart liquid handling devices, and includes the company's first Internet of Things (IoT) products: TRACKMAN Connected, an all-in-one kit that includes a tablet with the PipettePilot tracker application, and PIPETMAN M Connected, a Bluetooth-enabled smart electronic pipette. Gilson Connect devices can record and track pipette performance in real-time and transmit data to sciNote, a free, open-source electronic lab notebook. Researchers can check their pipetting data to detect errors and help improve traceability and experiment reproducibility. An environmental sensor wirelessly connects to the tablet and app, giving researchers a time-stamped record of environmental conditions that can affect pipetting accuracy. By partnering with sciNote, Gilson Connect makes it possible for researchers to store data and consolidate records in a secure location that is easily accessible and sharable, effectively eliminating lost data, a significant contributor to the irreproducibility crisis.
Gilson
For info: 800-445-7661
www.gilson.com

Substrates for Nanotechnology Applications
AMS Biotechnology is a leading supplier of gold-, silver-, and platinum-coated substrates for nanotechnology researchers looking to use these surfaces to characterize self-assembled monolayers using atomic force microscopy or scanning tunneling microscopy. Gold, silver, and platinum surfaces offer a clean, near atomically flat surface that is ideal for applications in nanotechnology, such as studies on self-assembly, single-molecule imaging, nano- or microcontact printing, DNA origami, or nanophotonics. Deposited under high vacuum (10^{-8} Torr) with 99.9% purity, noble metal presents researchers with an atomically flat coated substrate that is free from oxygen, organics, and other contaminants, and consequently does not require cleaning prior to use.
AMS Biotechnology
For info: 617-945-5033
www.amsbio.com/gold-coated-substrates-slides.aspx

Sintered Porous Materials for Chromatography
Developed for the Bioscience market, BioVyon from Porvair Sciences is a high-performance, porous, polymeric material manufactured to the highest cleanliness standards. This unique material, produced from high-density polyethylene resin using a modifiable proprietary process, is activated and then formed into filtration media of different void volumes according to the target application. Of special note is BioVyon's application in chromatography. Used in filter and pipette tips, and solid-phase extraction microplates (such as the Porvair Sciences MicroLute) and cartridges, BioVyon has found a niche with many blue-chip chromatography supply manufacturers because of the benefits it offers, particularly in demanding scientific applications. BioVyon co-sintered products are made using a solid-state media created from an ultrapure, highly modified polymeric material with the lowest levels of extractables and leachates. Porvair's proprietary BioVyon technology allows high-purity silica or divinylbenzene (DVB) resins to be supported in a matrix that provides a high surface area while reducing channeling through the column.
Porvair Sciences
For info: 800-552-3696
www.porvair-sciences.com/search/?q=biovyon

Centrifuge/Lyophilizer
Using LyoSpeed technology on SP Scientific's Genevac EZ-2 Elite and Series 3 HT evaporators, HPLC fractions can be automatically concentrated to a few milliliters, then frozen and rapidly lyophilized to produce a diffuse, dry powder that can easily be redissolved or weighed out. For certain compounds, a fully dried result can be hard to achieve with traditional methods due to compound interactions with water, resulting in formation of a gum or oil. Such samples are of little use in biological assays, since accurate weights cannot be obtained. In most samples, LyoSpeed technology produces a dry powder rather than the traditional thin film, making downstream processing more convenient, since compounds can be more easily removed from the evaporation vessel. The resultant powder is not excessively fluffy, as it would be if obtained from conventional freeze-drying. This avoids the problems associated with static formation, particularly when trying to weigh out such compounds, and helps prevent airborne contamination, which is important if the compound is harmful or toxic.
SP Scientific
For info: +44-(0)-1473-240000
www.spscientific.com/contentblock.aspx?id=3504

Electronically submit your new product description or product literature information! Go to www.sciencemag.org/about/new-products-section for more information.

Newly offered instrumentation, apparatus, and laboratory materials of interest to researchers in all disciplines in academic, industrial, and governmental organizations are featured in this space. Emphasis is given to purpose, chief characteristics, and availability of products and materials. Endorsement by *Science* or AAAS of any products or materials mentioned is not implied. Additional information may be obtained from the manufacturer or supplier.

UCLA

UCLA Division of Life Sciences– Lecturer with Potential for Security of Employment for the Quantitative Biology Curriculum

The Division of Life Sciences at the University of California, Los Angeles is seeking applicants for a full-time Lecturer with Potential for Security of Employment (LPSOE) in one of the Life Science Departments: Ecology & Evolutionary Biology, Integrative Biology & Physiology, Microbiology, Immunology & Molecular Genetics, Molecular, Cell & Developmental Biology, or Psychology. This position has a similar career progression to someone who enters as a tenure-track assistant professor. Faculty appointed as LPSOE are Academic Senate members whose expertise and responsibilities center on undergraduate education and scholarly analysis and improvement of teaching methods.

A successful candidate will be expected to provide leadership in innovative and inclusive teaching in the Life Science Quantitative Biology Curriculum. Their primary teaching responsibility will include our new introductory mathematics series for first-year life science majors, Mathematics for Life Scientists, based on the text Modeling Life (https://www.springer.com/us/book/9783319597300). These courses teach calculus and linear algebra with a focus on developing and analyzing models of nonlinear dynamical systems in ecology, biology, physiology, epidemiology and other subjects in the Life Sciences. The LPSOE will work with other faculty and the campus Center for Education Innovation and Learning in the Sciences to develop, implement, assess, and publish findings for new pedagogical initiatives. The appointee will also be expected to demonstrate continued professional growth that enhances their value to the University. Contributions and achievements supporting professional growth include: (i) acquisition of intramural and/or extramural funds to support educational initiatives, (ii) curriculum innovation to promote the retention of diverse students in Life Sciences, (iii) academic leadership within the University beyond normal service obligations, and (iv) involvement in professional organizations

Qualified applicants must have a Ph.D. in a Mathematical discipline (e.g., Mathematics, Biomathematics) or a Ph.D. in a Life Science discipline, with background in mathematical modeling. Candidates must have experience in teaching undergraduates and the ability to teach calculus and linear algebra in UCLA's Quantitative Biology Curriculum. Salary will be commensurate with education and experience and based on University of California pay scales.

To Apply: Candidates should submit a cover letter expressing their interest in the position, a curriculum vitae, a two-page teaching statement summarizing experience in undergraduate teaching at the university level that includes a description of pedagogical approaches used, a statement of previous research with an emphasis in Quantitative Biology, and a statement summarizing past or potential contributions to diversity, as well as the names and contact information for three professional references online to: **https://recruit.apo.ucla.edu/JPF04444**. Individuals with a history of mentoring students under-represented in the sciences are encouraged to apply and to describe their experience in a cover letter. Review of applications will begin on **April 30, 2019** and continue until the position is filled.

If available, candidates also should submit links to documentation of teaching excellence such as instructional or assessment materials developed by the candidate, summaries of student ratings of instruction, reports based on peer classroom observations, instructional video segments from previous courses taught, and any other materials candidates feel would assist the search committee with an evaluation of their application. Questions regarding the position should be sent to the chair of the search committee, Beth Lazazzera (bethl@microbio.ucla.edu).

The University of California is an Equal Opportunity/Affirmative Action Employer. All qualified applicants will receive consideration for employment without regard to race, color, religion, sex, sexual orientation, gender identity, national origin, disability, age or protected veteran status. For the complete University of California nondiscrimination and affirmative action policy see http://policy.ucop.edu/doc/4000376/NondiscrimAffirmAct

AWARDS

DGKL Deutsche Gesellschaft für Klinische Chemie und Laboratoriumsmedizin e.V.

DGKL Award „Biochemical Analytics 2019"

The German Society of Clinical Chemistry and Laboratory Medicine (DGKL) is the non-profit, scientific organization for clinical chemistry and laboratory medicine in Germany. We represent, promote and shape Clinical Chemistry and Laboratory Medicine in research, education and patient care.

The Biochemical Analytics award was established in 1970 and is awarded every two years to scientists who demonstrated outstanding achievements in research and analytical method development. Nominations are made by the Board of Directors of the DGKL, the Nominating Committee or by self-nominations.

The next award ceremony will be held at the 16th Annual Conference of the DGKL from 25th to 28th of September 2019 in Magdeburg, Germany. The award is sponsored by SARSTEDT AG & Co. KG and comprises an award sum of **EUR 50.000**. The award winner must be present at the prize giving ceremony.

Valid applications shall encompass a scientific CV, an abstract of scientific achievements and those papers the nomination is based on.

Please send the dossier using the keyword **„BIOCHEM2019"** by mail or email no later than **May 31st 2019** to:

Deutsche Gesellschaft für Klinische Chemie
und Laboratoriumsmedizin e.V.
BIOCHEM2019
attn. Anja Turkalj
Friesdorfer Straße 153
53175 Bonn
turkalj@dgkl.de

Search more jobs online

Access hundreds of job postings on ScienceCareers.org.

Expand your search today.

Alexander von Humboldt
Stiftung / Foundation

more independence + more opportunities + more scope search

Sofja Kovalevskaja Award – Become a research group leader in Germany

€ 1.65 million for young researchers from all disciplines

The Alexander von Humboldt Foundation is now calling for applications for the Sofja Kovalevskaja Award, one of the most valuable academic awards in Germany. With funding of up to € 1.65 million, it creates unique opportunities for excellent researchers to conduct their own research in Germany: award winners are invited to spend five years working at the institute of their choice and setting up their own research groups – independently and virtually free of bureaucracy.

Scientists and scholars of all disciplines from abroad who have completed their doctorates within the last six years are eligible to apply. The award targets outstanding talent and a creative approach to research.

The Humboldt Foundation actively promotes equal opportunities and therefore particularly welcomes applications from women researchers.

The closing date for applications is 31 July 2019. More information: **www.humboldt-foundation.de/SKP_en**

Exzellenz verbindet –
be part of a worldwide network.

Alexander von Humboldt Foundation
Jean-Paul-Str. 12
53173 Bonn
Germany

info@avh.de

www.humboldt-foundation.de

YOU'D SMILE TOO IF YOU JUST ADVANCED YOUR CAREER.

Find your next job at ScienceCareers.org

There's scientific proof that when you're happy with what you do, you're better at what you do. Access career opportunities, see who's hiring and take advantage of our proprietary career-search tools. Get tailored job alerts, post your resume and manage your applications all in one place: sciencecareers.org

Science Careers

FROM THE JOURNAL SCIENCE AAAS

Nanjing University of Information Science and Technology "Face to Face with NUIST Presidents" Frontier Forum

Time: May 12-14, 2019
Place: Nanjing, Jiangsu

I. Forum Introduction

The "Face to Face with NUIST Presidents" Frontier Forum aims to build a platform of exchanges and cooperation for young talents of different academic backgrounds from home and abroad. we encourage outstanding young scholars to come back to China with your innovation and entrepreneurship. Let's make NUIST a first-class high-level university with distinct characteristics. We warmly welcome young talents in the fields of atmospheric science, environmental ecology, remote sensing, electronic information, mathematical physics, chemical materials, humanities and business management, etc. to the forum!

II. Requirements for Participation

Well-known experts, scholars, leading talents and young talents with great academic potential, who have doctoral degrees from famous overseas universities or have domestic doctorates and work full-timely overseas for no less than one year are invited to apply for participation.

III. Schedule

May 12, 2019: Check-in
May 13, 2019: Opening Ceremony, President's Report; Policy Introduction, Communication with schools
May 14, 2019: Visit the city of Nanjing and Jiangbei New District

IV. Participation Treatment

Free local accommodation; participants can book their own air tickets and have the tickets reimbursed by the organizer. (economy class by plane or second-class seat by high-speed train, round-trip taxi fare between the airport/train station and NUIST; outstanding participants can apply for business class by plane or first-class seat by high-speed train).

V. Notice

1. Application deadline: April 30, 2019;
2. Application materials: Application Form and relevant personal information to email address forum@nuist.edu.cn, and name the subject of the email as "Frontier Forum + Name + applying XX School".

VI. Contact Information

DING Ni (+86-25-58731027)
CHEN Chen (+86-25-58731143)
SHI Wei (13805185107)
Email: forum@nuist.edu.cn

Please visit https://rsc.nuist.edu.cnto to have more details and download the Application Form, and scan the code for more information

High-End Global Talents Recruitment

Welcome back to hometown.
Thousands of academic job vacancies are in fast-developing China.

On-the-spot Recruitment in Russia
May 25, 2019 Lomonosov Moscow State University
May 26, 2019 Bauman Moscow State Technical University
May 27, 2019 Gubkin Russian State University of Oil and Gas

On-the-spot Recruitment in Poland
May 29, 2019 Warsaw University of Technology

Online Job Fair
June 2, 2019(GTM+8) http://www.edu.cn/cv

Qualification for Applicants
Overseas scholars, Doctor and Post-doctor

Participating Approach
Please send your CV to consultant@acabridge.edu.cn for on-the-spot Recruitment in Russia and Poland and Online Job Fair.

Job Vacancies in China's Universities and Institutes
Please visit http://www.acabridge.cn/
Contact consultant@acabridge.edu.cn

湖北大学　南京信息工程大学
江西理工大学　武汉纺织大学
上海外国语大学　中南民族大学

Scan the code for application

WORKING LIFE

By **Artaza Gilani**

The way I am

A year ago, I had one of the most significant interviews of my life. It was for a job I had worked toward for years, as a medical doctor doing research and teaching along with treating patients—a rare and highly competitive type of post in the United Kingdom. Toward the end of the interview, I was asked how I would balance the different parts of the role. I had expected this question and had thought about how I would answer. Still, I hesitated. I could say what I thought the members of the interview panel wanted to hear: I'm good at multitasking, prioritizing, and delegating, and I was confident that I would be able to juggle the various responsibilities. That would have been true—yet it didn't feel authentic. The more honest answer was that I knew it would be difficult, but I wanted to try anyway. I wasn't sure which answer to give.

I faced a similar problem 12 years earlier, when I applied to medical school. I was only 17 years old, and my education had left me believing that there were only right and wrong answers, especially in exams. In my mind, the interview was an exam—it, too, had right and wrong answers. But I didn't know what they were. No one in my family was a doctor. I come from the wrong side of the tracks, as they say. I had worked my way into a decent local school and done well in my classes, but I didn't speak the way my classmates did—or the way I imagined doctors did.

So, I found model answers on the internet, which put my mind at ease. But when I tried to use these answers as templates, it felt fake, as if I was trying to be somebody I wasn't.

This tension led me to stumble during the interviews. My own answers competed in my mind with those I'd found from other sources. The wires crossed on at least one occasion, when an interviewer asked me to give an example of a time when I had been caring. The answer that came to mind was that I volunteered at a nursing home and felt privileged to sit with the residents and listen to their stories. But I didn't think that was dramatic enough to impress the interviewers. So, instead I told them about when one of the residents got sick and I cleaned it up. I immediately felt embarrassed. That wasn't caring; that was basic cleanliness and hygiene, and it suggested that my best quality was skill with a mop. Right then and there, it was clear to me that trying to come across as someone other than myself was not the right approach.

My next interview attempt came a few years later, for a position I would start after medical school—a clinical job with a small academic research component. I wasn't sure what the panel was looking for, but I felt I had little to lose: New doctors in the United Kingdom are almost guaranteed a "normal" clinical job somewhere in the country, and I hadn't expected to be invited to interview for this more specialized position in the first place. So I was satisfied to present myself as I am, not as who I thought the panel members wanted me to be. I didn't second-guess myself. My answers were just that—they were mine. I was at ease and genuinely enjoyed the experience. And I was offered the job.

"Trying to come across as someone other than myself was not the right approach."

Fast-forward to my most recent interview and the question about how I would juggle the multiple responsibilities of the role. I hesitated—but not for long. I had learned the importance of being true to myself. So I answered simply: "With difficulty."

To my surprise and relief, the review panel members nodded knowingly and chuckled. They seemed to relate and to appreciate my candor and willingness to show my human side. I started the job a few months later.

I've come to realize that interviews don't have "right" or "wrong" answers. I still see them as exams, but they're not testing my ability to rehash somebody else's answers. The answers were always easier than I thought, because the exam is about something I am well acquainted with: me. ■

Artaza Gilani is an academic clinical fellow of the National Institute for Health Research School for Primary Care Research at University College London. Send your career story to SciCareerEditor@aaas.org.

ILLUSTRATION: ROBERT NEUBECKER

Science Webinars help you keep pace with emerging scientific fields!

Stay informed about scientific breakthroughs and discoveries.

Gain insights into current research from top scientists.

Take the opportunity to ask questions during live broadcasts.

Get alerts about upcoming free webinars.

Sign up at: webinar.sciencemag.org/stayinformed

PNAS Congratulates
2018 Cozzarelli Prize Recipients

PNAS has selected six outstanding PNAS papers for the 2018 Cozzarelli Prize. The award was established in 2005 as the PNAS Paper of the Year Prize and renamed the Cozzarelli Prize in 2007 to honor the late PNAS Editor-in-Chief Nicholas R. Cozzarelli. Papers receiving the Cozzarelli Prize were chosen from more than 3,200 research articles published by PNAS in 2018 and represent the six broadly defined classes under which the National Academy of Sciences is organized.

CLASS I: PHYSICAL AND MATHEMATICAL SCIENCES

Active learning machine learns to create new quantum experiments

Alexey A. Melnikov, Hendrik Poulsen Nautrup, Mario Krenn, Vedran Dunjko, Markus Tiersch, Anton Zeilinger, and Hans J. Briegel (2018) *Proc Natl Acad Sci USA* 115:1221–1226

CLASS II: BIOLOGICAL SCIENCES

Mechanism of tRNA-mediated +1 ribosomal frameshifting

Samuel Hong, S. Sunita, Tatsuya Maehigashi, Eric D. Hoffer, Jack A. Dunkle, and Christine M. Dunham (2018) *Proc Natl Acad Sci USA* 115:11226–11231

CLASS III: ENGINEERING AND APPLIED SCIENCES

Backbone-free duplex-stacked monomer nucleic acids exhibiting Watson–Crick selectivity

Gregory P. Smith, Tommaso P. Fraccia, Marco Todisco, Giuliano Zanchetta, Chenhui Zhu, Emily Hayden, Tommaso Bellini, and Noel A. Clark (2018) *Proc Natl Acad Sci USA* 115:E7658–E7664

CLASS IV: BIOMEDICAL SCIENCES

Platelets release pathogenic serotonin and return to circulation after immune complex-mediated sequestration

Nathalie Cloutier, Isabelle Allaeys, Genevieve Marcoux, Kellie R. Machlus, Benoit Mailhot, Anne Zufferey, Tania Levesque, Yann Becker, Nicolas Tessandier, Imene Melki, Huiying Zhi, Guy Poirier, Matthew T. Rondina, Joseph E. Italiano, Louis Flamand, Steven E. McKenzie, Francine Cote, Bernhard Nieswandt, Waliul I. Khan, Matthew J. Flick, Peter J. Newman, Steve Lacroix, Paul R. Fortin, and Eric Boilard (2018) *Proc Natl Acad Sci USA* 115:E1550–E1559

CLASS V: BEHAVIORAL AND SOCIAL SCIENCES

Individuals, institutions, and innovation in the debates of the French Revolution

Alexander T. J. Barron, Jenny Huang, Rebecca L. Spang, and Simon DeDeo (2018) *Proc Natl Acad Sci USA* 115:4607–4612

CLASS VI: APPLIED BIOLOGICAL, AGRICULTURAL, AND ENVIRONMENTAL SCIENCES

Long-term nutrient reductions lead to the unprecedented recovery of a temperate coastal region

Jonathan S. Lefcheck, Robert J. Orth, William C. Dennison, David J. Wilcox, Rebecca R. Murphy, Jennifer Keisman, Cassie Gurbisz, Michael Hannam, J. Brooke Landry, Kenneth A. Moore, Christopher J. Patrick, Jeremy Testa, Donald E. Weller, and Richard A. Batiuk (2018) *Proc Natl Acad Sci USA* 115:3658–3662

PNAS
www.pnas.org

Podcast interviews with the authors will be available at https://www.pnas.org/page/about/cozzarelli-prize